November 15, 1991

Analytical CHEMISTRY

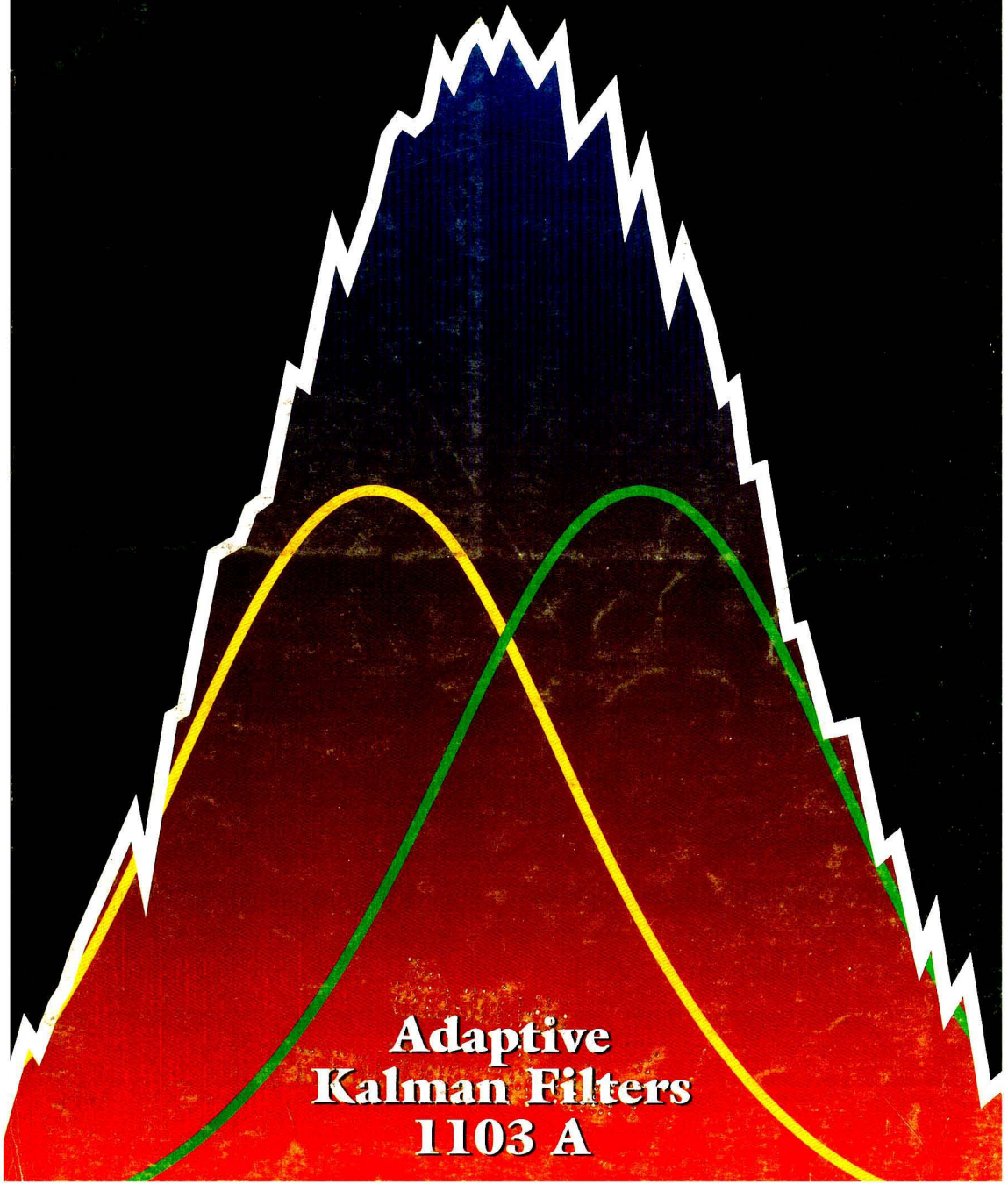

Adaptive Kalman Filters

1103 A

Important News for Chromatographers

Gilson's new software has more of the capabilities you've been asking for

Gilson's new 715 HPLC System Controller Software offers the versatility to meet virtually any gradient system control requirement. The 715 Software controls other Gilson system components – up to four pumps, collects data from up to four detector signals and offers four data analysis methods. But beyond these basic capabilities, 715 has more of the features you've always wanted in HPLC software.

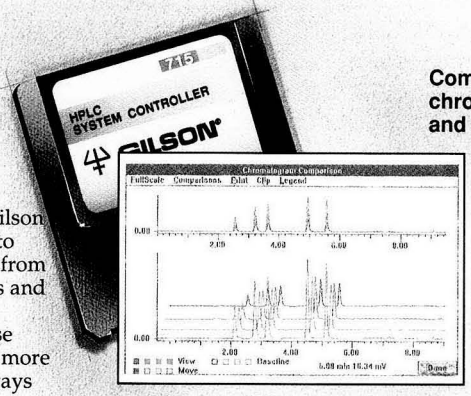

Compare chromatograms from run to run.

Compares up to four chromatograms quickly and easily

If you need to check and compare data files from run to run, 715 Software lets you do it quickly and easily. You simply move and overlay chromatograms to check peak shape, size and retention time. You can also subtract and ratio chromatograms and reduce non-peak heights to zero to simplify comparison of chromatograms with shifting baselines.

Allows manual adjustment of baselines to optimize peak integration

You can remove baselines from unwanted peaks, add baselines to previously non-integrated peaks and move baselines on integrated peaks. With manual baseline adjustment you can use your own method for peak integration and easily analyze abnormalities to optimize integration. All manual changes are automatically tracked according to GLP.

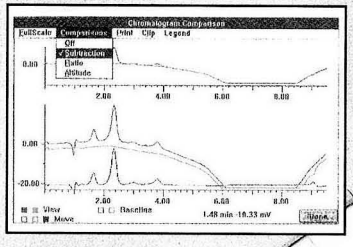

Subtract chromatograms to compensate for shifting baselines.

Plus, HPLC software has never been so easy to use

Communication commands have been simplified. Descriptive names can be entered for all samples. You can copy data files directly to a diskette. Or transfer data to word processing or spreadsheet programs. It all adds up to a versatile, easy-to-use controller for Gilson HPLC systems. Why not find out for yourself if 715 has everything you've always wanted in HPLC software? Mark the numbers below for free literature or a demonstration. Or call us toll-free.

Builds and stores calibration curves; saves hours of time

Creating calibration curves demands a lot of time. In fact, on a simple five-point curve with three repeats per level and each run taking 20 minutes, it could take up to five hours. But with 715 you can build a curve, store it and use it to calibrate unknown sample data at any time. Depending on your application, that could save you hours of tedious work daily.

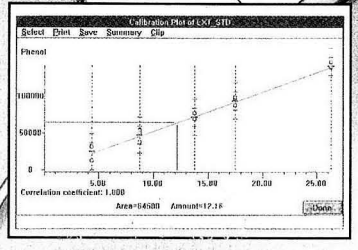

Build, store and recall calibration curves.

Call 800-445-7661

GILSON®

Gilson Medical Electronics, Inc., Box 27, 3000 W. Beltline Hwy., Middleton, WI 53562 USA, Tel: 608-836-1551, TLX: 26-5478, FAX: 608-831-4451
Gilson Medical Electronics (France) S.A., 72 rue Gambetta, B.P. No. 45, 95400 Villiers-le-Bel, France, Tel: (33) 1 34.29.50.00, TLX: 606682, FAX: (33) 1 34.29.50.80

CIRCLE 52 FOR LITERATURE
CIRCLE 53 FOR DEMONSTRATION

WHEN OUR ATOMSCAN 16 TELLS YOU YOUR UNKNOWN SAMPLE CONTAINS COBALT, IT'S NOT JUST HANDING YOU A LINE.

Perform a full qualitative and quantitative screening on an unknown sample using most scanning ICPs, and you'll get results at only one analytical line per element. In order to get interpretable results, you'll have to include standards for every element and wait several days.

In contrast, our new AtomScan 16 Sequential ICP Spectrometer performs the same screening on the same unknown sample using up to 5 lines/element. A single 4 element standard is required, and you'll get a complete list of the elements present, along with their concentrations, at accuracies of ±25%, in about 10 minutes.

The AtomScan 16 is able to perform this rapid screening because it is equipped with the high speed galvanometer grating drive and Multiquant software, a combination which allows the AtomScan 16 to collect more data in a shorter time than any other spectrometer. (Four typical spectra for cobalt and the related concentration data are shown in the photo below.)

High speed screening capability is only one of the many benefits of our new AtomScan 16 Sequential ICP Spectrometer. We'd like to show and tell you about the others. Please call (508) 520-1880 today for literature. Or write Thermo Jarrell Ash, 8E Forge Parkway, Franklin, MA 02038.

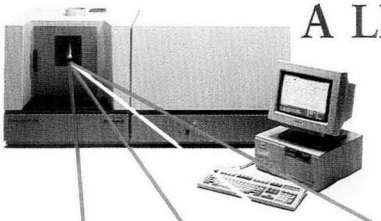

Thermo Jarrell Ash Corporation

A Subsidiary of Thermo Instrument Systems Inc.

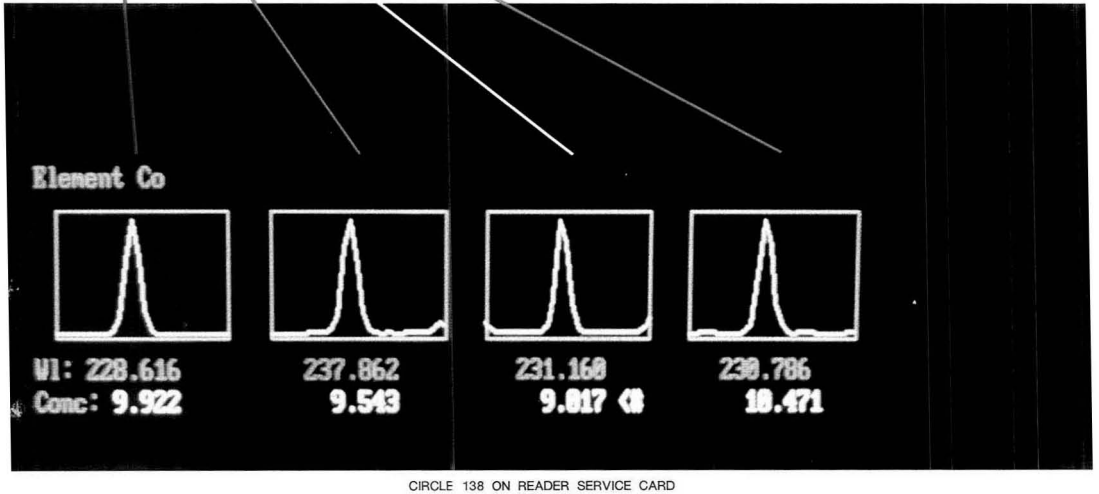

CIRCLE 138 ON READER SERVICE CARD

NOVEMBER 15, 1991
VOLUME 63
NUMBER 22

The Audit Bureau
ANCHAM
63(22) 1061A–1114A/2545–2672 (1991)
ISSN 0003-2700

ANALYTICAL CHEMISTRY (ISSN 0003-2700) is published semimonthly by the American Chemical Society at 1155 16th St., N.W., Washington, DC 20036. Editorial offices are located at the same ACS address (202-872-4570; fax 202-872-4574; Bitnet rmh96@cas; TDD 202-872-8733). Second-class postage paid at Washington, DC, and additional mailing offices. Postmaster: Send address changes to ANALYTICAL CHEMISTRY Member & Subscriber Services, P.O. Box 3337, Columbus, OH 43210.

Canadian GST Reg. No. R127571347

Claims for missing numbers will not be allowed if loss was due to failure of notice of change of address to be received in the time specified; if claim is dated (a) North America: more than 90 days beyond issue date, (b) all other foreign: more than one year beyond issue date, or if the reason given is "missing from files."

1991 subscription rates include air delivery outside the U.S., Canada, and Mexico

	Members	Nonmembers (personal)	Nonmembers (institutional)
U.S.	31	69	289
Canada and Mexico	67	105	325
Europe	112	210	370
Other countries	131	229	389

Nonmembers rates in Japan: Rates above do not apply to nonmember subscribers in Japan, who must enter subscription orders with Maruzen Company Ltd., 3–10. Nihonbashi 2-chrome, Chuo-ku, Tokyo 103, Japan. Tel: (03) 272-7211.

For multi-year and other rates, call toll free 800-227-5558 in the U.S. and Canada; in the Washington, DC, metropolitan area and outside the U.S., call 202-872-4363; fax 202-872-4615.

Subscription orders by phone may be charged to VISA, MasterCard, or American Express. Call toll free 800-333-9511 in the continental U.S.; in the Washington, DC, metropolitan area and outside the continental U.S., call 202-872-8065. Mail orders for new and renewal subscriptions should be sent with payment to American Chemical Society, Department L-0011, Columbus, OH 43268-0011

Subscription service inquiries and changes of address (include both old and new addresses with ZIP code and *recent mailing label*) should be directed to the ACS Columbus address noted above. Please allow six weeks for changes to become effective.

ACS membership information: Lorraine Bowlin (202-872-4567)

Single issues, current year, $13.00 except review issue, $26.00, and LabGuide, $50.00; **back issues and volumes and microform editions** available by single volume or back issue collection. For information or to order, call the number listed for subscription orders by phone; or write the Microform & Back Issues Office at the Washington address.

Analytical CHEMISTRY®

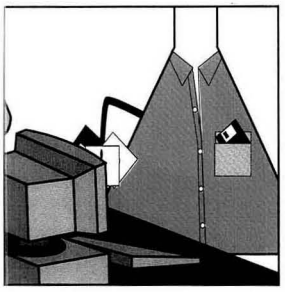

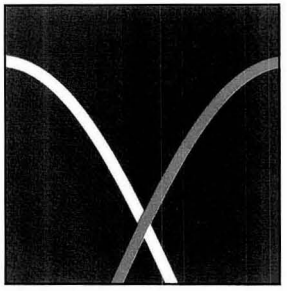

It's pronounced "kī-zen." It stands for "perpetual improvement." Our philosophy has created a new standard in HPLC...

The LC-10A HPLC System. The result of "perpetual improvement."

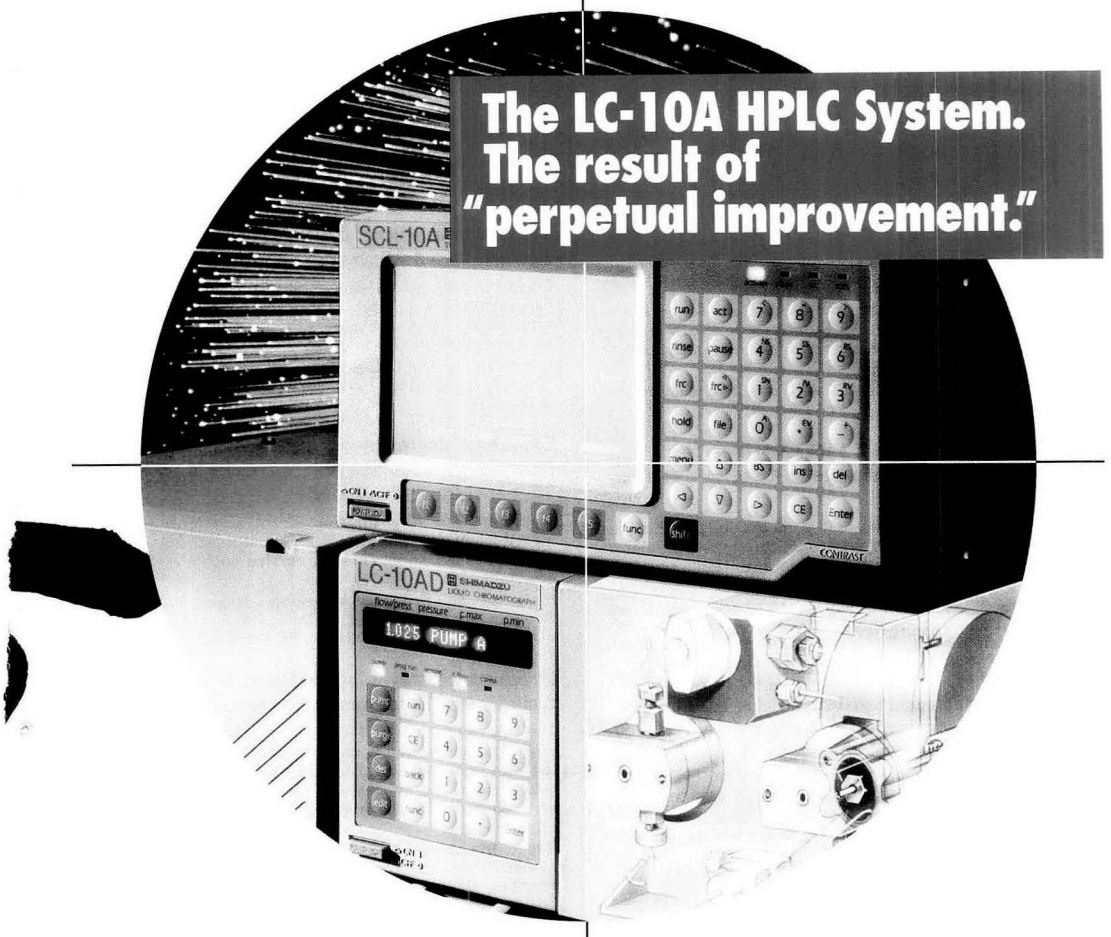

2x the pump life, 3x the UV sensitivity, 5x the reproducibility.

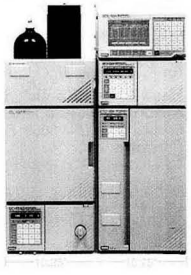

All LC-10A components are modular, stackable and just 10.25" wide. See them at one of the 50 Shimadzu locations in the U.S. and Canada.

Fiber optic communication...backlit LCD...miniaturization... the LC-10A HPLC system is the culmination of the most ambitious engineering project in HPLC history: 22 new integrated modules, simultaneously designed. We have rigorously followed our philosophy of "kaizen": steady, perpetual improvement. The result? Components that will outperform any on the market.

Our attention to detail has solved those little problems that cost you time, money and aggravation: seal replacement, cam lubrication, leak detection and handling, heating/cooling instability...the list goes on.

So, put some "kaizen" in your lab. *Call (800) 477-1227* for the full LC-10A story.

Shimadzu Scientific Instruments, Inc.
7102 Riverwood Drive, Columbia, MD 21046, (301) 381-1227

Proven Precision. Rely on it.

SHIMADZU

CIRCLE 126 ON READER SERVICE CARD

BRIEFS

Articles

*Corresponding author

Shape Discrimination in Liquid Chromatography Using Charge-Transfer Phases 2589

Molecular shape discrimination of polycyclic aromatic hydrocarbon isomers and polychlorinated biphenyl congeners is examined for charge-transfer columns. Dramatic separations of planar and nonplanar compounds are presented.

Lane C. Sander*, Reenie M. Parris, and Stephen A. Wise, National Institute of Standards and Technology, Gaithersburg, MD 20899 and **Philippe Garrigues,** UA 348 CNRS, Université de Bordeaux I, F-33405 Talence Cedex, France

Role of Charge Suppression and Ionic Strength in Free Zone Electrophoresis of Proteins 2597

A general model for calculating free solution electrophoretic mobility of proteins from their amino acid content is extended to encompass charge suppression and to account for other previously proposed empirical models.

Bruce Jon Compton* and Elizabeth A. O'Grady, Bristol-Myers Squibb Company, Industrial Division, P.O. Box 4755, Syracuse, NY 13221-4755

Stable Isotopes for Determining Biokinetic Parameters of Tellurium in Rabbits 2603

Stable tellurium isotopes are shown to be suitable for studies on the metabolism of this element. Results obtained using stable isotopes in combination with GFAAS and SIMS are in accordance with results derived from experiments involving radioactive isotope and gamma ray spectrometry.

Tomas Kron, Universität Frankfurt, Institut für Biophysik, Paul-Ehrlich-Strasse 20, D-6000 Frankfurt/Main 70, Germany, **Klaus Wittmaack*,** GSF, Institut für Strahlenschutz, D-8042 Neuherberg, Germany, and **Christine Hansen and Eckhard Werner,** GSF, Institut für Biophysikalische Strahlenforschung, Paul-Ehrlich-Strasse 20, D-6000 Frankfurt/Main 70, Germany

Adsorption Isotherm and Overloaded Elution Profiles of Phenyldodecane on Porous Carbon in Liquid Chromatography 2608

The adsorption isotherm of phenyldodecane between acetonitrile and graphitized carbon has two inflexion points. It can be accounted for by the sum of a quadratic and a Langmuir term. It permits the calculation of elution profiles for large samples that are in agreement with experimental results.

Moustapha Diack and Georges Guiochon*, Department of Chemistry, University of Tennessee, Knoxville, TN, 37996-1501, and Division of Analytical Chemistry, Oak Ridge National Laboratory, Oak Ridge, TN 37831-6120

Coriolis-Induced Secondary Flow in Sedimentation Field-Flow Fractionation 2614

A study of the effect of secondary flow is reported for sedimentation FFF using digital simulation techniques. Results suggest that the direction of spin relative to flow is critical in maximizing the zone quality.

Mark R. Schure*, Computer Applications Research, Rohm and Haas Company, 727 Norristown Road, Spring House, PA 19477 and **Sisira K. Weeratunga,** Numerical Aerodynamics Simulation Group, NASA/Ames Research Center, T045-1, Moffet Field, CA 94035

Fourier Analysis of Multicomponent Chromatograms. Theory of Nonconstant Peak Width Models 2627

The power spectrum method for determining the single component number is extended to cases of nonconstant peak width multicomponent chromatograms. The method is validated by numerical simulation.

Attila Felinger, Department of Analytical Chemistry, University of Veszprèm, P.O. Box 158, H-8201 Veszprèm, Hungary and **Luisa Pasti and Francesco Dondi*,** Department of Chemistry, University of Ferrara, I-44100 Ferrara, Italy

Hydrolytically Stable Bonded Chromatographic Phases Prepared through Hydrosilation of Olefins on a Hydride-Modified Silica Intermediate 2634

Heterogeneous olefin hydrosilation is used to form direct surface-to-carbon linkages on silica substrates. Spectroscopic and chemical characterization of the products as well as mechanistic interpretation of results are presented.

Junior E. Sandoval* and Joseph J. Pesek, Department of Chemistry, San Jose State University, San Jose, CA 95192

Centrifugal Partition Chromatography of Palladium(II) and the Influence of Chemical Kinetic Factors on Separation Efficiency 2642

Significantly lower centrifugal partition chromatographic efficiencies are encountered for a metal compared with an organic compound. The lower chromatographic efficiency for the metal is related to the kinetics of the metal complex decomposition reaction.

Y. Surakitbanharn, S. Muralidharan*, and H. Freiser, Strategic Metals Recovery Research Facility, Department of Chemistry, University of Arizona, Tucson, AZ 85721

Multivariate Statistics for Large Data Sets: Applications to Individual Aerosol Particles 2646

A generalized scheme is developed for cluster analysis of elemental compositions of aerosol particles. Discriminant, correlation, and principal components analysis are used to study temporal emission patterns for airborne particles.

Thomas W. Shattuck*, Mark S. Germani, and Peter R. Buseck, Chemistry and Geology Departments, Arizona State University, Tempe, AZ 85287

Harness A Workhorse.

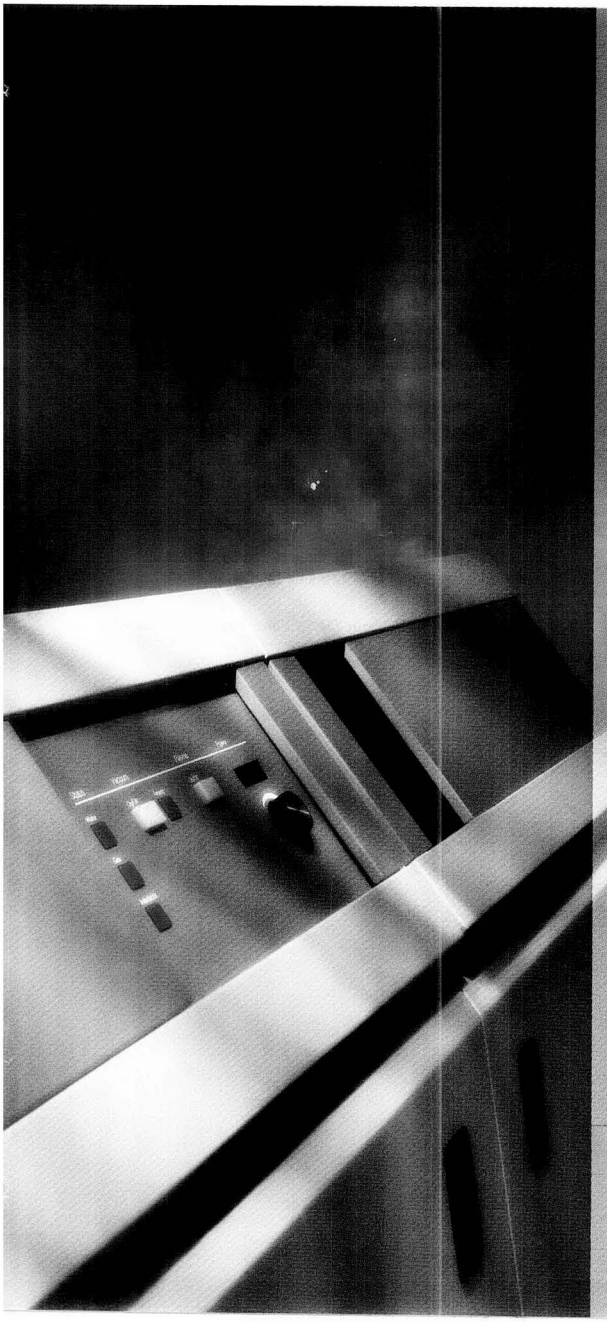

Perkin-Elmer Sciex takes ICP-MS out of the research lab and into the high productivity routine laboratory with the introduction of the ELAN 5000.

Fast and easy to use, the ELAN 5000's robust design will stand up to the rigors of routine high-throughput workloads, such as those found in environmental, semiconductor and clinical applications.

Unlike other ICP-MS systems, the ELAN 5000's new built-in RF generator and turbomolecular pumping system were designed specifically for ICP-MS to ensure maximum reliability.

And with PE XPRESS, all in-stock accessories and supplies are shipped within 24 hours.

For more information, or a demonstration of the ELAN 5000, contact your local Perkin-Elmer office. For product literature call 1-800-762-4000.

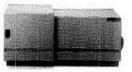

A full complement of accessories for maximum flexibility includes the Model 320 Laser Sampler, FIAS 200, ETV, Ultrasonic Nebulizer and Organics Sampler.

Ease of use and maintenance with PLASMALOK™ interface and QuickChange cones.

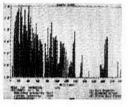

Exclusive software, designed for analysts by analysts. Such as TotalQuant,™ for the rapid semiquantitative analysis of 78 elements.

Perkin-Elmer combines experience, expertise and worldwide resources to provide unmatched products, service and support for analytical laboratories.

PERKIN ELMER SCIEX

The Perkin-Elmer Corporation
Norwalk, CT 06859-0012

110 Information Only

111 Sales Call

ELAN and PLASMALOK are trademarks of SCIEX, a division of MDS Health Group Limited.

TotalQuant is a trademark of The Perkin-Elmer Corporation.

BRIEFS

Technical Notes

All your chromatography lab needs is new Windows.*

Ever have a feeling of "running into walls" in your data handling? Stifled by the limitations of your system? Add Shimadzu EZChrom™: For advanced data handling and easy, single point control of your entire Shimadzu GC or HPLC lab.

Shimadzu EZChrom does it faster, easier, smarter. Imagine: No more menus to scroll, no more codes to remember, no more tedious editing, no more time-consuming manipulations. Just point and click—it's that intuitive and simple.

Shimadzu EZChrom gives you a broader view and a fresh outlook. Our new Windows™ 3.0 based software gives you enhanced customized reporting, colorful real-time display, permanent archiving, dynamic links to popular software, and provides a window to the whole world of IBM PC compatible computing: Shared peripherals, networks, LIMS connections, etc.

Shimadzu EZChrom opens a window of productivity. Cast new light on data previously acquired from your reliable Shimadzu GC, HPLC and Chromatopac™ data processors (C-R3A, C-R4A, C-R5A, CR 501 or CR 601): Just link up with a Shimadzu EZChrom PC system.

So, before you go "Windows-Shopping" let us show you ours! Better yet, ask for a demo disk and see for yourself. ***Call 800-477-1227*** or write:

Shimadzu Scientific Instruments,
7102 Riverwood Drive
Columbia, MD 21046, (301) 381-1227

Proven Precision. Rely on it.

SHIMADZU

*Trademark of Microsoft Corp.

Circle 127 for Demo. Circle 128 for Info.

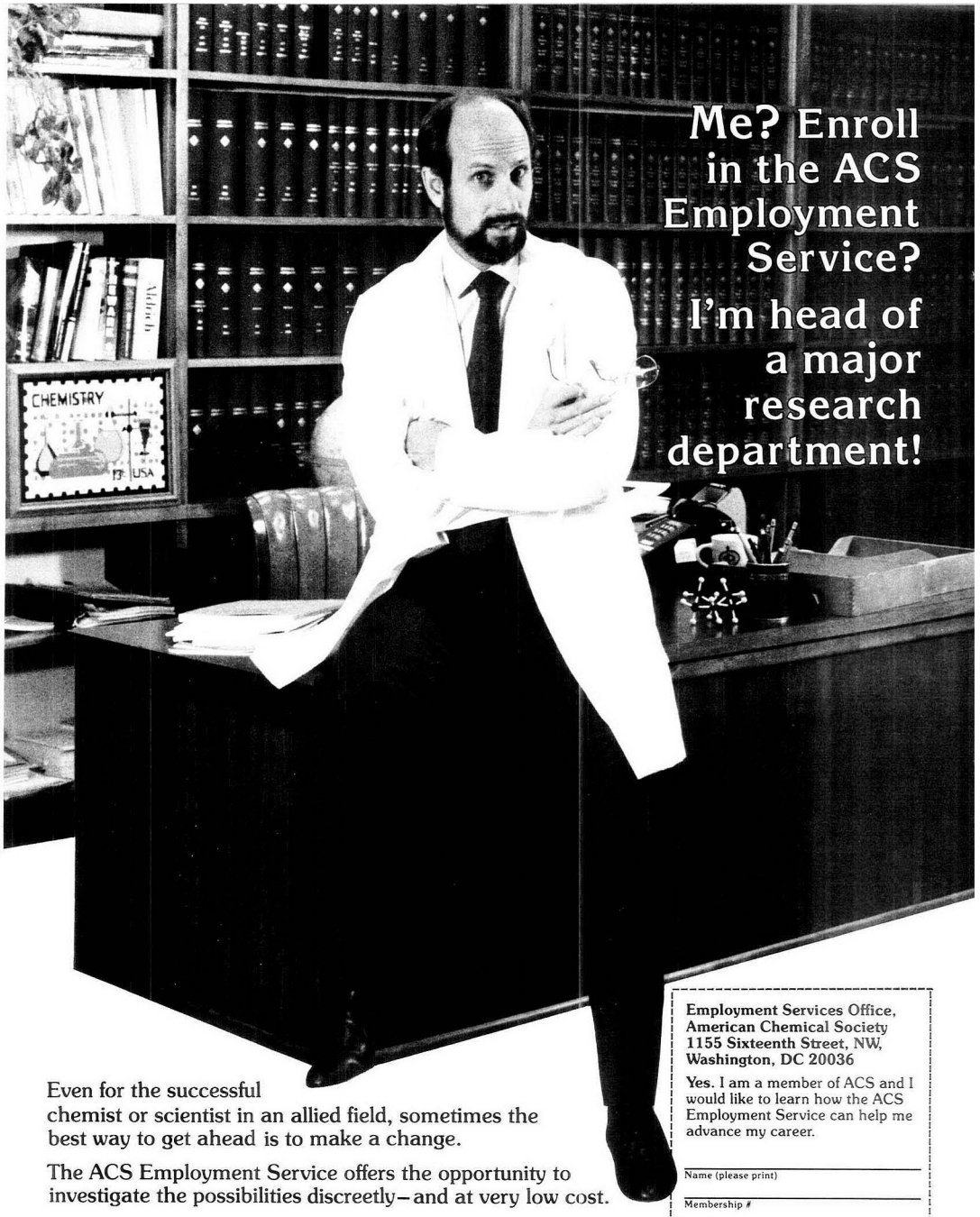

Me? Enroll in the ACS Employment Service? I'm head of a major research department!

Even for the successful chemist or scientist in an allied field, sometimes the best way to get ahead is to make a change.

The ACS Employment Service offers the opportunity to investigate the possibilities discreetly–and at very low cost.

Our Employment Service is free to all ACS members. If you request confidentiality from current employers or other designated organizations there is a nominal charge.

For more information write, use coupon, or CALL TOLL FREE 800-227-5558

Employment Services Office,
American Chemical Society
1155 Sixteenth Street, NW,
Washington, DC 20036

Yes. I am a member of ACS and I would like to learn how the ACS Employment Service can help me advance my career.

Name (please print) _____

Membership # _____

Address _____

_____

City _____

State _____ ZIP _____

NEWS

Division Seeks Opinions on Programming

The Division of Analytical Chemistry is evaluating its programming practices at both the ACS spring and fall national meetings and solicits opinions on this issue. Considerations for the evaluation of programming, the Division's major objective, include scientific needs, financial feasibility, and logistical details.

Scientific needs: Divisional award symposia at the fall meeting are normally well attended, but regular sessions are irregularly attended. The ACS spring meeting is always held shortly after the Pittsburgh Conference whereas the fall meeting is scheduled before the smaller FACSS meeting, making overlap in programming and speakers difficult to avoid. The Summer Symposium of the Division is a smaller and more intense meeting that has traditionally been well attended and well received.

Financial feasibility: Both programming and attendance costs for national meetings are very high. Programming one national meeting costs the Division approximately $18,000 for direct support of speakers, $9000 for printing and mailing the separate newsletter, and $2000 for miscellaneous expenses. Direct programming costs now account for about 40% of the Divisional funds in contrast to a traditional level of 30%.

Logistical details: Many chemists attend only a limited number of meetings per year. Personal expenses are increasing while travel budgets in both academe and industry are decreasing. In addition, ACS is constrained by the need to restrict national meeting sites to large cities with sufficient space.

You are invited to express your opinions concerning Divisional programming by writing to either Charles L. Wilkins, Department of Chemistry, University of California–Riverside, Riverside, CA 92521-0403 (714-787-3540) or Kenneth Busch, School of Chemistry and Biochemistry, Georgia Institute of Technology, Atlanta, GA 30332-0400 (404-894-4030).

NSF Announces New Programs for Young Science and Engineering Faculty

The National Science Foundation has announced two new award programs to recognize and support the scholarly activities of some of the nation's most promising young scientists and engineers. The Presidential Faculty Fellows (PFF) program will provide up to 30 awardees with $100,000 annually for five years. The president of any U.S. college or university offering baccalaureate or graduate degrees in science or engineering may nominate up to two young faculty members who were appointed to their first faculty positions within the last four years. NSF will manage the program, administer the evaluation process, and fund the awards, with final judgment from the White House.

The new NSF Young Investigator Awards (NYI) program replaces the Presidential Young Investigator Awards (PYI) program, first funded in 1984. Up to 150 NYI awardees each may receive a total of $100,000 per year for five years, provided they raise $37,500 in matching funds or equipment from industry and other eligible sources. Like the PYI program, NYI awardees are guaranteed a minimum of $25,000 a year for five years. Department chairpersons may nominate faculty members who began teaching after Jan. 1, 1988.

Nominees for the PFF and NYI programs may work in any discipline of science or engineering normally supported by NSF, and recipients may use their awards for both research and teaching purposes. The first awards in both programs will be made in fiscal year 1992. Further information can be obtained by contacting the appropriate program office at the National Science Foundation, 1800 G Street, N.W., Washington, DC 20550.

Test Kit Verification Program

AOAC International (formerly the Association of Official Analytical Chemists) has begun a new test kit verification program to examine the reliability of performance claims made by manufacturers. Test kit developers will submit an application to AOAC International, providing test kit performance specifications, information on intended uses and users, and other supporting data. AOAC International will then send the kit to an independently selected laboratory to assess its performance. The results will go to a team of technical experts who will evaluate the data from both the test kit applicant and the independent laboratory, using AOAC International-approved procedures and criteria. The team will make recommendations to a test kit review board, which will either grant or deny verification of the kit method. AOAC International hopes to be able to complete the review process within 90 days of accepting an application. For more details, contact George Heavner, AOAC International, 2200 Wilson Blvd., Suite 400, Arlington, VA 22201-3301 (703-522-3032; fax 703-522-5468).

For Your Information

The National Committee for Clinical Laboratory Standards (NCCLS) document C3-A2, "Preparation and Testing of Reagent Water in the Clinical Laboratory, 2nd Edition," is available. The updated guideline provides information on various **water purification and testing methods** as well as suggested applications for different types of water. Single copies of the guideline are $20 for member organizations and $30 for nonmembers. For overseas orders, add $5 for each copy. Discounts are available for multiple copy orders. For more information, contact NCCLS, 771 E. Lancaster Ave., Villanova, PA 19085 (215-525-2435; fax 215-527-8399).

Smaller, yet greater.

702 SET/MET Titrino from Metrohm

Benchspace is becoming more and more scarce
The 702 SET/MET Titrino is packed with outstanding features, yet is small and compact. This makes it unique among titrators.

Four modes for routine operation
Monotonic Endpoint-seeking Titration MET; Set Endpoint Titration SET; measuring mode MEAS for pH, voltage, temperature, I_{pol} or U_{pol} and pH calibration function CAL.

Simple operation
The separate keypad gives access to all the functions. Once programmed, the instrument can be operated for routine applications via the front panel keys. The result calculation can be formulated without restrictions.

Extensive communications
The two-line LCD display allows you to communicate with the instrument in English, Spanish, French or German. The built-in bi-directional RS 232C interface allows connection of a balance, printer and/or PC. Print results and titration curve ... download methods from PC to titrator or titrator to PC ... interface to sample changer or robotics.

Titration - quite simply with Metrohm.

Metrohm
Measurement in Chemistry
Worldwide with Metrohm

METROHM Ltd.
CH-9101 Herisau/Switzerland
Phone 071 53 11 33
Telefax 071 52 11 14
Telex 88 27 12 metr ch

BRINKMANN

Quality products for research and control.

One Cantiague Road
Westbury, NY 11590-9974
800-645-3050
(In New York **516-334-7500**)

In Canada:
416-675-7911
50 Galaxy Blvd.
Rexdale, Ont. M9W 4Y5

Role-Playing Analytical Chemistry Laboratories

Part 2: Physical Resources

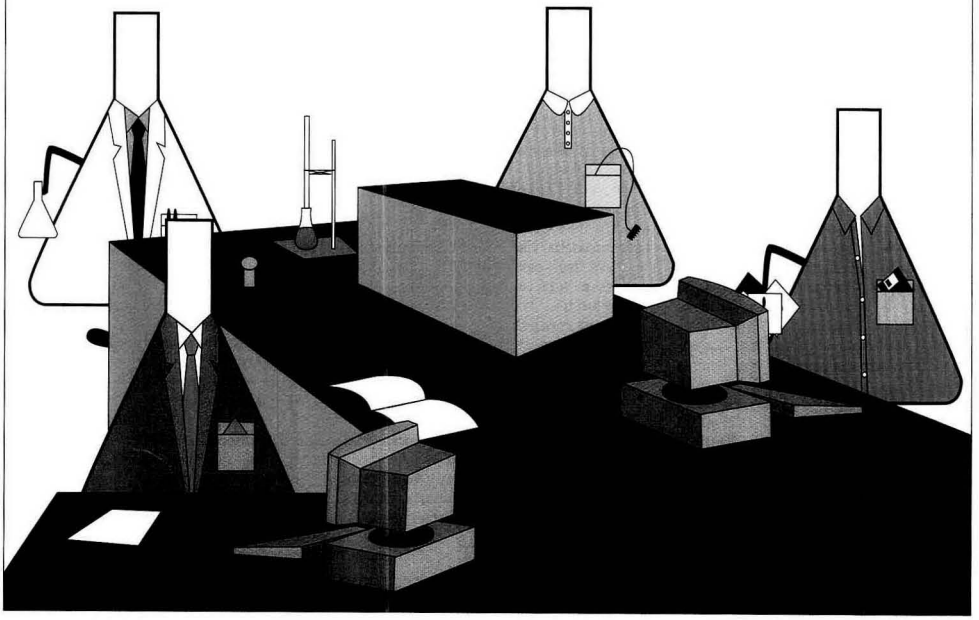

The structural ideas presented in Part I of this series (*Anal. Chem.* **1991,** *63,* 977 A) have been implemented through the use of physical resources (lab space and equipment), written lab experiments, and faculty time. Of these three, the most critical are the physical resources, especially for small colleges. For this reason, many innovations have been made in space management and equipment organization. A description of these innovations and the equipment used in the 1991 spring and fall course offerings will constitute the bulk of Part II. A discussion of the actual written lab experiments and a short evaluative summary will be presented in Part III, which will appear in the December 15 issue.

John P. Walters
Department of Chemistry
St. Olaf College
1520 St. Olaf Avenue
Northfield, MN
55057-1098

The entire role-playing approach is more readily understood when the physical layouts of the laboratories in the junior-level Analytical Chemistry and senior-level Instrumental Analysis courses are pictured (Figures 1 and 2). The junior course lab has four traditional benches in the center of the room, two end benches, and three large hoods. Each large center bench is designated as a company and given a name (Wendy, Laura, Bruce, and Deano). Each company actually is more than a lab bench. It is also a small, named, physical community that is set up, organized, identified, and equipped for problem solving.

Each bench has a wet end and a dry end and is connected by at least two 19,200-baud lines to the central Hewlett-Packard Xenix-based microcomputer. Each company is set up with its own equipment at both ends of the bench (see Figure 3). In the junior course, each company's instrumentation consists of digital analytical and top-loading balances, a Perkin Elmer Lambda-3B double-beam

REPORT

spectrophotometer and companion digital strip-chart recorder, a Perkin Elmer Tri-Det liquid chromatograph, a Corning Model 150 digital pH meter, a Sequoia-Turner digital readout colorimeter, and a magnetic stirrer. (See p. 1087 A for equipment sources.) An electrochemical analyzer will be added to each company's hard instrumental ensemble.

0003-2700/91/0363-1077A/$02.50/0

In small colleges, large lab rooms with fixed lab benches such as those in Figure 1 usually must be shared by students from multiple courses. The equipment infrastructure for role-playing is different from that used in most courses, especially those that equip students with their own individual drawers in a semi-isolated manner. Most role-playing equipment is mobile to allow other course participants access to the space. All computers are on carts, and other instruments (e.g., liquid chromatographs, pH meters, and balances) are on carts, cafeteria trays, or similar carrying devices. Only the large, heavy spectrophotometers are left on each bench.

At the start of each semester, the role-playing equipment is moved from hallway storage cabinets into the large lab room. Equipment is arranged and rearranged during the semester as required for individual experiments. Part of the work Hardware does in setting up an experiment is to add cables and small parts and arrange the apparatus. Although this degree of equipment portability was bothersome when the role-playing labs first started, the advent of smooth rolling carts and large locking hallway storage cabinets made it a preferred method of laboratory space management.

The natural extension to the portable equipment mode of shared space management is to avoid all capital purchases and use "just-in-time" lend-leasing procedures to set up each semester's experiments. This approach, although as yet untried, would handily avoid the need for permanent technical staff to maintain equipment that often is captured and customized by other individuals when not in use for an actual role-playing experiment.

An alternative method of space management, based on the availability of diverse instruments and locations in the building during the semester, was briefly tried and then rejected. The presence of four small groups working concurrently on the same tasks in a common room strengthens the sense of community within each company and gives Managers a way to caucus and compare approaches without copying each other or competing.

In the senior Instrumental Analysis course, two laboratory rooms are used: the large lab room in Figure 1 and the small room in Figure 2. The small room is set up anew biweekly to serve four students at a time. The maximum lab enrollment for this course is 16, and a typical class would have 12–16 students in the lab each week, four per afternoon. In Figure 2 the small room is set up for the third experiment in serial data acquisition. (Part III will include a discussion of this experiment.)

Some of the larger instruments from which data are acquired and sent to computers in the small laboratory room are located in the large laboratory room. Usually all of the robotic, electronic, and computer aspects of the work in the senior course occur in the small lab room; wet and large instrument work occur across the hall in the large room. Emphasis is placed on remote control and data acquisition to mimic the process control situations one encounters in industry.

An example of a remote data acquisition and control setup used in the senior course is shown in Figure 4. The Macintosh computer that acquires data, along with its Software role-player, is located in the small lab room. The HPLC instrument being run remotely, along with its Hardware role-player, is located in the large lab room, or occasionally on a hallway cart when space is tight because of conflicting class schedules. Visual and verbal command communication occurs between the two sites via closed-circuit television and voice intercom while the RS-232 serial line collects data from the instrument via an Omega type WB-31 smart serial A/D converter. Links such as these enhance the role-playing interaction, help diminish conflicts resulting from shared space, and add a pleasant sense of adventure to the methods development work.

Another example of this kind of spatial arrangement is shown in Figure 5. Here, the same closed-circuit TV and intercom approach is used to link a controlling Heath H-100 computer to the smart serial port on the spectrophotometer. The two parts of the experiment may be split over the length of a lab bench in the junior course, between the small and large lab rooms in the senior course, and between two large lab rooms in another experiment done in the first-year course.

In both the senior and junior courses one can make use of larger "departmental" instruments (atomic absorption spectrophotometer, gas chromatograph/mass spectrometer, FT-IR spectrometer, NMR spectrometer, and spectrofluorometer) when appropriate. These instruments are housed in other lab rooms. Whenever sensible, the control and data links to these instruments occur remotely, from the small lab room to the other

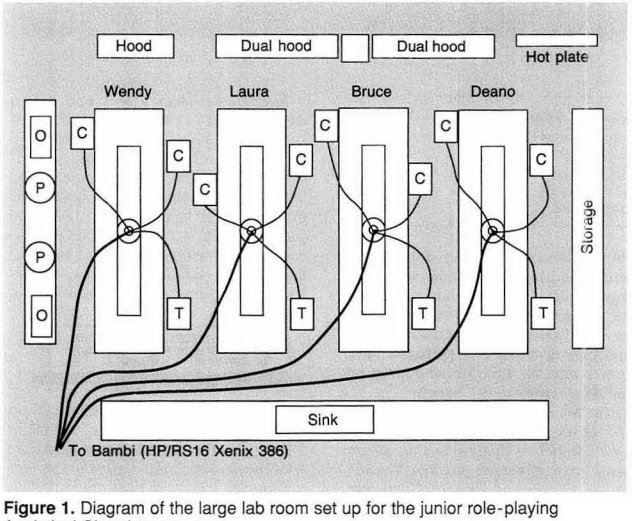

Figure 1. Diagram of the large lab room set up for the junior role-playing Analytical Chemistry course.

The four named companies (benches), company computers (C), company executive terminals (T), polarographs (P), drying ovens (O), and computer lines to the central Hewlett-Packard Xenix-based microcomputer (Bambi) are shown.

lab rooms. This is facilitated by using the smart serial ports in the course Xenix microcomputer.

An example of remote software switching between lab rooms, shown in Figure 6, involves connecting the individual desks set up in the small lab room with the fixed spectrophotometers in the large lab room. Permanent RJ-11 wiring is run between the two lab rooms to serial ports on the Xenix microcomputer. The terminal program, Kermit or TERM, cross-links these lines by choosing the proper "tty" port assignments and then makes a connection between students and instruments in the two rooms. The rooms do not have to be rewired between semesters or experiments. Instead, software selection of Xenix port cross-links accomplishes the setups.

In Figure 6, for example, the serial link is between ports of different baud and parity. These protocol differences are sorted out by the Kermit (or TERM) program. This type of remote instrument use can occur while other departmental courses are being conducted in the large lab room, even to the point of hour-by-hour sharing of the spectrophotometers. Visual contact with the instrument is made possible by closed-circuit television.

The small room thus becomes a larger example of the problem-solving community that is the company in the junior course, but one that is more tightly focused on methods development.

Mobile microcomputers

Communication between role-players and instruments in the senior course and between companies in the junior course is made possible by the use of many serially linked company computers and executive terminals. This equipment is present in each company in the junior course (see Figures 1 and 3) and is placed throughout the small room on an as-needed basis for the senior course (see Figure 2).

The function of these local, mobile microcomputers is to prepare reports (Manager), control instruments and acquire data from them (Software and Hardware), and store and exchange chemical material safety data sheet (MSDS) data and recipes (Chemist). They are true communication centers that provide a straightforward way to bond the role-players.

In both role-playing courses, it is expected that Hardware will be responsible for connecting the serial computer links on the computers and

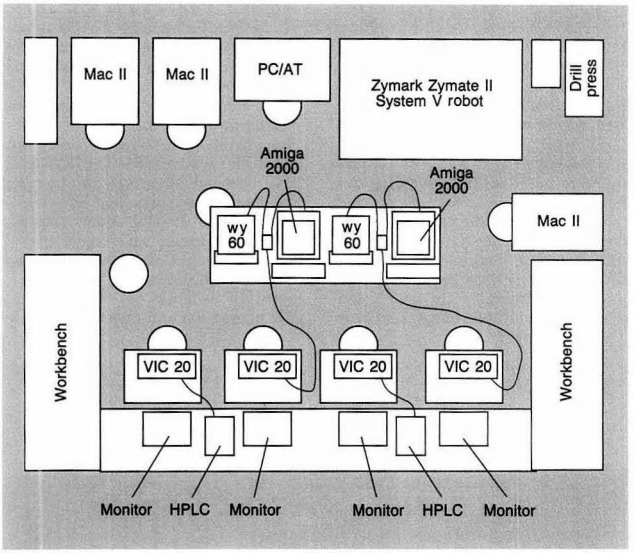

Figure 2. Diagram of the small lab room set up for one experiment on serial data acquisition and telemetry in the senior Instrumental Analysis course.

Individual desk and work spaces are shown for four students at six computers and terminals, together with other mobile Macintosh II computers and a semimobile Zymark Zymate II System V lab robot.

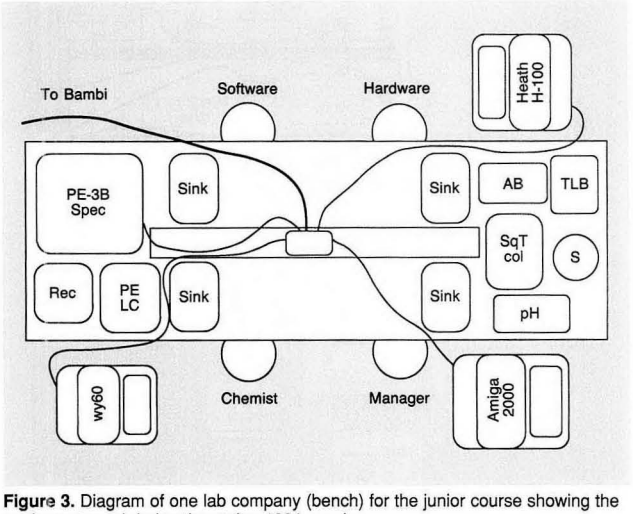

Figure 3. Diagram of one lab company (bench) for the junior course showing the equipment used during the spring 1991 session.

Key: PE-3B Spec: Perkin Elmer Lambda-3B double-beam recording spectrophotometer; Rec: Perkin Elmer R100A digital drive analog chart recorder (10 mV); PE LC: Perkin Elmer Tri-Det isocratic liquid chromatograph; AB: Ohaus Galaxy 200 electronic analytical balance with serial RS-232C interface; TLB: Mettler PM electronic top-loading balance with serial RS-232C interface; SqT col: Sequoia-Turner Model 390 digital readout single-beam colorimeter; pH: Corning Model 150 digital pH and specific ion meter with RS-232C printer output; S: magnetic stirrer; Heath H-100: Heath H-100 computer; Amiga 2000: Amiga 2000 computer with 2286 internal PC/AT DOS bridgeboard; and wy60: Wyse wy60 terminal (19,200 baud).

will handle interfacing and small circuit construction. Accomplishing these tasks in an afternoon's session, without rehearsal and especially with electronic novices, is difficult. Prefabricated junction boxes have been developed so that insulation displacement techniques can be used for making cables and connectors wherever possible, thus avoiding detailed soldering.

Figure 7 shows the types of input/output connections that facilitate interfacing with insulation displacement cabling for data acquisition and serial communication for one of the junior course H-100 computers. This computer is a stock Heath H-100 to which I/O Technology S-100 interface boards have been added. All of the board connections, whether parallel or serial, are brought out to DB25 connectors on the back of the computer, as shown.

In the H-100 machines, an A/D/A board and a parallel/serial I/O board have been added to the one parallel and two serial ports that are available on the H-100 motherboard. These computers, which are located on carts so that they can be moved from one end of the bench to another, have 768 K RAM (allowing RAM-disk operation) and eight-color 640 × 225 pixel graphics. Each is equipped with two floppy disk drives, an Epson LX-86 dot matrix printer, and a Zenith 1339 CGA color graphics monitor. All external hardware connections are made to the back of the H-100 using DB25 connectors, and these are easily assembled and attached to cables using insulation displacement techniques.

Often, Hardware must connect the H-100 I/O ports, or those of one of the other DOS or Macintosh lab microcomputers, to external instruments with an intermediate amplifier between the computer's A/D board and the instrument output. Such amplifiers are designed in the senior course and typically are wired by Hardware in the junior course on the day of the experiment in which they are needed. Special "plasticware" junction boxes, made from plastic food storage containers such as the examples shown in Figure 8, have been developed with this Hardware role in mind. (Any brand of plastic food storage container is satisfactory for this purpose.)

For example, in the weak acid titration experiment done in the junior course, Manager and Hardware must decide whether to build or buy the pH meter that they will use to conduct the titration. If Manager builds it, he or she will do so using the operational amplifier circuit shown in Figure 9 as the active device connecting the pH electrode to the serial A/D converter feeding one of the COM ports on one or another of the lab microcomputers. Hardware then will assemble this circuit into the plasticware box, and Chemist will prepare the buffers that will allow Software to calibrate the whole system.

When the Amiga 2000 DOS or Macintosh Mac II machines are used, serial port custom links are made externally to the computer, also using small plasticware junction boxes (Figure 8) to allow Hardware to make the connections. When high-speed A/D conversion is needed, the Macintosh machines carry a National Instruments NB-MIO-16L multifunction board that allows LabView2 or QuickBASIC drivers to carry out the task. In such cases, Software operates the programs and Hardware sets up coaxial, twisted pair, or differential connections to the instrumentation through these or equivalent plasticware junction boxes.

Multiples of plasticware boxes are available. Most are internally wire-wrapped between the insulation displacement experimenter's sockets

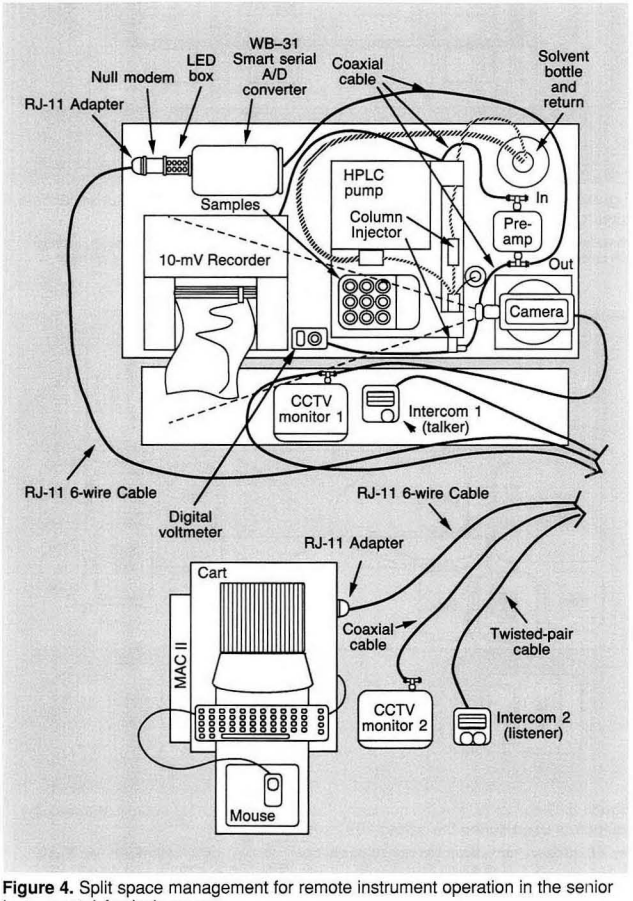

Figure 4. Split space management for remote instrument operation in the senior Instrumental Analysis course.

Software and Manager remotely operate the HPLC instrument from the small lab room (Figure 2) via Chemist and Hardware, who are located at the instrument in the large lab room (Figure 1) or another remote site.

and the DB25 connectors. The person playing Hardware in the senior course can develop the layouts for the person in the same role in the junior course, based on quick cabling needs that he or she has already experienced, and do so, without soldering, within a single lab period. Hardware in the junior course then concentrates more on cabling and connecting than on actual interfacing and linking, in keeping with the different natures of the two courses.

All of this interconnection structure has evolved over time and has proven effective; it has encouraged active participation by Hardware and good interdependent interaction with the other role-players.

In addition to the local lab microcomputers, each company has a Manager's executive terminal. Currently, wy60 terminals are used on small carts. These terminals link at 19,200 baud to each other and to the lab microcomputers via the serial ports on the course Xenix computer. Managers can use the terminals to prepare lab reports while the lab is in session and to communicate with each other using Xenix mail and Chat and Talk programs. Manager and Software also use this terminal for forecasting, predicting, analyzing, and reporting when the other lab microcomputers are tied up with data collection or analysis.

The laboratory robot

By far, the one device that has been most beneficial in catalyzing good small group dynamics is the Zymark Zymate II laboratory robot used in the senior Instrumental Analysis course. It may appear that a robot, as an automation device, is useful primarily for routine, programmed tasks that are too dangerous or mind-numbing to be done by a creative individual. However, another, more subtle side to the issue concerns the process of programming, or setting up, the robot in a role-playing lab.

Upon reflection, it is clear that the process of automating a chemical task, as opposed to simply observing an automation routine perform a preprogrammed task, requires more knowledge of the whole linked system of chemical steps than that needed to execute the method intuitively. Thus, if one sought a tool that would encourage a small group of students to look at all the linkages between steps before beginning a lab experiment, a device like a robot would be a natural choice. The key then would be to make automation a

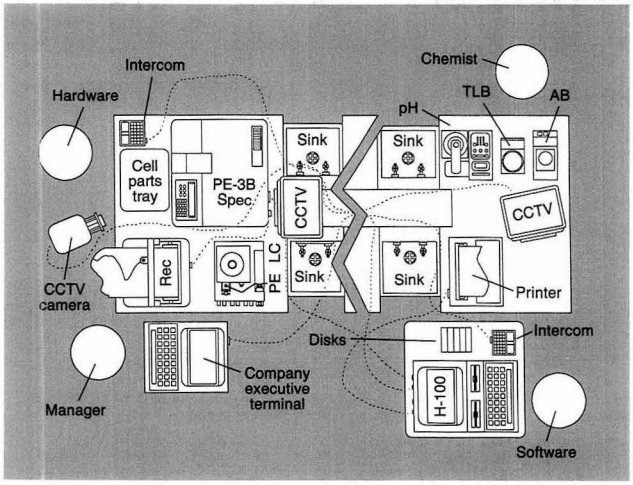

Figure 5. Split space management for remote instrument operation in the junior Quantitative Analysis course.

The roles indicated split physical locations between the controlling computer and the controlled spectrophotometer. Manager is free to move anywhere around the bench, Hardware and Chemist are free to move along the side of the bench where they are located, and Software cannot move from his or her location.

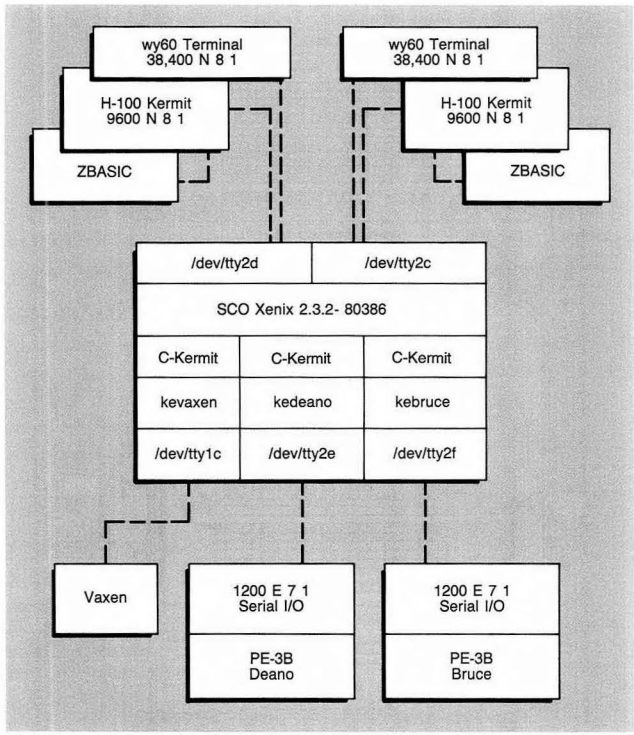

Figure 6. Serial line (RS-232) linkages between small and large lab rooms via the smart serial ports through the course Xenix microcomputer for implementing a remote spectrophotometer experiment in the senior Instrumental Analysis course.

A wy60 terminal or Heath H-100 computer driven by a ZBASIC program connects to port tty2d under one serial protocol. The Xenix program C-Kermit cross-connects port tty2e to tty2d, concurrently adjusting the protocol to that of the PE-3B spectrophotometer on the Deano lab bench.

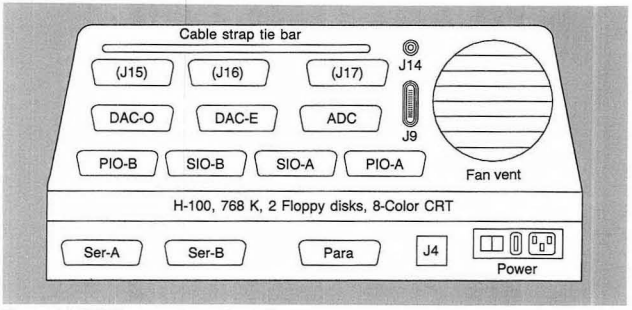

Figure 7. DB25 connector outputs for connecting serial ports and A/D/A devices between an H-100 microcomputer and laboratory instruments.

Key: (J15), (J16), and (J17): unused output sockets; J14 and J9: video port outlets; DAC-O: I/O Technology A/D/A board (8-channel, 12-bit DAC; pinouts for odd channels); DAC-E: I/O Technology A/D/A board (8-channel, 12-bit DAC; pinouts for even channels); ADC: I/O Technology A/D/A board (8-channel, 12-bit ADC); PIO-A and PIO-B: I/O Technology peripheral support boards with parallel I/O ports (16 bits); SIO-A and SIO-B: I/O Technology peripheral support boards with RS-232C serial I/O ports (DTE); Ser-A: H-100 motherboard with RS-232C serial I/O port (DCE); Ser-B: H-100 motherboard with RS-232C serial I/O port (DTE); Para: H-100 motherboard with parallel printer port (Centronics); and J4: RJ11 phone jack (unused).

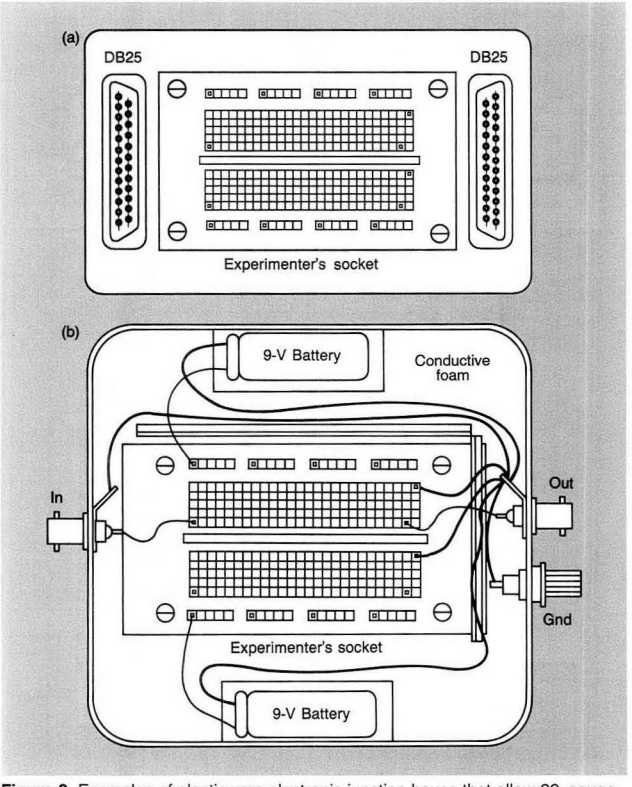

Figure 8. Examples of plasticware electronic junction boxes that allow 22-gauge wire patching between 24 pins of the plug and socket DB25 connectors via the two sides of the Radio Shack 276-175 experimenter's socket.

(a) Junction box that bridges all 25 pins between two DB25 connectors. (b) Junction box that allows insertion of battery-powered operational amplifiers between two bayonet coaxial connectors.

part of the experiment—for example, by filling in major parts of a skeletal program or creating an entire procedure.

In role-playing labs the Zymark robot is a marvelous physical representation of the roles of Chemist, Software, and Hardware while it is being set up to do a procedure. This one device embodies all of the functions that the entire company of role-players acts out. For example, when a robot is programmed by the four role-players, it is Manager who must perceive the entire linked system of chemical events needed to make the robot do the assigned task and communicate it to others in the group. It is Chemist who prepares the reagents. The group interaction is completed with Hardware, who actually tunes the robot sectors and installs the solutions, and Software, who executes the robot steps at the computer console. The robot programming activity thus exemplifies the interdependence on which the role-playing educational model is based.

The robot also adds new dimensions to some roles. For example, when the robot is running an experiment, Hardware is responsible for videotaping the automated process as it evolves under the direction of Manager and through the implementation of Chemist and Software. For Manager, the videotape adds new interest to the often onerous job of writing a technically accurate laboratory report about a methods development project. When it comes to reporting what actually happened in the methods development lab session, it is hard to argue with a videotape!

The robot configuration that will be used this fall in an experiment to determine the pseudo-first-order rate constant of the hydrolysis of aspirin is shown in Figure 10 together with the parts that make up the individual sectors. The colorimeter is not on a sector; it has been externally programmed into the system in the EasyLab language. Future plans call for limited-size versions of the Zymark robot in each junior course company.

The HP/RS16 Xenix-based central course microcomputer

The HP/RS16 Xenix machine, which is the hub of all communications for both junior and senior courses, is diagrammed by function in Figure 11. It services a total of 16 serial ports and one parallel I/O port. Eight serial ports typically connect with the

TASK MASTER.

The Rheodyne 7125 LC sample injector is equipped with two operating modes to master every injection task.

In the "partial-fill" mode, the sample from a syringe fills a sample loop only partially. No sample is lost. The amount injected is the exact volume dispensed from the syringe.

You use this mode when you need to conserve sample or change sample volume frequently. You can inject from 1 μL to 2.5 mL with a precision of 1%.

In the "complete-fill" mode, sample from a syringe fills the loop completely–using excess sample. The amount injected is the exact volume of the loop.

You use this mode when you need the maximum volumetric precision of 0.1%, or you wish to load sample without having to read syringe calibrations carefully. You can inject from 5 μL to 5 mL using one of ten interchangeable sample loops.

Variations of the Model 7125 perform yet other tasks. Model 8125 minimizes sample dispersion with micro columns. And Model 9125 uses inert plastic flow passages to prevent the mobile phase from contacting metal.

For more information about these versatile injectors, phone your Rheodyne dealer. Or contact Rheodyne, Inc., P.O. Box 996, Cotati, California, 94931, U.S.A. Phone (707) 664-9050.

RHEODYNE
THE LC CONNECTION COMPANY

CIRCLE 122 ON READER SERVICE CARD

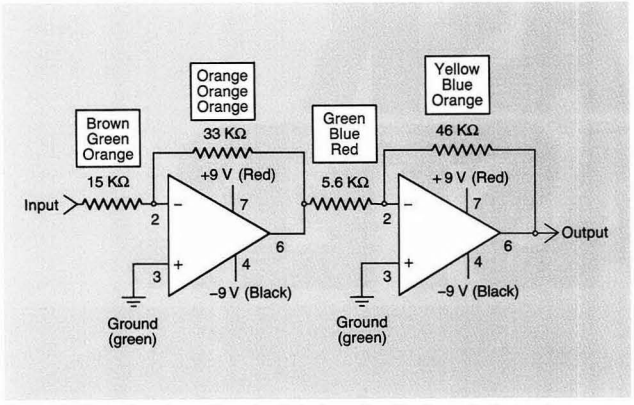

Figure 9. Operational amplifier circuit designed by Hardware in the senior Instrumental Analysis course.

In the junior course, Hardware assembles the circuit in the plasticware box shown in Figure 8b. The circuit, designed to connect an AmpHel amplifier pH electrode to an Omega D1131 smart serial A/D converter, is used by Software and Chemist in a weak acid–strong base titration.

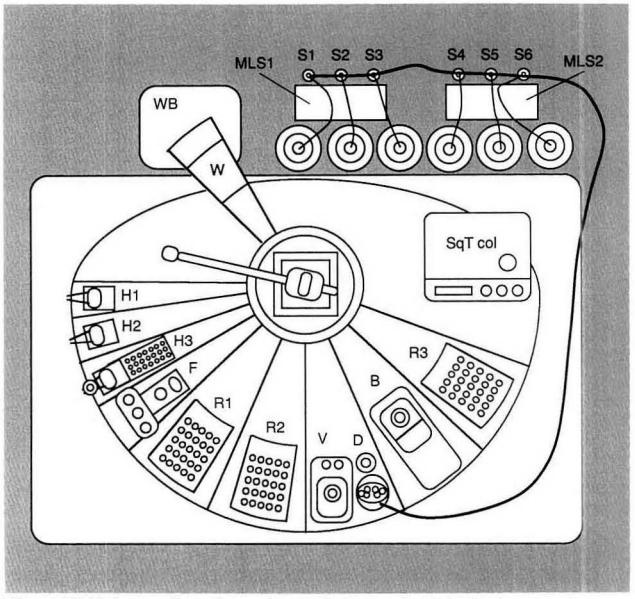

Figure 10. Robot configuration and parts that comprise individual sectors in an experiment to determine the pseudo-first-order rate constant of the hydrolysis of aspirin.

Key: WB: wastebasket used to catch used pipet tips and Gelman filter cups; W: waste disposal chute; MLS1 and MLS2: master laboratory station syringe dispensers; S1–S6: variable-volume solvent bottles; SqT col: Sequoia-Turner Model 390 visible colorimeter; R3: general-purpose rack for 25-mm test tubes; B: Mettler AE200 balance, which functions as the solid addition weighing station for the powder-pouring hand and 25 × 150 mm test tubes; D: custom six-reagent dilute and dissolve station for 25 × 150 mm tes: tubes; V: vortex mixer, part of the dilute and dissolve station; R2 and R1: general-purpose racks for 16-mm test tubes; F: membrane filtration station with Gelman filters; H3: 1.0–4.0-mL pipetting hand with tips; H2: general-purpose 25-mm hand; and H1: powder-pouring 16-mm general-purpose hand.

junior course companies in the large lab at 19,200 baud, two to a lab bench. Others connect with a multiplexer that provides 2400-baud time-sharing service between the college's two VAX 11/780 machines, 12 dial-in lines, and a collection of about 150 public microcomputers and terminals.

Additional serial ports service Upper Management's office and the consulting station in the large lab room; another is tied to a 2400-baud modem for communication with outside labs and offices or networks. The parallel port services one set of printers, and another serial port services the line printer used in the junior course large lab room.

The Xenix microcomputer carries professional software programs that Manager uses to do the quality reporting needed and that Software uses to develop spreadsheets. Programs include Microsoft Word 5.0, a full-featured word processor; SCO Professional, a Lotus 1-2-3 workalike; Foxbase+, a dBASEIII+ workalike; and TERM, a full-featured, programmable smart terminal program. All are operated under SCO Xenix 386, System V, version 2.3.2 supervision.

Additional local software includes UNIX Kermit; dejavu, a local file transfer program; and Basmark QuickBASIC, a compiling version of BASIC that is familiar to many students. Also available is the complete Xenix family of text-processing programs (including VI and Nroff).

The major function of the central Xenix microcomputer is to serve as a hub for software and data that Manager and Software use to design and report on experiments. It frees the role-playing labs from dependence on the lower speed college machines and offers a pleasing alternative to the "end of the semester press" that makes central time-sharing only partially effective.

The machine also serves as an electronic mail hub between Upper Management and local Managers, as a "chat" device between companies, and as a link to outside labs. It enhances timely reporting, advance lab preparation, and in-lab communication.

By providing the capability to route lines between labs using software linkups (as mentioned previously with regard to Figure 6), the Xenix computer frees Upper Management from constant electrical reorganization for remote instrument operation and data collection between rooms. Files from previous semesters can be stored and made

0.1 nm resolution.

5.0 absorbance.

Spectrum.

Report.

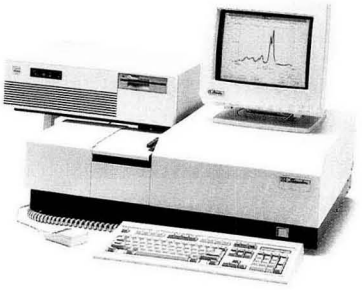

How to improve your productivity in UV-Vis.

Shimadzu gives you a whole new approach to UV-Vis spectroscopy with computer control. Result: Fast, easily produced, colorful, credible and publishable reports. It's the new UV-2101PC—your next powerful, personal spectrophotometer.

Obtaining meaningful data, whether in research or QC, is now as simple as operating a mouse. With a "click" you'll access the world's best single monochromator UV-Vis optics: Double-beam, high resolution, and wide dynamic range. Customized software with unique Microsoft Windows* adds ease of control and compatibility.

Of course, the UV-2101PC is but one of a range of personal UV-Vis and UV-Vis NIR systems designed to improve your productivity. Simply call or write for a demo or more information on how to get—click—UV-Vis productivity.

Shimadzu Scientific Instruments, Inc.
7102 Riverwood Drive
Columbia, MD 21046, (301) 381-1227
(800) 477-1227

* Microsoft Windows is a trademark of Microsoft Corp.

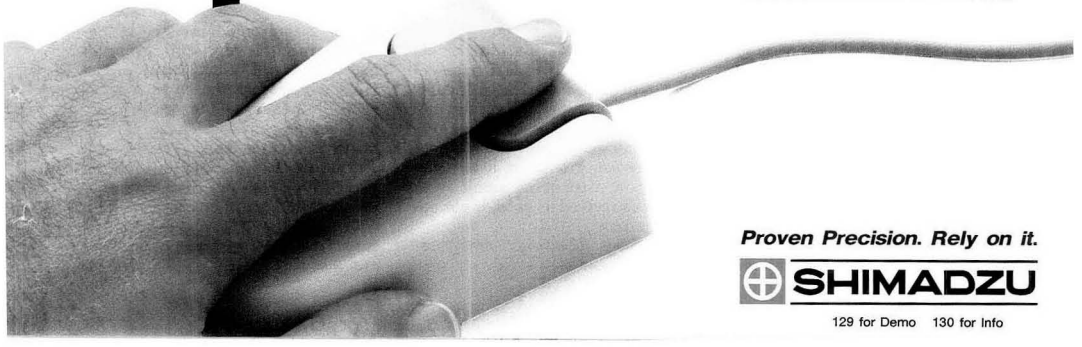

Proven Precision. Rely on it.

SHIMADZU

129 for Demo 130 for Info

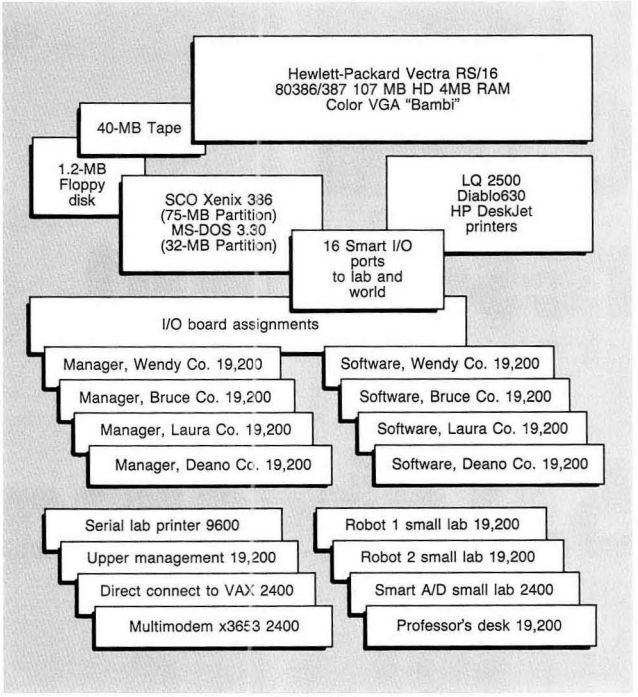

Figure 11. Diagram of the Hewlett-Packard Vectra RS/16 microcomputer.

available for new Managers to use as part of their strategic planning for their own labs. It allows bartering and swapping of spreadsheets, exchange of chemical recipes, and a way to prepare lab reports while the experimental work is being done.

This particular machine has been operational, more or less continuously, for more than three years without a crash or systems failure. The HP hardware and the SCO Xenix software form a robust combination that fits very well into the role-playing scheme.

Conclusion

Clearly, other physical arrangements can support the role-playing model for analytical laboratories. Still, after many iterations, it has been the mobile instruments, the remote linkages between lab rooms, and the presence of four-person groups at a common bench or in a common, small room that have survived as good, if not optimal, choices.

The concept of a semimobile "unit lab bench," complete with its own equipment keyed into these four roles and marketed as such by an analytical instrument company, has been suggested as an even better way to set up a program like this (personal communications with Merle Evenson of the University of Wisconsin–Madison). Whatever the future options, it is unlikely that any institution will face space and equipment restrictions much more severe than those in small colleges. Thus the current model should be equally applicable in large universities and high schools.

The way in which the role-playing construct presented in Part I combines with the physical resources shown here will be developed in Part III; I will discuss the current set of executable experiments for the junior and senior courses. These experiments originated from a core of work started in 1968 at the University of Wisconsin–Madison. They are substantially robust in any implementation and offer role-players significant freedom for decision making and group interaction.

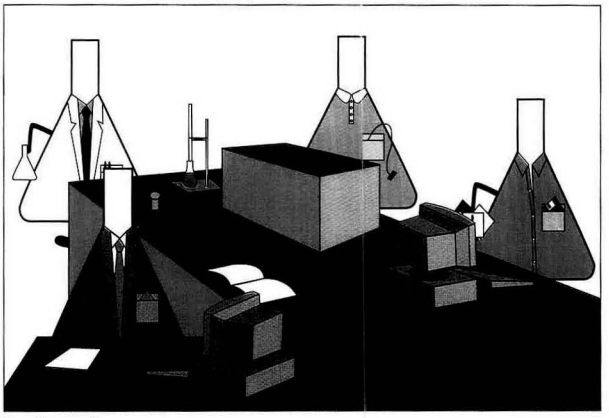

Equipment sources

Product	Vendor
Perkin Elmer Lambda-3B double-beam recording spectrophotometer	Perkin-Elmer Corp., Oak Brook Instrument Dept., 2000 York Rd., Oak Brook, IL 60521
Perkin Elmer R100A digital drive analog chart recorder (10 mV)	
Perkin Elmer Tri-Det isocratic liquid chromatograph	
Ohaus Galaxy 200 electronic analytical balance with serial RS-232C interface	Ohaus Corp., 29 Hanover Rd., P.O. Box 900, Florham Park, NJ 07932
Mettler PM electronic top-loading balance with serial RS-232C interface	Mettler Instrument Corp., Box 72, Hightstown, NJ 08520
Sequoia-Turner Model 390 digital readout single-beam colorimeter	Sequoia-Turner Corp., 850 Maude Ave., Mountain View, CA 94043
Corning Model 150 digital pH and specific ion meter with RS-232C printer output	Corning Scientific Instruments, Corning Glass Works, Medfield, MA 02052
Amiga 2000 computer	Commodore Business Machines, 1200 Wilson Dr., West Chester, PA 19380
Wyse wy60 terminal (19,200 baud)	Wyse Technology, Inc., 3571 N. First St., San Jose, CA 95134
Hewlett-Packard Vectra RS/16 80386 computer	Hewlett-Packard Corp., Personal Computer Group, 974 E. Argus Ave., P.O. Box 486, Sunnyvale, CA 94086
I/O Technology S-100 interface boards	I/O Technology Inc., 25327 Avenue Stanford, Unit 113, Valencia, CA 91355
National Instruments NB-MIO-16L multifunction board	National Instruments Corp., 6504 Bridge Point Parkway, Austin, TX 78730
QuickBASIC for the Mac	Microsoft Corp., 16011 N.E. 36th Way, P.O. Box 97018, Redmond, WA 98073
Experimenter's sockets	Tandy Radio Shack, Ft. Worth, TX, or any local outlet store
AmpHel glass electrodes	Cole-Parmer Instrument Co., 7425 N. Oak Park Ave., Chicago, IL 60648
Zymark Zymate II laboratory robot	Zymark Corp., Zymark Center, Hopkinton, MA 01748
SCO software programs	Santa Cruz Operation, Inc., 400 Encinal St., Santa Cruz, CA 95061
TERM smart terminal program	Century Software, 5284 South 320 West, Suite C-134, Salt Lake City, UT 84107
dejavu	IceTenPlus, The James River Group, 125 N. First St., Minneapolis, MN 55401
Basmark QuickBASIC	Basmark Corp., 1717 E. Ninth St., Cleveland, OH 44114
Omega WB-31 smart serial A/D converter	Omega Engineering Inc., 1 Omega Dr., P.O. Box 4047, Stamford, CT 06907

MEETINGS

43rd Pittsburgh Conference and Exposition

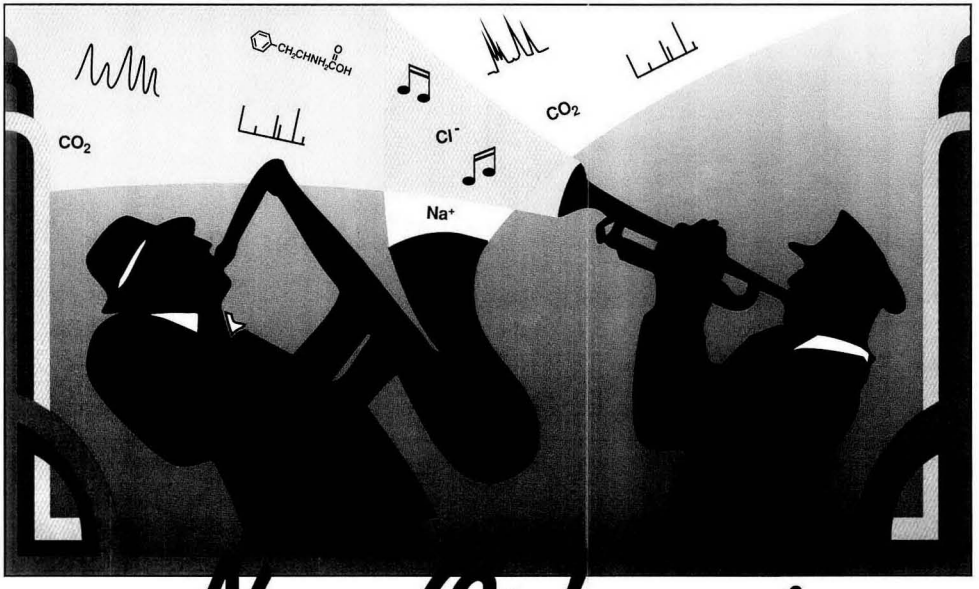

New Orleans

March 9–13, 1992

The 43rd Pittsburgh Conference and Exposition on Analytical Chemistry and Applied Spectroscopy will be held at the New Orleans Convention Center, March 9–13. This year's technical program will feature a plenary lecture presented by Carl Djerassi, professor of chemistry at Stanford University; more than 40 symposia; and a number of poster sessions. The Exposition of Modern Laboratory Equipment, showing the latest instruments and related chemicals, equipment, and publications, will include approximately 800 companies in more than 2500 booths.

The following symposia are scheduled as part of the technical program:

MONDAY MORNING

Advances in Raman Spectroscopy
Arranged by S. A. Asher, University of Pittsburgh

Bomem–Michelson Award Symposium
Arranged by W. G. Fateley, Kansas State University

Capillary Electrophoresis
Arranged by R. N. Zare, Stanford University

Diode Lasers: New/Old Tools for Spectroscopy
Arranged by P. M. Castle, Westinghouse Idaho Nuclear Co. and Lawrence Livermore National Laboratories

Exploration and Preservation of Ancient Art with Chemistry (Archaeometry)
Arranged by G. L. Vassilaros

Frontiers in Analytical and Clinical Toxicology
Arranged by S. H. Wong, Johns Hopkins University

Unique Medical Challenges in Operation Desert Shield/Desert Storm
Arranged by L. D. Mell, Jr., U.S. Navy, Navy Medical Research Institute

MONDAY AFTERNOON

Applied Surface Analysis
Arranged by S. Manocha, PPG Industries, Inc.

Capillary Electrophoresis
Arranged by R. N. Zare, Stanford University

Particle Beam and Electrospray LC/MS: Is Hard or Soft Ionization Better?
Arranged by R. F. Browner, Georgia Institute of Technology

James L. Waters Third Annual Symposium Recognizing Pioneers in the Development of Analytical Instrumentation: IR Spectroscopy
Arranged by R. Obrycki, PPG Industries, Inc.

TUESDAY MORNING

Analytical Chemistry at the Level of a Single Nerve Cell
Arranged by A. G. Ewing, The Pennsylvania State University

Current Analytical Challenges in Pharmaceuticals
Arranged by W. L. Zielinski, Jr., Food and Drug Administration

Dal Nogare Award Symposium
Arranged by M. E. McNally, E. I. du Pont de Nemours & Co., Inc.

Hubble Update
Arranged by J. C. Brandt, University of Colorado

Pittsburgh Spectroscopy Award Symposium
Arranged by B. L. Kirol, PPG Industries, Inc.

How many FT-IR Spectrometers does it take to do GC-IR, TG-IR, and IR Microscopy ....

... and then upgrade to FT-Raman next year

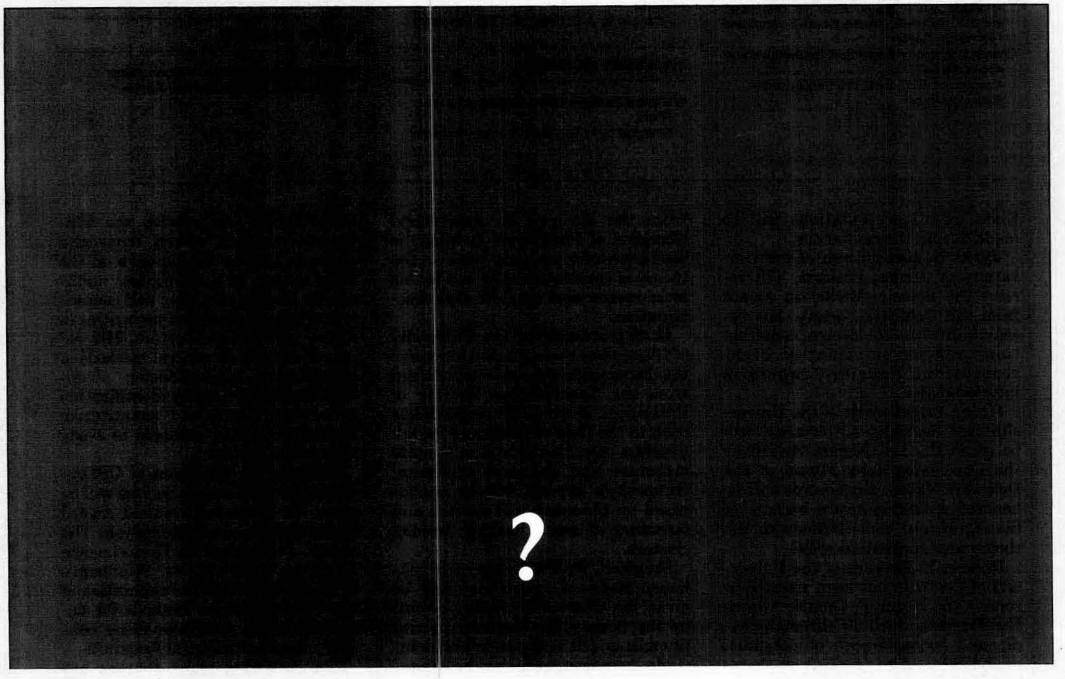

Time-of-Flight MS
Arranged by R. J. Cotter, Johns Hopkins University

TUESDAY AFTERNOON

Carbohydrate Analysis of Glycoprotein Pharmaceuticals
Arranged by D. T. Liu, Food and Drug Administration, and J. A. Feldman, Duquesne University

Pittsburgh Analytical Chemistry Award Symposium
Arranged by G. J. Meisner, University of Pittsburgh

Recent Advances in GC
Arranged by C. A. Cramers, Technical University of Eindhoven, The Netherlands, and H. M. McNair, Virginia Polytechnic Institute and State University

Shootout at the AS Corral
Arranged by G. M. Hieftje, Indiana University

Williams–Wright Award Symposium
Arranged by A. A. Garrison, University of Tennessee

Women and Minorities in the Chemical Sciences: The Untapped Potential
Arranged by R. P. Torrey, Tennessee Technological University

WEDNESDAY MORNING

Back to the Future: New Horizons in Electroanalytical Methods and Materials
Arranged by J. T. Maloy, Seton Hall University, and J. F. Jackovitz, Westinghouse Science and Technology Center

Chemical Property Prediction Techniques and Applications
Arranged by P. C. Jurs, The Pennsylvania State University

EPA Methods for Organics in Water: The Next Generation
Arranged by R. A. Hites, Indiana University

Keene P. Dimick Award Symposium—Chromatography: Broad Multidisciplinary Vistas
Arranged by A. E. Cibulas, Calgon Corp.

Fiber-Optic Sensors
Arranged by T. Vo-Dinh, Oak Ridge National Laboratory

Optimization of Supercritical Fluid Extraction
Arranged by M. E. McNally, E. I. du Pont de Nemours & Co., Inc.

WEDNESDAY AFTERNOON

Environmental Institute—Data Integrity in the Environmental Laboratory Community
Arranged by J. F. Fisk, U.S. Environmental Protection Agency

Frontiers in Chemometrics
Arranged by A. Lorber, Nuclear Research Center—Negev, Israel

Math and Science Education: How to Affect Improvements from a Corporate, Government, and Educator's Perspective
Arranged by D. Lebryk, Kraft General Foods

New Forms of Carbon: Analysis and Application
Arranged by R. L. Garrell, University of California, Los Angeles

Charles N. Reilley Award Symposium
Arranged by C. M. Elliott, Colorado State University

The Status of Analytical Chemistry in the World
Arranged by J. G. Grasselli, Ohio University

THURSDAY MORNING

Chemical Analysis Using Quadrupole Ion Traps
Arranged by R. G. Cooks, Purdue University

Environmental Institute—Risk Communication: Addressing the Public's Right to Know
Arranged by J. Slavick, Chemical Manufacturers Association

Managing the Analytical Laboratory
Arranged by P. D. LaFleur, Eastman Kodak

The Status of Analytical Chemistry in the World
Arranged by J. G. Grasselli, Ohio University

The Status of Analytical Methods for Use in Nutrition Labeling
Arranged by J. T. Tanner, Food and Drug Administration, and W. R. Wolf, U.S. Department of Agriculture

THURSDAY AFTERNOON

Environmental Institute—The Impact of Environmental Regulations on the Analytical Laboratory
Arranged by R. A. Cochran, Halliburton NUS Corp.

Managing Quality in the Analytical Laboratory
Arranged by P. D. LaFleur, Eastman Kodak

Near-IR Spectroscopy—Applications, New Directions
Arranged by B. Sparr and N. Dando, Alcoa Laboratories

Pesticide Residue Methodology in Foods
Arranged by W. G. Fong, Florida Department of Agriculture and Consumer Services

Scanning Tunneling and Atomic Force Microscopy of Biomolecules on Surfaces
Arranged by T. Beebe, University of Utah

FRIDAY MORNING

Environmental Institute—Round Table Discussion: Questions and Answers

Eight award presentations will be made during the conference.

Jyrki K. Kauppinen of the University of Turku, Finland, will receive the Bomem–Michelson Award from the Coblentz Society. His research involves the design, construction, and development of high-resolution, Fourier transform interferometers.

Heinz Engelhardt of the Universität des Saarlandes, Germany, will be given the Dal Nogare Award by the Chromatography Forum of the Delaware Valley. Engelhardt will be honored with this award because of his significant contributions to the theory and application of LC.

Robert E. Sievers of the University of Colorado has been selected to receive the Keene P. Dimick Award. His interests include chromatography and various aspects of inorganic, analytical, and environmental chemistry. He is cofounder of Sievers Instruments, Inc.

J. Calvin Giddings of the University of Utah will receive the Pittsburgh Analytical Chemistry Award from the Society for Analytical Chemists of Pittsburgh. Giddings is well known for his early work on the theory of chromatography and for his more recent work on field-flow fractionation.

H. S. Gutowsky of the University of Illinois has been selected to receive the Pittsburgh Spectroscopy Award from the Spectroscopy Society of Pittsburgh. Much of his research has been in the field of NMR and its application to molecular and solid-state structure and chemical dynamics. Gutowsky's current efforts are focused on the rotational spectra and structure of small, weakly bonded clusters.

Stephen W. Feldberg of Brookhaven National Laboratory will be given the Charles N. Reilley Award by the Society for Electroanalytical Chemistry. His research interests include homogeneous and heterogeneous kinetic phenomena, computer simulation of electrochemical phenomena, and electron transport phenomena in membranes.

Timothy D. Harris of AT&T Bell Laboratories will receive the Williams–Wright Award from the Coblentz Society for his work on the development of spectroscopic methods for the identification and concentration measurement of impurities in direct gap semiconductors. His research focuses on general methods of quantitative semiconductor photoluminescence, impurity identification in ternary alloys, and quantitative Raman scattering methods to study interface structure.

William R. Windham of USDA–Agricultural Research Service will be given the Tomas Hirschfeld Award for his work in near-IR analysis. The award is sponsored by Bran+Luebbe Analyzing Technologies. Windham's research focuses on the calibration of near-IR reflectance methods for determining the nutritive value constituents of agricultural foodstuffs.

The following short courses are tentatively scheduled as part of the continuing education program: Practical MS/MS Analysis, Getting Started with a PC in Your Lab, The Write Way to Success, Basic Statis-

MEETINGS

tics, Understanding Chemical Reactions: The Key for Developing Automated Chemical Methods, Professional Analytical Chemists in Industry, HPLC Method Validation with Computer-Aided Diode Array Detection, A Basic Introduction to Chirality and Its Impact on Industrial Analytical Separations, Public Speaking for Scientists, Near-IR Spectroscopy: An Overview, The Art of Sample Preparation, Effective and Practical Presentation Strategies for Scientists, Interpretation of Dynamic Mechanical Spectra, Laboratory PC Applications: Combining the Power of the Spreadsheet and Data Management Programs, Spreadsheets and Sail Away! A Motto To Teach Analytical Chemistry By, Precontrol as an Effective Method of Process Control, Time-of-Flight MS, Field-Flow Fractionation, Headspace GC, Supercritical Fluid Extraction: Practical Considerations and Applications in Environmental Analysis, LC and GC for Technicians, and Searching and Using Chemical Information. Registration information will be available in the preliminary program.

Advance registration is urged. Fees are $45 for advance and $90 for on-site registration, $10 for advance or on-site student registration, $25 for advance and $50 for on-site spouse registration, and $20 for advance and $40 for on-site exposition only registration. Preregistration forms will be provided in the preliminary program and can also be obtained from John Sember, Pittsburgh Conference, 300 Penn Center Blvd., Suite 332, Pittsburgh, PA 15235-5503 (412-825-3220). The Pittsburgh Conference *Update* will also contain registration forms as well as housing and travel information. All preregistration forms should be postmarked before Feb. 1, 1992.

An employment referral service will be provided during the conference. For more information, contact Dennis Balya at the Pittsburgh Conference address above.

The technical program will appear in the Feb. 1 issue of ANALYTICAL CHEMISTRY, along with additional details about the conference.

Conferences

■ **Sanibel Conference on Lasers in Mass Spectrometry.** Jan. 25–28. Sanibel Island, FL. *Contact: Judith A. Watson, ASMS, P.O. Box 1508, East Lansing, MI 48826 (517-337-2548; fax 517-332-7503)*

■ **Superfund Risk Assessment in Soil Contamination Studies.** Jan. 30–31. New Orleans, LA. *Contact: Keith Hoddinott, U.S. Army Environmental Hygiene Agency, Attn: HSHB-ME-SE, Aberdeen Proving Ground, MD 21010-5422 (301-671-2953)*

■ **Hydrotop '92: International Water Week.** April 7–10. Marseilles, France. *Contact: Association pour la Semaine Internationale de l'Eau à Marseille, 314 Avenue du Prado, 13008 Marseille, France (33-91-22-72-72; fax 33-91-22-71-71)*

■ **Spring Meeting of the Materials Research Society.** April 27–May 1. San Francisco, CA. *Contact: Materials Research Society, Meetings Dept., 9800 McKnight Rd., Pittsburgh, PA 15237 (412-367-3003)*

■ **4th International Symposium on Supercritical Fluid Chromatography and Extraction.** May 20–22. Cincinnati, OH. *Contact: Larry Taylor, Dept. of Chemistry, Virginia Polytechnic Institute and State University, Blacksburg, VA 24061-0212*

■ **14th International Symposium on Capillary Chromatography.** May 25–29. Baltimore, MD. *Contact: Leonard Schronk, Foundation for the ISCC, P.O. Box 663, Kennett Square, PA 19348 (215-692-4320)*

■ **Accuracy in Powder Diffraction II.** May 26–29. Gaithersburg, MD. *Contact: Carol O'Connor, E151 Reactor Bldg., NIST, Gaithersburg, MD 20899*

■ **40th ASMS Conference on Mass Spectrometry and Allied Topics.** May 31–June 5. Washington, DC. *Contact: Judith A. Watson, ASMS, P.O. Box 1508, East Lansing, MI 48826 (517-337-2548; fax 517-332-7503)*

■ **5th International Symposium on Polymer Analysis and Characterization.** June 1–4. Inuyama City, Japan. *Contact: Howard Barth, Du Pont Co., Experimental Station, P.O. Box 80228, Wilmington, DE 19880-0228 (302-695-4354)*

■ **16th Annual Conference of the International Precious Metals Institute.** June 7–11. Scottsdale, AZ. *Contact: IPMI, 4905 Tilghman St., Suite 160, Allentown, PA (215-395-9700; fax 215-395-5855)*

■ **11th Symposium of the Australian and New Zealand Forensic Science Society.** Aug. 17–21. Hobart, Tasmania, Australia. *Con-*

These events are newly listed in the JOURNAL. See back issues for other events of interest.

An Audiocassette Course from the American Chemical Society

INTERPRETATION OF MASS SPECTRA

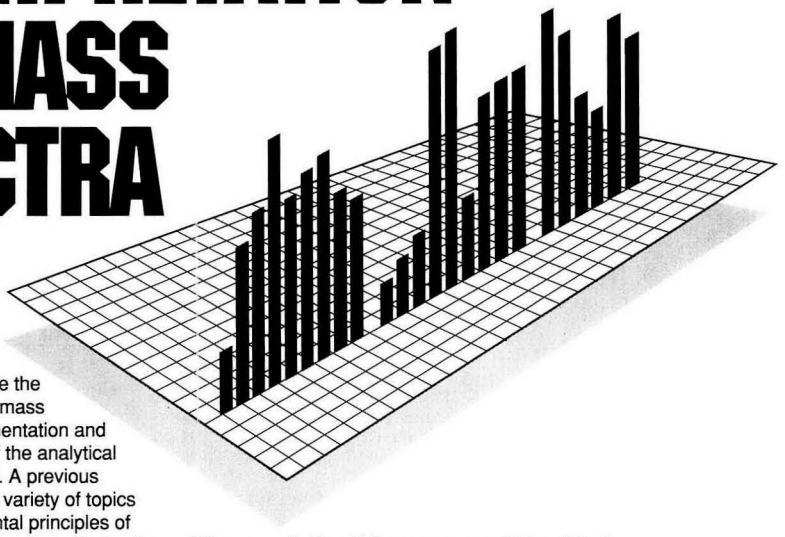

This new audiocassette course teaches you how to make the most effective use of mass spectrometric instrumentation and improve the quality of the analytical information produced. A previous bestseller, it covers a variety of topics — from the fundamental principles of mass spectrometry to newer, electronic forms of ionization and interpretation of the corresponding spectra. It also covers spectra produced by alternative ionization methods as well as additional mass spectrometry techniques that can provide valuable information.

Find out more on MS techniques

With five cassettes and the follow-along workbook, this course reviews the principles of tandem mass spectrometry. It gives you a better understanding of ancillary instrumental techniques — such as library search and accurate mass measurement. Ancillary chemical techniques, including the use of stable isotopes and derivative formation, are also examined.

In addition, this course will give you the know how to interpret spectra derived from alternative ionization techniques and apply mass spectrometry to problems in qualitative or quantitative analysis. You'll become more knowledgeable on how to select the appropriate ionization technique to solve a particular analytical problem.

After completing this course, you'll be able to:

- Use mass spectrometry with other spectroscopic techniques in elucidating chemical structures
- Effectively design experiments to provide a wide range of analytical information
- Improve the quality of analytical information in a wide range of disciplines, e.g., synthesis, structural elucidation, quality control, toxicology, environmental trace analysis
- Provide analytical information for a wide range of compound types
- Give advice on the purchase of mass spectrometric instrumentation

Instructor

John R. Chapman is currently Analytical Systems Manager in the Mass Spectrometry Division of Kratos Analytical. He received his B.S. in chemistry from Imperial College, London, in 1960 and Ph.D. from Oxford University in 1963. After leaving Oxford, he spent three years on the staff of the Medical Research Council. Dr. Chapman is the author of two text books and numerous research publications.

Unit

Five cassettes (5.0 hours playing time) and 200-page manual: $485.00, U.S. & Canada; $582.00, export. Additional manuals: $48.00 each, U.S. & Canada; $58.00, export. (Catalog No. B6)

Order from:

American Chemical Society, Distribution Office, Dept. 23
1155 Sixteenth Street, NW, Washington, DC 20036
or CALL TOLL FREE

1-800-227-5558

(in Washington, DC 872-4363) and use your credit card!
FAX: 202-872-6067

MEETINGS

tact: Conference Manager, Banks Paton Conference Management, GPO Box 558F, Hobart, Tasmania, Australia 7001

■ **International Conference on Solid-State Science and Technology.** Aug. 18–20. Penang, Malaysia. *Contact: K. Ibrahim, School of Physics, University Science Malaysia, 11800 USM, Penang, Malaysia (60-4-877888, ext. 3663 or 3200; fax 60-4-875113)*

■ **EUCMOS XXI: 21st European Congress on Molecular Spectroscopy.** Aug. 23–28. Vienna, Austria. *Contact: E. M. Schaup, Interconvention, Austria Center Vienna, A-1450 Vienna, Austria (43 222 2369 2647; fax 43 222 2369 648)*

■ **106th Annual International Meeting and Exposition of the Association of Official Analytical Chemists (AOAC).** Aug. 31–Sept. 3. Cincinnati, OH. *Contact: Margaret Ridgell, AOAC, 2200 Wilson Blvd., Suite 400, Arlington, VA 22201-3301 (703-522-3032; fax 703-522-5468)*

■ **12th International Symposium on Microchemical Techniques (ISM '92).** Sept. 7–12. Córdoba, Spain. *Contact: M. Valcarcel, Química Analítica, Facultad de Ciencias, 14004 Córdoba, Spain (34-57-234453; fax 43-57-452285)*

■ **SAC 92 and 150th Anniversary of the Laboratory of the Government Chemist.** Sept. 20–26. Reading, U.K. *Contact: P. E. Hutchinson, Analytical Division, The Royal Society of Chemistry, Burlington House, Piccadilly, London W1V 0BN, U.K. (44 71 437 8656; fax 44 71 734 1227)*

■ **9th Asilomar Conference on Mass Spectrometry—Trapped Ions: Principles, Instrumentation, and Applications.** Sept. 27–Oct. 1. Pacific Grove, CA. *Contact: Laszlo Tokes, Syntex Research, 3401 Hillview Ave., P.O. Box 10850, Palo Alto, CA 94303 (415-855-5713; fax 415-354-7363)*

■ **9th Montreux Symposium on Liquid Chromatography/Mass Spectrometry (LC/MS; SFC/MS; CZE/MS; MS/MS).** Nov. 4–6. Montreux, Switzerland. *Contact: M. Frei-Häusler, Postfach 46, CH-4123 Allschwil 2, Switzerland (41 61 63 27 89; fax 41 61 482 08 05)*

Short Courses and Workshops

■ **5th Summer Institute in Environmental Health Studies.** June 1–12. Baltimore, MD. *Contact: Jacqueline Corn or Catherine Walsh, Dept. of Environmental Health Sciences, The Johns Hopkins University, 615 N. Wolfe St., Room 6001, Baltimore, MD 21205 (301-955-2609)*

For information on the following courses, contact Office of Continuing Professional Education, Rutgers University, P.O. Box 231, New Brunswick, NJ 08903-0231 (908-932-9271; fax 908-932-8726)

■ **Monoclonal Antibodies: Principles, Production, and Applications.** Dec. 9–10. New Brunswick, NJ

■ **Protein Purification: A Comprehensive Hands-On Laboratory Course.** Jan. 5–10 and June 7–12

■ **Introduction to Recombinant DNA Techniques: A Hands-On Laboratory Course.** Jan. 14–17 and March 17–20

■ **Protein Electrophoresis and Western Blotting.** Jan. 8–9 and May 28–29

For information on the following courses, contact Joseph I. Goldstein, Dept. of Materials Science and Engineering, Bldg. 5, Lehigh University, Bethlehem, PA 18015 (215-758-5133; fax 215-758-4244)

■ **Scanning Electron Microscopy and X-ray Microanalysis.** June 8–12

■ **Analytical Electron Microscopy.** June 15–18

■ **Microcharacterization of Semiconductor Materials, Devices, and Packaging.** June 15–19

■ **Advanced Imaging in SEM.** June 15–19

■ **X-ray Microanalysis of Bulk Specimens and Particles.** June 15–19

■ **STM, AFM, and Other Scanned Probe Microscopies.** June 15–19

■ **Thin Specimen Preparation.** June 18–19

Call for Papers

■ **Symposium on Industrial Hygiene Chemistry.** San Francisco, CA. April 5–10. This half-day symposium, to be held in conjunction with the 203rd ACS national meeting, is cosponsored by the ACS Division of Chemical Health and Safety and the American Industrial Hygiene Association. The program will include papers on air-sampling techniques, analytical methods, and field sampling of workplace air. Abstracts (150 words) should be prepared on ACS abstract forms and submitted by Dec. 1 to John E. Adkins, E. I. Du Pont de Nemours and Co., Inc., P. O. Box 1089, Orange, TX 77630 (409-886-6402; fax 409-886-6241).

For You, from Cole-Parmer

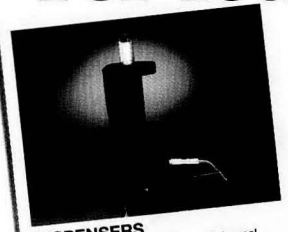

DISPENSERS
Thirty-six pages of standard, multichannel, repetitive, positive displacement, and programmable pipettors and syringe pumps.

FILTRATION
Twenty-one pages of micro, molecular, and macro filtration products including membranes, cartridges, and hardware.

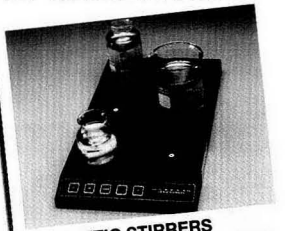

MAGNETIC STIRRERS
Twenty pages of single-position, large-volume, multi-position, hot plate, programmable, modular, and specialty stirrers plus stir bars.

PUMPS
One hundred fifty-five pages of Masterflex® tubing pumps plus centrifugal, metering, gear, vacuum pumps and more.

pH
Fifty-eight pages of pH, mV, ORP, and ion-selective meters and electrodes for pH measurement and control.

MAGNIFIERS/MICROSCOPES
Ten pages of monocular, binocular, trinocular, stereo, wide field, and illuminated microscopes plus camera, slide, and video zoom systems.

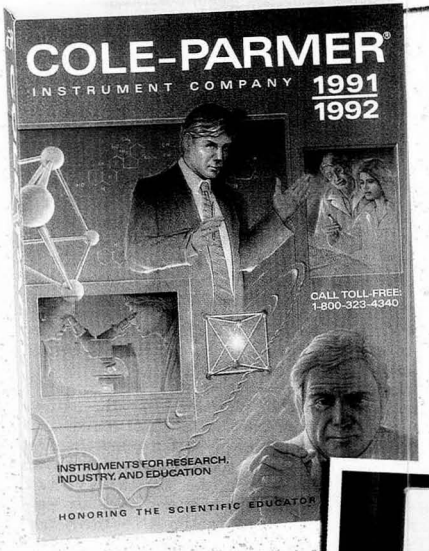

Send in the attached card for your free 1991-1992 Cole-Parmer catalog. Drop it in the mail today!

Our 1248-page catalog is filled with over 21,000 quality products for research, industry, and education.

To place an order, obtain technical support, or learn more about these NEW products, dial 1-800-323-4340.

NEW NEW

CONSTANT TEMPERATURE BATH
PID temperature control with 100 Ω RTD sensor for precise control of bath or external systems.
Circle for more information 27

NEW NEW

ENERGY EFFICIENT OVENS
Fully insulated with airtight interior seams and gas-proof silicone seal to keep your lab cool.
Circle for more information 25

NEW NEW

ANALYTICAL BALANCE
Weighs up to 210 grams of sample with a readability of 0.05 mg; movable display panel.
Circle for more information 26

Cole Parmer

Cole-Parmer® Instrument Company
7425 North Oak Park Avenue
Chicago, Illinois 60648

For your free catalog, circle 24

BOOKS

Chromatography and Biological Magnetic Resonance

Biological Magnetic Resonance. Lawrence J. Berliner and Jacques Reuben, Eds. 251 pp. Plenum Press, 233 Spring St., New York, NY 10013. 1990. $65

Reviewed by Robert London, Laboratory of Molecular Biophysics, NIEHS, P.O. Box 12233, MD17-05, Research Triangle Park, NC 27709

The rapid expansion of the literature on magnetic resonance studies of biological systems increasingly forces researchers to rely on review articles to keep abreast of developments outside their specialties. The series Biological Magnetic Resonance is one of the most useful, sustained sources of information in this rapidly evolving area. The coverage of Volume 9 is typical, ranging from summaries of highly active areas, such as methods for resonance assignment in proteins, to more specialized topics, such as the structure of ribosomal RNA. It is also very well organized; a table of contents is provided for each article, and there are relatively few typographical errors.

Articles by Robertson and Markley ("Methods of Proton Resonance Assignment for Proteins") and by Opella ("Solid-State NMR Spectroscopy of Proteins") are pitched at a fairly introductory level and directed toward an audience with a good NMR background but little specific experience in these areas. For example, the first article is much less detailed than the recent reviews by Bax (*Annual Review of Biochemistry*) and Zuiderweg (*Practical Spectroscopy*), limiting the discussion to "proteins containing natural abundance levels of NMR-sensitive isotopes."

The application of ^{31}P NMR measurements to the study of membrane structure, reviewed in somewhat greater detail by Yeagle, provides a brief theoretical background, outlines the relationship of ^{31}P NMR lineshapes to lipid morphology, and discusses applications in the area of membrane structure and dynamics. I found this to be a very useful review for workers not specializing in spectroscopic studies of membranes, apart from limitations such as inadequate figure captions and inadequate discussion of the need for transient rather than steady-state nuclear Overhauser effect (NOE) studies when dealing with macromolecules for which spin diffusion is significant. In the article on the structure of ribosomal 5S RNA, Marshall and Wu provide a more exhaustive discussion of the investigation of this class of molecules; they point out most of the relevant literature and some information derived from other types of measurement. This more problem-oriented review will probably be useful both to researchers studying RNA structure and to students new to the field. The relatively large size (40 kD) and poor resolution of the most informative imino protons poses major experimental problems; the best solution thus far relies on the characterization of fragments. Their strong conclusion that "^{19}F and ^{13}C labeling were historically important, but no longer justify the major effort and expense required for their bioincorporation" is of particular interest in light of the increased reliance on isotopic labeling strategies in NMR studies of proteins, although they conclude that ^{15}N labeling is worth the effort.

> "... useful source of information in this rapidly evolving area ..."

Two remaining chapters on (experimental) methods for water suppression and (theoretical) methods for the determination of molecular structure using a complete relaxation matrix analysis approach are also included. Meier and Marshall's review on water suppression is particularly timely and provides a more thorough discussion than the briefer treatment by Hore in Volume 176 of *Methods in Enzymology*. A brief experimental comparison of several water suppression methodologies is given for a sample of 0.5 mM tRNA. The review by Borgias and James on relaxation matrix analysis is similar to, although less detailed than, their recent article in *Methods in Enzymolgy*. They present an extremely useful discussion of an approach used increasingly for the evaluation of molecular structure from NOE data. Unfortunately, the early matrix calculations of transient NOE behavior by Gerig and co-workers are not cited.

Chromatography and Modification of Nucleosides, Part B: Biological Roles and Function of Modification. C. W. Gehrke and K. C. Kuo, Eds. xliv + 370 pp. Elsevier Science Publishers, 22 Vanderbilt Ave., New York, NY 10017. 1990. $154

Reviewed by Ram P. Singhal, Department of Chemistry, Wichita State University, Wichita, KS 67208

In this second volume the editors (from the University of Missouri at Columbia) present a comprehensive review of the procedures employed for studying the structure–function relationship of minor, modified components in transfer RNA (tRNA) and DNA structures. Scientists representing a wide spectrum of disciplines discuss biosynthesis, biological functions and regulations, structural conformation, and the occurrence of minor-modified components of tRNAs as well as DNA modification and solid-phase immunoassay for determining the specificity of modification.

Bjork and Kohli (Universities of Umeå and Bern, respectively) pre-

sent the synthesis and function of modified nucleosides in tRNAs. They describe the presence of modified nucleosides in tRNAs from different organisms and address the role of tRNA-modifying enzymes and functions of modified nucleosides next to the 3′ side of the anticodon that is in the wobble position.

H. Kersten and W. Kersten (University of Erlangen–Nurnberg) present an excellent review of the biosynthesis and function of queuine (Q) and Q-containing tRNAs from a variety of sources, explaining the consequences of variations in the Q contents (vs. G34 residue) in the tRNA structure.

In describing Q-base modification, protein synthesis, and development, Kubli (Zoological Institute at the University of Zurich) explains that codon usage is nonrandom, genome specific, and within a species. He discusses codon usage and Q-base modification in highly and weakly expressed genes in *D. melanogaster* and presents a set of codon usage tables for unicellular organisms and vertebrates. According to Kubli, Q appears to have many roles and may integrate a variety of functions within a cell.

Kretz et al. (The Ohio State University) describe solid-phase immunoassay techniques for measuring the inosine content in tRNAs, including site-directed replacement of nucleotides in the loop of tRNA with application to the study of inosine biosynthesis in yeast tRNA.

Joshi and Haenni (Institut Jacques Monod, Paris) describe tRNAs in translation as molecules that fulfill an amino acid donor function in mRNA-dependent ribosomal protein synthesis, molecules that resemble tRNAs but cannot act as tRNAs and therefore exhibit different specialized functions, and structural elements in nucleic acids that are related to tRNAs.

Dirheimer and Martin (Institut de Biologie Moléculaire et Cellulaire, Strasbourg) review the structure and codon recognition patterns of mitochondrial (mt) tRNAs. They describe the present state of mt RNAs and mt DNAs and discuss how to isolate mt tRNAs from diverse sources as well as modify mt tRNAs that exhibit highly unusual chemical structures.

Maden (University of Liverpool) describes the modification of ribosomal RNA (rRNA), especially the methylation, and concludes that perhaps all modifications in this molecule occur in the specific sequences of the precursor molecule.

Yokoyam and Miyazawa (University of Tokyo) present the relationship between modified uridines in the first position of anticodons and mechanisms of codon recognition and discuss the general concept of regulating this residue in post-transcriptional modification of tRNAs.

Ehrlich and Zhang (Tulane University) describe existing information on minor, modified nucleosides in DNA from different sources and discuss the significance of these modifications to biological functions.

References appear through 1989, but for a book of this scope, this does not seem to be a drawback. The type font used for references is hard to read, but each chapter is well written and has been carefully edited. The monograph would be an excellent reference and experimental manual for researchers doing analytical work in the nucleic acid field, and it is a must for every chemistry or biochemistry library.

NEW PRODUCTS

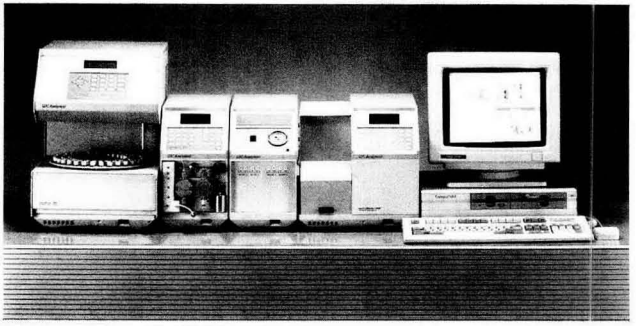

LCtalk, an automated HPLC system, features single keyboard control and multitask Windows 3 based software. The system is available for high- or low-pressure gradient applications. LDC Analytical **401**

Instrumentation

NMR. Four-nucleus probes (200 and 300 Hz) allow users of the UNITY and GEMINI FT-NMR spectrometers to observe four nuclei (^{1}H, ^{19}F, ^{13}C, and ^{31}P) within a sample without retuning. When coupled with an autosampler, the probe can be used to study up to 100 samples. Varian **402**

FT-IR. Model MB-160 FT-IR spectrometer features 0.05-nm wavelength accuracy and 0.01-nm wavelength repeatability. The standard software packages are designed for laboratory and continuous process monitoring applications. Bomem/Hartmann & Braun **403**

Fourier analyzer. Model 2642A Fourier analyzer provides precision time-domain waveform analysis as well as spectral and network analysis and has the capability of an arbitrary waveform generator. The system features a 200-kHz frequency range, two or four input channels, and high computational bandwidth. Tektronix **404**

Titration. DL70 autotitrator can run complex multistage titrations and switch up to four burettes and three electrodes automatically. It has 20 built-in standard methods, and up to 50 additional methods can be stored in memory. Mettler **405**

Near-IR. Quantum 1200 PLUS near-IR rapid scanning analyzer has a monochromator designed for applications in the petrochemical, food, chemical, polymer, and pharmaceutical industries. Measurements can be made in transmittance, reflectance, or transflectance modes. LT Industries **406**

Air analysis. Model PC-2 cascade impactor air particle analyzer determines aerosol particle mass concentration and size distribution. The impactor employs a piezoelectric quartz crystal microbalance mass sensor to weigh particles electronically in each impactor stage. California Measurements **407**

Thermal analysis. D_2-DTA thermal analysis system, designed for freeze-drying applications, measures degree of supercooling, eutectic temperature or freezing point, and collapse temperature. Characterization is achieved in the original process bottle. FTS Systems **408**

Thermal desorption. Model 810TD system automates the thermal desorption of air-sampling tubes or solids. The two-stage gradient trapping system is used to isolate desorbed components, refocus them, and transfer them in a sharp band onto the head of a GC capillary column. Envirochem **409**

Cell disrupter. Virsonic 50 ultrasonic cell disrupter is designed for small samples. The unit provides up to 50 W to disrupt bacterial cells, viruses, spores, and emulsifications; disperse solids in liquid; accelerate enzymatic and chemical reactions; and de-gas liquids. VirTis **410**

Scale. CW250 portable electronic scale is available in 12 different models with capacities ranging from 300 to 2000 lbs. Two weigh platforms of different sizes are available. The scales are battery operated and allow up to 8 h of continuous use between charges. Intercomp **411**

HPLC. Model 760 pump is designed for all facets of HPLC, including analytical, microbore, and preparative applications. Flows from 20 μL/min to 20 mL/min can be achieved using interchangeable pump heads. Alcott **412**

Software

Data acquisition. NOTEBOOK/XE, an extended version of NOTEBOOK, adds new capabilities to DOS, Windows 3.0, and OS/2 versions of the software. The data acquisition, analysis, and control software is expanded to include multiple real-time screen displays, additional windows per screen and display types, and larger setup capabilities. LABTECH **413**

Data retrieval. Easi-Disk Instrumentation Partner can retrieve data from instruments for archival purposes, statistical analysis, and in-

Companies interested in a listing in this department should send their releases directly to ANALYTICAL CHEMISTRY, Attn: New Products, 1155 16th Street, N.W., Washington, DC 20036.

strument data monitoring. The software is designed to link a variety of instruments, including mass spectrometers, chromatographs, digital storage oscilloscopes, logic analyzers, power line monitors, particle counters, and data loggers, to IBM PCs or compatible computers. ADPI **414**

Chromatography. DryLab G/plus software program allows chromatographers to simulate gradient HPLC separations on the computer for method development purposes. The program runs on IBM PCs or compatible computers. LC Resources **415**

ACS Publications and Services

Biotechnology. Information pamphlet defines and describes the growing field of biotechnology, explains its applications, and addresses its present and future benefits and risks. 12 pp. **416**

Chemical Risk Communication: Preparing for Community Interest in Chemical Release Data. Written for public health officials and other community leaders, this handbook presents a basic understanding of risk assessment concepts and risk communication techniques that can be used when a community is affected by chemicals in the environment. A list of resources is included. 28 pp. **418**

RCRA & Laboratories. Developed for generators of laboratory wastes, this handbook describes responsibilities for proper disposal of hazardous wastes under federal Resource Conservation and Recovery Act regulations and suggests general procedures for management and disposal of laboratory chemicals. A list of information sources is included. 24 pp. **419**

Program summaries. Brochure describes educational activities managed by the ACS Education Division that are directed toward high school and college students, chemistry teachers and practitioners, and persons interested in the chemical sciences. 12 pp. **420**

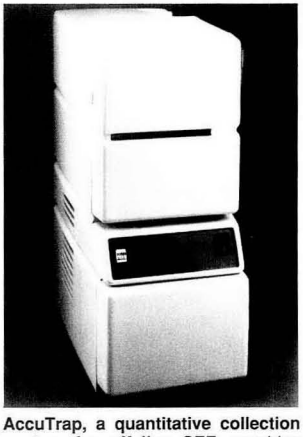

AccuTrap, a quantitative collection system for off-line SFE, provides > 90% collection efficiency. Unlike other solvent-based collection methods, recovery does not depend on the flow of CO_2 extraction solvent. Suprex **417**

Manufacturers' Literature

Columns. *Focused Ion and Electron Beam Columns* discusses capabilities and applications of sources and focusing columns for nanometer-scale technology. Brochure also features supporting electronic components and accessories. 8 pp. FEI **421**

GC. Brochure describes the porous layer open tube (PLOT) GC columns that are designed for extended hydrocarbon analysis and provide resolution of typical mixes in refinery and natural gas from C_1 to C_{10}. 4 pp. J&W Scientific **422**

MS. *BioSpec* issues 1, 2, and 3 are entitled "An Introduction to Protein Electrospray Mass Spectrometry," "Rapid Detection and Identification of Post-Translational Modifications by Electrospray Mass Spectrometry," and "Protein Mixture Profiling: Applications of an Improved Method of Presenting Electrospray Data from Protein Mixtures." Fisons Instruments **423**

HPLC. Application note 505 describes a preparative procedure for purifying porcine adrenocorticotropic hormone (ACTH), a peptide containing 39 amino acid residues, using the Prep 50 HPLC system and SuperPac Pep-S C_2/C_{18} reversed-phase LC columns. Pharmacia **424**

Opiates. Data sheet describes a method for determining opiates in urine using Bond Elut Certify solid-phase extraction columns and GC/MS. The method provides relative recoveries > 90% with concentrations as low as 100 ng/mL using a 2-mL spiked urine sample. Varian **425**

Catalogs

HPLC. Catalog provides information on HPLC columns, methods, and applications, and describes the advantages, limitations, and uses of specific techniques. More than 500 references to published applications are included. 120 pp. Bio-Rad **426**

MS. Catalog features supplies and services for users of mass spectrometers, gas chromatographs, and vacuum systems. Accessories for related instruments are included. 480 pp. Scientific Instrument Services **427**

Chemicals. Catalog includes more than 10,000 organic and inorganic chemicals, including high-purity metals and organometallic compounds. 1000 pp. Crescent Chemical **428**

Organofluorine. Catalog lists 1169 reagents, including more than 900 organofluorine compounds and more than 260 organosilane compounds. Literature references, hazard and handling information, CAS numbers, and physical property data also are presented. 232 pp. PCR **429**

Temperature. Catalog presents information on precision thermometers, temperature probes, indicating decals, calibration instruments, and IR probes and sensors for use in chemical and food processing, plant maintenance, manufacturing, waste management, and research applications. 31 pp. Wahl **430**

GC. Catalog features capillary columns for GC and provides information on stationary phases; column efficiency, resolution, installation, and care; sample capacity; and film thickness. An EPA methods reference chart and applications information for steroids, flavors/fragrances, petrochemicals, and triglycerides also are included. 80 pp. Quadrex **431**

For more information on instrumentation and software products, and/or to obtain the free available information on other listed items, please circle the appropriate numbers on one of our Readers' Service Cards.

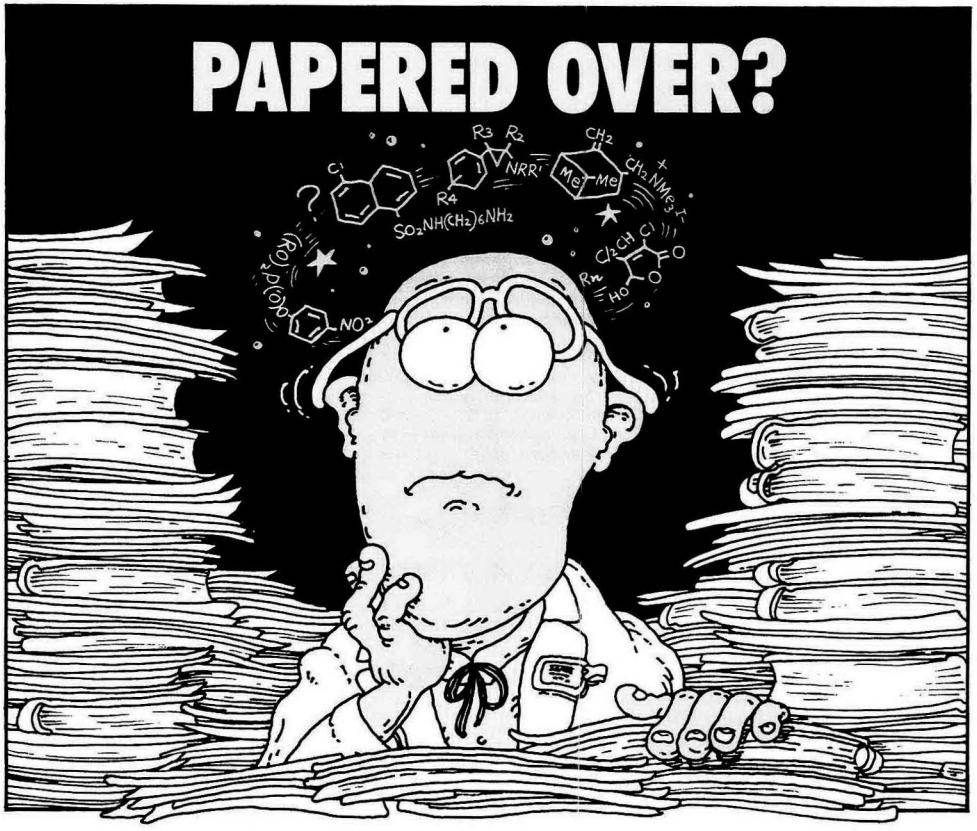

Let CA SELECTS® Uncover You!

Subscribe to CA SELECTS. We will free you from mounds of extraneous papers... and uncover the information you need.

CA SELECTS is a series of 237 different current-awareness bulletins. These printed bulletins give you the same bibliographic information, abstracts, and structure diagrams (when available) that you find in CHEMICAL ABSTRACTS, only focused on specialized topics.

With CA SELECTS, you can relax while a computer profile searches for current literature relevant to your interests. The information you need will flow effortlessly across your doorstep.

All this is yours for just $180.00 a year—$6.92 a biweekly issue—only pennies per abstract! Ask for our FREE catalog.

Let CA SELECTS strip away your mounting mass of papers!

YES! Please send me the descriptions of all 237 topics.

NAME

JOB TITLE

ORGANIZATION

ADDRESS

STATE ZIP

CITY

COUNTRY

PHONE NUMBER

For faster response, complete the coupon, and FAX this ad to 614/447-3713!

CAS

Marketing, Dept. 47991
2540 Olentangy River Road
P.O. Box 3012
Columbus, Ohio 43210-0012, U.S.A.

Adaptive Kalman Filtering

Sarah C. Rutan
Department of Chemistry
Box 2006
Virginia Commonwealth University
Richmond, VA 23284

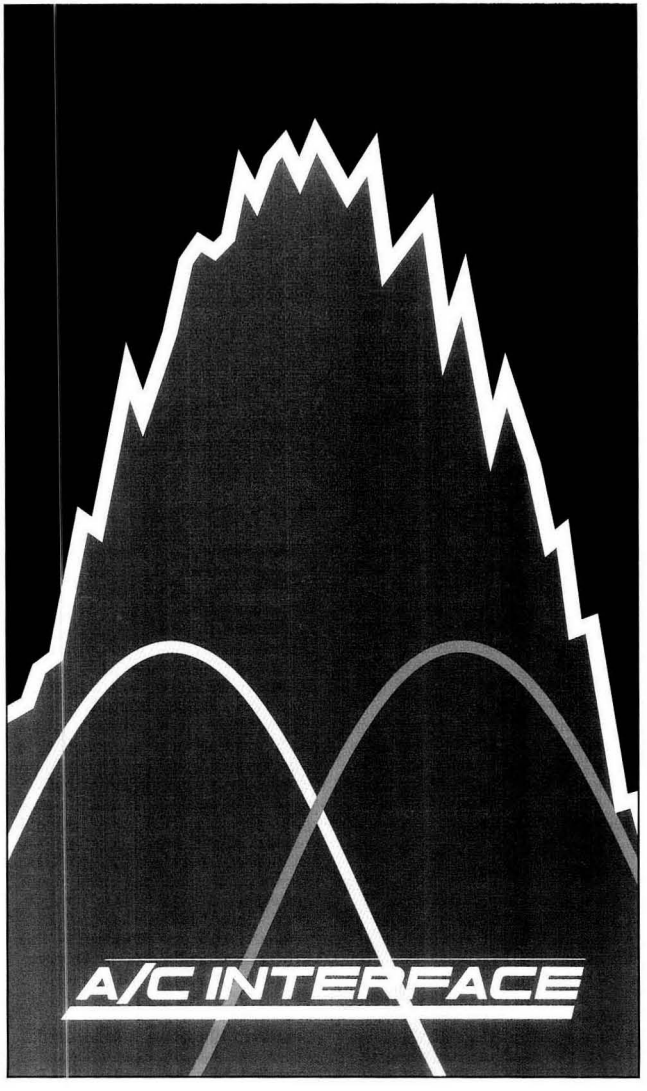

Computer methods have become increasingly important as analytical chemists continue their attempts to understand the nature of chemical systems. To interpret the results obtained from analytical experiments, data are fit to some sort of model describing the chemical system. By examining the results from such studies, researchers can explore new models for chemical behavior and identify and quantify the components in complex mixtures.

When data obtained experimentally are consistent with the proposed model, the fitting procedure provides valuable information. Several models commonly used in analytical chemistry include simple straight lines, multiple linear models, and nonlinear models. These models can be used to fit data from calibration experiments, multicomponent spectroscopic measurements, and kinetic experiments.

These standard models assume that all data points are consistent with the model selected, within the noise of the experiment. This assumption, however, may not be valid. To verify that the model is representative of all data, the residuals of the fit are examined. For simple models, such as straight lines, examination of residuals can sometimes lend insight into the nature of the model's inadequacy. For example, a single large residual indicates an outlier, whereas an observed trend in the residuals might indicate nonlinearity of the data. For complex models, it may not be possible to draw conclusions from the residuals about model adequacy and the nature of the lack of fit. The adaptive Kalman filter is most useful for such cases.

The examples described above correspond to situations in which the

0003-2700/91/0363-1103A/$02.50/0

model selected is at least partially correct. It would be convenient to interpret the modeling results for the correct portion of the model and still gain some insight into the nature of the model inadequacy for the incorrect portion. For example, a signal obtained from an analytical instrument gives information about the analyte of interest yet also contains contributions from interferences such as background signals. Subtraction of a measured background signal from an analyte response is a standard way to correct this; however, if the background response is not precisely characterized in terms of either amplitude or shape, the background subtraction step will fail to completely remove the interference from the analytical signal. Adaptive Kalman filters have been useful in these instances (*1, 2*).

Another example of the use of the adaptive Kalman filter is the spectroscopic characterization of chemical species that cannot be physically isolated from related species with similar spectral characteristics because of equilibrium considerations. In this case, the spectral characteristics of the interfering species may be known and the adaptive Kalman filter can be used to determine the spectral characteristics of the target species.

The Kalman filter was developed in 1960 by R. E. Kalman (*3*) for processing data for problems in orbital mechanics. Several reviews on the applications of Kalman filters to analytical problems have appeared recently (*4–7*). This A/C INTERFACE will focus on the adaptive modification of the Kalman filter that is used to fit chemical data when the model is incomplete or inaccurate. A brief summary of the regular Kalman filter will be given before expanding on the adaptive modification of the algorithm. (Throughout this discussion, scalars are denoted by lower case italic characters, vectors by lower case bold characters, and matrices by upper case bold characters. A superscript T denotes a transposed vector.)

Kalman filter algorithm

In its simplest form, the Kalman filter is no different from the recursive least-squares fitting approach originally suggested by Gauss and discussed by Young (*8*). A recursive procedure processes the data points one at a time. The previous best estimate for the parameters (e.g., mean, slope, intercept) is used in computing the updated estimate of the parameter

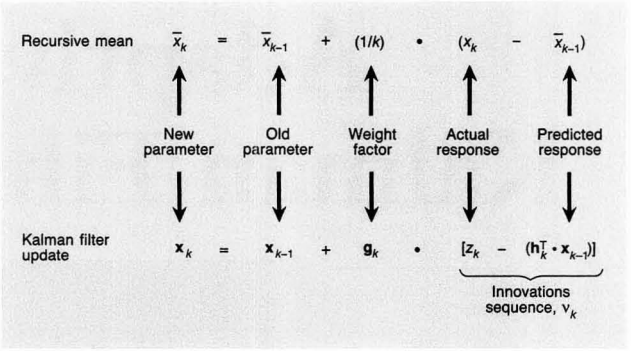

Figure 1. Recursive parameter estimation.

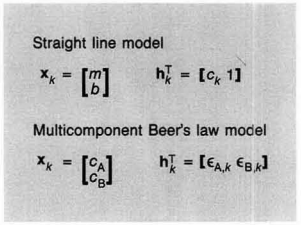

Figure 2. Kalman filter model information for straight line and multicomponent Beer's law expressions.

for each successive data point.

To calculate a mean value, the recursive estimation procedure takes the form shown at the top of Figure 1, where k is the number of values processed, x_k is the most recent measurement, and $\bar{x}_k$ and $\bar{x}_{k-1}$ are the means of k and $k-1$ responses, respectively. The Kalman filter update equation (the central equation of the algorithm), shown at the bottom of Figure 1, takes a similar form: $\mathbf{x}_k$ is a vector containing all parameters to be estimated from the fit after k responses have been measured and filtered. The vector $\mathbf{g}_k$ is the Kalman gain, and $\mathbf{h}_k^T$ is the measurement function vector, which describes the relationship between the kth measurement, z_k, and the most recent best estimates for the model parameters contained in the vector $\mathbf{x}_{k-1}$.

For the examples described in this article, the Kalman filter model equation for the measurement process is

$$z_k = (\mathbf{h}_k^T \bullet \mathbf{x}_k) + v_k \qquad (1)$$

Equation 1 illustrates a linear model, where the measurement function is described by a row vector, $\mathbf{h}_k^T$. The scalar value v_k is the noise contribution to the measurement, which has a variance of r_k. A simple straight line calibration model takes the form

$$z_k = (m \bullet c_k) + b + v_k \qquad (2)$$

where c_k is the concentration of the kth standard solution. In this case, the values for the standard concentrations c_k are known and m and b are the parameters to be determined. Equations 1 and 2 are equivalent when the $\mathbf{h}_k^T$ and $\mathbf{x}_k$ vectors are specified for the straight line model, as shown in Figure 2.

Another important model in analytical chemistry is represented by the multicomponent Beer's law expression

$$z_k = (\epsilon_{A,k} \bullet c_A) + (\epsilon_{B,k} \bullet c_B) + v_k \qquad (3)$$

where $\epsilon_{A,k}$ and $\epsilon_{B,k}$ are the molar absorptivities of species A and B, respectively, at wavelength λ_k (the cell pathlength is assumed to be 1 cm). In this instance, the values for the molar absorptivities are known, and the concentrations, c_A and c_B, are the parameters to be determined from the filtering procedure. The $\mathbf{h}_k^T$ and $\mathbf{x}_k$ vectors required for the solution to this problem are shown in Figure 2. This model allows for the resolution of overlapped spectra so that the concentrations of each individual species can be determined, provided that a pure component spectrum for each of the chemical species has been measured. Figure 3 shows a two-component overlapped spectral response fit to the model expressed by Equation 3. The spectral response shapes of the contributing components are known and are used to generate the $\mathbf{h}_k^T$ vector for each wavelength λ_k.

To use the Kalman filter for these problems, a weighting factor called

the Kalman gain, $\mathbf{g}_k$, must be calculated for each data point. The most important factor affecting the gain calculation is the variance of the measurement noise, r_k. The gain is inversely proportional to the variance of the measurement noise. This means that relatively noise-free data will be weighted heavily in the update calculation, whereas noisy data will be given correspondingly less weight (see Figure 1). Because the data are processed point by point, it is fairly easy to change the variance of the noise (and hence the weighting factors), yielding a convenient implementation of weighted least-squares fitting. For the regular Kalman filter, value(s) for r_k must be determined before beginning the fitting process.

The covariance matrix, $\mathbf{P}_k$, is also computed during the Kalman fitting routine and describes the error in the parameter estimates contained in the vector $\mathbf{x}_k$ after k measurements have been processed by the filter. Once the fitting process is complete, the square roots of the diagonal elements of $\mathbf{P}_k$ give the standard deviations of the parameter estimates. When the Kalman filter is used as described above, the results obtained are identical to those obtained using standard linear least squares. However, because the calculations are done recursively, an additional diagnostic of the fit quality is available.

The innovations sequence, v_k, is defined as the difference between the predicted and the actual response and is given by the bracketed term in the update equation shown in Figure 1. These values are also known as on-line residuals. They are simply residuals of the fit, but they are calculated during the fitting process instead of being computed after the fitting process is complete. Once the first few data points have been processed, this innovations sequence should resemble a zero-mean, white-noise process (provided that the original data are affected only by zero-mean, white-noise processes). Characteristics of the innovations sequence under these conditions are shown at the bottom right of Figure 3.

When the chosen model is incomplete or inaccurate, the normal Kalman filter fitting process will be altered by the presence of data points inconsistent with that model. The values for the on-line residuals will be large and will directly affect the computation of the updated estimates for the parameters. In turn, these values will be adjusted by large amounts and will usually result in final parameter estimates that are inaccurate. Adaptive filters are designed to overcome this limitation of the normal Kalman filter algorithm.

Adaptive Kalman filter algorithm

For adaptive Kalman filters, the measurement variance, r_k, plays an important role. The value for the measurement variance can be adjusted to compensate for the presence of model errors or outlying data points. The idea is to attribute data points that are inconsistent with the model to random noise by artificially increasing the measurement variance so that the data points are not used to corrupt the parameter estimates. The variance of the measurement noise is recalculated as

$$r_k = (1/q)\left(\sum_{j=1}^{q} v_{k-j} \bullet v_{k-j}\right) - \mathbf{h}_k^T \bullet \mathbf{P}_k \bullet \mathbf{h}_k \qquad (4)$$

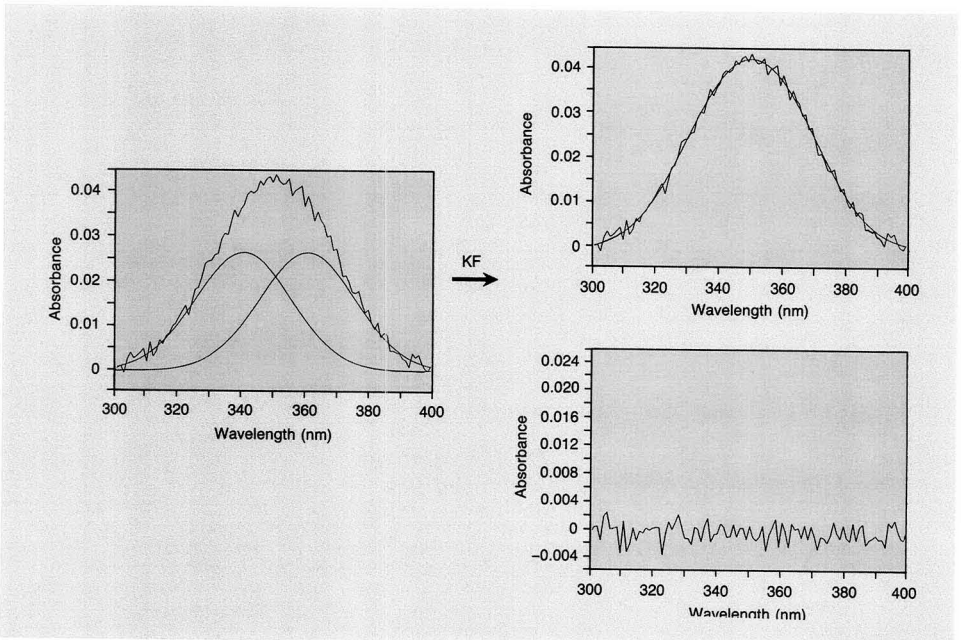

Figure 3. Kalman filter (KF) fit (top right) and innovations sequence (bottom right) for fitting noisy data to an accurate two-component Beer's law model (left).

where q is the number of points corresponding to a predetermined smoothing window and j is the index. Equation 4 effectively allows the filter to disregard any data points associated with large values for the innovations sequence, thereby giving accurate estimates for the parameters. In addition, examination of the resulting fit residuals can help to determine the nature of the modeling errors.

For most adaptive filters used for analytical applications, the method for "turning off" the filter to "bad" data points is based on the computation of Equation 4 (*9*). In contrast to the regular Kalman filter, computation of the value(s) for r_k for the adapted filter is based on the progress of the fitting process. When the innovations sequence is large, the calculated value for r_k takes a large value, a result that affects the calculation of the Kalman gain. The gain becomes very small, effectively turning off the filter to incoming measurements, and the parameter estimates are not significantly altered by the update calculation shown in Figure 1. If the innovations sequence values decrease to a range consistent with the known measurement errors, the filter can "open up" to subsequent responses. This approach depends on the model errors, or outlying data points, to follow a significant trend within the q data point window used to average the innovations sequence in Equation 4.

Multicomponent Beer's law model

The principles of the adaptive filter can be demonstrated by using a multicomponent Beer's law model. Figure 4 shows the results obtained for filtering a hypothetical spectrum of a two-component mixture, where one of the components is "left out" of the filter model. Here, spectral characterization of an unknown species in the presence of a known, spectrally similar species is desired. When the adaptive algorithm begins to filter the region of data where the missing component contributes, the filter is turned off and the concentration estimate for the known component is not affected by the presence of the second, contaminating component. In addition, the innovations sequence of the fit gives a more accurate estimate for the shape of the unmodeled component, compared with the innovations sequence obtained for the regular Kalman filter algorithm (Figure 4).

When the regular Kalman filter is used, the contribution of the known component to the total signal is overestimated, as shown by the fit in the upper right of Figure 5. The adaptive filter algorithm can be used to avoid significant overestimation of the concentration for this component (also shown in Figure 5, bottom right). The main limitation of this approach is that the data must be consistent with the model for some portion of the observed, nonzero response. For example, if the unmodeled component is completely overlapped by components included in the model, the concentrations of the known components may be overestimated by the adaptive filter. For the system shown in Figure 5, the concentration of the component included in the model is slightly overestimated by the adaptive filter for this reason.

When the above approach is used, the first few points processed by the filter should be modeled accurately.

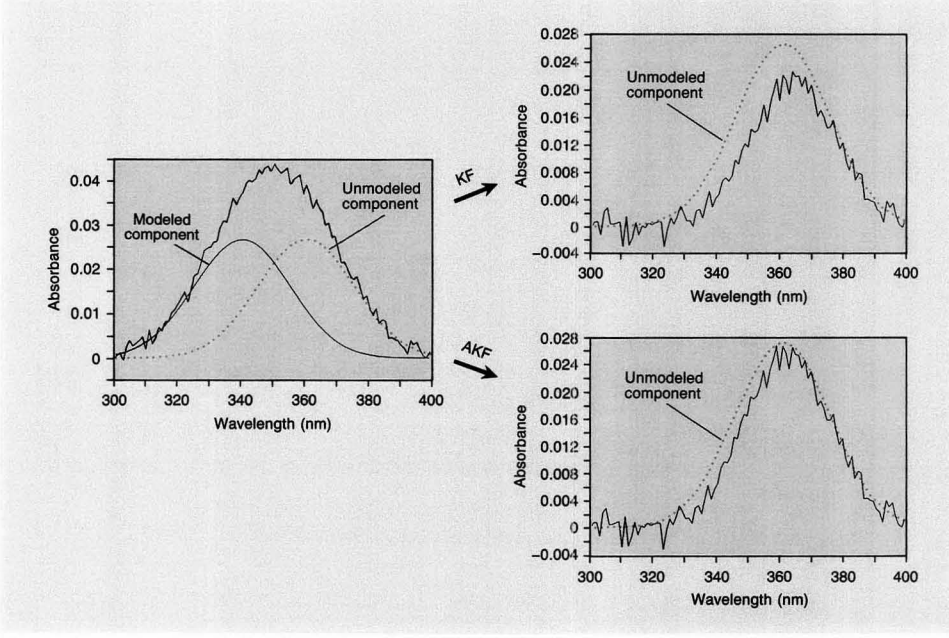

Figure 4. Kalman filter and adaptive Kalman filter (AKF) innovations sequence for inaccurate multicomponent model.
The second component is not included as part of the model information.

If this is not the case, a simplex-optimized adaptive filter is useful (*10*). This algorithm is based on repetitive passes through the data, where the diagonal elements of the covariance matrix, $\mathbf{P}_k$, are minimized, after the last available data point has been processed. This step is equivalent to fitting the maximum amount of data consistent with the model selected. Other methods for optimization of the adaptive filter have been investigated, and minimization of the area under the innovations sequence has given accurate parameter estimates with reduced computation times (*11*).

Zero-lag adaptive Kalman filter

Another difficulty occurs if the data and the model are inconsistent for a single point rather than for a sequence of several data points. In this case, Equation 4 can still be used to calculate corrected r_k values when the smoothing window, q, is set to 1. The filter processes the data twice. The first pass is used to establish the values for r_k, which will be used during the second pass of the filter. This method is called a zero-lag adaptive filter because the corrected r_k values are used for computing the updated estimates based on the same data point.

This approach has been used successfully to reject one or more outlying data points from calibration data sets fit to the straight line model described above (*12*). The main restriction is that some correct data points must be processed initially by the filter. For problems of this type the data can be processed in any order desired. Therefore, the data points can be ranked in approximate order of reliability, and accurate results from the adaptive filter should be obtained. One convenient way of processing data points in a different order is to filter them in reverse. If this processing is not successful, the data points must be rearranged in a different order so that the first few points processed are accurately modeled.

Modeling of gas–liquid partition coefficients

To illustrate the application of the zero-lag filter, consider linear free energy models for examining the factors contributing to gas–liquid partition coefficients, K_i, given by

$$K_i = [C_i]_g / [C_i]_s \qquad (5)$$

and where $[C_i]_g$ is the concentration of a solute i in the gas phase and $[C_i]_s$ is the concentration of the solute in solvent s. A better understanding of the chemical and physical contributions to these equilibrium constants is important in many areas, such as chromatography, because devices such as Snyder's solvent triangle are based on gas–liquid partition coefficient data (*13*).

These equilibrium constants are normalized by the partition coefficient of a similar-sized alkane solute, giving K_i'' values. The logarithms of these normalized partition coefficients for selected probe solutes are fit to a multiple linear model of dipolarity/polarizability and hydrogen bonding parameters for several common solvents (*14*).

The fit obtained for toluene as a solute is shown in Figure 6a. These fit results show evidence of errors in the model; however, no conclusions can be drawn from the pattern of the residuals. In addition, the coefficient

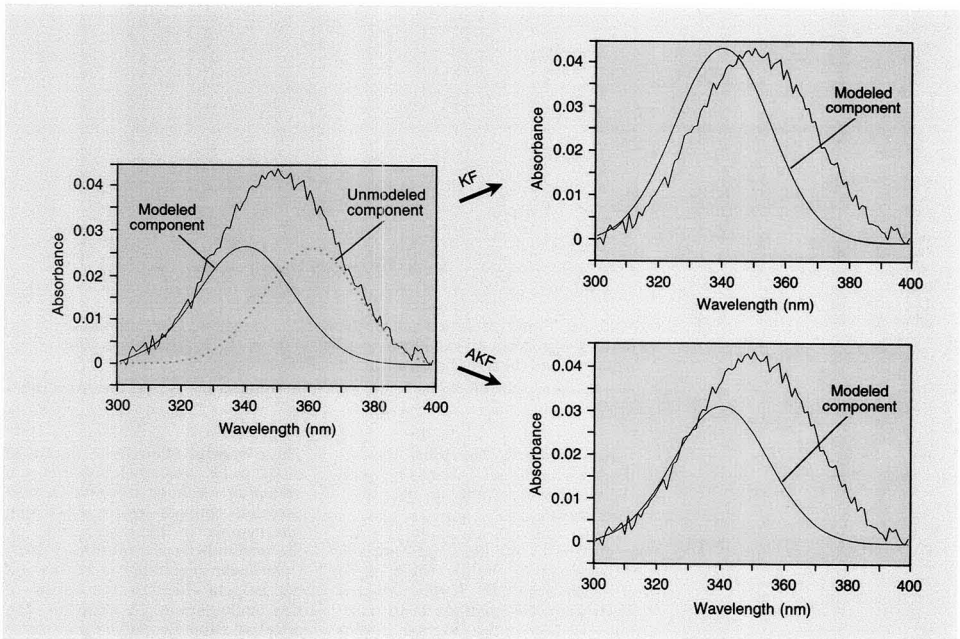

Figure 5. Kalman filter and adaptive Kalman filter fit results for inaccurate multicomponent model.
The second component is not included as part of the model information.

LEGAL NOTICE

U.S. POSTAL SERVICE
STATEMENT OF OWNERSHIP, MANAGEMENT AND CIRCULATION

(Required by 39 U.S.C. 3685)

1A. Title of publication: Analytical Chemistry
1B. Publication no.: 00032700
2. Date of filing: Oct. 1, 1991
3. Frequency of issue: Semimonthly
3A. No. of issues published annually: 23
3B. Annual subscription price: $31.00
4. Complete mailing address of known office of publication:
American Chemical Society
1155 16th Street, N.W.
Washington, D.C. 20036
5. Complete mailing address of headquarters of general business offices of the publisher:
American Chemical Society
1155 16th Street, N.W.
Washington, D.C. 20036
6. Names and addresses of publisher, editor and managing editors:
Royce W. Murray
Department of Chemistry
University of North Carolina
Chapel Hill, NC 27514
7. Owner:
American Chemical Society
1155 16th Street, N.W.
Washington, D.C. 20036
8. Not applicable
9. The purpose, function, and nonprofit status of this organization and the exempt status for Federal income tax purposes has not changed during the preceding 12 months.
10. Extent and nature of circulation

	Average No. Copies Each Issue During Preceding 12 Months	Actual No. Copies of Single Issue Published Nearest to Filing Date
A. Total no. copies printed	25,231	24,136
B. Paid Circulation		
1.Sales through dealers and carriers, street vendors and counter sales	0	0
2.Mail subscriptions	21,275	21,345
C. Total paid circulation	21,275	21,345
D. Free distribution by mail, carrier or other means, samples, complimentary, and other free copies	2,116	1,565
E. Total distribution	23,391	22,190
F. Copies not distributed		
1.Office, use, left over, unaccounted, spoiled after printing	1,840	1,946
2.Return from news agents	0	0
G. Total	25,231	24,136

11. I certify that the statements made by me above are correct and complete

Director, Publications Division-ACS
Robert H. Marks

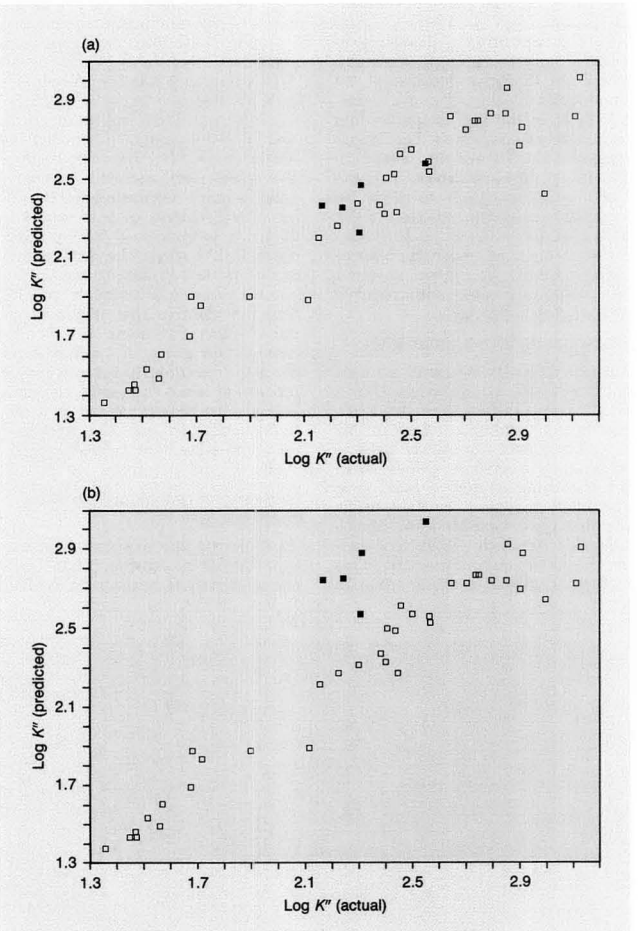

Figure 6. Predicted versus actual values of the logarithm of the gas–liquid partition coefficient for toluene in 44 solvents using (a) normal Kalman filter algorithm and (b) zero-lag adaptive Kalman filter algorithm.

Solid squares represent the alcoholic solvents included in the data set. Open squares represent all other solvents.

values obtained, describing the hydrogen bonding interactions between the solute and solvent, are not physically logical.

When the zero-lag adaptive filter is used to fit the data, substantially different fit results are obtained, as shown in Figure 6b. A clear trend is observed in the residuals for the alcoholic solvents in the data set, in contrast to the results obtained using standard regression procedures such as the regular Kalman filter. These results allowed an improved model to be postulated, based on the ability of alcoholic solvents to self-associate through hydrogen bonding interactions. In this case, examining the residuals from a traditional multiple linear regression procedure did not help to elucidate the nature of the model error. In addition, the adaptive filter fit yielded parameter estimates that were more consistent with an intuitive evaluation of the chemical system (*14*).

There is nothing magic about using the adaptive Kalman filter. The results are obtained from fitting only those portions of the data that can be accurately modeled. However, this method does not require the analyst to decide which data points to use and which to omit from the fitting procedure. The use of this algorithm can aid in the development of chemically valid models, a result that cannot always be obtained by examining the residuals of simple multiple linear least-squares fits. In addition, more accurate parameter estimates can be obtained, despite the presence of errors in the model.

The author acknowledges support from the U.S. Department of Energy, Grant No. DE-FG05-88ER13833.

References

(1) Gerow, D. D.; Rutan, S. C. *Anal. Chim. Acta* **1986**, *184*, 53.
(2) Gerow, D. D.; Rutan, S. C. *Anal. Chem.* **1988**, *60*, 847.
(3) Kalman, R. E. *J. Basic Eng.* **1960**, *82*, 34.
(4) Brown, S. D. *Anal. Chim. Acta* **1986**, *181*, 1.
(5) Rutan, S. C. *J. Chemometrics* **1987**, *1*, 7.
(6) Rutan, S. C. *Chemometrics and Intelligent Laboratory Systems* **1989**, *6*, 191.
(7) Rutan, S. C. *J. Chemometrics* **1990**, *4*, 103.
(8) Young, P. *Recursive Estimation and Time-Series Analysis*; Springer-Verlag: New York, 1984.
(9) Rutan, S. C.; Brown, S. D. *Anal. Chim. Acta* **1984**, *160*, 99.
(10) Rutan, S. C.; Brown, S. D. *Anal. Chim. Acta* **1985**, *167*, 39.
(11) Wilk, H. R.; Brown, S. D. *Anal. Chim. Acta* **1989**, *225*, 37.
(12) Rutan, S. C.; Carr, P. W. *Anal. Chim. Acta* **1988**, *215*, 131.
(13) Snyder, L. R. *J. Chromatogr. Sci.* **1978**, *16*, 223.
(14) Rutan, S. C.; Carr, P. W.; Taft, R. W. *J. Phys. Chem.* **1989**, *93*, 4292.

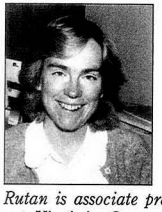

Sarah C. Rutan is associate professor of chemistry at Virginia Commonwealth University. She received her B.S. degree in chemistry in 1980 from Bates College (Lewiston, ME) and her Ph.D. in analytical chemistry in 1984 from Washington State University. Her research interests include chemometrics applied to solving problems in chromatographic and spectroscopic analyses.

LABORATORY SERVICE CENTER

CLASSIFIED—HELP WANTED

INDEX TO ADVERTISERS IN THIS ISSUE

Classified advertising section, see page 1110A.
Directory section, see page 1110A.
** See ad in ACS Laboratory Guide.*

Advertising Management for the American Chemical Society Publications

CENTCOM, LTD.

President
James A. Byrne
Executive Vice President
Benjamin W. Jones

Robert L. Voepel, *Vice President*
Joseph P. Stenza, *Production Director*

500 Post Road East
P.O. Box 231
Westport, Connecticut 06880
(Area Code 203) 226-7131
Telex No. 643310
Fax No. 203-454-9939

ADVERTISING SALES MANAGER
Bruce E. Poorman

ADVERTISING PRODUCTION MANAGER
Jane F. Gatenby

SALES REPRESENTATIVES

Philadelphia, PA. . . . CENTCOM, LTD. GSB Building, Suite 405, 1 Belmont Ave., Bala Cynwyd, PA. 19004. Telephone: 215-667-9666, FAX: 215-667-9353

New York/New Jersey . . . Dean A. Baldwin, John F. Raftery, CENTCOM, LTD., Schoolhouse Plaza, 720 King Georges Post Road, Fords, NJ 08863, Telephone: 908-738-8200, FAX: 908-738-6128

Westport, CT. . . . Edward M. Black, CENTCOM, LTD., 500 Post Road East, P.O. Box 231, Westport, CT 06880. Telephone: 203-226-7131, Telex 643310, FAX: 203-454-9939

Cleveland, OH. . . . Bruce E. Poorman, CENTCOM, LTD., 325 Front St., Suite 2, Berea, OH 44017. Telephone: 216-234-1333, FAX: 216-234-3425

Chicago, IL. . . . Michael J. Pak, CENTCOM, LTD., 540 Frontage Rd., Northfield, Ill. 60093. Telephone: 708-441-6383, FAX: 708-441-6382

Houston, TX. . . . Michael J. Pak, CENTCOM, LTD. Telephone 708-441-6383

San Francisco, CA. . . . Paul M. Butts, CENTCOM, LTD., Suite 808, 2672 Bayshore Parkway, Mountain View, CA 94043. Telephone: 415-969-4604, FAX: 415-969-2104

Los Angeles, CA. . . . Paul M. Butts, CENTCOM, LTD. Telephone: 415-969-4604

Boston, MA. . . . Edward M. Black, CENTCOM, LTD. Telephone: 203-226-7131

Atlanta, GA. . . . CENTCOM, LTD. Telephone 216-234-1333

Denver, CO. . . . Paul M. Butts, CENTCOM, LTD. Telephone: 415-969-4604

United Kingdom
Reading, England . . . Malcolm Thiele, Technomedia Ltd., Wood Cottage, Shurlock Row, Reading RG10 OQE, Berkshire, England. Telephone: 0734-343302, Telex #848800, FAX: 0734-343848

Continental Europe . . . Andre Jamar, International Communications, Inc., Rue Mallar 1, 4800 Verviers, Begium. Telephone: (087) 22-53-85, FAX: (087) 23-03-29

Tokyo, Japan . . . Sumio Oka, International Media Representatives Ltd., Room 100, 21 Bldg., 2-2-22 Okusawa, Setagaya-ku, Tokyo 158 Japan. Telephone: 502-0656, Telex #22633, FAX: 5706-7349

Analytical CHEMISTRY

EDITOR: **ROYCE W. MURRAY**

ASSOCIATE EDITORS: **Catherine C. Fenselau, Georges Guiochon, Walter C. Herlihy, Robert A. Osteryoung, Edward S. Yeung**

Editorial Headquarters
1155 Sixteenth St., N.W.
Washington, DC 20036
Phone: 202-872-4570
Telefax: 202-872-4574
Bitnet: rmh96@cas

Managing Editor: Mary Warner

Senior Editor: Louise Voress

Associate Editor: Grace K. Lee

Assistant Editors: Jane K. Baker, Felicia Wach

Contributing Editor: Marcia Vogel

Director, Operational Support: C. Michael Phillippe

Head, Production Department: Leroy L. Corcoran

Art Director: Alan Kahan

Composition Systems Administrator: Vincent L. Parker

Designers: Peggy Corrigan, Robert Sargent

Production Editors: John W. Laine, Elizabeth Wood

Circulation: David Schulbaum

Editorial Assistant, LabGuide: Joanne Mullican

Journals Dept., Columbus, Ohio

Associate Head: Marianne Brogan

Editorial Office Manager: Mary Scanlan

Journals Editing Managers: Kathleen E. Duffy, Joseph E. Yurvati

Assistant Editors: Stephanie R. Harrell, Brenda S. Wooten

Published by the
AMERICAN CHEMICAL SOCIETY
1155 16th Street, N.W.
Washington, DC 20036

Publications Division

Director: Robert H. Marks

Journals: Charles R. Bertsch

Manuscript requirements are published in the January 1, 1991 issue, page 89. Manuscripts for publication (4 copies) should be submitted to ANALYTICAL CHEMISTRY at the ACS Washington address.

AUTHOR INDEX

Chemical Modulation of the Electron Work Function

Jiří Janata

Department of Materials Science, University of Utah, Salt Lake City, Utah 84112

Theory explaining the chemical modulation of Fermi level of a chemically selective layer is presented. It is shown that a measurable potentiometric signal can be obtained which is due to a partial electron transfer between the electrically neutral molecule, e.g. a gas, and a p-type or an n-type semiconductor. In this scheme a charge-transfer complex is formed between the guest molecule and an ionizable donor or an acceptor state in the semiconductor, which results in the shift of work function. It is logarithmically related to the activity of the neutral molecule in the solid phase; however, the slope is a fraction of *kT*. There is a formal analogy between this relationship and the Nernst equation, which corresponds to a complete charge separation. The changes of work function can be measured with a Kelvin probe or an insulated gate semiconductor device.

INTRODUCTION

The design of new selective layers is probably the most important issue of chemical sensor research today. Both the integration of these layers with the physical part of the sensor and the origin of the signal, the so-called mode of transduction influences the choice of methods by which these layers are prepared. Chemical modulation of the work function (WF) is a mode of transduction on which a whole new class of chemical sensors is based. It requires that the chemically sensitive layer is capacitively coupled to the rest of the sensor at one interface (*1*). This requirement is satisfied in the vibrating capacitor (Kelvin probe) and in all solid-state devices utilizing a so-called insulated gate. The typical examples are so-called chemically sensitive diodes and chemically sensitive field-effect transistors.

The Kelvin probe is the best known technique for the measurement of surface potential and of the contact potential. A brief explanation of its function is shown in Figure 1. A chemically sensitive layer is deposited on one plate of the capacitor. The choice of the metal on which it is deposited is arbitrary, the only requirement is that it is electronically conducting and that it forms an ohmic contact with the layer. The opposing reference plate is also an electronic conductor. If the two materials adjacent to the dielectric, i.e. the reference plate and the sensitive layer, are different, a voltage is established between them which is the consequence of the difference of their affinity for electron and of the difference of their surface dipoles. These two terms define the WF, i.e. the energy which is required to remove an electron from the bulk of the phase (Fermi level) and to place it just outside the reach of the image forces, in so-called vacuum reference level.

When two materials are brought into contact, forming an ohmic junction, electrons flow from the material of low WF to that of the higher WF. Thus, for example, if the electronically coupled chemical layer attracts electrons more strongly (i.e. it has a higher WF), electrons are transferred from the reference plate to the chemical layer and the reference plate becomes positively charged with respect to the plate carrying the layer. We can quantify this charge separation and estimate the difference of the WF of the two materials from which the plates are made. This is the principle of the Kelvin probe measurement but also an operating mechanism of some solid-state devices which have been proposed as potentiometric microsensors (*1*). They differ only in the method of measurement of the charge separation. In the Kelvin probe the distance between the two plates is periodically varied, hence its name "vibrating capacitor". The vibration produces an alternating current in the external circuit. If a source of electrons (e.g. a battery) is placed in series with the plates, a compensating voltage can be applied which pushes the electrons back to the reference plate. As the electric field decreases, the ac current vanishes to zero, indicating that the compensating voltage equals exactly the difference of the WF which caused the displacement of the electrons. Under these conditions the electric field between the plates is zero.

A similar situation exists in an insulated gate structure: The difference between the WF of the semiconductor and the gate metal adjacent to the insulator causes a deficiency or an excess of electrons in the semiconductor at its interface with the insulator. The amount of the excess charge at the semiconductor plate is determined from so-called capacitance–voltage curves. In a field-effect transistor the excess charge at the semiconductor/insulator interface determines the magnitude of the drain-to-source current. The important difference is that in solid-state structures it is possible to perform the measurement of WF difference in a state which is not completely compensated, i.e. in the presence of an electric field. In either case the observed WF difference contains the contribution from both the bulk and the surface (or interface).

If a gaseous electron donor or acceptor enters the sensitive layer it may change the bulk component of its WF, thus forcing a new value of the compensating voltage. One assumption which has to be made, and cannot be verified, is that the WF of the reference plate remains unaffected by the change of the gaseous environment.

Solution potentiometric sensors such as ion-selective electrodes and ISFETs rely on measurement of the potential difference between two electrodes, the indicator (working) and the auxiliary (reference). This signal has its origin in the separation of charge due to the partitioning process which occurs, more or less selectively, at the interface between the indicator electrode and the fluid medium, the sample. The thermodynamics and kinetics of this process have been described extensively, can be found in standard textbooks, and will not be repeated here. Its characteristic feature is the fact that *integral values* of charge are involved, giving rise to the familiar "Nernstian slopes" of e.g. 59.16 mV/decade or 29.6 mV/decade etc., for uni and divalent ions, respectively (at 25 °C).

The WF difference is also responsible for the existence of so-called contact potential at the junction of two electronically conducting condensed phases. Although the contact potentials are abundantly present in any electrical circuit they are not accessible to a conventional direct potentiometric measurement. The usual technique for measurement of contact potential is again the vibrating capacitor.

The purpose of this paper is to examine another type of interaction which also gives rise to an equilibrium potentiometric signal for which the dependence of the observed voltage

0003-2700/91/0363-2546$02.50/0

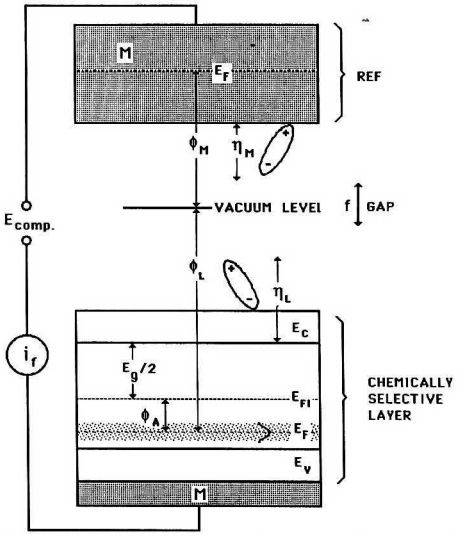

Figure 1. Schematic diagram of the Kelvin probe. The chemically selective layer deposited on metal M forms one plate of the vibrating capacitor while the identical metal M forms the reference plate. The layer is shown as a p-type semiconductor. The frequency of the mechanical vibration is f, the compensating voltage is $E_{comp.}$ and the ac current is i_f. Other symbols have their usual meaning and/or are explained in the text.

on concentration has a predictable but *fractional slope*.

Let us consider a gas G which dissolves in an electronically conducting solid phase according to Henry's law. The concentration of the gas in the solid, $G(s)$, is given by the solubility coefficient α and by the partial pressure of the gas, P_G

$$G(s) = \alpha P_G \tag{1}$$

Gas molecules are electrically neutral. However, upon entering the solid they exchange *partial electron density* (δe) with the matrix according to the equilibrium

$$G(s) = G_\delta + \delta e \tag{2}$$

where δe is the number of moles of charge transferred from the gas molecules to the matrix. For $|\delta| < 1$ we talk about formation of a *charge-transfer complex* between the solid matrix and the gas molecule. Let us assume that the solid has a discrete energy band structure. If the gas is an electron donor (i.e. a Lewis base), the charge density is transferred to the conduction band, while for an electron-accepting gas (i.e. a Lewis acid), the charge-transfer complex is formed between the gas and the valence band. In either case the direction in which the charge flows is governed by the difference of the electron affinity of the solid and of the gas molecule. This interaction can be viewed as a normal doping process in which the distribution of electrons is given by the Fermi–Dirac statistics.

The formation of a charge-transfer complex is a common chemical notion when this type of interaction involves individual molecules. However, it occurs also between solid phase and individual molecules. For example the partial charge transfer causes chemisorption in which the adsorbing molecule strongly interacts with the surface of the solid phase.

The affinity of electron for the gas molecule is described by so-called Mullikan electronegativity (e.g. ref 2), χ, which is the average of the value of the ionization potential I_p and of the electron affinity E_a of the molecule

$$\chi = 0.5(I_p + E_a) \tag{3}$$

while the affinity of electron for the solid, ther Fermi level E_F, is the bulk component of the WF ϕ

$$\phi = E_F - \eta e \tag{4}$$

The second term on the right-hand side of eq 4 is the work required to transfer electron across the surface dipolar layer η.

It has been shown experimentally (*3*) that that the charge-transfer coefficient δ (per molecule) is proportional to the difference between the Fermi level, E_F, and the Mullikan electronegativity

$$\delta = \beta(E_F - \chi) \tag{5}$$

where β is an unspecified constant. The gas/solid equilibrium is therefore written as

$$K_G = [e]^{2\delta}/\alpha P_G \tag{6}$$

The charge-transfer coefficient δ simply reflects the fact that δ number of molecules participate in the process which results in the exchange of an integral value of charge with the energy bands of the solid matrix. Thus, it is a stoichiometry factor which enters into the equilibrium expression as an exponent in eq 6. Its integral values of −1 and +1 correspond to the complete ionization of the gas molecule. In other words the interaction between the semiconductor matrix and the gas molecule which involves a partial transfer of electron is a redox relationship. Obviously, such a process is of little value in classical potentiometry because the partial separation of charge, for $|n| < 1$, results in formation of a dipole which does not lead to a measurable potential difference between the two phases. From this point of view the Nernst equation is a unique case of formation of the potential difference, so-called Galvani potential difference, between the bulks of the two phases. It is due to the separation of integral values of charge. The partial charge transfer is not fundamentally different, but it requires the measurement of the WF. In the case of the hydrogen-sensitive Pd-MOSFET (*11*) the formation of the dipole layer at the Pd/insulator interface is responsible for the signal. This device is again based on the modulation of the WF, specifically of its interfacial component.

The practical implementation of the "vacuum reference level" gives rise to several different experimental techniques which are as diverse as calorimetry, photoionization measurements, studies with a vibrating capacitor, and studies with devices based on insulated solid-state junctions, the last two being electrostatic in nature. These different techniques lead to values of the WF which, unfortunately, do not completely agree with each other. This problem is related to the fact that the electron which is removed from the primary phase has to be deposited in some reference phase. What is then measured is the net amount of energy corresponding to these two steps. This is the familiar problem of solution potentiometry which always requires two electrodes, working and reference, in order to perform a thermodynamically sound measurement. It is also a fundamental reason for the impossibility of establishing the absolute value of the WF of a phase, absolute value of an electrode potential, and also the absolute value of the ionization potential and electron affinities of individual molecules. In other words, the WF measurement is always relative, relative with respect to an arbitrarily chosen reference phase into which the electron is deposited.

The affinity of the phase for electron can be looked upon as a local redox potential with respect to the guest molecule. Therefore, if the affinity, given by the bulk component of the WF of the matrix is low, electrons are transferred to the guest molecule. In other words, the matrix behaves as a reducing agent with respect to the guest molecule. On the other hand,

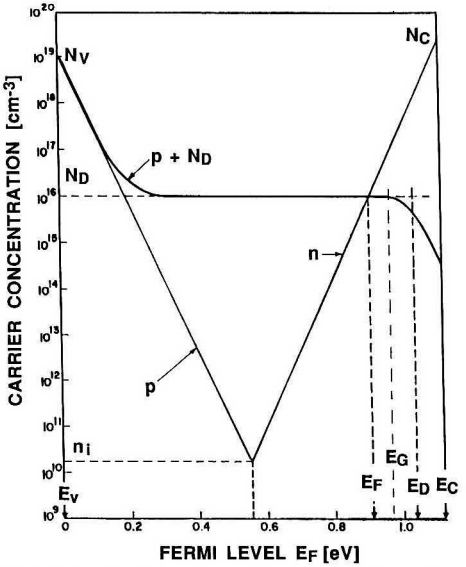

Figure 2. Logarithmic dependence of Fermi level, E_F, for an n-type semiconductor, on the concentration of the donor impurity N_D. The gas energy level E_G is shown here for arbitrary $\delta < 0$ (see text for discussion).

if the value of the E_F is high, electrons move from the guest molecule to the matrix; i.e. the molecule is oxidized. The relative character of this charge sharing, on a molecular scale, is again the consequence of the same thermodynamical requirement "to close the electron return path", which explains the necessity for the reference phase in a macroscopic measurement of the WF. In other words, the electron taken out of one moiety must be transferred to another. The important point to realize here is that the formation of the charge-transfer complex described in eq 2 is an *internal* phenomenon while the measurement of the WF is a process which implies a formal electron transfer out of the solid phase and thus can be classified as *external*. In the latter case the measured value of the WF difference contains the contribution from the two dipolar layers (eq 4) located at the surface of the two sides of the insulator.

The Fermi–Dirac statistics describe the distribution of indistinguishable, *noninteracting* particles in n available energy levels. It can be used for electrons or holes, the chief formal difference being in the presence of the degeneracy factor g, which in silicon is 2 for a donor and 4 for an electron acceptor. However, the values of g for an organic semiconductor is not known a priori. Otherwise, the arguments concerning the donor and acceptor are the same. The non-Fermi–Dirac distribution of indistinguishable *interacting* particles has been also developed (*4*). Both statistics lead to the same final result in this analysis. The occupancy of the levels by the donor molecules D is

$$N_{D^+} = N\left[1 - \frac{1}{1 + (1/g_D)\exp[(E_D - E_F)/kT]}\right] \quad (7)$$

where $N = N_D + N_{D^+}$, the Fermi level, E_F, is the average value of energy of electrons in the phase, and E_D is the dopant energy level. N_D and N_{D^+} are the concentrations (in inverse cubic centimeters) of the neutral and of the fully ionized dopant in the phase. The basic premise of calculation of the Fermi level is the condition of charge neutrality in the phase (*5*). In other words there is no electrical field in the bulk of the phase. As long as the charge remains inside the phase, the Fermi level equals the chemical potential of electron. The experimental observation of the charge-transfer complex formation under these conditions can be made, e.g., spectroscopically (*3, 4*). On the other hand the Kelvin probe method yields the value based on the *electrochemical potential of electron* and contains the experimental uncertainty due to the contribution from the dipolar layers which is experienced by the electron passing through them.

Rearrangement of eq 7 yields

$$E_F = E_D + kT \ln N_D/g_D N_{D^+} \quad (8)$$

The dependence of the Fermi level on the concentration of donors (acceptors) in silicon is shown in Figure 2, as an example. From this diagram we see that E_F varies logarithmically with the concentration of the primary dopant. The energy band structure of organic semiconductors is undoubtedly more complicated. The coupling of the secondary dopant, such as a gas molecule, is expected to occur through one of the energy levels defined by the primary dopants. For the time being it is not necessary to specify what this state may be. In the case of some organic semiconductors it could be the polarons or bipolarons which have been shown to form charge-transfer complexes with various organic vapors (*3*).

We shall now retain N as the total primary dopant level (e.g. a donor) and link it to the charge transfer from the gas molecules through the electron-exchange equilibrium. The ionization equilibrium involving this level is

$$N_D = N_{D^+} + e \quad (9)$$

$$K_D = N_{D^+}[e]/N_D \quad (10)$$

Combining eqs 8 and 6 then yields

$$N_D/N_{D^+} = (K_G \alpha P_G)^{1/2\delta} \quad (11)$$

and substitution into eq 8 yields for a n-type semiconductor

$$E_F = E_D + (kT/2\delta) \ln K_G\alpha/(g_D K_D)^{2\delta} + (kT/2\delta) \ln P_G \quad (12a)$$

or

$$E_F = E_D{}^* + (kT/2\delta) \ln P_G \quad (12b)$$

Equations 12 quantify the relationship between the position of the Fermi level in a n-type semiconductor and the fugacity of the donor molecules in the gas phase. A similar relationship can be derived for the p-type semiconductor for which the ionization of a discrete acceptor state N_A is given as

$$N_A + e = N_{A^-} \quad (13)$$

$$K_A = \frac{N_{A^-}}{N_A[e]} \quad (14)$$

The Fermi–Dirac distribution for electron acceptors (in which $N = N_A + N_{A^-}$ is then

$$N_{A^-} = \frac{N}{1 + (1/g_A)\exp[(E_A - E_F)/kT]} \quad (15)$$

Combination of eqs 6, 14, and 15 yields for a p-type semiconductor

$$E_F = E_A + (kT/2\delta) \ln K_G\alpha(g_A K_A)^{2\delta} + (kT/2\delta) \ln P_G \quad (16a)$$

or

$$E_F = E_A{}^* + (kT/2\delta) \ln P_G \quad (16b)$$

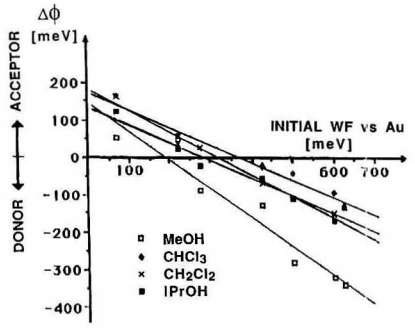

Figure 3. Dependence of the change of work function difference $\Delta\phi$ on the initial value of the WF of polypyrrole tosylate. Concentrations of the injected vapors in nitrogen: methanol, 4.6 mM L^{-1}; 2-propanol, 0.8 mM L^{-1}; CH_2Cl_2, 8.5 mM L^{-1}; $CHCl_3$, 1.2 mM L^{-1}. (Reprinted with permission of the author from ref 3.)

Equations 12 and 16 have the familiar characteristics of the Nernst equation for ion and electron transfer across the interface of two condensed phases, except that they account for the *fractional charge transfer*. The standard potentials E_D^* and E_A^* differ only in the value of the degeneracy factor g and in the value of the dopant ionization equilibrium constants of the donor K_D and the acceptor K_A levels. Equations 16 convert formally to eqs 12 for $\delta < 0$. Because the polarity and magnitude of the response depends on the value of δ (eq 5) they also explain why the same molecule, at a given concentration, can yield a positive or a negative change of the WF. In other words a gas molecule can act as an electron donor or an electron acceptor in either type of the semiconductor. It is not surprising to find this kind of coupling for the formation of charge-transfer complexes. The amount of interaction energy is much smaller than the corresponding energy required for electrodes based on charge transfer of integral values of electron.

It is known (*3*, *7*, *8*) that electrochemically prepared organic semiconductors formed under different conditions have a different initial value of the WF. It may be difficult to control because it depends both on the conditions of the electrochemical preparation and on the postpreparation treatment. Nevertheless, it has been shown (*3*, *9*), in agreement with eq 5, that for the same guest molecule the slope of the ΔWF vs ln P_G dependence (eq 12) indeed varies with the initial value of the WF_{init} of the matrix (Figure 3). The initial value of WF is typically 4 eV, while the ΔWF is usually 0.1–0.2 eV. Thus, for a small overall change of WF, the variation of δ is less than 5%.

The data in Figure 3 show that for certain values of WF_{init} the ΔWF is zero, i.e. the molecule does not form a charge-transfer complex. At higher values of WF_{init} the molecule behaves as an electron donor, while at values below the zero-crossing point the molecule becomes an electron acceptor. The fact that these zero-crossing points lie at different values of WF_{init} indicates that, in principle, the "reference materials" could be obtained by adjusting the WF_{init} accordingly.

SELECTIVITY

From the point of view of this analysis, the selectivity enters into the picture in two places: in the solubility of the gas in the condensed phase (eq 1) and in the donor/acceptor relationship between the guest molecule and the condensed phase (eq 5). If the gas is not soluble in it, it is not expected to modulate its work function through the above mechanism. However, it is obvious that the molecule which cannot partition to the condensed phase can still *adsorb* at its surface and thus modulate the surface component of its WF. This is particularly true in the case of WF sensors using a gaseous dielectric, e.g. the Kelvin probe and the suspended gate field-effect transistor (SGFET) (*10*), in which both the *surface* and the bulk may contribute to the overall signal. Because of the limited number of available adsorption sites, the contribution from the surface (adsorption) is expected to occur mostly at the low concentrations and saturate at the high concentrations. To complicate the matter even further, the occupancy of the surface by the adsorbing molecules is governed by a specific form of the adsorption isotherm which is given by the nature of the interactions between the adsorbing molecules themselves and between the adsorbing molecules and the surface. Because there is no physical restriction on the access of all molecules to the surface, this mode of interaction makes these sensors vulnerable to a broad range of nonspecific interferences which have to be dealt with in a rational way. On the other hand the effect of adsorption of interferants, e.g. in the case of Pd–hydrogen MOSFET (*11*), is of a kinetic nature. In these devices the modulation of the WF originates in the bulk of the sensitive layer (in this case Pd) and at the Pd/solid insulator *interface*. This is a rather unique situation given by the fact that Pd serves both as the gate material *and* the selective layer at the same time. Anyway, it is important to realize the fundamental difference between the surface (i.e. solid/gas) and the interface (e.g. solid/solid) in this context.

As we have seen (Figure 3), the selectivity is also given by the value of the charge-transfer parameter δ. There is no charge transfer for $\delta = 0$, i.e. no change in the position of the Fermi level, even though the guest molecules may absorb in the condensed phase.

In the case of a mixture of gases, each species has its own value of the Mullikan electronegativity, therefore its own value of the charge-transfer coefficient δ. Clearly, for a matrix of a given WF some gases may act as electron donors, some may act as electron acceptors, and some may be inert. For a matrix of a different value of the WF these proportions will be different. In a formal analogy with the Eisenman–Nikolskij equation governing the selectivity of ion-selective electrodes, we can formulate the response of the WF sensor in a mixture as

$$E_F = \text{constant} + (kT/2\delta_1) \ln [P_{G1} + K_{1/2}(P_{G2})^{\delta 1/\delta 2} + ... + (K_{1/i}P_{Gi})^{\delta 1/\delta i}] \quad (17)$$

A formal analogy apparently also exists between the partial charge-transfer coefficients δ and the exchange current densities of charged species participating in the formation of the equilibrium potential of the ion-selective electrode. However, the origin of the selectivity coefficients $K_{1/i}$ depends on the mechanism of the interaction of individual species. The important conclusion is that the magnitude of the contribution of the interfering species to the overall signal can be manipulated through the adjustment of the WF of the selective layer which was proposed earlier (*9*). This greatly increases the range of the species that can be quantified by this transduction principle.

It is possible to speculate on yet another analogy between the partial charge-transfer mechanism and a complete ionization process. It has been shown that the above gas/solid interactions can be quantified spectroscopically (*3*, *6*). This is analogous to a spectroscopic evaluation of the ionization equilibria which are the basis of various optrodes. In both cases the photons "count the molecules" and provide the information about the concentration rather than activity of the species participating in the charge-transfer equilibrium. Different specific and nonspecific interactions then give rise to a multitude of acidity functions (*12*). For the same reason,

the optically determined value of E_F (and of ΔWF) is likely to contain an error which is due to the undetermined variation of the activity coefficient of the dissolved and partially ionized gas in the condensed phase.

The specific nature of the semiconductor doping process is also reflected in the fact that one dopant can have several different doping energy levels in different materials. Thus, for example, there are three acceptor and one donor energy level for Au in Ge. On the other hand, in Si gold has only one acceptor and one donor level (5), both at entirely different energies than in germanium. This material-dependent multiplicity exists for most elements and semiconductors. It is tempting to speculate that a similar situation will exist in the realm of the gas/organic semiconductor interactions, leading to a wide range of selective materials.

LIST OF SYMBOLS

E_A	acceptor energy level
E_a	electron affinity
E_C	energy of the conduction band edge
E_D	donor energy level
E_{Fi}	intrinsic Fermi level
E_V	energy of the valence band edge
$G(s)$	concentration of gas in the solid
g_A	degeneracy factor for acceptors
g_D	degeneracy factor for donors
I_p	ionization potential
k	Boltzmann constant
$K_{1/i}$	potentiometric selectivity coefficient
K_D	donor ionization equilibrium constant
K_G	gas ionization equilibrium constant
N	total concentration of dopant atoms
N_D	concentration of nonionized donors
N_{D^+}	concentration of ionized donors
P_G	partial pressure of gas
T	absolute temperature
α	solubility coefficient
δ	charge-transfer coefficient
χ	Mullikan electronegativity
η	surface dipole
ϕ	work function (energy per electron)

LITERATURE CITED

(1) Janata, J. *Principles of Chemical Sensors*; Plenum: New York, 1989.
(2) Barrow, G. M. *Physical Chemistry*, 5th ed.; McGraw-Hill: New York, 1988; p 524.
(3) Blackwood, D.; Josowicz, M. *J. Phys. Chem.* **1991**, *95*, 493.
(4) Reiss, H. *J. Phys. Chem.* **1985**, *89*, 3783.
(5) Sze, S. M. *Physics of Semiconductor Devices*; Wiley: New York, 1969; p 20.
(6) Cabala, R.; Josowicz, M. Private communication, 1991.
(7) Heinze, J.; Bilger, R.; Meerholz, K. *Ber. Buns-Ges. Phys. Chem.* **1988**, *92*, 1266.
(8) Duan-Fu, Hsu; Gratzl, M.; Riley, A. M.; Janata, J. *J. Phys. Chem.* **1990**, *94*, 5982.
(9) Josowicz, M.; Janata, J. *Anal. Chem.* **1986**, *58*, 514.
(10) Josowicz, M.; Janata, J. In *Chemical Sensor Technology*; Seiyama, T., Ed.; Elsevier: Amsterdam, 1988; Vol. 1.
(11) Lundström, I. In *Chemical Sensor Technology*; Seiyama, T., Ed.; Elsevier: Amsterdam, 1989; Vol. 2.
(12) Janata, J. *Anal. Chem.* **1987**, *59*, 1351.

RECEIVED for review April 15, 1991. Accepted August 20, 1991. This work was supported by Grant No. R-816491-01-0 from the Office of Exploratory Research of the Environmental Protection Agency.

Performance Characteristics of Sodium Super Ionic Conductor Prepared by the Sol–Gel Route for Sodium Ion Sensors

Alberto Caneiro,[1] Pierre Fabry,* Hafit Khireddine, and Elisabeth Siebert

Laboratoire d'Ionique et d'Electrochimie du Solide de Grenoble, Enseeg, B.P. 75, 38402 Saint Martin d'Hères, France

NASICON ($Na_{1+x}Zr_2Si_xP_{3-x}O_{12}$) is a new ceramic material and is a fast ionic conductor by Na^+. It was initially proposed for use as an ion-sensitive membrane for ISE or ISFET devices some years ago. The sol–gel route is used here to prepare high-density samples. Some physicochemical characteristics such as structure, conductivity, and solubility are described. Results on ISEs made with this material are presented including ion-exchange kinetics, detection limit, and selectivity coefficients. A sintering temperature influence is observed. The performance characteristics are compared to those of a commercial glass membrane; the detection limit is slightly poorer than for the commercial ISEs but selectivity is always better (up to 10 times). A considerable sintering temperature influence is observed on the interfering proton phenomenon: the higher the temperature, the smaller the effect.

INTRODUCTION

Solid-state sensors for use in ion analysis present some advantages compared to classic ones which have a liquid internal reference system. For instance they are stronger, they can accept thermal treatments and can be prepared by thin-layer technologies for microsensor mass production. As reported in the literature (*1–3*), such solid materials have generally been glasses which are often poor ionic conductors. Crystalline membranes such as LaF_3 (*4*) or silver salts (*5*) are still relatively poor conductors. In the last 10 years, numerous new solid ionic conductors have been synthesized and studied essentially for electrochemical battery applications. Ceramics are promising materials and their use as ion-sensitive membranes for analytical applications has been discussed in preceding papers (*6, 7*).

Among these new materials, 3D framework conductors are of particular interest. One such example is NASICON (Na super ionic conductor). This compound, which has the chemical formula $Na_{1+x}Zr_2Si_xP_{3-x}O_{12}$, was first synthesized by Hong and Goodenough (*8, 9*). Its ionic conductivity is high and very close to that of β-alumina ($\sigma = 10^{-3}$ S·cm^{-1} at room temperature). According to some studies, NASICON does not seem to be altered by water, contrary to β-alumina (*10, 11*). It has been reported to exhibit a monoclinic symmetry for $1.8 < x < 2.2$. Its framework can be described as a rigid skeleton constituted by $(Si,P)O_4$ tetrahedra and ZrO_6 octahedra (*8, 9, 12*). The Na^+ ions are placed in the interstices of this skeleton and occupy several kinds of sites whose size is perfect for the sodium ion. Sodium ions move in this skeleton structure

*To whom correspondence must be addressed.
[1] Present address: Centro Atomico Bariloche, 8400 SC de Bariloche, Argentina.

0003-2700/91/0363-2550$02.50/0

through narrow bottlenecks, also perfectly sized. The ionic conductivity is therefore assumed to be three-dimensional. Its maximum is obtained for about $x = 2$ (*13*). For this reason, we have chosen the stoichiometric composition $Na_3Zr_2Si_2PO_{12}$ to make ion-sensitive membranes.

The adjustment of conduction sites promotes sodium ion crossing in regard to potassium which is too big or lithium which is too small and tends to fix itself on the edge of the sites. Considering the selectivity phenomenon from a kinetics viewpoint, the exchange current of sodium should be greater than that of the interfering potassium or lithium because of this geometrical reason. The first results obtained on NASICON sintered by the traditional route have been very promising (*14*, *15*). The selectivity characteristics of NASICON pellets were better than those of a sodium aluminosilicate glass.

It was also shown (*14*) that the densification of sintered pellets is an essential criterion: below about 90–95% compactness, the open porosity leads to an ionic short circuit by the aqueous solution which penetrates into the bulk toward the internal reference system. If this system is based on a silver salt, the sensor will also respond to other ions, for instance Cl^-. The classical ball-milling route used to prepare polycrystallized NASICON ceramic does not allow us to obtain high-density materials. A densification of about 100% can be obtained by hot pressing; however this process is not easy to carry out.

The sol–gel route using organo-metallic precursors is now a common procedure for ceramic preparation (*16*). It was applied to NASICON preparation in the 80's with many processes (*17–21*). As a principal advantage, it easily gives very fine powders. Therefore, the sintering temperature can be lowered considerably, avoiding the ZrO_2 formation observed when the sintering temperature is higher than 1150 °C in air (*10*, *22–25*). In the present work, we will report some performance characteristics of an Na^+ ISE based on NASICON ceramics prepared by the sol–gel route.

EXPERIMENTAL SECTION

(1) Synthesis and Physicochemical Characterization of NASICON Ceramics. Among the different published processes, we have chosen the route proposed by Colomban (*21*). The starting materials $Si(OC_2H_5)_4$ and $Zr(OC_3H_7)_4$ were provided by Alpha Ventron and NaOH and $NH_4H_2PO_4$ by Fluka. A mixture of $Si(OC_2H_5)_4$ and $Zr(OC_3H_7)_4$ diluted in C_3H_7OH was hydrolyzed by an aqueous solution containing NaOH and $NH_4H_2PO_4$. Additional water was introduced in excess to complete the hydrolysis of Si and Zr alkoxides. All the solutions were preheated to approximately 60–80 °C before the hydrolysis step. As this reaction is very fast, the reagents must be added quickly.

Some modifications were introduced to the route proposed by Colomban, the essential being a washing with acetone to eliminate water (*26*) and to avoid the formation of hard agglomerates. This procedure allows us to recover a greater quantity of powder and to eliminate the screening step (*21*). After this washing, the powder is dried under a primary vacuum at 200 °C. The very fine powder was then prepressed at 500 bars in a double-punch die and finally pressed isostatically at 4000 bars for severals tens of minutes.

The green densities (before sintering) obtained at this step were 70% of the theoretical value, which is 3.26 $g \cdot cm^{-3}$. The sintering at different temperatures (between 800 and 1250 °C) was carried out at a heating rate of about 100 °C/h with one step of 3–4 h at 380 °C. The sintering time was 2 h for most of the samples, and the atmosphere was air. For sintering temperatures lower than 1100 °C, the samples were covered with platinum foil to reduce Na^+ departure and accidental contamination in the furnace. For temperatures higher than 1100 °C, some samples were sintered in a sealed platinum capsule. The final dimensions were about 1 cm^2 in area and 2 or 3 mm in thickness.

In order to determine the sintering conditions, the shrinkage as a function of the temperature was determined by an Adhamel dilatometer using cylinders of 5 mm in diameter and 15 mm in length. Figure 1 shows the shrinkage of NASICON samples for a normalized y axis defined by

$$(l_o - l)/(l_f - l_o) \qquad (1)$$

where l is the length at a given temperature, l_o and l_f respectively, the initial and final length. The heating rate was 100 °C/h. A small expansion was observed near 100 °C probably due to the residual water departure. The maximum shrinkage occurs at 850 °C.

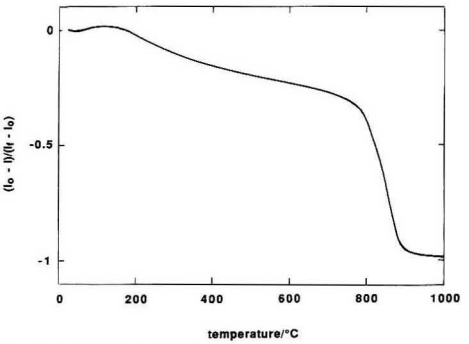

Figure 1. Shrinkage vs temperature curve for NASICON ($x = 2$).

After the sintering procedures, we obtained highly dense samples, with a compactness generally higher than 97%, even at low sintering temperatures (800 °C).

To identify the crystallized form, X-ray analysis was performed with an X-ray powder diffractometer using Cu Kα radiation. Ultrapure silicon was used as a standard element. The lattice parameters were smoothed by means of a square regression program.

Electrical conductivity measurements were determined by the complex impedance method using a Hewlett Packard 4192 impedance analyzer controlled by a Hewlett Packard 9845 computer. Carbon blocking electrodes as well as platinum electrodes were used. No differences in the complex impedance spectra were observed between these two types of electrodes in the high-frequency range characteristic of the material.

(2) Electrochemical Characterization. The kinetics of Na^+ ion exchange between NASICON and aqueous solutions and the interface behavior in the presence of interfering ions such as K^+, Li^+, and Ca^{2+} were studied by four electrode impedance measurements. This technique is well suited to the study of ion-transfer reactions in ion-selective electrodes (*27–29*). The NASICON sample was symmetrically submerged in buffered aqueous solutions (Tris-8 from Tacussel), and impedance measurements were performed after a controlled soaking time. Before being contacted with the solution, the solid electrolyte surface was polished with successive waterproof silicon carbide papers and diamond paste down to 1 μm. The experimental setup and the impedance measurement conditions have been reported in detail in ref *30*.

(3) Preparation of Ion Sensors and Experimental Conditions. Sintered NASICON was used in two types of ion sensors: (a) traditional devices with a liquid internal reference which can be represented by the following electrochemical chain

$$Ag/AgCl/NaCl\ 0.1\ M,\ pH\ 8/NASICON/$$

(b) solid-state devices with a polymer (POE) as an internal ionic bridge (*31*)

$$Ag/POE\ (AgI_x^{(x-1)-},\ Na^+,\ I^-)/NASICON/$$

For the last case we can also use an internal reference system based on copper (*31*). Schematic diagrams of the sensors are represented on Figure 2. The performance characteristics of the sensors for a given NASICON sample were identical whatever the device.

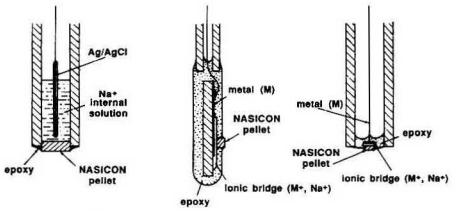

Figure 2. Na^+ sensor devices.

All tests were made in buffered solution (Tris-8, from Tacussel), except for the study of proton interference. Since its ionic strength is not very high (2×10^{-2}), for the high concentrations a corrective calculation is necessary. The activity coefficient was approximated by the Debye–Huckel theory.

To avoid any K^+ contamination from the saturated calomel electrode (SCE), we used double junctions. For the determination of the detection limit, the intermediate solution was identical to the working solution. For the interference study, it consisted of the initial solution.

The detection limit was determined graphically by the intersection between the Nernst straight line and the horizontal asymptote, as it is generally defined (*2*). The experimental points were determined from standard solutions obtained by successive dilutions from a mother solution at 1 mol/L NaCl. To avoid any contamination from the concentrated solution, the measurements were made by increasing the concentrations. The time required to reach steady-state conditions was long for the small concentrations and we systematically waited 15–30 min for each point.

The selectivity coefficients of interfering ions were determined from the extended Nernst equation

$$E = E^\circ + RT/F \ln (a_{Na} + K^{pot}_{Na/i}(a_i)^{1/zi}) \quad (2)$$

where E° is a constant, a_{Na} and a_i are respectively the activity of sodium and interfering ion i^{zi+}, and $K^{pot}_{Na/i}$ is the selectivity coefficient relative to the i^{zi+} ion.

Two different methods were used: (a) The *separate solution method* is well-known (*32*); we have followed the traditional procedure. It is advantageous because it is very fast and simple. We will discuss its suitability later on. It nevertheless gives a rapid comparison between several sensors. (b) A *fixed primary ion concentration* (*32*) (Na^+) is provided during the measurement by adding a solution containing the interfering ion at high concentration and the primary ion at the same initial concentration. The concentration of primary ion is then a constant. The interfering ion concentration C_i is calculated by dilution of the added volume into the initial volume of the primary solution. The activity values can be calculated from the concentrations by the Debye Huckel approximation.

The Nickolskii relation can be approximated by two asymptote equations corresponding to the following limit cases:

$$a_{Na} \gg K^{pot}_{Na/i}(a_i)^{1/zi}: \quad (3)$$

$$E(\mathrm{Na}) = E^\circ + RT/F \ln (a_{Na}) \quad (4)$$

which is a horizontal asymptote for a given value of a_{Na},

$$a_{Na} \ll K^{pot}_{Na/i}(a_i)^{1/zi}: \quad (5)$$

$$E(i) = E^\circ + RT/ziF \ln (a_i) + RT/F \ln (K^{pot}_{Na/i}) \quad (6)$$

which is the Nersnt's law asymptote for the interfering ion.

For the particular case

$$a_{Na} = K^{pot}_{Na/i}(a_i)^{1/zi} \quad (7)$$

the voltage is given by the relation

$$E(1/2) = E^\circ + RT/F \ln (a_{Na}) + RT/F \ln (2) \quad (8)$$

The theoretical shift between $E(1/2)$ and $E(\mathrm{Na})$ is 18 mV at room temperature.

If these theoretical relations hold experimentally, the selectivity coefficient can be easily determined from the abscissa of the intersection of the two asymptotes. It is nevertheless necessary to verify that the shift value is equal to 18 mV at this point.

When the selectivity coefficients are too small, the interfering ion concentration necessary to observe a deviation on the voltage is too high and the proposed corrections are not accurate enough. In this case, the selectivity coefficient is better determined from the point on the curve corresponding to a shift of 18 mV relative to the $E(\mathrm{Na})$ value. This limiting value is generally recommended (*32*). A more accurate determination can be made by evaluating the Na^+ activity coefficient (γ) as a function of the ionic strength. As a first approximation, this value can be calculated from the concentration determined on the curve at the 18 mV point. The difference between $E(1/2)$ and $E(\mathrm{Na})$ is then equal to

$$\Delta E = RT/F \ln (1 + \gamma) \quad (9)$$

which is equivalent to the difference between eqs 8 and 4 if $\gamma = 1$. An iteration is theoretically necessary to calculate this value, but it converges quickly: generally, just one loop is sufficient.

Table I. Lattice Parameters (Å) of NASICON ($x = 2$) Sintered at Different Temperatures (T_s)

T_s = 903 °C	T_s = 1000 °C	T_s = 1150 °C[b]	T_s = 1200 °C[b]
a_r = 9.046 ± 0.005	a_r = 9.044 ± 0.005	a_m = 15.63 ± 0.03	a_m = 15.64 ± 0.01
		b_m = 9.05 ± 0.02	b_m = 9.053 ± 0.005
c_r = 22.88 ± 0.01	c_r = 22.95 ± 0.01	c_m = 9.24 ± 0.03	c_m = 9.223 ± 0.008
		β = 123.7 ± 0.1	β = 123.65 ± 0.05

[a] For 903 and 1000 °C, the quoted parameters correspond to the rhombohedral structure (a_r, c_r) and to the monoclinic structure for 1150 and 1200 °C (a_m, b_m, c_m, β); see ref 34. [b] Sealed capsule.

RESULTS AND DISCUSSION

(1) Structural and Electrical Properties of NASICON Membranes. NASICON $x = 2$ composition has been reported to be monoclinic at room temperature. However, when the sol–gel process is used (*25*), rhombohedral symmetry can be obtained if the processing temperature is lower than 1100 °C and monoclinic symmetry is observed for temperatures higher than 1100 °C.

As we have quoted, we have obtained highly dense samples even for processing temperatures of 800 °C. However the NASICON framework is not developed at this temperature since X-ray diffraction patterns show only traces of tetragonal zirconia. The NASICON framework is formed from processing temperatures of 900 °C.

For sintering temperatures of 903 and 1000 °C, the symmetry is rhombohedral, while for 1200 °C (sintering for 72 h in a sealed platinum capsule) it is monoclinic. For intermediate temperatures such as 1150 °C, both phases are present but the symmetry seems to be mainly monoclinic (see Table I). The values of the lattice parameters of the monoclinic form agree with those determined in a recent study of the structure of a NASICON single crystal (*33*) (for structural description of these symmetries, see ref 34).

To simplify the making of ion sensors, we also characterized some samples sintered at 1200 °C in air atmosphere. As quoted in the literature, we also observed a zirconia phase.

Table II summarizes the conductivity values at room temperature and the activation energy determined in the temperature interval 20–140 °C.

The sample processed at 800 °C is a poor conductor while all samples processed at higher temperatures have approximately the same value of conductivity, except the one sintered at 1200 °C in air, which has a conductivity 10 times lower. This value is certainly due to the zirconia phase, which is an insulator at room temperature. The impedance diagrams of samples sintered at 1200 °C are constituted by two semicircles

Table II. Values of the Ionic Conductivity at Room Temperature and the Activation Energy Determined within the Temperature Range 20–140 °C for NASICON ($x = 2$) Sintered in Air[a]

sint temp, °C	ionic conductivity Ω^{-1} cm^{-1} (at 25 °C)	activation energy, eV
806	2.17×10^{-8}	0.66
915	5.74×10^{-4}	0.37
1000	8.43×10^{-4}	0.34
1074	9.03×10^{-4}	0.38
1141[b]	8.6×10^{-4}	0.36
1200	5.31×10^{-5}	0.24
	(8.34×10^{-4})	(0.34)

[a] The values quoted in parentheses correspond to the pure phase for NASICON sintered in air at 1200 °C (see text).
[b] Sealed capsule.

equivalent to two resistance–capacitance (RC) circuits in series. The high-frequency semicircle (characteristic frequency of about 2 MHz) corresponds to the pure NASICON phase, and the lower frequency semicircle (characteristic frequency of about 13 kHz) corresponds to the poor conductor phase. The conductivity characteristics determined from the high-frequency semicircle are very similar to the pure NASICON characteristics (see Table II). Such a phenomenon was not observed on other samples; impedance diagrams were constituted of one semicircle with a characteristic frequency of about 1 MHz.

(2) Stability in Water. Studies of NASICON stability in water (*10*, *11*) have been essentially qualitative; few quantitative observations have been made, except in the work of Ahmad et al. (*24*) comparing the behavior of NASICON samples of different compositions obtained from different processes at high sintering temperatures ($T > 1150$ °C).

We have observed the membrane surface by scanning electron microscopy (SEM) after a treatment in boiling water to determine the destroying effect. The samples were first polished. Micrographs have shown the difference, after water treatment for 1 h, between a sample sintered at 806 °C and another sintered at 915 °C. The phase processed at about 800 °C is not stable in water; on the other hand, for the samples sintered at about 900 °C and higher, no macroscopic effect was observed.

We have made a qualitative study of the behavior of NASICON in water by introducing powder in distilled water. The conductivity, pH, and pNa of the aqueous solution were measured simultaneously. Unfortunately, no quantitative correlation was observed between the values to establish a model. Nevertheless, we can draw some qualitative conclusions: (a) the pNa value tends slowly toward a limit (the Na^+ concentration is about $(1–6) \times 10^{-3}$ mol/L, dependent on the sintering temperature) which is not a function of the powder quantity. This observation shows the existence of a solubility product effect; (b) as the sintering temperature increases, the dissolution process decreases; (c) the noncrystallized material obtained below 900 °C is clearly more soluble and cannot be used for sensor making; (d) the pH value becomes always quickly basic.

From these first results, two phenomena are evidenced: a solubility product effect and a proton fixation. To determine a model, other experiments must be conducted.

(3) NASICON/Solution Interface. (*a*) *Na^+ Ion Transfer: Influence of the Sintering Temperature of NASICON.* It has been shown that when NASICON is contacted with a NaCl solution, the impedance diagram in the frequency range 65 kHz to 10^{-2} Hz shows only one semicircle which can be related to the Na^+ ion transfer across the interface (*30*). The process is equivalent to a resistance in parallel with a capacitance. In the present work, the impedance was measured in 0.1 M NaCl solutions for the various NASICON samples sintered at 800, 900, 1000, 1074, and 1150 °C. For the samples sintered at 800 °C, the interface resistance was too small compared to the ohmic drop to be measured. The impedance diagram was somewhat related to the bulk properties of NASICON since the conductivity of the sample was very low.

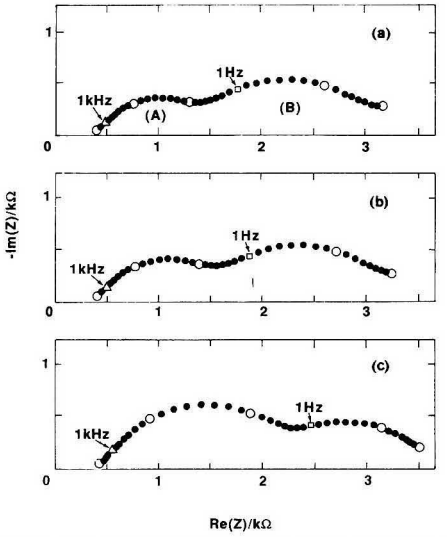

Figure 3. Change in the impedance diagram with the soaking time in 0.01 M NaCl + 1 M KCl solution (Tris): (a) 1 h 40 min; (b) 2 h 50 min; (c) 18 h 40 min. The empty dots represent the frequency decades.

At temperatures higher than 900 °C, the interface semicircle can be observed. No trend as a function of the sintering temperature was evidenced. The impedance data do not vary significantly. The order of magnitude of the polarization resistance was 25 Ω·cm^2, and that of the capacitance was 1 μF·cm^{-2}.

(*b*) *Na^+ Exchange in the Presence of Interfering Ions.* When the membrane was contacted with solutions containing other cations such as K^+, Li^+, or Ca^{2+} the general form of the impedance diagram was modified. The interface impedance increased and a second low-frequency semicircle, which was hardly noticeable with NaCl solution, could be observed clearly for all our polished samples. Figure 3 gives an example of impedance diagrams for a membrane in a 10^{-2} M NaCl solution in which K^+ ions were added so that their concentration was raised to 1 M. The impedance spectra variations were monitored as a function of the soaking time for 19 h. The resistance of the high-frequency semicircle (A) increases roughly as the square root of time. By the end of the experiment, the resistance had increased by a factor of 5 and the capacitance by a factor of 10. The second semicircle reaches a steady-state more rapidly.

A study as a function of the K^+ concentration in 10^{-2} M NaCl was performed. The interface impedances are reported in Figure 4. For comparison, they were measured after the same time of immersion (1 h). A significant influence was noticed as soon as the K^+/Na^+ ratio reached 1.

At the end of the experiment, the 10^{-2} M NaCl + 1 M KCl solution was removed and replaced by the original 10^{-2} M NaCl solution (containing no K^+ ions). The impedance was measured immediately. The resistance of the first semicircle

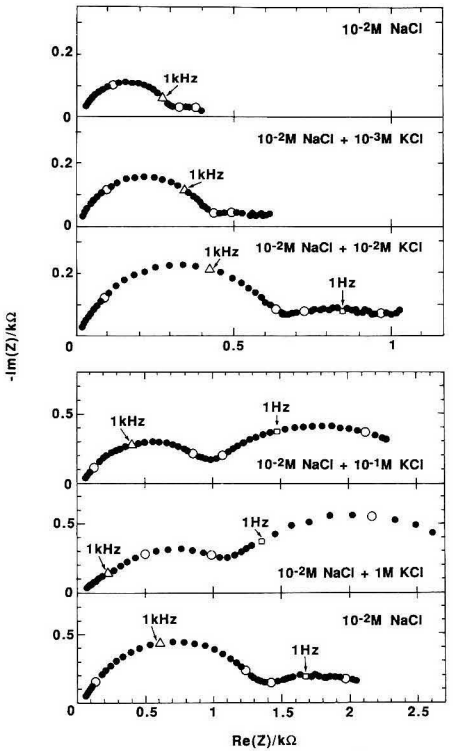

Figure 4. Change in the impedance diagram with the K^+ concentration in 0.01 M NaCl solution (Tris).

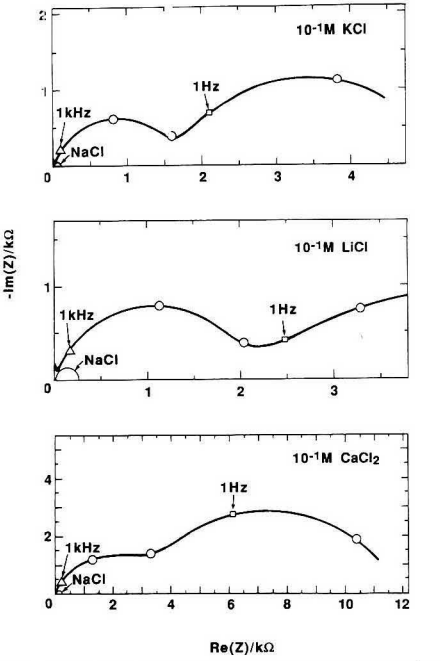

Figure 5. Change in the impedance diagram as a function of interfering ions. The fine continuous lines represent the diagram obtained with 0.1 M NaCl.

(A) was of the same order of magnitude and then diminished slowly whereas the second semicircle (B) disappeared immediately. Polishing the surface of the membrane allowed faster recovery of the initial size of the first semicircle. We concluded that the change in size of the high-frequency semicircle was caused by a process occurring in NASICON. Na^+ substitution by K^+ ions on the Na sites in NASICON may partially block the Na^+ exchange, resulting in an increase of the polarization resistance. The second semicircle can be related to the interfering cation present in the solution.

When the membrane was contacted with a pure 0.1 M KCl solution, the interface impedance increased, but the general form of the impedance diagrams was not modified. In similar experiments with other kinds of ISE membranes, Xie et al. (*28*) have observed only one semicircle attributed to the interfering ion transfer across the interface. Our impedance spectra indicate that the mechanism is more complex. Indeed, contact with aqueous KCl causes the Na^+ ions in the membrane to be exchanged for K^+ so that Na^+ ions are present in the solution near the surface. The resulting impedance spectra are similar to the preceding ones. A study as a function of the sintering temperature shows that the lowest polarization resistance (R_p) was obtained for the samples sintered at 1150 °C.

Comparison of the impedance spectra for the various cations (0.1 M KCl, 0.1 M LiCl, 0.1 M $CaCl_2$) shows that the general form of the diagram was the same for all the tested solutions (cf. Figure 5). Whatever the nature of the interfering ion, the resistance of the first semicircle is approximately of the same order of magnitude (10–20 times higher than the initial value), whereas the resistance of the second loop was dependent on the nature of the interfering cation. In the case of K^+ or Ca^{2+} interfering ions, the polarization resistance (R_p) is about 100 times higher than that obtained for a membrane contacted with the same concentration of Na^+ ions. For Li^+ ion, an accurate evaluation is difficult.

(4) Performance Characteristics of Na^+ Sensors. (*a*) *Detection Limit.* The detection limits were determined for several NASICON samples sintered at different temperatures: 800, 900, 1000, 1150, and 1200 °C. The experimental results are respectively 1×10^{-2}, 8×10^{-4}, 1.6×10^{-4}, 2.5×10^{-4} and $(3–6) \times 10^{-4}$ mol/L. For comparison, the detection limit of a commercial PNAV electrode (from Tacussel) measured simultaneously was 2×10^{-5} mol/L.

The highest value for the samples sintered at 1200 °C was obtained for the sample sintered in the sealed platinum capsule. Note that this value is similar to the one which was obtained with the sample processed by ball-milling (*14*). The optimal value corresponds to the sample sintered at about 1000 °C. With one sample immerged several hours in boiling water, the limit was slightly better (1×10^{-4} mol/L), but this improvement is not very significant. On the other hand, we have observed a sample densification influence: for 1150 °C the limit was 1×10^{-4} mol/L for 99% and 2.7×10^{-4} mol/L for 90% densification, for a sample sintered at 1200 °C it was 1.5×10^{-4} mol/L for 90% and 3.2×10^{-4} mol/L for 85% densification.

For low sintering temperature (800 °C), the high value obtained is due to the unstability of this membrane in water, and the theoretical Nernst slope is founded only near 1 mol/L. This result agrees with the qualitative solubility study, but the correlation between the pNa measured in this study and

Table III. Logarithm of Selectivity Coefficients as a Function of the Sintering Temperature Determined by the Fixed Primary Ion Concentration Method[a]

interf ion	sint temp, °C 900	1000	1150	1200	PNAV	preceding results (*14*)
K^+		−2.52 to −4.22	−2.22 to −2.6	−2.6 to −3.22	−1.26 to −1.52	−1.82
	(−1.74)	(−2.52 to −3.52)	(−1.26)	(−1.27 to −1.36)	(−0.92 to −1.1)	
Li^+		−2.7 to −3	−2.3 to −2.47	−2.64	−1.7 to −2	−1.8
	(−1.4 to −1.52)	(−1.1 to −1.92)	(−1 to 1.3)	(−1.4 to −1.7)	(−1.59 to −1.7)	
Ca^{2+}		−3.34	−3.33 to −3.52	−3.62	−3.4	−1.66
	(−2)	(−1.7 to −2.4)	(−1.52)	(−2.46)		
NH_4^+		−3.82		−2.51	−2.15 to −2.22	
H_3O^+		+0.84 to +1.7	+0.6 to +1	+0.48 to +0.6	+1.76 to +1.9	0.3

[a] The values quoted in parentheses were obtained by the separate solution method.

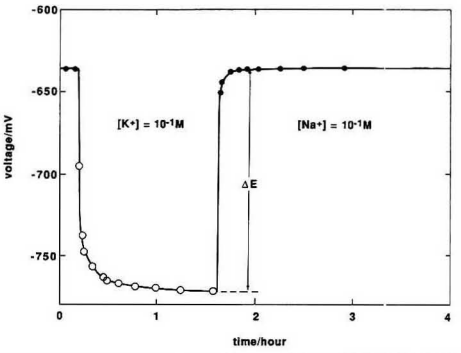

Figure 6. Determination of selectivity coefficient of NASICON (1100 °C) for K^+ interfering ions (separate solution method).

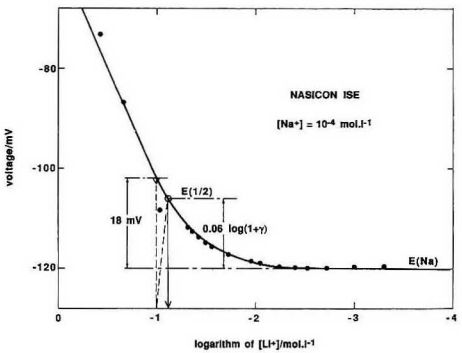

Figure 7. Determination of selectivity coefficient of NASICON (1000 °C) for Li^+ interfering ions (fixed Na^+ concentration): voltage vs Li^+ concentration.

the detection limit is not obvious, certainly due to kinetics phenomena in the vicinity of the NASICON/solution interface. In the solubility study of NASICON powder, the area of the interface was very much greater than that of the sintered sample in ISE testing and the time scale was also much higher. The exchange between powder and water is certainly faster. This point is in agreement with the detection limit observed for poorly densified NASICON samples which have a greater interface area.

(*b*) *Selectivity.* The selectivity coefficients determined by the separate solution method for $a_{Na} = 10^{-1}$ are quoted in Table III. For comparison, the results obtained for a commercial PNAV electrode (from Tacussel) are reported. An example of determination is given on Figure 6. We can observe a response to interfering ion which is very slow (empty dots). The corresponding response time (about 1 hour) is higher than that obtained when the membrane is contacted again with sodium ions (full dots on Figure 6). This phenomenon is certainly due to a poisoning effect by the interfering ions since the real response time to sodium (measured with a double jet setup) is equal to a few tens of milliseconds (*35*).

For the proton, the values obtained with this method showed poor reproducibility and were too high (the scale was between 10 and 100).

Depending on the experiment, the values fluctuated for the same NASICON sample. They increased as the NASICON aged; for instance for a sample sintered at 1000 °C, $K^{pot}_{Na/i}$ became 1×10^{-1} after 1400 h in aqueous solution while the initial value was 3×10^{-3} (simultaneously, the detection limit decreased slightly). An analogous phenomenon has been observed for lithium interfering ions.

Measurements were made with dry sensors just after introducing them into the solutions and were compared with those obtained after 30 h in distilled water. We observed no influence of moistening on the responses and the measurements on different electrodes were reproducible to within about 10%.

Note that the selectivity coefficients determined with this method are of the same order of magnitude as the polarization resistance ratios already described.

Table III summarizes also the selectivity coefficients measured by the fixed primary ion concentration method (an example of determination is given on Figure 7). All the measurements were made for a Na^+ concentration equal to 10^{-4} mol/L except for the H_3O^+ interference, which was studied with solutions containing 10^{-2} mol/L of Na^+. The surface of the samples was polished with silicon carbide before each measurement series in order to eliminate the influence of the ageing phenomenon observed when samples were contacted with a solution for a long time.

The different values quoted in the same box correspond to sensors made with different NASICON samples obtained from identical processes. The NASICON pellets were all sintered in air for the results mentioned here. For comparison we have also quoted the preceding results obtained with a sample processed by ball-milling (*14*). The determination method was similar to this one, but the Na^+ concentration was higher (10^{-2} mol/L). For our new measurements, we have preferred to use more diluted solutions (Na^+ concentration = 10^{-4} mol/L) to avoid excessive interfering ion concentrations. Some determinations were made also for 10^{-3} mol/L, but the results were very similar. For the proton, the sodium concentration is higher because the interfering effect is greater and it is necessary to obtain the horizontal asymptote for the determination.

If we compare the results, we can see that the values de-

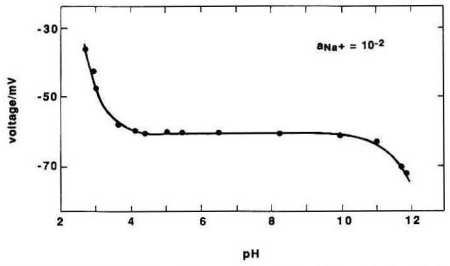

Figure 8. Change of the voltage as a function of the solution pH for NASICON (1150 °C).

termined by the separate solution method are always higher. This observation is in agreement with the results obtained by Gadzekpo et al. (*36*) on another ISE. This can be explained by the main difference between the two methods: in the first, the interfering ion is present alone and only the thermodynamical aspect of selectivity is taken into account (assuming that there are no sodium ions in the solution). In reality, the sodium activity was fixed by the solubility phenomenon and it was not well-known. In the second method, there is a real concurrence between the different ions and the kinetics aspect must be considered. The values obtained by the second method are more accurate.

From our results, we can conclude that the selectivity of NASICON material is always better than that of a glass membrane. The selectivity with respect to K^+ and Li^+ interfering ions is improved by at last a factor of 10. For Ca^{2+}, similar performance is obtained.

A slight sintering temperature influence is observed, 1150 °C giving often the worst results. This phenomenon could be attributed to the existence at this temperature of both phases (monoclinic and rhombohedral) which create nonhomogeneous grain boundaries, leading to a performance similar to that of glass. On the other hand, for the single-phased samples, a very significant difference in selectivity has not been found, except for NH_4^+ which seems slightly more interfering with the monoclinic symmetry (sintered at 1200 °C). Indeed, the variations of these selectivity coefficients are not sufficiently significant and the sizes of conduction sites too similar to support seriously an accurate model of selectivity based on structural considerations.

For proton interference, the influence of the sintering temperature is clearly demonstrated: the lower the sintering temperature, the higher the interference phenomenon which becomes similar to that of the glass electrode. We explain this result by the existence of residual M–OH groups from the sol–gel route. These groups can be sensitive to the protons in the same way as are the silanol groups involved in the pH sensitivity of SiO_2. As mentioned by Guizard (*37*), these are very numerous and difficult to eliminate from powders obtained by the sol–gel process. Engell et al. (*20*) have indicated, from TG and DTA analyses, that the last OH groups are not released from NASICON gel until a temperature between 900 and 1000 °C. From our results, it seems necessary to reach temperatures higher than 1000 °C, for instance around 1150 °C, to clear a NASICON pellet of these groups. In this case, the selectivity coefficient becomes equal to a few unities only, constituting a good improvement. The pH range for the use of NASICON as an ion-sensitive material is then clearly larger than for a glass electrode in an acid medium. This result is in agreement with our first results obtained with NASICON processed by ball-milling and sintered at 1250 °C (*14*). Nevertheless, as is shown in Figure 8, the sensor responses became erroneous in basic media at pH values higher than 10. This is attributed to a deterioration of NASICON in this medium.

CONCLUSION

The sol–gel route is a very effective process for making high-density ceramic samples, for instance for densification to more than 90% which is necessary to make ion-sensitive membranes for ISEs. The results with NASICON are better than those obtained previously on a sample processed by the ball-milling method. The detection limit is not very low, somewhat poorer than the one for an alumino–silicate glass membrane, but it is sufficient for instance for biomedical and food industry applications or Na^+ monitoring in drinking water. The selectivity coefficients are better with a NASICON membrane, especially for interfering alkaline ions. The selectivity assumption based on the size of conduction sites at the interface between the membrane and the aqueous solution can be considered to hold qualitatively, except for proton interference. The latter is probably due to the surface OH groups, similar to silanol groups, which are sensitive to the pH.

The choice of the sintering temperature is a function of the pH zone of the working medium in analysis applications. For a neutral pH, 1000 °C is a sufficient temperature allowing better selectivity with respect to potassium and lithium interfering ions. For an acid medium, 1200 °C is the best temperature. The nature of the sintering atmosphere (air or closed platinum) does not seem to be important. Only the membrane impedance is slightly increased. The selectivity coefficients are not very affected by this heat treatment, but the detection limit is slightly modified.

The intermediate sintering temperature (1150 °C) appears to be a bad compromise, since the selectivity coefficients are the highest for alkaline interferences, whatever the determination method. The correlation between the interference coefficient and the impedance data of primary and interfering ions is not obvious for NASICON membranes. Indeed, the impedance diagram for a membrane immersed for 1 h in an aqueous solution of the interfering ion is made of two semicircles. The ratios between the polarization resistances of primary and interfering ions do not correspond accurately to the selectivity coefficient values, but the order of magnitude is similar and the conclusion on the choice of the sintering temperature is confirmed.

ACKNOWLEDGMENT

We gratefully acknowledge the contributions of B. Bochu (X-ray analysis), J. Garden (SEM observations), M. Henault (technical assistance on ceramic elaboration), and M. Chalaron (manuscript typewriting). We also wish to thank P. Colomban and J. P. Boilot (Ecole Polytechnique de Palaiseau, France) for their advices on the sol–gel route.

LITERATURE CITED

(1) Koryta, J.; Stulik, K. *Ion-Selective Electrodes*; Cambridge University Press: Cambridge, U.K., 1983.
(2) Morf, W. E. *The Principles of Ion-Selective Electrodes and of Membrane Transport*; Elsevier: New York, 1981.
(3) Covington, A. K. *Ion Selective Electrode Methodology*; CRC Press: Boca Raton, FL, 1979.
(4) Frant, M. S.; Ross, J. W., Jr. *Science* **1966**, *154*, 1553.
(5) Pungor, E.; Hollos-Rokosinyi, E. *Acta Chim. Hung.* **1981**, *27*, 63.
(6) Fabry, P.; Gros, J. P.; Kleitz, M. Symposium on Electrochemical Sensors, Rome, June 12–14, 1984.
(7) Kleitz, M.; Million-Brodaz, J. F.; Fabry, P. *Solid State Ionics* **1987**, *22*, 295.
(8) Hong, H. Y. P. *Mater. Res. Bull.* **1976**, *11*, 173.
(9) Goodenough, J. B.; Hong, H. Y. P.; Kafalas, J. A. *Mater. Res. Bull.* **1976**, *11*, 203.
(10) Miller, G. R.; McEntire, B. J.; Hadnagy, T. D.; Rasmussen, J. R.; Gordon, R. S.; Virkar, A. V. In *Fast Ion Transport in Solids*; Vashista, P., Mundy, J. N., Shenoy, G. K., Eds.; Elsevier: Amsterdam, 1979; p 83.
(11) Auborn, J. J.; Johnson, D. W., Jr. *Solid State Ionics* **1981**, *5*, 315.
(12) Kohler, H.; Schulz, H. *Mater. Res. Bull.* **1985**, *20*, 1461.
(13) Tran Qui, D.; Capponi, J. J.; Gondrand, M.; Saib, M.; Joubert, J. C. *Solid State Ionics* **1981**, *3–4*, 219.

(14) Fabry, P.; Gros, J. P.; Million-Brodaz, J. F.; Kleitz, M. *Sens. Actuators* **1988**, *15*, 33.
(15) Engell, J. E.; Mortensen, S. Radiometer Int. Patent WO 84/01829, 1984.
(16) Zelinski, B. J. J.; Uhlmann, D. R. *J. Phys. Chem. Solids* **1984**, *45*, 1069.
(17) Quon, D. H. H.; Wheat, T. A.; Nesbitt, W. *Mater. Res. Bull.* **1980**, *15*, 1533.
(18) Gordon, R. S.; Miller, G. R.; McEntire, B. J.; Beck, E. D.; Rasmussen, J. R. *Solid State Ionics* **1981**, *3-4*, 243.
(19) Bollot, J. P.; Colomban, Ph.; Blanchard, N. *Solid State Ionics* **1983**, *9-10*, 639.
(20) Engell, J.; Mortensen, S.; Moller, L. *Solid State Ionics* **1983**, *9-10*, 877.
(21) Colomban, Ph. *Ceram. Int.* **1989**, *15*, 23.
(22) Bayard, M. L.; Barna, G. G. *J. Electroanal. Chem. Interfacial Electrochem.* **1978**, *91*, 201.
(23) Lloyd, I. K.; Gupta, T. K.; Hall, B. O. *Solid State Ionics* **1983**, *11*, 39.
(24) Ahmad, A.; Wheat, T. A.; Kuriakose, A. K.; Canaday, J. D.; McDonald, A. G. *Solid State Ionics* **1987**, *24*, 89.
(25) Colomban, Ph. *Solid State Ionics* **1986**, *21*, 97.
(26) Bernier, J. C. GRECO Précurseurs Moléculaires de Matériaux Inorganiques 93. Procédés SOL-GEL, Bombannes, France, Sept 28-Oct 2, 1987; Part II.
(27) Buck, R. P. *Ion-Sel. Electrode Rev.* **1982**, *4*, 3.
(28) Xie, S.; Camman, K. In *Ion-Selective Electrodes 5*; Pungor, E., Ed.; Pergamon Press: New York, 1989; p 639.
(29) Armstrong, R. D. *Electrochim. Acta* **1987**, *32*, 1549.
(30) Siebert, E.; Caneiro, A.; Fabry, P.; Levy, M. *J. Electroanal. Chem. Interfacial Electrochem.* **1990**, *286*, 245.
(31) Fabry, P.; Montero-Ocampo, C.; Armand, M. *Sens. Actuators* **1988**, *15*, 1.
(32) Macca, C.; Cakrt, M. *Anal. Chim. Acta* **1983**, *154*, 51.
(33) Bollot, J. P.; Collin, G.; Colomban, Ph. *Mater. Res. Bull.* **1987**, *22*, 669.
(34) Schmid, H.; De Jonghe, L. C.; Cameron, C. *Solid State Ionics* **1982**, *57*, 6.
(35) Attari, M. Thesis, Université J. Fourier, Grenoble, France, 1991.
(36) Gadzekpo, V. P. Y.; Christian, G. D. *Anal. Chim. Acta* **1984**, *164*, 279.
(37) Guizard, G.; Larbot, A.; Cot, L. GRECO Précurseurs Moléculaires de Matériaux Inorganiques 93. Procédés SOL-GEL, Bombannes France, Sept 28-Oct 2, 1987; Part I.

RECEIVED for review January 2, 1991. Accepted August, 12, 1991.

Comparison of Fourier Self-Deconvolution and Maximum Likelihood Restoration for Curve-Fitting

Richard S. Jackson[1] and Peter R. Griffiths*

Department of Chemistry, University of Idaho, Moscow, Idaho 83843

The advantages of combining deconvolution and curve-fitting for the analysis of spectra with heavily overlapped bands in the presence of noise and baseline errors are examined. Two methods of deconvolution are used, namely Fourier self-deconvolution (FSD) and maximum likelihood restoration (MLR). It is shown that for spectra with heavily overlapped bands and baseline errors there is an improvement in the conditioning if spectra are deconvolved prior to curve-fitting, so that more accurate band parameters are derived. This result is true for both FSD and MLR, but it is more difficult to determine the optimum degree of deconvolution when MLR is used. The combination of deconvolution and curve-fitting also allows the objective optimization of the parameters used in either FSD or MLR.

INTRODUCTION

In a recent paper (*1*) we reported the advantages of curve-fitting unresolved or poorly resolved spectra for which the natural peak widths had been reduced using Fourier self-deconvolution (FSD). It was shown that the combination of FSD and subsequent least-squares curve-fitting allowed objective optimization of the parameters used in FSD, assisted in the determination of the number of bands, and significantly improved the mathematical conditioning of the curve-fitting when compared with fitting the original spectrum. This last advantage is perhaps the most significant, since curve-fitting is inherently ill-conditioned and even small errors in the input data or the assumptions can lead to very large errors in the fitted parameters (*2-6*). In our initial studies the synthetic spectra used were all noise free; in this paper those studies have been extended to include the effects of noise.

* To whom correspondence should be addressed.
[1] Current address: Mattson Instruments, Inc., Madison, WI 53717.

Two methods of deconvolution, FSD and maximum likelihood restoration (MLR), are compared in this paper. The method used for FSD was the same as that described in the first paper and was originally developed by Kauppinen et al. (*7, 8*). The application of MLR to this problem was also studied because MLR deals explicitly with noise and has been shown to provide greater resolution enhancement than FSD if the spectrum has a moderate or high noise level (*9, 10*).

Fourier Self-Deconvolution. FSD is the method of deconvolution that is most commonly used in spectroscopy. If an infrared spectrum is assumed to consist of N Lorentzian bands, then the absorbance at wavenumber $\bar{\nu}$ can be represented as

$$A(\bar{\nu}) = \sum_{i=1}^{N} A_i^0 \frac{\gamma_i^2}{\gamma_i^2 + 4(\bar{\nu} - \bar{\nu}_i^0)^2} \quad (1)$$

where A_i^0, γ_i, and $\bar{\nu}_i^0$ are the height, full width at half-height (FWHH), and center peak position, respectively, of the ith band. The inverse Fourier transform of $A(\bar{\nu})$ is

$$Y(x) = 0.25 \sum_{i=0}^{N} \gamma_i A_i^0 \exp(-2\pi j \bar{\nu}_i^0 x) \exp(-\pi \gamma_i x) \quad \text{for } |x| \le R^{-1} \quad (2)$$

where $j = \sqrt{(-1)}$, R is the nominal resolution, and x is the spatial frequency. In FSD, $Y(x)$ is multiplied by $\exp(\pi\gamma' x)$, where $\gamma' < \gamma$, to yield $Y'(x)$:

$$Y'(x) = 0.25 \sum_{i=0}^{N} \gamma_i A_i^0 \exp(-2\pi j \bar{\nu}_i^0 x) \exp[-\pi(\gamma_i - \gamma')x] \quad \text{for } |x| \le R^{-1} \quad (3)$$

When the forward Fourier transform of $Y'(x)$ is calculated, we obtain

$$A'(\bar{\nu}) = \sum_{i=1}^{N} \frac{A_i^0 \gamma_i}{(\gamma_i - \gamma')} \frac{(\gamma_i - \gamma')^2}{(\gamma_i - \gamma')^2 + 4(\bar{\nu} - \bar{\nu}_i^0)^2} \quad (4)$$

0003-2700/91/0363-2557$02.50/0

(This equation has not been simplified, to permit comparison with eq 1.) This "deconvolved" spectrum still has Lorentzian bands in the same positions, but the width of each band has been decreased by an amount γ' and the peak absorbance has been increased by the factor $\gamma_i/(\gamma_i - \gamma')$. Although originally developed for infrared spectra in which each band has a Lorentzian shape (*7, 8*), FSD is equally valid for spectra in which the band shapes can be represented as the convolution of a Lorentzian and some other function.

In the Fourier domain array, $Y(x)$, the signal decreases exponentially as the spatial frequency increases, whereas the noise level remains constant. Thus multiplication by $\exp(\pi\gamma' x)$ to yield $Y'(x)$ can result in the signal at high spatial frequencies having a very high noise level. This can seriously degrade the quality of the deconvolved spectrum after the forward Fourier transform. In practice $Y'(x)$ is therefore truncated at some fraction, F, of the Fourier domain array, which is equivalent to multiplying $Y'(x)$ by a boxcar truncation function, $D(x)$, where

$$D(x) = 1 \qquad \text{for } |x| \le FR^{-1} \tag{5}$$

$$D(x) = 0 \qquad \text{for } |x| > FR^{-1}$$

The spectrum is therefore convolved with a sinc function, $[\sin(2\pi FR^{-1}\bar{\nu})]/(2\pi FR^{-1}\bar{\nu})$, which is the Fourier transform of $D(x)$. When F is significantly less than unity, the maximum achievable resolution is reduced from R to R/F. In addition side lobes appear in the spectrum that may either mask real weak spectral features or appear as artifacts (*7, 11*). If F is too large, however, the noise level in the spectrum becomes excessive. It has been shown (*8*) that the use of a suitable apodization function, $A(x)$, instead of simple boxcar truncation, can reduce the noise and/or side lobe amplitude, but these effects cannot be completely suppressed. Bessel apodization has been shown to be a good choice for FSD (*8*) and was used in all the work presented here. In this case the deconvolved spectrum is convolved with a Bessel function, which has smaller side lobes than a sinc function but a greater FWHH. In the previous paper (*1*) the choice of F was somewhat arbitrary because the spectra were noise free, and the method described therefore involved the optimization only of γ'. The present studies were carried out on noisy data and extend the method described earlier (*1*) to allow optimization of both γ' and F such that the maximum possible resolution enhancement concomitant with the absence of side lobes or excessive noise is obtained.

Maximum Likelihood Restoration. Unlike FSD, maximum likelihood restoration is based on a statistical approach (*12, 13*). If a data set $\{y_1, y_2, y_3, ..., y_n\}$ is measured, with noise components $\{\epsilon_1, \epsilon_2, \epsilon_3, ..., \epsilon_n\}$, then we can write

$$y_i = (o \otimes s)_i + \epsilon_i \tag{6}$$

where $\{o_i\}$ is the more highly resolved spectrum, $\{s_i\}$ is some peak shape function, and $\otimes$ denotes convolution. There are, however, many possible spectra, $\{o_i\}$, that will satisfy this equation to within experimental error. The maximum likelihood principle requires that we find the most likely restored spectrum, $\{o_i\}$, that when convolved with the peak shape function, $\{s_i\}$, and added to the noise, $\{\epsilon_i\}$, yields our measured data set, $\{y_i\}$.

If the statistics of the noise are known and the peak shape function is defined, the probability of obtaining the measured spectrum, $\{y_i\}$, is clearly conditional upon the choice of restored spectrum, $\{o_i\}$. The probability $P(y_1, ..., y_n|o_1, ..., o_n)$ (where | denotes conditional upon) must therefore be maximized by some suitable choice of $\{o_i\}$. To define $P(y_1, ..., y_n|o_1, ..., o_n)$, we consider the fact that, for a given restored spectrum, $\{o_i\}$, and peak shape, $\{s_i\}$, this probability is equal to the probability of obtaining the noise, $\{\epsilon_i\}$:

$$P(y_1, ..., y_n|o_1, ..., o_n) = P(\epsilon_1, ..., \epsilon_n|o_1, ..., o_n) \tag{7}$$

Furthermore, if it is decided, a priori, that all possible restored spectra, $\{o_i\}$, are equally likely, then

$$P(\epsilon_1, ..., \epsilon_n|o_1, ..., o_n) = P(\epsilon_1, ..., \epsilon_n) \tag{8}$$

To define the probability, $P(\epsilon_1, ..., \epsilon_n)$, of obtaining the noise, $\{\epsilon_i\}$, it must be assumed that all the errors in the data can be represented statistically and the statistics of the noise must be defined. If we assume that the noise is random, normally distributed with position-dependent variance $\{\sigma_i^2\}$, and independent of the signal and that noise component ϵ_i is uncorrelated with noise component ϵ_j for all i,j $(i \neq j)$, then the probability of obtaining a noise set $\{\epsilon_i\}$ is given by

$$P(\epsilon_1, ..., \epsilon_n) = \prod_{i=1}^{n} \frac{1}{\sqrt{2\pi}\sigma_i} \exp\left(-\frac{\epsilon_i^2}{2\sigma_i^2}\right) \tag{9}$$

The assumption that the noise is independent of signal is valid for the synthetic spectra described here, and for FT-Raman spectra. For infrared spectra that are output linear in absorbance, this assumption is not strictly true, but if the absorbances are small ($A_i° < 0.5$) it is an adequate approximation. Combining eqs 6–9 yields

$$P(y_1, ..., y_n|o_1, ..., o_n) = \prod_{i=1}^{n} \frac{1}{\sqrt{2\pi}\sigma_i} \exp\left(-\frac{[y_i - (o \otimes s)_i]^2}{2\sigma_i^2}\right) \tag{10}$$

To obtain the restored spectrum, the probability $P(y_1, ..., y_n|o_1, ..., o_n)$ must be maximized, under an appropriate set of constraints, by a suitable choice of $\{o_i\}$.

EXPERIMENTAL SECTION

The programs used to perform FSD, MLR, and curve-fitting were all run under the Spectra Calc software package from Galactic Industries Corp. (Salem, NH). The curve-fitting program uses an iterative least-squares criterion for optimization based on the method of Levenberg (*14*). Convergence was deemed to have been achieved when the change in the standard deviation was less than 0.01%. The MLR program was a proprietary algorithm supplied by Spectrum Square Associates, Inc. (Ithaca, NY). This program imposes the constraint that the solution must always be positive and assumes that all the standard deviations, $\sigma = \{\sigma_i\}$, are equal. The user is required to supply an estimate of the standard deviation at run time. The shape of the peak, s, used in this work was Lorentzian, with a FWHH of γ'.

To investigate the potential advantages of combining deconvolution and curve-fitting techniques for the analysis of noisy spectra, several spectra were synthesized from two or more Lorentzian bands. Moderate amounts of noise were then added to these spectra. The presence of noise, if it is the only source of error, is not expected to seriously affect the curve-fit unless either the noise levels are very high or there is a large number of overlapping bands. This is because, if the only source of error is noise which is normally distributed, curve-fitting not only yields a statistically valid solution but it can also be shown to yield the maximum likelihood solution (*15*). Other systematic errors, such as a poor knowledge of the baseline, can seriously reduce the accuracy of the parameters obtained by curve-fitting, however. The main advantage of performing FSD prior to curve-fitting in our previous work (*1*) was an improvement in the conditioning of the curve-fitting, and this will probably also be the main advantage if other forms of deconvolution (e.g. MLR) are applied prior to curve-fitting. Baseline errors were therefore introduced into some of the spectra. A linear baseline was included as a variable in each curve-fit, but this cannot, of course compensate for nonlinear baseline errors.

Although it was shown in our first paper (*1*) that the more quantitatively accurate results were obtained by curve-fitting using a Lorentzian band shape with some Gaussian character, a pure Lorentzian band shape was used in all the curve-fits in this work to reduce the number of variables and thereby simplify the

Table I. Parameters of Synthetic Band Multiplets Discussed in This Paper

	spectrum A		spectrum B		spectrum C			
	1	2	1	2	1	2	3	4
position, cm^{-1}	3003	2997	3003	2997	3007	3003	2997	2992
FWHH, cm^{-1}	12.0	14.0	12.0	14.0	12.0	13.0	14.0	12.0
height	1.50	1.00	1.50	1.00	1.00	0.75	1.30	0.90

analysis and reduce the overall time for this investigation.

As in the first paper, two parameters were used to determine the goodness of fit. The first of these, the deviation in the fit, D, is defined as

$$D = \sum_{i=1}^{n} (d_i - f_i)^2 \tag{11}$$

where d_i and f_i are the ith data point and the ith point in the fitted spectrum, respectively, and n is the number of data points. When fitting real spectra, this is the only available measure of the goodness of fit. The second parameter, E, is the sum of the absolute percentage errors in the area of each band:

$$E = \sum_{i=1}^{l} \frac{|A_i^t - A_i^m|}{A_i^t} \times 100 \tag{12}$$

where A_i^t and A_i^m are the true and the measured band areas, respectively, of the ith band and l is the number of bands. Obviously, this metric can only be used for synthetic spectra, for which the true areas of each band, A_i^t, are known accurately. A comparison of these two parameters allows an assessment of the effectiveness of combining deconvolution and curve-fitting to be obtained.

Of the various synthetic spectra used in this investigation, only representative examples will be discussed specifically in this paper. Table I shows the band parameters used to synthesize these spectra. Spectra A and B were composed of two completely unresolved bands, with a separation of 6 cm^{-1} and an average FWHH of 13 cm^{-1}. Spectrum C was composed of four unresolved bands of varying heights and widths. In all cases the data point spacing was 0.5 cm^{-1}. All spectra subsequently had 0.5% peak-to-peak (~0.1% root mean square) noise added to them. Spectra B and C also had baseline errors introduced. For spectrum B the "baseline" was a broad, small Lorentzian band centered at 2985 cm^{-1} with a height of 0.05 and a FWHH of 50 cm^{-1} (see later, Figure 4). This type of function was chosen because in a real spectrum it is unlikely that a small, broad band would be allowed for in a curve-fit. Spectrum C was "baseline-corrected" by subtraction of linear sections of baseline from regions of low absorbance, such that the ordinate points at 3200, 3100, 2900, and 2800 cm^{-1} were zero (see later, Figure 7). This type of baseline correction is commonly applied to real spectra but will rarely be exactly right.

RESULTS AND DISCUSSION

Effects of Noise in Combined Deconvolution and Curve-Fitting. To investigate the effects of noise on combined FSD and curve-fitting and to derive a method for optimizing the fraction, F, of the Fourier domain array retained during FSD, spectrum A was studied. This spectrum had 0.5% added noise, but no baseline errors. The two bands in this spectrum are completely unresolved prior to deconvolution. Although the effects of changing the values of γ' and F used in FSD on the parameters D and E obtained from the subsequent curve-fit are clearly interrelated, they will be treated separately for clarity. As already pointed out, for any given value of γ' there is an optimum value of F that gives the maximum possible resolution enhancement without leading to excessive noise in the deconvolved spectrum. This optimum value must lie between the values of F that lead to side lobe formation and serious degradation of the resolution (low F) or to excessive noise (large F). It should be noted, however, that if the noise levels are high and a large value of

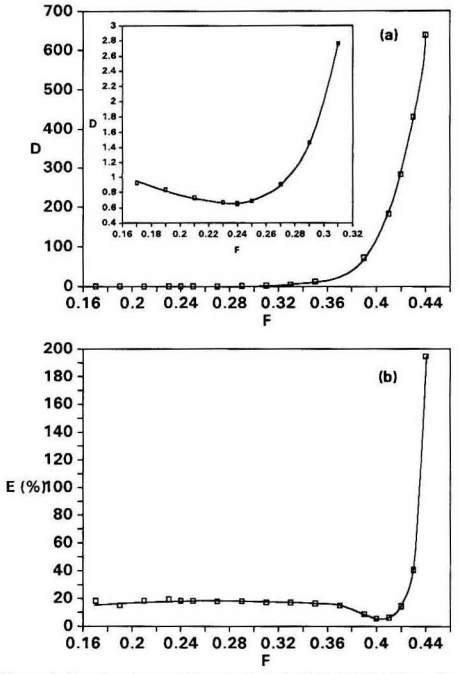

Figure 1. Results of curve-fitting spectrum A after deconvolution using FSD with $\gamma' = 8$ cm^{-1}. (a) Variation of D as the fraction of the Fourier domain array, F, retained during deconvolution is changed. An expanded plot for $0.16 < F < 0.32$ is shown in the insert. (b) Variation of E as the fraction of the Fourier domain array, F, retained during deconvolution is changed.

γ' is used, the ranges of F that lead to these two sources of error may overlap. In this case there is no good choice for the fraction of the Fourier domain array to be retained. Thus the value of γ' at which this situation begins to occur effectively defines an upper limit on the level of resolution enhancement that can be achieved.

As an example of the effects of the value of F used in FSD on the parameters D and E obtained from the subsequent curve-fit, a spectrum deconvolved with a moderately high value of γ' will be considered. Parts a and b of Figure 1 show the effects on the parameters D and E of changing the fraction of the Fourier domain array, F, when the spectrum was deconvolved using a value of $\gamma' = 8$ cm^{-1}. The functional forms of these plots are not always the same for different spectra or even for the same spectrum deconvolved using different values of γ', but they do always show certain characteristics. Both plots have always exhibited a minimum, although any occurrence of the minimum in D and the minimum in E at the same value of F is fortuitous. Both D and E also always show a very rapid and large rise if F is increased beyond a certain point. This latter characteristic is perhaps not surprising, since after multiplication by $\exp(\pi\gamma' x)$ the noise in the Fourier domain array increases exponentially with x, and therefore the noise level in the deconvolved spectrum will rise exponentially as F is increased.

The result of deconvolving spectrum A using FSD with $\gamma' = 8$ cm^{-1} and various values of F is shown in Figure 2. A comparison of the spectra in this figure with the plots in Figure 1 shows that although there is a minimum in the parameter E that occurs at the value of F that minimizes the errors in

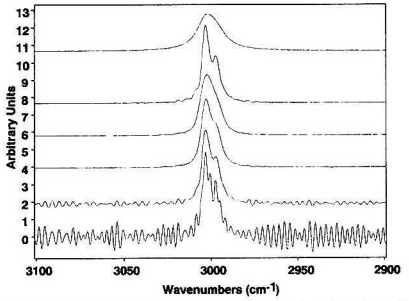

Figure 2. Spectrum A deconvolved using MLR with $\gamma' = 8$ cm^{-1} and FSD with $\gamma' = 8$ cm^{-1} and various values of F (top to bottom): (A) original spectrum; (B) spectrum deconvolved using MLR; (C–F) spectra deconvolved using FSD with $F = 0.17$, $F = 0.24$, $F = 0.33$, and $F = 0.40$, respectively.

the band areas (i.e. $F = 0.40$), this minimum occurs when the deconvolved spectrum has a very high noise level. It would therefore be difficult or impossible to estimate the number of bands from the lowest trace in Figure 2 correctly. This appears to be generally true, both for different spectra and different levels of deconvolution. This behavior occurs because the band shapes are closer to Lorentzian in spectra computed with higher values of F and the noise levels are still not sufficiently high to affect the curve-fit seriously.

When a real spectrum is analyzed, the only parameter available is D. It would therefore not be possible to determine the value of F that would minimize the errors in the band areas. Consequently, it was decided to use the value of F that minimized the deviations in the fit; in this case $F = 0.24$. The choice of this value of F allows the correct number of component bands to be determined, and although it does not minimize the errors in the band areas, it will be shown later that these errors are still significantly smaller than if the original spectrum was curve-fitted.

There is a second possible criterion for choosing the fraction of the Fourier domain array that is to be retained during FSD. Choosing the value of F that occurs just before the deviations begin to rise rapidly (in this case $F = 0.30$–0.35) gives a spectrum that does not have excessively high noise levels and shows the correct number of component bands. In practice this criterion would have the advantage that a good choice of F could be found by looking at a series of deconvolved spectra and choosing the largest value of F that does not lead to excessive noise. For example, in the series of spectra seen in Figure 2C through 2F, the noise level in Figure 2C and 2D is low, leading to the conclusion that a higher value of F can be applied, while the noise level in Figure 2F is obviously excessive. The optimum value of F would be close to the one used to calculate the spectrum shown in Figure 2E. Small differences in the value of F used in the deconvolution do not greatly affect the errors in the band parameters found from the subsequent curve-fit. In this example, any value of F between 0.30 and 0.33 leads to a similar result, as can be seen from Figure 1B. Choosing F in this fashion would save a considerable amount of time and it would therefore be the method of choice if a large number of spectra must be analyzed. To investigate the magnitude of the errors incurred by curve-fitting as quantitatively as possible, however, it was decided to use a more precisely defined method of finding the optimum value of F.

When a noisy spectrum is deconvolved by MLR, the noise level in the resultant spectrum is always lower than when the same degree of band narrowing is achieved by FSD. For example, deconvolution of spectrum A using MLR with $\gamma' =$ 8 cm^{-1} is shown in Figure 2 for comparison with the corresponding data obtained by FSD. The potential advantages of using MLR for the deconvolution of noisy spectra are evident: the two component bands have been clearly resolved, but without the high noise levels seen when FSD is used to achieve an equivalent level of band narrowing.

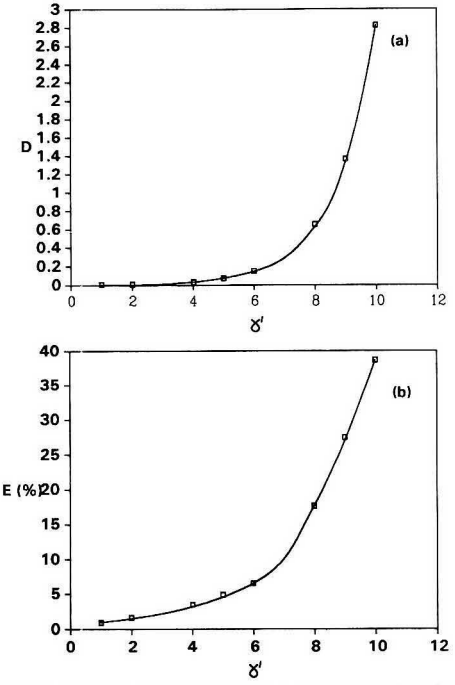

Figure 3. Results of curve-fitting spectrum A after deconvolution using FSD, shown as plots of (a) D vs γ' and (b) E vs γ'.

Figure 3 shows the variation in the parameters D and E obtained from the curve-fit as the degree of deconvolution, γ', is changed. For each point on these plots, the parameter F was chosen to give the minimum value of D in the subsequent curve-fit. The deviations begin to rise rapidly near the point at which there is no good choice for F, and side lobes and severe band shape distortion and/or noise are always present. Although not shown in this paper, the results for the parameter E obtained by curve-fitting spectrum A after deconvolution using MLR are very similar to the results obtained by FSD. (In fact, the results for the parameter D are very similar to those shown later in Figure 9a.) It should be noted that when either FSD or MLR was used, the errors in the fitted band areas were always greater than when the original spectrum was curve-fitted. Thus when noise constitutes the only error in the original data, there is no advantage in using deconvolution prior to curve-fitting, and the errors in the band areas increase considerably as the degree of deconvolution (using FSD or MLR) is increased and the band shapes deviate more from pure Lorentzian.

Spectra with Added Noise and Baseline Errors. As noted above, spectrum B is identical to spectrum A, but with a small, curved baseline added as previously described. Figure 4 shows spectrum B, in the absence of noise, and the baseline to indicate their relative magnitudes. As with spectrum A, for any particular value of γ' the fraction of the Fourier do-

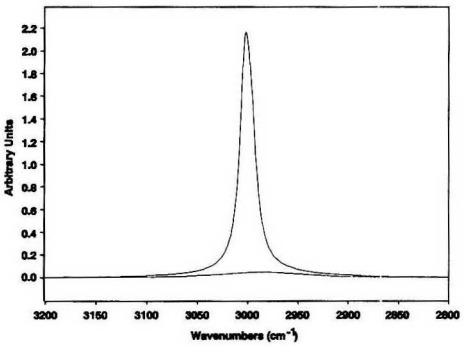

Figure 4. Spectrum B, in the absence of noise, and the baseline error that was introduced to this spectrum.

main array that was retained during deconvolution was chosen as the value that minimized the deviations in the subsequent curve-fit. This spectrum was chosen as an example because two minima, one global and one local, were found in some of the curve-fits. The convergence of the curve-fit to one or the other of these minima depended on the initial estimates for the peak parameters. If the original spectrum (i.e., spectrum B) was curve-fitted, two minima were found with values of $D = 0.0446$ and $D = 0.0592$. The values of E found for these two curve-fits were $E = 136.4\%$ and 13.4%, respectively. The latter result gave an average error in each band area of only 6.7%, but this is obtained from the local minimum. In practice, when only the parameter D is available as a measure of the goodness of fit, the global minimum would be chosen as the best fit and the band areas would therefore be in error by an average of 68.2%. If spectrum B was Fourier-transformed and truncated in the Fourier domain array with a value of F chosen as described above, but with $\gamma' = 0$ cm^{-1} (i.e. no deconvolution), and then transformed back to the spectral domain and curve-fitted, two minima, were also found. In this case values of $D = 0.0365$ and $D = 0.0429$ were obtained at the minima, with corresponding errors $E = 116.3\%$ and 15.5%, respectively. As with the original spectrum, the choice of the global minimum would lead to band areas that were seriously in error.

Figure 5 shows the parameters D and E obtained from the curve-fit as a function of the value of γ' used in the FSD. The most notable effect of curve-fitting the deconvolved spectra is that the two minima degenerate into a single minimum as the value of γ' is increased much beyond $\gamma' = 5$ cm^{-1}. This is due to the improved conditioning of the curve-fit. It can also be seen that the errors in the band areas, E, are reduced significantly when compared to those obtained by curve-fitting the undeconvolved spectrum and taking the band parameters found at the global minimum as correct. As with the examples presented in the previous paper (*1*), in which noise-free spectra were used, the errors in the peak areas are minimized by fitting the spectrum deconvolved with the value of γ' at which the deviations, D, in the curve-fit just begin to show a significant increase. At this point the average percentage error in each peak area is only 8.6%. It is notable that this point is less well defined than in the examples given in the previous paper. This happens because the presence of noise in the spectrum leads to more severe truncation requirements in the Fourier domain array, and therefore greater distortion of the peak shapes. Addition of a small, fixed Gaussian fraction to the fitted peaks, as was used in the first paper (*1*), would probably improve this situation and may also reduce the errors in the band areas.

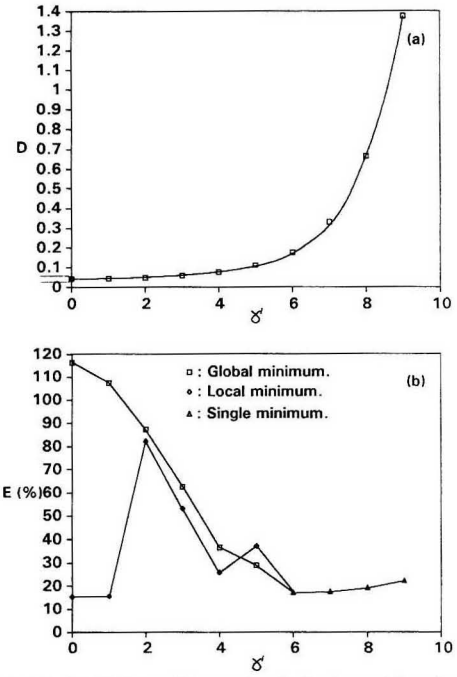

Figure 5. Results of curve-fitting spectrum B after deconvolution using FSD, shown as plots of (a) D vs γ' and (b) E vs γ'. The values of D found for the local and global minima ($0 \leq \gamma' \leq 5$ cm^{-1}) at a particular value of γ' are very close on this plot, and therefore only the averages are shown.

The variation of the parameters D and E as a function of γ', obtained by curve-fitting spectrum B after deconvolution using MLR, is shown in Figure 6a,b. An estimate of $\sigma = 0.5\%$ of the most intense band was used for all the restorations. This estimate of the standard deviation of the noise is actually somewhat high, since the peak-to-peak noise level of the original spectrum was 0.5% of the maximum intensity, so that the standard deviation was about 0.1%. In practice, however, an estimate that is too low can produce artifacts or noise in the deconvolved spectrum and it was found that the estimate should always be conservative. It can be seen that the results are similar to those obtained using FSD, although there are certain notable differences. One obvious major difference is seen in the variation of D as a function of γ' (cf. Figure 5a). Although there is a rapid rise in the deviations in the curve-fit as γ' is increased, it does not occur at the same value of γ' that was found using FSD. There is also a maximum in D at approximately $\gamma' = 5.5$ cm^{-1}. The fact that this occurs at about the same value of γ' that minimizes the errors in the band areas is fortuitous. The position of this maximum can vary considerably from one example to another and can even vary somewhat if the noise estimate, σ, is changed. This maximum is caused by sharp features, in particular noise, being interpreted as real when low values of γ' are used. Alternative MLR formulations are available (see for example Jansson (*13*)) that may help solve this problem, but these still need to be investigated.

The other major difference is that the minimum error in the peak areas is only an average of 1.7%, compared to 8.6% when the spectra were deconvolved using FSD. Despite this

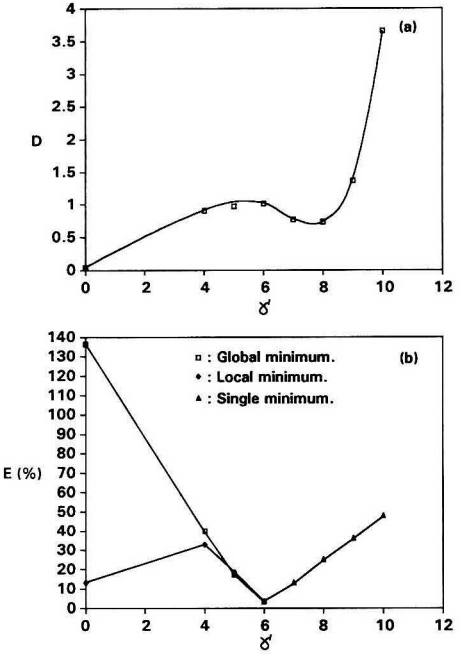

Figure 6. Results of curve-fitting spectrum B after deconvolution using MLR, shown as plots of (a) D vs γ' and (b) E vs γ'. The values of D found for the local and global minima ($0 \leq \gamma' \leq 5$ cm^{-1}) at a particular value of γ' are very close on this plot, and therefore only the averages are shown.

improvement in the accuracy of the band areas, however, the correspondence between the deviations in the fit and the errors in the band areas is not as clear as when the deconvolution is performed using FSD. Because of this, if a real spectrum (with noise and baseline errors) were being analyzed and only the parameter D were available, it would be very difficult to choose the optimum value of γ'.

One other example of a spectrum with added noise and baseline errors will be considered. This is spectrum C in Table I and is somewhat more complex than those already considered. Figure 7 shows this spectrum, in the absence of noise, and the baseline that was added to it. The separations of adjacent bands of 4, 5, and 6 cm^{-1} were chosen so that after truncation of the Fourier domain array they were close to (or even less than) the nominal resolution. Because of the small band separations, both FSD and MLR were incapable of completely resolving all four bands. After FSD, bands 1 and 2 and bands 3 and 4 were still unresolved. After MLR only bands 1 and 2 remained unresolved. This spectrum therefore provides a good test of the ability of spectral deconvolution to improve the conditioning of subsequent curve-fitting.

The parameters D and E, obtained from the curve-fit, are shown as a function of the value of γ' used in the FSD in Figure 8a,b. The results are not as good as in the previous example, but this is not surprising since after deconvolution some of the bands are still unresolved. An appreciable improvement in the accuracy to which the band areas could be estimated was nonetheless observed. When the original spectrum was curve-fitted, the average error in the band area was 50.2%, whereas if the optimally deconvolved spectrum ($\gamma' = 6$ cm^{-1}) was curve-fitted, the error in the band area was

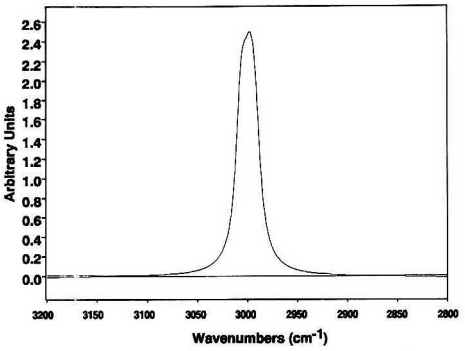

Figure 7. Spectrum C, in the absence of noise, and the baseline error that was introduced to this spectrum.

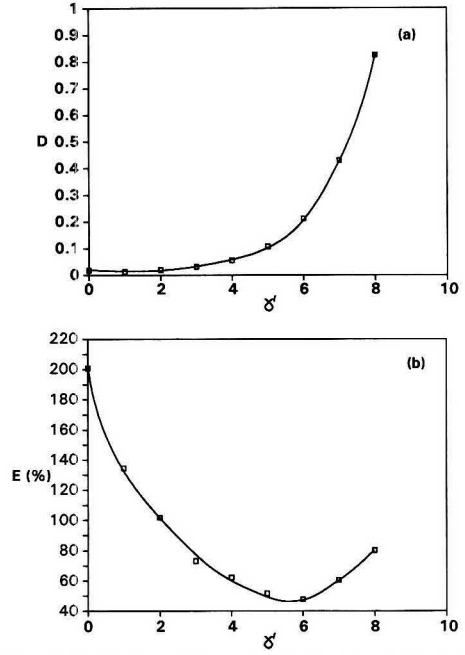

Figure 8. Results of curve-fitting spectrum C after deconvolution using FSD, shown as plots of (a) D vs γ' and (b) E vs γ'.

reduced to an average of 12.0%. It is also clear from this example that complete resolution of the component peaks after deconvolution is not necessary for the conditioning of the curve-fitting to be improved significantly.

Parts a and b of Figure 9 show the results of curve-fitting spectrum C after deconvolution using MLR. As in the previous example the estimate of the noise, σ, was chosen as 0.5% of the most intense point of the spectrum. In this example there are clearly substantial differences between the results obtained using FSD and MLR. The most obvious of these is the difference in the minimum errors found in the band areas. Using MLR two minima were found, one at approximately $\gamma' = 4$ cm^{-1} and the other at $\gamma' = 9$ cm^{-1}. (Results for 0 cm$^{-1} < \gamma' < 4$ cm^{-1} were not available because of restrictions

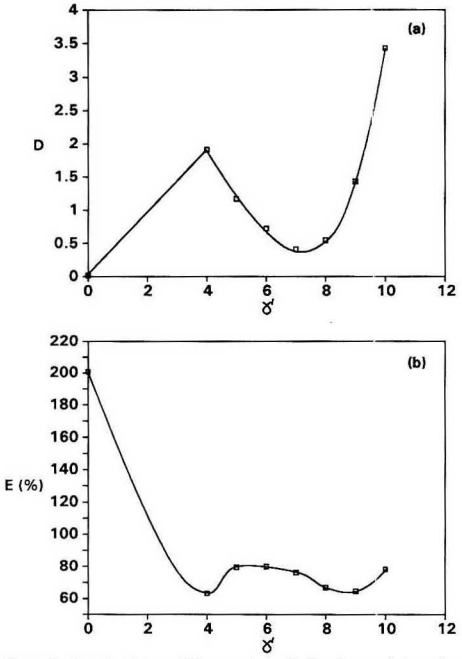

Figure 9. Results of curve-fitting spectrum C after deconvolution using MLR, shown as plots of (a) D vs γ' and (b) E vs γ'.

imposed by the MLR algorithm.) These values of γ' gave average errors in the fitted band areas of 15.9% and 16.2%, respectively, compared with 12.0% found using FSD. As in the previous example, the deviations, D, in the curve-fit show a minimum, in this case at $\gamma' = 7$ cm^{-1}. Since the position of this minimum does not coincide with the position of either minimum in E, estimation of the optimum level of deconvolution using only the parameter D would be effectively impossible. Nevertheless, fitting the spectrum that had been deconvolved by MLR with a value of $\gamma' = 7$ cm^{-1} would produce more accurate band areas (an average error of 19.0%) than fitting the original spectrum.

CONCLUSIONS

In a previous paper (*1*) we showed that the combination of Fourier self-deconvolution and curve-fitting overcame many of the limitations of the individual methods when applied to noise-free synthetic spectra with highly overlapped bands. The value of γ' used in the FSD can be objectively optimized, the conditioning of the curve-fit is significantly improved, and quantitative information is available directly.

In the present study, this work has been extended to include the effects of noise when deconvolution is effected using both FSD and MLR. The combination of either FSD or MLR and curve-fitting for the analysis of overlapping bands in noisy spectra has been shown to provide more accurate band areas when compared to curve-fitting the original spectrum, if the original spectrum has small baseline errors. If noise is the only nonnegligible source of error in the measured spectrum, there is no advantage to using deconvolution prior to curve-fitting, and the accuracy of the band areas calculated for unresolved multiplets will almost certainly be reduced.

Although MLR can provide greater resolution enhancement than FSD, the errors in the band areas found by subsequent curve-fitting are not much lower, and in some cases may even be higher. It is also more difficult to identify the optimum value of γ' using the deviations from the curve-fit when MLR is used instead of FSD. In the context of combined deconvolution and curve-fitting, FSD is therefore the technique of choice, although MLR may be useful for the initial identification of the number of component bands and their approximate positions.

It has also been shown that complete resolution of the overlapping bands is not necessary for quantitative information to be obtained, although the bands in the deconvolved spectrum have to show some structure for curve-fitting to be reasonably well conditioned. In this case the application of deconvolution prior to curve-fitting will lead to more accurate band areas than if the original spectrum were curve-fitted, unless there are no appreciable sources of error other than noise. The improvement in accuracy may not, however, be as great as would be achieved if the component bands were completely resolved after deconvolution.

LITERATURE CITED

(1) Pierce, J. A.; Jackson, R. S.; Van Every, K. W.; Griffiths, P. R.; Hongjin, G. *Anal. Chem.* **1990**, *62*, 477.
(2) Vandeginste, B. G. M.; De Galen, L. *Anal. Chem.* **1975**, *47*, 2124.
(3) Audo, D.; Armand, Y.; Arnaud, P. *J. Mol. Struct.* **1968**, *2*, 287.
(4) Audo, D.; Armand, Y.; Arnaud, P. *J. Mol. Struct.* **1968**, *2*, 409.
(5) Anderson, A. H.; Gibb, T. C.; Littlewood, A. B. *Anal. Chem.* **1970**, *42*, 434.
(6) Anderson, A. H.; Gibb, T. C.; Littlewood, A. B. *J. Chromatogr. Sci.* **1970**, *8*, 640.
(7) Kauppinen, J. K.; Moffatt, D. J.; Mantsch, H. H.; Cameron, D. G. *Appl. Spectrosc.* **1981**, *35*, 271.
(8) Kauppinen, J. K.; Moffatt, D. J.; Cameron, D. G.; Mantsch, H. H. *Appl. Opt.* **1981**, *20*, 1866.
(9) Palmo, K.; Manntors, B.; Pietila, L.-O. *J. Mol. Struct.* **1988**, *174*, 101.
(10) Ni, F.; Scheraga, H. A. *J. Raman Spectrosc.* **1985**, *16*, 337.
(11) Pariente, G. A.; Griffiths, P. R. *TrAC, Trends Anal. Chem. (Pers. Ed.)* **1986**, *5*, 209.
(12) *Manual for "SSRES" Maximum Likelihood Restoration Program*; Spectrum Square Associates, Inc.: Ithaca, NY, 1989.
(13) Jansson, P. A. *Deconvolution With Applications in Spectroscopy*; Academic Press Inc.: Orlando, FL, 1984.
(14) Levenberg, K. *Q. Appl. Math.* **1944**, *2*, 164.
(15) Press, W. H.; Flannery, B. P.; Teukolsky, S. A.; Vettering, W. T. *Numerical Recipes in C. The Art of Scientific Computing*; Cambridge University Press: Cambridge, 1988.

RECEIVED for review February 20, 1991. Revised manuscript received August 14, 1991. Accepted August 22, 1991. This work was supported by Grant No. DE-FG22-87PC79907 from the U.S. Department of Energy, Pittsburgh Energy Technology Center.

Photovoltaic Detection Method for Condensed-Phase Photoionization

John W. Judge and Victoria L. McGuffin*

Department of Chemistry, Michigan State University, East Lansing, Michigan 48824

A novel method is examined for the detection of photoinduced ions in the absence of an applied electric field. The analyte solution is enclosed between two optically transparent electrodes and is irradiated transversely by a pulsed laser. After irradiation, the extent of photoionization differs at the two electrodes and a transient photopotential is developed. This photovoltaic response is characterized with respect to electrode composition and film thickness, electrode separation distance, illuminated area, and laser pulse energy. In addition, the dependence of the photopotential on solute concentration is examined in a variety of polar solvents. Detection limits of 5×10^{-7} M potassium permanganate in water are reported, with a linear range exceeding 3 orders of magnitude.

INTRODUCTION

Photoionization phenomena in the condensed phase have been investigated for several decades and continue to be of great interest. Previous studies have been concerned with the determination of ionization spectra, ionization energies, mechanisms of ionization, and the nature of ionic products for pure aromatic liquids and for aromatic compounds in alkane solvents (*1–3*). Important physical parameters such as solvated ionic radii (*4*), electron mobility (*5, 6*), electron transport and reactivity (*6, 7*) have also been examined. In addition, the fluorescence emission produced during ionization and from highly excited states has been investigated (*1, 8*). Although analytical applications have been reported in both static and dynamic systems (see refs 9–13 and references therein), the high sensitivity and selectivity of this technique have yet to be fully exploited for analytical purposes.

Photoionization in the condensed phase is complicated by many problems that do not occur to a great extent in the gas phase, where much of our present knowledge resides. In the condensed phase, the excess kinetic energy of the ejected electron is dissipated more rapidly by collision (*4*). Consequently, it is possible to have geminate ion recombination, formation of radical anions, electron capture, molecular rearrangement or fragmentation, in addition to simple solvation of the product ions. Another important difference is that the ionic products are stabilized by solvation, which causes a reduction of the ionization threshold by approximately 2–4 eV for most pure organic compounds in the liquid phase when compared to the gas phase (*9*). If the compound is not pure but dispersed in another medium, the ionization energy and efficiency are highly dependent on the physical properties of the solvent (*14*). Furthermore, many polar solvents are themselves more readily photoionized in the condensed state; most notably, the photoionization of water occurs in the gas phase at 12.6 eV and in the liquid phase at 6.05 eV (*9*). The interference of solvent photoionization complicates the acquisition and interpretation of spectral information for the analyte molecule. Consequently, quantitative detection of photoionization in the condensed phase may be complicated and difficult.

The most commonly employed detection technique for condensed-phase photoionization is the measurement of electrical conduction. In this technique, large bias voltages (up to several thousand volts) are applied across a solution to drive photoinduced ions to a collection electrode, where the net charge flux (current) is measured (*2–4, 15, 16*). Since any naturally occurring ions or ionic impurities are also detected, extensive purification procedures may be required (*2, 16*). In addition, solvents with intrinsically high conductivity, such as water and other highly associated liquids, cannot be readily employed due to the high background current.

A novel alternative to conduction measurement, proposed by Coleman and co-workers (*17*), is to detect the photopotential induced at the electrode–solution interface in the absence of an applied electric field. By elimination of the bias voltage, contributions from intrinsic solvent conduction are substantially reduced or eliminated. Consequently, measurements of the photovoltaic response may be accomplished in polar solvents and in solutions of relatively high ionic strength, where a photoconduction measurement may not be possible. Furthermore, this detection method may reduce background current from the photoelectric effect, which is caused by electron ejection from the electrodes when directly irradiated in an applied electric field.

Coleman and co-workers (*17*) have reported such photovoltaic measurements for the photoreduction of potassium permanganate in aqueous solution. In these studies, the sample was enclosed between two optically transparent electrodes (n-type tin oxide semiconductor overcoated with an insulating quartz layer) and was irradiated transversely by a nitrogen-pumped dye laser. The photopotential developed across the unbiased electrodes after illumination was measured with an oscilloscope relative to external ground. The signals were characterized by a rapid rise (<1 μs) to a maximum potential of 100–1000 μV, which then decayed over approximately 250 μs. The photopotential was shown to be dependent on the laser power and wavelength, as well as the pH and ionic strength of the aqueous solvent system. To explain the origin of the observed signal, Coleman and coworkers (*17*) noted that the potential difference at the beginning of the experiment is zero, since all interfacial potentials at the two electrodes are exactly equal and therefore cancel. Following irradiation, the light intensity at the front electrode is greater than that at the rear electrode, due to analyte absorption as the light traverses the cell. The extent of photoreduction of the permanganate ion varies concurrently with radiant power; hence, the electrodes are present in different chemical environments and a transient potential difference is developed. Although the proposed explanation of the phenomenon seems plausible, no interpretation of the magnitude, sign, or temporal decay of the photopotential was offered, and a detailed mechanism has yet to be reported.

In this paper, more extensive and detailed investigations of the photovoltaic detection method of Coleman and coworkers (*17*) are described. The photovoltaic response is characterized with respect to optically transparent electrode

* To whom correspondence should be addressed.

0003-2700/91/0363-2564$02.50/0

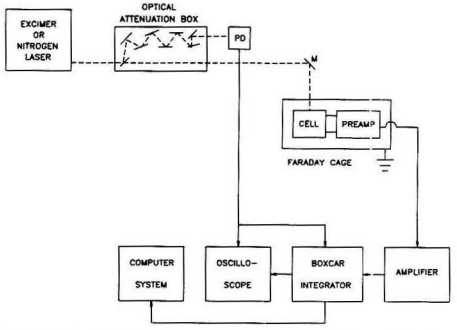

Figure 1. Schematic diagram of the analytical system used for photovoltaic detection of condensed-phase photoionization: (M) mirror; (PD) photodiode.

Table I. Comparison of Optically Transparent Electrode Characteristics

property	gold electrode		tin oxide electrode
substrate	fused silica		Pyrex
film thickness, Å	100	200	400
resistivity, Ω cm	4×10^{-5}	2×10^{-5}	2×10^{-4}
transmittance (248 nm)	0.32	0.12	<0.01
transmittance (337.1 nm)	0.38	0.16	0.45

material, film thickness, illuminated area, and electrode separation distance. In addition, the response for several nonpolar, polar, and ionic solutes at varying concentrations is reported in water, alcohols, and other polar solvent systems. This detection technique is promising, as it offers the opportunity to detect photoionization and related photoelectrochemical phenomena under experimental conditions where a traditional conduction measurement may not be appropriate.

EXPERIMENTAL SECTION

Optical System. The experimental apparatus for these studies is shown schematically in Figure 1. When the krypton fluoride excimer laser (Lambda Physik, Model EMG 101, 248 nm, 180 mJ, 23 ns) is used as the excitation source, the radiation enters an optical attenuation box where a fraction (~8%) is diverted and attenuated by a series of fused-silica plates. This attenuated beam is used to produce a trigger signal using a fast-response photodiode (Hamamatsu Corp., Model S1722-02). The remainder of the beam is reflected from another fused-silica plate and is directed onto the sample cell. The laser pulse energy measured at the cell is approximately 6.8 mJ. When the low-power nitrogen laser (National Research Group, Inc., Model 0.5-5-150, 337.1 nm, 0.5 mJ, 8 ns) is used, the optical attenuation box is replaced by a single fused-silica plate to produce a suitable trigger pulse from the photodiode. The remainder of the beam is then delivered to the sample cell by using a front-surface aluminum mirror overcoated with magnesium fluoride (Esco Products Inc.). The laser pulse energy reaching the cell in this case is approximately 0.23 mJ.

Cell Construction. Two different types of optically transparent electrodes (OTE) are used in these studies: gold (conductor) and antimony-doped tin oxide (n-type semiconductor). Physical characteristics of these thin-film electrodes are summarized in Table I. The gold films are produced in-house by vapor deposition on a fused-silica substrate (Esco Products Inc., 2.54-cm diameter, 0.159–0.476-cm thickness). The antimony-doped tin oxide films, obtained from PPG Industries, are deposited on a Pyrex substrate (0.8 cm × 2.0 cm, 0.318-cm thickness). Electrical connection to the OTE is made by using a commercially available, silver conductive epoxy (TRA-CON Inc.). A thin layer of the epoxy is coated from the electrode surface onto the side of the substrate, to which a copper wire is attached. The epoxy

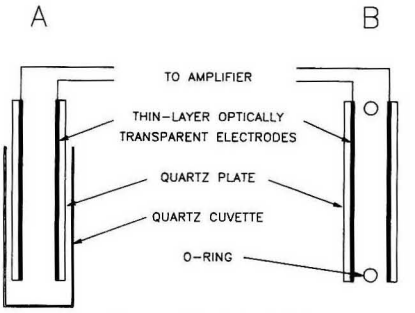

Figure 2. Schematic diagram of the photovoltaic detection cells: (A) cuvette cell; (B) sandwich-type cell.

is cured at room temperature for 12 h and then at 110 °C for 1 h or longer. Total resistance across a typical gold electrode (100-Å film thickness), including electrical connections, is 120 Ω.

Two types of static cells are shown schematically in Figure 2. The first cell consists of a quartz cuvette containing the solution into which the OTEs are immersed. The second cell is a sandwich-type arrangement with either a silicone rubber O-ring or a Teflon gasket to separate the plates. Electrode separation distance in the sandwich-type cell is controlled by the thickness of the spacer material (0.125, 0.25, 1.6, and 4.7 mm), while the cuvette cell allows for continuous variation of separation distance from 3 to 8 mm.

Detection System. The potential between the electrodes is amplified using a two-stage differential amplifier that was manufactured in-house. The preamplifier, located immediately adjacent to the cell inside a Faraday cage, has a nominal gain of 10, while the second-stage amplifier has a nominal gain of 40. The time constant of the complete circuit was originally selected to be 5 ns but, based on preliminary investigations, has been increased to approximately 2 μs to reduce high-frequency noise without sacrificing signal integrity. A boxcar integrator (Stanford Research Systems, Model SR250) is used to sample the amplifier output at a fixed time interval corresponding to the maximum photopotential (12 μs after the trigger pulse), or to scan the amplifier output across a specified time interval. An analog-to-digital converter (Stanford Research Systems, Model SR245) is used in conjunction with an IBM PC-XT computer to collect data. Both the boxcar integrator and the A/D converter are controlled by a commercially available software package (Stanford Research Systems, SR265). An oscilloscope (Tektronix Inc., Model 2235) is used to monitor the photovoltaic signal in real time during the experiment.

The data are acquired by averaging five trials of 500 points, either at constant or scanned time intervals. The potential is measured under both illuminated (signal) and nonilluminated (noise) conditions. Corrected photopotentials are calculated by subtracting the systematic noise, predominantly due to radio-frequency (rf) interference and amplifier null offset, from the signal measurement. The photopotentials are then reported as the average of five corrected data sets, with the confidence interval expressed by the standard deviation.

Reagents. *N,N,N′,N′*-Tetramethyl-1,4-phenylenediamine (TMPD) is liberated from its dihydrochloride salt (Aldrich Chemical Co.) with aqueous ammonia. The free amine is then purified by vacuum sublimation at 50 °C and stored in the dark. Reagent-grade potassium permanganate (J. T. Baker Chemical Co.) is used without further purification. Stock solutions (10^{-2} to 10^{-7} M) of these reagents are prepared freshly as needed in the appropriate solvent.

Other reagents examined in the photoionization studies include fluorescein and its disodium salt (Eastman Kodak Co.) and Rhodamine B and Coumarin 460 (Aldrich Chemical Co.), which are laser-dye-grade reagents.

High-purity methanol and acetonitrile are distilled-in-glass grade (Baxter Healthcare Corp., Burdick and Jackson Division); all other solvents are reagent grade (J. T. Baker Chemical Co.).

Water is deionized and doubly distilled in glass (Corning Glass Works, Model MP-3A).

RESULTS AND DISCUSSION

Potassium permanganate was selected as the analyte molecule for initial studies because it has been used previously to characterize the photovoltaic detection method (*17*) and because its photochemical properties have been studied extensively (*18*, *19*). Although the exact mechanism remains in question, the photodecomposition of permanganate ion in neutral or basic aqueous solution is reported to yield the following products (*18*, *19*):

$$MnO_4^- \rightarrow MnO_2(s) + O_2^- \quad \text{or} \quad MnO_2^- + O_2(g)$$

From isotopic studies (*18*), the O_2 produced is known to arise directly from decomposition of permanganate ion rather than from decomposition of water. Consequently, the reaction written above is essentially irreversible in deoxygenated solvents, due to the change in physical state of the decomposition products. By interpolation of literature data (*17*, *18*), the quantum yield for photodecomposition of permanganate in aqueous solution is estimated to be 3.5×10^{-3} at 337.1 nm and 5.5×10^{-2} at 248 nm. The quantum yield is reported to be independent of permanganate ion concentration (10^{-2} to 10^{-4} M), hydrogen ion concentration (pH 7–14), temperature (0–45 °C), and irradiance under the experimental conditions employed herein (*18*).

Origin of the Photovoltaic Response. At present, we have examined two different types of electrode materials, gold (conductor) and antimony-doped tin oxide (n-type semiconductor), whose properties are indicated in Table I. The commercially available n-type tin oxide films provide reasonably low resistance and high optical transparency. Because they are deposited on a Pyrex substrate, however, these films can only be used with the nitrogen laser (337.1 nm), not with the KrF excimer laser (248 nm). The gold films, manufactured in-house, show generally lower resistance and lower transparency than the semiconductor materials but can be used with both laser systems. Gold films less than 75 Å in thickness have an infinite resistance due to formation of isolated gold islands (*20*), whereas those with thickness greater than 300 Å show almost no transmittance. Consequently, gold films of approximately 100 ± 10 Å thickness provide a reasonable compromise between film resistance and optical transparency for these studies.

In general, little or no photovoltaic response is observed for water, organic solvents, or nonabsorbing electrolyte solutions using either n-type tin oxide or gold electrodes. Solutions containing species that are photoionizable or otherwise photoelectrochemically active produce a transient photopotential, whose characteristics are dependent upon the electrode composition. Typical response observed for the photodecomposition of permanganate ion in aqueous solution is shown in Figure 3. In general, the signal is characterized by a rapid rise (2 μs) to the peak photopotential, followed by a complex decay over approximately 100–500 μs. In the case of permanganate ion, the most highly illuminated (front) electrode exhibits a negative photopotential with respect to ground for both n-type tin oxide and gold electrodes. The magnitude of the maximum photopotential is approximately equal for n-type tin oxide and gold electrodes with similar transmittance and resistance, as shown in Figure 3A,B. The signal decay in both cases is not characterized by a simple exponential (exp $[t/\tau]$) or power ($[t/\tau]^n$) time dependence but, rather, appears to be a convolution of these functions. The decay time, expressed as the time required for the signal to decay to 1/e of the maximum photopotential, is 300 μs for n-type tin oxide and 100 μs for gold electrodes. Although the signal characteristics vary slightly with electrode material, the sign, magnitude, and temporal behavior are comparable to those reported previously by Coleman and co-workers (*17*). The peak photopotential in our studies (Figure 3A) is approximately 5-fold smaller and the temporal decay is approximately 2-fold longer than reported previously with n-type tin oxide electrodes irradiated by a nitrogen laser (*17*); however, this discrepancy may be attributed to the method of signal acquisition. Coleman and co-workers measured the photopotential arising after a single laser pulse, and noted that the magnitude decreased and the time constant increased with repeated irradiation (*17*). In our experiments, the photopotential from multiple laser pulses at 10–30 Hz is averaged to yield a steady-state response that is smaller but more reproducible than single-shot experiments (Figure 4).

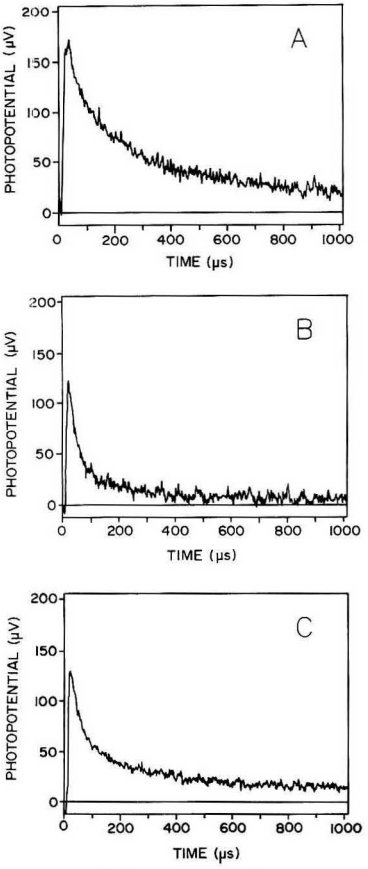

Figure 3. Photopotential for aqueous potassium permanganate solutions: (A) nitrogen laser excitation (337.1 nm, 0.23 mJ) using 400-Å n-type tin oxide electrodes at 4.7-mm separation distance, 10^{-3} M $KMnO_4$; (B) nitrogen laser excitation using 95-Å gold-film electrodes at 4.7-mm separation distance, 10^{-3} M $KMnO_4$; (C) KrF excimer laser excitation (248 nm, 6.8 mJ) using 95-Å gold-film electrodes at 4.7-mm separation distance, 10^{-4} M $KMnO_4$.

In addition to the dependence on electrode composition, the photovoltaic response is also a function of the film thickness, illuminated area, and illumination geometry. By using gold electrodes of 75–300-Å film thickness, the magnitude of the maximum photopotential for aqueous per-

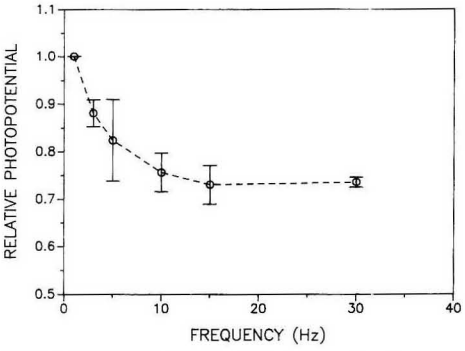

Figure 4. Dependence of relative photopotential on laser frequency. KrF excimer laser excitation (248 nm, 6.8 mJ) using 95-Å gold-film electrodes at 4.7-mm separation distance, 5×10^{-4} M $KMnO_4$.

manganate ion is observed to increase in direct proportion with transmittance, while the temporal characteristics remain constant. Likewise, the signal magnitude varies linearly with the total illuminated area of the gold electrode. Illumination normal to the electrode surface produces a photopotential that decreases in magnitude as the angle of illumination approaches grazing incidence. Reversal of the irradiation direction or of the electrical connection to the electrodes reverses the sign, but does not affect the magnitude or temporal behavior of the signal. When the sample between the electrodes is illuminated, but not the electrode surface itself, no photopotential is observed. Illumination of the front electrode alone, at normal incidence, produces signal magnitude and temporal decay comparable to that obtained by illumination of both electrodes. Moreover, replacement of the rear electrode with any solid metal conductor (nonilluminated) produces the same signal as the optically transparent electrode. Finally, overcoating the surface of either gold or n-type tin oxide electrodes with an insulating layer of silicon dioxide (600–5000 Å) produces no apparent change in the signal characteristics.

These observations support a number of important conclusions concerning the origin of the photovoltaic signal. First, since no signal is observed for nonabsorbing solvents and electrolytes, thermal or optical excitation of the electrode surface does not appear to be responsible for the photovoltaic response. While excitation of the electrode material undoubtedly occurs, as reported by Fox and Tien (*21*), it is not the predominant signal mechanism in this system. It is noteworthy that the maximum photopotentials developed for aqueous permanganate ion using the nitrogen and KrF excimer lasers (Figure 3B,C) differ by slightly less than 1 order of magnitude, as expected from the quantum yields for photodecomposition estimated above. This result indicates that the photovoltaic signal arises from photoexcitation and subsequent electron transfer from the solute molecules, rather than from the electrode surface. The studies of illumination geometry (grazing incidence and sample-only illumination) suggest that a surface phenomenon, rather than a bulk-phase phenomenon, is responsible for the signal. Finally, the investigations using electrodes overcoated with an insulating layer of silicon dioxide support the conclusion that thermally assisted adsorption/desorption of the solute is not the predominant signal mechanism. In consideration of these results, the most probable origin of the photovoltaic response is from photoionization, photodecomposition, or photooxidation/reduction of the solute at or near the front electrode surface. Further characterization studies of this phenomenon and a discussion of the possible mechanism are reported below.

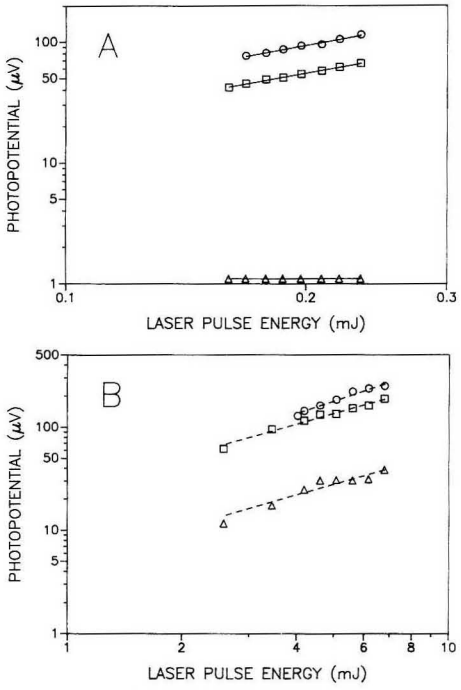

Figure 5. Dependence of log (photopotential) on log (laser pulse energy). (A) Nitrogen laser excitation (337.1 nm) using 400-Å n-type tin oxide electrodes: (○) 10^{-4} M $KMnO_4$; (□) 10^{-3} M TMPD; (△) water solvent. (B) KrF excimer laser excitation (248 nm) using 95-Å gold-film electrodes: (○) 10^{-4} M $KMnO_4$; (□) 10^{-4} M TMPD; (△) water solvent.

Characterization of the Photovoltaic Response. The response of the photovoltaic detection method is dependent upon a number of experimental parameters, including the laser wavelength and pulse energy, the separation distance between electrodes, the solute concentration, and the solvent composition. These characterization studies were performed using gold optically transparent electrodes in the sandwich-type cell. The maximum photopotential for the analyte, generally permanganate ion, was measured 12 μs after irradiation with the nitrogen or KrF excimer laser.

The dependence of the photovoltaic signal on laser pulse energy is shown in Figure 5 for the photodecomposition of an aqueous solution of 10^{-4} M permanganate ion. The logarithmic graph of photopotential versus pulse energy is linear with a slope of 1.1 for both the nitrogen laser (Figure 5A) and the KrF excimer laser (Figure 5B). This indicates that the photovoltaic signal arises from a one-photon excitation process, regardless of the differences in photon energy (3.7 and 5.0 eV, respectively) and total laser pulse energy (0.23 and 6.8 mJ, respectively), which is consistent with previous studies of the permanganate photodecomposition (*18*). In general, when the solvent water is freshly distilled, no background signal is observed with either the nitrogen or KrF excimer laser systems. However, if the water has been stored for more than a few days, a background signal is observed on an intermittent basis. This signal, shown in Figure 5B, arises from a one-photon excitation process and is believed to be due to the accumulation of atmospheric ammonia or volatile amines. To examine this hypothesis, samples of freshly distilled water were saturated with various gases including helium, nitrogen, carbon

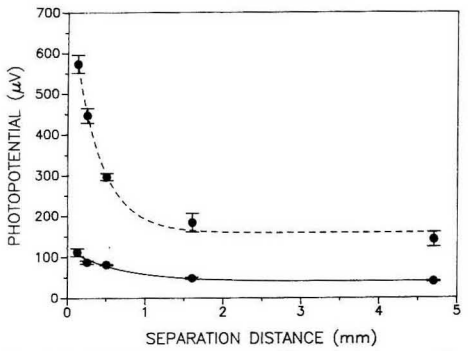

Figure 6. Dependence of photopotential on electrode separation distance for 10^{-4} M $KMnO_4$ using 95-Å gold-film electrodes: (—) nitrogen laser (0.23 mJ); (---) KrF excimer laser (6.8 mJ).

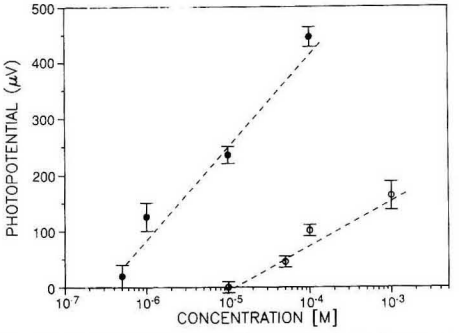

Figure 7. Dependence of photopotential on concentration for aqueous potassium permanganate solutions. Conditions: KrF excimer laser excitation (248 nm, 6.8 mJ) using 95-Å gold-film electrodes. Separation distance: (○) 4.7 mm; (●) 0.25 mm.

dioxide, oxygen, hydrogen peroxide, and ammonia. Of these potential interferences, only ammonia generated a detectable photovoltaic signal, which is consistent with the low ionization energy of ammonia and substituted amines in the condensed phase. This source of interference may be eliminated by using freshly distilled solvents or by removing dissolved gases by ultrasonication or sparging prior to use.

The maximum photopotential is also a function of the separation distance or optical path length between the two electrodes. This dependence is examined using both the nitrogen and KrF excimer laser systems to induce photodecomposition of an aqueous solution of 10^{-4} M permanganate ion. The photopotential is measured as a function of separation distance between 0.125 and 4.7 mm using gold electrodes in the sandwich-type cell. As shown in Figure 6, the photopotential decreases exponentially with increasing separation distance. When the distance between the electrodes exceeds 1 mm, the magnitude of the photopotential remains relatively constant. These results suggest that the simple model proposed by Coleman and co-workers (*17*), in which the photopotential is thought to arise because of the difference in light intensity at the two electrodes (vide supra), may not be completely accurate. If this model were correct, the difference in light intensity would be expected to increase with optical path length; thus, the photopotential should increase rather than decrease with separation distance. While a reduction in separation distance has an exponential effect on the magnitude of the photopotential, the temporal characteristics do not appear to be affected. These results indicate that a substantial increase in sensitivity could be realized by miniaturization of the detection cell.

The dependence of signal magnitude on sample concentration has also been investigated, as shown in Figure 7 for aqueous solutions of permanganate ion. These data were acquired using gold electrodes in the sandwich-type cell at separation distances of 0.25 and 4.7 mm. At both separation distances, a semilogarithmic relationship between photopotential and permanganate ion concentration is observed. Because the signal increases exponentially as the separation distance is decreased, the sensitivity or slope of the calibration curve is commensurately greater at 0.25 mm. The minimum detectable concentration is 5×10^{-7} M potassium permanganate, measured at a signal-to-noise ratio of 2.1 (99% confidence level), which corresponds to a total mass of 80 ng in the detector cell. The linear dynamic range shown in Figure 7 exceeds 3 orders of magnitude. Although these results are not optimal, they clearly indicate the high sensitivity inherent in this detection method.

Proposed Model of the Photovoltaic Response. The response of photoelectrochemical systems is of two general types: (1) those in which a photochemical reaction forms products which react at the electrodes and (2) those in which direct irradiation of a photosensitive electrode or membrane produces charge injection across the phase boundary (*22*). On the basis of the studies described herein, the photovoltaic detection method appears to be of the former type. Consequently, we may attempt to describe the response of this system using the model developed by Albery and Archer (*22*) and extended by Quickenden and Yim (*23, 24*). In this model, the photoelectrochemical system is presumed to consist of two inert metal electrodes, one illuminated and the other dark. These electrodes are immersed in a solution containing two redox couples, only one of which is photosensitive. For the purposes of this study, the photoactive species (permanganate ion) is the electron donor (Z) and the Y/Z redox couple is irreversible, while the electron acceptor couple (A/B) is reversible. The perturbations in concentration caused by irradiation are presumed to be small in comparison with the steady-state concentration of reactants in the dark. Under these conditions, the open-circuit photopotential (V) developed upon continuous illumination at low irradiance (E) is given by the following equation (*24*):

$$V = (RT/F) \ln [1 + (K_2'/K_3)E] \quad (1)$$

where R is the gas constant, T is the absolute temperature, and F is the Faraday constant. The constants K_2' and K_3 are complex functions of the steady-state concentrations of the Y/Z and A/B redox couples at the electrode surface and in bulk solution and of the rate constants for excitation, electron transfer, adsorption, photochemical reactions, etc.

This model predicts a semilogarithmic relationship between the photopotential and the concentration of photoelectrochemically active species, which is confirmed by the experimental results for permanganate ion shown in Figure 7. In addition, eq 1 predicts that the photopotential will be logarithmically related to the irradiance, if the light intensity is sufficiently low. When the data for the permanganate ion in Figure 5A,B are replotted in semilogarithmic form (photopotential versus log (laser pulse energy)), the resulting graphs are linear with correlation coefficients (R^2) of 0.986 and 0.993 for the nitrogen and KrF excimer lasers, respectively. Although the instantaneous irradiance produced by the pulsed lasers is quite high (18.7–28.5 kW/cm^2 for the nitrogen laser, 99.4–166 kW/cm^2 for the KrF excimer laser), the time-averaged irradiance at 10 Hz repetition rate is relatively low (1.5–2.3 mW/cm^2 for the nitrogen laser, 22.9–38.7 mW/cm^2

for the KrF excimer laser). These average irradiances are well within the range typically used under the conditions of continuous illumination, for which the theory of eq 1 was derived (*22*). Finally, the model predicts a linear dependence of photopotential on absolute temperature. While preliminary studies were not conclusive, due to thermal decomposition of permanganate ion, the photovoltaic signal does appear to increase slightly with temperature in the range 10–65 °C. It is interesting to note that the decay time decreases concurrently over this temperature range from approximately 160 to 90 μs.

The general trends of this theoretical model agree well with our experimental results. However, the assumptions implicit in the model may only be rigorously applicable at large electrode separation distances (>1 mm), where the back electrode may be considered nonilluminated. Further investigations of the photovoltaic detection mechanism at short separation distances are presently underway.

Effect of Solvent on Photoionization Energy. In the condensed phase, the nature of both the solute and the solvent directly influence the photoionization process. The ionization threshold and efficiency may vary substantially for a given solute, since nonpolar solvents will stabilize the neutral molecule relative to the product ions, whereas polar solvents will do the converse. Jortner and co-workers (*25, 26*) have proposed a relationship between the gas-phase (I_G) and liquid-phase (I_L) ionization energies that expresses this solvent dependence:

$$I_L = I_G + P_+ + V_0 \qquad (2)$$

where P_+ is the electronic polarization energy of the medium by the cation and V_0 is the energy of the electronic conduction level of the solvent.

The polarization energy term (P_+) represents the stabilization of the cation by the solvent medium. The extent of stabilization is known to be dependent upon the effective cationic radius (r_+) and the solvent optical dielectric constant (ϵ):

$$P_+ = -(1/(4\pi\epsilon_0))(e^2/2r_+)(\epsilon - 1)/\epsilon \qquad (3)$$

where ϵ_0 is the permittivity of a vacuum, and e is the charge of a proton. The optical dielectric constant of the solvent is commonly estimated as the square of the refractive index at 589 nm (n_D), regardless of the excitation wavelength. Equation 3 has been demonstrated to be a reasonable approximation of the polarization energy for simple dense fluids, such as liquified rare gases (*25, 26*), and for nonpolar, nonassociating solvents (*14, 27*).

The electronic conduction term (V_0) represents the stabilization of the electron injected into the solvent medium and has been measured as the difference in work functions between vacuum and solvent (*28*). In many nonpolar solvents, the lowest energy state of the electron is a delocalized or quasi-free state. Although the solvation mechanism in polar solvents remains in dispute (*29*), it is generally presumed that the electron is injected initially into the quasi-free state, after which the solvent undergoes rapid rearrangement to produce a localized, solvated electron of lower energy. The V_0 term, which adequately describes solvation of the electron in nonpolar solvents, is not wholly appropriate in polar media. The lack of a suitable theoretical model and the difficulty in experimental measurement have severely restricted the study of photoionization in polar solvents (*30*). In this work, we report the use of the photovoltaic method for detection of photoionization in water, alcohols, and other polar solvents and compare the results with ionization energies estimated using eq 2.

N,N,N′,N′-Tetramethyl-1,4-phenylenediamine (TMPD) was chosen for these studies because visual verification of the photoionization process is possible: the neutral molecule is colorless in solution, whereas the cation has an intense and characteristic blue color (*31*). For all of the solvent systems examined herein, photovoltaic signals are observed only when the blue cation color appears and persists during irradiation of the TMPD solution. These results strongly support the conclusion that the photovoltaic detection method is directly responsive to photoionization of the solute.

Table II. Effect of Solvent on the Photoionization of *N,N,N′,N′*-Tetramethyl-1,4-phenylenediamine (TMPD)

solvent	n_D[a]	P_+,[b] eV	V_0,[c] eV	I_L,[d] eV	photopotential,[e] μV: N_2 laser (3.7 eV)	photopotential,[e] μV: excimer laser (5.0 eV)
water	1.3330	−1.42	−1.3	3.48	66.3	187.0
methanol	1.3288	−1.41	−1.0	3.79	50.0	133.3
ethanol	1.3611	−1.50	−0.65	4.05	ND[f]	37.7
1-propanol	1.3850	−1.56	−0.30	4.34	ND	ND
ethylene glycol	1.4318	−1.67	NA	NA	ND	33.3
acetonitrile	1.3442	−1.45	NA	NA	ND	51.0
hexane	1.3755	−1.54	+0.04	4.70	ND	ND

[a] From ref 35 at 589 nm. [b] Calculated from eq 3, assuming $r_+ = 2.21 \times 10^{-10}$ m for TMPD. [c] From ref 30. [d] Calculated from eq 2, assuming $I_G = 6.20$ eV for TMPD. [e] Measured for 10^{-4} M TMPD solution using 95-Å gold-film electrodes at 4.7-mm separation distance. [f] NA = not available, ND = not detectable.

The choice of TMPD is also advantageous because of the extensive information available in the literature (*4, 14, 27, 31–34*). The adiabatic gas-phase ionization energy of TMPD is approximately 6.20 eV (*31*), and photoionization is reported to arise through a two-photon excitation process. Absorption of the first photon produces the excited singlet state of TMPD, which undergoes intersystem crossing. The second photon is subsequently absorbed by the triplet state to effect ionization. Although this two-photon excitation process has been verified for TMPD in the liquid (*3*) and solid (*32*) states, a single-photon process has also been implicated in both nonpolar (*33*) and polar (*34*) liquid solvents. Single-photon ionization energies ranging from 4.3 to 4.9 eV have been reported in nonpolar solvents (*14, 27*). These previous measurements may be in error, however, since photoionization may be assisted by the externally applied electric field used for photoconductive detection, yielding systematically low threshold values. Such errors do not occur in the photovoltaic detection method.

As shown in Figure 5, the logarithmic graph of the observed photopotential for TMPD in water versus the laser pulse energy is linear with a slope of 1.1 for both the nitrogen laser (337.1 nm, 3.7 eV) and the KrF excimer laser (248 nm, 5.0 eV). These results indicate that the photoionization of TMPD proceeds through a single-photon process in the absence of an applied electric field, and that the ionization energy in water is less than 3.7 eV. By use of eq 2, the ionization energy for TMPD in water is estimated to be 3.48 eV, which is consistent with these experimental data.

Table II summarizes the photopotentials measured for TMPD in a variety of polar solvents. In general, the magnitude of the photopotential shows direct correlation with solvent polarity. With increasing polarity, solvent stabilization of the TMPD cation decreases slightly (P_+ term), while stabilization of the electron increases markedly (V_0 term). Thus, the ionization energy decreases with increasing solvent polarity, as predicted by eq 2. The photoionization of TMPD in the homologous series of alcohols provides a clear illustration of this trend. If no signal is observed with either laser system (i.e., TMPD in 1-propanol), then the ionization threshold must be greater than 5.0 eV or, alternatively, the

ionization efficiency in that solvent is too low to produce a detectable signal. When a signal is observed with the excimer laser but not with the nitrogen laser (i.e., TMPD in ethanol), then the ionization threshold must lie between 5.0 and 3.7 eV. If signals are observed from both lasers (i.e., TMPD in methanol), then the ionization threshold is less than 3.7 eV. These estimations for the ionization energy of TMPD in alcohols are in reasonable agreement with the values calculated using eq 2.

CONCLUSIONS

The photovoltaic detection method, first reported by Coleman and co-workers (*17*), shows promise for sensitive and selective detection of photoionization and related photoelectrochemical phenomena. Because no bias voltage is applied to the electrodes, contributions from the photoelectric effect and from intrinsic solvent conduction are substantially reduced or eliminated. Consequently, measurements of the photopotential can be accomplished in polar solvents and in solutions of relatively high ionic strength, where a conductance measurement may not be possible.

In this work, the photovoltaic detection method is characterized with respect to the optically transparent electrode material, electrode separation distance, laser pulse energy, sample concentration, and solvent composition. Although these characterization studies have been limited to potassium permanganate and TMPD, a variety of other solutes have been examined. Neutral organic molecules, both nonpolar such as pyrene and polar such as aniline and coumarin, can be readily detected. In addition, ionic solutes such as disodium fluorescein and Rhodamine B dyes are detectable in a variety of polar solvents. While the results presented here are limited to static systems, preliminary studies indicate that this detection method may be easily adapted to flowing systems such as chromatographic or electrophoretic separations.

ACKNOWLEDGMENT

We thank Dr. Richard D. Sacks (University of Michigan) and Dr. Stephen W. Brewer (Eastern Michigan University) for help in producing the gold-film electrodes, Dr. Stanley R. Crouch (Michigan State University) for use of the nitrogen laser, Randall D. King for tin oxide electrodes, and Martin Rabb for design and construction of the amplifier circuit. Special acknowledgment is given to Christine E. Evans, Lawrence E. Bowman, and Stephen V. Medlin for helpful discussions.

Registry No. TMPD, 100-22-1; $KMnO_4$, 7722-64-7; gold, 7440-57-5; antimony, 7440-36-0; tin oxide, 18282-10-5.

LITERATURE CITED

(1) Schwarz, F. P.; Mautner, M. *Chem. Phys. Lett.* **1982**, *85*, 239.
(2) Scott, T. W.; Twarowski, A. J.; Albrecht, A. C. *Chem. Phys. Lett.* **1979**, *66*, 1.
(3) Braun, C. L.; Scott, T. W.; Albrecht, A. C. *Chem. Phys. Lett.* **1981**, *84*, 243.
(4) Yakovlev, B. S.; Lukin, L. V. In *Advances in Chemical Physics*; Lawley, K. P., Ed.; Wiley: New York, 1985; Vol. 60, Chapter 3.
(5) Schmidt, W. F. *Can. J. Chem.* **1977**, *55*, 2197.
(6) Jortner, J.; Gaathon, A. *Can. J. Chem.* **1977**, *55*, 1801.
(7) Casanovas, J.; Grob, R.; Delacroix, D.; Guelfucci, J. P.; Blanc, D. *J. Chem. Phys.* **1981**, *75*, 4661.
(8) Scott, T. W.; Albrecht, A. C. In *Advances in Laser Spectroscopy*; Garetz, B. A., Lombardi, J. R., Eds.; Heyden: London, 1982; Vol. 1, Chapter 3.
(9) Locke, D. C.; Dhingra, B. S.; Baker, A. D. *Anal. Chem.* **1982**, *54*, 477.
(10) Voigtman, E.; Winefordner, J. D. *Anal. Chem.* **1982**, *54*, 1834.
(11) Voigtman, E.; Winefordner, J. D. *Talanta* **1983**, *30*, 75.
(12) Berthod, A.; Mellone, T.; Voigtman, E.; Winefordner, J. D. *Anal. Sci.* **1987**, *3*, 405.
(13) Yamada, S.; Ogawa, T. *Prog. Anal. Spectrosc.* **1986**, *9*, 429.
(14) Holroyd, R. A.; Russell, R. L. *J. Phys. Chem.* **1974**, *78*, 2128.
(15) Siomos, K.; Christophorou, L. G. *Chem. Phys. Lett.* **1980**, *72*, 43.
(16) Scott, T. W.; Braun, C. L.; Albrecht, A. C. *J. Chem. Phys.* **1982**, *76*, 5195.
(17) Coleman, W. F.; Prisant, M. G.; Zare, R. N. *J. Phys. Chem.* **1980**, *84*, 2685.
(18) Zimmerman, G. *J. Chem. Phys.* **1955**, *23*, 825.
(19) Adamson, A. W.; Waltz, W. L.; Zinato, E.; Watts, D. W.; Fleischauer, P. D.; Lindholm, R. D. *Chem. Rev.* **1968**, *68*, 541.
(20) Holland, L. *Vacuum Deposition of Thin Films*; Wiley: New York, 1956; Chapter 7.
(21) Fox, M. A.; Tien, T. *Anal. Chem.* **1988**, *60*, 2278.
(22) Albery, W. J.; Archer, M. D. *Electrochim. Acta* **1976**, *21*, 1155.
(23) Quickenden, T. I.; Yim, G. K. *Electrochim. Acta* **1979**, *24*, 143.
(24) Quickenden, T. I.; Yim, G. K. *J. Phys. Chem.* **1979**, *83*, 2796.
(25) Raz, B.; Jortner, J. *Chem. Phys. Lett.* **1969**, *4*, 155.
(26) Messing, I.; Jortner, J. *Chem. Phys.* **1977**, *24*, 183.
(27) Bullot, J.; Gauthier, M. *Can. J. Chem.* **1977**, *55*, 1821.
(28) Holroyd, R. A.; Allen, M. *J. Chem. Phys.* **1971**, *54*, 5014.
(29) Krohn, C. E.; Thompson, J. C. *Phys. Rev. B* **1979**, *20*, 4365.
(30) Bernas, A.; Grand, D.; Amouyal, E. *J. Phys. Chem.* **1980**, *84*, 1259.
(31) Nakato, Y.; Ozaki, M.; Egawa, A.; Tsubomura, H. *Chem. Phys. Lett.* **1971**, *9*, 615.
(32) Cadogan, K. D.; Albrecht, A. C. *J. Chem. Phys.* **1965**, *43*, 2550.
(33) Richards, J. T.; Thomas, J. K. *Trans. Faraday Soc.* **1970**, *66*, 621.
(34) Takeda, S. S.; Houser, N. E.; Jarnagin, R. C. *J. Chem. Phys.* **1971**, *54*, 3195.
(35) Weast, R. C.; Astle, M. J. *CRC Handbook of Chemistry and Physics*; CRC Press: Boca Raton, FL, 1981.

RECEIVED for review June 28, 1991. Accepted August 16, 1991. This work was supported in part by the Michigan State University Foundation, the Alcoa Foundation, and the Dow Chemical Co. Preliminary results were presented at the Pittsburgh Conference on Analytical Chemistry and Applied Spectroscopy, New Orleans, LA, 1988.

Factors Influencing Ion Signal Profiles in Pulsed Glow Discharge Mass Spectrometry

J. A. Klingler,[1] C. M. Barshick, and W. W. Harrison*

Department of Chemistry, University of Florida, Gainesville, Florida 32611-2046

Ionization mechanisms responsible for the formation of prepeaks and afterpeaks on ion signals observed in pulsed glow discharges and potential analytical use of pulsed glow-discharge mass spectrometry have been investigated. The formation of a prepeak at the beginning of the pulse is related to the ionization efficiency of electrons accelerated across the cathode fall region. The appearance of an afterpeak at the termination of the discharge is associated with the energy, population, and ionization efficiency of metastable discharge gas atoms. As a result of the differences in pulse profiles, it is possible to acquire data over specific regions of the pulse that permit discrimination against interfering signals in the mass spectrum.

INTRODUCTION

The glow discharge is growing in scope as an atomization and ionization source in the elemental analysis of solids (*1*). In optical spectroscopy, the abundant atom population and steady emission intensity, coupled with the rugged source design, have made the glow discharge well suited for routine trace analysis. In mass spectrometric analysis, features such as ease of sample preparation and the ability to analyze a wide variety of samples with minimal matrix effects have contributed to widespread interest in the glow discharge as an elemental ion source.

Numerous glow discharge source configurations are possible (*2*), all relying on the application of high voltage, either as a direct current (dc) or as an oscillating potential in the radio frequency (rf) range. The glow discharge in this study, a variation of a dc coaxial cathode type source, is pulsed between ground and a high negative potential. Pulsed glow discharges have been used in several areas of analytical chemistry; for example, hollow cathode lamps show an increase in emission output by applying a pulsed voltage instead of the more conventional dc voltage (*3*). Laser excited fluorescence in the "dark period" between pulses of a hollow cathode discharge yields signals with reduced background noise and femptogram detection limits for some elements (*4*). Research in our laboratory indicates that pulsed glow discharges enjoy increased sputter yield and higher ion signal intensity over conventional dc sources (*5*).

Of greater interest in glow discharge mass spectrometry (GDMS) is the time-dependent response of the individual ion signals; both sputtered and contaminant gas species exhibit reproducible anomalies that do not match the square-wave signal driving the pulse power supply. The time period after glow discharge termination has been investigated by other researchers. Strauss et al. (*6*) have used atomic absorption spectroscopy to measure the metastable atom concentration in the time domain immediately after the discharge is extinguished. Similarly, Biondi (*7*) monitored the electron density in the postpulse time period using resonant cavity microwave techniques. The objectives of this paper are to report potential analytical uses of a pulsed glow discharge and to examine possible processes controlling the shape of the ion signal at different times during the pulse period. Various features of the pulsed discharge are described, on the basis of their occurrence relative to the applied voltage.

* To whom correspondences should be addressed.
[1] Current address: Shell Development Co., Westhollow Research Center, Houston, TX.

EXPERIMENTAL SECTION

The instrumental layout used in this paper for atomic absorption (*8*) and mass analysis (*9*) has been described elsewhere. Modifications used to investigate the time-dependent nature of the pulsed glow discharge are described in this section.

Atomic Absorption Analysis. In order to correlate the glow discharge pulse and hollow cathode lamp (HCL) emission, the discharge pulse rate is controlled by a synchronization signal from a mechanical light chopper. The chopper is fed into the external control terminal of a square-wave pulse generator (Hewlett-Packard, Model HP8003A). The variable 0–5-V output from the HP8003A generator is then used to drive an operational power supply (Kepco, Model OPS3500) and to trigger the data collection system. The position of the data gate with respect to the discharge pulse and HCL signal is controlled by delaying the arrival of the trigger signal using a variable signal-delay circuit; the delayed trigger pulse is fed into a signal processor (EG&G Princeton Applied Research, Model 1112) to control the sychronization of data acquisition.

Mass Analysis. Pulsed discharge experiments permit analysis of the ion signal relative to the applied voltage. Figure 1 is a schematic of the equipment used to collect and analyze individual ion signals. The system centers around a waveform generator (Hewlett-Packard, Model HP3325A) that is capable of producing square, sine, triangle, and sawtooth waves. The amplitude and shape of the waveform generator output controls the operational power supply that drives the glow discharge.

Individual ion signals of a selected mass-to-charge ratio are collected using a multichannel analyzer (MCA, Tracor Northern, Model 7200). The ion signal from the mass spectrometer passes through a peak height discriminator (SSR Instruments, Model 1120) and is then converted to a TTL compatible pulse before being directed to the MCA. The start of data acquisition is synchronized with the applied voltage by a trigger pulse from the waveform generator. The duration of each MCA channel controls how much of the waveform is displayed for analysis. Data taken in this study typically use 1024 MCA channels with a collection time of 19 μs/channel, allowing sufficient time to record the on portion and signal decay of a 50-Hz pulse period with a 50% duty cycle. In order to correlate the peak shape with the applied voltage, a 1000:1 voltage divider (Tektronix, Model P6013A) is attached to the high-voltage terminal of the discharge probe and the reduced voltage fed into a voltage-to-frequency (V/F) converter. The V/F converter produces a TTL-compatible signal for accumulation with the MCA.

Samples were prepared from standard reference materials of low alloy steel, copper, and brass obtained from the National Institute for Standards and Technology. All metal samples were machined into pins 2 mm in diameter with 5 mm exposed to the discharge. Experiments were performed using reagent grade argon or neon as the discharge gas; metastable quenching experiments used commercially available mixtures of methane in argon (Spectra Gas).

A thermal filament source was built in this laboratory consisting of a tungsten wire 7.5 mm in length × 0.125 mm in diameter that

0003-2700/91/0363-2571$02.50/0

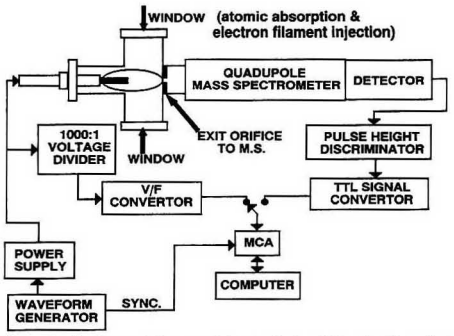

Figure 1. Instrumentation used for analysis of ion signal profiles.

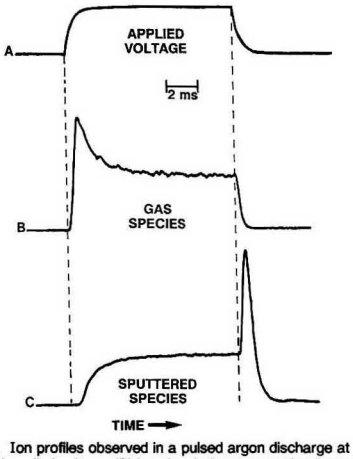

Figure 2. Ion profiles observed in a pulsed argon discharge at 1 Torr: (A) typical applied voltage; (B) ion signals for gas species (here, H_2O^+); (C) sputtered species ($^{56}Fe^+$).

can be heated to white hot with currents up to 6.0 A. To accelerate electrons into the discharge, a variable 0- to -500-V dc bias (relative to the discharge housing) is applied the filament. The injection of electrons into the discharge is controlled by a ring electrode 4.75 mm in length × 19.05 mm in diameter, mounted between the filament and the discharge. This electrode operates at the same potential as the filament when electrons are allowed to enter the discharge and is switched to a +100-V bias to prevent electron injection.

RESULTS AND DISCUSSION

Typical Pulsed Profiles. The dc glow discharge produces a steady-state source of ions for analysis. Pulsed glow discharges, on the other hand, exhibit (1) a transition period as the high voltage is first applied to the sample, (2) an interval of steady-state output (as in a dc discharge) when the voltage stabilizes, and (3) another transition period at the termination of the applied voltage.

Figure 2 shows the two types of ion signal profiles observed in a pulsed discharge, relative to the applied voltage. Application of the high voltage (Figure 2A) does not immediately yield an ion signal. There is a brief induction time before any signal is observed, followed by a period in which the discharge gas and the contaminant gas species (e.g., H_2O, CO_2, N_2, and CO) in the discharge chamber show a sudden increase in their ion signal (termed a "prepeak") before decaying to a plateau

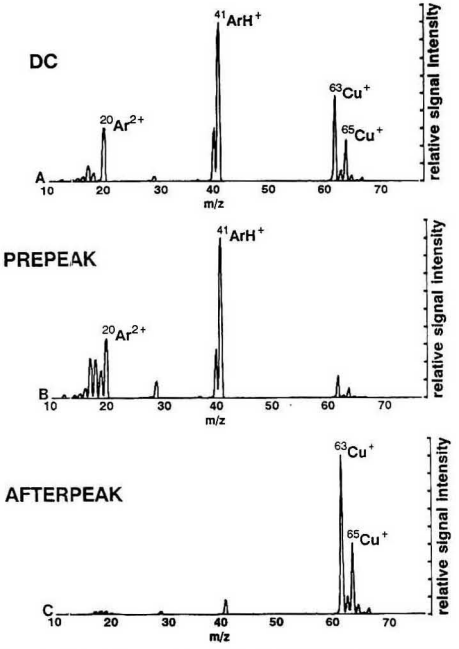

Figure 3. Effect of gate position on the mass spectrum of C1101 brass in a 1-Torr, 4-mA argon discharge. All spectra were accumulated using a 1-ms data gate: (A, top) dc glow discharge; (B, middle) 50-Hz, pulsed glow discharge with data gate placed in the prepeak region of the pulse signal; (C, bottom) same pulsed discharge with data gate placed in the afterpeak region.

value (Figure 2B). During the corresponding period, no prepeaks are observed for atoms sputtered from the sample surface. Instead, after a slightly longer induction period than for contaminant gas species, the sputtered species signal rises to a plateau value (Figure 2C). Plateau values for both sputtered and gas species hold at this level until termination of the applied voltage.

At the end of the discharge cycle, both gas and sputtered species signals remain constant for ca. 0.15 ms, after which each type of species behaves differently. For contaminant gas species, the ion signal decays to the baseline. In contrast, sputtered species signals display a sudden increase in intensity (termed an "afterpeak", Figure 2C) to a value above the plateau steady state, decaying to the baseline within several milliseconds.

As a result of the differences in pulse profiles, it is possible to acquire data over specific regions of the pulse. These time-resolved spectra permit discrimination against interfering signals in the mass spectrum. Figure 3 compares the spectra resulting from a dc discharge versus a time-resolved system in which data are collected through a narrow gate placed over different portions of the pulse period. Figure 3A is the dc mass spectrum for a C1101 brass pin. Figure 3B is a mass spectrum using the same pin, except the data are collected only during the prepeak region of the pulse discharge. Because ions of sputtered species are not yet in abundance, the resulting spectrum is deficient in analytical signal. Figure 3C is a mass spectrum taken through a data gate placed over the afterpeak region. Sputtered species become dominant while contaminant gas species are significantly reduced in intensity.

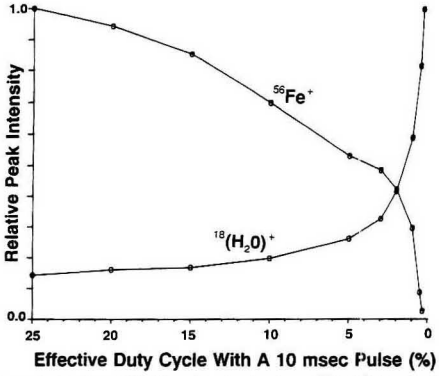

Figure 4. Sputtered ($^{56}Fe^+$) and contaminant gas ($^{18}(H_2O)^+$) ion signals as the pulsed discharge off time increases while maintaining a constant 10-ms on time. The duty cycle is the fraction of the total pulse period represented by the 10-ms discharge on time.

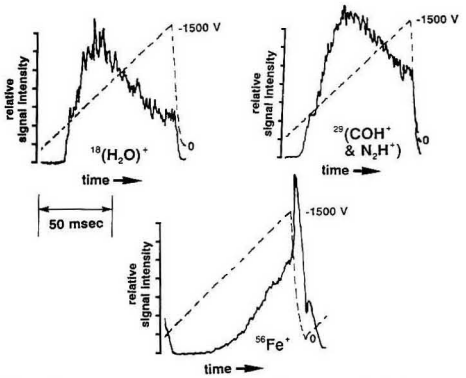

Figure 5. Pulsed discharge ion signals using a sawtooth high-voltage waveform.

A specific example of selectively collecting data over a limited time period of the pulse discharge to reduce or eliminate spectral interferences involves the m/z 28–29 region of the mass spectrum, where contaminant ions CO^+, N_2^+, COH^+, and N_2H^+ can be troublesome in the analysis of silicon. When data are collected through a gate placed over the decaying portion of the afterpeak, the contaminant gas interferences can be virtually eliminated from the mass spectrum, revealing isotope ratios for silicon to within 1% of their accepted values (*5*).

Sample Surface between Pulses. At 1 Torr, the sample is exposed to a flux of argon atoms that can physisorb onto the sample surface (*10*). Coabsorbing with the argon will be contaminant gases such as water, nitrogen, oxygen, carbon monoxide, and carbon dioxide. While these gases are a minor component compared to argon, they may react with the surface to form a variety of compounds (e.g., oxides). The displacement of physically adsorbed argon atoms by species that can chemically bond to the surface creates a barrier that becomes increasingly difficult to remove as additional reactive species interact with the surface.

To evaluate the effect of adsorbed gases on the ion signal, the duration and peak voltage of the on portion of the pulsed discharge were kept constant while the off portion was increased (effectively increasing the pulse period and the time between pulses while the pulse duty cycle was decreased). Figure 4 illustrates the effect on the observed signal intensities by increasing the off time of a 1-Torr argon discharge using a constant 10-ms on time. Ion signal intensities were recorded in the plateau region in order to sample ions from the steady-state portion of the pulsed discharge. The x axis denotes the percentage of the total pulse period represented by the 10-ms on time. For example, a 1% duty cycle (at 10-ms on time) represents a total pulse period of 1000 ms; a 25% duty cycle yields a 40-ms pulse period. As the off-time increases (moving left to right on the x axis), there is little change in the H_2O^+ signal until approximately a 5% duty cycle is reached, after which there is a sharp increase in the water signal. This corresponds to the point where the iron signal, already regularly decreasing with increasing off-time, sharply decreases in intensity. These data indicate that off times greater than 190 ms are detrimental to the iron ion signal due to the adsorption of contaminant gases, increasing thickness of adsorbed layers, cooling of the cathode, or the formation of oxides on the surface. It is not clear at this point whether the effect is strictly a sputtering phenomenon or if changes in ionization are also occurring. Fortunately, within the pulse cycles normally used in pulsed GDMS (<100-ms off-time, >10% duty cycle), there is little effect in duty cycle variation.

Prepeak Region. As illustrated in Figure 2B, contaminant gas species produce a rapid rise in signal before decaying to a steady-state plateau value. The prepeak is observed only for contaminant gas species, appearing after a short induction period (ca. 0.3 ms).

Previous studies (*11*) have shown that ions observed with the mass spectrometer originate with reactions occurring in close proximity to the exit orifice. The rate at which sputtered species arrive at the exit orifice depends on the time required for atoms to diffuse across the dark space and negative glow (a pressure-dependent characteristic). At 1 Torr, ion signals from sputtered atoms are not detected until approximately 0.8 ms after the discharge voltage is applied. Moving the cathode closer to the exit orifice decreases the induction period of sputtered species yet has little effect on the gas species, indicating that the sputtered species signal is tied to the drift velocity of atoms across the discharge space. The source of the gas ion signal is presumably due to electron impact ionization of the steady-state population of contaminant gas atoms near the exit orifice (because of their uniform presence in the discharge environment). For these reasons, gas species signals always appear before sputtered species in the time frame of a pulse period.

In order to identify the factors influencing formation of the prepeak, application of the high voltage was altered by replacing the rapidly changing square wave with a slowly increasing sawtooth wave (see Figure 5). As indicated in the figure, the observed signal for the gas species initially increases with applied voltage, reaches a maximum value, then decreases as the applied voltage continues to increase. The same effect is observed at approximately the same voltages if the applied potential is slowly decreased. The sputtered species (Figure 5, $^{56}Fe^+$) follows its normal pattern of producing an afterpeak when the applied voltage terminates. These results suggest that the potential difference across the cathode fall region (*12*) is a significant factor in affecting contaminant gas ionization.

To explain the prepeak, it is necessary to consider how contaminant gases are ionized in a glow discharge. In an argon discharge, the only significant source of contaminant gas ionization is electron impact (Penning ionization energies are insufficient to ionize common contaminant gases). The energies of electrons present in the negative glow are often modeled to have a Boltzmann distribution, though Langmuir probe experiments indicate there may be a deficiency of higher

energy electrons such that the distribution is not truly Boltzmann (*13*). Of particular interest is the 2-eV mean energy of secondary electrons (electrons resulting from ionizing collisions (*14*)), meaning that only a small fraction of these electrons is energetic enough to ionize contaminant gases. Factors that influence the electron energy distribution are expected to change the overall ionization in the discharge.

Primary electrons (electrons emitted from the sample surface and accelerated to high velocity by the electric field across the dark space (*15*)) are thought to influence the secondary electron energy distribution. As primary electrons pass through the negative glow, their energy can be attenuated as they interact with slower moving secondary electrons via Coulombic interactions (*16*). These interactions are expected to be more efficient with slower moving primary electrons due to the reduced collisional cross section of electrons at higher velocities (*17*). Again referring to Figure 5, when the high voltage is first applied to the sample in a pulsed discharge, a brief delay is required for the discharge to be initiated. Once argon ions begin to bombard the surface, electrons emitted from the surface experience the changing electric field as the applied voltage increases. At first, these slow primary electrons are efficient in transferring their energy to the secondary electrons, temporarily increasing the population of high-energy electrons in the plasma. As the applied voltage continues to increase, the efficiency of the primary–secondary interaction decreases and the high-energy electron population is reduced. Hence, the prepeak may be the result of a temporary increase in the population of electrons energetic enough to ionize contaminant gases as the electric field passes from low to high voltage.

The effect of voltage on the observed gas species signal is not unique to pulsed discharges. Conventional dc discharges also show increased gas signals, particularly H_2O^+ and H_3O^+, at lower operating voltages. Moreover, we have observed the same relationship between voltage and gas species signals in radio frequency discharges as the dc bias voltage is varied (*18*).

Plateau Region. A mass spectrum obtained in the plateau region of a pulsed discharge is similar to a dc spectrum. Once the discharge has stabilized to form the plateau, the signal remains steady until the applied voltage is terminated, regardless of the duration of the pulse period. An examination of the kinetic energy of ions sampled by the mass spectrometer indicates that the temperature of the plasma is slightly higher in the plateau region of a pulsed discharge than for a dc discharge at the same average current. This results from the higher voltage required to maintain the same number of ions striking the cathode in the shorter time period of a pulsed discharge. No other significant differences in the two types of discharges were observed in the plateau region.

Afterpeak Region. The afterpeak region of the pulsed discharge displays the striking feature of a large surge in ion signal intensity for the sputter species after the discharge is turned off. In an argon glow discharge this feature is unique to sputtered elements and other species with sputtered components, such as metal–argide diatomic molecules. The afterpeak commences shortly after termination of the applied voltage, reaching its peak value in less than 1 ms, followed by a decay to the baseline. Factors affecting the afterpeak and possible mechanisms for its formation are of direct analytical interest.

Termination of the Applied Voltage. In the 1950s, Biondi (*7*) investigated the electron density in pulsed neon and helium discharges using resonant cavity microwave techniques at pressures between 1.5 and 3.3 Torr. Those experiments indicated an increase in the electron population during the first 0.10 ms following termination of the applied voltage, thought to result from collisions of argon metastable atoms releasing electrons. Using atomic absorption spectroscopy, Strauss et al. have observed an increase in the argon metastable population in a 1.8-Torr discharge during the first 0.15–0.20 ms after the discharge is terminated (*6*), an effect they attribute to the recombination of low-energy electrons with argon ions to form argon metastable atoms. The formation of afterpeaks in our pulsed glow discharges, as observed mass spectrometrically, begins approximately 0.15 ms after the applied voltage is terminated. During this delay, ion signals remain at the same intensity as the plateau region, followed by appearance of the afterpeak. In our consideration of glow discharge afterpeaks, attention is focused on a time in the pulse sequence later than for either Strauss' or Biondi's study.

Afterpeak Formation. Our work has shown that the formation of an afterpeak requires the pulsed voltage to change rapidly over a potential difference of at least 400 V (at 1 Torr of argon). Since the operational power supply used in these studies closely follows the shape of a controlling waveform, it is possible to influence the rate of change of the applied voltage by using different waveform shapes to regulate the power supply or by placing a dc bias on the controlling wave to prevent the discharge from completely shutting off.

Studies using triangle-shaped pulses, with steadily increasing and decreasing voltage, do not show a significant afterpeak because the change in potential is too gradual. A sawtooth wave, on the other hand, exhibits an afterpeak comparable in size to a square wave as the potential slowly increases and then rapidly falls to zero (like a square wave). Using a reversed sawtooth, whereby the waveform rapidly increases followed by a slow decay to zero, little or no afterpeak is observed. Furthermore, the size of the afterpeak appears to be directly proportional to the magnitude of the voltage change. Experiments using a square wave in conjunction with a dc bias voltage show that as the difference between the bias voltage and the applied square wave becomes smaller, the intensity of the afterpeak is reduced. These results indicate that a rapid shift in the average electron energy and population is required to form an afterpeak. The 0.15-ms delay in the formation of the afterpeak may represent the time required for the energetic electrons to thermalize through elastic collisions with neutral atoms (*7*). Any additional metastable atom formation is expected to occur in this delay period.

The afterpeaks observed with our quadrupole mass spectrometer maximize at einzel lens and Bessel box energy discriminator values different from those normally used in optimizing dc discharge ion signals. Figure 6 illustrates that changing the center of the energy band-pass of the Bessel box alters the shape of the plateau and afterpeak. These data indicate that the average energy of ions in the afterpeak is slightly higher than in the plateau. The difference in energy may result from metastable argon atoms being the only source of ionization in the afterpeak region, electrons having rapidly disappeared with discharge termination, transferring kinetic energy during the ionization process that increases the average energy of ions in the afterpeak.

Penning Ionization in the Afterpeak. Only atoms with ionization potentials below the argon metastable energy level produce afterpeaks, pointing to Penning ionization as the principal mechanism for ionization after termination of the discharge voltage. Several experiments were carried out to study this possibility: (1) the use of an alternative discharge gas with higher metastable energy, (2) monitoring of the metastable population by atomic absorption, (3) the use of auxiliary sources of ionization to alter the metastable population, and (4) introduction of metastable quenching reagents.

If the formation of the afterpeak depends on discharge gas metastable atoms, then the energy level of the metastable state should dictate which atoms and molecules display afterpeaks.

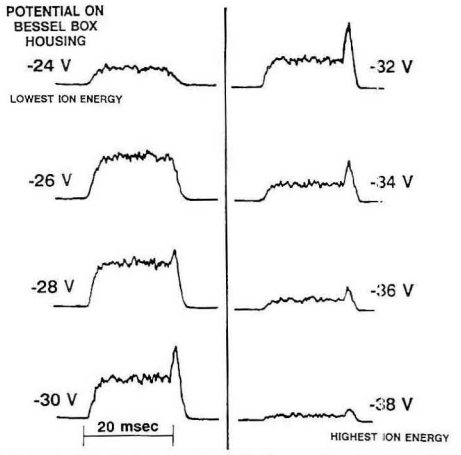

Figure 6. Effect of energy discrimination on the afterpeak. The housing potentials indicate only relative ion energy.

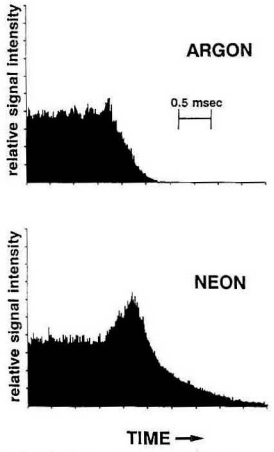

Figure 7. Pulse termination region for H_2O^+ in (a) argon and (b) neon discharges showing afterpeak formation for a nonsputtered species.

Argon metastable energy levels (11.55 and 11.72 eV) are too low to ionize water (ionization energy 12.6 eV) or other contaminant gas species with ionization potentials above the highest energy level of the argon metastable states, and these ion signals do not exhibit an afterpeak (*5*). In contrast, neon has metastable states of sufficient energy (16.62 and 16.72 eV) to ionize most common contaminant gas molecules. Figure 7 is a trace of the afterpeak region of H_2O^+ using first an argon discharge and then neon. The discharge gas with higher energy metastable states yields afterpeaks for water and other gas species.

The population of metastable atoms in the glow discharge is a balance between formation processes (e.g., argon atoms and ions colliding with low-energy electrons) and destruction processes (e.g., metastable atoms colliding with the walls and other atoms in the glow region and collisions with electrons of sufficient energy to ionize the metastable atoms) (*19*). A study to monitor the argon metastable atom population in the negative glow after termination of the applied voltage was

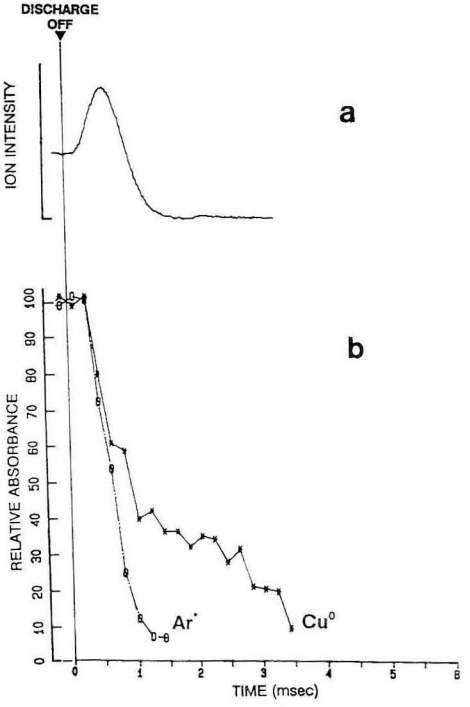

Figure 8. Simultaneous measurements of the ion signals and atomic absorption signals in the termination region of a −2200-V dc, 2-mA average current argon discharge at a pressure of 1.0 Torr: (a) the ^{63}Cu ion signal (mass spectrometer); (b) absorbance intensity of the argon metastable atom, Ar^* (811 nm), and neutral copper, Cu^0 (324 nm).

undertaken using atomic absorption. Figure 8 compares the time relationship of the applied pulse waveform, the resulting ion signal for ^{63}Cu, and the absorption intensity for copper atoms and argon metastable species. The argon metastable atom absorbance at 811.5 nm (*20*) and the copper atom absorbance at 324.7 nm are monitored from 0.5 ms prior to and 3.5 ms after termination of the applied voltage. Note that at the apex of the afterpeak ion signal the argon metastable population has already fallen to 65% of its plateau value and the copper atom population to 75% of its plateau value. Beyond the maximum of the afterpeak ion signal, the decline of the argon metastable signal is more rapid than the copper atom signal, indicating the decay of the copper ion afterpeak is controlled by the loss of the ionizing agent (argon metastables) rather than the loss of analyte atoms diffusing to the walls of the discharge chamber.

Another method for investigating the role of metastable atoms in the afterpeak region is to reduce the metastable population with an appropriate quenching reagent. Hess et al. (*21*) used this technique to investigate the role of Penning ionization in the glow discharge. In that study, methane served as a metastable quenching reagent, resulting in a decrease in argon metastable atomic absorption signal with increasing methane concentration. If metastable species are responsible for formation of the afterpeak, then the addition of methane to the discharge gas should affect the observed afterpeaks.

The sputtered species ion signal in a copper discharge was monitored with the mass spectrometer as a function of the

Table I. Effect of Methane Concentration on the Observed Copper Signal

% methane in argon	% plateau	% afterpeak	ratio of afterpeak to plateau
0.0	100	100	1.00
1.0	82	47	0.57
2.5	37	18	0.49
5.0	19	8	0.42
7.5	9	4	0.44
10.0	5	2	0.40

methane concentration. A 0.50-ms data gate was first placed over the plateau region of the pulse discharge and then over the center of the afterpeak. Table I illustrates the effect on the relative copper signal in each region while the methane concentration is varied from 0 to 10%. Both the plateau and afterpeak signal are reduced with increasing methane concentration; however, the effect is more pronounced on the afterpeak. For example, the addition of 1% methane reduces the copper ion signal in the plateau ca. 18%, but the afterpeak region is reduced by 53%. Since atomic absorption experiments (*21*) have shown that the metastable concentration, and not the sputtered atomic population, is changing with the addition of methane, the change in the ion signal in the two regions is likely attributable to the loss of metastable atoms. The smaller decrease exhibited by the plateau is attributed to a steady-state condition that results in this region of the pulse. In addition to providing electron impact ionization of gas and analyte atoms, energetic electrons keep the metastable population in a pseudo steady-state equilibrium. This is in contrast to the afterpeak region where ionizing species cannot be replenished until the next pulse. Hence the loss of metastable argon atoms is more dramatic in the afterpeak region.

Thus, while our work indicates that the metastable population decreases in the afterpeak region, the sputtered ion signal actually increases to form the afterpeak. After the discharge is terminated, sputtered atoms are still randomly moving in the discharge region, because these atoms require several milliseconds to diffuse to the walls of the discharge chamber (Figure 8 and ref 21). Upon discharge termination, electrons thermalize rapidly with the discharge gas; after this equilibration, argon metastable atoms no longer experience collisions with electrons sufficiently energetic to reduce their population. Long-lived metastable atoms (approximately 5–10 ms (22)) that would have otherwise been deactivated by electron impact are available to ionize analyte atoms still in the discharge region. Because the collision cross sectional area for metastable atoms is generally 1 order of magnitude higher than the ionization cross section for electrons (*23*), analyte atoms are ionized more efficiently. The improved ionization in the afterpeak regions briefly yields an ion signal higher than is observed in the electron-rich plateaul region.

Effect of Electron Flux. While the glow discharge features an intrinsic source of electrons, the use of a thermal filament permits the addition of controlled quantities of electrons accelerated to a fixed potential. If electron–ion recombination is a major source of ion destruction, ion signals in both the discharge plateau and in the afterpeak should be affected similarly. If, however, the electron flux serves primarily to destroy argon metastable species, a greater change should be observed in the afterpeak, on the basis of the proposed ionization mechanisms in that region of the pulse. In the plateau region, operation of the filament would merely supplement the overall discharge electron current. In the afterpeak, wherein the free-electron population is depleted by diffusion loss, the filament becomes the only or major source of electrons and a corresponding decrease in ion signal would result.

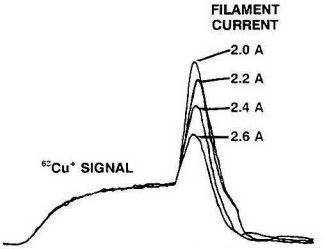

Figure 9. ^{63}Cu ion signal response as the electron filament current is varied from 2.0 to 2.6 A with a constant –300-V dc bias voltage on the filament.

In order to investigate the effect of a flux of electrons on the plateau and afterpeak regions, initial experiments using a 2.6-A filament current with a constant accelerating potential of –300-V dc showed that the copper ion signal decreased only slightly in the plateau (ca. 15%), while the afterpeak intensity dropped significantly (up to 60%). Under these conditions, the argon signal was unaffected in either the prepeak or the plateau region. This could be the result of the electron energies being insufficient to provide additional ionization but energetic enough to deexcite the argon metastable levels. Because of the many collisions in a 1-Torr environment, the actual electron energies will show a wide distribution. Of the three pulse regions, only the afterpeak is strongly dependent on electron excitation of the argon atoms. Figure 9 illustrates the effect of a variable flux of electrons at constant energy. It may be seen from the overlaid traces that the plateau signal remains virtually unchanged with increasing current, while the afterpeaks are being reduced by the electron flux. One explanation consistent with the data is that argon metastable atoms, giving rise to afterpeak formation, are being deexcited by the electron flux, although it is not clear why deexcitation is favored over excitation. The filament currents could also affect extraction dynamics of the afterpeak ions, which are normally slightly higher in energy than the plateau ions.

LITERATURE CITED

(1) Harrison, W. W. *J. Anal. At. Spectrom.* **1988**, *3*, 867.
(2) Harrison, W. W.; Bentz, B. L. *Prog. Anal. Spectrosc.* **1988**, *11*, 53.
(3) Barnett, W. B.; Kahn, H. L. *Anal. Chem.* **1972**, *44*, 935.
(4) Glick, M.; Smith, B. W.; Winefordner, J. D. *Anal. Chem.* **1990**, *62*, 157.
(5) Klingler, J. A.; Savickas, P. J.; Harrison, W. W. *J. Am. Soc. Mass Spectrom.* **1990**, *1*, 138.
(6) Strauss, J. A.; Ferreira, N. P.; Human, H. G. C. *Spectrochim. Acta* **1982**, *37B*, 947.
(7) Biondi, M. A. *Phys. Rev.* **1952**, *88*, 660.
(8) Loving, T. J.; Harrison, W. W. *Anal. Chem.* **1983**, *55*, 1523.
(9) Bruhn, C. G.; Bentz, B. L.; Harrison, W. W. *Anal. Chem.* **1978**, *50*, 373.
(10) Adamson, A. W. *Physical Chemistry of Surfaces*, 3rd ed.; Wiley: New York, 1976; p 548.
(11) Savickas, P. J. Ph.D. Dissertation, University of Virginia, 1984.
(12) Nahemow, M.; Wainfan, N. *J. Appl. Phys.* **1963**, *10*, 2988.
(13) Fang, D.; Marcus, R. K. *Spectrochim. Acta* **1990**, *45B*, 1053.
(14) Chapman, B. *Glow Discharge Processes*; Wiley: New York, 1980; p 129
(15) Cobine, J. D. *Gaseous Conductors*; Dover: New York, 1958; p 214.
(16) Bohm, D.; Gross, E. P. *Phys. Rev.* **1949**, *75*, 1864.
(17) Massey, H. S. W.; Burhop, E. H. S. *Electronic and Ionic Impact Phenomena*, 2nd ed.; Oxford: New York, 1969; Vol. 1, p 25.
(18) Klingler, J. A.; Harrison, W. W. Unpublished results.
(19) Hardy, K. A.; Sheldon, J. W. *J. Appl. Phys.* **1982**, *53*, 8532.
(20) Phelps, A. V.; Molnar, J. P. *Phys. Rev.* **1953**, *89*, 1202.
(21) Smith, R. L.; Serxner, D.; Hess, K. R. *Anal. Chem.* **1989**, *61*, 1103.
(22) Van Dijk, C.; Smith, B. W.; Winefordner, J. D. *Spectrochim. Acta* **1982**, *37B*, 759.
(23) Muschlitz, E. E. *Science* **1968**, *159*, 599.

RECEIVED for review May 15, 1991. Accepted August 22, 1991. This work has been supported by a grant from the U.S. Department of Energy, Basic Energy Sources.

Continuous-Flow Fast Atom Bombardment and Field Desorption Mass Spectrometry of Oligomers of 3,3,3-Trifluoro-1-phenylpropyne

Richard B. van Breemen,* Chien-Hua Huang, and Carl L. Bumgardner

Department of Chemistry, Box 8204, North Carolina State University, Raleigh, North Carolina 27695-8204

Field desorption mass spectrometry was used to determine the chain length, molecular weight range, and identities of the end-capping groups of synthetic oligomers of 3,3,3-trifluoro-1-phenylpropyne. In order to obtain structurally significant fragment ions of selected molecular ion precursors, the MS/MS technique of *B/E*-linked scanning with collisional activation (CAD) was used. Because of the short duration and low intensity of the signal, no useful MS/MS data could be obtained using FD as the ionization method. However, *B/E*-linked scans following CAD could be obtained using fast atom bombardment (FAB) mass spectrometry. To overcome ion "suppression" of components in the unpurified oligomeric mixture and reduce the chemical noise during FAB, continuous-flow FAB liquid chromatography/mass spectrometry (LC/MS) was used to obtain molecular weight information comparable to field desorption mass spectrometry. Finally, *B/E*-linked scanning with CAD was carried out during LC/MS in order to obtain fragment ions confirming the presence of phenyl and trifluoromethyl substituents on the polyacetylene chain.

INTRODUCTION

Polyacetylenes and related synthetic polymers such as polyphenylacetylenes have been demonstrated to conduct electric current because of their extended series of conjugated double bonds (*1*). Potential applications of these polymers include use as organic semiconductors or use as components of electrolytic capacitors or rechargeable batteries (*2*). In order to determine the factors that influence the conductivity of these polymers, accurate methods are needed to measure their chain length, molecular weight, and structure, including defects in the polymeric chain.

In studies of polyanilines (*3*), gel permeation chromatography was used to show a bimodal distribution of molecular weights that consisted of a light fraction weighing approximately 4800 and a heavy fraction weighing between 200 000 and 350 000. However, this method provided no information regarding the structure of the polymer such as the mass of the monomeric unit, sites of defects in the chain, or the nature of the end-capping groups. For the determination of molecular weight range, structure of the repeating unit, and identity of the capping groups that terminate the polymeric chains, field desorption (FD) mass spectrometry has been used to analyze oligomers and low molecular weight polymers such as poly(ethylenimine) (*4*) and polybutadiene (*5*).

A newer technique than FD, fast atom bombardment (FAB) mass spectrometry has been applied to the analysis of a variety of compounds including biological polymers such as peptides (*6*) and some synthetic organic oligomers and polymers (*4*). During FAB, sample ions are desorbed into the gas phase from a liquid matrix of low volatility as a result of bombardment by a beam of energetic atoms (*7*). Although FD can generate molecular ions with relatively low background noise, the signal is transient and typically lasts only seconds to a few minutes at most. Compared to FD, FAB ionization has the advantage of generating ions over a longer period of time, which can extend from a few minutes to 1 h or more. Prolonged ionization facilitates collisional activation of selected-ion precursors and then structural analysis of the product ions by using MS/MS.

Recently, FAB mass spectrometry has been combined online with reversed-phase HPLC in a system called continuous-flow FAB mass spectrometry. Continuous-flow FAB mass spectrometry has been applied to the analysis of a variety of compounds including peptides (*8*), oligonucleotides (*9*), and chlorophylls (*10*). However, no continuous-flow FAB mass spectrometric analyses of polyacetylenes or other conductive polymers have been reported. In this study, a frit-FAB version of continuous-flow FAB mass spectrometry will be used. During continuous-flow FAB using a frit, the HPLC mobile phase is pumped through a fused-silica capillary and then through a stainless steel frit located inside the ion source of the mass spectrometer (*11*). The fast atom beam is focused onto the opposite side of the frit from the capillary, so that sample ions are desorbed into the gas phase as they flow through the frit. The HPLC solvent rapidly evaporates and is pumped away by the vacuum pumps of the mass spectrometer.

As part of our studies on the free radical reactions of fluorinated alkynes and related compounds, we have been investigating the free radical polymerization of 3,3,3-trifluoro-1-phenylpropyne to form a fluorinated polyacetylene. Although fluorinated polyacetylenes lack heteroatoms that might serve as sites of protonation or deprotonation, which are common ionization pathways in FAB mass spectrometry, molecular ions, $M^{\bullet+}$, can be formed during FAB, especially if the analyte contains delocalized π electrons. We report here the analysis of oligomers of 3,3,3-trifluoro-1-phenylpropyne (1) using continuous-flow FAB liquid chromatography–mass spectrometry (LC/MS) and, for comparison, FD mass spectrometry.

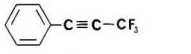

1

EXPERIMENTAL SECTION

The monomer, 3,3,3-trifluoro-1-phenylpropyne (1), was synthesized according to the method of Bumgardner and Bunch (*12*) and purified by distillation under reduced pressure. Oligomerization was carried out without solvent in a sealed vial at 90 °C for 72 h using benzoyl peroxide as the free radical initiator. The molar ratio of monomer to benzoyl peroxide was 10:1. The products of the reaction were dissolved in methylene chloride and diluted to a final concentration of approximately 1 μg/μL. All analyses were carried out using aliquots of this stock solution. Further details of the chemistry of the polymerization of 1 and related acetylene derivatives are presented elsewhere (*13*).

* Corresponding author.

0003-2700/91/0363-2577$02.50/0

HPLC separation of oligomers was carried out using an Applied Biosystems (Foster City, CA) model 140A dual-syringe solvent delivery system, which had been modified so that the dynamic mixer was replaced with a "T" union to minimize dead volume. The HPLC system was equipped with a Rheodyne (Cotati, CA) Model 8125 injector and Vydac (Hesperia, CA) C_{18} narrow-bore column (15 cm × 2.1 mm) packed with 300 Å pore size, 5 μm diameter silica particles. Oligomers were eluted from the column using a 20-min gradient from 50:50:0:0.25 (v/v/v/w) to 10:30:60:0.25 water/methanol/ethyl acetate/3-nitrobenzyl alcohol. The solvent flow rate was 70 μL/min, and 20 μL was injected onto the reversed-phase column per analysis.

Positive-ion FAB mass spectra were obtained using a JEOL (Tokyo, Japan) JMS-HX110HF double-focusing mass spectrometer equipped with a JMA-DA5000 data system and continuous-flow FAB interface. Xenon fast atoms at 6 kV were used for FAB ionization. For standard probe FAB mass spectrometry, 2 μg of the oligomeric mixture in methylene chloride was loaded onto 1 μL of the FAB matrix, 3-nitrobenzyl alcohol. For continuous-flow FAB mass spectrometry, 3-nitrobenzyl alcohol in the mobile phase functioned as the matrix. The accelerating voltage was 10 keV, and the resolving power was 1000 for all FD and low-resolution FAB measurements. Exact mass measurements were carried out using FAB mass spectrometry at a resolving power of 10 000. The ion source was maintained at a temperature of 46 °C. The range m/z 10–1500 was scanned over approximately 10 s. For compatibility with the vacuum system of the mass spectrometer, the HPLC column eluate was split so that approximately 5 μL/min entered the continuous-flow FAB interface. At a column flow rate of 70 μL/min, this resulted in a split ratio of 1:14. For analysis using LC/MS, 20 μL of a 1 μg/μL solution of the oligomeric mixture in methylene chloride was injected onto the HPLC column. Because the column eluant was split, approximately 1.4 μg of the oligomers was analyzed by continuous-flow FAB mass spectrometry.

Under controlled-pressure conditions, acetone was introduced into the FD ion source using the reservoir inlet. The FD ion source, equipped with a silicon emitter, was tuned while monitoring the acetone signal at m/z 58. For each analysis using FD mass spectrometry, approximately 2 μg of the oligomeric mixture was loaded onto the silicon emitter from a microsyringe. Silicon emitters were used because they are more durable and less expensive than carbon emitters, although carbon emitters can produce a more abundant ion current for some compounds. However, Schulten and Lattimer reported that there is no particular advantage to using silicon emitters (*14*). Using a cathode potential of −1.2 kV and emitter and accelerating voltage of +10 kV, FD mass spectra were recorded continuously over the range of emitter currents from 10 to 35 mA. The higher molecular weight oligomers desorbed at higher emitter currents. These spectra were summed to produce a single mass spectrum representing the entire mass range of oligomers. The sensitivities of FD and static FAB mass spectrometry were compared for the analysis of the oligomer detected at m/z 834 in 2 μg of the unpurified oligomeric mixture and were 1.4×10^{-13} and 2.7×10^{-12} A/μg, respectively.

MS/MS analyses were carried out using B/E-linked scanning and collisional activation (CAD). Fragmentation of the precursor ion was enhanced by CAD using helium gas in the first field-free region of the double-focusing mass spectrometer. The helium gas pressure was adjusted so that the abundance of the selected-ion precursor was attenuated 70%.

RESULTS AND DISCUSSION

After polymerization, a 2-μg aliquot of the unpurified reaction product mixture in methylene chloride was analyzed using FD mass spectrometry to determine the extent of polymerization and the molecular weights of the products. This FD mass spectrum is shown in Figure 1. Molecular ions, $M^{\bullet+}$, of the different oligomers were detected over a mass range extending from the cyclic dimer at m/z 416 to the linear octamer at m/z 1514. Three series of oligomers were detected, one containing the capping groups –H and $-C_6H_5$ (series A), another containing two phenyl capping groups (series B), and a less abundant third series consisting of two hydrogen capping groups (series C) (Figure 2). Ions within each series differed

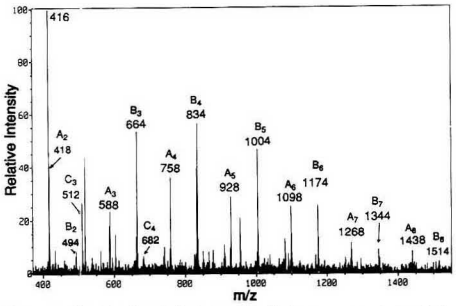

Figure 1. Positive-ion field desorption (FD) mass spectrum of the unpurified oligomeric products following polymerization of 3,3,3-trifluoro-1-phenylpropyne (**1**). Approximately 2 μg of the reaction product mixture was used in the analysis. The structures of the ions designated A, B, and C are shown in Figure 2.

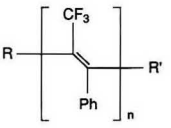

Series A R=H, R'=Ph

Series B R=R'=Ph

Series C R=R'=H

Figure 2. Structures of the three series of oligomers formed by free radical polymerization of 3,3,3-trifluoro-1-phenylpropyne (**1**).

in mass by multiples of 170 mass units, which corresponded to the molecular weight of the expected monomeric unit, $-(CF_3)C{=}C(C_6H_5)-$. The ion at m/z 416 was probably an A-series dimer that had undergone cyclization with loss of a hydrogen atom. The structure of the ion at m/z 416 was investigated more rigorously using FAB mass spectrometry as described below. The corresponding linear dimer was detected at m/z 418, although at lower relative abundance.

Because the FD mass spectrum contained primarily molecular ions, B/E-linked scanning of a selected precursor ion was carried out following CAD in order to obtain structurally significant fragment ions. The most abundant ion in the FD mass spectrum, m/z 416, was selected as the initial molecular ion precursor. Because the number of ions formed during FD mass spectrometry of each oligomer in the mixture was low and the duration of ionization for each oligomer was less than approximately 30 s, the signal-to-noise ratio of fragment ions in the B/E-linked scan was not adequate for the recording of an MS/MS spectrum. For the same reason, exact mass measurements at high resolution are difficult to obtain using field desorption.

In order to generate more abundant molecular ions over a longer period of time for MS/MS analysis, FAB ionization was investigated as an alternative to FD. The unpurified mixture of polyacetylene oligomers was analyzed by positive-ion FAB mass spectrometry using either glycerol, thioglycerol, or 3-nitrobenzyl alcohol as the matrix. No molecular ion species were observed using glycerol or thioglycerol. However, using a matrix of 3-nitrobenzyl alcohol, $M^{\bullet+}$ ions were detected at m/z 664, 834, and 1004, which corresponded to trimers, tetramers, and pentamers in the B series (Figure 3). Oligomers in the B series were less polar than those in the A series because both end-capping groups were phenyl

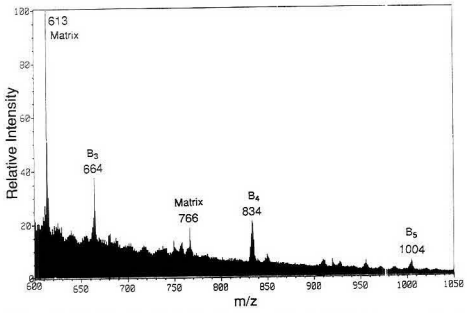

Figure 3. Positive-ion fast atom bombardment (FAB) mass spectrum of 2 μg of polymerized **1**.

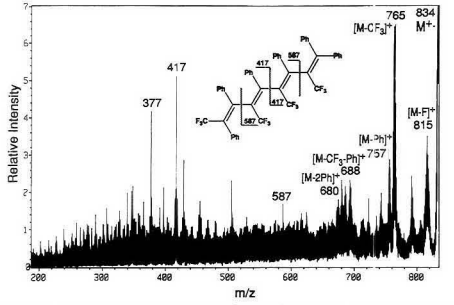

Figure 4. *B*/*E*-linked scan of *m*/*z* 834 obtained using positive-ion FAB mass spectrometry and collisional activation.

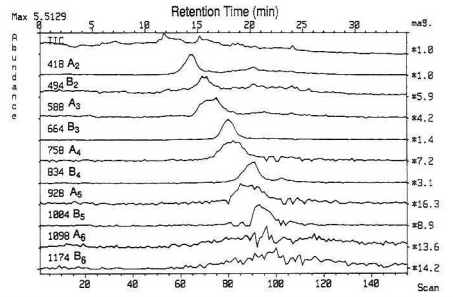

Figure 5. Reconstructed total-ion chromatogram (TIC) and selected-ion chromatograms for the continuous-flow FAB LC/MS analysis of oligomeric **1** (mag = magnification factor).

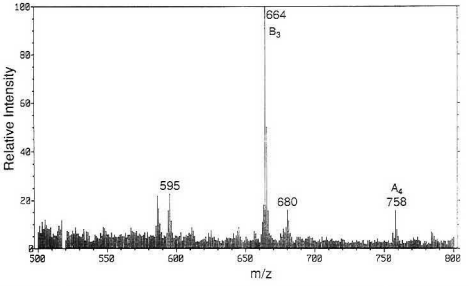

Figure 6. Positive-ion continuous-flow FAB mass spectrum of *m*/*z* 664 corresponding to oligomer B_3 detected at a retention time of approximately 18 min during the LC/MS analysis shown in Figure 5.

groups instead of one phenyl and one hydrogen. In the analysis of peptide mixtures by FAB mass spectrometry, hydrophobic peptides in the mixture are usually detected in much greater abundance relative to the more polar peptides (*15*, *16*). Similar surface activity properties probably facilitated the selective ionization of the more hydrophobic polyacetylenes.

Collisional activation and *B*/*E*-linked scanning were used to obtain structurally significant fragment ions of the molecular ion of the tetramer at *m*/*z* 834 in the positive-ion FAB mass spectrum (Figure 4). An abundant fragment ion was detected at *m*/*z* 765, indicating loss of a trifluoromethyl radical. Although less abundant, fragment ions were observed corresponding to $[M - F]^+$ at *m*/*z* 815, $[M - Ph]^+$ at *m*/*z* 757, $[M - CF_3 - Ph]^+$ at *m*/*z* 688, and $[M - 2Ph]^+$ at *m*/*z* 680. These fragment ions confirmed the identities of the substituents on the polyacetylene chain as phenyl and trifluoromethyl groups. Finally, the fragment ions detected at *m*/*z* 417 and 587 were formed by cleavage of carbon–carbon bonds of the oligomer, as indicated in Figure 4. These ions were unusual because they were formed by fragmentation of the backbone of the oligomer instead of elimination of substituents from the chain.

Although a partial set of B-series ions from the oligomeric mixture was detected using FAB mass spectrometry, ions corresponding to several less abundant B-series oligomers and the entire A series were not observed. Therefore, reversed-phase HPLC separation followed on-line by continuous-flow FAB mass spectrometry was investigated as a method to obtain a more complete profile of oligomers in the mixture. The reconstructed total-ion and selected-ion chromatograms for the continuous-flow FAB LC/MS analysis of the polyacetylene mixture is shown in Figure 5. Because abundant FAB matrix ions were continuously detected in the low molecular weight region of the LC/MS mass spectra, the total-ion chromatogram shows relatively little variation during the analysis. Necessary for FAB ionization, the 3-nitrobenzyl alcohol matrix was included in the mobile phase for simplicity of analysis instead of being added postcolumn (*17*) or by using coaxial flow (*18*). Compared to reversed-phase HPLC without the presence of the FAB matrix (data not shown), addition of 3-nitrobenzyl alcohol to the mobile phase reduced chromatographic resolution so that some overlapping of A- and B-series oligomers was observed. However, chromatographic resolution was sufficient to at least partially resolve each oligomer belonging to each series.

During the LC/MS analysis, both series of oligomers were detected beginning with A_2 and B_2 and extending through A_6 and B_6. An example of the FAB mass spectrum of B_3 at *m*/*z* 664 obtained using LC/MS is shown in Figure 6. Background subtraction was used to eliminate matrix ions and ions from other oligomers that partially coeluted with B_3. Because the oligomer A_4 virtually coeluted with B_3, the A_4 molecular ion was detected at *m*/*z* 758 in Figure 6. The only ions detected using FD mass spectrometry that were not observed during LC/MS were the heptamers and octamers, probably because these oligomers were present in trace amounts and were lost in the chemical noise during FAB ionization.

Like FD, continuous-flow FAB provided a molecular ion profile for a mixture of synthetic polyacetylenes with little fragmentation. However, MS/MS with CAD could be carried out successfully during continuous-flow FAB in order to obtain structurally significant fragment ions of molecular ion precursors. For example, the *B*/*E*-linked scan with CAD of *m*/*z* 416 obtained during LC/MS is shown in Figure 7. Fragment ions were observed that confirmed the presence of –F, $–CF_3$, and phenyl groups on the precursor ion. For example, $[M - F]^+$ was detected at *m*/*z* 397, $[M - CF_3]^+$ at *m*/*z* 347, [M –

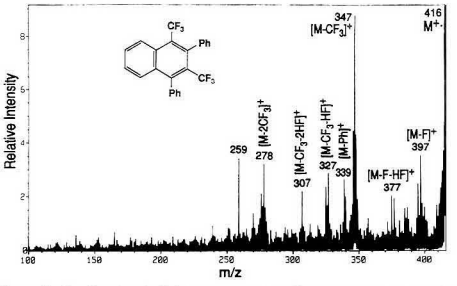

Figure 7. Positive-ion *B*/*E*-linked scan with collisional activation of *m*/*z* 416 obtained during continuous-flow FAB LC/MS analysis of oligomers of **1**.

$2CF_3]^+$ at *m*/*z* 278, $[M - F - HF]^+$ at *m*/*z* 377, $[M - CF_3 - HF]^+$ at *m*/*z* 327, $[M - CF_3 - 2HF]^+$ at *m*/*z* 307, and loss of a phenyl group was detected at *m*/*z* 339.

The same limitations that precluded MS/MS analysis of the molecular ions formed during FD prevented exact mass measurements of these ions from being carried out using FD mass spectrometry. Therefore, the exact mass of the molecular ion at *m*/*z* 416 was determined by high-resolution FAB mass spectrometry to be 416.0100, which corresponded exactly to an elemental composition of $C_{24}H_{14}F_6$. Prior to analysis, this compound had been purified by using HPLC. The structure of this molecule was probably a dimer with one phenyl end-capping group that eliminated a hydrogen atom to form a cyclic, aromatic molecule. The absence of fragment ions of the polymeric chain supports the assignment of this structure as a resonance stabilized, cyclic molecule.

CONCLUSIONS

Although FD mass spectrometry continues to be a useful technique for the determination of the relative chain length of low molecular weight polymers, MS/MS analysis of selected molecular ions of the oligomeric mixture can be hampered by low abundance of individual molecular ions and the short duration of their formation. Because of the longer duration of sample ionization, FAB mass spectrometry can be used to obtain MS/MS spectra and exact mass measurements, as well as molecular weights of synthetic polymers. However, because of chemical noise and ion "suppression", not all components of oligomeric mixtures can be detected using FAB ionization. In addition to FD mass spectrometry, continuous-flow FAB LC/MS of a substituted polyacetylene has been demonstrated to be a useful technique for the determination of the chain lengths of the various oligomers present and the identities of their end capping groups. Finally, LC/MS/MS was used to obtain fragment ions that confirmed the identities of the substituent groups along the polyacetylene chain.

LITERATURE CITED

(1) Tokura, Y.; Koda, T.; Itsubo, A.; Miyabayashi, M.; Okuhara, K.; Ueda, T. *J. Chem. Phys.* **1986**, *85*, 99–104.
(2) Baughman, R. H.; Bredas, J. L.; Chance, R. R.; Elsenbaumer, R. L.; Shacklette, L. W. *Chem. Rev.* **1982**, *82*, 209–222.
(3) MacDiarmid, A. G.; Epstein, A. J. *Faraday Discuss. Chem. Soc.* **1989**, *88*, 317–332.
(4) Lattimer, R. P.; Schulten, H.-R. *Int. J. Mass Spectrom. Ion Processes* **1985**, *67*, 277–284.
(5) Craig, A. G.; Cullis, P. G.; Derrick, P. J. *Int. J. Mass Spectrom. Ion Phys.* **1981**, *38*, 297–304.
(6) Biemann, K.; Scoble, H. A. *Science* **1987**, *237*, 992–998.
(7) Fenselau, C.; Cotter, R. J. *Chem. Rev.* **1987**, *87*, 501–512.
(8) Capricli, R. M.; Moore, W. T.; Dague, B.; Martin, M. J. *Chromatogr.* **1988**, *443*, 355–362.
(9) van Breemen, R. B.; Martin, L. B.; Le, J. C. *J. Am. Soc. Mass Spectrom.* **1991**, *2*, 157–163.
(10) van Breemen, R. B.; Canjura, F. L.; Schwartz, S. J. *J. Chromatogr.* **1991**, *542*, 373–383.
(11) Ito, Y.; Takeuchi, T.; Ishii, D.; Goto, M. *J. Chromatogr.* **1985**, *346*, 161–166.
(12) Bumgardner, C.; Bunch, J. *J. Fluorine Chem.* **1987**, *36*, 313–317.
(13) Bumgardner, C. L.; Huang, C.-H.; van Breemen, R. B. *J. Fluorine Chem.*, in press.
(14) Schulten, H.-R.; Lattimer, R. P. *Mass Spectrom. Rev.* **1984**, *3*, 231–315.
(15) Capricli, R. M.; Moore, W. T.; Fan, T. *Rapid Commun. Mass Spectrom.* **1987**, *1*, 15–18.
(16) Capricli, R. M.; Moore, W. T.; Petrie, G.; Wilson, K. *Int. J. Mass Spectrom. Ion Processes* **1988**, *86*, 187–199.
(17) Games, D. E.; Pleasance, S.; Ramsey, E. D.; McDowall, M. A. *Biomed. Environ. Mass Spectrom.* **1988**, *15*, 179–182.
(18) Determling, L. J.; Moseley, M. A.; Tomer, K. B.; Jorgenson, J. W. *Anal. Chem.* **1989**, *61*, 2504–2511.

RECEIVED for review June 10, 1991. Accepted August 22, 1991. This research was supported by the North Carolina Biotechnology Center (R.v.B.) and the Ethyl Corp. (C.L.B.).

Mathematical Theory of Complex Ligand-Binding Systems Applied to Free Triiodothyronine Immunoassays

Kaj R. Blomberg*[1]

Department of Physical Chemistry, Åbo Akademi, Porthansgatan 3, SF-20500 Åbo, Finland

Sten O. Engblom

Department of Analytical Chemistry, Åbo Akademi, Biskopsgatan 8, SF-20500 Åbo, Finland

A theoretical basis for direct immunoassays of free hormones in serum is presented. The multiple-ligand/multiple-site binding theory employed makes it possible to predict the distribution of hormones among exogenous and endogenous binding proteins in the assay mixture. The model allows simulation of assay systems involving any number of ligands and binding sites. The simulation of an assay of free triiodothyronine illustrates the way in which assay parameters such as antibody concentration, antibody affinity, serum dilution, and labeled hormone interactions with serum binding proteins affect the validity of free hormone assays. The simultaneous equations describing these complex binding systems at equilibrium were solved on a personal computer, with the use of commercial mathematics software. This general method for solving and modeling free hormone assay systems provides a tool for predicting the behavior of free-hormone assays.

INTRODUCTION

In serum, structurally related hormones of low molecular weight (thyroid hormones, steroids) compete for the same binding sites on endogenous binding proteins. The concentration of free (unbound) hormone is measured in direct immunoassays by incubating the serum sample with an antibody specific for the hormone to be measured. In this complex ligand-binding system the amount of hormone bound to the antibody is under certain conditions a function of the free hormone concentration in the serum. Determination of antibody sites occupied gives the free-hormone concentration.

The mathematical theory of free hormone immunoassay has been developed by several researchers. Ekins has given dose–response curves for the situation in which one univalent antibody binds two antigens (labeled and unlabeled ligand) with the same avidity and has also considered the equilibrium system in which one antigen reacts with many binding sites (*1*). The same author has also extensively discussed the pros and cons of different free-hormone methodologies and assay designs (*2*). Geiseler and Ritter have studied the system in which labeled and unlabeled analyte reacts with any number of binding sites, employing a model assuming one strong binding site and a simplified expression for the rest of the binding sites (*3*). Midgley and Wilkins have used equations based on the mathematical model of complex ligand binding by Feldman (*4*) for computer simulation of a free thyroxine assay based on the use of a thyroxine–analogue label (two ligands, many binding sites) (*5*, *6*).

In this paper the mathematical theory of complex ligand-binding systems at equilibrium, introduced and used by Feldman et al. (*7*) for modeling of immunoassays for determination of total analyte concentrations, has been applied to immunoassays of free hormones. The mathematical model formulated is applicable to free-hormone assay systems involving any number of hormones and binding sites. This technique made it possible to simulate an assay system for free triiodothyronine in which four ligands react with up to 12 binding sites. The mass law equations determining the composition of the assay mixture at equilibrium were solved using a personal computer equipped with commercial software. The general method for simulation of the complex equilibrium state, together with the standard computer equipment used, provides a convenient tool for predicting sufficient assay conditions.

[1] Current address: Wallac Biochemical Laboratory, P.O. Box 10, SF-20101 Turku, Finland.

THEORY

The mathematical model is based on the following assumptions: each reaction is reversible and proceeds to equilibrium obeying the law of mass–action, binding sites compete independently for univalent ligands, and no reactions other than

$$H_i + B_j \rightleftharpoons H_iB_j \qquad (1)$$

$$i = 1, 2, ..., n \qquad j = 1, 2, ..., m$$

take place. The number of ligands involved in the reaction is n, and they are denoted by H_1 to H_n. Similarly, the number of binding sites involved is m and the denotations used are B_1 to B_m. The equilibrium composition of the solution is given by

$$K_{H_iB_j} = [H_iB_j]/[fH_i][fB_j] \qquad (2)$$

$$i = 1, 2, ..., n \qquad j = 1, 2, ..., m$$

$$[tH_i] = [fH_i] + \sum_{j=1}^{m} [H_iB_j] \qquad (3)$$

$$[tB_j] = [fB_j] + \sum_{i=1}^{n} [H_iB_j] \qquad (4)$$

where $K_{H_iB_j}$ denotes the affinity constant for each reaction, $[fH_i]$ is the free concentration of the ith hormone, $[fB_j]$ is the concentration of the jth unreacted binding site, $[tH_i]$ is the total concentration of the ith hormone, $[tB_j]$ is the total concentration of the jth binding site, $[H_iB_j]$ is the concentration of the complex formed between the ith hormone and jth binding site. Combination of eqs 2–4 yields a set of n equations:

$$[tH_i] = [fH_i] + \sum_{j=1}^{m} \frac{K_{H_iB_j}[tB_j][fH_i]}{1 + \sum_{k=1}^{n} K_{H_kB_j}[fH_k]} \qquad (5)$$

$$i = 1, 2, ..., n$$

When $[tH_i]$, $[tB_j]$, and $K_{H_iB_j}$ are known, this system of n nonlinear equations can be solved numerically to find the free concentrations of the hormones involved.

0003-2700/91/0363-2581$02.50/0

Using the relation $[tH_i] - [fH_i] = \sum_{j=1}^{m}[H_iB_j]$ (from eq 3), the concentration of bound hormone H_i is given by

$$\sum_{j=1}^{m}[H_iB_j] = \sum_{j=1}^{m}\frac{K_{H_iB_j}[tB_j][fH_i]}{1 + \sum_{k=1}^{n}K_{H_kB_j}[fH_k]} \qquad (6)$$

$$i = 1, 2, ..., n$$

Assume now that an antibody Ab with two binding sites, Ab_1 and Ab_2, is present in the solution. This situation is reflected in the simulations described in a later section of this paper. It follows from eq 6 that the concentration of antibody-bound hormone can be expressed as

$$[H_iAb] = [H_iAb_1] + [H_iAb_2] =$$

$$[tAb][fH_i]\left(\frac{K_{H_iAb_1}}{1 + \sum_{k=1}^{n}K_{H_kAb_1}[fH_k]} + \frac{K_{H_iAb_2}}{1 + \sum_{k=1}^{n}K_{H_kAb_2}[fH_k]}\right) \qquad (7)$$

$$i = 1, 2, ..., n$$

where $[tAb] = [tAb_1] = [tAb_2]$ is the total concentration of the antibody and $[H_iAb]$ is the concentration of hormone H_i bound to the antibody. If the antibody is absolutely specific for the hormone H_a we wish to measure and if the two affinity constants are equal, then eq 7 reduces to

$$\frac{[H_aAb]}{[tAb]} = \frac{2K_{H_aAb}[fH_a]}{1 + K_{H_aAb}[fH_a]} \qquad (8)$$

The fraction of antibody binding sites occupied is determined solely by the free-hormone concentration in the solution. Thus, the free-hormone concentration can be quantified by measuring the fraction of binding sites occupied. A commonly employed technique for determination of occupied binding sites is the titration of unoccupied binding sites with labeled hormone after the serum binding proteins have been removed (*8*, *9*). Constructing a dose–response curve from standards with known free-hormone concentrations relates the antibody occupancy to the free-hormone concentration. The sequestering antibody need not be absolutely specific for the analyte of interest. If $[H_aAb] \gg [H_iAb]$, $i \neq a$, holds, then binding of hormones other than the one to be measured to the antibody, is negligible. This is the case when the antibody has a sufficiently low affinity for cross-reacting hormones present in high concentrations or when the antibody binds cross-reacting substances, present in sufficiently low concentrations, with a high affinity.

Dilution of the sample and addition of antibody reduces the free-hormone concentration initially present in the sample. Nevertheless, the free-hormone concentration in the sample can be quantified with a neglible systematic error if the alteration of the free-hormone concentration is insignificant. The extent of the alteration can be expressed as

$$A = [fH_a]/[fH'_a] \qquad (9)$$

where $[fH'_a]$ is the free-hormone concentration in the sample, $[fH_a]$ is the free-hormone concentration of the assay mixture, and A is their ratio. The unavoidable alteration of the free-hormone concentration affects the accuracy of the assay. In a well-optimized assay with maximized accuracy, the ratio A should be close to 1.

Another technique which is also widely used for determination of the free-hormone concentration is the one-step, analogue assay (*6*), where sample, antibody, and a hormone–analogue label are incubated simultaneously. A criterion for an analogue assay is that the antibody reacts only with the hormone of interest and the labeled hormone, and that the latter is unreactive with serum binding proteins. Assuming again a divalent antibody with identical binding sites, we obtain the concentration of antibody-bound analogue from eq 6 as

$$[H_a{*}Ab] = [H_a{*}Ab_1] + [H_a{*}Ab_2] =$$

$$\frac{2K_{H_a{*}Ab}[tAb][fH_a{*}]}{1 + K_{H_a{*}Ab}[fH_a{*}] + K_{H_aAb}[fH_a]} \qquad (10)$$

Since total concentrations of antibody and analogue are identical in each tube in an assay run and since only analogue and analyte compete for binding sites on the antibody, it is the free-hormone concentration in the solution that determines the amount of analogue sequestered onto the antibody. Measurement of $[H_a{*}Ab]$ in eq 10 gives the free-hormone concentration in the sample, provided A is close to 1. The amount of antibody-bound analogue is related to the free-hormone concentration by constructing a dose–response curve from standards with known free-hormone concentrations.

Useful Equations and Numerical Methods. When eq 5 is solved for the free-hormone concentrations $[fH_i]$, the concentrations of free binding sites $[fB_j]$ can easily be calculated from

$$[fB_j] = \frac{[tB_j]}{1 + \sum_{i=1}^{n}K_{H_iB_j}[fH_i]} \qquad (11)$$

$$j = 1, 2, ..., m$$

With known values of the variables $[fH_i]$ and $[fB_j]$ and the affinity constants, the concentrations of complexes formed are obtained from eq 2.

The numerical solutions of the equations used for simulations were obtained on a personal computer equipped commercially available mathematics software. Information on the computer program and the algorithm it used to solve simultaneous nonlinear equations can be found in the program manual (*10*).

EXPERIMENTAL SECTION

We used the reagents of the DELFIA Free T3 (Wallac OY, Turku, Finland) solid phase, fluoroimmunoassay, for the quantitative measurement of free T3 in serum. The buffer used for the incubations was a 0.05 M tris(hydroxymethyl)aminomethane buffer, pH 7.4, containing 0.9% sodium chloride and 0.05% sodium azide. This buffer was also used for the washings after addition of 0.01% Tween.

Specimens. Serum samples from various patient groups with known concentrations of total thyroxine (T4), thyroxine-binding globulin (TBG), and prealbumin (PA) were obtained from Dr. Med.Sc. Tom Petterson, Danderyd Hospital, Danderyd, Sweden. The methods used for the determination of these parameters have been reported (*11*). Total triiodothyronine (T3) was determined with the DELFIA T3 kit (Wallac OY).

Apparatus. The fluorescence was measured with a time-resolved fluorometer (1232 DELFIA, Wallac OY).

Principle of the Assay. Standards and samples are first reacted with anti-T3 monoclonal antibody (derived from mouse) which binds to anti-mouse IgG immobilized onto the wells of microtitration strips. After incubation, buffer and serum are washed away and in a second incubation step the remaining empty sites on the anti-T3 antibody are back-titrated with europium-labeled T3 (Eu–T3). Then the bound europium is dissociated into DELFIA enhancement solution where it forms highly fluorescent chelates with components of the enhancement solution. The fluorescence is measured in the time-resolved fluorometer.

Assay Procedure. In the assay, 50 μL of standard, serum sample, and diluted serum sample (diluted with buffer solution) were pipetted in duplicate into the coated wells and 200 μL of antibody solution was added to each well. In order to demonstrate the effect of antibody concentration on the free-T3 concentration the samples were assayed using two concentrations of antibody,

Table I. Affinities of T4, T3, and rT3 for Serum Binding Proteins

		affinity constants (M^{-1}) at 37 °C, pH 7.4, phosphate buffer, 0.1 M NaCl					
protein	binding site	T4	ref	T3	ref	rT3	ref
TBG[a]	1	1.0×10^{10}	12[b]	4.6×10^{8}	12[b]	3.1×10^{8}	18[c]
PA	1	2.2×10^{8}	14[d]	1.8×10^{7}	14[d]	1.1×10^{7}	19[e]
	2	3.5×10^{6}	14[d]	8.8×10^{5}	14[d]	3.0×10^{5}	*f*
Alb	1	7.0×10^{5}	15	1.2×10^{5}	16, 17[g]	7.0×10^{5}	16[h]
	2–6	4.8×10^{4}	15	8.0×10^{3}	16, 17[g]	4.8×10^{4}	16[h]

[a] TBG, thyroxine binding protein; PA, prealbumin; Alb, human serum albumin. [b] Affinity constant in phosphate buffer at 25 °C, adjusted to 37 °C by Robbins and Rall (*13*). [c] Value in phosphate buffer. [d] Literature value at 25 °C multiplied by 0.7 to adjust to 37 °C (*13*). [e] Value at 37 °C, pH 8, in 0.1 M Tris–NaCl. [f] Estimated. [g] For each binding site, the affinity of T3 for albumin is assumed to be 16.7% of that of T4. [h] The affinity of rT3 for albumin is assumed to be equal to that of T4.

Table II. Serum Concentration of Binding Proteins, T4, T3, and rT3

protein	hormone	normal serum[a]	low TBG serum[a]
TBG		340 nM	3.4 nM
PA		5.0 μM	5.0 μM
Alb		640 μM	640 μM
	T4	100 nM	30 nM
	T3	2 nM	1.2 nM
	rT3	500 pM	400 pM

[a] Values are within the range of mean values, for various reference populations, quoted by Pettersson (*11*), Ramsden et al. (*20*), and authors listed by Robbins and Rall (*13*).

4.4×10^{-11} and 4.4×10^{-10} M. The wells were incubated for 90 min at 37 °C and then washed two times with wash solution. After dispensing 200 μL of Eu–T3 buffer solution into each well, the wells were incubated for 30 min at 4 °C and then washed four times. Before the fluorescence was measured, 200 μL of enhancement solution was added to each well.

Mathematical Calculation. The calculation of the free-T3 concentration in each sample was made from the equilibrium model using the affinity constants in Table I and the measured total T3, T4, TBG, and PA concentrations. The concentration of albumin was not measured for each individual sample but given a value of 640 μM. Since the concentration of reverse T3 has no effect on the calculated T3 concentration, a value of 0.5 nM was used in the calculations. The affinity of the antibody was 10^{10} M^{-1}. Calculated and experimentally obtained free-T3 values for the serum samples from the various groups at different dilutions and two antibody concentrations are presented.

RESULTS AND DISCUSSION

Free concentrations of thyroid hormones triiodothyronine (T3) and thyroxine (T4) are of diagnostic value in assessing thyroid function. In serum they compete with different affinities for the same binding sites on binding proteins. Affinities of T3, T4, and the thyroid hormone metabolite 3,3′,5′-triiodothyronine (reverse T3, rT3) for the major serum binding proteins are presented in Table I. The serum concentrations of these compounds and the major serum binding proteins in normal serum and in serum from subjects with congenitally low thyroxine-binding globulin concentrations are listed in Table II. Minor binding proteins and thyroid hormone metabolites have been excluded, since very little data on their binding parameters is available and their low concentration and affinity are not expected to significantly affect the distribution of T3 among the binding proteins. This seems to be a justifiable assumption since excluding rT3 from the calculations has an insignificant effect on the computed results presented here. The calculated free-T3 concentration in the normal serum is 6.28 pM, and in the serum with low TBG, 5.96 pM. The corresponding free-T4 concentrations are 22.5 and 17.8 pM, which is in agreement with measured values (*21–23*). The binding parameters, if not separately measured, listed in Tables I and II have been used in the computations throughout this paper.

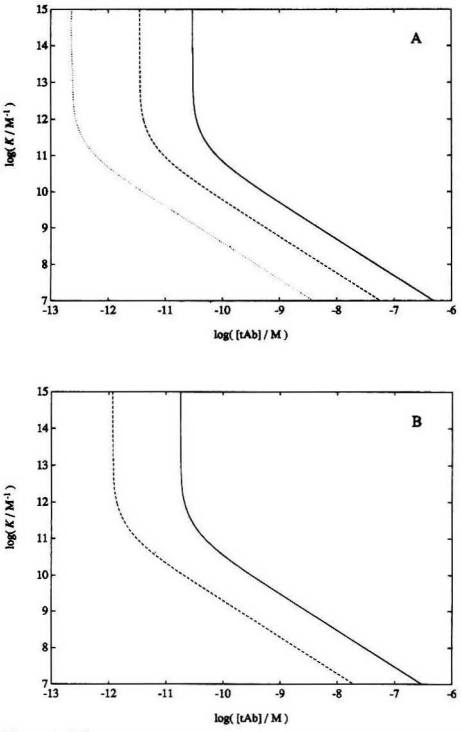

Figure 1. Effect of dilution, antibody affinity, and antibody concentration on the free T3 concentration in serum was simulated using the parameters listed in Tables I and II. The decrease in the free T3 concentration is less than 3% in a free T3 assay if antibody affinity and concentration are in the area delimited by the *x* axis (antibody concentration), the *y* axis (antibody affinity), and the curves showing antibody affinities and concentrations causing a decrease of 3% in the free T3 concentration. The curves refer to different serum dilutions. Figure 1A is for normal serum: (solid line) undiluted serum, (dashed line) serum diluted by a factor of 5 in the assay; (dotted line) serum diluted by a factor of 10 in the assay. Figure 1B is for serum with low TBG: (solid line) undiluted serum; (dashed line) serum sample diluted by a factor of 5 in the assay.

Introduction of antibody and dilution of a serum sample causes a decrease in the free-hormone concentration. The fall in the free-T3 concentration is less than 3% if antibody affinity, antibody concentration, and the dilution factor are selected as depicted in Figure 1. A 10-fold dilution of the TBG-deficient serum decreases the free-T3 concentration by 4.5%, and addition of antibody, even more. The computation

Table III. Effect of Dilution and Antibody Addition on the Free T3 Concentration, pM (Percent Decrease) in Normal Serum[a]

antibody affinity, M^{-1}	dilution factor	antibody concentration					
			10^{-9} M	10^{-10} M	10^{-11} M	10^{-12} M	10^{13} M
	1	6.28[b]					
	5	6.21 (1.2)					
	10	6.11 (2.8)					
	100	4.79 (24)					
10^{10}	1		5.93 (5.6)	6.25 (0.6)	6.28 (–)	6.28 (–)	6.28 (–)
	5		4.79 (24)	6.03 (4.1)	6.19 (1.5)	6.20 (1.3)	6.21 (1.2)
	10		3.85 (39)	5.78 (8.1)	6.07 (3.3)	6.11 (2.8)	6.11 (2.8)
	100		0.83 (87)	3.27 (48)	4.58 (27)	4.76 (24)	4.78 (24)
10^{11}	1		4.37 (30)	6.05 (3.8)	6.26 (0.4)	6.28 (–)	6.28 (–)
	5		1.70 (73)	5.15 (18)	6.09 (3.1)	6.19 (1.4)	6.20 (1.3)
	10		0.93 (85)	4.28 (32)	5.88 (6.4)	6.09 (3.1)	6.11 (2.8)
	100		0.10 (98)	0.89 (86)	3.54 (44)	4.63 (26)	4.17 (24)
10^{12}	1		2.06 (67)	5.75 (8.5)	6.23 (0.9)	6.28 (–)	6.28 (–)
	5		0.24 (96)	3.75 (40)	5.94 (5.5)	6.18 (1.7)	6.20 (1.3)
	10		0.11 (98)	2.02 (68)	5.59 (11)	6.06 (3.6)	6.10 (2.8)
	100		0.01 (100)	0.11 (98)	1.74 (72)	4.39 (30)	4.74 (29.5)

[a] Binding parameters from Tables I and II have been used in these computations. [b] Concentration of free T3 in undiluted normal serum.

Table IV. Measured and Calculated Effect of Antibody Concentration and Sample Dilution on Free T3 Values (pM) in Various Groups[a]

	antibody concn, M	measured free T3						calculated free T3					
		dilution factor[b]						dilution factor[c]					
		1	2	4	6	10	20	1	10	20	30	50	100
								5.57	5.41	5.24	5.09	4.79	4.20
normal	4.4×10^{-11}	5.01[d]	4.81	4.59	4.25	3.67	2.73	5.51	5.24	4.95	4.70	4.25	3.46
$n = 10$	4.4×10^{-10}	5.05	4.13	3.05	2.43	1.92	1.52	5.27	4.24	3.43	2.87	2.17	1.35
hypothyroidism	4.4×10^{-11}	2.60	2.53	2.63	2.49	2.24	1.98	2.55	2.43	2.31	2.20	2.00	1.66
$n = 2$	4.4×10^{-10}	2.60	2.15	1.80	1.42	1.18	1.40	2.50	2.00	1.63	1.38	1.05	0.66
hyperthyroidism	4.4×10^{-11}	19.0	18.8	16.9	15.0	12.5	8.09	15.2	14.4	13.5	12.7	11.4	9.00
$n = 6$	4.4×10^{-10}	15.8	10.5	6.14	4.50	3.06	2.32	14.4	11.4	8.96	7.43	5.45	3.26
low TBG	4.4×10^{-11}	4.77	4.69	4.20	3.75	3.11	2.08	3.68	3.43	3.19	2.98	2.63	2.04
$n = 10$	4.4×10^{-10}	4.39	3.14	2.06	1.50	0.98	0.83	3.56	2.62	2.01	1.63	1.19	0.67

[a] The mean concentrations of total T3, T4, TBG, and PA in the normal, hypothyroid, hyperthyroid, and low TBG groups were 1.74 nM, 105 nM, 360 nM, and 4.37 μM; 0.87 nM, 28 nM, 361 nM, and 4.49 μM; 3.94 nM, 216 nM, 346 nM, and 3.55 μM; and 0.84 nM, 61 nM, 124 nM, and 4.39 μM, respectively. [b] The samples were diluted by these factors before measurement. [c] Sample dilution factor in the assay mixture. [d] Mean values are shown.

suggests that a dilution factor of about 5 should be used if one wants the fall in the free-T3 concentration to be less than 3% also in samples with very low TBG concentrations. Increasing the dilution factor and antibody concentration may cause a considerable decrease in the free-T3 concentration (Table III). As long as the reduction (even a large one) in the free-T3 concentration in standards and unknowns is similar or negligible, a reliable estimate of the free-T3 concentration is obtained. However, if too much antibody is used, a substantial variation in the extent of the reduction of the free-T3 concentration between samples occurs due to the presence of serum samples with altered protein binding. Hence, too much antibody results in a biased estimate of the free-T3 concentration in samples with abnormal binding protein affinities and in samples with concentrations of binding proteins differing from the average level. Therefore it is essential in a free-T3 assay (and in all free-hormone assays) that the antibody concentration and dilution factor are selected in such a way that the alteration of the free-hormone concentration in standards and samples is negligible.

A simple way to test the effect of the antibody concentration on a free-T3 assay is to perform the dilution test (*24*). In an assay where the antibody concentration causes a negligible fall in the free-T3 concentration, normal serum diluted with buffer free of binding substances follows at moderate dilutions the theoretically predicted dilution curve for normal serum. If antibody is used at a concentration resulting in a substantial reduction in the free-hormone concentration, a deviation from the theoretically predicted dilution curve is seen also for low sample dilution factors. However, even with high concentrations of antibody, the estimated free-T3 concentration in normal serum will be close to that initially present in the undiluted serum provided the dilution factor and the binding parameters in standards and normal serum are identical. The results in Table IV show that the measured free-T3 concentration in normal samples and samples from hypothyroids is unchanged after a 10-fold increase in the antibody concentration (standards and samples are diluted 5-fold in the assay, and the standards are made in normal human serum). An increased antibody concentration causes a decrease in the estimated free-T3 concentration in the low TBG group because binding parameters in standards and samples are different. There is, overall, a fairly good agreement between calculated and measured free-T3 concentrations for the groups investigated, although the computed values for the hypothyroid and low TBG groups are somewhat lower than the experimentally obtained result. The magnitude of the theoretically predicted decrease in the FT3 concentration in diluted serum samples is similar to that obtained experimentally. Increasing the antibody concentration results in a further reduction in the free-T3 concentration in diluted samples, wich is in accordance with the calculated results.

Figure 2A shows theoretical dose–response curves for analogue assays of free T3 where antibody and labeled analyte concentrations and affinities have been varied. Under these assay conditions and the assumption of a sample dilution

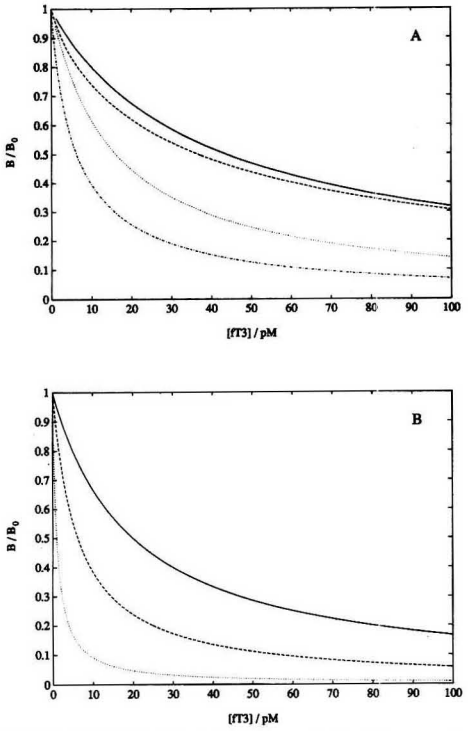

Figure 2. Theoretical dose–response curves for free T3 assays. A divalent antibody is assumed. B = T3–analogue label bound to antibody, B_0 = T3–analogue label bound to antibody at zero T3 dose, T = total concentration of T3–analogue label. Figure 2A is for the analogue assay: (solid line) the antibody binds T3 and T3–analogue label with the same affinity, $K = 8.0 \times 10^{10}$ M^{-1}, [tAb] = 1.25×10^{-11} M, $T = 2.5 \times 10^{-11}$ M, $B_0/T = 0.5$; (dashed line) the antibody binds T3 and the T3–analogue label with the same affinity, $K = 8.0 \times 10^{11}$ M^{-1}, [tAb] = 1.87×10^{-11} M, $T = 5.0 \times 10^{-11}$ M, $B_0/T = 0.7$; (dotted line) the antibody affinity for the T3–analogue label is 1.0×10^{10} M^{-1}, and for T3, 1.0×10^{11} M^{-1}, [tAb] = 1.0×10^{-11} M, $T = 5.0 \times 10^{-11}$ M, $B_0/T = 0.12$; (dash-dotted line) the antibody binds the T3–analogue and T3 with the same affinity, $K = 8.0 \times 10^{11}$ M^{-1}, [tAb] = 1.87×10^{-12} M, $T = 5.0 \times 10^{-12}$ M, $B_0/T = 0.5$. Figure 2B is for the back-titration assays: (solid line) the affinity of T3 for the antibody is 5.0×10^{10} M^{-1}; (dashed line) the affinity constant for T3-antibody binding is 1.6×10^{11} M^{-1}, which is the reciprocal of the calculated free T3 concentration (6.28 pM) in a normal serum; (dotted line) the affinity constant for the T3-antibody binding is 1.0×10^{12} M^{-1}.

factor of 5, the free-T3 concentration in normal serum is reduced by 1.8–3.2% and 0.5–2% of the total amount of T3 available is sequestered onto the antibody. Theoretical dose–response curves for back-titration assays of free T3 are depicted in Figure 2B. These over-simplified curves are based on the assumption that all unoccupied binding sites on the antibody can be titrated with labeled T3 without any dissociation of antibody-bound T3. For back-titration assays, Ekins has suggested an affinity constant of the antibody that is roughly the reciprocal of the free-hormone concentration (2). Among the "best" curves is the one where the antibody possesses an affinity that is the reciprocal of the calculated free-T3 concentration (6.28 pM) in normal serum. In order to obtain an acceptable measurement range and sufficient slope of the standard curve, the computed results suggest that in a free-T3 assay the antibody should possess an affinity that is in the range 10^{11}–10^{12} M^{-1} and the antibody concentration should be less than 10^{-11} M when the sample is diluted by a factor of 5. Working assays can be constructed using antibodies of lower affinity but then the clinically important dose region is at the very beginning of the standard curve.

In the computations in this paper a decrease of 3% or less in the free-T3 concentration is considered arbitrarily to be insignificant and acceptable. If a greater deviation is considered acceptable, higher antibody concentrations than those recommended can be used and still the estimated free-T3 concentration in samples with normal binding parameters will be close to that in undiluted serum. In samples with abnormal binding parameters the free-T3 estimate will be biased, depending on the antibody concentration, dilution factor, and binding parameters, to a degree that may or may not be clinically important.

Under assay conditions as in Figure 2A (dotted line) and with the assumption that the affinity of the T3 specific antibody for T4 is 1.0×10^8 M^{-1}, the calculated concentrations of antibody-bound T3 and antibody-bound T4 are 5.9×10^{-12} and 2.2×10^{-14} M, respectively. The cross-reactivity of the antibody is insignificant since [T3Ab] $\gg$ [T4Ab]. The antibody cross-reacts insignificantly with T4 in all assays in Figure 2 when the antibody affinity for T4 is 1000 times lower than for T3, since in comparison to the amount of T3 bound to antibody, about 270 times less T4 is bound.

In an analogue assay where the analogue reacts with serum binding proteins, the amount of analogue bound to antibody is not only determined by the free-T3 concentration but is also affected by variations in binding protein concentrations and affinities. This fact can be illustrated in the following way. Assay conditions are as in Figure 2A (dotted line), except for the tracer concentration, which is doubled. When normal serum samples are analyzed, 59% of the T3-analogue label is bound to the serum albumin, because of the reaction of the analogue with albumin. Two samples are assayed, both with 6.28 pM of free T3. One of the samples is a low-albumin sample (2.0×10^{-6} M), the other one contains normal concentrations of binding proteins. The calculated values for antibody-bound T3-analogue label are 5.9×10^{-13} M for the normal sample and 1.4×10^{-12} M for the low-albumin sample. In a valid free-T3 assay with negligible cross-reactivity of the analogue with serum albumin, these two concentrations are identical.

The approach presented here makes is possible to quantitatively describe and solve the equations of the complex binding system free-hormone assays constitutes. The effect of important assay parameters, such as antibody concentration and affinity, dilution factors, altered protein binding, reactivity of hormone-analogue label with serum binding proteins, drug interference, and cross-reactivity of the antibody can be predicted. In combination with experiments this theoretical method provides a powerful tool for optimization and evaluation of free-hormone assays.

Registry No. T3, 6893-02-3.

LITERATURE CITED

(1) Ekins, R. P. In *Free Hormones in Blood*; Albertini, A., Ekins, R. P., Ed.; Elsevier Biomedical Press: Amsterdam, 1982; pp 73–90.
(2) Ekins, R. P. *NucCompact* **1985**, *16*, 305–313.
(3) Geiseler, D.; Ritter, M. *Anal. Chem.* **1982**, *54*, 2062–2067.
(4) Feldman, A. H. *Anal. Biochem.* **1972**, *48*, 317–338.
(5) Wilkins, T. A.; Midgley, J. E. M. In *Radioimmunoassay and Related Procedures in Medicine*; IAEA: Vienna, 1982; pp 221–240.
(6) Wilkins, T. A.; Midgley, J. E. M.; Barron, N. *Clin. Chem.* **1985**, *31*, 1644–1653.
(7) Feldman, H.; Rodbard, D.; Levine, D. *Anal. Biochem.* **1972**, *45*, 530–556.
(8) Bunting, J. In *Free Hormones in Blood*; Albertini, A., Ekins, R. P., Eds.; Elsevier Biomedical Press: Amsterdam, 1982; pp 139–149.
(9) Ekins, R. P. In *Immunoassays for Clinical Chemistry*, 2nd ed.; Hunter, W. M., Corrie, J. E. T., Eds.; Churchill, Livingstone: Edinburgh, 1983; pp 319–339.

(10) User's Guide: MathCad; MathSoft Inc.: Cambridge, MA, 1989.
(11) Pettersson, T. M. Ph.D. Thesis, Karolinska Institutet, Stockholm, Sweden, 1989.
(12) Korcek, L.; Tabachnick, M. J. Biol. Chem. 1976, 251, 3558-3562.
(13) Robbins, J.; Rall, J. E. In Hormones in Blood I, 3rd ed.; Gray, C. H., James, V. H. T., Eds.; Academic Press: London, 1979; pp 575-688.
(14) Cheng, S. Y.; Pages, R. A.; Saroff, H. A.; Edelhoch, H.; Robbins, J. Biochemistry 1977, 16, 3707-3713.
(15) Tabachnick, M. J. Biol. Chem. 1967, 242, 1646-1650.
(16) Tabachnick, M.; Giorgio, N. A. Arch. Biochim. Biophys. 1964, 105, 563-569.
(17) Steiner, R. F.; Roth, J.; Robbins, J. J. Biol. Chem. 1966, 241, 560-565.
(18) Tabachnick, M.; Korcek, L. Biochem. Biophys. Acta 1978, 537, 169-175.
(19) Andrea, A. T.; Cavalieri, R. R.; Goldfine, I. D.; Jorgensen, C. J. Biochemistry 1980, 19, 55-63.
(20) Ramsden, D. B.; Sheppard, M. C.; Hoffenberg, R. In Free Hormones in Blood; Albertini, A., Ekins, R. P., Eds.; Elsevier Biomedical Press: Amsterdam, 1982; pp 187-193.
(21) Liewendahl, K.; Tikanoja, S.; Helenius, T.; Välimäki, M. Clin. Chem. 1984, 30, 760-762.
(22) Rajan, M. G.; Samuel, A. M. Clin. Chem. 1987, 3, 372-376.
(23) Tikanoja, H. S.; Liewendahl, K. B. Clin. Chem. 1990, 36, 800-804.
(24) Ekins, R. Clin. Chem. 1987, 12, 2137-2152.

RECEIVED for review December 10, 1990. Revised manuscript received July 9, 1991. Accepted August 13, 1991.

A High-Performance Liquid Chromatography System with an Immobilized Enzyme Reactor for Detection of Hydrophilic Organic Peroxides

Hans-Hagen Kurth,* Siegmar Gäb, Walter V. Turner, and Antonius Kettrup

GSF-Institut für Ökologische Chemie, Schulstrasse 10, 8050 Freising-Attaching, Federal Republic of Germany

A short reactor column containing horseradish peroxidase immobilized on controlled-pore glass can replace the continuous flow of a solution of the enzyme in the detection of hydroperoxides in an HPLC system, thereby allowing the elimination of one of the three pumps previously required. The immobilized enzyme catalyzes the oxidation by hydroperoxides of (*p*-hydroxyphenyl)acetic acid to a fluorescent biphenyl derivative, which is the species actually detected. The simplified HPLC system is optimized for the analysis of H_2O_2 and a number of alkyl and 1-hydroxyalkyl hydroperoxides. The detection limit of the H_2O_2 analysis is 5×10^{-8} M (34 pg in a 20-μL sample), and the response is linear down to at least 10^{-7} M.

INTRODUCTION

Our research group recently described an HPLC system for the quantitative analysis of H_2O_2 and hydrophilic organic peroxides (*1*). The peroxides are separated on a cooled RP18 column with dilute H_3PO_4 (pH 3.5) as eluent and then allowed to react with peroxidase and (*p*-hydroxyphenyl)acetic acid (PHOPA). This postcolumn reaction is specific for hydroperoxides, and the product is detected by its fluorescence (*2*). The great advantages of the system are the selectivity afforded by the enzyme reaction and the sensitivity of fluorescence detection. The detection limit of around 5×10^{-8} M peroxide means that the method is excellently suited for determining H_2O_2 and hydrophilic organic peroxides from air, in precipitation and in laboratory simulations of natural peroxide-forming processes without a preconcentration step.

Enzyme reactors in flow injection analysis (FIA) systems are routine nowadays, but their application to HPLC is an active area of research (*3*). The present work was undertaken to ascertain the characteristics of the HPLC system when a reactor containing immobilized peroxidase is substituted for the continuous addition of peroxidase to the eluate. The use of such a peroxidase reactor would allow us to reduce from 3 to 2 the number of pumps necessary for the HPLC analysis of hydroperoxides, to considerable economic advantage.

In making an enzyme reactor, the enzyme-immobilization strategy is crucial. The application of peroxidase as a marker in immunoassays (*4*) and in FIA systems has led to the development of a variety of ways to attach the enzyme to both synthetic and biological supports (*5*). We selected a method developed by Nakane and Kawaoi (*6*) for coupling peroxidase to biological materials and extended by Hayashi et al. (*7*) to coupling to controlled-pore glass (CPG). In this method carbohydrate side chains of the glycoprotein peroxidase are oxidized with periodate to aldehyde groups, which react with aminopropyl groups of the CPG. Since we followed the scheme of Hayashi et al. with little change, we are concentrating in this report on the optimization of the HPLC system with the enzyme reactor.

EXPERIMENTAL SECTION

Apparatus (Figure 1). Two Gilson Model 302 pumps were utilized for the HPLC system, the eluent pump being connected with a Gilson Model 802 C manometer and a Rheodyne Model 7125 injection valve with a 20-μL sample loop. The fluorescence detector and integrator were Hewlett Packard Models HP 1046 A (λ_{ex} = 285 nm, λ_{em} = 410 nm) and HP 3390, respectively. The column, 250 mm × 4 mm i.d., was packed with 5-μm Shandon ODS Hypersil and surrounded by a circulating mixture of water/methanol cooled to 1 °C by a Lauda Model K2R cryostat. All connections and the 2-m reaction coil were of stainless-steel capillaries $^1/_{16}$ in. o.d., 0.12 mm i.d. An HPLC column 17 mm × 4 mm i.d. was used for the enzyme reactor. The eluent flow rate was optimized at 0.5 mL/min, and that of the reagent at 0.4 mL/min (see text).

Reagents. Sodium borohydride and aminopropyl-CPG beads (mean pore size 1400 Å, 120-200 mesh) were purchased from Riedel-de Haën (Seelze, Germany) and Serva (Heidelberg, Germany), respectively. Horseradish peroxidase (EC 1.11.1.7) was from Merck (Darmstadt, Germany); all other chemicals were of reagent grade and were also from Merck. Water was deionized, distilled from $KMnO_4$, redistilled and stored in glass bottles protected from light. For use as the mobile phase it was brought to pH 3.5 with H_3PO_4. The reagent solution was optimized (see

0003-2700/91/0363-2586$02.50/0

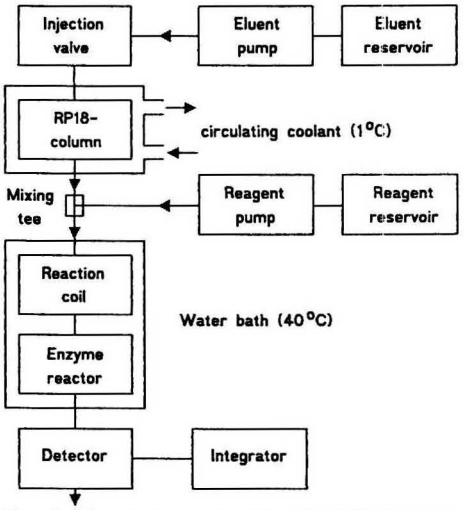

Figure 1. Schematic diagram of the HPLC system utilizing the enzyme reactor.

text) as 10 mg of PHOPA in 250 mL of 0.05 M K_2HPO_4. Commercial H_2O_2 (35%) was standardized by iodometric titration and diluted each day to make standards; these should be kept at 0 °C and protected from light.

Procedures. The immobilization of peroxidase was carried out according to the procedure of Hayashi et al. (7) scaled up to 45 mg of enzyme and 300 mg of CPG beads; the only exception was to extend the time allowed for the coupling reaction to 48 h.

The alkyl hydroperoxides were synthesized by reaction of H_2O_2 under basic conditions with the corresponding sulfates (methyl and ethyl, by a procedure (8) for methyl hydroperoxide) or methanesulfonates (1-propyl and 2-propyl, by a procedure (9) for 1-propyl hydroperoxide). The products were distilled at reduced pressure and identified by ^1H and ^{13}C NMR spectroscopy. Their peroxide content was determined by iodometric titration in acetic acid, and any residual H_2O_2 was determined by HPLC.

To prepare the 1-hydroxyalkyl hydroperoxides, 10 mmol of the appropriate aldehyde was warmed for 20 min at 40 °C with 5 mL of 35% H_2O_2 and 2 mL of pH 3.5 H_2O, the inhomogeneous reactions being shaken occasionally. Water at pH 3.5 was used to dilute the mixture to 100 mL and then by a factor of 10^4 for HPLC analysis. Except for hydroxymethyl hydroperoxide (10), these peroxides were not isolated or characterized by spectroscopy; if desired, several of them can be prepared in the same reaction by starting with a mixture of aldehydes.

RESULTS AND DISCUSSION

Design of the Analytical System. With the HPLC system as originally described, it is possible to analyze for low-molecular-weight alkyl hydroperoxides, 2-hydroxyalkyl hydroperoxides, 1-hydroxyalkyl hydroperoxides, and alkyl 1-hydroxyalkyl peroxides, as well as H_2O_2, and it was desired that the new system be equally versatile. Because these peroxides are all moderately polar and are stable in cold aqueous acid, they are separated by reversed-phase HPLC on a cooled column with dilute H_3PO_4 (pH 3.5) as eluent. The first two classes of hydroperoxides are also stable at pH > 7 and at somewhat higher temperatures; in addition, they are acceptable substrates for peroxidase and can thus enter directly into the catalytic postcolumn oxidation of PHOPA. Alkyl 1-hydroxyalkyl peroxides cannot react directly with the enzyme. These compounds and 1-hydroxyalkyl hydroperoxides are formally the addition products of aldehydes with alkyl hydroperoxides and H_2O_2, respectively, and at pH > 7 they revert rapidly to aldehyde and peroxide. The strategy for detecting these two peroxide classes is thus to raise the pH of the eluate after the column to convert them to alkyl hydroperoxides and H_2O_2, which then react with the enzyme.

Conversion of the 1-hydroxyalkyl hydroperoxides and alkyl 1-hydroxyalkyl peroxides is important, however, for another reason as well. Hydroxymethyl hydroperoxide is known to inhibit horseradish peroxidase irreversibly (11), and its homologues may act similarly. This would not have been very detrimental to the HPLC system as originally described, since peroxidase was continuously added, and the only effect observed would have been a reduction in the response to these peroxides. In a system with an enzyme reactor, however, all inhibitors must be prevented from reaching the immobilized peroxidase, in order to maintain the efficiency of the reactor. To assure complete conversion of the 1-hydroxyalkyl hydroperoxides to H_2O_2, the eluate, after being made basic by addition of the PHOPA/buffer solution, is passed through a coil at 40 °C before it enters the reactor.

Table I. Partial List of Peroxides Determined

peroxide	formula	retention time, min
hydrogen peroxide	H_2O_2	5.54
methyl hydroperoxide	CH_3OOH	8.04
ethyl hydroperoxide	CH_3CH_2OOH	14.75
2-propyl hydroperoxide	$(CH_3)_2CHOOH$	35.89
1-propyl hydroperoxide	$CH_3CH_2CH_2OOH$	42.11
hydroxymethyl hydroperoxide	$HOCH_2OOH$	6.22
1-hydroxyethyl hydroperoxide	$CH_3CH(OH)OOH$	7.87
1-hydroxypropyl hydroperoxide	$CH_3CH_2CH(OH)OOH$	14.08
1-hydroxy-2-methylpropyl hydroperoxide	$(CH_3)_2CHCH(OH)OOH$	37.15
1-hydroxybutyl hydroperoxide	$CH_3CH_2CH_2CH(OH)OOH$	41.62

Quantification of the Peroxides. Table I presents a list of the retention times of the peroxides which have been studied most extensively with the modified HPLC system. In separate calibration experiments all the alkyl hydroperoxides in the table gave the same response as H_2O_2 solutions of the same concentration. These peroxides can thus be quantified by comparison of their peak areas with those of fresh H_2O_2 standards. A comparable experimental proof that the 1-hydroxyalkyl hydroperoxides and alkyl 1-hydroxyalkyl peroxides also give the same response as H_2O_2 would be very welcome, but such a proof is currently unavailable, because most of these unstable substances cannot be prepared pure as standards. Bis(hydroxymethyl) peroxide is an exception in this regard; in dilute solution it is quantitatively converted to H_2O_2 on neutralization (1). In addition, we have shown that when a ca. 10^{-5} M solution of the 1-hydroxyalkyl peroxides is brought to pH 7 at room temperature immediately before it is injected into the HPLC system, no trace of the original peroxide can be detected. We presume, therefore, that the conversion to H_2O_2 and alkyl hydroperoxides is complete in the postcolumn reaction coil, where the solution is basic and warm (40 °C).

Examination of Table I reveals that H_2O_2 and the alkyl hydroperoxides (C_n) have retention times similar to those of certain 1-hydroxyalkyl hydroperoxides (C_{n+1}); this results in overlapping of the following pairs of peaks: H_2O_2/hydroxymethyl hydroperoxide, methyl hydroperoxide/1-hydroxyethyl hydroperoxide, ethyl hydroperoxide/1-hydroxypropyl hydroperoxide, and 1-propyl hydroperoxide/1-hydroxybutyl hydroperoxide. This overlapping increases with the retention

Table II. Influence of pH on Sensitivity of the HPLC System to H_2O_2[a]

pH	rel peak area	pH	rel peak area
7.0	78.7	9.5	96.1
8.0	91.3	10.0	91.4
9.0	100.0	10.5	66.4

[a] Based on 20 measurements of 10^{-6} M H_2O_2 at each pH.

time and is greater when the enzyme reactor is used, because the peaks are somewhat broader. If the sample is neutralized before analysis, the 1-hydroxyalkyl hydroperoxides are eliminated, and if the sample is analyzed twice, before and after being neutralized, both the *n*-alkyl and the 1-hydroxyalkyl hydroperoxides can be quantified.

Optimization of the Analytical System. Separation of the peak pairs mentioned above improves as the flow rate is reduced. These separations are never complete, even at very slow elution, and the desirability of quick analyses and sharp peaks for compounds with longer retention times makes it necessary to raise the flow rate. The optimum eluent flow rate of 0.5 mL/min is a compromise between these two conflicting requirements.

To determine the best conditions for the postcolumn enzyme reaction, the flow rate, concentration, and pH of the reagent solution were independently optimized.

(1) At pH 9.0 and a PHOPA concentration of 10 mg/250 mL of 0.05 M K_2HPO_4, the reagent flow rate was raised systematically from 0.1 to 0.8 mL/min. At flow rates <0.2 mL/min, all the peaks exhibited tailing. This phenomenon would be expected if the oxidation of the enzyme by the hydroperoxide is very rapid, but there is too little PHOPA to reduce the enzyme back at the same rate (cf. ref 12). As the flow rate increases above 0.2 mL/min, the peaks gain in symmetry, but the peak areas decrease. At a rate of 0.4 mL/min, symmetrical peaks were obtained without an unacceptable loss in peak area.

(2) At less than 1 mg of PHOPA/250 mL of 0.05 M K_2HPO_4, all the peaks tailed, just as when the flow rate was too low. Over the range 2–20 mg/250 mL, there was a continuous increase in both peak area and baseline noise; above 20 mg/250 mL, baseline noise increased further, but there was no longer any improvement in the peak area. A concentration of 10 mg/250 mL was chosen as giving good peak areas without too much noise.

(3) As mentioned above, the pH of the eluate after mixing with the reagent must be at least 7 to assure decomposition of the 1-hydroxyalkyl peroxides and 1-hydroxyalkyl hydroperoxides. Values between 7.0 and 10.5 were investigated, with the results shown in Table II. The optimum at pH 9.0 is probably the result of two opposing trends: at higher pH the sensitivity of the fluorescence detection is better, but the reactivity of the enzyme decreases above pH 8. Prolonged use of the system at high pH would also be destructive to the bound enzyme itself. The optimum excitation wavelength for the fluorescence detection is a function of the pH, the composition of the buffer, and the concentration of PHOPA. With our pH limits and PHOPA concentration, the optimum is 285–295 nm.

Detection Limit and Linear Range. With freshly prepared H_2O_2 standards the detection limit (the concentration that gave a peak height equal to 3 times the standard deviation of the background fluorescence) was determined as 5×10^{-8} M H_2O_2. To measure the linear range, fresh H_2O_2 standards were injected 20 times in succession, each concentration having been independently prepared from 35% H_2O_2. The mean peak area and standard deviation were found for each concentration, and the results are shown in Table III. Linear

Table III. Calibration of the HPLC System

concn[a]	peak area[b]	RSD,[c] %
10.0	35.91	1.8
5.0	17.66	1.2
1.0	3.27	5.5
0.5	1.71	9.1

[a] Of H_2O_2 in 10^{-6} M. [b] Arbitrary units. [c] Based on 20 measurements at each concentration under optimum conditions.

regression reveals a linear range of (5–100) $\times 10^{-7}$ M with a correlation coefficient of >99.99%. Below 5×10^{-7} M the integrator interpreted noise as peaks, so that we were unable to measure peak areas accurately; nevertheless, measurement of the peak heights showed that the linearity extends down to 10^{-7} M H_2O_2. Because of peak broadening at longer retention times, the detection limit is considerably higher for the larger peroxide homologues (ca. 5×10^{-7} M for *n*-propyl hydroperoxide).

By raising the PHOPA concentration, the linear range can be extended to higher peroxide concentrations, but at the expense of the detection limit, because higher PHOPA concentrations lead to more baseline noise.

Limitations of the Analytical System. The analytical system with the enzyme reactor is subject to the same chromatographic and enzymatic limitations as the system described earlier. The chromatographic limitations arise from the inability of dilute aqueous acid to elute hydroperoxides with more than four carbon atoms in a reasonable time; studies are underway to determine to what extent other eluents can extend the range of peroxides we can analyze. The steric requirements of the enzyme, however, will restrict the peroxides to those that are not too bulky. We know, for example, that *tert*-butyl hydroperoxide gives no signal in our analysis, and certain other hydroperoxides appear to react so much more slowly than the alkyl hydroperoxides in Table I that a quantitative analysis of them is not possible with the peroxidase/PHOPA system.

Useful Lifetime of the Enzyme Reactor. No signs of a loss in activity of the enzyme reactor could be discerned, even after several months of constant use (8–10 h/day). This indicates either that there was no loss in the activity of the immobilized enzyme or that over this period any such loss was smaller than the "initial overcapacity" (*5*) of the reactor.

Enzyme Reactor in a "Single-Pump System". If a 0.05 M phosphate buffer (pH 7.0) containing 10 mg of PHOPA is used as eluent, the pump used for the reagent solution in the system described above (Figure 1) can also be dispensed with; the result is what we refer to as the "single-pump system". Under these conditions the 1-hydroxyalkyl hydroperoxides and the alkyl 1-hydroxyalkyl peroxides are converted immediately to H_2O_2 and alkyl hydroperoxides, respectively, so that no reaction coil after the column is necessary. If one is willing to sacrifice information about the original concentrations of these two peroxide classes that are only stable in acid, the simplified system can be used quite profitably.

ACKNOWLEDGMENT

We are grateful to Edgar Grom of the M. Grom Co., Herrenberg, Federal Republic of Germany, for helpful discussions and for assistance in filling the enzyme reactor, and to the referees for useful comments.

LITERATURE CITED

(1) Hellpointner, E.; Gäb, S. *Nature* **1989**, *337*, 631–634.
(2) Guilbault, G. G.; Brignac, P. J., Jr.; Juneau, M. *Anal. Chem.* **1968**, *40*, 1256–1263.
(3) Bowers, L. D. In *Reaction Detection in Liquid Chromatography*; Krull, I. S., Ed.; Chromatographic Science 34; Marcel Dekker: New York, 1986; pp 195–226.

(4) Tijssen, P.; Kurstak, E. *Anal. Biochem.* **1984**, *136*, 451–457.
(5) Olsson, B. *Mikrochim. Acta* **1985**, II, 211–221.
(6) Nakane, P. K.; Kawaoi, A. *J. Histochem. Cytochem.* **1974**, *22*, 1084–1091.
(7) Hayashi, Y.; Zaitsu, K.; Ohkura, Y. *Anal. Sci.* **1985**, *1*, 65–68.
(8) Rieche, A.; Hitz, F. *Ber. Dtsch. Chem. Ges.* **1929**, *62*, 2458–2474.
(9) Williams, H. R.; Mosher, H. S. *J. Am. Chem. Soc.* **1954**, *76*, 2984–2987.
(10) Rieche, A.; Meister, R. *Ber. Dtsch. Chem. Ges.* **1935**, *68*, 1465–1473.
(11) Marklund, S. *Arch. Biochem. Biophys.* **1973**, *154*, 614–622.
(12) Goldstein, L. In *Immobilized Enzymes*; Mosbach, K., Ed.; Methods in Enzymology 44; Academic Press: New York, 1976; pp 397–443.

RECEIVED for review May 29, 1991. Accepted August 14, 1991.

Shape Discrimination in Liquid Chromatography Using Charge-Transfer Phases

Lane C. Sander,* Reenie M. Parris, and Stephen A. Wise

National Institute of Standards and Technology, Gaithersburg, Maryland 20899

Philippe Garrigues

UA 348 CNRS, Université de Bordeaux I, F-33405 Talence Cedex, France

A variety of factors affect the ability of a given column to discriminate between compounds on the basis of shape (shape selectivity). In reversed-phase systems, bonded phases based on monomeric surface modification exhibit low shape selectivity; phases based on polymeric surface modifications exhibit enhanced shape selectivity. Even greater shape specificity is exhibited by charge-transfer columns, operated in the normal-phase mode. In this work, the retention behavior of electron-acceptor and electron-donor charge-transfer phases was studied for the separation of polycyclic aromatic hydrocarbon isomers (PAHs), methyl-substituted PAHs, and polychlorinated biphenyl congeners (PCBs). In all cases, planar compounds were retained in preference to corresponding nonplanar analogues.

INTRODUCTION

Polycyclic aromatic hydrocarbons (PAHs) and polychlorinated biphenyls (PCBs) are found ubiquitously in the environment in air, water, and soil samples. The health risks associated with PAHs and PCBs are highly variable but depend largely on the size and shape (e.g., substitution pattern) of the individual compounds. Therefore, the separation and identification of individual PAHs and PCBs is a problem of considerable practical significance.

Because of the complexity of PAH and PCB mixtures, the isolation and measurement of individual compounds is challenging. PAHs are highly isomeric, particularly with the addition of alkyl substitution, adding to the difficulty in making measurements. Although capillary gas chromatography (GC) is capable of separating large numbers of PAHs because of high efficiency, enhanced selectivity toward PAH isomers is achieved in liquid chromatography (LC) through the use of polymeric C_{18} phases (i.e., phases prepared with trifunctional silanes in the presence of water) and other novel phases. The retention behavior of PAH isomers has been reviewed by Sander and Wise (*1*). PAHs are primarily nonpolar in nature, and in a general sense LC separations are governed by solvophobic interactions. Solvophobic retention theory, however, cannot fully explain separations of PAH isomers, since these compounds have similar van der Waals surface areas and volumes. Wise et al. (*2*) first reported that the retention of PAH isomers on polymeric C_{18} phases was correlated closely with solute shape; i.e., retention increased with the length-to-breadth ratio (L/B) of the solute. An empirical model of solute retention has been advanced that describes possible solute/stationary phase interactions for rigid solutes (*3*). Referred to as the "slot model", this schematic representation is consistent with the correlation of solute retention and L/B, as well as the discrimination observed between planar and nonplanar isomers. Rigorous theoretical treatments of solute shape effects have been presented by Martire and Boehm (*4*, *5*) and Dill (*6*, *7*).

In general, conventional monomeric C_{18} phases (i.e., phases prepared with monofunctional silanes) provide only limited inherent ability to separate isomers on the basis of shape (shape selectivity). Enhanced shape recognition is possible with polymeric C_{18} phases. Differences in selectivity between these types of phases have been compared to the differences between nonpolar and liquid crystalline phases in GC (*8*). Polymeric C_{18} phases in LC exhibit similar retention characteristics to liquid crystalline phases in GC (and supercritical fluid chromatography, SFC) and, by analogy, polymeric C_{18} phases are thought to be more ordered than monomeric C_{18} phases. The technique of small-angle neutron scattering (SANS) has been used to show that polymeric C_{18} phases are slightly thicker and significantly denser than monomeric C_{18} phases (*9*). The difference in selectivity of monomeric and polymeric C_{18} phases has been particularly useful in the analytical approach to identify individual methyl-substituted PAHs in natural environmental samples (*10–12*). Monomeric C_{18} phases have been used to isolate methyl-PAH isomers as a group followed by separation of individual isomers on a polymeric C_{18} phase.

In this paper the retention behavior of a variety of PAH isomers on several novel LC stationary phases is described. The retention characteristics of electron-acceptor and electron-donor charge-transfer columns are examined and compared to monomeric and polymeric C_{18} columns. The effect of solute shape, as determined by molecular modeling, is discussed in relation to solute retention. An additional example of shape discrimination is presented for the separation of planar and nonplanar PCB congeners using an electron-

donor charge-transfer column.

EXPERIMENTAL SECTION

Materials. Chromatographic grade solvents were used to prepare all mobile-phase solutions. PAH standards were obtained from a variety of sources: molecular weight (MW) 278 and 302 isomers were from sources previously identified (*3*, *13*); MW 328 isomers (Institut für PAH-Forschung, Greifenburg am Ammersee, Germany); methylchrysene isomers (Community Bureau of Reference, Belgium); methylbenz[*a*]anthracene isomers (NCI Chemical Carcinogen Repository, c/o Midwest Research Institute, Kansas City, KS). Individual PCB standards were obtained from the Community Bureau of Reference (BCR, Brussels, Belgium). A solution containing 28 PCB congeners, designated NIST Candidate Standard Reference Material 2262, "Polychlorinated Biphenyl Congeners in 2,2,4-Trimethylpentane", was obtained from the Standard Reference Materials Program (NIST, Gaithersburg, MD). Standard Reference Material 869, "Column Selectivity Test Mixture for Liquid Chromatography (Polycyclic Aromatic Hydrocarbons), was also obtained from the Standard Reference Materials Program (NIST).

Chromatography. Separations were performed with a reciprocating piston liquid chromatograph utilizing low-pressure solvent mixing. Injection volumes varied from 25 to 50 μL and were carried out either with a fixed-loop injector or autosampler. Analytes were dissolved in solvents compatible with the mobile phase employed, i.e., acetonitrile for reversed-phase separations and methylene chloride for normal-phase separations. Normal-phase separations were performed with premixed mobile phases; mobile-phase compositions for reversed-phase separations were controlled by the pumping system. Mobile-phase compositions for the various retention studies are specified in the Results and Discussion. The flow rate for the separations was 2 mL/min (1 mL/min for the separation of PCBs with the pyrene column). Detection for all analytes was at 254 nm with a fixed-wavelength detector.

Six columns were utilized in this study: monomeric C_{18} column (Zorbax C_{18}, MacMod, Chadds Ford, PA); polymeric C_{18} column (Bakerbond Wide Pore C18, J. T. Baker, Phillipsburg, NJ); experimental heavy-loaded polymeric C_{18} column (J. T. Baker); tetrachlorophthalimidopropyl (TCPP) column ("Colonne HPA", Societe Francaise Chromato Colonne, Neuilly-Plaisance, France); tetranitrofluoreniminopropyl (TENF) column (TENF column, ES Industries, Marlton, NJ); pyrene column (Cosmosil PYE, Nacalai Tesque, Kyoto, Japan) (see Figure 1). The C_{18}, TCPP, and TENF columns were 25 cm × 4.6 mm, 5 μm particle size configurations; the pyrene column was 15 cm × 4.6 mm, 5 μm particle size configuration.

Molecular Modeling. Space-filling structures of PAH isomers were generated using PC-Model and MMX molecular modeling programs (Serena Software, Bloomington, IN). The force field used in MMX is derived from MM2 (QCPE-395 by N. L. Allinger, Quantum Chemistry Program Exchange, Bloomington, IN) with pi-VESCF routines from MMP1 (QCPE-318, by N. L. Allinger). Structures were plotted with PC-Display (Serena Software).

RESULTS AND DISCUSSION

In comparison to reversed-phase systems, charge-transfer phases have received only limited study. The use of electron-acceptor (EA) and electron-donor (ED) phases in liquid chromatography has been reviewed by Nondek (*14*) and by Sander and Wise (*15*). Electron-acceptor phases are based on ligands with a deficit of electrons, e.g., nitrated or halogenated aromatic species and are commonly used in the normal-phase mode. One of the first such bonded phases for liquid chromatography was reported by Lochmüller and Amoss in 1975 (*16*). They observed strong complexation (high retention) for PAHs with a tetranitrofluoreniminopropylsilane (TENF) stationary phase. Nondek and co-workers prepared phases based on various polynitrated phenyl substituents (*17–19*) and discussed solute retention in terms of the energies of lowest unoccupied (LUMO) and highest occupied (HOMO) molecular orbitals of the acceptor (bonded ligand) and donor (solute) (*19*). More recently, Jadaud, Caude, and Rosset (*20*, *21*) have prepared EA phases based on tetrachlorophthalimidopropyl (TCPP) ligands, using the procedure of Holstein (*22*). PAH retention for this phase was shown to depend on mobile-phase strength, the number of π electrons in the molecule and π electron density, and substituent effects. Although the effect of L/B was briefly examined for three solutes, molecular shape and planarity effects were not examined in these retention studies.

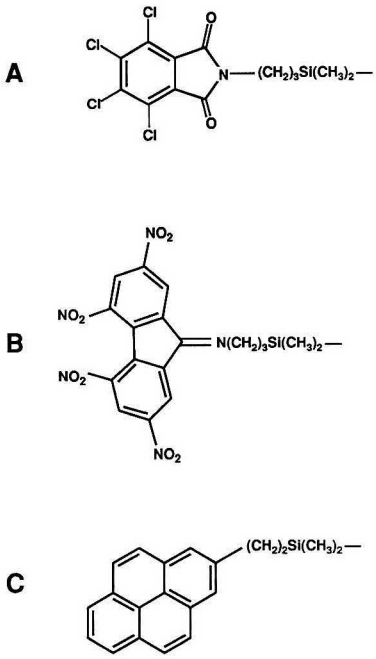

Figure 1. Ligand structures for charge-transfer phases: (A) tetrachlorophthalimidopropyl (TCPP); (B) tetranitrofluoreniminopropyl (TENF); (C) pyrene (PYE).

PAH Isomers. To further probe the retention behavior of PAHs on electron-acceptor charge-transfer phases, a series of PAH isomers of molecular weights 278, 302, and 328 were studied (Figure 2). While most of these PAHs have nearly planar conformations, some of the compounds exhibit marked nonplanarity. Structures for two representative nonplanar PAHs (MW 328) are shown in Figure 3. These compounds are also the nonplanar components of SRM 869, "Column Selectivity Test Mixture". Space-filling models for the compounds represent van der Waals surfaces as determined by molecular modeling. In general, PAHs that contain the fragment benzo[*c*]phenanthrene (i.e., four-ring helicene) are sterically strained by opposing "bay region" hydrogens and exhibit a degree of nonplanarity. This nonplanarity can be expressed by the dihedral angles of adjacent carbons in the bay region. For unsubstituted PAH isomers (e.g., benzo[*g*]-chrysene, benzo[*c*]chrysene, dibenzo[*b,g*]phenanthrene, and dibenzo[*c,g*]phenanthrene), these angles of distortion typically range from 20 to 30°. Substitution in the bay region increases steric hindrance and nonplanarity.

The retention times on the TCPP column for each of the available isomers were determined individually. Normal-phase separations of mixtures of the isomers are shown in Figure 4, and several observations can be made from these chroma-

MW 278 Isomers

		L/B
1.	Dibenzo[c,g]phenanthrene	1.12
2.	Benzo[g]chrysene	1.32
3.	Dibenzo[b,g]phenanthrene	1.33
4.	Benzo[c]chrysene	1.47
5.	Pentaphene	1.73
6.	Dibenz[a,j]anthracene	1.47
7.	Dibenz[a,h]anthracene	1.79
8.	Dibenz[a,c]anthracene	1.24
9.	Benzo[a]naphthacene	1.77
10.	Benzo[b]chrysene	1.84
11.	Picene	1.99

MW 302 Isomers

		L/B
1.	Benzo[a]perylene	1.19
2.	Dibenzo[def,p]chrysene	1.19
3.	Dibenzo[de,qr]naphthacene	1.28
4.	Naphtho[2,1,8-qra]naphthacene	1.69
5.	Benzo[b]perylene	1.38
6.	Dibenzo[fg,op]naphthacene	1.32
7.	Naphtho[1,2,3,4-def]chrysene	1.23
8.	Benzo[rst]pentaphene	1.73
9.	Dibenzo[b,def]chrysene	1.73

MW 328 Isomers

		L/B
1.	Tetrabenzonaphthalene	1.07
2.	Phenanthro[3,4-c]phenanthrene	1.00
3.	Dibenzo[a,m]triphenylene	1.08
4.	Naphtho[1',2'-a]naphthacene	1.52
5.	Benzo[h]pentaphene	1.36
6.	Tribenzo[a,c,h]anthracene	1.40
7.	Benzo[c]pentaphene	1.96
8.	Dibenzo[a,c]naphthacene	1.41
9.	Naphtho[1',2'-b]chrysene	2.05
10.	Benzo[b]pentaphene	1.82
11.	Dibenzo[b,k]chrysene	2.10
12.	Naphtho[b',b]chrysene	2.34
13.	Benzo[c]picene	2.26
14.	Benzo[b]picene	2.01

Figure 2. Structures and length-to-breadth ratios (L/B) for PAH isomer sets employed in this study. Compounds are listed in the order of elution with the TCPP charge-transfer column, and identification numbers correspond to those in Figure 5.

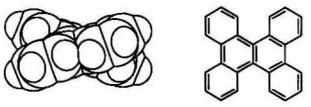

1,2:3,4:5,6:7,8-Tetrabenzonaphthalene

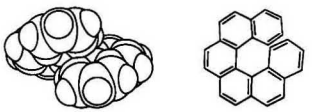

Phenanthro[3,4-c]phenanthrene

Figure 3. Space-filling models for representative nonplanar PAH isomers, as determined by molecular modeling.

tograms. Dramatic differences exist in the retention of nonplanar and planar PAH isomers. Nonplanar PAH isomers elute very early, in several cases near the void volume (e.g., helicene and tetrabenzonaphthalene). Planar isomers are strongly retained by the TCPP phase, and consequently, "class" separations of planar and nonplanar PAHs are possible. Retention of planar isomers follows trends outlined by Jadaud et al. (*20*, *21*); i.e., retention increases with the number of π electrons and with the L/B of the solute. Furthermore, the retention of pericondensed PAHs is disproportionally greater than catacondensed PAHs. For example, under the same mobile-phase conditions, MW 302 planar isomers were retained longer than MW 328 isomers. This is significant since the MW 302 isomers contain fewer π electrons than the MW 328 isomers. It appears that more stable donor–acceptor complexes are possible with pericondensed PAHs than with the more extended catacondensed structures.

The capacity factors (k') for these isomers are plotted against elution order in Figure 5. The sigmoidal shape of these curves is indicative of the planar/nonplanar shape discrimination provided by the charge-transfer column. The "plateau regions" are a consequence of relatively low shape discrimination among the planar PAHs in each isomer set. For example, seven of the MW 328 isomers coelute on the TCPP column; however, a somewhat better separation was obtained for the planar MW 278 isomers.

The shape discrimination that results with the TCPP column is not unique to the tetrachlorophthalimidopropyl ligand. The retention behavior of a dissimilar EA charge-transfer column (tetranitrofluoreniminopropyl column (TENF)) was briefly examined using the MW 278 PAH iso-

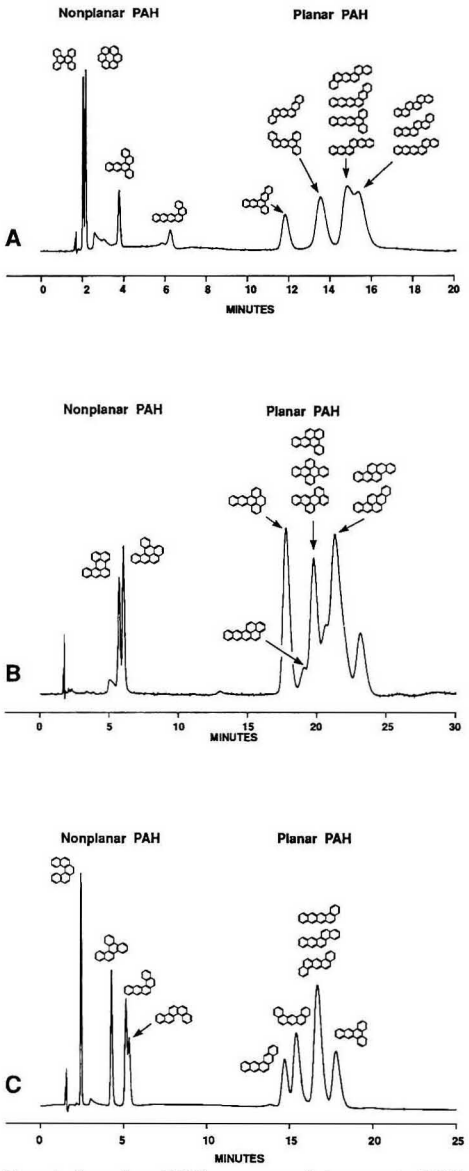

Figure 4. Separations of PAH isomers on an electron-acceptor (TCPP) charge-transfer column: (A) MW 328 isomers, mobile phase 75/25 methylene chloride/hexane; (B) MW 302 isomers, mobile phase 75/25 methylene chloride/hexane; (C) MW 278 isomers, mobile phase 50/50 methylene chloride/hexane. Note that the time scales are different for each chromatogram.

mers. A mixture of these isomers was separated on the TENF column operated in the normal-phase mode (Figure 6A). Although peak shapes were poor, the mixture was resolved into two broad bands. These fractions were collected and further separated using a wide-pore polymeric C_{18} column

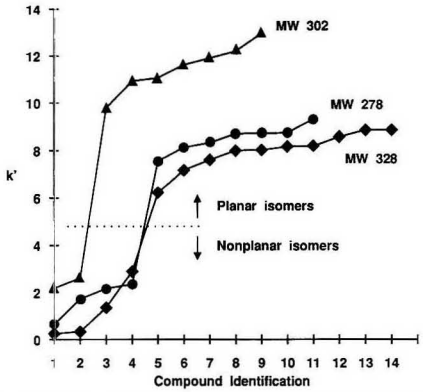

Figure 5. Solute retention plotted as a function of elution order for PAH isomer sets. For compound identification, see Figure 2.

(Figure 6B,C). Peak assignments were made by comparison to standards. It is evident from this figure that planar isomers are preferentially retained compared to nonplanar isomers on the TENF column. This trend is comparable to the retention behavior of PAH isomers with the TCPP column, although better peak shape and better resolution of individual components is possible with the TCPP column.

A simplified view of retention for charge-transfer phases can be envisioned that results from a face-to-face contact of the electron-donor and -acceptor moieties. Enhanced overlap and sharing of π electrons is achieved with planar solute molecules. Strong donor/acceptor complexes are also favored by condensed ring structures. This contact model is subtly different from the slot model, since interaction is relatively insensitive to the L/B of the solute, especially when the contacting solute is spatially large compared to the ligand. Overlap of π electrons would appear to change little for the higher molecular weight PAH isomers, since these compounds are large in relation to TCPP or TENF ligands, and changes in ring position may not be probed by a spatially small EA ligand. The enhanced selectivity that is exhibited by the TCPP column for the MW 278 isomers suggests that more of the solute molecule can interact with the charge-transfer ligand because of the smaller size of these isomers. One could predict that greater shape specificity for PAH isomers would result if charge-transfer phases were designed using larger EA ligands.

It is interesting to compare this mode of retention for the EA charge-transfer phase to the retention behavior of reversed-phase columns. Such a comparison is given in Figure 7 for the separation of MW 302 isomers on several reversed-phase columns (see also ref 13). The best overall separation of these isomers was achieved using polymeric C_{18} phases (Figure 7A). Nearly complete resolution of the 10 isomers was possible with the polymeric wide-pore C_{18} column; similar selectivity toward PAH isomers has been observed for other polymeric C_{18} columns (*3*, *8*, *23–26*). Even more complete separation of the MW 302 PAH isomers was achieved using an experimental, heavily loaded polymeric C_{18} column ($\alpha_{TBN/BaF} \approx 0.2$; see below). The order of elution of the isomers generally follows L/B; however nonplanar isomers elute earlier than would be expected on the basis of L/B alone (*3*, *27*). The slot model suggests that interactions of nonplanar solutes with the stationary phase are hindered by the difficulty of fitting a bulky, nonplanar solute between the alkyl chains.

By comparison to the polymeric C_{18} phase, separation of the MW 302 isomers was very limited on the monomeric C_{18}

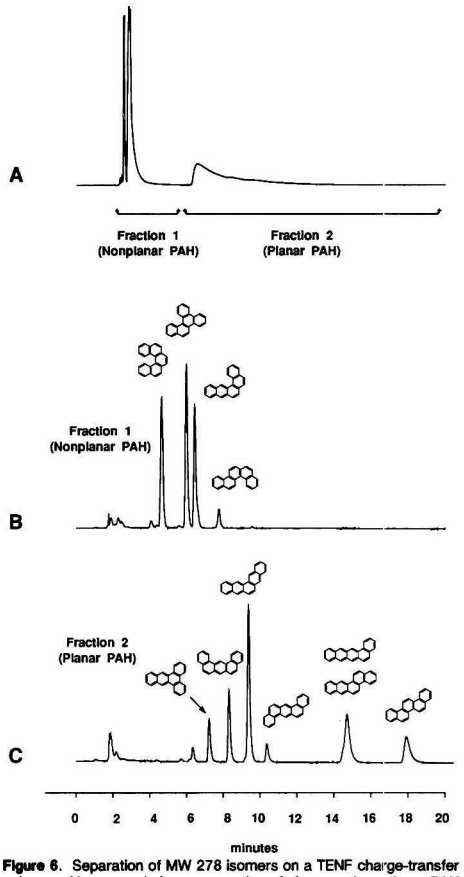

Figure 6. Separation of MW 278 isomers on a TENF charge-transfer column, with reversed-phase separation of planar and nonplanar PAH fractions: (A) TENF column, 50/50 (v/v) methylene chloride/pentane; (B) fraction 1, polymeric C_{18} column, with gradient elution, 85 → 100% (v/v) acetonitrile in water over 5 min with subsequent hold; (C) fraction 2, same conditions as in part B.

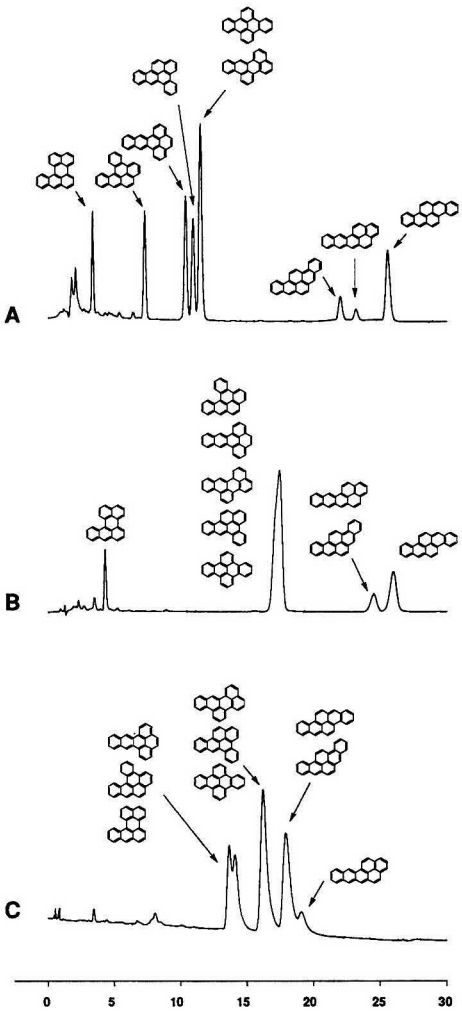

Figure 7. Separation of MW 302 PAH isomers on three reversed-phase columns: (A) polymeric C_{18} column with gradient elution, 85 → 100% (v/v) acetonitrile in water over 20 min with a subsequent hold; (B) monomeric C_{18} column, 85/15 (v/v) acetonitrile/water (isocratic); (C) pyrene column, 70/30 (v/v) acetonitrile/water (isocratic).

phase. With the same mobile-phase gradient as with the polymeric C_{18} phase, little separation of the isomers was achieved. A slightly improved separation resulted with an isocratic mobile phase (Figure 7B). The composition (85% (v/v) acetonitrile/water) was selected to give overall retention comparable to the separation with the polymeric C_{18} phase. Five of the isomers coeluted in a band at approximately 17 min; only two of the nine isomers were completely resolved. One of the nonplanar isomers eluted early (as with the polymeric C_{18} and charge-transfer phases), and the other nonplanar isomer coeluted with four other components. The results strengthen conclusions presented in previous studies—in general, better separations of PAH isomers are possible with polymeric C_{18} phases than with monomeric C_{18} phases. An empirical test has been developed that is useful in classifying C_{18} phase selectivity as "monomeric-like" or "polymeric-like" (*25*, *28*, *29*). This test is based on the relative retention of nonplanar and planar PAH probes, namely tetrabenzonaphthalene (TBN, alternate name dibenzo[*g*,*p*]-chrysene) and benzo[*a*]pyrene (BaP), and the selectivity factor $\alpha_{TBN/BaP}$ is used as a measure of this retention behavior. A column with $\alpha_{TBN/BaP} < 1$ is representative of polymeric C_{18} phases; whereas $\alpha_{TBN/BaP} > 1.7$ is indicative of monomeric C_{18} phases. The $\alpha_{TBN/BaP}$ value for the polymeric C_{18} column in this study was 0.72; for the monomeric C_{18} phase, $\alpha_{TBN/BaP}$ was 1.74. The chromatograms in Figure 7A,B are typical of each phase type, and columns from other manufacturers with comparable $\alpha_{TBN/BaP}$ values should give similar separations.

Bonded phases based on unsubstituted aromatic ligands have the potential for two modes of interaction with solutes—solvophobic interactions and electron-donor charge-transfer interactions. However, unless solutes are potential electron acceptors (such as halogenated or nitrated

Table I. Capacity Factors and Shape Parameters for Methyl-Substituted PAHs

	monomeric C_{18} 70% ACN (v/v)	polymeric C_{18} 70% ACN (v/v)	polymeric C_{18} (high load) 85% ACN (v/v)	pyrene column 60% ANC (v/v)	charge transfer	L/B	dihedral angle of distortion, deg	
			k'				α	β
methylchrysenes								
chrysene	10.2	6.59	2.27	8.21	12.4[a]	1.72		
1-methyl-	16.7	12.2	4.92	12.3	15.7[a]	1.71	0.1	0
2-methyl-	18.2	14.9	6.01	11.3	13.6[a]	1.85	0	0
3-methyl-	16.1	10.1	3.13	10.4	14.1[a]	1.63	0	0
4-methyl-	14.7	8.34	2.07	10.4	10.2[a]	1.51	−3.6	−8.7
5-methyl-	14.7	7.69	2.03	10.6	11.3[a]	1.48	4.3	−11.4
6-methyl-	14.7	7.69	1.78	10.7	18.1[a]	1.48	0	0
methylbenz[a]anthracenes								
benz[a]anthracene			1.49	8.15	4.31[b]	1.60		
1-methyl-			2.05	10.2	4.62[b]	1.47	−24.7	
2-methyl-			1.55	10.1	5.08[b]	1.50	0	
3-methyl-			4.50	11.0	4.96[b]	1.71	0.05	
4-methyl-			1.66	10.9	6.63[b]	1.64	0.6	
5-methyl-			2.88	11.7	6.13[b]	1.43	0.2	
6-methyl-			1.59	10.7	6.11[b]	1.38	6.9	
7-methyl-			2.13	10.9	7.36[b]	1.50	11.2	
8-methyl-			2.43	10.2	5.31[b]	1.57	0.5	
10-methyl-			2.09	10.8	7.39[b]	1.59	−0.5	
11-methyl-			2.12	10.0	5.88[b]	1.45	0	
12-methyl-			1.95	10.5	2.48[b]	1.51	−26.7	
methylbenzo[c]phenanthrenes								
benzo[c]phenanthrene(BcP)			0.77	6.87	1.34[b]	1.22	−23.7[c]	−24.0[d]
1-methyl-			0.69	8.55	0.50[b]	1.21	−32.0[c]	−22.9[d]
2-methyl-			0.91	8.86	1.36[b]	1.17	−24.0[c]	−23.6[d]
3-methyl-			1.37	9.85	1.39[b]	1.36	−23.9[c]	−23.8[d]
4-methyl-			1.13	9.51	1.28[b]	1.36	−26.2[c]	−22.6[d]
5-methyl-			1.17	9.91	1.41[b]	1.22	−25.2[c]	−23.2[d]
6-methyl-			1.07	10.3	1.37[b]	1.12	−24.6[c]	−25.6[d]
1,12-dimethyl-			0.88	10.8	0.26[b]	1.26	−30.7[c]	−30.1[d]
5,8-dimethyl-			1.69	14.2	1.58[b]	1.25	−22.4[c]	−22.7[d]

[a] Separation with 75/25 hexane/CH_2Cl_2 (v/v). [b] Separation with 50/50 hexane/CH_2Cl_2 (v/v). [c] Angle "pqr". [d] Angle "opq".

PAHs), solvophobic mechanisms will dominate retention. The retention behavior of a bonded pyrene column was briefly examined for the MW 302 isomers (Figure 7C). A weaker mobile phase (70% acetonitrile/water) was required to give overall retention comparable to the two C_{18} phases. Little separation of the isomers was possible with this column. Despite the limited resolution, the two nonplanar isomers eluted first as with the polymeric C_{18} and charge-transfer phases. No retention of PAH isomers was observed for the pyrene column operated in the normal-phase mode (100% pentane). This is as expected, since pyrene ligands (electron donors) and PAHs (also electron donors) should not associate to form a donor–acceptor complex.

Methyl-Substituted PAHs. PAH isomers resulting from methyl substitution display many of the trends observed for unsubstituted isomers. While methyl substitution usually results in increased retention compared to the retention of the parent compound, Wise et al. reported that certain methyl isomers elute before the unsubstituted parent compound (27). This anomalous retention behavior was attributed to the nonplanarity of certain methyl isomers and the resulting hindered interaction with the bonded-phase chains. In the current work, the retention behavior of several sets of methyl-substituted PAHs was examined on the charge-transfer and pyrene columns, for comparison with monomeric and polymeric C_{18} phases, as well as with retention trends observed with unsubstituted PAHs.

Relative retention data for various methyl-substituted chrysene, benz[a]anthracene, and benzo[c]phenanthrene isomers (see Figure 8) are presented in Table I. L/B ratios were calculated using procedures previously described (2). For nonplanar molecules, the L/B values listed were calculated

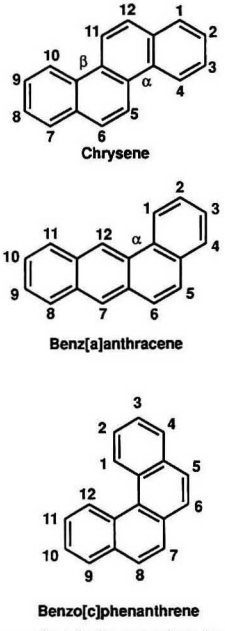

Figure 8. Structures and numbering conventions for methyl-substituted four-ring PAH isomers.

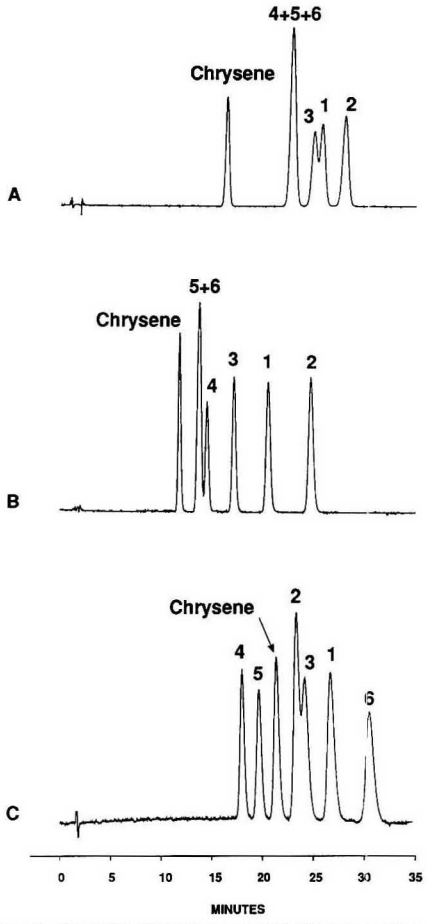

Figure 9. Separation of chrysene and methylchrysene isomers on various columns: (A) monomeric C_{18} column (mobile phase 70/30 (v/v) acetonitrile/water); (B) polymeric C_{18} column (70/30 (v/v) acetonitrile/water); (C) TCPP charge-transfer column (25/75 (v/v) methylene chloride/hexane). Peak numbers refer to the position of methyl substitution.

for the planar representation of the molecule. Dihedral angles of distortion were determined from modeled structures using the carbon atoms that define the bay region (*27*). Trends in retention for the methyl isomers are less defined than trends for the MW 278, 302, and 328 isomer sets. Separations of the six methylchrysene isomers are shown in Figure 9, and in Figure 10 retention (k') is plotted as a function of L/B for the charge-transfer and polymeric C_{18} columns. 4- and 5-methylchrysene have nonplanar conformations due to steric hindrance of the methyl group in the bay region (see Table I). These isomers elute early on the TCPP charge-transfer phase, in a similar fashion to the nonplanar MW 278, 302, and 328 isomers. Complete separation of the methylchrysene isomers was not possible with either of the C_{18} columns. All of the methyl isomers eluted after chrysene for the reversed-phase separations; however, Wise et al. (*27*) demonstrated that nonplanar methyl–PAH isomers (including

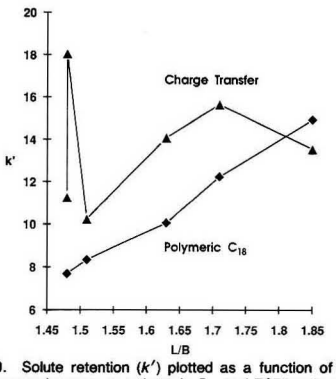

Figure 10. Solute retention (k') plotted as a function of L/B for methylchrysene isomers on polymeric C_{18} and TCPP columns.

nonplanar methylchrysene isomers) elute before the planar unsubstituted parent PAH on heavily loaded, highly shape selective polymeric C_{18} phases. The elution order of 4-, 5-, and 6-methylchrysene on the C_{18} phases deserves a brief comment. Although 4- and 5-methylchrysene are nonplanar, 6-methylchrysene is planar. Complete resolution of these isomers was not possible with either C_{18} phase. With the polymeric C_{18} column, 6-methylchrysene eluted before 4-methylchrysene and coeluted with 5-methylchrysene. Even though the polymeric C_{18} phases exhibited considerable selectivity toward this isomer set, planar and nonplanar isomers were not separated in groups, as with the charge-transfer column. The overall elution order of the isomers is very different for the reversed-phase separations and the charge-transfer separation. Retention of methylchrysene isomers with polymeric C_{18} phases follows the L/B of the solute (Figure 10) (*1*, *30*). Retention with the charge-transfer phase is not as closely correlated to L/B, and it seems probable that in addition to shape effects, positive inductive effects of the methyl substituent play a significant role in retention with the charge-transfer phase. From a practical viewpoint, it is interesting to note that 6-methylchrysene is well separated from the other isomers on the charge-transfer phase. The separation of 5- and 6-methylchrysene, which have identical L/B values, is very difficult using reversed-phase methods (*24*). Little selectivity toward this isomer set was observed with the pyrene column (not shown), and all methyl isomers eluted after the unsubstituted parent.

Structures determined for 1- and 12-methylbenz[*a*]anthracene isomers exhibited appreciable nonplanarity (the distortion angle of 7-methylbenz[*a*]anthracene determined with molecular modeling was ~11°, even though the methyl substitution was not in the bay region). With the TCPP charge-transfer column, 1- and 12-methylbenz[*a*]anthracene eluted before the other isomers; however, the 1-methyl isomer eluted slightly after benz[*a*]anthracene. All methyl isomers eluted after unsubstituted benz[*a*]anthracene on the pyrene column, with little apparent selectivity.

The methyl-substituted benzo[*c*]phenanthrene isomers are interesting in that all of the compounds, including the unsubstituted parent, are nonplanar. Substitution in the bay region (the 1- and/or 12-position) increases this nonplanarity. Two dimethyl isomers are included in this set, 1,12- and 5,8-dimethylbenzo[*c*]phenanthrene. For all of the methyl- and dimethyl-substituted benzo[*c*]phenanthrene isomers, the 1,12-dimethyl isomer was retained the least with the TCPP charge-transfer column, even though the addition of two methyl groups would ordinarily be expected to increase retention substantially compared to the parent compound. In

fact, the 5,8-dimethyl isomer, which is not substituted in the crowded bay region has the greatest retention of the benzo[c]phenanthrene isomers studied. It is interesting to note that with the exception of the 1-methyl and 1,12-dimethyl-substituted compounds, almost no separation of the benzo[c]-phenanthrenes was possible with the charge-transfer column. Low selectivity was also observed with the polymeric C_{18} column. The difficulty in separating these isomers can be attributed to the similarities in their overall shapes. The L/B values for the methylbenzo[c]phenanthrenes are within 0.24 units of each other, and the dihedral angles of distortion are also similar. Because of these similarities, molecular shape provides little basis for discrimination.

Polychlorinated Biphenyls (PCBs). Like PAHs, PCBs are widely distributed throughout the environment and due to their toxicity, the measurement of PCBs in environmental samples is of considerable importance. PCBs are the subject of intense study, and several excellent reviews have been published (*31–33*). There are 209 different PCB configurations (congeners) possible; however, only about half of these congeners are present in the environment, and a much smaller fraction are toxic (*31*). Among the most toxic PCBs are planar congeners with multiple chlorination at ring positions 3, 4, and 5. Chlorinated biphenyls for which no substitution is present at ortho positions (i.e., 2, 2′, 6, or 6′ positions) are classified as non-ortho or planar (often denoted as "coplanar") PCBs, since planar conformations are permitted sterically. PCBs with two or more ortho chlorines are sterically constrained from the planar conformation; these compounds are referred to as nonplanar PCBs. Chlorinated biphenyls with a single ortho chlorine (mono-ortho PCBs) have intermediate properties and are usually grouped separately. McKinney et al. have reported that all non-ortho PCBs have rotational energy minima at ~42°, with rotational barriers of 3.6 and 2.3 kcal mol^{-1} at 0 and 90°, respectively (*34*). A shift in this minimum toward 90° occurs with ortho substitution.

Because PCBs are highly halogenated, these compounds form complexes with electron-donor (ED) charge-transfer phases. Separations of PCBs have been reported on carbon-based sorbents (*35, 36*), and retention is attributed to formation of a charge-transfer complex between the electron-rich graphite surface and the electron-deficient PCB. Recently, Haglund et al. have reported the use of a bonded pyrene column to separate planar and nonplanar PCBs using hexane as the mobile phase (*37*). In the current study, enhanced separation of planar and nonplanar PCB congeners was achieved using a pyrene bonded phase at subambient temperatures. A separation of a mixture of PCB congeners is shown in Figure 11. Peak identifications refer to IUPAC numbering convention for PCB congeners (*31*). At room temperature, PCB retention is limited. Since retention cannot be increased by using weaker normal-phase solvents (the elutropic strength parameter for pentane is 0.00), retention was increased by reducing column temperature. Reduced column temperature was conveniently obtained by immersion of the column into a ice water slurry in a Dewar flask. Temperature stability with this simple apparatus was excellent (±0.1 °C). Nonplanar PCBs were observed to elute before mono-ortho substituted PCBs. Planar (non-ortho) PCBs eluted last, with significant separation of the individual isomers. The nonplanar conformation of the ortho-substituted PCBs reduces the strength of charge-transfer complexes with the pyrene moiety, and retention is reduced compared with planar PCBs. As with PAHs separated on EA charge-transfer columns, class separations of planar and nonplanar PCBs are possible on ED phases. This result is of considerable practical significance since separation of planar and nonplanar PCB fractions are required with many GC methods to eliminate

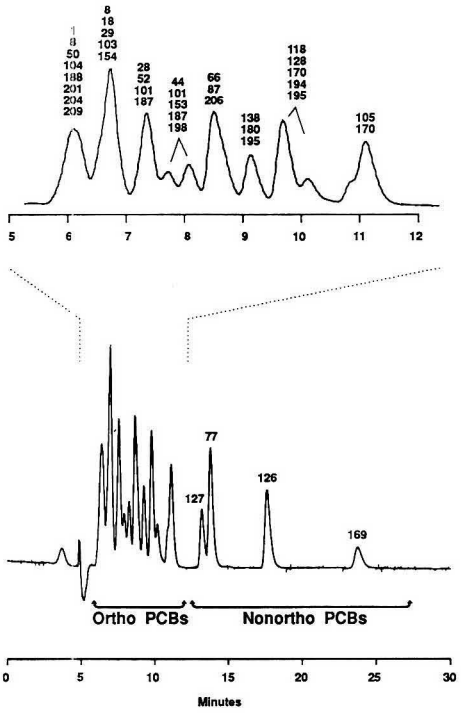

Figure 11. Separation of selected planar and nonplanar PCB congeners (SRM 2262 + PCBs 103, 127, 169, 198, and 204) on a bonded pyrene column at T = 0 °C and pentane mobile phase. Peak identifications refer to IUPAC numbering convention for PCB congeners.

coelution of critical PCB pairs. Use of subambient column temperature improves this class separation and thus facilitates fraction collection in real samples. The application of pyrene columns at subambient temperatures to the fractionation of planar and nonplanar PCBs in environmental samples will be reported in detail elsewhere.

CONCLUSIONS

Shape recognition in liquid chromatography varies dramatically with stationary phase properties. Among reversed-phase C_{18} columns, better separations of PAH isomers are usually possible with polymeric phases than with monomeric phases. Electron-acceptor charge-transfer phases based on tetrachlorophthalimidopropyl or tetranitrofluoreniminopropyl ligands provide class separations of PAH isomers. Nonplanar isomers form weak charge-transfer complexes and have low retention; planar isomers form strong complexes which result in high retention. Similar class separations of ortho and non-ortho PCBs are possible with electron-donor charge-transfer phases. Because charge-transfer phases are used in the normal-phase mode, samples can be prepared in nonpolar solvents, thus eliminating solubility limitations. The unique retention mechanisms of electron-acceptor and electron-donor charge-transfer phases make these columns an excellent complement to polymeric C_{18} phases for the separation of rigidly structured aromatic compounds.

ACKNOWLEDGMENT

The authors thank J. Bellocq for preliminary experiments involving the TCPP column, P. Aznar for providing a TCPP column, and N. Tanaka for providing a pyrene column.

LITERATURE CITED

(1) Sander, L. C.; Wise, S. A. In *Advances in Chromatography*; Giddings, J. C., Grushka, E., Cazes, J., Brown, P. R., Eds.; Marcel Dekker: New York, 1986; Vol. 25, p 139–218.
(2) Wise, S. A.; Bonnett, W. J.; Guenther, F. R.; May, W. E. *J. Chromatogr. Sci.* **1981**, *19*, 457–465.
(3) Wise, S. A.; Sander, L. C. *HRC&CC, J. High Resolut Chromatogr. Chromatogr. Commun.* **1985**, *8*, 248–255.
(4) Martire, D. E.; Boehm, R. E. *J. Phys. Chem.* **1983**, *87*, 1045–1062.
(5) Jaroniec, M.; Martire, D. E. *J. Chromatogr.* **1987**, *387*, 55–64.
(6) Dill, K. A. *J. Phys. Chem.* **1987**, *91*, 1980–1988.
(7) Marqusee, J. A.; Dill, K. A. *J. Chem. Phys.* **1986**, *85*, 434–444.
(8) Wise, S. A.; Sander, L. C.; Chang, H.; Markides, K. E.; Lee, M. L. *Chromatographia* **1988**, *25*, 473–480.
(9) Sander, L. C.; Glinka, C. J.; Wise, S. A. *Anal. Chem.* **1990**, *62*, 1099–1101.
(10) Garrigues, P.; Radke, M.; Druez, O.; Willsch, H.; Bellocq, J. *J. Chromatogr.* **1989**, *473*, 207–213.
(11) Garrigues, P.; De Sury, R.; Angelin, M. L.; Bellocq, J. Oudin, J. L.; Ewald, M. *Geochim. Cosmochim. Acta* **1990**, *52*, 375–384.
(12) Garrigues, P.; Marniesse, M. P.; Wise, S. A.; Bellocq, J.; Ewald, M. *Anal. Chem.* **1987**, *59*, 1695–1700.
(13) Wise, S. A.; Benner, B. A.; Liu, H.; Byrd, G. D.; Colmsjo, A. *Anal. Chem.* **1988**, *60*, 630–637.
(14) Nondek, L. *J. Chromatogr.* **1986**, *373*, 61–80.
(15) Sander, L. C.; Wise, S. A. *CRC Crit. Rev. Anal. Chem.* **1987**, *18*, 299–415.
(16) Lochmüller, C. H.; Amoss, C. W. *J. Chromatogr.* **1975**, *108*, 85–93.
(17) Nondek, L.; Malek, J. *J. Chromatogr.* **1978**, *155*, 187–190.
(18) Nondek, L.; Minarik, M.; Malek, J. *J. Chromatogr.* **1979**, *178*, 427–434.
(19) Nondek, L.; Ponec, R. *J. Chromatogr.* **1984**, *294*, 175–183.
(20) Jadaud, P.; Caude, M.; Rosset, R. *J. Chromatogr.* **1987**, *393*, 39–49.
(21) Jadaud, P.; Caude, M.; Rosset, R. *J. Chromatogr.* **1988**, *439*, 195–211.
(22) Holstein, W. *Chromatographia* **1981**, *14*, 468–477.
(23) Sander, L. C.; Wise, S. A. *Anal. Chem.* **1984**, *56*, 504–510.
(24) Sander, L. C.; Wise, S. A. *Anal. Chem.* **1989**, *61*, 1749–1754.
(25) Sander, L. C.; Wise, S. A. *LC-GC* **1990**, *8*, 378–390.
(26) Sander, L. C.; Wise, S. A. In *Polynuclear Aromatic Hydrocarbons: Eighth International Symposium on Mechanism, Method and Metabolism*; Cooke, M. W.; Dennis, A. J., Eds.; Battelle Press: Columbus, OH, 1983; p 1133–1144.
(27) Wise, S. A.; Sander, L. C.; Lapouyade, R.; Garrigues, P. *J. Chromatogr.* **1990**, *514*, 111–122.
(28) Sander, L. C.; Wise, S. A. *HRC&CC, J. High Resolut. Chromatogr. Chromatogr. Commun.* **1988**, *11*, 383–387.
(29) Sander, L. C. *J. Chromatogr. Sci.* **1988**, *26*, 380–387.
(30) Wise, S. A.; Bonnett, W. J.; Guenther, F. R.; May, W. E. In *Polynuclear Aromatic Hydrocarbons: Chemistry and Biological Effects*; Bjorseth, A., Dennis, A. J., Eds.; Battelle Press: Columbus, OH, 1980; p 791–806.
(31) McFarland, V. A.; Clarke, J. U. *Environ. Health Perspect.* **1989**, *81*, 225–239.
(32) Safe, S.; Bandiera, S.; Sawyer, T.; Robertson, L.; Safe, L.; Parkinson, A.; Thomas, P. E.; Ryan, D. E.; Reik, L. M.; Levin, W.; Denomme, M. A.; Fujita, T. *Environ. Health Perspect.* **1985**, *60*, 47–56.
(33) Miller, S. *Environ. Sci. Technol.* **1983**, *17*, 11a–14a.
(34) McKinney, J. D.; Gottschalk, K. E.; Pedersen, L. *J. Mol. Struct.* **1983**, *104*, 445–450.
(35) Tuinstra, L. G.; van Rhijn, J. A.; Roos, A. H.; Traag, W. A.; van Mazijk, R. J.; Kolkman, P. J. *J. HRC, J. High Resolut. Chromatogr.* **1990**, *13*, 797–802.
(36) Hanai, T.; Walton, H. F. *Anal. Chem.* **1977**, *49*, 1954–1958.
(37) Haglund, P.; Asplund, L.; Jarnberg, U.; Jansson, B. *J. Chromatogr.* **1990**, *507*, 389–398.

RECEIVED for review June 5, 1991. Accepted August 26, 1991. This work was supported in part by NATO Grant No. 870486. Certain commercial equipment, instruments, or materials are identified in this report to specify adequately the experimental procedure. Such identification does not imply recommendation or endorsement by the National Institute of Standards and Technology, nor does it imply that the materials or equipment identified are necessarily the best available for the purpose.

Role of Charge Suppression and Ionic Strength in Free Zone Electrophoresis of Proteins

Bruce Jon Compton*,[1] and Elizabeth A. O'Grady

Bristol-Myers Squibb Company, Industrial Division, P.O. Box 4755, Syracuse, New York 13221-4755

The free zone electrophoretic mobility of proteins can be predicted from the protein's amino acid content by applying a model based on the Debye–Hückle–Henry theory and Henderson–Hasselbalch equation. Calculated mobilities are always greater than actual mobility but a pH-independent proportionality (described by the constant F_Z) is found between the two. Thus, determination of a protein's mobility at one pH allows, with the use of the model and F_Z, calculation of its mobility at other pH conditions. This leads directly to optimum conditions for the electrophoretic resolution of proteins in capillary zone electrophoresis. The fundamental nature of F_Z is examined and found to be a function of a proteins molecular weight, charge, and solution ionic strength. This work aids in explaining the form of previously proposed empirically based equations for peptide and protein mobility.

*Corresponding author.
[1]Current address: ZymoGenetics, 4225 Roosevelt Way NE, Seattle, WA 98105.

INTRODUCTION

Optimization of the electrophoretic behavior of solutes such as proteins in the free zone capillary mode (CZE) requires an understanding of how experimental parameters and the intrinsic features of the protein itself interact to give a result. The most common way of describing such behavior is by a protein's electrophoretic mobility, u, which is defined as the steady-state velocity of a protein under unit field strength. As a starting point, a summary of various electrophoretic mobility functions previously derived for a variety of solutes is presented in Table I. Though this list is not comprehensive, it illustrates the variety and differing complexity of relationships describing how u varies with solute parameters such as size, charge, and shape and solution parameters such as temperature, viscosity, dielectric constant, and ionic strength. More exact theories than those used to derive the cited expressions have been developed. For instance, Booth (*7*), Overbeek (*8*), and Gorin (*9*) have all introduced detailed and insightful treatments. These works are considered useful for

0003-2700/91/0363-2597$02.50/0

Table I. Summary of Electrophoretic Mobility Relationships

equation	application	comment
(1) $u = \frac{Z_a e}{6\pi r_S n}$	general expression for zero ionic strength	based on Stokes' law of viscosity (*1*)
(2) $u = \frac{Z_a e \Phi(kr)}{6\pi n r_S} \frac{1}{1+k}$	approximate expression for conducting solutions	Debye–Hückel–Henry theory (*1*)
(3) $u = \frac{k(1)Z_a}{K(2)M^{1/3} + K(3)I^{1/2}M^{2/3}}$	derived for proteins	from eq 2 (*2*)
(4) $u = \frac{Z_a e(f/f_o)}{5r_W n}$	small ions	used to study ion (f/f_o) (*3*)
(5) $u = \frac{k'Z_a}{M^{2/3}}$	peptides in paper electrophoresis	Offord's equation, empirically based (*4*)
(6) $u = \frac{k' \ln (Z_c + 1) + k''}{n r^{0.43}}$	peptides in free zone CZE	empirically based on eq 7 (*5*)
(7) $u = \frac{Ce'\zeta}{n}$	colloids in ionic solutions	basis for the ζ potential (*6*)

$C = {}^1/_6$(Hückel equation) to ${}^1/_4$(Helmholz–Smoluchowski equation)
e = electronic charge
e' = medium dielectric constant
e_0 = permissivity of free space
(f/f_o) = frictional ratio
I = solution ionic strength
$K(1) = \Phi(kr)e$
$K(2) = 6\pi n(f/f_o)(4\pi N/3\upsilon)^{-1/3}$
$K(3) = 6\pi n(2^{1/2}Ne(e_0e'RT)^{-1/2})(f/f_o)^2(4\pi N/3\upsilon)^{-2/3}$
k', k'' = empirical constants
M = protein molecular weight
N = Avogadro's number
n = solution viscosity
n_r = number of amino acid residues
$\Phi(kr)$ = Henry's function
R = gas constant
r_S = Stokes radius
r_W = van der Waals radii
T = absolute temperature
υ = partial specific volume
Z_a = actual solute valence
Z_c = calculated solute valence
ζ = ζ potential (particle surface charge density)

illustrating the complexity of the subject but do not easily lend themselves to practical solutions.

With regards to Table I, eq 1 is the classic electrophoretic mobility function, based on Stokes' Law, which states that solute mobility is a direct function of its charge ($Z_a e$, where Z_a is the actual or effective valence of the solute and e is the charge of an electron) and inversely related to the frictional drag on the solute ($6\pi r_s n$, where r_s is the solute Stokes radius and n is the medium viscosity). Though widely cited and applied to CZE, it has limited utility because it does not take ionic effects on mobility into consideration.

Equation 1 can be made more useful by applying the Debye–Hückel theory, as shown in eq 2, to account for ionic affects. This expression also incorporates Henry's function ($\Phi(kr)$) and is relatively accurate in principle for describing how u varies with both the nature of a solute and its environment (*1*, *6*, *10–13*). The main limitation of utilizing this expression for the optimization of CZE separations is that its solution requires knowledge of both a solute's Stokes radius (r_s) and actual valence (Z_a). The Stokes radius is obtained from diffusion or sedimentation studies, while Z_a is most accurately determined from membrane potential measurements (*12*, *14*). Since both r_s and Z_a are dependent on solution conditions such as pH, ionic strength, the nature of the ions present, dielectric constant, and temperature, they must be measured under conditions identical to those used for electrophoresis.

Equation 3 was derived from eq 2 in an attempt to arrive at a more useful, albeit more approximate, expression for describing protein mobility. This involved the substitution of protein molecular weight (M) for protein equivalent radii and calculating valence from protein sequence information and the Henderson–Hasselbalch equation (2). Thus, a protein's amino acid content is used for direct calculation of a protein's molecular weight and, with an estimate of a protein's partial specific volume (υ) and frictional ratio (f/f_o), allows calculation of a radius equivalent to Stokes' radius (*15*, *16*). A protein's amino acid content is best determined from sequence information as opposed to amino acid analysis, due to the lability of certain amino acids to protein hydrolysis conditions. Also, it is noteworthy that once calculated valence (Z_c) is determined as a function of pH, the resulting pH–valence curve is of limited usefulness because of the requirement for the determination of a proportionality constant (F_Z) to equate Z_a with Z_c ($Z_a = Z_c/F_Z$, see ref 2). Since the nature of F_Z is currently unknown, F_Z will be investigated here with respect to the role that charge suppression plays on determining net protein charge.

Equation 4 is similar to 1 but based on van der Waals radii and has been used to account for the frictional ratio (f/f_o), a measure of solute symmetry, of small solutes (*3*). It is mentioned because it aids in understanding the limitations of eq 1 for applications involving solutions of high ionic strength but also shows under what conditions eq 1 is applicable.

Due to the complexity of the subject, attempts at describing mobility of macromolecules such as peptides and proteins has often required an empirical approach. Thus, eqs 5 and 6 resulted from mobility data of model peptides and proteins. The former expression was originally developed for paper electrophoresis and has recently been successfully applied to the free zone capillary mode (*16–19*). The latter expression was specifically developed for describing mobility of peptides in the free zone capillary mode (*5*). This expression (eq 6) is of interest since it shows that calculated valence (Z_c) is proportional, as will be discussed further, to actual valence (Z_a) by a complex logarithmic function. It also illustrates that the molecular weight dependency of mobility can be different than that predicted by the other expressions, with the exception of eq 3. Equation 3 was actually derived to account

for the discrepancies between eqs 5 and 6 and the fundamental expressions (eqs 1, 2, and 4).

Equation 7 is an interesting and familiar expression for describing the mobility of colloids. The basic form of this equation has been attributed both to Hückel and to Helmholtz and Smoluchowski, and the difference between their results has been reconciled by the work of Henry (*1, 6, 11*). It should be noted that this equation can be derived from eq 2 when one considers that the ζ potential of a particle (its surface charge density) determines particle mobility at high solution ionic strength and large solute radii, as noted indirectly during the derivation of eq 3 (*2*). It is mentioned since it is often cited in reference to the mobility of nonmacroscopic solutes in CZE, but since it is a direct extrapolation of eq 2 to the limiting case of solutes of large size in high ionic strength buffer, this many not be an appropriate use of the expression.

This brief survey indicates that the subject of solute electrophoretic mobility is complex. This is particularly true for proteins since these large molecules show zwitterionic characteristics and secondary structure which make simple description of their charge and size difficult. Since there is a compelling need for analyzing this type of material, the understanding of CZE for this application requires a practical solution. With this in mind, as mentioned, eq 3 was derived from eq 2 such that the solute size dependency can be expressed in terms of molecular weight rather than solute radii. Thus, this equation is an initial attempt at adding practicality to the use of eq 2. This is further manifested in the use of Z_c, rather than Z_a, since Z_c is easily calculated for a particular solution pH from the amino acid content of a protein. Unfortunately, as noted, the difference between Z_c and Z_a requires the use of a proportionality factor, F_Z. Interestingly, the complex u dependency on Z_c seen in eq 6, as has been previously noted, must be due to the nature of F_Z since this eq 6 actually equates Z_c and Z_a. Though the nature of F_Z is expected to be complex, it warrants further study.

Role of Protein Electrostatics on Charge Suppression. The classic work of Longsworth (*20*), Abramson (*21, 22*), and Beychok (*23*), to name a few, have shown that a direct proportionality exists between the valence of a protein determined by titration (Z_t) and u. Furthermore, this proportionality is independent of pH. As mentioned, membrane potential measurements have been shown to give a more exact measure of effective protein valence in that they agree with valence measured by electrophoresis (*12, 14*).

To explain these results, we refer to the classic work done on protein electrostatics. Kirkwood and Tanford (*24*) have shown that the measured titration curves, both for free constituent amino acids and the protein itself, overestimates actual valence because of surface electrostatic charge suppression. The determination of detailed protein surface charge distribution directly from sequence data is an unsolved problem, but an approximate relationship can be utilized to help explain the differences between Z_t, Z_c, and Z_a, and between eqs 1–4 and 6, particularly the complex form of the charge relationship seen in the latter.

To determine the nature of F_Z, albeit in an approximate fashion, the classic expression for charge suppression is used (*24*)

$$\mathrm{pH} = \mathrm{p}K_{\mathrm{int}} - 0.868wZ_a + \log\,(\alpha/(1-\alpha)) \qquad (8)$$

where pH is solution pH, $\mathrm{p}K_{\mathrm{int}}$ is the intrinsic ionization constant for a particular amino acid side chain, and $w = [e^2N/2e'e_oRT]\,[r^{-1} - [k/(1 + kr_i)]$, where e' is the solution dielectric constant, e_o is permissivity of free space, R is the gas constant, T is the solution temperature, k is the Debye parameter, and r_i is the sum of the radii of solute and solution ions. Thus, w is a complex variable whose magnitude is dependent on protein and solution ion radii and solution ionic strength. Also, α is the degree of ionization of the amino acid in question. In the past, Z_c was calculated from

$$Z_c = \sum \frac{P_n}{1 + 10^{\mathrm{pH}-\mathrm{p}K(P_n)}} - \sum \frac{N_n}{1 + 10^{\mathrm{p}K(N_n)-\mathrm{pH}}} \qquad (9)$$

where P_n and N_n are the number of cationic and anionic amino acids of a particular type (eg. n = 1–5), respectively, and the pK values refer to their respective ionization constants (*26*). This is a general expression that can be applied to other non amino acid ionizable groups, such as those attributed to posttranslational modification of proteins, by treating these groups in an fashion analogous to that of the amino acids.

An expression for actual protein valence results from substituting eq 8 into eq 9 to give

$$Z_a = \sum \frac{P_n}{1 + 10^{\mathrm{pH}-\mathrm{p}K(P_n)+0.868wZ_a}} - \sum \frac{N_n}{1 + 10^{\mathrm{p}K(N_n)-\mathrm{pH}-0.0868wZ_a}} \qquad (10)$$

Given that $F_Z = Z_c/Z_a$, the ratio of eqs 9 and 10 gives

$$F_Z = \frac{1 + 10^{\mathrm{pH}-\mathrm{p}K(P_n)+0.868wZ_a}}{1 + 10^{\mathrm{pH}-\mathrm{p}K(P_n)}} \qquad (11)$$

where, for simplicity, it is assumed that n = 1 and N_n = 0. Since F_Z is independent of solution pH, we can solve for F_Z in the limiting case of pH − p$K(P_n) \rightarrow 0$ to arrive at

$$\log\,(F_Z - \tfrac{1}{2}) = 0.868wZ_a + \log\,\tfrac{1}{2} \qquad (12)$$

and substituting for w gives

$$\log\,(F_Z - \tfrac{1}{2}) = \frac{0.868e^2NZ_a}{2e'e_oRT[r^{-1} - (k/(1 + kr_i))]} + \log\,\tfrac{1}{2} \qquad (13)$$

A further substitution of molecular weight (M) for protein radii (r) can be made, as was done in deriving eq 3, by using the expression $r_e = (3Mv/4\pi N)^{1/3}(f/f_o)$. We also assume that, for the case of large solutes such as proteins, r_e approximates r_i. Upon substitution of this into eq 13, we arrive at

$$\log\,(F_Z - \tfrac{1}{2}) = Z_ak_1k_2[M^{1/3} + kk_1M^{2/3}] + \log\,\tfrac{1}{2} \qquad (14)$$

where $k_1 = [3v/(4\pi N)]^{1/3}(f/f_o)$ and $k_2 = (0.868e^2N)/(2e'e_oRT)$.

There are a number of interesting aspects to eq 14. First, its general form is similar to the mobility–charge dependency seen in eq 6 and gives one explanation as to why valence calculated from amino acid content of peptides or proteins (Z_c) results in a charge dependency different from the direct proportionality otherwise shown in Table I. Secondly, the expression indicates that the magnitude of F_Z depends on the actual charge of a protein (Z_a), its molecular weight (M), and solution ionic strength (as $I^{1/2}$ through the Debye parameter, k). The molecular weight dependency is complex and varies between $M^{1/3}$ and $M^{2/3}$ depending on I. Substitution of I = 70 mol/m^3, $v = 7.3 \times 10^{-4}$ m^3/Kg, and (f/f_o) = 1.0 into eq 14 gives $kk_1 = 0.57$, which indicates that under this condition of ionic strength, F_Z tends to have a dependency intermediate between $M^{1/3}$ and $M^{2/3}$ (ie. $M^{1/2}$).

Since eq 14 is based on a simplistic model of charge surpression, it is not surprising that further attempts at its use for quantitative predictions of F_Z fail. The main limitation of the model is that it does not account for the differential suppression of individual amino acid side chains. The results of this become obvious when one examines eq 10, which does not give the constant proportionality with eq 9 that is described for actual titration and mobility results. Also, eq 12 fails in providing reasonable quantities for F_Z as well. Though not completely satisfactory, these expressions, particularly eq 14, can be used in a semiempirical fashion to study the nature

Table II. Summary of Calculated and Measured Mobility

protein	calcd M, kg/mol	pH 2.5 Z_c	pH 2.5 Z_a	$10^8 u$, $m^2/(V\ s)$ u_c	$10^8 u$, $m^2/(V\ s)$ u_a	F_Z
α-lactalbumin	14.186	16.2	5.85	9.84	1.56	2.77
trypsin inhibitor	20.100	21.0	5.14	11.4	1.31	4.08
carbonic anhydrase	28.851	38.0	9.03	18.2	1.41	4.21
chicken ovalbumin	42.749	41.8	10.2	17.6	1.39	4.10
human serum albumin	66.407	98.5	17.4	35.5	1.85	5.66
phosphorylase *b*	97.288	130.9	19.3	41.7	1.66	6.77
β-galactosidase	116.00	117.4	19.7	35.5	1.52	5.97
chimeric-L6 IgG	147.76	152.9	18.3	42.6	1.23	8.37

[a] Calculated from eq 9 and respective amino acid content at pH 2.5. [b] Determined from mobility data (u_a) and eq 3 as described in the text. [c] Calculated from eq 3 and Z_c. [d] Relative standard deviation for the measurement is estimated to be 5%. Most errors associated with this measurement were systematic and corrected for using adenosine as an internal marker of mobility.

of F_Z for model proteins. A more elaborate model has been developed which significantly modifies eq 8, but its complexity limits its practicality (25).

EXPERIMENTAL SECTION

Experimental conditions and equipment have previously been described (2). Briefly, free zone capillary electrophoresis (CZE) was used for mobility determinations using a Biorad HPE 100 (Biorad Corp., Richmond, CA) and a 25 μm i.d. coated capillary that is 20 cm between electrode reservoirs (L_t) and 17.2 cm from site of sample introduction to detection (L_d). A variety of different ionic strength orthophosphoric acid buffers (sodium salt), as described in the text, were used at a pH of 2.5. All chemicals except the model proteins were reagent grade from Fisher Scientific (Pittsburgh, PA). All determinations of mobility were done in triplicate with buffer flushes between individual runs. Except for chimeric L6, an antineoplastic human-mouse chimeric antibody, which was prepared in-house (2), all model proteins were purchased from Sigma Chemical Co. (St. Louis, MO) and prepared as approximately 1 mg/mL in physiological phosphate-buffered saline. They were subsequently diluted with deionized water to 50–100 μg/mL concentration prior to analysis and applied to capillary by electromigration. Previous studies regarding the sample buffer composition effects on solute migration indicated that solute band shape and size were greatly affected by variations in this parameter but not solute mobility (2).

Sequence and amino acid data were obtained from the data base GenePro (Riverside Scientific Enterprises, Bainbridge Island, WA). The pK_a values chosen for respective amino acid side chains have been given in ref 2.

The nature of F_Z can be examined by determining u for a variety of proteins, calculating Z_a from these determinations and eq 3 and Z_c at the pH of interest from eq 9, and determining F_Z from Z_c/Z_a. Alternatively, F_Z can be determined from the ratio of calculated to actual protein mobility (u_c/u_a) as is done here, where u_a is measured and u_c is derived from eqs 3 and 9 (2). This was done by determination of the mobility of the series of model proteins shown in Table II at pH 2.5 in a sodium ortho phosphate buffer solution at ionic strength 70 mol/m^3 (0.1 M). These conditions were chosen because at this pH electroosmotic flow within the capillaries is low, the titration curves of the proteins indicate that this is a relatively unchanging portion of the curve (i.e. a region which is insensitive to changes in experimental conditions), and the proteins under investigation were all positively charged, simplifying measurements.

The resulting migration times (t) for each protein were used to determine u_a from the expression $u = L_d L_t / Vt$, where L_d and L_t are previously defined, V was 8.0 kV, and t was measured in seconds.

Alternatively, studies on varying ionic strength were conducted at 2.0 kV to reduce capillary Joule heating as previously discussed (2). All work was conducted at room temperature (25 °C).

In calculation of the values for u_c (from eqs 3 and 9 and the respective amino acid contents of the proteins), values for (f/f_o) and Henry's function were taken to be unity, v was assumed to be $7.3 \times 10^{-4}\ m^3/kg$ (2, 16), and $K(1) = 9.50 \times 10^{-18}\ m^3/(V\ s)$, $K(2) = 6.62 \times 10^{-10}\ (mol^{1/3}\ m)/kg^{1/3}$, and $K(3) = 4.55 \times 10^{-11}\ (m^{5/2}\ mol^{1/6})/kg^{2/3}$. Coefficient $K(3)$ is defined differently here than in ref 2; in this instance, it does not incorporate the ionic strength term. This term is shown directly in eq 3 to emphasize the role this attribute of the system buffer plays in determining solute mobility. Table II is a compilation of the information resulting from these calculations and measurements.

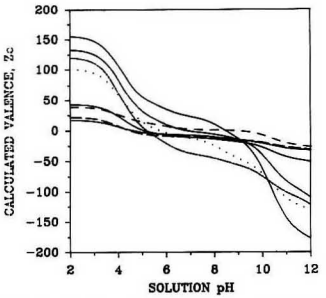

Figure 1. Calculated valence (Z_c) as a function of pH for (at pH 2 in descending order of charge) chimeric L6 IgG, phosphorylase *b*, β-galactosidase, human serum albumin, chicken ovalbumin, carbonic anhydrase, trypsin inhibitor, and α-lactalbumin. While Z_c is calculated to be large for some proteins, charge suppression as determined using capillary zone electrophoresis, results in much lower actual charges (Z_a) as tabulated for pH 2.5 in Table II.

RESULTS AND DISCUSSION

A practical means of optimizing resolution in CZE is to predict the mobility of respective solutes as a function of experimental conditions. The most effective means of controlling protein mobility is by changing solution pH, since this directly changes protein valence and valence is the solute parameter which determines mobility to the greatest extent. Given the amino acid content of a protein, its titration curve can be calculated from the Henderson–Hasselbalch equation (26). The resultant titration curve has two features of interest. Firstly, it predicts with reasonable accuracy (±0.2 pH unit) the isoelectric point (p*I*) of a protein, as has been demonstrated with regard to showing the validity of these calculations (26). However, no attempt has been made at demonstrating that calculated valences at pH conditions different from the p*I* of the protein are valid since this is not easily accomplished. Thus, the second feature of these titration curves is that they most likely do not predict correctly the valence of a protein at conditions where the protein has reasonable charge. The basis for this statement is that eq 6 is empirically based on calculated valence and yet does not conform to well-established mobility relationships with regard to the charge–mobility relationship described. The inconsistent form of this equation must be due to the way in which valence is estimated, i.e. calculated rather than measured by titration or membrane potential, since eqs 1–4 show that a direct relationship exists between valence and mobility. This inconsistency can be accounted for, in a general fashion, by classic concepts regarding protein electrostatics (24, 25).

The use of calculated valence–titration curves is particularly compelling since, as shown in Figure 1 for the model proteins examined here, their direct inspection illustrates solution pH conditions where CZE resolution of respective proteins should occur. Similar mobility–pH curves can be generated using eq 2 or 3. This is illustrated in Figure 2 for human serum albumin (HSA), where mobility is calculated using the parameters mentioned in the Experimental Section. Also shown in this figure are CZE mobility results measured below and

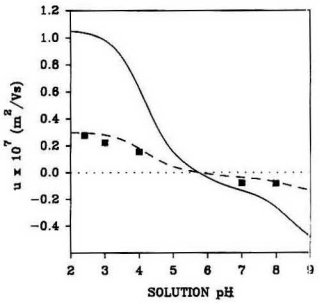

Figure 2. Calculated (solid line) and measured (solid squares) mobility (u)–pH dependency for human serum albumin, illustrating charge and mobility reversal above and below the pI of the protein. Also shown is the mobility–pH curve when corrected for charge suppression (F_Z = 3.42), which results in a coincident between experimental and calculated results.

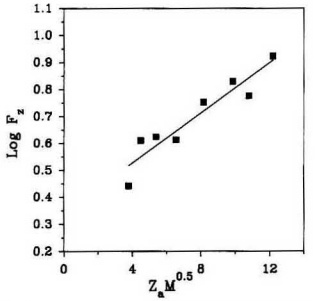

Figure 3. Correlation of protein charge suppression (F_Z) to molecular weight according to eq 15 (data taken from Table II). While eq 15 is expected to be inexact, additional scatter in the data probably results from using a constant value for (f/f_o) and v when u_c is calculated using eq 3.

above the pI of HSA. The difference in the predicted and actual mobilities can be accounted for by calculating a charge suppression factor (F_Z) at pH 2.5 and recalculating the predicted curve using this factor. When this is done, the predicted and measured curves are coincident. This relationship is not surprising, considering the classic free zone electrophoresis and corresponding membrane potential and titration work previously cited. It has also been previously demonstrated for isoelectrotype resolution of IgG (2).

The calculated values of F_Z for the eight model proteins are listed in Table II and plotted according to eq 14 using the simplified expression

$$\log F_Z = aZ_e M^{1/2} + b \tag{15}$$

as shown in Figure 3. The line shown in the figure represents linear regression analysis of the experimental data fit to eq 15 where a = 0.0466 (standard error 0.00668), b = 0.341 (standard error 0.0546), and R^2 = 0.890. Thus, for an ionic strength of 70 mol/m^3, the log F_Z of a protein is proportional to $M^{1/2}$, which is intermediate between radii and surface area. The charge suppression model expressed by eq 14 appears to fail in a quantitative sense. This is not surprising when one examines in detail eq 8, the basis for eq 14, since this equation does not correctly predict the relationship between Z_v, Z_c, and Z_e. The reason for this is that the expression is based on a model that assumes all charges on the surface of a protein are suppressed to a similar extent as the charge density increases. This is clearly not the case since protein surface charge distribution is not expected to be uniform. A more detailed model has been proposed but is difficult to apply due to its complexity and requirements with regard to knowledge of the actual spatial distribution of surface charges (24). Other limitations of the approach discussed here, that the assumption that peptides have similar secondary structure and that their Stokes radii can be approximated from M and v, are all simplifications that attempt to add practicality to the subject. Also, this work assumes the proteins under investigation have similar v and f/f_o on the basis of average values for generalized proteins (2), and again, this is not valid. Considering the complexity of the subject and the diverse nature of the model proteins, it is interesting that a reasonable relationship does exist between F_Z and M. This not only aids in explaining the difference between eq 6 and the other equations mentioned in Table I but also shows that approximate values for F_Z may be predicted a priori.

Though eq 14 is an approximation, it can be used in its simplified form (eq 15) by substitution into eq 3 to give a generalized expression for the electrophoretic mobility of proteins

$$u = \frac{K(1)Z_c 10^{-aMb+c}}{K(2)M^{1/3} + K(3)/I^{1/2}M^{2/3}} \tag{16}$$

where a, b, and c are experimentally derived factors. This expression indicates that, in dealing with calculated charge (Z_c) and ionic solutions, eqs 1 and 2 take on different and complex forms. For instance, the molecular weight dependency of u is not simply based on solute radius (eq 1) or surface area (eq 7) but is a complex continuous function of $M^{1/3}$ to $M^{2/3}$. The charge dependency is equally complex, due to charge suppression and ionic factors.

For any particular protein, eq 16 functionally reduces to

$$u = Z_C/C'M^m \tag{17}$$

where Z_c is from eq 9 and the amino acid content of a protein, C', is experimentally determined (for instance, at pH 2.5) and becomes an aggregate constant encompassing $I^{1/2}$, $K(1)$, $K(2)$, $K(3)$, and $m = {}^1/_3$–$^2/_3$, depending on I and M. The predictive nature of this equation, used in a semiempirical fashion, has been demonstrated for the case of IgG isoelectrotype resolution (2).

One shortcoming of the empirical models that resulted in eqs 5 and 6 was that in their derivation the respective roles of solution pH and ionic strength were not considered nor extensively discussed. Equation 16 indicates that I has relatively general affects on u. According to the Debye–Hückel model, the mobility relationship should be that u is proportional to $I^{-1/2}$, as has been previously demonstrated (14). Figure 4 illustrates this relationship for human serum albumin. As ionic strength increases, the ionic shell of the protein also increases, effectively increasing r_S and decreasing u. Complimentary to this, the effect of I on F_Z is shown in Figure 5. As with u, ionic strength effects on F_Z are seen to be nonselective in nature. Thus, changes in solution ionic strength are not expected to change solute resolution dramatically unless specific ionic interactions between a particular ion and solute occur. This in turn indicates, as is generally accepted, that solution pH plays the most significant role with regard to solution parameters, in determining free zone mobility and selectivity of proteins.

While this work attempts to aid in understanding how the mobility of complex solutes such as proteins are dependent on the nature of both the protein and the surrounding solution and does offer a predictive value with respect to equating mobility results to the calculated charge of a protein as a function of pH, the complexity of the subject does not appear

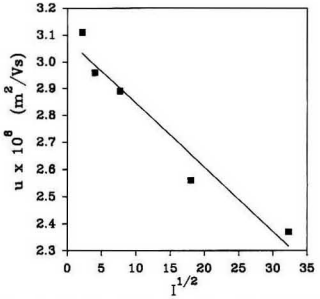

Figure 4. Plot showing the relationship of u to I at pH 2.5 for human serum albumin. The plot agrees with what is predicted from eqs 2 and 3. The line is the result of linear-regression analysis of the data, which gives an x coefficient of -2.36×10^{-10} (standard error 3.31×10^{-11}), y intercept of 3.08×10^{-8} (standard error 8.25×10^{-10}), and R^2 of 0.945.

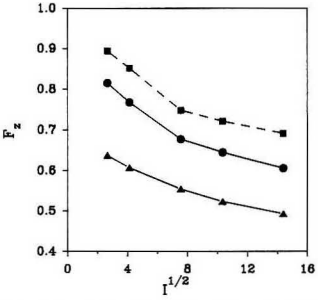

Figure 5. Plot of the relationship of F_z and I at pH 2.5 for (top-to-bottom) human serum albumin, phosphorylase b, and carbonic anhydrase, using the functional form of eq 14. These results are consistent with the expected relationship of F_z to I, in that as solution ionic strength increases, a protein can carry greater surface charge and F_z should decrease. The general nature of F_z is also illustrated by its observed proportional decreases being similar, and t therefore nonselective, for each protein.

to lend itself to a simple exact solution. One aspect of CZE that is often overlooked is that this technique presents itself as an elegant and convenient tool for investigating surface charge characteristics and specific ionic interaction of proteins. As more work is done using CZE, a better and more satisfying understanding of the behavior of protein mobility should present itself.

ACKNOWLEDGMENT

We are grateful to Bristol-Myers Squibb Industrial Division personnel, Jerrery A. Schrimsher (Protein Purification Group), and Jeffery A. Titus (Antitumor Fermentation Development) for assistance in preparing this manuscript and to William V. Burnett (Genetic Engineering) for helpful discussions and sequence information.

Registry No. Trypsin inhibitor, 9035-81-8; carbonic anhydrase, 9001-03-0; phosphorylase b, 9012-69-5; β-galactosidase, 9031-11-2.

LITERATURE CITED

(1) Abramson, H. A.; Moyer, L. S.; Gorin, M. H. *Electrophoresis of Proteins*; Hafner Publishing Co. Inc.: New York, 1964; pp 105–172.
(2) Compton, B. J. *J. Chromatogr.*, in press.
(3) Edwards, J. T. In *Advances in Chromatography*; Giddings, J. C., Keller, R. A., Eds.; Marcel Dekker Inc.: New York, 1966; Vol. 2, pp 63–98.
(4) Offord, R. E. *Nature* **1966**, *211*, 591–593.
(5) Grossman, P. D.; Colburn, J. C.; Lauer, H. H. *Anal. Biochem.* **1989**, *179*, 28–33.
(6) Overbeek, J. Th. G. In *Advances in Colloid Science*; Mark, H., Verwey, E. J. W., Eds.; Wiley-Interscience: New York, 1950; Vol. 3, pp 97–134.
(7) Booth, F. *Proc. R. Soc. London, A* **1950**, *203*, 514–533.
(8) Overbeek, J. Th. G. *Kolloid-Beih.* **1943**, *54*, 287–364.
(9) Gorin, M. H. *J. Chem. Phys.* **1939**, *7*, 405–414.
(10) Hiemenz, P. C. In *Principles of Colloid and Surface Chemistry*; Marcel Dekker, Inc.: New York, 1977.
(11) Henry, D. C. *Proc. R. Soc. London, A* **1931**, *133*, 106–129.
(12) Adair, G. S.; Adair, M. E. *Trans. Faraday Soc.* **1940**, *36*, 23–32.
(13) Mosher, R. A.; Dewey, D.; Thorman, W.; Saville, D. A.; Bier, M. *Anal. Chem.* **1989**, *61*, 362–366.
(14) Tiselius, A.; Svensson, H. *Trans. Faraday Soc.* **1940**, *36*, 16–22.
(15) Oncley, J. L. *Ann. N.Y. Acad. Sci.* **1941**, *41*, 121–150.
(16) Zamyatnin, A. A. *Annu. Rev. Biophys. Bioeng.* **1984**, *13*, 145–165.
(17) Frenz, J.; Wu, S.-L.; Hancock, W. S. *J. Chromatogr.* **1989**, *480*, 379–391.
(18) Wu, S.-L.; Teshima, G.; Cacia, J.; Hancock, W. S. *J. Chromatogr.* **1990**, *516*, 115–122.
(19) Rickard, E. C.; Strohl, M. M.; Nielsen, R. G. *Anal. Biochem.* **1991**, *197*, 197–207.
(20) Longsworth, L. G. *Ann. N.Y. Acad. Sci.* **1941**, *41*, 276–284.
(21) Abramson, H. A. *J. Gen. Physiol.* **1931–1932**, *15*, 575–603.
(22) Abramson, H. A.; Gorin, M. H.; Moyer, L. S. *Chem. Rev.* **1939**, *24*, 345–366.
(23) Beychok, S.; Warner, R. C. *J. Am. Chem. Soc.* **1959**, *81*, 1892–1897.
(24) Tanford, C.; Kirkwood, J. G. *J. Am. Chem. Soc.* **1957**, *79*, 5333–5347.
(25) Matthew, J. B. *Ann. Rev. Biophys. Biophys. Chem.* **1985**, *14*, 387–417.
(26) Sillero, A.; Ribeiro, J. M. *Anal. Biochem.* **1989**, *179*, 319–325.

RECEIVED for review June 12, 1991. Accepted August 29, 1991.

Stable Isotopes for Determining Biokinetic Parameters of Tellurium in Rabbits

Tomas Kron[1]

Universität Frankfurt, Institut für Biophysik, Paul-Ehrlich-Strasse 20, D-6000 Frankfurt/Main 70, Germany

Klaus Wittmaack*

GSF, Institut für Strahlenschutz, D-8042 Neuherberg, Germany

Christine Hansen and Eckhard Werner

GSF, Institut für Biophysikalische Strahlenforschung, Paul-Ehrlich-Strasse 20, D-6000 Frankfurt/Main 70, Germany

We have compared the use of stable and radioactive isotopes for determining the concentration of tellurium in body fluids of animals and man, specifically in the blood plasma of rabbits. Particular effort has been devoted to developing a sample-processing technique that allows the total amount of tellurium and isotope ratios to be measured by graphite furnace atomic absorption spectrometry (GFAAS) and secondary ion mass spectrometry (SIMS), respectively. The procedure employed in the SIMS analysis is discussed in detail. Investigations on the plasma clearance and the fractional intestinal absorption were carried out on four rabbits. Tracer solutions containing stable tellurium enriched in ^{124}Te or ^{126}Te and radioactive tellurium (^{121m}Te or ^{123m}Te) were administered by gavage and/or intravenously. Blood samples were drawn during the first 2 days after application. The activity of the separated plasma was measured by standard γ ray spectrometry. After wet ashing and solvent extraction with MIBK the samples were analyzed for stable tellurium. A detection limit of 1 ng/mL of plasma could be achieved with GFAAS. For SIMS analysis the processed samples were deposited on high-purity graphite backings. Reliable isotope ratios could be determined with sample fractions containing 1 ng of tellurium or even less. The results obtained by applying stable isotopes were found to be in good agreement with the data achieved by using radioactive tracers. Studies on the intestinal absorption and the metabolic behavior of tellurium in human volunteers may thus be performed with stable isotopes.

INTRODUCTION

Tellurium is a rare nonessential trace element. It enters the environment of man mainly due to its increasing usage in industry, particularly in semiconductor device fabrication (*1*). Information on the intestinal absorption and the metabolic behavior of tellurium after incorporation is of concern from the point of view of occupational medicine and environmental protection. Interest in the metabolism of this element is also stimulated by the recent discovery of the new tellurium–based immunomodulating compound AS-101 (*2*, *3*). Very few experimental studies on the metabolism of tellurium have been reported previously, and available data relate to animals only (*4*, *5*). Studies on tellurium in human beings are highly desirable, therefore.

[1]Present address: The Prince of Wales Hospital, Department of Radiation Oncology, Randwick, NSW 2031, Australia.

In the past the biokinetic parameters of trace elements in animals and man have commonly been derived from experiments involving radioactive tracers. Due to the increasing number of restrictions limiting the in vivo use of radioactive substances in both women and men there is a need for methods based upon the application of stable isotopes. The purpose of this work was to develop procedures for determining the absolute and the relative content of tellurium in body fluids, specifically in the blood plasma, which constitutes the major transfer compartment in the organism.

Investigations on the plasma clearance and retention merely require a measurement of the total amount of tellurium in a known quantity of plasma. Atomic absorption spectrometry (AAS) appears to be the method of choice for this purpose. Background problems would not be expected to be critical since the natural concentration of tellurium in blood is rather low (*6*). In order to determine the fractional intestinal absorption it is necessary to distinguish the administered tracer from another tracer applied via the intravenous route. The desired information can be derived by using a double-isotope technique, provided suitable isotopes are available. The concentration ratio of the employed isotopes may generally be measured by mass spectrometric means or, in favorable cases, by activation analysis. In this work we have explored the use of secondary ion mass spectrometry (SIMS). On the basis of the experience recently gained from studies on iron in blood (*7*, *8*), we had to expect that chemical processing of the blood samples would be required prior to a meaningful SIMS analysis.

EXPERIMENTAL SECTION

γ Ray Spectrometry. The radioisotopes ^{121m}Te and ^{123m}Te employed in this work were prepared at the research reactor Geesthacht, Germany, by neutron activation of the enriched stable isotopes ^{120}Te and ^{122}Te (purchased from AERE, Harwell, U.K.). The half-times $t_{1/2}$ and the major γ energies E_γ are as follows: ^{121m}Te $t_{1/2}$ = 154 days, E_γ = 212 keV; ^{123m}Te $t_{1/2}$ = 119.7 days, E_γ = 159 keV. The activity in the administered solution as well as in the unprocessed plasma samples was measured with a well-type sodium iodide detector (Packard Auto-Gamma scintillation spectrometer 5260 with a Canberra Series 35 multichannel analyzer) and standard data acquisition techniques.

Graphite Furnace Atomic Absorption Spectrometry (GFAAS). The tellurium content in the administered solution and in the chemically processed plasma samples was determined by using an atomic absorption spectrometer (Perkin-Elmer PE 2380) in combination with a hollow cathode lamp and graphite furnace atomization (Perkin-Elmer HGA 500). The absorption was measured at a wavelength of 214.3 nm by applying deuterium background correction in the peak height mode.

Secondary Ion Mass Spectrometry (SIMS). The concentration ratio of the enriched stable tellurium isotopes was de-

Table I. Isotopic Abundance (in Percent) of Natural Tellurium and of the Two Tracers Te(124) and Te(126)

mass no., u	natural tellurium	Te(124)	Te(126)
120	0.09	0.05	<0.03
122	2.57	0.12	<0.03
123	0.89	0.34	0.08
124	4.76	91.70	0.09
125	7.10	2.98	0.16
126	18.89	2.29	98.40
128	31.73	1.54	0.93
130	33.97	1.03	0.34

termined by SIMS. For reasons discussed in detail with reference to Figures 1–3, we used tracers enriched in ^{124}Te and ^{126}Te. These isotopes were purchased from AERE Harwell, U.K., and Medgenix, Ratingen, Germany, respectively. The isotopic abundances of the enriched tellurium tracers, as quoted by the manufacturers, are listed in Table I. The data for naturally occurring tellurium (*9*) are given for comparison.

The SIMS measurements were carried out by using the dual-beam raster scanning ion microprobe DORAMIS (named after the German term "*Do*ppelstrahl-*Ra*sterionen*mi*krosonde"). The instrument constitutes an improved version of the DIDA ion microprobe described elsewhere (*10*). The analysis chamber and the quadrupole-based secondary ion mass spectrometer of DIDA were integrated into DORAMIS without any changes. Different from the previous design, however, the new instrument features two primary ion guns that are symmetrically arranged with respect to a beam-switching and mass-selecting sector magnet (deflection angles ±30°). A thermal surface ionization source (for generating cesium ions) and a plasma source (for generating ions of permanent gases) are at the disposal of the operator. Primary ions with the desired mass-to-charge ratio can be fed into the common beam line between the magnet and the analysis chamber. An einzel lens located in this section serves to focus the beam onto a multiaperture diaphragm. This intermediate aperture acts as the object for the final lens and also defines the primary ion mass resolution.

In this work we used 8-keV primary ion beams of O_2^+, Ar^+, and Cs^+ for sputtering and, desirably, for secondary ion yield enhancement. Focused beams with a spot of about 30 μm on target were raster-scanned over an area of typically 300 μm. The impact angle was 2° to the surface normal of the target. Beam currents ranged from 20 to 300 nA. The pass energy of the secondary ion energy filter was tuned for maximum signal, i.e. for analysis and detection of ions ejected with the most probable energy. During the SIMS measurements the total pressure in the analysis chamber was typically 2×10^{-9} mbar.

Reagents. Tridistilled water (Millipore) was used throughout. The employed reagents were all analytical grade (Merck, Darmstadt, Germany). The tellurium concentration in the reagents, measured with AAS, was below the detection limit of 4 pmol/mL. Tellurium titrisol (Aldrich, Steinheim, Germany) with a tellurium concentration of 79 μmol/mL (1 mg/mL) served as one standard solution. Another standard of the same nominal concentration was prepared by dissolving 125 mg of TeO_2 (Merck) in 5 mL of concentrated HCl and diluting with water to 100 mL (*11*). According to analysis by AAS the tellurium concentrations in the two standards were the same to within 2%.

Treatment of Rabbits. Tellurium was administered to four rabbits (breed "Kleine Gelbsilber") in the form of sodium tellurate (Na_2TeO_3). The animals were anaesthetized with Urethan and kept under narcosis during the whole experiment. The body weight of the rabbits, the administered quantities of tellurium and the employed tracer isotopes are listed in Table II. Intravenous (iv) application of tellurium was carried out by using a catheter inserted in the vena formalis. Rabbit no. 1 merely received an injection of an isotonic solution containing tellurium while rabbit no. 2 incorporated sodium tellurate only per gavage (perorally, po). The other two rabbits first received tellurium intravenously and, 70 min later, a differently labeled tellurium tracer by gavage. The administered activities were typically 300 kBq (iv) and 800 kBq (po). Blood samples of about 3 mL were drawn repeatedly from the femoral arteria via another catheter

Table II. Body Weight of the Rabbits and Administered Amount of the Respective Tellurium Tracers[a]

rabbit no.	body wt, kg	amt of iv dose, μg	tracers used	amt of po dose, μg	tracers used
1	3.5	260 ± 30	^{124}Te ^{123m}Te		
2	2.7			160 ± 15	^{124}Te ^{123m}Te
3	3.7	180 ± 20	^{124}Te ^{123m}Te	2500 ± 500	^{126}Te ^{121m}Te
4	3.7	120 ± 20	^{124}Te ^{123m}Te	2800 ± 200	^{126}Te ^{121m}Te

[a] The total concentration of tellurium in the applied solution was measured by AAS. The quoted error in the po dose partly reflects the uncertainty in tellurium uptake per gavage. The total amount of radioactive tellurium in the solution is estimated to 1 ng or less.

(the amount of blood in a rabbit of this breed is typically 70 mL/kg of body weight (*12*)). Sampling was continued up to about 40 h after tracer application.

Sample Processing. The extracted blood samples were first centrifuged to separate the plasma. After measuring the γ activity, 0.5-mL aliquots of the plasma were transferred to 10-mL Teflon containers and dried therein. The GFAAS measurements were performed by using the standard addition technique. To at least one aliquot of each sample was added 10 ng of a natural isotope mixture of tellurium. In the closed Teflon vessels the samples were wet-ashed with 700 μL of concentrated HNO_3 under pressure at 135 °C (*13*). The ashing procedure was repeated if the remaining solution was not clear and slightly yellow in color. The clear solution was evaporated ($T \leq 100$ °C) and redissolved in 400 μL of concentrated HCl. In order to reduce hexavalent tellurium to the tetravalent stage, the solution was heated to 100 °C for 1 h, then evaporated, and redissolved in 600 μL of 5 M HCl. Solvation was assisted by moderate heating ($T < 50$ °C) in an ultrasonic bath. The properly dissolved sample was transferred to a 1-mL polypropylene test tube and 150 μL of methyl isobutyl ketone (MIBK) was added. MIBK is known to extract tetravalent tellurium from a hydrochloric solution (*14*). After shaking for 2 min the tubes were centrifuged. Aliquots of 20 μL of MIBK were directly transferred to the graphite furnace of the atomic absorption spectrometer for a determination of the tellurium content.

Sample preparation for SIMS analysis proceeded along the same lines as for the GFAAS measurements up to the point at which tellurium was extracted with MIBK. Natural tellurium was not added. After shaking and centrifugation the MIBK was separated and transferred to another test tube. The tellurium was reextracted from the organic solvent with 150 μL of tridistilled water. MIBK was taken off, and the water was evaporated. The residue was dissolved in 50 μL of KOH, 0.5 M.

Using a micropipet, aliquots of 10 μL (1–3 μL for human blood plasma) were deposited in units of 2 μL (1 μL) on high-purity graphite backings and dried (Spectral purity graphite disks, diameter 12.5 mm, thickness 1 mm, Ringsdorff, Bonn-Bad Godesberg, Germany. As in previous work (*7, 8*) this material was found to be particularly suited as a backing for SIMS analysis because the signals due to surface and bulk contaminations were rather low compared to other nominally pure backing materials). The residue on the graphite disks was brownish-red and between 2 and 4 mm in diameter. Prior to sample deposition the graphite disks were "conditioned" with KOH by dropping 1 μL of a 1 M lye onto the backing. A total of 19 graphite disks were mounted on an aluminum sample caroussel and stored in a Teflon box. SIMS analysis was carried out at GSF, Neuherberg, several days (sometimes weeks) after sample preparation in Frankfurt.

Optimization of Sample Preparation for SIMS Analysis. The technique described above for processing the blood plasma prior to SIMS analysis was the result of an elaborate optimization procedure. Tellurium is known to exhibit a very low yield of positively charged secondary ions but a rather high yield of negatively charged ions (*15*). This observation is closely related to the fact that tellurium features a high ionization potential (9.01 eV), which results in a small degree of ionization, and a rather

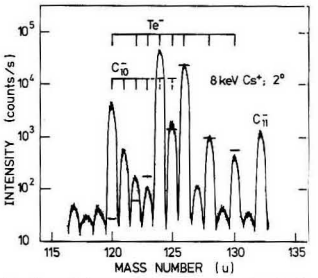

Figure 1. Section of the mass spectrum of chemically processed human blood plasma deposited on a graphite backing, bombarded with a defocused cesium beam at near-normal incidence (2° off normal, beam diameter 300 μm, beam current 50 nA). The deposited sample contained the two enriched tracers Te(124), 20 ng, and Te(126), 10 ng. The horizontal bars indicate the normalized Te^- intensities expect from the isotopic abundances listed in Table I (reference signal $^{124}Te^-$).

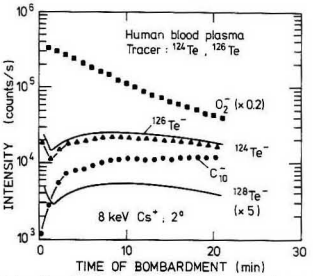

Figure 2. Intensity of selected secondary ion species emitted from a sample of chemically processed human blood plasma as a function of the time of bombardment with a raster scanned cesium beam (raster area 300 μm^2, beam current 20 nA). Tracer content of the sample: 5 ng of both Te(124) and Te(126).

high electron affinity (1.97 eV), which favors electron attachment. In agreement with previous work (*15*) we found that negative tellurium ions provide a much higher sensitivity than positive ions. It has also been known that in order to maximize the degree of ionization in the negative SIMS mode, the sample surface should be covered by a submonolayer of an alkali metal like cesium (*16, 17*). Deposition of alkali metals has the desirable effect of lowering the work function of the substrate. The yield of negative secondary ions can also be enhanced by several orders of magnitude if primary ions of cesium are used for sputter erosion of the sample (*18, 19*).

On the basis of these findings, we have also performed SIMS analysis under cesium bombardment. In the course of the initial test measurements it turned out, however, that with "good" samples, i.e. samples yielding high SIMS signals of Te^-, the use of Cs^+ beams was often not mandatory. In fact, whenever sample preparation involved the use of KOH, the yields of negative secondary ions were often rather high even with primary ions of Ar^+ or O_2^+. Only in very few cases the results obtained by using Cs^+ bombardment were superior to those obtained with the other two primary ion species. The reason for the somewhat erratic sample quality could not be identified. Apparently, the simple work function model of negative ion yield enhancement is not directly applicable to the situation encountered with the samples of chemically processed blood plasma. It is conceivable that tellurium and alkali-metal atoms like potassium or cesium form a compound with a strong ionic bond. This ionic compound may then act as a site for strong emission of positive alkali ions and negative tellurium ions, a process which is commonly termed "bond breaking" (*20*). Alternatively, one could argue that, under the "dynamic" bombardment conditions employed in this work, potassium can migrate to the instantaneous surface where it generates the desired lowering of the work function. More work will be necessary to clarify the mechanism of negative secondary ion yield enhancement due the deposition of alkali-metal compounds.

Mass Spectrum and Analysis of Tracer Composition. In order to achieve the best possible SIMS data with the processed plasma samples, the measurements to be discussed now were all obtained with primary ions of cesium. Quantitative aspects of tellurium analysis were explored with samples to which known quantities of isotopically enriched tellurium were added. Figure 1 shows a section of the mass spectrum of a sample that was prepared from human blood plasma. The total amount of tellurium in the two enriched stable tracers Te(124) and Te(126), which were contained in the sample material on the graphite backings, was 10 and 5 ng, respectively. Since the sample was spread out over an area of about 10 mm^2, only about 100 and 50 pg, respectively, of tracer material were contained within the area hit by the probing beam ($\approx$0.1 mm^2).

The major peaks in the mass spectrum of Figure 1 are easily identified as the tellurium isotopes and molecular ions of carbon, i.e. C_{10}^- and C_{11}^-, the latter originating from the graphite backing. Since natural carbon is composed of the two isotopes ^{12}C (isotopic abundance β_{12} = 98.89%) and ^{13}C (β_{13} = 1.11%), the spectrum due to C_{10}^- will extend from mass number 120 to 130 units (u), with relative intensities according to permutation statistics. For example, the relative intensity $R(121/120) = I(121)/I(120) = 10\beta_{13}/\beta_{12} = 11.2\%$, in reasonable agreement with the results of Figure 1. Even the intensity of C_{10}^- at mass number 122 u is not negligible. ^{122}Te would thus not be very well suited for tracer studies involving a graphite backing. At mass number 123 u and beyond, however, the C_{10}^- signals become so small that they can be ignored in evaluating the isotopic composition of tellurium in the sample. If we ratio the measured intensities at mass numbers between 120 and 130 u to the intensity of $^{124}Te^-$ we expect the signal heights denoted in Figure 1 by horizontal bars. These estimates are based upon the assumption that the quoted abundances in the tracer materials are correct (see Table I). Very good agreement between expected and measured intensities is evident at mass numbers 126 and 128 u, whereas deviations in either direction are seen at mass numbers 123 (−60%), 125 (+30%), and 130 u (−25%). Since the background signals at mass numbers 117–119, 127, 129, and 131 u are rather small, we attribute the observed discrepancies to a deviation of the quoted isotopic abundance in the tracer materials from the true value. Fortunately, this deviation is not of great concern here because the tracer studies reported below relate only to the isotopes ^{124}Te and ^{126}Te. Therefore, we have not investigated the observed discrepancy any further. Generally, it appears advisable, however, to check the composition of commercially available enriched stable tracer materials by an independent test.

Time Dependence of SIMS Signals and Background Problems. An important aspect in the SIMS measurements is the time dependence of the secondary ion signals. As an example Figure 2 shows the intensity of C_{10}^-, O_2^-, $^{124}Te^-$, $^{126}Te^-$, and, presumably, $^{128}Te^-$ versus the time of bombardment with cesium. The sample was prepared from 1 mL of human blood plasma to which 500 ng of each of the two tracer materials was added prior to chemical processing. Only 1% of the final sample material was deposited on the graphite backing.

Whereas the effect of cesium implantation on the degree of ionization is quite pronounced for C_{10}^- (10-fold increase in ion yield), only a relativel small yield enhancement is evident for the Te isotopes (as already mentioned above). The same statement holds true for O_2^-. As is the case of the spectrum shown in Figure 1, the data in Figure 2 suggest that the area probed by the primary ion beam is not completely covered with the chemically processed sample material. Therefore, the observed time dependence of the different signals cannot be interpreted readily.

Even though all signals in Figure 2 vary with the time of bombardment, the intensity ratio $R(126/124)$ is constant within statistical uncertainty and agrees well with the number calculated from the applied 1:1 ratio of employed two-tracer materials, $R(126/124) = (98.40 + 2.29)/(91.70 + 0.09) = 1.10$ (see Table I). By contrast, $R(128/124)$ varies with time of bombardment, from 0.047 to 0.054, and is significantly larger than the expected ratio of 0.027. Apparently, the $^{128}Te^-$ signal is superimposed by an

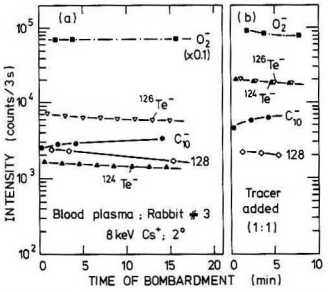

Figure 3. (a) Same as Figure 2, but for a sample of chemically processed blood plasma of a rabbit. (b) Same sample material as in (a), but after adding about 10 ng of the isotopes ^{124}Te and ^{126}Te in a 1:1 ratio.

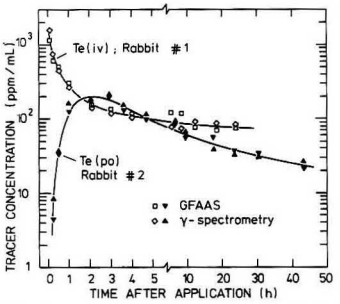

Figure 4. Time dependence of the tellurium concentration in the blood plasma of two rabbits as measured by GFAAS and γ ray spectrometry. Rabbit no. 1 received tellurium intravenously (iv), rabbit no. 2 by gavage, i.e. perorally (po).

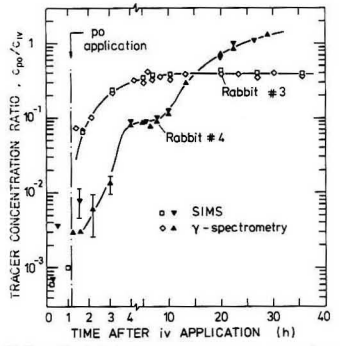

Figure 5. Ratio of the tellurium concentrations, c_{po}/c_{iv}, after oral (c_{po}) and intravenous (c_{iv}) application, measured in the blood plasma of two rabbits by SIMS and γ ray spectrometry. The vertical arrow indicates the time of peroral (po) tellurium application.

unknown background signal of the same magnitude. If such background signals were also present at mass numbers 124 and 126 u, this would determine the detection limit for the employed conditions of sample preparation. Data analysis suggests that about 10 ng of the two isotopes contained in 1 mL of plasma should be clearly detectable.

Results on the time dependence of secondary ion intensities, observed with a sample from a tracer experiment on rabbit no. 3 are shown in Figure 3. Panel a relates to a plasma sample drawn 35.5 h after intravenous application of tracer Te(124), and panel b to another portion of the same plasma sample, but after adding 58.6 ng of Te(124) and 52 ng of Te(126) with the aim of assessing the amount of tracer material in the sample of panel a. The stability of the Te^- signals is seen to be even better than in Figure 2. In contrast to the results of Figure 2, a yield enhancement effect is barely detectable in Figure 3, even with C_{10}^-. Apparently, a large fraction of the area hit by the cesium beam was covered with sample material of a composition that already favored negative secondary ion emission. For this kind of samples, bombardment with cesium was not mandatory.

The intensity ratio $R(126/124)$ in Figure 3b is in very good agreement with the 126/124 isotope ratio in the added tracers, i.e. 1.0. This finding implies that the amount of tracer material in the sample of panel a did not exceed a few percent of the added quantities. A more precise estimate is not possible with this approach since the absolute intensities of Te^- differed from sample to sample, sometimes by more than a factor of 10. Note, however, that by adding a sufficiently large amount of merely one tracer one can produce an internal standard. Thus it would be possible to determine not only the ratio but also the absolute value of the tracer concentrations in the sample by SIMS alone. In this exploratory study, however, we have relied on GFAAS for determining absolute concentrations.

RESULTS AND DISCUSSION

Prior to tracer application the tellurium concentration in the plasma of the rabbits was below the detection limit of GFAAS, which was found to be 1 ng/mL of plasma. Due to the absence of a detectable background signal, the tellurium signal measured by GFAAS is directly proportional to the tellurium concentration. Figure 4 shows the tellurium concentration in the plasma of two rabbits (labeled no. 1 and no. 2) as a function of the time after tracer application. The two rabbits received tellurium only via one route. The data are presented in normalized form, i.e. as the fraction of the administered dose per milliliter of plasma.

It is evident from Figure 4 that the agreement between the results obtained by GFAAS and γ ray spectrometry is quite satisfactory. The data for each rabbit may be described by a common time dependence, represented by full lines. The individual data points deviate from these curves by no more than ±25%. This number is very similar to the accuracy of the GFAAS measurements.

To first order the decay of the tracer concentration $c_{Te,iv}(t)$ after intravenous application may be described by a function of the form

$$c_{Te,iv}(t) = c_1 \exp(-t/\tau_1) + c_2 \exp(-t/\tau_2) \qquad (1)$$

where τ_1 and τ_2 are characteristic time constants of the plasma clearance. The decay function was fitted to the experimental data by means of a least-squares procedure employing the SAAM-27 program developed for compartmental analysis (*21*). The data from both the GFAAS and the γ spectrometry measurements were taken into account in the fitting routine. The results were as follows: $c_1 = (1160 \pm 360)$ ppm/mL, $\tau_1 = (0.65 \pm 0.05)$ h, $c_2 = (110 \pm 45)$ ppm/mL, and $\tau_2 = (70 \pm 20)$ h.

In a kinetic analysis of the po data one has to take into account both uptake and loss terms (*22*)

$$c_{Te,po}(t) = c_a - c_u \exp(-t/\tau_u) + c_l \exp(-t/\tau_l) \qquad (2)$$

The following characteristic parameters were derived by least-squares fitting: $c_a = (27 \pm 3)$ ppm/mL, $c_u = (240 \pm 20)$ ppm/mL, $\tau_u = (1.6 \pm 0.2)$ h, $c_l = (215 \pm 25)$ ppm/mL, and $\tau_l = (6.3 \pm 1.0)$ h. A detailed discussion of the derived biokinetic parameters is beyond the scope of the present paper. The main purpose here is to demonstrate that the quality of the results derived from tracer studies involving stable isotopes is good enough for determining such parameters.

Rabbits no. 3 and no. 4 received tellurium intravenously (iv) at time $t = 0$ and, 70 min later, another differently labeled

tellurium fraction by gavage (po). Figure 5 shows the ratio, c_{po}/c_{iv}, of the normalized tellurium concentrations as a function of the time after iv application. As in Figure 4 the agreement between the results derived from measurements involving stable and radioactive isotopes is rather good, except for the very lowest concentrations where the uncertainty is on the same order as the absolute value of the concentration ratio.

About 5 h after peroral application of tellurium to rabbit no. 3 the concentration ratio has reached a constant level, c_{po}/c_{iv}(SIMS) = 0.40 ± 0.03 and c_{po}/c_{iv}(γ ray spectrometry) = 0.39 ± 0.04. The constant ratio implies that after this time interval a common metabolism is present for the orally and intravenously administered tracers. For this rabbit the fractional intestinal absorption of tellurium from sodium tellurate thus amounts to about 40%. Similarly, about 4 h after peroral application a constant ratio c_{po}/c_{iv} was derived from the data for rabbit no. 4. The increase in c_{po}/c_{iv} observed after about 8 h was due to a complete occlusion of the intestine in the continuously anaesthetized animal. It is completely artificial and has no physiological meaning. In the present context the data are nevertheless useful, since they substantiate the agreement between the SIMS and γ spectrometry data. Furthermore the results for rabbit no. 4 demonstrate that with the described procedure tracer concentration ratios can be measured over 2 orders of magnitude.

CONCLUSION

The results of this study provide safe evidence that tracers of stable tellurium isotopes can be used for performing biokinetic studies on animals as well as on man. GFAAS is very useful whenever information about the total concentration of tracer material in the body fluid is needed. Such experiments do not even require enriched isotopes, but the background may be a problem if the element of interest is already present in the body. Much more complete biokinetic information can be derived with a mass spectrometric technique like SIMS. As pointed out above, it is possible, with full use of the double-tracer technique, to determine both the absolute values as well as the ratio of the concentration of tracers incorporated via different routes. With elements like tellurium analysis and detection of negative secondary ions appears to be mandatory.

The present study has again shown that chemical processing of the body fluid and details of the sample deposition technique are very crucial. As in previous work (*6*, *7*) the quality of the SIMS data described here might have been adversely affected by the need for transporting the samples from Frankfurt to Neuherberg, as well as by the sometimes long storage in air (up to 4 weeks). It is very likely that much improved data (higher secondary ion intensities, less background) could be achieved if SIMS analysis would be carried out immediately following the completion of sample preparation. Note also that the samples were deposited on the graphite backing by the simple droplet technique. It is conceivable that other techniques like spin casting (*23*) or electrospraying (*24*) will result in improved sample quality as well as in less variation from sample to sample.

Irrespective of these potential improvements one can state that stable isotopes may be used to study the metabolism of tellurium on human volunteers. Since, from the point of view of occupational medicine, there is a need for the knowledge of biokinetic parameters of toxic substances like tellurium, the techniques described here may very well serve to provide the required data.

LITERATURE CITED

(1) Einbrodt, H. J.; Michels, S. In *Metalle in der Umwelt*; Merian, E., Ed.; Verlag Chemie: Weinheim, 1984; pp 561–569.
(2) Sredni, B.; Caspi, R. R.; Klein, A.; Kalechman, Y.; Danziger, Y.; Ben-Ya'akov, M.; Tamari, T.; Shalit, F.; Albeck, M. *Nature* **1987**, *330*, 173–176.
(3) Nyska, A.; Waner, T.; Pirak, M.; Albock, M.; Sredni, B. *Arch. Toxicol.* **1988**, *63*, 386–393.
(4) *International Commission on Radiological Protection Evaluation of Radiation Doses to Body Tissue from Internal Contamination due to Occupational Exposure*; ICRP Publication 10; Pergamon Press: Oxford, U.K., 1969; pp 74–84.
(5) Coughtrey, P. C.; Jackson, D.; Thorne, M. *Radionuclide Distribution and Transport in Terrestrial and Aquatic Ecosystems*; Balkema: Rotterdam, The Netherlands, 1983.
(6) Kron, T.; Hansen, Ch.; Werner, E. In *Trace Element Analytical Chemistry in Medicine and Biology*; Brätter, P., Schramel, P., Eds.; Walter de Gruyter & Co.: Berlin, New York, 1988; pp 412–417.
(7) Hansen, Ch.; Wittmaack, K.; Roth, P.; Werner, E. In *Trace Element Analytical Chemistry in Medicine and Biology*; Brätter, P., Schramel, P., Eds.; Walter de Gruyter & Co: Berlin, New York, 1983; Vol. 2, pp 849–857.
(8) Wittmaack, K.; Hansen, Ch.; Werner, E. *Nucl. Instrum. Methods* **1986**, *B15*, 222–225.
(9) Weast, R. C.; Lide, D. R.; Astle, M. J.; Beyer, W. H. *CRC Handbook of Chemistry and Physics*, 70th ed.; CRC Press: Boca Raton, FL, 1989.
(10) Wittmaack, K. *Vacuum* **1982**, *32*, 65–89.
(11) Kamada, T.; Sugita, N.; Yamamoto, Y. *Talanta* **1979**, *26*, 337–340.
(12) Altman, P. L. In *Blood and Other Body Fluids*; Dittmer, D. S., Ed.; Federal American Society of Experimental Biology: Washington, DC, 1961.
(13) Kotz, L.; Kaiser, G.; Tschöpel, P.; Tölg, G. Z. *Anal. Chem.* **1972**, *260*, 207–209.
(14) Havezov, I.; Jordanov, N. *Talanta* **1974**, *21*, 1013–1023.
(15) Storms, H. A.; Brown, K. F.; Stein, J. D. *Anal. Chem.* **1977**, *49*, 2023–2030.
(16) Yu, M. L. *Phys. Rev. Lett.* **1978**, *40*, 574–577; *Phys. Rev.* **1982**, *B26*, 4731–4734.
(17) Bernheim, M.; Le Bourse, F. *Nucl. Instrum. Methods* **1988**, *B27*, 94–103.
(18) Andersen, C. A. *Int. J. Mass Spectrom. Ion Phys.* **1970**, *3*, 413–428.
(19) Wittmaack, K. *Surf. Sci.* **1983**, *126*, 573–580.
(20) Yu, M. L.; Mann, K. *Phys. Rev. Lett.* **1986**, *57*, 1476–1479. Yu, M. L. *Nucl. Instrum. Methods* **1987**, *B18*, 542–548.
(21) Foster, D. M.; Boston, R. C. In *Compartmental Distribution of Radiotracers*; Robertson, J. S., Ed.; CRC Press: Boca Raton, FL, 1983; pp 73–142.
(22) Marshall, D. H.; Nordin, B. E. C. *Nature* **1969**, *222*, 797.
(23) Säve, G.; Håkansson, P.; Sundqvist, B. U. R. Jönsson, U.; Olofsson, G.; Malmquist, M. *Anal. Chem.* **1987**, *59*, 2059–2063.
(24) McNeal, C. J.; Macfarlane, R. D.; Thurston, E. L. *Anal. Chem.* **1979**, *51*, 2036–2039.

RECEIVED for review March 13, 1991. Accepted July 11, 1991.

Adsorption Isotherm and Overloaded Elution Profiles of Phenyldodecane on Porous Carbon in Liquid Chromatography

Moustapha Diack and Georges Guiochon*

Department of Chemistry, University of Tennessee, Knoxville, Tennessee 37996-1501, and Division of Analytical Chemistry, Oak Ridge National Laboratory, Oak Ridge, Tennessee 37831-6120

The adsorption isotherm of phenyldodecane from acetonitrile solutions onto porous carbon has been measured at 50 °C, by frontal analysis. This isotherm exhibits two inflexion points. It can be accounted for by the sum of a quadratic and a Langmuir term. The Langmuir term accounts for adsorption at very low surface coverages and could be explained by selective adsorption of the alkyl chains on surface defects. The quadratic term accounts for the adsorbate–adsorbate interactions involving the alkyl groups at moderate degrees of surface coverage. The semiequilibrium model of chromatography permits the calculation of the profiles of high concentration bands when the equilibrium isotherm is known. The model is applied successfully here to the computation of the profiles of bands of increasingly large samples of phenyldodecane. In spite of the complexity of the profiles observed with this sigmoidal isotherm, satisfactory agreement is observed between the experimental profiles and those predicted by theory.

INTRODUCTION

There is a close relationship between the equilibrium isotherm of a compound in a chromatographic system and the elution profile of its high concentration bands on the corresponding column (*1–3*). The theory of nonlinear chromatography permits the calculation of these profiles if the mass-transfer kinetics and the kinetics of adsorption–desorption are fast enough and the column efficiency exceeds a few hundred theoretical plates (*4*). Numerous systematic investigations have demonstrated an excellent agreement between the experimental band profiles and the profiles calculated from the equilibrium isotherms (*5–8*). In all cases reported, however, the isotherms were convex upward. The aim of the present paper is to examine the more complex problem of an isotherm exhibiting inflexion points. In this case, theory predicts that shock layers or quasi-discontinuities of the eluent concentration will take place simultaneously on the front and the rear parts of the band profile (*3*).

We know that the behavior of long-chain normal alkanes and alkyl derivatives on hydrophobic carbon adsorbents is peculiar (*9*). In gas–solid chromatography and in other adsorption studies, adsorbate–adsorbate interactions involving the alkyl chains are observed to take place at moderate concentrations. Thus, the adsorption energy of a second molecule is higher than that of the first one (*9*). The equilibrium isotherms are convex downward at the origin and belong to either class V or class III (*9, 10*). It was expected that in liquid–solid equilibria as well, the equilibrium isotherms of long-chain alkyl derivatives would be convex downward at the origin, contrary to what is observed for more bulky molecules for which the energy of the adsorbate–adsorbate interactions is weak compared to the adsorption energy. Since no phenomenon analogous to capillary condensation can take place in liquid–solid equilibria, the isotherm should be of class V.

Graphitized carbon black has been widely and successfully used in gas–solid chromatography (*9, 11*). Unfortunately, the very small carbon particles are loosely bound by van der Waals interactions and form agglomerates with very poor mechanical stability that cannot be used to pack columns for liquid chromatography (*12*). Knox et al. have prepared spherical particles of porous graphitized carbon which are made of porous two-dimensional graphite (*13*). These particles have the proper mechanical stability, specific surface area and porosity for use as a stationary phase in liquid chromatography. We have decided to study the equilibrium isotherm and the elution band profiles of phenyldodecane on this carbon material.

THEORY

I. Isotherm Models. The simplest isotherm model used in adsorption studies is the Langmuir isotherm (*14*):

$$\theta = \frac{q}{q_s} = \frac{bC}{1 + bC} \tag{1}$$

In this equation, θ is the surface coverage, q_s is the specific saturation capacity of the adsorbent, and b is a numerical coefficient. The Langmuir isotherm assumes that the solution is ideal, that the adsorbate forms a monolayer which is ideal, that there are no adsorbate–adsorbate interactions in this monolayer, and that the adsorption is localized. These conditions are usually not met in practice. In many cases, however, and at low to moderate concentrations, the Langmuir isotherm remains a satisfactory empirical model for fitting adsorption data (*15*).

Simple statistical thermodynamics suggests a model of adsorption that is the ratio of two related polynomials of the same degree (*16*). The Langmuir isotherm (eq 1) is the simplest, first-order such model (*14*). The second-order model is the quadratic isotherm:

$$\theta = \frac{q}{q_s} = \frac{C(b_1 + 2b_2C)}{1 + b_1C + b_2C^2} \tag{2}$$

In this equation, b_1 and b_2 are numercial coefficients and q_s is the specific saturation capacity of the adsorbent. However, in the corresponding model, there are two molecules adsorbed per site in the saturated monolayer. For this reason, the limit of θ for infinitely large values of C is $2q_s$. While the Langmuir isotherm is always convex upward and cannot have an inflexion point, the quadratic isotherm may be used to represent isotherms with an inflexion point. Thus, this model can be used to account for adsorption either at higher degrees of surface coverage than the Langmuir model or when one of the basic assumptions of this model falters. We shall use this model to account for the adsorption data of phenyldodecane, a compound for which adsorbate–adsorbate interactions are significant.

Adsorbent surfaces are rarely homogeneous (*17*). Several different types of sites may coexist on a surface and have different adsorption behavior for a given compound (*17, 18*). In general, the adsorption on the different types of sites is

* To whom correspondence should be sent at the University of Tennessee.

0003-2700/91/0363-2608$02.50/0

not cooperative (*18*). Thus, a multiterm isotherm may be necessary to account for the equilibrium behavior observed with such surfaces, each term accounting for the adsorption on a given type of sites. For example, different authors have used a bi-Langmuir isotherm in studying adsorption on heterogeneous surfaces (*8*, *18–20*).

II. The Semiideal Model of Chromatography. The profiles of elution bands in chromatography can be derived from the study of the response of the column to an input perturbation. This is conveniently done by using the equilibrium–diffusive model (*1–4*), a model based on the integration of the differential mass balance of the compound considered in a chromatographic column, given the proper set of initial and boundary conditions. The exact balance is written as follows:

$$\frac{\partial C}{\partial t} + F\frac{\partial C_s}{\partial t} + u\frac{\partial C}{\partial x} = D_{ap}\frac{\partial^2 C}{\partial x^2} \qquad (3)$$

In this equation, C and C_s are the concentrations of the compound in the mobile and stationary phases, respectively, x and t are the length and time, respectively, F is the phase ratio ($F = (1 - \epsilon)/\epsilon$, ϵ packing porosity), u is the mobile-phase flow velocity, and D_a is the axial dispersion coefficient. D_a accounts for the axial diffusion, the tortuosity of the packing, and the eddy diffusion (*2*, *4*).

To solve eq 3, we need a relationship between C_s and C. Most chromatographic columns have a high efficiency, demonstrating that the stationary and the mobile phases are close to equilibrium. Thus, we may replace C_s in eq 3 by the equilibrium isotherm (e.g., q, as given by eq 1 or 2 or a more complex combination) and take into account the contribution of a finite rate of the mass-transfer kinetics in the column by replacing D_a by D_{ap}, the axial dispersion coefficient. D_{ap} is related to the column efficiency by

$$D_{ap} = HL/2t_0 \qquad (4)$$

It has been shown that the solutions of the equation

$$\frac{\partial C}{\partial t} + F\frac{\partial q}{\partial t} + u\frac{\partial C}{\partial x} = \frac{HL}{2t_0}\frac{\partial^2 C}{\partial x^2} \qquad (5)$$

corresponding to the injection profile (boundary condition) are the elution profiles, provided the column efficiency exceeds a few hundred theoretical plates (*4*, *21–25*).

In this work, we have used the calculation procedure based on the semiideal model, which has been previously described (*3*, *4*) and discussed (*25*).

EXPERIMENTAL SECTION

I. Equipment. The determination of the equilibrium isotherm and the acquisition of the elution profiles of large-size samples of phenyldodecane were carried out with an HP1090 liquid chromatograph (Hewlett-Packard, Palo Alto, CA), equipped with a multisolvent delivery system, an automatic sample injector with a 250-μL sample loop, a rapid UV photodiode array detector, and a computer data acquisition system.

The detector was calibrated directly, by flushing its cell with solutions of known concentrations and recording the signal.

II. Materials. *Stationary Phase.* Microcrystalline porous graphitic carbon (PGC) supplied by Professor John H. Knox (Wolfson Liquid Chromatography Unit, Department of Chemistry, University of Edinburgh, U.K.) was used as the adsorbent (*13*). The spherical particles are ca 7 μm in diameter. The packing porosity is approximately 60%; the adsorbent has a specific surface area of about 150 m^2/g, measured with nitrogen, by using the BET method (*13*, *26*).

Column Packing. The stainless steel chromatographic column (150 mm long, 4.6 mm i.d., geometrical volume 2.49 mL) was packed by using a slurry technique, slightly different from the one recommended by Knox et al. (*26*). An acetone slurry containing approximately 5% (w/w) of adsorbent was prepared and treated in an ultrasonic bath for 10 min at ambient temperature. The slurry was then pushed downward into the column by using acetone pumped under a pressure of 3000 psi. The efficiency was much better than when the column was packed at the recommended 2000 psi. After packing completion, the column was conditioned for several hours, under a stream of acetonitrile, at 50 °C before use. As a consequence of the use of a higher packing pressure, the back-pressure for a flow rate of 1 mL/min of a (90/10) mixture of methanol and water was 90–100 atm instead of 60–70 atm as reported by Knox et al. (*26*).

Column Characteristics. The column contains 1.4 g of PGC. The retention volume of deuterated water, which is less adsorbed by carbon than acetonitrile (*9*), was 1.0 mL. This value was taken as the void volume. The column efficiency (1000 theoretical plates) was determined with naphthalene ($k' = 3$).

Mobile Phase and Chemicals. All experiments were performed under isocratic conditions, using pure acetonitrile (J. T. Baker, Philipsburg, NJ). Phenyldodecane (97% grade) and acetonitrile were purchased from Aldrich (Milwaukee, WI) and used without further purification.

III. Procedures. During all the experiments, the mobile-phase flow rate (1 mL/min) and the column temperature (50 °C) were kept constant. The UV detector was set at wavelengths of either 260 or 220 nm, depending on the concentration range considered. The raw data were acquired with the HP 9133 data station, then transferred to the VAX 8700 of the University of Tennessee Computer Center for processing.

Determination of the Isotherm. Two methods were used for the determination of the equilibrium isotherms. Frontal analysis (*27*, *28*) was carried out at high concentrations, using the experimental procedure already described (*5*). At low concentrations, elution by characteristic point (ECP) was preferred (*5*, *29*).

Overloaded Elution. The elution profiles of samples of a wide range of sizes were recorded by injecting different volumes (5–180 μL) of a concentrated solution of phenyldodecane (67 mM) in pure acetonitrile. The elution profiles (concentration of phenyldodecane in the eluent versus time) were derived from the detector signal (time profile of the optical density of the eluent) by using a calibration curve of the detector in the range considered.

RESULTS AND DISCUSSION

PGC is prepared by impregnating high-porosity spherical silica gel particles with a mixture of hexamethylenetetramine and phenol, heating at 150 °C to react the mixture into phenol–formaldehyde resin within the pores of the inorganic matrix, then pyrolyzing at 900 °C under nitrogen into a compact carbon (*13*, *26*). After the silica is dissolved in a concentrated solution of sodium hydroxide, a porous glassy carbon (BET specific surface area 450–600 m^2/g) is obtained. Finally, this carbon is treated at 2500 °C and becomes porous two-dimensional carbon. The porosity is unchanged by this last treatment, but the specific surface area is reduced to ca 150 m^2/g (*13*, *26*). The adsorbent properties are similar to those of graphitized carbon black, and the surface is essentially made of the 001 graphite planes. However, the intermediate product is similar to an activated carbon; its surface is highly heterogeneous and contains mesopores arising from the silica template and micropores from the pyrolytic carbon (*26*). A large fraction of the micropores disappears during the high-temperature treatment, but the surface remains heterogeneous. The presence of micropores in the intermediate product is demonstrated by the considerable decrease in surface area observed during the high-temperature treatment; the heterogeneity of the surface of the final product is demonstrated by the poor quality of the chromatograms obtained without the use of "tailing reducers", especially for compounds with an *n*-alkyl chain (*13*). However, while we observed strong tailing with long-chain alkyl compounds, the bands of compounds with more bulky molecules were symmetrical.

When a molecule is adsorbed onto graphitized carbon, it tends to lie as flat as possible, to maximize the interaction energy between its heavy atoms (carbon, oxygen, and heteroatoms) and the flat 001 graphite planes that constitute most of the surface (*9*, *11*). Thus, the energetically favored con-

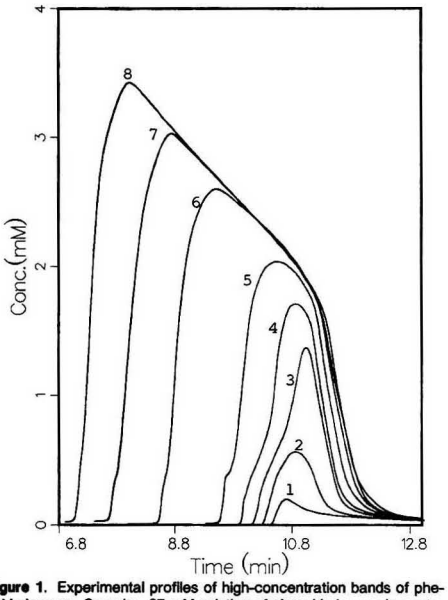

Figure 1. Experimental profiles of high-concentration bands of phenyldodecane. Sample: 67 mM solution of phenyldodecane in acetonitrile. Sample volume: (1) 5 μL; (2) 10 μL; (3) 20 μL; (4) 30 μL; (5) 50 μL; (6) 100 μL; (7) 140 μL; (8) 180 μL. Experimental conditions: column L = 15 cm, i.d. = 0.46 cm; temperature = 50 °C; mobile-phase flow rate = 1 mL/min.

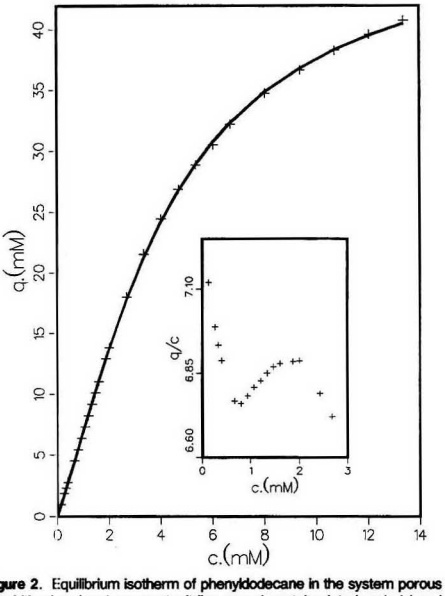

Figure 2. Equilibrium isotherm of phenyldodecane in the system porous graphitized carbon/pure acetonitrile: experimental points (symbols) and best isotherm model (solid line). The model is given in eq 4, and numerical coefficients are in Table I. Experimental conditions are the same as in Figure 1. The inset gives a plot of q/C versus C in the low-concentration range.

formation in the adsorbed state of long-chain alkyl derivatives such as phenyldodecane is the gauche conformation (*9*). Strong lateral interactions take place between these chains (*9*, *30*, *31*). Accordingly, at low values of the surface coverage ratio, the adsorption energy increases with increasing concentration. An anti-Langmuir isotherm is expected (*9*). This was the reason why we decided to study the chromatographic band profiles of phenyldodecane under nonlinear conditions. A phenyl group permits the convenient use of a UV detector, while similar studies with alkanes or fatty acid methyl esters would have required a differential refractometric detector. The results obtained are more complicated than anticipated, as shown in Figure 1, which reports the band profiles obtained with a series of samples of increasing sizes, from 82 μg to 3 mg.

Instead of the anti-Langmuir profiles expected at low sample sizes, a typical Langmuir adsorption behavior was observed when very small size samples were injected (Figure 1, profiles 1 and 2). The elution bands of 82- and 165-μg samples exhibit a steep front and a long tailing rear (the slope of the front is not as steep as usual with a Langmuir type behavior because the efficiency of the column is unusually low, only 1000 theoretical plates). When the sample size was reduced further, the retention time of the peak kept increasing with decreasing sample size, and it was not possible to record a detectable band with a Gaussian profile. This indicates that the surface of the adsorbent is highly inhomogeneous. The band profiles recorded for stilbene are symmetrical, however. Benzene is not retained and naphthalene is weakly retained but eluted with a symmetrical peak, even at very low sample sizes, which is expected for carbon. Polar compounds with bulky hydrophobic groups give Gaussian elution bands. The surface heterogeneity seems to affect essentially the long-chain normal alkyl groups.

On the contrary, the adsorption behavior observed for large-size samples was as expected (Figure 1, profiles 6–8). The equilibrium concentration at the surface increases faster than the concentration in the solution, and the isotherm exhibits a region that is convex downward. Then, as the mobile-phase concentration is increased further, the monolayer saturation is approached and the equilibrium isotherm becomes eventually convex upward. Accounting for such a complex isotherm and for the profile of the elution bands reported in Figure 1 raises a few interesting challenges.

I. Adsorption Isotherm. The adsorption isotherm of phenyldodecane was determined by using frontal analysis at high and moderate concentrations in the mobile phase and the ECP method at low concentrations. In the high-concentration range of the isotherm, the breakthrough fronts are self-sharpening and frontal analysis is easy and accurate in the classical mode, in spite of the low column efficiency. In the intermediate range (between ca. 2 and 10 mM), however, the breakthrough fronts are diffuse, confirming a reversal of the sign of the isotherm curvature. In this region of the isotherm, which is convex downward, frontal analysis can still be carried out accurately, provided the measurements are made with the rare boundaries, which are self-sharpening. Instead of the stepwise increase of the concentration, which is performed for the determination of conventional, convex upwards isotherms, the experimental procedures use a stepwise decrease of the concentration (*9*). Isotherm data points are derived from the retention times of the rear fronts obtained. At very low concentrations, ECP was found to be more accurate and certainly much easier to carry out.

The adsorption data provided by frontal analysis at mobile-phase concentrations exceeding 1.5 mM are consistent with an S-shape isotherm (Figure 2). The simplest model for such an isotherm is provided by the quadratic isotherm

Table I. Parameters of the Adsorption Isotherm Models

model 1	$q = Q_s C(b_1 + 2b_2C)/(1 + b_1C + b_2C^2)$
params	$Q_s = 24.605$ mM, $b_1 = 0.246$ mM^{-1}, $b_2 = 0.060$ mM^{-2}
model 2	$q = Q_{s,1}C(b_1 + 2b_2C)/(1 + b_1C + b_2C^2) + Q_{s,2}bC/(1 + bC)$
params	$Q_{s,1} = 24.450$ mM, $b_1 = 0.238$ mM^{-1}, $b_2 = 0.059$ mM^{-2}, $Q_{s,2} = 0.149$ mM, $b = 26.790$

(eq 3). The least-squares fit of the frontal analysis data to the quadratic isotherm model gives very good results in the high-concentration range (see parameters in Table I, first model). Satisfactory agreement was also obtained between the experimental band profiles and the profiles calculated with the semiideal model at high column loadings (see next section and Figures 3–5), although the long shallow tail exhibited by all the bands cannot be accounted for by a simple S-shaped isotherm (*3*). In the moderate and low concentration range, considerable differences were observed between the band profiles calculated with the quadratic isotherm and the experimental chromatograms that exhibit a strongly tailing rear boundary and a sharp front, a behavior typical of convex upward or of mixed isotherms.

With the ECP method applied to the rear profile of the band obtained with an 82-μg sample (smallest sample in Figure 1), the adsorption isotherm at low concentration was determined (inset in Figure 2). The experimental data exhibit a significant upward curvature, typical of a Langmuir isotherm with a small specific saturation capacity. This is in marked deviation from the prediction of the quadratic isotherm that is convex downward ("anti-Langmuir" isotherm), as shown by the inset in Figure 2. The least-squares fit of these low-concentration experimental data to a Langmuir equation gives the parameters in Table I (second model). Assuming the isotherm to be the sum of a Langmuir and a quadratic term, we can determine the coefficients of the quadratic term by correcting the experimental data at moderate and high concentrations for the Langmuir term contribution and fitting the difference to the quadratic equation. This results in minor corrections to the numerical values of the coefficients of this quadratic isotherm (Table I, second model). The global isotherm shown in Figure 2 demonstrates that it accounts much better for the experimental data at low concentrations than did the quadratic isotherm, while it is as good at high concentrations. For the sake of clarity, the inset in Figure 2 provides a plot of q/C versus C, with an expanded scale for q/C, which clearly illustrates the presence of two inflection points.

Although the surface of graphitized carbon black tends to be highly homogeneous (*9*), the surface of many carbon samples prepared by pyrolysis of organic materials is not necessarily so. The surface of the adsorbents obtained by pyrolysis of highly aromatic materials such as phenol–formaldehyde resins is heterogeneous (*9*). It includes micropores and is fragmented with numerous incomplete aromatic sheets. The surface of the porous two-dimension carbons prepared by different procedures to be used as stationary phases in liquid chromatography has micropores, other defects of the atomic arrangement, and active sites originating from differences in the reactivity of the carbon atoms in the basal or prismatic faces (*12, 32, 33*). A prolonged high-temperature treatment under an inert atmosphere is required to eliminate the micropores of these adsorbents and to rearrange the aromatic sheets into planar surfaces. This treatment was incomplete for the sample used in this work.

From the numerical coefficients of the isotherm, we derive that the specific saturation capacities of the carbon corresponding to the two isotherms are 2(24.45) = 48.9 mmol of phenyldodecane/L and 0.149 mmol/mL for the quadratic and the Langmuir terms of the isotherm, respectively. The high-energy sites remaining at the carbon surface occupy only 0.6% of the total area, which is small but still sufficient to transform the chromatographic properties of the surface and make it highly active toward alkyl groups. The column has an inner volume of 2.49 mL and was packed with 1.4 g of carbon, i.e., a packing density of 0.56 g/mL. The adsorbent has a specific surface area of approximately 150 m^2/g. Thus, the surface occupied by one molecule of phenyldodecane in the saturated monolayer would be 285 Å^2/molecule.

This value is somewhat high, approximately 3 times larger than the cross-sectional area of a phenyldodecane molecule, but the discrepancy can be explained if we assume that the micropores are too narrow to let the phenyl group enter them. The nitrogen molecules used for the determination of the surface area, as well as the alkyl groups can enter freely. Then, only one phenyldodecane molecule can enter the opening of a micropore. This mechanism may explain an important increase in the apparent surface area occupied by one molecule of adsorbate.

II. Experimental Band Profiles. The band profiles recorded for samples of increasing sizes (5–180 μL) are shown in Figure 1. These band profiles are compatible with an equilibrium isotherm following a Langmuir model at very low concentrations and having two inflexion points, as the isotherm in Figure 2. It is remarkable, however, how an apparently minor kink in this isotherm results in band profiles that are extremely different from those obtained with a classical Langmuir or quasi-Langmuir isotherm, i.e., one which is convex upward in the entire concentration range. The kink is barely visible in the main Figure 2, where the isotherm appears to be linear. It is clearly seen in the inset, which shows a plot of q/C versus C, much more sensitive to minor changes in the isotherm differential. As we know, it is the isotherm differential that controls the velocity associated with a concentration (*2–5, 23–25*). This result confirms the extreme sensitivity of the chromatographic band profiles to minor changes in the equilibrium isotherm (*3–8*).

The main features of this series of profiles are the two shock layers (*2, 4, 23, 24*), on the front and the rear of the band profiles of the large-size samples (Figure 1, profiles 5–8), the long tail of all the profiles, and the front shoulder which appears on all the profiles 3–8 but is especially noticeable on the front of the profile 5. The shock layers are not very steep because the column efficiency is poor. All features of these profiles are explained by the properties of the equilibrium isotherm. For low-size samples, the profile is Langmuirian (profile 1). It has even the long tail characterizing the bi-Langmuir isotherms. For larger size samples, the band front moves forward very slowly with increasing size, while the retention time of the band maximum increases and the band rear becomes steeper and steeper (profiles 2 and 3). A prominent shoulder is seen on the band front. Then, when the sample size is increased further, the direction of variation of the retention time changes again. For profiles 4–8, the retention time decreases with increasing sample size. The band rear remains stationary while the front becomes steep and moves toward shorter and shorter retention times.

The features of the last four experimental profiles are very similar to those predicted for compounds having isotherms with an inflexion point in several previous theoretical studies (*1, 3, 34*). Although this type of profile has been classical for a long time in gas–solid chromatography (*9*), there are few examples reported in liquid chromatography. In most cases, the anti-Langmuir profiles reported have been observed in normal-phase HPLC, when a mixture of a weak and a strong solvent is used as the mobile phase (*34, 35*). It has been shown, however, that in this case the competition between the strong solvent and the solute is intense. It results in solute band

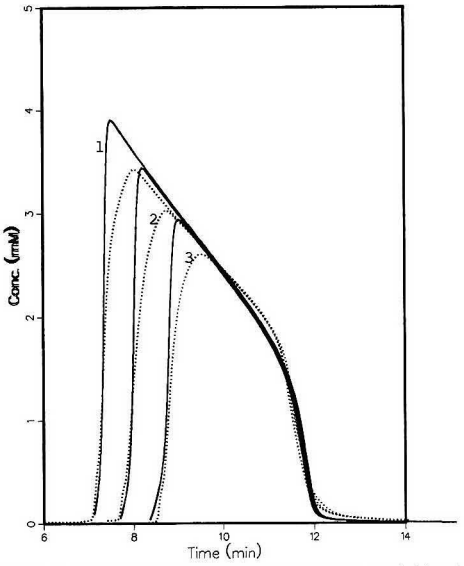

Figure 3. Comparison between experimental elution bands (dotted lines) of phenyldodecane and calculated profiles (solid lines), for different masses injected. The isotherm model is given in eq 4, and numerical coefficients are in Table I. Experimental conditions are the same as for Figure 1. Sample concentration: 67 mM. Sample volume: (curve 1) 180 μL; (curve 2) 140 μL; (curve 3) 100 μL.

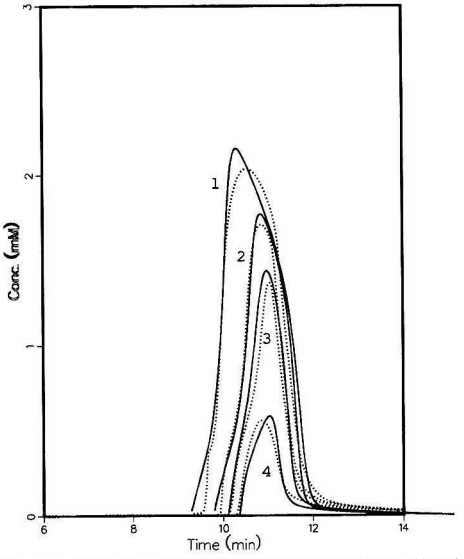

Figure 4. Comparison between experimental elution peaks (dotted lines) of phenyldodecane and the calculated profiles (solid lines), for different masses injected. Conditions are the same as for Figure 3, except sample volume: (curve 1) 50 μL; (curve 2) 30 μL; (curve 3) 20 μL.

profiles that appear like those due to an anti-Langmuir or S-shaped isotherm even when the equilibrium isotherms of both the solute and the strong solvent are Langmuirian (*36, 37*). Complex isotherms involving mixtures of strong and weak solvents have been reported in a number of cases, e.g., Souteyrand et al. (*38*), but no study of band profiles on these systems has been performed. Complex band profiles have been reported but not investigated in detail (*39*).

III. Comparison between Experimental and Predicted Band Profiles. Calculations of the band profiles corresponding to the different samples injected (Figure 1) conducted by using the simple quadratic isotherm (eq 3, coefficients in Table I) and assuming a rectangular pulse injection profile gave satisfactory results only for the three large-size profiles. Even in this case, the profiles did not exhibit the front shoulder nor the long tail but ended at 12 min. This isotherm model does not contain the Langmuir term needed to account for these two features.

In Figures 3–5, we compare the experimental chromatograms (dotted lines) recorded with a range of sample sizes (see Figure 1) and those calculated (solid lines) by using the composite isotherm (Table I, model 2). In Figure 3, we show the three largest bands recorded (sample sizes of 180, 140, and 100 μL, corresponding to amounts of 3, 2.3, and 1.6 mg of phenyldodecane, respectively) and the predicted profiles. A very good agreement is observed between the two series of curves. The most significant differences are found around the band maxima and tails. The maxima are quite lower and rounder than calculated, maybe the result of more sluggish mass transfers at high concentration than estimated by the model. The band tail is underestimated (see below).

In Figure 4, we compare the calculated and experimental profiles for three intermediate sample sizes, 0.8, 0.5, and 0.3 mg of phenyldodecane, respectively. Good agreement is observed again between the two series of band profiles. In this second series, the agreement is much better than in the previous case for the profiles around the band maximum. The deviations are observed mainly at the front (the shoulder of the calculated band is not as conspicuous as the one of the experimental profile) and the tail of the profile.

Finally, in Figure 5, we compare the experimental and calculated profiles for the smallest two sample sizes used, 82 and 165 μg, respectively. The agreement observed between experimental and calculated profiles for the tails of these two bands is only fair, however. The band tails are much longer than expected for a Langmuir isotherm. In comparing with previous results (*8*), we anticipated that an excellent agreement would be achieved when a bi-Langmuir isotherm was used. Analysis of the experimental adsorption data failed, however, to justify the use in the adsorption isotherm of a second Langmuir term to account for the strong band tail. At this stage, it seems rather that the tailing observed is due to the slow rate of desorption from the adsorption sites corresponding to the Langmuir isotherm, a conclusion which would also support the identification of these sites with micropores.

CONCLUSION

Our initial goal was to find a chromatographic system in which some compounds would exhibit equilibrium isotherms having an inflexion point, to determine these isotherms, and to compare the band profiles calculated from these isotherms with the experimental profiles at various degrees of column overloading. This goal has been successfully met. The agreement between calculated and experimental profiles is another demonstration of the validity of the current theory of nonlinear chromatography (*4*).

The results reported here demonstrate that phenyldodecane has a complex equilibrium isotherm in the system acetonitrile/graphitized carbon used in this study. This isotherm exhibits two inflexion points at low concentrations. It can be approximated by the sum of two terms, (i) a Langmuir iso-

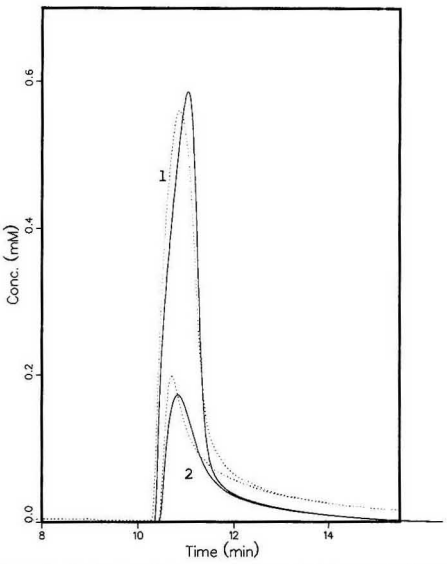

Figure 5. Comparison between experimental elution peaks (dotted lines) of phenyldodecane and the calculated profiles (solid lines), for different masses injected. Conditions are the same as for Figure 3, except sample volume: (curve 1) 10 μL; (curve 2) 5 μL.

therm with a very small specific saturation capacity, accounting for the strong initial slope and downward curvature of the isotherm at very low concentrations; and (ii) a quadratic isotherm, accounting for the more conventional S-shape observed at moderate concentrations and due to adsorbate–adsorbate interactions. The combination of the two terms provides for the reversal of the curvature sign and the second inflexion point at intermediate concentrations. This result raises several questions.

Further elucidation of the adsorption mechanism needs the determination of the enthalpy and entropy of adsorption corresponding to the Langmuir and the quadratic terms, hence the measurement of the temperature dependence of the parameters of the isotherm. It is expected that longer chain alkylbenzenes, alkylphenols, and similar compounds will give similar isotherms. Shorter chain alkyl compounds of the same series should progressively lose this feature when the chain length decreases, as the intensity of molecular interactions between alkyl chains decrease with decreasing length. This phenomenon is currently under investigation (*40*). Phenyltridecane and phenyldecane give results similar to those reported here. The adsorption isotherm of phenyloctane has no inflexion point but still cannot be accounted for by a bi-Langmuir isotherm. Gas chromatographic measurements (using a porous layer open tubular column) could give useful data regarding the adsorption behavior in the absence of competition with a solvent.

The use of short alkanes (e.g., *n*-pentane) as the mobile phase should provide effective competition to the adsorption of phenyldodecane in the micropores (*40*). It would also alter the adsorption behavior of this compound. System peaks would be observed only if the mobile phase is a mixture of acetonitrile and pentane, provided the adsorption of *n*-pentane is not insignificant compared to that of phenyldodecane (*36*, *37*).

Finally, a variety of carbon samples are available, notably materials prepared by using a more effective heat treatment (*26*). Comparison between the results of this study and those obtained with more homogeneous surfaces could provide a more complete understanding of the complex adsorption behavior of alkyl derivatives on carbon. The results of these studies currently in progress will be reported later (*40*).

ACKNOWLEDGMENT

We thank John H. Knox (Wolfson Liquid Chromatography Unit, Department of Chemistry, University of Edinburgh, U.K.) for the generous gift of a sample of microcrystalline porous graphitic carbon. We are grateful to the Hewlett-Packard Corp. for the gift of a 1090A liquid chromatograph with its data system.

Registry No. Phenyldodecane, 29986-57-0; carbon, 7440-44-0.

LITERATURE CITED

(1) Glueckauf, E. *Proc. R. Soc. (London)*, **1946**, *A186*, 35.
(2) Aris, R.; Amundson, N. R. *Mathematical Methods in Chemical Engineering*; Prentice Hall: Englewood Cliffs, NJ, 1973.
(3) Guiochon, G.; Golshan-Shirazi, S.; Jaulmes, A. *Anal. Chem.* **1988**, *60*, 1856.
(4) Golshan-Shirazi, S.; Guiochon, G. *J. Chromatogr.* **1990**, *506*, 495.
(5) Golshan-Shirazi, S.; Ghodbane, S.; Guiochon, G. *Anal. Chem.* **1988**, *60*, 2630.
(6) Golshan-Shirazi, S.; Guiochon, G. *Anal. Chem.* **1988**, *60*, 2634.
(7) Katti, A. M.; Guiochon, G. *J. Chromatogr.* **1989**, *461*, 1.
(8) Jacobson, S.; Golshan-Shirazi, S.; Guiochon, G. *J. Am. Chem. Soc.* **1990**, *112*, 6492.
(9) Kiselev, A. V.; Yashin, I. A. *Gas Solid Chromatography*; Plenum Press: New York, 1970.
(10) Brunauer, S.; Emmett, P. H.; Teller, E. *J. Am. Chem. Soc.* **1938**, *60*, 309.
(11) Vidal-Madjar, C.; Guiochon, G. In *Separation and Purification Methods*; Perry, E. S., Van Oss, C. J., Eds.; M. Dekker: New York, 1973; Vol. 2, p 1.
(12) Colin, H.; Guiochon, G. *J. Chromatogr.* **1977**, *137*, 19.
(13) Gilbert, M. T.; Knox, J. H. *Chromatographia* **1982**, *16*, 138.
(14) Langmuir, I. *J. Am. Chem. Soc.* **1916**, *38*, 2221.
(15) Ruthven, D. M. *Principles of Adsorption and Adsorption Processes*; Wiley: New York, 1984.
(16) Hill, T. L. *Introduction to Statistical Thermodynamics*; Addison-Wesley: Reading, MA, 1960.
(17) Jaroniec, M.; Madey, R. *Physical Adsorption on Heterogeneous Solids*; Elsevier: Amsterdam, 1988.
(18) Andrade, J. D. In *Surface and Interfacial Aspects of Biomedical Polymers*; Andrade, J. D., Ed.; Plenum Press: New York, 1985; Vol. 2, p 35.
(19) Graham, D. *J. Phys. Chem.* **1953**, *57*, 665.
(20) Laub, R. J. *ACS Symp. Ser.* **1986**, *297*, 1.
(21) Giddings, J. C. *Dynamics of Chromatography*; M. Dekker: New York, 1965.
(22) Haarhoff, P. C.; Van der Linde, H. J. *Anal. Chem.* **1966**, *38*, 573.
(23) Rouchon, P.; Schonauer, M.; Valentin, P.; Guiochon, G. *Sep. Sci. Technol.* **1987**, *22*, 1793.
(24) Lin, B.; Ma, Z.; Golshan-Shirazi, S.; Guiochon, G. *J. Chromatogr.* **1990**, *500*, 185.
(25) Czok, M.; Guiochon, G. *Anal. Chem.* **1990**, *62*, 189.
(26) Knox, J. H.; Kaur, B.; Millward, G. R. *J. Chromatogr.* **1986**, *352*, 3.
(27) James, D. H.; Phillips, C. S. G. *J. Chem. Soc.* **1954**, 1066.
(28) Schay, G.; Szekely, G. *Acta Chim. Hung.* **1954**, *5*, 167.
(29) Cremer, E.; Huber, J. F. K. *Angew. Chem.* **1961**, *73*, 461.
(30) Vidal-Madjar, C.; Gonnord, M. F.; Guiochon, G. In *Advances in Chromatography*; Giddings, J. C., Grushka, E., Eds.; M. Dekker: New York, 1975; Vol. 13, p 177.
(31) Vidal-Madjar, C.; Gonnord, M. F.; Goedert, M.; Guiochon, G. *J. Phys. Chem.* **1974**, *79*, 732.
(32) Lahaye, J.; Ehrburger, P. *Pure Appl. Chem.* **1963**, *61*, 1853.
(33) Golkiewicz, W.; Verkhoven-Goevie, C. E.; Brinkman, U. A. T.; Frei, R. W.; Colin, H.; Guiochon, G. *J. Chromatogr. Sci.* **1983**, *21*, 27.
(34) Svoboda, V. *J. Chromatogr.* **1990**, *518*, 177.
(35) Puncocharova, J.; Kriz, L.; Vodicka, L.; Prusova, D. *J. Chromatogr.* **1980**, *191*, 81.
(36) Golshan-Shirazi, S.; Guiochon, G. *J. Chromatogr.* **1989**, *479*, 1.
(37) Golshan-Shirazi, S.; Guiochon, G. *J. Chromatogr.* **1989**, *479*, 19.
(38) Souteyrand, C.; Thibert, M.; Caude, M.; Rosset, R. *J. Chromatogr.* **1983**, *262*, 1.
(39) Kirkland, J. J. *J. Chromatogr.* **1973**, *83*, 149.
(40) Diack, M.; Guiochon, G. Unpublished work.

RECEIVED for review April 25, 1991. Accepted July 9, 1991. This work was supported in part by Grant CHE-8901382 from the National Science Foundation and by the cooperative agreement between the University of Tennessee and the Oak Ridge National Laboratory. We acknowledge support of our computational effort by the University of Tennessee Computing Center.

Coriolis-Induced Secondary Flow in Sedimentation Field-Flow Fractionation

Mark R. Schure*

Computer Applications Research, Rohm and Haas Company, 727 Norristown Road, Spring House, Pennsylvania 19477

Sisira K. Weeratunga

Numerical Aerodynamics Simulation Group, NASA/Ames Research Center, T045-1, Moffet Field, California 94035

In an attempt to examine the effect of smaller channel breadth in sedimentation field-flow fractionation channels, computer simulations of zone profiles are reported which utilize the complete fully developed flow field obtained from Navier–Stokes calculations. The flow field displays Coriolis-induced secondary flow which results when a moving fluid is rotated regardless of the radius of curvature of the channel. By inclusion of secondary flow in the simulation, it is suggested that channel breadths smaller than those used in commercial fractionators will lead to zone leakage; i.e. a small concentration of particles will be found between the void peak and retained peak. Simulation demonstrates that when channel rotation is in the same direction as flow, zone leakage is enhanced compared with the case where flow and rotation are in opposing directions. To reduce zone dilution, which is found to be linear in channel breadth, it is recommended that channel thickness be reduced because of its $^3/_2$ power dependence on the dilution factor. Smaller channel thickness also allows the channel breadth to be reduced because of the reduction in secondary flow. Considerations of flow in a circular channel are also given to explain why circular channels fail to perform adequately in sedimentation FFF.

INTRODUCTION

Sedimentation field-flow fractionation, one of the most powerful subtechniques of the field-flow fractionation (FFF) method of separation, performs both separation and quantitation of particles and other colloidal-based substances (*1*, *2*). Sedimentation FFF is particularly suited for separation in the particle diameter range 0.05–1.0 μm when the normal FFF mode (*1*, *2*) of operation is used; this diameter range may be extended beyond 50 μm by using the steric mode of operation (*1–4*). Quantitation of particle sizes using the normal mode of sedimentation FFF operation has been the subject of a recent publication (*5*).

The sedimentation field used in sedimentation FFF is produced by rotating a channel most commonly formed from two concentric strips of metal or plastic and separated by a spacer system (*6–8*). These strips are assembled together so as to allow a curved rectangular duct to be formed between them. This duct is typically 254 μm in thickness and 2 cm in breadth and has a radius of curvature between 7 and 16 cm. Alternatively, one of the concentric rings may be milled to form the channel. The channel is shown in Figure 1 along with the coordinate system and terminology commonly used in the sedimentation FFF literature.

The first sedimentation FFF fractionators differed from the present day design in many respects. For instance, the apparatus of Berg and Purcell (*9*) utilized the annular space between two concentric rotating cylinders. Particles were sedimented radially and flow was introduced at the annular edge; elution took place down the length of the annular region. In this configuration satisfactory results were obtained, however, further experimental work (*10*) on this configuration revealed a region of flow instability near the annular edge where solute was introduced. This design has not been used further in sedimentation FFF possibly due to the combination of the large radius, which is needed to obtain reasonable field strength, and the large annular cylinder length, which is needed to obtain reasonable separation efficiency. A different approach was utilized in the laboratory of Giddings and coworkers where circular channels of small internal diameter were used in the configuration shown in Figure 1. These channels produced the unanticipated result of particles eluting prior to the channel void peak (*11*). Upon refinement of the sedimentation FFF technique it was learned that unidirectional laminar flow conditions will not exist in a rotating circular channel due to secondary flow (*6*, *12*, *13*). Secondary flow normally arises when a fluid moving in a duct is subject to rotation or when flow takes place in a stationary curved duct or a combination of both. Secondary flow is characterized by the presence of regions of flow perpendicular to the direction of bulk flow. This perpendicular velocity component will cause the solute zone to be convectively driven across the bulk flow lines to produce a mixing effect. To minimize this mixing effect, which is undesirable for practical FFF separations, rectangular channels with a large breadth to thickness ratio (aspect ratio) were used (*6*); this configuration is now utilized in all modern sedimentation FFF fractionators.

In rotating channels the major driving force for secondary flow is the Coriolis acceleration (*14*) which must be included in the equations of motion describing the fluid flow for a complete analysis of the flow profile. The Coriolis force arises whenever a fluid particle is undergoing motion relative to a rotating frame of reference, in a direction not aligned with the axis of rotation, as the fluid does when flowing through a sedimentation FFF channel. This force is mathematically represented by the vector (cross) product of the angular velocity of rotation and the fluid velocity; hence the Coriolis force acts in a direction perpendicular to both the axis of rotation and the fluid motion. The Coriolis force is most commonly observed in meteorological applications such as winds, hurricanes, tornadoes, and ocean currents; chemical applications include the coupling between vibrational and rotational modes of motion in polyatomic gasses and liquids. For readers unfamiliar with Coriolis forces, a simple introductory explanation of the origins and effects are given in refs 15 and 16.

The aspect ratio used in laboratory fractionators is typically greater than 70. No published systematic study has been performed which examines the effects of varying the channel breadth and hence the aspect ratio. It is known, however, that the concentration enhancement of particles from zone compression against the outer wall will be reduced by dilution of particles across the channel breadth. Hence, the larger the channel breadth, the less probable is particle aggregation

0003-2700/91/0363-2614$02.50/0

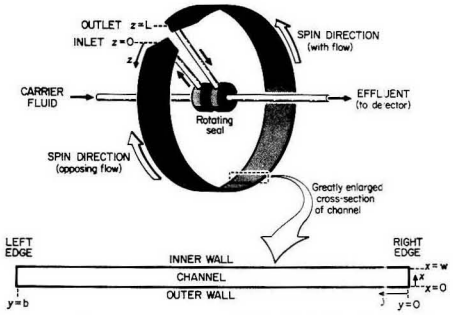

Figure 1. Sedimentation FFF apparatus illustrating the coordinate system x, y, and z and the channel thickness w, breadth b, and length L. Note that the wall at $y = 0.0$ and $y = b$ will be referred to as edges and walls at $x = 0.0$ and $x = w$ will be referred to as the "outer" wall and "inner" wall, respectively. The radius of curvature is the distance between the axis of rotation (the axis formed by the carrier fluid and effluent arrows) and the channel midpoint, $x = w/2$.

during zone relaxation when the particle population is in the most concentrated stage of the separation process. This dilution is impossible for circular channels because the field tends to concentrate particles at one point in the channel. On the other hand, large aspect ratio channels will dilute the zone, leading to a higher limit of detection; this may be important when the sample is either dilute or available in limited amounts or when detector sensitivity to the sample is low.

One experimental investigation (*13*) has been performed where the retention times of zones were compared for flow in the same direction as rotation and flow in the opposite direction to that of rotation. It was determined from this study that the retention times showed no dependence on the flow direction, relative to rotation, therefore the choice of flow and rotation direction was deemed not important. As will be seen from the results given below, there appears to be no measurable difference in retention times of zones; however, the quality of the separation is highly influenced by the choice of relative rotation and flow direction.

The velocity profile in a straight rectangular duct, under fully developed laminar flow conditions, was derived from theory and experimentally verified (*17*) in 1926. This profile or an approximation of it has been used in many FFF studies (*18–21*) where edge effects have been studied. This velocity profile does not, however, consider the effects of curvature nor the rotation which produces secondary flow. Although the effect of channel curvature has been studied in the context of sedimentation FFF for the infinite parallel plate model (*22*), a more exacting treatment of flow in a curved, rectangular duct (but with no rotation) has recently been given (*23, 24*). In addition, some studies have explored flow in rotating straight rectangular ducts (*25, 26*); however, these studies were concerned with high Reynolds number flows in moderate aspect ratio channels. The stability of flow in a rotating curved rectangular duct was recently published (*27*); however, the flow field was not computed.

In the work reported in this paper we use a complete solution to the Navier–Stokes equations for fully-developed flow in rotating curved ducts of rectangular cross section. The flow fields are calculated at the aspect ratios, bulk flow rates, and rotation rates pertinent to sedimentation FFF. The complete numerical solution of the Navier–Stokes equations for this problem provides a detailed velocity profile which includes $U(x,y)$, the flow velocity in the x direction at each point in the x–y plane (i.e. the channel cross section) along with $V(x,y)$ and $W(x,y)$, which are the flow velocities in the y and z directions, respectively, at each point in the x–y plane. This is in contrast to the previous approximations used in FFF of ideal unidirectional laminar fluid flow where the U and V velocity components are zero, except in flow FFF where U is considered to be constant throughout the channel cross section. The Navier–Stokes equations are formulated to include the appropriate terms for the Coriolis effect, which arises as a direct result of motion of the fluid relative to the rotating duct, and channel curvature, which generates secondary flow through centrifugal acceleration of the moving fluid, independent of rotation. The detailed theory and numerical method used for the evaluation of these flows is given in a recent publication (*28*). We will consider the effect that channel breadth has on practical separations in terms of peak shape by including the secondary flow effect in a digital simulation. In addition, a detailed view of particle flow in the edge region will be offered by viewing particle trajectories so that a microscopic explanation of zone evolution is revealed. We will also briefly consider the flow profile in a curved circular duct undergoing rotation in an attempt to explain why early attempts at sedimentation FFF with circular channels failed.

THEORY

Classical Sedimentation FFF Theory. We will discuss the classical analytical theory of Giddings and co-workers (*6*) as it applies to the problem of retention and zone broadening because simulation parameters will be cast in the parameters from this theory where possible. This theory, although simplistic in nature, is highly useful because of the clear correspondence between the theory and experimental quantities. Implicit assumptions in this theory include the use of infinite parallel plates as a duct model and that the zone is dispersed according to the limit of long times, resulting in Gaussian peaks. In addition, Coriolis and channel curvature effects are not considered in the theory and particles are treated as point masses with no wall interaction and no concentration effects. Lift forces, which are important for larger particles and higher velocity separations, are not included in the theory.

Retention in sedimentation FFF is easily estimated through the retention ratio R, which is the ratio of the void time t_0 to the retention time t_r. The retention ratio is easily related to the nondimensional mean layer thickness λ for small particles not showing an appreciable steric effect (*3–5*):

$$R = 6\lambda \coth(1/2\lambda) - 12\lambda^2 \tag{1}$$

The quantity λ may be expressed in terms of fundamental physical parameters for sedimentation FFF:

$$\lambda = 6k_B T/\pi d^3 G w|\Delta\rho| \tag{2}$$

where k_B is Boltzmann's constant, T is absolute temperature, d is the particle diameter, G is the centrifugal acceleration, w is the channel thickness, and $\Delta\rho$ is the density difference between the particle and fluid. For well-retained zones, λ is an excellent approximation of the nondimensional distance (x/w) from the outer wall to the point where half of the zone concentration is found. This definition of λ applies only to the case where the particle is denser than the fluid; however, this is the most important experimentally observed case as well as the primary case we will consider in this paper. For any level of retention the point in x/w where half the solute mass lies above and half the solute mass lies below may be calculated as (*29*)

$$\lambda_e = \lambda - \frac{1}{\exp(1/\lambda) - 1} \tag{3}$$

so that λ_e is equal to 0.5 in the limit $\lambda \to \infty$ and λ_e approaches λ in the limit $\lambda \to 0$.

Zone broadening, as measured by the plate height H, may be expressed easily for sedimentation FFF:

$$H = \frac{2D}{R\langle v\rangle} + \frac{\chi w^2\langle v\rangle}{D} + \sum H_k \tag{4}$$

where $\langle v\rangle$ is the cross sectional average fluid velocity, D is the diffusion coefficient, χ is the nondimensional nonequilibrium parameter (*30*), and H_k represents additional secondary sources of zone broadening such as finite detector volume, finite injection volume, and channel imperfections. The symbol W will be used interchangeably with v, the velocity component of primary flow; v is the standard notation in unidirectional laminar flow models of FFF. Where convenient the notation $\bar{W}$ will replace $\langle v\rangle$ for consistency. The plate height may be obtained from an experiment through the use of the relationship

$$H = \frac{\sigma_t^2}{t_r^2}L \tag{5}$$

where L is the channel length and σ_t is the standard deviation of the zone profile in time units.

Dilution. The limit of detection concept has been previously discussed for chromatography (*31–34*) and is important because band-broadening mechanisms cause dilution of the component zones resulting in a reduction in the concentration of solute present in the detection system (*31*). Understanding this dilution in quantitative terms with respect to channel dimensions and experimental parameters should aid in understanding how to minimize the dilution and create the lowest limit of detection separation system possible.

The dilution effect is quantitatively given by using previously developed chromatographic theory (*31*). We consider the dilution as a volume factor that will reduce the mass concentration of solute at the peak maximum, C_{max}, relative to the mass of solute injected, m_{inj}, so that

$$C_{max} = m_{inj}/\left\{V_R\sqrt{2\pi}/\sqrt{N}\right\} \tag{6}$$

where N is the number of theoretical plates (equal to the channel length L divided by the plate height H), V_R is the retention volume, and the term in braces represents the explicit volume dilution of the zone. The factor of $\sqrt{2\pi}$ enters into this equation through the assumption of Gaussian zone profiles (*31*). It is also assumed that the injection volume is small compared with the volume term in eq 6. The combination of eq 4, the above definition of N, and neglecting the longitudinal diffusion and secondary sources of broadening terms in eq 4, which are known to be negligible compared to the purely nonequilibrium term (*13*), yields for N

$$N = LD/\chi w^2\langle v\rangle \tag{7}$$

Combining eqs 6 and 7 yields

$$C_{max} = m_{inj}/\{wV_R\sqrt{2\pi\chi\langle v\rangle/LD}\} \tag{8}$$

For the case of well-retained zones we use the approximations $\chi = 24\lambda^3$ and $R = 6\lambda$ (*13*) along with the Stokes–Einstein relationship, $D = kT/3\pi\eta d$, (η is viscosity), and V_0, the channel void volume, which is equal to the product bwL to give

$$C_{max} = m_{inj}/\{2\pi bw^2\sqrt{\eta d\langle v\rangle L\lambda/kT}\} \tag{9}$$

Finally, eq 2 is substituted for λ in eq 9

$$C_{max} = m_{inj}/\left\{\frac{2\sqrt{6\pi}bw^{3/2}}{d}\sqrt{\frac{\eta\langle v\rangle L}{G|\Delta\rho|}}\right\} \tag{10}$$

Dilution is explicitly linked to a first-order dependence of channel breadth and a $^3/_2$ power dependence on channel thickness, as seen from eq 10. This suggests that using smaller channel breadths is very advantageous in decreasing the dilution (and the limit of detection) in sedimentation FFF. However, the $^3/_2$ power dependence on channel thickness is more dominant. If very thin channels can be engineered, the zone dilution can be further reduced. The penalty here is that to maintain an equivalent λ with a reduced w, the speed of rotation must be increased, which places an additional burden on the instrument. Although channel thickness may be difficult to reduce, the channel breadth is easily reduced. As will be shortly demonstrated, reducing the channel breadth, although decreasing the dilution, may under certain conditions have deleterious consequences for multicomponent separations.

COMPUTATIONAL DETAILS

Flow Calculations. The flow velocities U, V, and W are calculated according to the theory and computational procedures recently developed for flow in rotating, curved ducts of rectangular cross section, and the reader is urged to consult this paper for the computational details of the flow field (*28*). Typically, a computational grid of size 41 (x) by 81 (y) is used for the rectangular channel. The grid is nonuniform with finer mesh spacing near the edges, where the gradients of the flow variables are expected to be large. Due to the symmetry of the flow field, only the right half (referring to Figure 1) of the channel ($y/b \leq 0.5$) need be computed. The input parameters necessary for the calculation of the velocities include the streamwise pressure gradient dP/dz, the duct aspect ratio, the rotation rate (through the Ekman number described below), and the nondimensional radius of curvature, which is simply the radius of curvature divided by the channel thickness. Using the computed flow field based on these parameters the nondimensional velocities and the Reynolds number (equal to $w\bar{W}\rho/\eta$) of the flow are calculated. The nondimensional velocities $U(x,y)/\bar{W}$, $V(x,y)/\bar{W}$, and $W(x,y)/\bar{W}$ are then stored on disk and converted by another computer program to corresponding dimensional velocities suitable for particle simulation.

Particle Simulation. There are a number of numerical methods which can be used to obtain the elution profiles of particles in solution under the combined influence of force and flow fields, once the flow field is computed. The most general of these is the numerical solution of the partial differential equations (PDE's) governing FFF. Theses PDE's have been given previously (*19*, *20*); however their previous usage did not consider the convective effects due to flow velocity components U and V. Through additional terms these flow components can be included in the PDE formulation describing FFF. Numerical methods which solve these PDE's have a number of advantages and disadvantages which depend highly on the detail to be provided in problem formulation. Some advantages of the PDE solution methodology include fast computational speed and the fact that the channel walls are specified distinctly through the boundary conditions. Some disadvantages include issues such as robustness in terms of solution convergence, difficulties near sharp gradients in the solution and the accuracy in calculating transport near walls when the diffusion coefficient is made to be a function of the distance between wall and particle center of mass. Note that in the PDE solution, the spatial concentration gradient drives diffusion on a macroscopic scale and in this regard the mathematical foundation of the method allows for the effect of finite zone concentration to be modeled explicitly, if additional equations describing particle–particle concentration effects are known.

An alternative method, based on a stochastic derivation of the FFF problem (*29*), and used previously (*18*) and in this paper, is that of discrete random walks under the influence

of force field and convective bias. In this method, zone simulation is carried out by allowing a particle starting at some initial point in the channel to repeatedly diffuse in the flow field, with movement in the x direction biased by the force field, and convect in the flow field components U, V, and W. These discrete convection and diffusion/force bias steps are repeated until the particle is transported past the channel length, L. At this point, the time of transport and the x and y positions are written to disk and this procedure is continued for typically 6000 or more particles. The initial starting point is sampled from an exponential distribution in x and a uniform distribution in y, as previously described (*18*). Some of the advantages of this method include the ability to specify complex boundary and initial conditions since these may be easily described in discrete locations, and the simplicity in implementing this algorithm on both course-grained and fine-grained (massively) parallel computers. Some of the disadvantages include long run times when single processor computers are used, and the ad hoc method through which a boundary is implemented. This type of transport algorithm only considers particles in the limit of zero concentration, i.e. there is no provision for modeling particle concentration effects. Diffusion is implemented through the introduction of a microscopic random force of Brownian collisions. The simulation methodology does recognize, however, that particles have finite volume in that the particle center of mass may not contact a wall less than half of the effective particle diameter away. This effect may also be incorporated into the PDE approach by proper assignment of the boundary conditions. The particle simulation methodology used here is expected to be quite realistic when transport is due to the presence of flow gradients (e.g. secondary flow) and/or when time-dependent behavior (e.g. in flow and field-programming) is to be considered for small-diameter, low-concentration elution problems. Laboratory experiments utilizing fast field decays which are difficult to describe by analytical mathematics have shown very good agreement with the stochastic particle simulation (*35*).

In both the PDE solution technique and discrete particle simulation, transport is modeled as a passive process; i.e. the fluid flow influences particle motion through the convective components but the presence of the particle does not perturb the flow field. This ultimately limits the utility of this simple simulation methodology in FFF when large particles, which exhibit lift forces (*3*, *36*, *37*), are to be modeled. The reason for this is that the presence of a large particle modifies the flow field in the vicinity of the particle and the fluid forces on the particle are highly complex as the particle drifts near a wall, causing the lifting to occur. The computer resources needed to model the full interaction of a distinct collection of large particles and the flow field near a wall, in the context of a complete moving boundary problem is beyond that of the largest supercomputer currently available.

Mathematically, the random-walk algorithm may be stated as follows: Upon selection of the Cartesian coordinate starting positions x_0, y_0, and z_0, the particle is allowed to diffuse according to

$$x_{i+1/2} = x_i + s \quad \text{for} \quad \xi < P_+$$

and

$$x_{i+1/2} = x_i - s \quad \text{for} \quad \xi \geq P_+ \tag{11a}$$
$$y_{i+1/2} = y_i + s \quad \text{for} \quad \xi < 0.5$$

and

$$y_{i+1/2} = y_i - s \quad \text{for} \quad \xi \geq 0.5 \tag{11b}$$
$$z_{i+1/2} = z_i + s \quad \text{for} \quad \xi < 0.5$$

and

$$z_{i+1/2} = z_i - s \quad \text{for} \quad \xi \geq 0.5 \tag{11c}$$

where $P_+(x)$ is the probability of a particle moving to higher x, s distance away, the subscripts denote iteration number, and ξ is a random number with uniform density so that $0 \leq \xi < 1$. By combination of the effects of isotropic diffusion and force field bias on particle movement in the x direction, a probabilistic equation can be derived (*18*) which gives

$$P_+(x) = \frac{1}{1 + \exp(-s/l)} \tag{12}$$

The sum of $P_+(x)$ and $P_-(x)$ (where $P_-(x)$ is the probability of a particle moving to lower x, s distance away) is unity. The dimensional mean layer thickness, l, is given as the product λw. The distance s that a particle may move in time t_s is given as

$$s = \sqrt{2Dt_s} \tag{13}$$

where t_s is typically a millisecond or less in practical simulations. The probabilities of moving to higher or lower y and z are equal to $^1/_2$ because there is no force field to bias movement in the y and z directions.

After the particle is moved by the combined effects of diffusion and force field bias, it is transported by convection for time t_s so that

$$x_{i+1} = x_{i+1/2} + U(x_{i+1/2}, y_{i+1/2})t_s \tag{14a}$$
$$y_{i+1} = y_{i+1/2} + V(x_{i+1/2}, y_{i+1/2})t_s \tag{14b}$$
$$z_{i+1} = z_{i+1/2} + W(x_{i+1/2}, y_{i+1/2})t_s \tag{14c}$$

The stochastic algorithm assumes that diffusion and convection can be split into separate and successive operations; the PDE formulation explicitly gives these operations occurring simultaneously. Using the numerical method of operator splitting (*38*), it can be shown that this separate and successive application is valid even for nonlinear operators when the time step, t_s, is sufficiently small. The original stochastic derivation (*29*) states that $s \ll l$, which through eq 13 gives $t_s \ll l^2/2D$. Typically, $l^2/2D$ is 100 times greater than t_s in the calculations given in this paper.

The computational details of the simulations presented here are similar to those presented previously (*18*). A number of important differences exist, however, and these will be discussed in detail here. First, the velocities of fluid in the channel are no longer broken up into wall region flow and infinite parallel-plate flow. Second, the computational grid which was superimposed in the $x - y$ plane (*18*) is no longer used because the particle now has additional convective components which will certainly cause the particle to end up between grid points. If the particle surface touches a wall (or artificially diffuses inside the wall), the particle center of mass is placed at a distance of one-half of the particle diameter away from the wall at the point of particle-wall contact. Subrandom numbers (*39*) are now used for sampling from these initial distributions with maximum sampling efficiency.

Interpolation of velocity components U, V, and W in the x and y coordinates of the channel cross section is necessary because the particle positions do not at all times coincide with the grid points used for fluid flow calculation. Interpolation is implemented by the following steps. Upon program initialization, four grid points defining a rectangular element in x and y are identified. An additional five points are identified such that the original four points of each rectangle comprise the lower right one-fourth of a three by three patch of grid points (except for the largest values of x and y corresponding to the inner wall and left edge of the channel). This three by three patch of velocities in U, V, and W are individually

fit to a biquadratic function (*38*) and the resulting nine coefficients for U, V, and W are stored for each rectangular element. These coefficients are then used to calculate U, V, and W, at the locations $x_{i+1/2}$ and $y_{i+1/2}$ for each rectangular element. When the particle moves out of the local rectangular element, the new element is found by separately searching the x grid and y grid locations in order of nearest location to the former grid locations. The new rectangular element number is then easily calculated from the x and y grid locations.

Analysis of the resulting data is presented in the form of unsmoothed arrival time histograms and particle concentration density plots. Production of smooth elution curves, as was done for a previous study (*18*), is not attempted here because the simulations generate a very wide range of arrival times, from the void peak to the retained peak, as will be shown below. Even with 6000 particles, there are regions of undersampling which result in the production of unphysical bumps and gaps in the elution curves unless a large amount of filtering is used. This is, however, only a cosmetic situation and no further information is gained by smooth curve generation. The simulation code, written in FORTRAN-77, was developed and tested on a VAX 8800 computer (Digital Equipment Corp.) using the VMS operating system. Data were also analyzed on this computer. Production run data were obtained on RISC System/6000 Model 530 and 540 computers (International Business Machines Corp.) using the AIX operating system. All computer programs are executed with 64-bit precision.

RESULTS AND DISCUSSION

Channel Flow. To simplify the presentation of results, we introduce additional notation here. For graphs which contrast the importance of the direction of channel rotation with respect to the bulk flow direction, two arrows pointing up (↑↑) signifies the case where flow and rotation are in the same direction; this will be called the parallel case from previously introduced terminology (*13*). Two arrows pointing in opposite directions (↑↓) denotes the case where flow and rotation are in opposing directions; this will be called the antiparallel case (*13*). A single arrow (↑) denotes flow but no rotation. Other terminology for these cases exists in the fluid mechanics literature; for instance the terms codirectional (↑↑) and counterdirectional (↑↓).

The secondary flow in a curved rectangular duct without rotation is illustrated in Figure 2A via a vector plot for the right-edge region of the channel cross section shown in Figure 1. The dimensions of the channel used here are typical of those used in one type of commercial sedimentation FFF instrument. As can be seen from Figure 2A, there is a flow very near the channel edge ($y = 0.0$) in the direction of the inner wall ($x = w$). Approximately one channel thickness away from the edge there is a lower velocity flow toward the outer wall ($x = 0.0$) forming a counterclockwise rotating vortex. Between these regions is a small inner region where the secondary flow components U and V are essentially zero; this region is identified as the center of the vortex. Away from the edge region ($y/w > 1$) the secondary flow rapidly diminishes in magnitude. We show only one of the edge regions for the purpose of giving an expanded view; the vortex region at the opposite edge is exactly the same except that the direction of vortex rotation is reversed. The placement of vector arrows seen here is nonuniform in x and y, and these arrows lie on the grid points where U, V, and W are calculated. For the purpose of clarity we show only half the actual density of grid point locations used in calculating the flow field.

Under the conditions of curvature and rotation at a moderate spin rate (1000 rpm) and antiparallel operation, Figure 2B shows that the secondary flow is seen to be opposite in

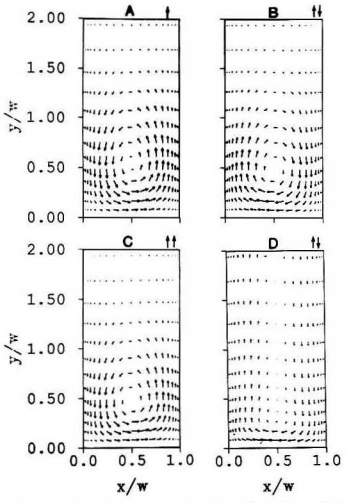

Figure 2. Vector plots of the secondary flow for a flow of 1 mL/min, $w = 254$ μm, $b = 2.0$ cm, radius of curvature of 15 cm: (A) without rotation; (B) 1000 rpm in the antiparallel mode of operation; (C) 1000 rpm in the parallel mode of operation; (D) as in (B) but at 15 000 rpm. The arrow convention is described in the Results.

direction to that of the case of curvature but with no rotation shown in Figure 2A. In both cases the secondary flow component is present with approximately the same extent of importance in terms of channel cross-sectional occupation; the region of secondary flow extends about two channel thickness values inward from the edge. The velocities of the secondary flow components are very different for these cases; however, a vector plot tends to obscure absolute velocity comparison between plots. For a typical radius of curvature found in sedimentation FFF fractionators, the absolute velocities of the secondary flow are about 3 orders of magnitude larger from rotation due to Coriolis forces as compared to the centrifugal acceleration component due to channel curvature. The domination of secondary flow by Coriolis forces takes place at rotation speeds of just a few rpm for channel dimensions typically used in sedimentation FFF.

Secondary flow under parallel conditions is given in Figure 2C. As can be seen, vortex rotation is of the same relative extent of that given in Figure 2B but of opposite rotation direction. In this case the fluid motion is up the edge at $y = 0.0$ to the inner wall and then toward the channel interior with motion toward the outer wall, culminating in full counterclockwise rotation. In all cases, secondary flow tends toward zero as a wall is approached.

The case of high field strength (15 000 rpm) is shown in Figure 2D for antiparallel operation. Again, the clockwise motion of the vortex occurs, but now the vortex region is rectangular shaped with the V component of the secondary flow being of long range and U being mostly confined to one channel thickness away from the edge in the y direction. The U component here is also confined more toward the center, with respect to the channel thickness, away from where particles will be concentrated under normal retentive conditions. This type of secondary flow is most desirable from the viewpoint of particle separations, as will be discussed below.

The four vector plots shown in Figure 2 are normalized so that the maximum velocity of secondary flow at a point in the channel cross section fits in each plot, through the length of

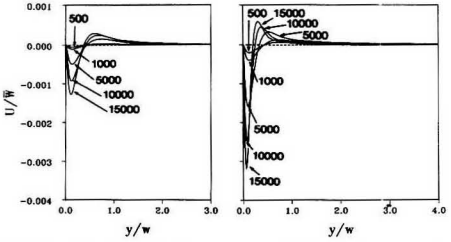

Figure 3. The secondary flow component $U(l,y)/\bar{W}$ near an edge under a variety of rotation speeds (speed in revolutions per minute) and in the antiparallel mode of operation: (left graph) w = 127 μm, b = 1.0 cm; (right graph) w = 254 μm, b = 2.0 cm. $\bar{W}$ = 0.328 and radius of curvature equals 15 cm for both cases.

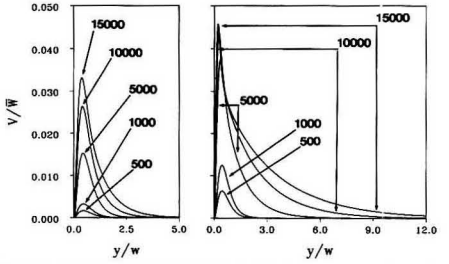

Figure 4. Secondary flow component $V(l,y)/\bar{W}$ near an edge under a variety of rotation speeds (speed in revolutions per minute) and in the antiparallel mode of operation: (left graph) w = 127 μm, b = 1.0 cm; (right graph) w = 254 μm, b = 2.0 cm. $\bar{W}$ = 0.328 and radius of curvature equals 15 cm for both cases.

the vector. Although this is convenient to show direction, only the relative magnitude of the secondary flow can be visualized. A better indication of the secondary flow velocity is to plot the flow velocity along a line in the x–y plane. These types of plots are shown in Figures 3–5 for selected regions of the channel cross section for U, V, and W, respectively, under conditions pertinent to sedimentation FFF.

In Figure 3 the x-directed component of the secondary flow, U, scaled to the mean bulk flow velocity, $\bar{W}$, is shown for the antiparallel case at different rotation speeds for the channel region $x = l$ when the retention ratio, R, is equal to 0.1. Results are given in Figure 3 for two cases of channel thickness, w, equal to 127 and 254 μm. In both cases shown in Figure 3, the aspect ratio is 78.74 because the channel breadth is varied for these two cases. These calculations are strictly valid when $\bar{W}$ is 0.328 cm/s; however, these plots vary only by a maximum of a few percent for $\bar{W}$ as high as 4 cm/s, a value far in excess of that commonly practiced in FFF. The value of $x = l$ is chosen for these calculations because a solute particle is most often found statistically at l distance from the outer wall. As can be seen from Figure 3, the U component at $x = l$ achieves a small fraction of the bulk flow velocity, $\bar{W}$. The sign of U is negative when secondary flow is toward decreasing x; this is shown in Figure 2 near the outer wall. Although U appears to be small, it does control particle motion on a short-length scale near the edge until it diminishes asymptotically to zero a few channel thicknesses in from the edge. This can be shown by considering when $\bar{W}$ is 0.328 cm/s, and $U/\bar{W}$ is approximately −0.0005 (referring to Figure 3) then U will be on the order of 1 μm/s; in 1 s the particle can travel a sizeable fraction of l in this edge region. The main concern, however, is when U is positive, because the particle will be convectively lifted away from the wall causing premature elution. Although the positive U values are small, they are significant. Comparison

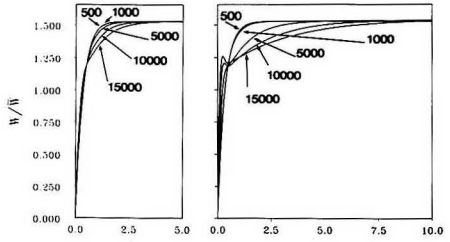

Figure 5. Primary flow component $W(x = w/2,y)$ near an edge under a variety of rotation speeds (speed in revolutions per minute) and in the antiparallel mode of operation. Other conditions are as in Figures 2 and 3.

of the two plots shown in Figure 3 demonstrates that the secondary flow in the x direction is stronger under equal $\bar{W}$ for the thicker channel than for the thinner channel. For low rotation speeds it can be seen that positive U values are much higher for the thicker channel than for the thinner channel. This is explained by considering the driving force for secondary flow which is given by the nondimensional Ekman number; the Ekman number is the ratio of the viscous force to Coriolis force and is given as

$$E = \nu/w^2\Omega \tag{15}$$

where ν is the kinematic viscosity (equal to η/ρ where ρ is the fluid density) and Ω is the rotation rate in radians per second (equal to 2π rpm/60). The larger is the Ekman number, the smaller is the extent of secondary flow. Because w appears in the definition of the Ekman number, larger channel thickness will result in a smaller Ekman number, leading to higher velocities and cross-sectional extent of the secondary flow. Figure 3 shows that U diminishes along $x = l$ for both thickness values roughly the same relative distance (as viewed by the ratio y/w) away from the edge. However, U diminishes to zero in a much shorter absolute distance from the edge for the smaller thickness channel; this is seen by multiplying the abscissas in Figure 3 by the respective w values.

Because the nondimensional radius of curvature is so large in sedimentation FFF instrumentation (250–1200), the secondary flow component from curvature alone is insignificant compared with the secondary flow induced by rotation, as determined by extensive calculation with the computer program described in ref 28 under conditions pertinent to sedimentation FFF. This means that in sedimentation FFF $U_{\uparrow\uparrow} \simeq -U_{\uparrow\downarrow}$ and $V_{\uparrow\uparrow} \simeq -V_{\uparrow\downarrow}$ over all of the channel cross section when all variables except the relative direction of flow, with respect to rotation, are held constant. These approximations hold true down to the case where the nondimensional radius of curvature is less than 100. Below this value curvature must be considered as a unique source of secondary flow and the approximations mentioned above will no longer be valid. Hence, Figure 3 is valid for the parallel mode of operation by scaling the ordinate by a multiplicative factor of −1.

Figure 4 shows the y-directed component of the secondary flow, V, also scaled to the average bulk flow, $\bar{W}$, for different rotation rates in the antiparallel mode of operation and again at the line where $x = l$ for R = 0.1. From Figure 4 it is seen that the V component is larger than the U component shown in Figure 3 and is of longer range in terms of its transport capability. V is larger and of longer range for the larger w case than for the smaller w case. The V component, unlike the U component of secondary flow, is desirable because it will carry the solute zone away from the edge region where the U component will cause x-directed convection. A stronger

V component is also desirable in minimizing the diffusion of a particle back into the vortex region once it is convectively transported away from the edge region. As was the case in Figure 3, the results of Figure 4 are strictly valid for $\bar{W} = 0.328$ cm/s; only a few percent error is incurred from using Figure 4 up to $\bar{W} = 4$ cm/s. In addition, the results given in Figure 4 can be used for the parallel case by multiplying the ordinate scale by −1.

The edge profile of the bulk flow, W, scaled to $\bar{W}$, is shown in Figure 5 for antiparallel operation at the channel midsection line $x = w/2$ and for the two channel thickness values used in Figures 3 and 4. On the basis of the analytical solution for laminar flow in straight rectangular, nonrotating ducts (*17*), $W/\bar{W}$ is equal to 1.512 and 1.506 at the channel midsection for the two channel aspect ratios, 78.74 and 157.48, under consideration in Figure 5. For rotating channel flow investigated in this paper, this value turns out to be approximately equal to 1.525 at the center of the channel for both channel thickness values. This difference is primarily due to the modification of parallel plate flow by the Coriolis forces and to a much lesser degree by the centrifugal forces arising from channel curvature. As can be seen from Figure 5, there is a large difference in the flow profiles between the two thickness values as the rotation speed is increased. For the larger channel thickness, it is shown that the velocity component $W/\bar{W}$ is no longer monotonically increasing away from the edge for rotation rates in excess of 5000 rpm. Also of interest in Figure 5 is the observation that $W/\bar{W}$ reaches a nearly constant value at a much longer distance away from the edge region for high rotation rates and thicker channels than for the thinner channels.

These observations are explained as follows. Under zero rotation the velocity of fluid near an edge is governed exclusively by the viscous drag that the fluid experiences near the edge and the only non-zero velocity component is W. However, the introduction of Coriolis forces through channel rotation causes the flow field to assume a dramatically different structure, especially in the planes perpendicular to the bulk-flow direction. At relatively low rotation rates, Coriolis, viscous, inertial, and pressure forces interact in a complex manner to produce the resulting flow field. As the rotation rate is increased, a well-defined asymptotic flow structure emerges, with regions where distinct force balances are established. At high rotation rates, i.e. small Ekman numbers, the basic flow structure in the x–y plane is divided into an essentially nonviscous core and very thin (relative to the channel thickness) viscous layers along the channel edges. The qualitative features of these regions is described in the following paragraphs.

The interior region (i.e. the region away from all channel edges), which occupies most of the channel cross section, is established by a balance between Coriolis and pressure forces. This core region, where inertial and viscous forces are negligible, is referred to as the Taylor–Proudman region in the classical fluid mechanics literature. The significant velocity component in this region is W, and it is responsible for the mass flux associated with the bulk flow. The other two velocity components, U and V, are vanishingly small for small Ekman numbers, and are proportional to $E^{1/2}$.

The thin layers near the channel edges at $y = 0$ and $y = b$ that are perpendicular to the axis of rotation are referred to as the Ekman layers in the fluid mechanics literature. Within each Ekman layer, for which the thickness is proportional to $E^{1/2}$, the Coriolis force is balanced by viscous forces; the pressure is nearly constant and the inertial forces are negligible. Within the Ekman layer, U is the dominant flow component, whereas the other two velocity components are small and proportional to $E^{1/2}$. This results in a mass flux

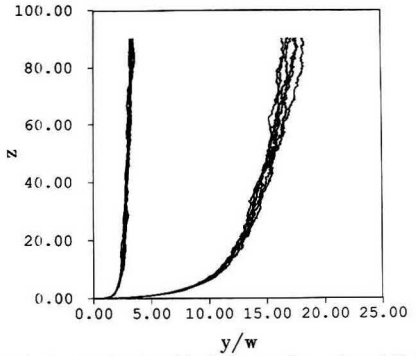

Figure 6. Trajectories of particles in the y–z plane not caught in the vortex; antiparallel mode of operation: (left bundle) 1000 rpm, $d = 0.27$ μm, $\lambda = 0.0190$; (right bundle) 15 000 rpm, $d = 0.045$ μm, $\lambda = 0.018\,23$. Conditions: flow rate 1 mL/min, $w = 254$ μm, $b = 2.0$ cm, $L = 90$ cm, radius of curvature of 15 cm. All particles are initially placed at $x/w = \lambda$, $y/w = 1.0$, $z = 0.0$. $\Delta\rho = 0.05$ g/mL in all cases.

proportional to $E^{1/2}$ within the Ekman layers along the x axis and leads to what is termed Ekman suction, which is the primary cause of the secondary flow in the x–y plane. The presence of Ekman layers at high rotation rates is substantiated by the appearance of the characteristic overshoot shown in Figure 5 for the W component of fluid velocity, at a distance approximately in agreement with the position of overshoot predicted by the linear Ekman layer theory.

The viscous layers along the edges $x = 0$ and $x = w$, that are parallel to the axis of rotation, evolve from a different and more complex balance of forces than that responsible for the Ekman layers. This results in a complex sandwich structure, consisting of two transition regions, one completely embedded inside the other. The outer viscous layer, whose thickness is proportional to $E^{1/4}$, occupies the region between the wall and the core region, whereas the inner sublayer extends from the wall to a distance proportional to $E^{1/3}$ that is inside the outer layer. The primary function of the inner layer is to provide a return path for the fluid flow within the Ekman layers, such that the net mass flux in the side layers is the same as that carried in the Ekman layers. A secondary function of these layers is to provide a region for smooth adjustment of the fluid velocity from its value in the Taylor–Proudman region to the no-slip condition (zero velocity) at the wall.

As can be discerned from the above discussion, at high rotation rates most of the mass flux associated with the secondary flow is confined to these thin viscous layers. A direct consequence of this is the shrinking of the extent of the vortical region, as the rotation rate increases.

Particle Motion in the Vortex. For a complete understanding of particle transport in the edge region, we pick an initial starting point for a particle in the edge region and record the particle's x, y, and z coordinates at each time step of the convection–diffusion cycle. In this way it is possible to follow a particle's trajectory through the vortex or any other part of the channel flow. Such trajectories are shown in Figures 6 through 8 under a variety of different conditions; these will be explained individually in this section.

In Figure 6 the trajectories of particles in the y–z plane are shown for the antiparallel mode of operation. As can be seen, there are two bundles of trajectories, those on the left side which are run under weak field (1000 rpm) conditions and moderate particle size ($d = 0.27$ μm) and those on the right which are run under strong field (15 000 rpm) conditions and small particle size ($d = 0.045$ μm). In both cases R is ap-

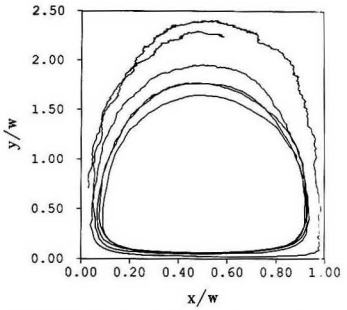

Figure 7. Trajectory of particle in the x–y plane caught in the vortex. Conditions are as in left bundle shown in Figure 6 except the particle is initially placed at $y/w = 0.6875$.

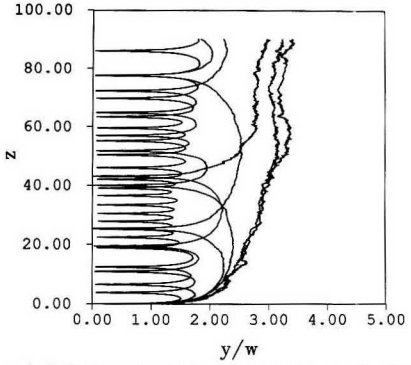

Figure 8. Trajectories of particles in the y–z plane showing the exchange of particles between the wall-displaced secondary flow driven by $V(x,y)$ and the fluctuation-induced crossing into the vortex region of flow driven by both $U(x,y)$ and $V(x,y)$. Conditions are as in Figure 6 except the particles are initially placed between $y/w = 0.78$ and $y/w = 1.0$.

proximately 0.1. The initial starting point for all particles is $x = l$, $y/w = 1.0$, and $z = 0.0$. For both cases it is shown that the secondary flow convectively drives the particles away from the edge region of the channel and into the interior of the channel breadth where the corresponding secondary flow component in V becomes negligible; at this point only diffusion governs motion in the y direction. This particular case is very favorable in terms of separation quality because it prevents particles from being trapped in the edge region where the bulk flow velocity W becomes very sluggish and would normally cause zone broadening (*18*, *21*). For particles which initially start out closer to the edge, as depicted in Figure 7, the U component of the secondary flow is relatively large, causing the particle to lift away from the outer wall and to be convectively driven by the vortex. In Figure 7 the trajectory is projected in the x–y plane and shows how the particle will swirl down the channel. For the case of small molecules, such as an unreacted monomer that may be injected with the macromolecular sample, the diffusional component is sufficient to cause a very erratic trajectory, as compared with Figure 7. This is caused because diffusion across the vortex causes a rapid sampling of the different convective paths offered by the vortical flow. Although not shown here, this case is very favorable because small molecules will diffuse in and out of the vortical region and will therefore spend little time in the edge region where the bulk flow W tends to be retarded. For large particles which start in an edge-confined region similar to the case depicted in Figure 7, inertial effects may also play a role in terms of ejecting the particle into the interior regions of the channel with respect to the y direction. This may be important for sedimentation FFF separations run under the steric mode of operation.

Due to diffusional fluctuations in position, a particle initially in one of the two modes depicted previously may cross over to the other mode of transport. This is shown in Figure 8 for the low field case, via projection in the y–z plane, where particles initially in the vortex region (shown here as the periodic oscillatory motion next to the edge) may diffuse out of the vortex region and be convectively driven into a channel location where U is minimal. Also shown in Figure 8 is the situation where a particle initially in the edge region comes under the influence of the vortex after traversing a few channel thickness values out from the edge in the y direction. This suggests that there exists an edge region from where particles will end up in the vortical region with a high degree of probability. This will lead to the presence of solute in the void peak and beyond, the amount of solute being proportional to the area of the edge region where the vortex contains a significant positive U velocity.

Trajectories under the same conditions, except for the parallel mode of operation, show that the secondary flow actively promotes the convection of retained particles into the vortex where V is negative along the line where $x = l$; in this case premature elution is more probable, as demonstrated in the next section. This behavior is central to the findings of this paper in that particle zones with small mean layer thicknesses and, initially, in the edge region will not experience edge flow for long because the secondary flow, in the antiparallel mode of operation, will convectively carry the particles away from the edge and into regions where there is very little flow in both x and y directions. However, in the parallel mode of operation, particles starting at the edge or near the edge will almost surely end up in the vortex through the secondary flow in V which promotes convective transport to the edge. A small change in initial particle position near the edges may cause the particle to elute somewhere between the void peak and the retained peak. In this regard particle transport at the edge region is noted to be chaotic for both parallel and antiparallel modes of operation, the use of the term chaotic referring to systems which exhibit a large sensitivity to initial conditions (*40*).

Zone Profiles. In this section we will examine the zone profile that results from the repeated application of convection–diffusion cycles to thousands of particles under retentive conditions. Figure 9 shows the elution profile of a zone which would be expected for the case of retention in a large aspect ratio (78.84) sedimentation FFF fractionator ($w = 254$ μm, $b = 2.0$ cm) for both parallel and antiparallel modes of operation. As can be seen from Figure 9, the presence of secondary flow causes a substantial number of particles to elute prematurely before the main peak in both cases. As explained in the trajectory section above, the fraction of particles which prematurely elute before the main peak is substantially higher for the parallel case as compared to the antiparallel case. This suggests that sedimentation FFF fractionators should be run with flow in the direction opposite to that of rotation so as to minimize the predicted zone leakage, the term leakage being used here to denote particles that do not elute with the main peak but, rather, are prematurely eluted by vortex flow. The mechanism discussed above is also verified by considering the concentration density profile of the particles at the end of the channel, shown in Figure 9 for the two cases. In the antiparallel mode of operation, there is a depletion of particles near the channel edges at $y/b = 0.0$ and $y/b = 1.0$. Again,

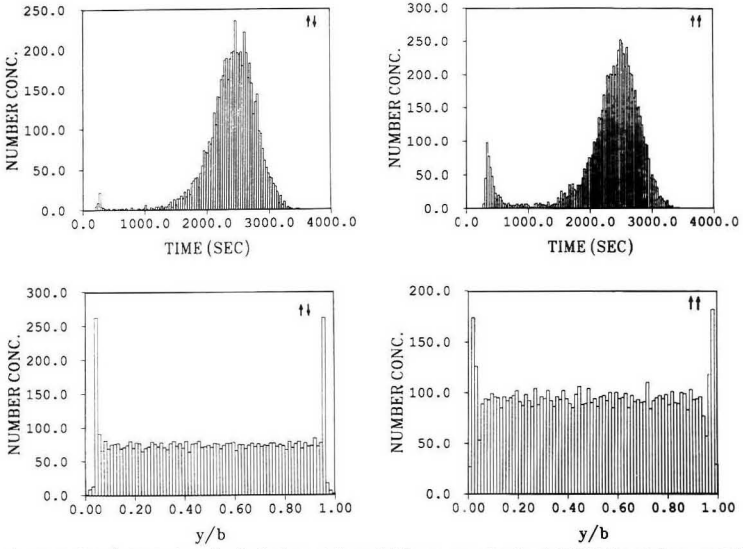

Figure 9. Time elution profiles and zone breadth distributions at the outlet for an aspect ratio of 78.740 (b = 2.0 cm, w = 254 μm), L = 90 cm, d = 0.27 μm, rotation rate of 1000 rpm, flow rate of 1 mL/min, $\langle v \rangle = \bar{W}$ = 0.328 cm/s, $\Delta\rho$ = 0.05 g/mL, radius of curvature 15 cm.

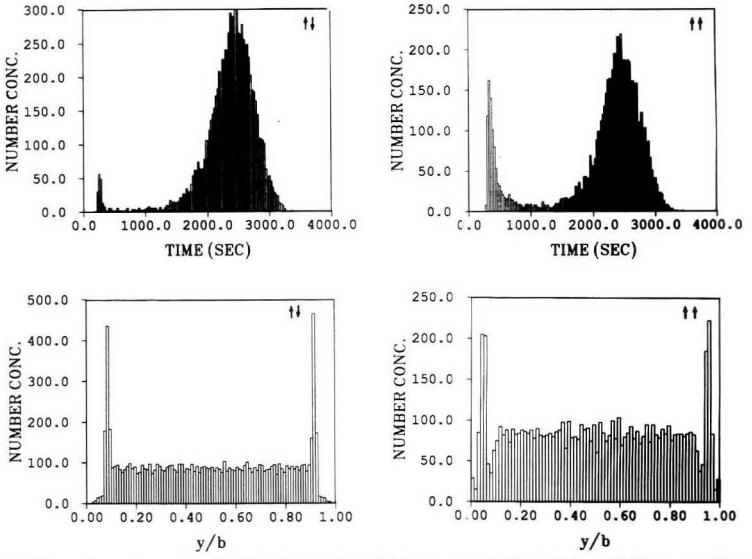

Figure 10. Time elution profiles and zone breadth distributions at the outlet for an aspect ratio of 40 (b = 1.016 cm, w = 254 μm), L = 90 cm, d = 0.27 μm, rotation rate of 1000 rpm, flow rate of 0.507 mL/min, $\langle v \rangle = \bar{W}$ = 0.328 cm/s, $\Delta\rho$ = 0.05 g/mL, radius of curvature 15 cm.

secondary flow in V is pushing the majority of particles away from the edges and into the interior of the channel. This is contrasted with the concentration density profile at the end of the channel for the parallel case where the particles enter the vortex and mostly reside in the vortex, until the particles leave the channel. For multicomponent zones, zone leakage will contaminate each peak with solute from more retained zones, causing a loss in the purity of the recovered fractions when sedimentation FFF is used to isolate a pure component. Simulation also suggests that baseline irregularity will be more dominant in the parallel mode of operation; under this mode of operation, peak area and statistical moment quantification may be difficult.

In an attempt to reduce the dilution caused by large channel breadth, simulations are performed with smaller breadths. These are shown in Figures 10 and 11 for aspect ratios of 40 (b = 1.016 cm) and 20 (b = 0.508 cm), respectively. Note that the comparison of these cases is facilitated by holding the

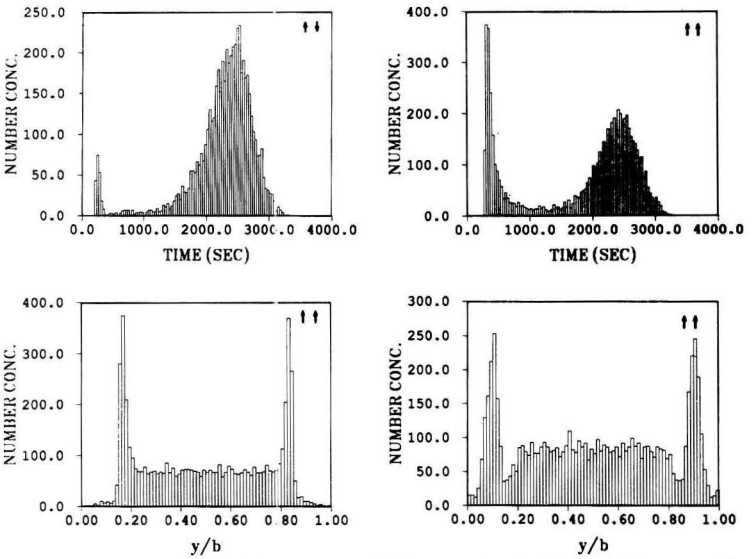

Figure 11. Time elution profiles and zone breadth distributions at the outlet for an aspect ratio of 20 (b = 0.508 cm, w = 254 μm), L = 90 cm, d = 0.27 μm, rotation rate of 1000 rpm, flow rate of 0.254 mL/min, $\langle v \rangle = \bar{W}$ = 0.328 cm/s, $\Delta\rho$ = 0.05 g/mL, radius of curvature 15 cm.

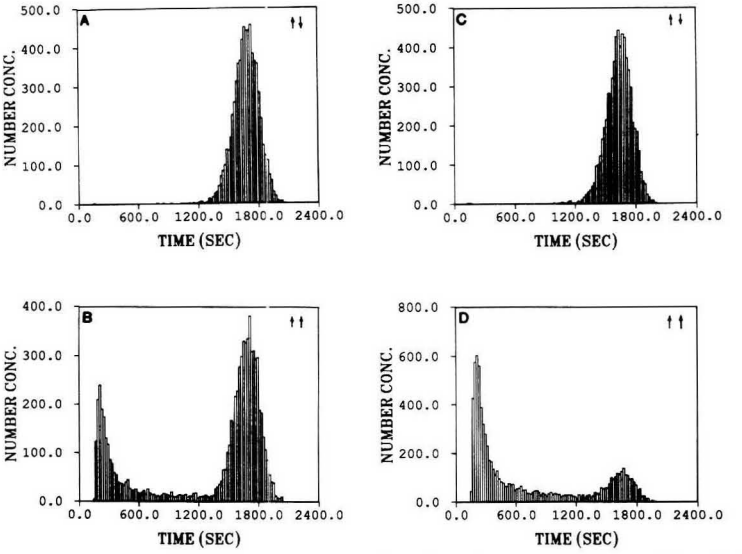

Figure 12. Time elution profiles for high rotation rate (15 000 rpm) separations. Parameters are w = 254 μm, L = 57 cm, d = 0.045 μm, $\langle v \rangle$ = 0.328 cm/s, $\Delta\rho$ = 0.05 g/mL, and radius of curvature 9.75 cm. For A and B: b = 2.54 cm (aspect ratio of 100), flow rate of 1.27 mL/min. For C and D: b = 1.016 cm (aspect ratio of 40), flow rate of 0.508 mL/min.

average linear velocity, $\bar{W}$, constant, which is the more fundamental parameter controlling elution and zone broadening, as compared to flow rate. These figures demonstrate that as channel breadth is reduced, more solute is found proportionally near the void peak region. This may be attributed to the simple fact that the actual vortex area remains constant and the interior area of the channel, which is devoid of rotational flow, decreases proportionately with reduction in channel breadth. This is most unfortunate since it implies that decreasing the channel breadth, in an attempt to decrease dilution, will result in a higher amount of zone leakage with a subsequent reduction in zone purity. Even for the more favorable case of antiparallel operation, enhanced zone leakage can be seen from these lower channel breadth results.

As was shown in Figure 2D, the secondary flow in U and V is very important in terms of cross-sectional occupation for

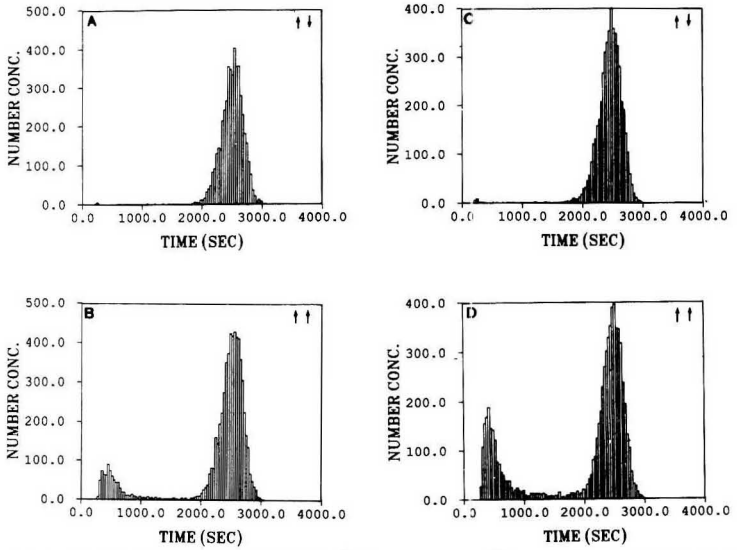

Figure 13. Time elution profiles for small channel thickness case. Parameters are w = 127 μm, L = 90 cm, d = 0.35 μm, $\langle v \rangle = \bar{W}$ = 0.328 cm/s, $\Delta\rho$ = 0.05 g/mL, and radius of curvature 15 cm. For A and B: b = 0.508 cm (aspect ratio of 40), flow rate of 0.127 mL/min. For C and D: b = 0.254 cm (aspect ratio of 20), flow rate of 0.0635 mL/min.

very high rotation speed. In Figure 12 simulated elution profiles are shown for very small particles at a high rotation speed (15 000 rpm) with parallel and antiparallel operation at two aspect ratios. In the case where the channel dimensions are chosen to be those of a typical high rotational speed fractionator (Figure 12A,B), the direction of spin with respect to flow is seen to be critical in maintaining a high-quality separation. For the parallel mode of operation, the void region is seen to be occupied by particles all the way from the void peak to the main peak. This situation highlights a potentially serious problem in that most experimentalists would interpret a fractogram like Figure 12B as having a sizable population of low and medium molecular weight material that was never resolved from the high molecular weight material composing the main peak. This, of course, is not correct and is a direct consequence of the zone leakage effect in its most extreme case. This is contrasted to the antiparallel case shown in Figure 12A where very few particles were detected between the void region and the main peak. Simulation, in this case, demonstrates a very high quality fractionation of the particle population with negligible leakage. The reason for the large contrast in results between parts A and B of Figure 12 is that, in the case of high rotation, the flow field is elongated (as shown in Figure 2D) so that the V component is strong and of a relatively long range away from the edge. This causes particles to be convected laterally along the channel breadth either into the edge and the vortex region (for parallel operation) or out of the edge region (for antiparallel operation) where the U component is very weak and cannot convect the particle into the vortex. This would indicate that higher fields are more favorable to reducing leakage when in the antiparallel mode of operation.

Because of the elongation of the flow field under high spin rate conditions, reduced channel breadth operation is possible under this condition as shown in Figure 12C for antiparallel operation. However, for the parallel mode of operation shown in Figure 12D, simulation reveals that reduced channel breadth, as expected, leads to unacceptable levels of zone leakage. Because not all experiments are conducted at such high rotation rate, the reduced breadth fractionator, for the given channel thickness of 254 μm, does not appear to be a promising configuration for routine high-quality separations.

From the results given in this paper it is suggested that the field programmed mode of operation is conducive to minimizing zone leakage in the early elution time part of the fractogram, when the initial rotation speed is high. However, as rotation speed is reduced as a function of time, it is possible that later eluting zones will have more zone leakage than earlier zones in the antiparallel mode of operation.

Because commercial fractionators have employed channel thickness dimensions of approximately 254 μm, the simulation studies reported in this paper have been performed mostly with this w value. It is important, however, to examine the reduced channel breadth scenario in the context of smaller channel thickness because zone dilution is more favorably dealt with by lowering channel thickness. As was shown in Figures 3 and 4, secondary flow is smaller at lower channel thickness because smaller w values will give larger Ekman numbers, yielding less secondary flow.

Simulation results for w = 127 μm, a value where some of the earlier sedimentation FFF experiments have been performed (*13*), are given in Figure 13, where $\bar{W}$ is identical to the results given previously. As can be seen from parts A and C of Figure 13, where simulations at aspect ratios of 40 and 20 are shown for the antiparallel mode of operation, zone leakage is minimal. Even for the lowest aspect ratio of 20, zone leakage is far less than that shown in Figure 9 where the dimensions of one commercial fractionator are used for simulation. This finding suggests that for the highest quality separation, channel thickness should be made smaller than is currently commercially available. In addition, simulation suggests that smaller channel breadths can be used with the reduced thickness channels. The dilution factor is decreased significantly in these cases as compared to the standard commercial dimensions of 254 μm by 2.00 to 2.54 cm. By using eq 9, the ratio of dilution factors for the 254-μm channel by

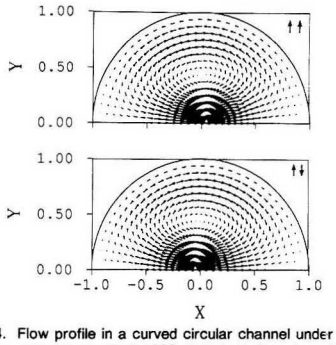

Figure 14. Flow profile in a curved circular channel under rotation. Conditions: rotation speed of 1000 rpm, duct diameter of 254 μm, radius of curvature 15 cm, and $\langle v \rangle = \bar{W} = 0.328$ cm/s. Note that the zone would accumulate at the three o'clock position in both cases and that the axis of rotation is perpendicular to the nine o'clock position.

a 2.00-cm channel to the 127-μm channel by a 0.508-cm channel at constant λ is seen to be approximately 16 when the particle diameter is equal for the two cases. It should be noted, however, that the use of eq 9 in this way is only approximate because a constant λ with different w necessitates different d values. Nonetheless, a factor of 16 less dilution results in the ability to lower the detection limit by a factor of 16. In addition, solvent consumption is reduced by approximately a factor of 8 for the reduced channel thickness and breadth case mentioned above. The only foreseeable problem with this suggestion, as was mentioned previously, is that under reduced channel thickness conditions, the centrifuge must be rotated at a higher speed to maintain the equivalent λ. This is only a consideration, however, until the secondary flow flattens out, as shown in Figure 2D, so that retained particles are isolated from the deleterious effects of the U secondary flow component. As was the case for previous simulations, the parallel mode of operation gives poor results and this is shown vividly in parts B and D of Figure 13 for the reduced thickness and breadth case (aspect ratios of 40 and 20) mentioned above. Simulation suggests that for the case of reduced thickness and breadth it is of paramount importance to use the antiparallel mode of operation to maintain high-quality separations free of zone leakage.

The results presented in this paper demonstrate the importance of secondary flow considerations in sedimentation FFF. Perhaps the most important and certainly the most practical finding of this paper is that the proper choice of rotation direction with respect to bulk flow direction is critical in minimizing zone leakage. Although these findings have been obtained through computer simulation, recent experimental verification has been obtained and will be given in a later paper.

Circular Channels. Because the mathematical formulation of the flow in a rotating curved duct was derived in generalized curvilinear coordinates (*28*), it is a relatively easy matter to compute the flow field for a rotating curved channel with circular cross section. This flow field was very recently computed (*41*) for the limiting case of small curvature. As mentioned previously, early attempts at achieving separation using a sedimentation field with circular channels failed. The velocity profiles calculated for a circular channel will be shown here to demonstrate that there is no vortex-free cross-sectional area of a circular channel; hence sedimentation FFF must be performed with relatively large aspect ratio channels.

Figure 14 shows the secondary flow via vector plots for circular channel sedimentation FFF. As was the case for rectangular channels, only half of the flow field need be calculated due to symmetry considerations. In this figure, the upper part of the semicircles correspond to the location $x = w/2$ and $y = 0.0$ and the lower right-most point corresponds to $x = 0.0$ and $y = b/2$ (the accumulation point for particles with density greater than the carrier fluid), where for circular channels the channel thickness, w, and channel breadth, b, are equal to the tube diameter. The conditions chosen for this calculation parallel the operating conditions for rectangular channels; i.e. the rotation speed, radius of curvature, and average cross-sectional velocity, $\bar{W}$, are similar to those given in Figure 9. The flow rate is, however, very much reduced because of the smaller cross-sectional area of the circular channel. As can be seen from this figure, secondary flow is prevalent over the whole channel cross section for both configurations. The absolute magnitude of the secondary flow, relative to bulk mean velocity, $\bar{W}$, although not shown, is large enough to convectively transport particles over the whole tube cross section a few times during the journey down the tube, rendering the principle of retention in sedimentation FFF useless in this type of experiment.

Although we have simulated elution profiles with particles possessing a density higher than that of the fluid, which causes the sample zone to accumulate at the outer wall under retentive conditions, the same behavior is expected for the occasional case of particles less dense than the carrier fluid. In this case the particles will be concentrated at the inner wall rather than the outer wall when particles are relaxed under the influence of the force field. It is easy to see from the vector plots in Figure 2 that under antiparallel conditions, particles which are initially present at the inner wall ($x = w$) will be swept into the vortex causing premature particle elution. This suggests that the experimentalist should use the parallel mode of operation if particles less dense than the fluid are to be fractionated.

One aspect of these studies which has not been previously discussed is the effect that high flow rates will have on practical separations. Because the absolute values of U and V secondary flow components increase with higher flow rates (flow rate being proportional to $\bar{W}$), zone leakage will be expected to increase with higher flow rates. It may be argued, however, that although U is larger at higher flow rate, causing more lifting into the vortex, V is also larger and should convect the particles at the edge into the channel interior faster, minimizing the effects of higher U. Simulations at higher flow rates, although not presented here, have shown that there is a mild effect from higher flow rates causing more zone leakage, although not substantially higher, at elevated flow rates. For separations performed at much higher flow rates than normally encountered, the use of channels with larger breadths or higher rotation rates may be advantageous in minimizing zone leakage. It has been suggested (*18*) that large flow rates may cause poorer agreement between theory and experiment due to the incomplete flow field sampling of the particle for low retention in the normal mode of FFF operation. In this regard, higher retention will be advantageous under higher flow conditions to minimize both secondary flow (U is smaller for small x) and to facilitate complete sampling of the flow field (l is smaller). In addition, operation of sedimentation FFF in the hyperlayer mode of operation utilizing the lift force to generate the hyperlayer may be especially susceptible to zone leakage because of the high flow rates necessary to lift the particle and because the particle will experience the higher U velocity due to the higher zone position in x where U is larger.

Finally, we note that a great deal of effort has been expended in attempting to include the effects of channel breadth in general treatments of FFF (*18–21*). The results presented here suggest that a reasonably accurate model of sedimen-

tation FFF is that of the infinite parallel plate model, for the antiparallel mode of operation and particles more dense than the fluid, due to the particles being convectively driven away from the channel edges for retained zones. The three-dimensional model of a channel which includes edge-retarded flow may be simplified through the findings of this paper because the edge retardation does not occur. Through careful quantitation of the edge retardation effect (*18*) it was found that this effect is suggested to be slight for sedimentation FFF but the results presented here establish the validity of the infinite parallel plate model as a very good approximation for use in sedimentation FFF.

ACKNOWLEDGMENT

We thank Prof. Karin D. Caldwell and Dr. Jianmin Li of the Center for Biopolymers at Interfaces at the University of Utah and Dr. Bhajendra N. Barman of FFFractionation Inc., Salt Lake City, UT, for experimental fractograms which support some of the findings of this paper.

SYMBOLS

b	channel breadth
C_{max}	concentration of particles at the peak maximum
D	diffusion coefficient
d	particle diameter
E	Ekman number
G	acceleration due to channel rotation
H	plate height
H_k	plate height due to secondary contributions
k_B	Boltzmann's constant
l	dimensional mean layer thickness
L	channel length
m_{inj}	mass of solute injected
N	number of theoretical plates
P	inlet pressure
R	retention ratio
s	average diffusion distance of a particle in t_s
T	absolute temperature
t_o	passage time for an unretained zone
t_r	retention time
t_s	time between iterations
U, $U(x,y)$	secondary flow velocity in the x direction
V, $V(x,y)$	secondary flow velocity in the y direction
V_0	void volume
V_R	retention volume
$\langle v \rangle$, $\bar{W}$	average axial flow velocity
v, W, $W(x,y)$	axial flow velocity
w	channel thickness
x	coordinate in channel thickness
y	coordinate in channel breadth
z	coordinate in channel length
η	absolute viscosity
ν	kinematic viscosity
ρ	fluid density
$\Delta\rho$	difference between particle and fluid density
λ	nondimensional mean layer thickness
λ_e	exact nondimensional mean layer thickness
χ	nondimensional nonequilibrium coefficient
Ω	rotation rate in radians per second
$\uparrow$	notation for curvature but no rotation
$\uparrow\uparrow$	notation for flow and rotation in the same direction
$\uparrow\downarrow$	notation for flow and rotation in opposite directions

LITERATURE CITED

(1) Caldwell, K. D. *Anal. Chem.* **1988**, *60*, 959A–971A.
(2) Giddings, J. C. *Chem. Eng. News* **1988**, Oct 10, 34–45.
(3) Koch, T.; Giddings, J. C. *Anal. Chem.* **1986**, *58*, 994–997.
(4) Peterson, R. E.; Myers, M. N.; Giddings, J. C. *Sep. Sci. Technol.* **1984**, *19*, 307–319.
(5) Li, J.; Caldwell, K. D.; Mächtle, W. *J. Chromatogr.* **1990**, *517*, 361–376.
(6) Giddings, J. C.; Yang, F. J. F.; Myers, M. N. *Anal. Chem.* **1974**, *46*, 1917–1924.
(7) Kirkland, J. J.; Dilks, C. H.; Yau, W. W. *J. Chromatogr.* **1983**, *255*, 255–271.
(8) Janca, J. *Field-Flow Fractionation*; Marcel Dekker: New York, 1988.
(9) Berg, H. C.; Purcell, E. M. *Proc. Natl. Acad. Sci. U.S.A.* **1967**, *58*, 1821–1828.
(10) Barcilon, V.; Berg, H. C. *J. Fluid Mech.* **1971**, *47*, 469–479.
(11) K. D. Caldwell, Department of Bioengineering, University of Utah, personal communication.
(12) Grushka, E.; Caldwell, K. D.; Myers, M. N.; Giddings, J. C. *Sep. Purif. Methods* **1973**, *2*, 127–151.
(13) Karaiskakis, G.; Myers, M. N.; Caldwell, K. D.; Giddings, J. C. *Anal. Chem.* **1981**, *53*, 1314–1317.
(14) Greenspan, H. P. *The Theory of Rotating Fluids*; Cambridge University Press: Cambridge, U.K., 1968.
(15) Feynman, R. P.; Leighton, R. B.; Sands, M. *The Feynman Lectures on Physics*; Addison-Wesley Publishing Co.: Reading, MA, 1977; Vol. I, 19-7 to 19-9.
(16) Goldstein, H. *Classical Mechanics*, 2nd ed.; Addison-Wesley Publishing Co.: Reading, MA, 1980; pp 174–182.
(17) Cornish, R. *Proc. R. Soc.* **1926**, *120*, 691–700.
(18) Schure, M. R. *Anal. Chem.* **1988**, *60*, 1109–1119.
(19) Kim, E.-K.; Chung, I. *Chem. Eng. Commun.* **1986**, *42*, 349–365.
(20) Takahashi, T.; Gill, W. N. *Chem. Eng. Commun.* **1980**, *5*, 367–385.
(21) Giddings, J. C.; Schure, M. R. *Chem. Eng. Sci.* **1977**, *42*, 1471–1477.
(22) Davis, J. M. *Anal. Chem.* **1986**, *58*, 161–164.
(23) Siragami, N.; Inoue, I. *Int. J. Eng. Fluid Mech.* **1988**, *1*, 101–133.
(24) Cheng, K. C.; Lin, R.-C.; Ou, J. W. *J. Fluids Eng.* **1976**, 41–48.
(25) Speziale, C. G. *J. Fluid Mech.* **1982**, *122*, 251–271.
(26) Speziale, C. G.; Thangam, S. *J. Fluid Mech.* **1983**, *130*, 377–395.
(27) Matsson, O. J. E.; Alfredsson, P. H. *J. Fluid Mech.* **1990**, *210*, 537–563.
(28) Weeratunga, S. K.; Schure, M. R. To be submitted for publication in *J. Fluids Eng.*
(29) Berg, H. C.; Purcell, E. M. *Proc. Natl. Acad. Sci. U.S.A.* **1967**, *58*, 862–869.
(30) Giddings, J. C.; Yoon, Y. H.; Caldwell, K. D.; Myers, M. N.; Hovingh, M. E. *Sep. Sci. Technol.* **1975**, *10*, 447–460.
(31) Karger, B. L.; Martin, M.; Guiochon, G. *Anal. Chem.* **1974**, *46*, 1640–1647.
(32) Foley, J. P.; Dorsey, J. G. *Chromatographia* **1984**, *18*, 503–511.
(33) Long, G. L.; Winefordner, J. D. *Anal. Chem.* **1983**, *55*, 712A–724A.
(34) Pal, F.; Pungor, E.; Kovats, E. sz. *Anal. Chem.* **1988**, *60*, 2254–2258.
(35) Hansen, M. E.; Giddings, J. C.; Schure, M. R.; Beckett, R. *Anal. Chem.* **1988**, *60*, 1434–1442.
(36) Saffman, P. G. *J. Fluid Mech.* **1965**, *22*, 385–400.
(37) Ho, B. P.; Leal, L. G. *J. Fluid Mech.* **1974**, *65*, 365–400.
(38) Press, W. H.; Flannery, B. P.; Teukolsky, S. A.; Vetterling, W. T. *Numerical Recipes*; Cambridge University Press: New York, 1986.
(39) Press, W. H.; Teukolsky, S. A. *Comp. Phys.* **1989**, *3* (6), 76–79.
(40) Evans, D. J.; Morriss, G. P. *Statistical Mechanics of Nonequilibrium Liquids*; Academic Press: New York, 1990; Chapter 10.
(41) Daskopoulos, P.; Lenhoff, A. M. *J. Fluid Mech.* **1990**, *217*, 575–593.

RECEIVED for review April 30, 1991. Accepted August 14, 1991.

Fourier Analysis of Multicomponent Chromatograms. Theory of Nonconstant Peak Width Models

Attila Felinger[1]

Department of Analytical Chemistry, University of Veszprēm, P.O. Box 158, H-8201 Veszprēm, Hungary

Luisa Pasti and Francesco Dondi*

Department of Chemistry, University of Ferrara, I-44100 Ferrara, Italy

Power spectrum (PS) based analysis of multicomponent chromatograms is extended to chromatograms containing peaks of different widths. For Poissonian chromatograms the PS is derived both for cases where peak width and retention time are independent of one another and for cases of linear peak broadening. Computer-generated chromatograms were used to test the derived model equations. The shape parameters and the number of single-component peaks can be estimated with good precision, although the precision of the estimated minimum and maximum peak widths is lower than that of their average. The results obtained by simulation are explored on the basis of the theoretically derived equations, and the relevance of the results in handling practical cases is emphasized.

INTRODUCTION

Fourier analysis of multicomponent chromatograms has recently been elaborated (*1*) and a general theoretical model of the chromatogram power spectrum (PS; see Glossary) was derived by representing the chromatogram as a random (i.e. stochastic) and stationary sequence of single-component (SC) peaks. In this initial treatment the peak standard deviations (for the sake of simplicity these will be called peak width, PW; see Glossary) were assumed to be constant and both SC peak heights and positions were random variables independent of one another. From this PS approach a new method was derived for determining the SC number m—that is the number of individual components which can be detected above a given concentration level—and other attributes of the multicomponent chromatograms such as peak shape parameters and peak capacity N_c. The method was tested on a substantial number of computer-simulated chromatograms (*2*), and it was found superior to the previously reported methods (*3–10*), since it appears applicable under conditions of greater overlapping, where other methods begin to fail. In addition, the PS method is insensitive to white noise, at least for signal-to-noise ratios greater than 20 (*2*).

This PS method may be applied under programmed elution conditions where constancy of SC PW is more closely met. However when such real cases are examined and the chromatogram is carefully viewed, it becomes clear that PW constancy is not perfectly respected. For example, one can easily check this failure in a programmed temperature chromatogram of a homologous series of linear hydrocarbons (*11*). Even if the temperature program is carefully controlled, variations of about 20–30% in PWs cannot be prevented. This exact perception is not so easily singled out in the chromatogram of a complex multicomponent mixture where the peak-overlapping effect hinders direct control over SC peak shape. However, in these cases, the above-mentioned figures are certainly higher since differences in physicochemical properties of the SCs in the mixture could determine an additional random, more unpredictable peak broadening.

The other constraint of the PS method, i.e. the condition of SC peak density constancy along the entire chromatographic space, are less critical since carefully controlling the elution program can improve resolution of the regions with greater peak density or compress the less dense regions. Another possibility is to cut the global chromatogram into a number of smaller windows, where SC peak density can be assumed constant, and to process them separately. Moreover, even from a mathematical point of view, such nonuniformity in the density of SCs is not of specific interest. This is, in fact, a case of a nonstationary stochastic process, which can be referred to stationary random cases under convenient compression or expansion of the time axis (*12*). However, the main point here is that we cannot easily keep both PW and SC peak density constant and, of these the PW proves the more difficult to control.

In order to check the relevance of PW constancy in applying the PS method to experimental chromatograms, the following two model cases were thus considered: (1) In the first case PW is a random variable independent of peak position and peak height (model A). Two distribution cases were considered: the normal distribution and the uniform distribution. (2) In the second model dependence of PW on retention time is assumed (model B). Parts a and b of Figure 1 report sections of these two kinds of model cases.

The Fourier analysis approach for obtaining theoretical expression of the PS is here again applied. In both cases SC peak density was assumed to be constant and Poissonian while the peak shape is taken as strictly Gaussian. The preference for Poissonian SC interdistance distribution is based on the fact that it is the limit distribution case holding true for very complex multicomponent chromatograms (*1*). The method will be validated under simulated chromatographic conditions closely related to those mentioned above, by applying the same numerical procedure previously set up (*2*).

THEORY

Derivation of a PS of nonconstant PW multicomponent chromatogram is similar to the one presented in ref 1. The only differences are that now the peak area characterizes the amount of a SC instead of peak height and the peak shape contribution to the PS is a function of the PW distribution.

Let the equation describing the shape of a single-component peak be

$$u(t,m,\sigma) = \frac{1}{(2\pi)^{1/2}\sigma} \exp\left[-\frac{(t-m)^2}{2\sigma^2}\right] \qquad (1)$$

u is a Gaussian peak of unit area, whose standard deviation and center are σ and m, respectively. When shifted to the origin, the Fourier transform (*13*) of such a peak is

$$g(\omega,\sigma) = \exp[-\omega^2\sigma^2/2] \qquad (2)$$

The quantity of a single component cannot be characterized

[1] Present address: University of Tennessee, Knoxville, TN.

0003-2700/91/0363-2627$02.50/0

Table I. Evaluation of the Terms in eq 10 for the Gaussian Peak Shape Case

peak width type[a]	$E\{\|g(\omega)\|^2\}$	$\|E\{g(\omega)\}\|^2$
1	$e^{-\omega^2\sigma^2}$	$e^{-\omega^2\sigma^2}$
2	$\dfrac{\sqrt{\pi}[\mathrm{erf}(\omega\sigma_2) - \mathrm{erf}(\omega\sigma_1)]}{2\omega(\sigma_2 - \sigma_1)}$	$\dfrac{\sqrt{\pi}[\mathrm{erf}(\omega\sigma_2/\sqrt{2}) - \mathrm{erf}(\omega\sigma_1/\sqrt{2})]^2}{2\omega^2(\sigma_2 - \sigma_1)^2}$
3	$\dfrac{\exp\left[-\dfrac{\sigma_{av}^2\omega^2}{2s^2\omega^2 + 1}\right]}{2s\omega^2 + 1}$	$\dfrac{\exp\left[-\dfrac{\sigma_{av}^2\omega^2}{s^2\omega^2 + 1}\right]}{s^2\omega^2 + 1}$

[a] 1 = constant PW, 2 = uniform PW distribution, 3 = normal PW distribution.

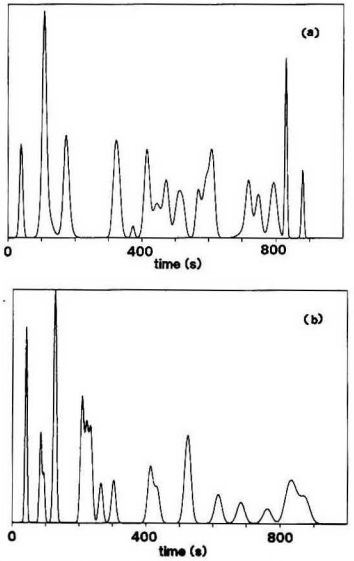

Figure 1. Simulated Poissonian chromatograms with nonconstant peak width (PW), $m = 25$ ($\alpha = 0.5$, $R_s = 0.5$). (a) PW is independent of retention time and uniformly distributed between $\sigma_1 = 2.8$ and $\sigma_2 = 14$. (b) PW is linear function of retention time ($\sigma_1 = 2.8$, $\sigma_2 = 14$).

here by the peak height since the PW is not constant, the amount of a component being indeed more generally related to the peak area. This is why, when the chromatogram is assumed to be built up as a random sequence of a given number of SC peaks, the random characteristics are the area (a), the center (m), and the standard deviation (σ) of the SC peaks.

The "ensemble" approach previously described is followed here in deriving the PS (*1*). An ensemble model containing $2N + 1$ components is considered. If the random chromatogram contains $2N + 1$ components distributed within the time interval $-NT < t < NT$ then its kth representation is

$$Y^k(t) = \sum_{n=-N}^{N} a_n{}^k u(t, m_n{}^k, \sigma_n{}^k) \tag{3}$$

The PS of such a random sequence is

$$F(\omega) = \lim_{N\to\infty} \frac{2}{(2N+1)T} E\{|Z_N{}^k(\omega)|^2\} \tag{4}$$

where

$$Z_N{}^k(\omega) = \sum_{n=-N}^{N} a_n{}^k g(\omega, \sigma_n{}^k) \exp(-i\omega m_n{}^k) \tag{5}$$

is the Fourier transform of the kth representation of the stochastic chromatogram. A derivation for the power spectrum of a stochastic chromatogram is given in eqs 16–42 in ref 1.

A. Random Distributions of Peak Width along the Time Axis. By consideration of the deviations mentioned above, the important differences can be summed up as follows. For the final form of $K(\omega)$ (see eq 22 in ref 1) we now get

$$K(\omega) = (2N + 1)(a_a{}^2 + \sigma_a{}^2)E\{|g(\omega, \sigma_n{}^k)|^2\} \tag{6}$$

where a_a and σ_a are the average and the standard deviations of the SC peak areas, respectively, and E is the expected value of a function defined as (*14*)

$$E\{g(\xi)\} = \int_{-\infty}^{\infty} g(\xi)\, f(\xi)\, d\xi \tag{7}$$

where $f(\xi)$ is the frequency function of the ξ distribution. For $q_{n-j}(\omega)$ (see eq 35 in ref 1) we have

$$q_{n-j}(\omega) = a_a{}^2 |E\{g(\omega, \sigma_n{}^k)\}|^2 \theta^{n-j}(\omega) \tag{8}$$

where $\theta(\omega)$ is the characteristic function of the interdistance between subsequent SC peak positions (*1*, *14*). Thus, when PW is also a random variable, the PS of a stochastic chromatogram is

$$F(\omega) = \frac{2a_a{}^2}{T}\left\{(\sigma_a{}^2/a_a{}^2 + 1)E\{|g(\omega,\sigma)|^2\} + |E\{g(\omega,\sigma)\}|^2 2\mathrm{Re}\frac{\theta(\omega)}{1 - \theta(\omega)}\right\} \tag{9}$$

By introducing chromatographic quantities (i.e. taking into account that $A_T = ma_a$ and $X = mT$) into eq 8, one gets

$$F(\omega) = \frac{2A_T{}^2}{mX}\left\{(\sigma_a{}^2/a_a{}^2 + 1)E\{|g(\omega,\sigma)|^2\} + |E\{g(\omega,\sigma)\}|^2 2\mathrm{Re}\frac{\theta(\omega)}{1 - \theta(\omega)}\right\} \tag{10}$$

The expected values found in eqs 9 and 10 are given in Table I, for the cases of uniform and normal PW distribution and under the hypothesis of Gaussian peak shape. Expressions for the term $2\mathrm{Re}\theta(\omega)/[1 - \theta(\omega)]$ were reported in Table I of ref 1 for the cases of exponential, uniform, gamma, and deterministic interdistance distribution between subsequent peaks. By use of a specific expression for general terms in eq 10, a consistent number of PS theoretical models are obtained.

In the present paper the Poissonian case is considered for which the interdistance between subsequent peaks is exponentially distributed. In this case $\mathrm{Re}\theta(\omega)/[1 - \theta(\omega)] = 0$ (*1*). If SC PW are uniformly distributed within the interval $\sigma_1 < \sigma < \sigma_2$, then the PS is

$$F(\omega) = \frac{A_T^2\pi^{1/2}}{mX\omega}\left(\frac{\sigma_a^2}{a_a^2} + 1\right)\frac{\mathrm{erf}(\omega\sigma_2) - \mathrm{erf}(\omega\sigma_1)}{\sigma_2 - \sigma_1} \quad (11)$$

When the distribution of PW is normal with σ_{av} (the average PW) and s (the standard deviation of the PW), then the PS is

$$F(\omega) = \frac{2A_T^2}{mX(2s^2\omega^2 + 1)^{1/2}}\left(\frac{\sigma_a^2}{a_a^2} + 1\right)\exp\left[\frac{\sigma_{av}^2\omega^2}{2s^2\omega^2 + 1}\right] \quad (12)$$

B. Deterministic PW Variation along the Time Axis. Up to this point peak position and PW were assumed independent random variables. In real cases it is often found that PW is a monotone function of retention time. If, e.g., the components elute with a constant plate number, $N = (V_r/\sigma)^2$, then the relationship between PW and retention volume is strictly linear

$$\sigma = V_r/N^{1/2} \quad (13)$$

Equation 13 emphasizes the importance of the investigation of linear PW–peak position relationship. When linear peak broadening is detected, the PS of a Poissonian chromatogram can easily be derived. The expected value in eq 4 can be written as

$$E\{|Z_N^k(\omega)|^2\} = E\{\sum_{n=-N}^{N}\sum_{j=-N}^{N} a_n^k a_j^k g(\omega,\sigma_n^k)g(\omega,\sigma_j^k) \times \exp(-i\omega m_n^k)\exp(-i\omega m_j^k)\} \quad (14)$$

Distinguishing the cases $n = j$ and $n \neq j$ allows the above expression to be written as

$$E\{|Z_N^k(\omega)|^2\} = K(\omega) + L(\omega) \quad (15)$$

where

$$K(\omega) = \sum_{n=-N}^{N} E\{(a_n^k)^2|g(\omega,\sigma_n^k)\exp(-i\omega m_n^k)|^2\} \quad (16)$$

$$L(\omega) = \sum_{\substack{n=-N\\ n\neq j}}^{N}\sum_{j=-N}^{N} E\left\{(a_n^k a_j^k g(\omega,\sigma_n^k)\overline{g(\omega,\sigma_j^k)}\exp(-i\omega m_n^k)\overline{\exp(-i\omega m_j^k)}\right\} \quad (17)$$

When peak area and PW are independent, the first sum of the above expression is

$$K(\omega) = \sum_{n=-N}^{N} E\{(a_n^k)^2\}E\{|g(\omega,\sigma_n^k)|^2|\exp(-i\omega m_n^k)|^2\} \quad (18)$$

since the expected value of a product of random independent quantities is the product of the expected values (*1*, *14*). Utilizing the expected value of $(a_n^k)^2$ as $a_a^2 + \sigma_a^2$ (see eq 21 in ref 1) and $|\exp(-i\omega m_n^k)|^2 = 1$, we obtain for $K(\omega)$

$$K(\omega) = (2N + 1)(a_a^2 + \sigma_a^2)E\{|g(\omega,\sigma_n^k)|^2\} \quad (19)$$

$L(\omega)$ can be written as

$$L(\omega) = 2N(2N + 1)a_a^2|E\{g(\omega,\sigma_n^k)\exp(-i\omega m_n^k)\}|^2 \quad (20)$$

since peak area was assumed to be independent of PW and position.

Writing eqs 19 and 20 into eq 4, we get

$$F(\omega) = \lim_{N\to\infty}\frac{2}{(2N+1)T}[K(\omega) + L(\omega)] = \frac{2(a_a^2 + \sigma_a^2)}{T}E\{|g(\omega,\sigma_n^k)|^2\} + \frac{4a_a^2}{T}\lim_{N\to\infty} N|E\{g(\omega,\sigma_n^k)\exp(-i\omega m_n^k)\}|^2 \quad (21)$$

Supposing that the dependence of PW on retention time is a linear function, that is

$$\sigma_n^k = Am_n^k + B \quad (22)$$

and taking into account that if the chromatogram is Poissonian, then the distribution of peak positions is uniform inside the region $-NT < m_n^k < NT$, one can calculate the limit in eq 21 as

$$\lim_{N\to\infty} N\left|\frac{\int_{-NT}^{NT}\exp\left[-\frac{\omega^2(Am+B)^2}{2}\right]\exp(-i\omega m)\,dm}{2NT}\right|^2 \quad (23)$$

The integral in the above expression is finite, since when the limit of the integration is extended to plus and minus infinity, it resembles the Fourier transform of a Gaussian function. By the use of the following Fourier transform property (*13*)

$$\mathcal{F}\{e^{-(t-t')^2/2\sigma^2}\} = (2\pi)^{1/2}\sigma e^{-\omega^2\sigma^2/2 - i\omega t'} \quad (24)$$

the above integral can be calculated as

$$\int_{-\infty}^{\infty}\exp\left[\frac{\omega^2(Am+B)^2}{2}\right]\exp(-i\omega m)\,dm = \frac{(2\pi)^{1/2}}{A\omega}e^{-1/2A^2}e^{i\omega B/A} \quad (25)$$

by considering in eq 24 $\sigma = 1/(\omega A)$ and $t' = -(B/A)$. Thus, by consideration of eq 23, the limit in eq 21 is

$$\lim_{N\to\infty} N|E\{g(\omega,\sigma_n^k)\exp(-i\omega m_n^k)\}|^2 = \lim_{N\to\infty} N\frac{2\pi}{4N^2T^2A^2\omega^2}e^{-1/A^2} = 0 \quad (26)$$

The PS of a Poissonian chromatogram in the case of linear peak broadening is

$$F(\omega) = \frac{2a_a^2}{T}\{(\sigma_a^2/a_a^2 + 1)E\{|g(\omega,\sigma)|^2\}\} \quad (27)$$

The expected quantity in eq 27 for the case of linear PW variation between two boundary values σ_1 and σ_2 is found in Table I for uniform PW distribution (case 2). In this way, for linear PW variation, one obtains a theoretical PS expression exactly equal to eq 9, which holds true for the uniform peak width distribution model. In order to understand this finding, one must consider that the distribution of PWs is determined by the distribution of peak positions via the PW vs retention time function. When the position vs PW relationship is linear and the peak position distribution is uniform, the PW distribution will be uniform as well. The PS of such a chromatogram is the same as that in eq 11 independent of whether the variation of the PW is ordered or disordered along the time axis.

The point here is much more than a mathematical result. It can be explained as the consequence of the "memory loss" intrinsic to the PS approach. The hypothesis of "stationariness" of the statistical attributes of the chromatogram which was assumed in deriving PS by Fourier analysis is mathematical artifice which allows us to derive the PS by the "ensemble average" process. The same "lack of memory" arises when the autocovariance function (ACVF) is numerically computed over an experimental digitized chromatogram by the expression (*15*)

$$C_{xx}(\mathbf{k}) = \frac{1}{N}\sum_{j=1}^{N-\mathbf{k}}(Y_j - \hat{Y})(Y_{j+\mathbf{k}} - \hat{Y}) \quad \mathbf{k} = 0, 1, 2 \ldots, M-1 \quad (28)$$

Table II. Random Peak Width with Uniform Distribution between σ_1 and σ_2 (m = 200)

original values					estimated values				
α	σ_1	σ_2	σ_a	r	m	σ_1	σ_2	σ_{av}	r
0.333	1.68	5.05	3.37	3	222 ± 15	2.66 ± 0.43	5.29 ± 1.03	3.97 ± 0.36	2.09 ± 0.73
0.5	2.51	7.53	5.02	3	217 ± 19	2.60 ± 0.61	8.67 ± 2.05	5.63 ± 0.78	3.67 ± 1.6
0.5	1.67	8.36	5.02	5	213 ± 19	3.36 ± 0.62	10.27 ± 2.39	6.82 ± 0.93	3.27 ± 1.3
0.667	3.32	9.97	6.64	3	222 ± 19	3.81 ± 0.81	9.75 ± 1.86	6.78 ± 0.67	2.77 ± 1.8
0.667	2.21	11.07	6.64	5	214 ± 25	2.41 ± 0.62	11.77 ± 3.17	7.09 ± 1.4	5.50 ± 2.0
1	4.92	14.75	9.83	3	220 ± 32	5.51 ± 1.2	15.21 ± 4.39	9.36 ± 1.8	3.04 ± 1.5
1	2.21	11.07	6.64	5	219 ± 19	2.45 ± 0.53	11.49 ± 2.37	6.97 ± 1.1	5.00 ± 1.9

Table III. Linear Peak Broadening ($\sigma = \sigma_1$ at $t = 0$ and $\sigma = \sigma_2$ at $t = X$) (m = 200)

original values					estimated values				
α	σ_1	σ_2	σ_{av}	r	m	σ_1	σ_2	σ_{av}	r
0.333	1.68	5.05	3.37	3	223 ± 18	1.75 ± 0.37	5.51 ± 1.13	3.63 ± 0.41	3.39 ± 1.29
0.5	2.51	7.53	5.02	3	228 ± 20	3.03 ± 0.74	7.43 ± 2.28	5.23 ± 0.86	2.81 ± 1.84
0.5	1.67	8.36	5.02	5	228 ± 13	1.82 ± 0.49	8.47 ± 1.90	5.14 ± 0.78	5.16 ± 2.38
0.667	3.32	9.97	6.64	3	207 ± 17	3.74 ± 0.68	9.90 ± 2.59	6.82 ± 1.0	2.87 ± 1.36
0.667	2.21	11.07	6.64	5	209 ± 16	2.38 ± 0.56	11.59 ± 2.12	6.98 ± 0.90	5.30 ± 2.02
1	4.92	14.75	9.83	3	207 ± 23	5.93 ± 1.3	13.79 ± 4.31	9.86 ± 1.6	2.59 ± 1.46
1	2.21	11.07	6.64	5	203 ± 14	2.51 ± 0.48	10.86 ± 2.15	6.69 ± 0.92	4.57 ± 1.69

Table IV. Random Peak Width With Uniform Distribution between σ_1 and σ_2 (Using the Theoretical Value of $^1/_3$ for σ_a^2/s_a^2) (m = 200)

original values					estimated values				
α	σ_1	σ_2	σ_{av}	r	m	σ_1	σ_2	σ_{av}	r
0.333	1.68	5.05	3.37	3	208 ± 20	1.86 ± 0.31	4.79 ± 1.01	3.33 ± 0.39	2.72 ± 1.00
0.5	2.51	7.53	5.02	3	206 ± 24	2.76 ± 0.70	7.62 ± 2.47	5.19 ± 0.98	3.13 ± 1.79
0.5	1.67	8.36	5.02	5	193 ± 18	1.75 ± 0.34	9.28 ± 1.76	5.51 ± 0.76	5.66 ± 2.09
0.667	3.32	9.97	6.64	3	218 ± 27	3.27 ± 0.80	11.90 ± 3.38	7.59 ± 1.4	4.08 ± 2.08
0.667	2.21	11.07	6.64	5	227 ± 16	2.29 ± 0.44	11.87 ± 3.38	7.08 ± 1.6	5.58 ± 2.84
1	4.92	14.75	9.83	3	224 ± 20	5.67 ± 1.7	15.31 ± 3.96	10.49 ± 1.4	3.12 ± 1.73
1	3.28	16.38	9.83	5	235 ± 26	3.62 ± 0.95	17.77 ± 3.65	10.69 ± 1.6	5.31 ± 1.92

where Y is the digitized chromatogram and $\hat{Y}$ its mean value of Y. M is the truncation point of the computed ACVF. From ACVF the experimental PS is evaluated by taking its Fourier transform (*2*, *15*)

$$F(\omega) = 2\{C_{xx}(0) + 2\sum_{k=1}^{M-1} C_{xx}(\mathbf{k})\, w(\mathbf{k}) \cos(\omega\mathbf{k})\} \qquad 0 \le \omega \le \pi \tag{29}$$

where $w(\mathbf{k})$ is a weighing function introduced to filter the effect of random fluctuations of the ACVF function (*2*). In the above equation M is the truncation point in the ACVF.

Since the ACVF is the sum of products of time-scaled chromatographic responses (see eq 28), the specific order of different terms in the sum does not have any relevance. The only relevance is the abundance with which terms with the same sign at the same time shift appear, that is the frequency response. The order with which these terms appear along the time axis of the chromatogram is instead immaterial. Full exploration of these aspects of lack of memory lies beyond the aims of the present paper. What is important in this context is rather the implications of the method when it is applied in practice. Since estimates of parameters like σ_1, σ_2, and m are obtained by the nonlinear fitting to theoretical PS expression (like eqs 11 and 12) of the experimentally determined PS (eq 29), the determined quantities will be statistical mean values referred to the total time span over which the numerical treatment is applied. The determined SC number m cannot be considered as an exact value but as an estimate with its own bias. This last point was carefully discussed in a previous work where it was indeed shown by simulation that the determined number of single components is a typical, unbiased Poisson quantity with variance equal to its value (*2*).

COMPUTATIONS

All the programs were written in Basic and run on an IBM PS/2 Model 50 computer. Poissonian chromatograms were simulated that contained 200 Gaussian peaks at different saturation values, α, and had a varying range of PW by following the procedure previously described (*2*). The distribution of peak areas was uniform with a maximum A_{max}/A_{min} ratio of 150. To calculate peak areas, a perpendicular drop was used when a valley was found between two adjacent peaks. For each parameter combination 25 runs were performed using different random sequences.

The experimental PS was computed by using eqs 28 and 29 with the procedure described in ref 2, method I. The theoretical PS was computed by using eq 11. The nonlinear parameter estimation was performed by the SIMPLEX method as described in ref 2. Tables II–VIII report the mean values and the standard deviations of the fitted model parameters computed over these repeated runs. All the data reported in Tables II–VIII refer to a resolution R_S (*3*) equal to 0.5.

RESULTS AND DISCUSSION

The two cases of type A models for which the theoretical expression of PS was derived—the uniform PW distribution, eq 11 and the normal one, eq 12—are compared in Figure 2. It can be seen that the ratio either of the largest over the smallest PW, $r = (\sigma_2/\sigma_1)$, or of relative standard deviation (RSD = s/σ_{av}), respectively, for the uniform and for the normal distribution case, have significant influence on the PS shape. However, it can be seen that the cases of the two distributions display significant congruence once they are compared together. In order to check this point, a comparison at common RSD values was made (see Figure 3). It can be easily shown

Table V. Linear Peak Broadening ($\sigma = \sigma_1$ at $t = 0$ and $\sigma = \sigma_2$ at $t = X$) (Using the Theoretical Value of $^1/_3$ for σ_a^2/a_a^2) (m = 200)

original values					estimated values				
α	σ_1	σ_2	σ_{av}	r	m	σ_1	σ_2	σ_{av}	r
0.333	1.68	5.05	3.37	3	210 ± 16	1.90 ± 0.43	4.92 ± 1.06	3.41 ± 0.39	2.80 ± 1.11
0.5	2.51	7.53	5.02	3	210 ± 23	2.75 ± 0.54	7.37 ± 2.04	5.06 ± 0.81	2.91 ± 1.36
0.5	1.67	8.36	5.02	5	209 ± 22	1.96 ± 0.50	8.10 ± 1.39	5.03 ± 0.60	4.45 ± 1.55
0.667	3.32	9.97	6.64	3	208 ± 30	3.68 ± 0.95	10.22 ± 2.88	6.95 ± 1.0	3.13 ± 1.56
0.667	2.21	11.07	6.64	5	208 ± 15	2.59 ± 0.58	10.38 ± 2.03	6.49 ± 0.87	4.32 ± 1.73
1	4.92	14.74	9.83	3	199 ± 18	5.85 ± 1.5	13.95 ± 4.30	9.90 ± 1.5	2.72 ± 1.58
1	3.28	16.38	9.83	5	214 ± 24	3.94 ± 1.2	15.80 ± 4.07	9.87 ± 1.6	4.57 ± 2.08

Table VI. Partial Processing of the Total Chromatogram with Uniform PW Distribution (m = 200, α = 0.500)

	original values				estimated values				
processed part	σ_1	σ_2	σ_a	r	m	σ_1	σ_2	σ_{av}	r
total	2.51	7.53	5.02	3	216 ± 14	3.03 ± 0.45	6.87 ± 1.0	4.95 ± 0.37	2.36 ± 0.66
first half	2.51	7.53	5.02	3	109 ± 6	3.23 ± 0.45	6.87 ± 1.0	4.95 ± 0.37	2.36 ± 0.66
second half	2.51	7.53	5.02	3	105 ± 12	3.36 ± 0.59	6.48 ± 1.2	4.86 ± 0.44	2.08 ± 0.67
first quarter	2.51	7.53	5.02	3	47 ± 8	3.55 ± 0.72	6.73 ± 1.7	5.14 ± 0.72	2.05 ± 0.95
second quarter	2.51	7.53	5.02	3	49 ± 7	3.66 ± 0.78	6.27 ± 1.4	4.96 ± 0.68	1.82 ± 0.68
third quarter	2.51	7.53	5.02	3	49 ± 8	3.73 ± 0.88	6.06 ± 1.4	4.90 ± 0.77	1.74 ± 0.72
fourth quarter	2.51	7.53	5.02	3	51 ± 6	3.40 ± 0.77	6.34 ± 0.92	4.87 ± 0.54	1.97 ± 0.56

Table VII. Partial Processing of the Total Chromatogram with Linear PW increase (m = 200)

	original values					estimated values				
processed part	α	σ_1	σ_2	σ_{av}	r	m	σ_1	σ_2	σ_{av}	r
total	0.500	2.51	7.53	5.02	3	231 ± 17	2.89 ± 0.58	6.97 ± 1.59	4.93 ± 0.57	2.59 ± 1.02
first half	0.375	2.51	5.02	5.77	2	112 ± 12	2.70 ± 0.54	5.08 ± 1.51	3.89 ± 0.54	2.09 ± 1.15
second half	0.625	5.02	7.53	6.28	1.5	116 ± 7	5.43 ± 0.64	7.33 ± 1.14	6.38 ± 0.43	1.39 ± 0.38
first quarter	0.312	2.51	3.77	3.14	1.5	54 ± 7	2.56 ± 0.35	3.66 ± 0.56	3.11 ± 0.23	1.48 ± 0.42
second quarter	0.437	3.77	5.02	4.39	1.33	51 ± 7	3.91 ± 0.36	5.22 ± 1.07	4.56 ± 0.52	1.35 ± 0.35
third quarter	0.563	5.02	6.38	5.65	1.25	55 ± 9	5.20 ± 0.84	6.55 ± 1.20	5.87 ± 0.77	1.30 ± 0.40
fourth quarter	0.687	6.28	7.53	6.90	1.20	50 ± 10	6.66 ± 0.83	7.37 ± 0.75	7.01 ± 0.72	1.11 ± 0.12

Table VIII. Parameter Estimations Obtained by Using the Constant PW PS Model m = 200 (Method I of ref 2)

Case 1: Random Peak Width with Normal Distribution

original value			estimated value	
α	RSD	σ_{av}	m	σ_{av}
0.500	0.1	4.00	209 ± 21	3.99 ± 0.20
0.500	0.3	4.00	207 ± 22	4.04 ± 0.19
0.500	0.5	4.00	191 ± 25	4.31 ± 0.31
0.500	0.7	4.00	178 ± 21	4.64 ± 0.31
0.500	0.9	4.00	163 ± 21	5.25 ± 0.45

Case 2: Linear Peak Broadening

original values					estimated value	
α	σ_1	σ_2	σ_{av}	r	m	σ_{av}
0.500	3.81	4.19	4.00	1.1	200 ± 22	4.22 ± 0.27
0.500	4.00	5.20	4.60	1.3	197 ± 22	4.68 ± 0.35
0.500	4.00	6.00	5.00	1.5	193 ± 24	5.16 ± 0.51
0.500	4.00	6.80	5.40	1.7	188 ± 25	5.76 ± 0.62
0.500	4.00	7.60	5.80	1.9	182 ± 25	6.21 ± 0.49

that for the uniform distribution, the relationship between r and RSD is

$$\mathrm{RSD} = \frac{1}{\sqrt{3}} \frac{r-1}{r+1} \tag{30}$$

since the standard deviation of the uniform type PW distribution is $(\sigma_1 - \sigma_2)/\sqrt{12}$ (*16*). From eq 30, one can get

$$r = \frac{(\sqrt{3}\mathrm{RSD} + 1)}{(1 - \sqrt{3}\mathrm{RSD})} \tag{31}$$

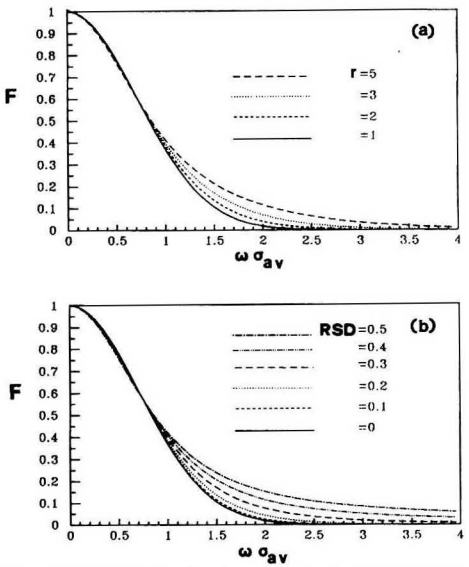

Figure 2. PS of a Poissonian chromatogram with nonconstant PW distribution: (a) uniform PW distribution of different $r = \sigma_2/\sigma_1$ values; (b) normal PW distribution of different RSD = s/σ_{av} values.

Therefore, the correspondence between the cases in Figure 3 for the uniform distribution is r = 2.06 if RSD is 0.2 and

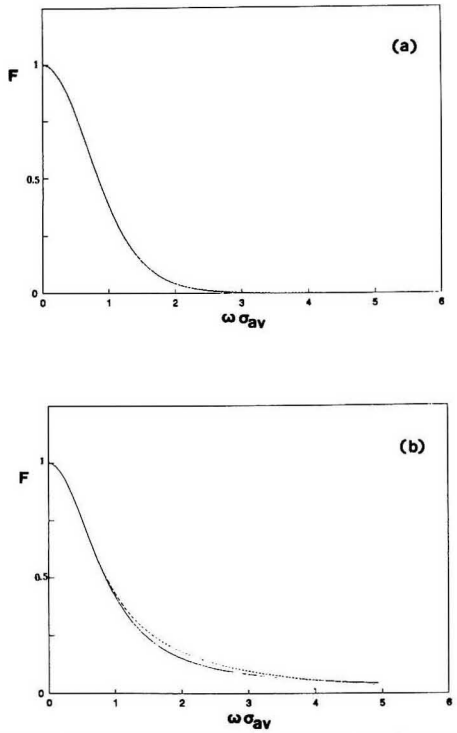

Figure 3. Effect of PW distribution type on PS shape: (a) RSD = 0.2; (b) RSD = 0.5; (continuous line) normal PW distribution; (dashed line) uniform PW distribution.

r = 13.93 if RSD = 0.5, a very high r value indeed. Otherwise RSD values greater than 0.5 for the normal PW distribution are meaningless, since this would imply a significant probability of having negative PW values. It can thus be seen that, for all cases of practical interest, PSs of different distribution types, with common RSD values, in practice yield superimposable profiles and, consequently, the distribution type—whether it be uniform or normal—cannot be inferred from PS analysis. In the following description the uniform distribution type and the linear increase type of PW will be extensively considered.

An extended set of parameter estimation results for simulated chromatograms is presented in Tables II–V. Data refer to chromatograms of 200 SCs, with α values ranging from 0.3 to 1. Two cases of PW variation ratio ($r = \sigma_2/\sigma_1$) were considered: r = 3 and r = 5, respectively. These values correspond to a significant PW variation which could be found under programmed elution conditions. When isothermal gas or isocratic liquid chromatographic elution conditions are followed, even greater PW variations are expected. Nevertheless this topic lies beyond the aims of the present investigation.

The theoretical expression of PS (see eq 11), to which the experimental PS, computed over a simulated chromatogram, is to be fitted in the procedure of nonlinear parameter estimation, contains the SC area dispersion ratio (σ_a/a_a). This quantity cannot be determined from an experimental multicomponent chromatogram where SC peaks cannot be located but only "bands" containing an unknown number of SC peaks can be singled out. The SC area dispersion ratio (σ_a/a_a) was thus estimated through the corresponding quantities determined over detected bands (σ_b/a_b) (see Computation on how bands are detected here). This is the same problem previously faced when the PS method was first set up under conditions of constant PW (2). In that case the SC peak height dispersion ratio was approximated with the peak maxima dispersion ratio.

Data reported in Tables II and III show that the PS method applied to cases of nonconstant PW allows unbiased determination not only of the SC number m but also of the mean PW value, σ_{av}. The latter result is of particular interest since the method is validated once a correct and independent estimate of σ_{av} has been made, e.g. from chromatograms of separated components.

The precision on σ_1 and σ_2 estimation and on their relative ratio r, is lower (see Tables II and III). The bias on r estimation is significant (20–30%), especially at low α values and for the uniform distribution (see Table II). The dispersion on r determination is always around 40–60% (see Tables II and III). In Tables IV and V, results obtained by using correct values of σ_a/a_a instead of σ_b/a_b are reported. It can be seen that congruency of the results is improved with a significant reduction of the bias on r estimation, especially for low α values where the most significant error was previously found. The general conclusion is that the PS method can work even under nonconstant PW effects. Furthermore, better results could be expected if more sophisticated integration routines are employed for better estimation of the peak area dispersion ratio.

The effect of processing separated windows of an extended multicomponent chromatogram—i.e. cases of lower number of detectable SC peaks—is reported in Tables VI–VII for uniform distribution and linear increase of the PW, respectively. As far as the m and the σ_{av} estimates are concerned, it can be seen that the PS method works pretty well even for 50 SCs, meanwhile the estimated σ_2/σ_1 ratio is poorer and the same behavior is exhibited by both the examined PW variation cases.

The reason the PS method is less accurate in determining boundary σ_1 and σ_2 values is explained by analyzing its dependence on r (see Figure 2a). It can be seen that in the region of low $\omega\sigma_{av}$ values, r has no significant influence over PS shape. Only at greater $\omega\sigma_{av}$ values does r dependence appear, but this last part of the PS is less important to the fitting procedure since it is heavily filtered during the the windowing step of the numerical procedure (2).

The point is further exploited by analyzing the limiting expressions of the PS equation at height and low r values. Two boundaries can be calculated for the shape of the PS of a nonconstant PW model. The PS is narrowest when each peak is of the same width (i.e. $\sigma_{av} = \sigma_1 = \sigma_2$). For this case the PS is

$$\lim_{\sigma_1 \to \sigma_2} \frac{A_T^2 \pi^{1/2}}{mX\omega}\left(\frac{\sigma_a^2}{a_a^2} + 1\right)\frac{\operatorname{erf}(\omega\sigma_2) - \operatorname{erf}(\omega\sigma_1)}{\sigma_2 - \sigma_1} = \frac{2A_T^2}{mX}\left(\frac{\sigma_a^2}{a_a^2} + 1\right)e^{-\omega^2\sigma_{av}^2} \quad (32)$$

The other boundary can be set when the ratio of the widest and narrowest peak is infinity (e.g. $\sigma_1 = 0$ and $\sigma_{av} = \sigma_2/2$). Now the PS is

$$F(\omega) = \frac{A_T^2 \pi^{1/2}}{mX}\left(\frac{\sigma_a^2}{a_a^2} + 1\right)\frac{\operatorname{erf}(2\omega\sigma_{av})}{2\omega\sigma_{av}} \quad (33)$$

All the other PSs lie between these two boundaries. It can be seen that eq 29 is the case of constant PW of a Poissonian model (1). The fact that almost all the PSs plotted in Figure 2a can hardly be distinguished below the inflection point

(which appears approximately at or below $\omega = 0.7/\sigma$) and that, in this region, all the considered PS cases of nonconstant PWs which can be approximated by eq 32 can be usefully applied. In fact, this behavior suggests that by using only the frequency interval below the inflection point, the number of components can be correctly estimated even in the case of moderate nonconstant PWs by using the simple model of constant PW (eq 32). Full exploration of this aspect would require a specific setup of the numerical procedure of PS computation, although this point lies beyond the aims of the present work.

What can be done in the present status of both theoretical and numerical development of the PS approach is actually a trial of the application of the model based on the constant PW hypothesis (2) to cases of limited PW variation. Some results of numerical simulations are presented in Table VIII for two cases of PW variations, the normal distribution and the linear increase. It can be seen that both σ_{av} and the m estimation are equally good. Obviously, with this procedure the separated values of σ_1 and σ_2 cannot be estimated.

In conclusion, the PS method performs under an extended set of conditions. Other points will be explored, such as peak position patterns other than Poisonian or complex noise structure effects other than the white noise (2). These points, however, deserve separate handling.

GLOSSARY

a	single-component peak area
a_a	mean value of single-component peak area
a_b	mean value of the separate bands (see Computation)
a_n	estimated peak value of single-component peak area
$a_n{}^k$	area of the nth single-component peak in the kth representation of the chromatogram as stochastic process
A	slope parameter of function of linear peak broadening
A_{max}	maximum single-component peak area
A_{min}	minimum single-component peak area
A_T	total area of the multicomponent chromatogram
B	intercept parameter of function of linear peak broadening
$C_{xx}(\mathbf{k})$	numerically computed autocovariance function at point $\mathbf{k}$
$E\{\}$	expected value of the quantity
erf	error function
$f(\xi)$	frequency function of the variable ξ
$F(\omega)$	PS value at frequency ω
$g(\omega,\sigma)$	Fourier transform of a unit area peak of width σ when shifted to the origin
$\theta(\omega)$	characteristic function of the interdistance between subsequent SC peak positions
$K(\omega)$	part of the PS not dependent on peak position
$L(\omega)$	part of the PS dependent on peak position
m	retention time
$m_n{}^k$	as above but referred to the nth component in the kth representation in the chromatogram as stochastic process
m	number of single components
M	truncation point in the ACVF computation
N	ensemble parameter referred to the number of components $(2N + 1)$
N	number of theoretical plates
N_c	peak capacity
PS	power spectrum
PW	SC peak standard deviation
$q_{n-j}(\omega)$	part of the PS dependent on retention time referring to all the possible interdistances between components n and j
r	ratio of the width of the widest and narrowest peak present in the chromatogram (σ_2/σ_1)
Re	real part
RSD	relative standard deviation of the normal PW distribution (s/σ_{av})
R_s	chromatographic resolution (0.5)
s	standard deviation of the normally distributed peak widths
SC	single component
t	time axis
T	mean value of interdistances between adjacent single-component peaks
$u(t,m,\sigma)$	function of the single-component peak shape
V_r	retention volume
X	time range of the chromatogram
$Y^k(t)$	kth representation of the multicomponent chromatogram
$Z_N{}^k(\omega)$	Fourier transform of $Y^k(t)$
α	Saturation factor (m/N_c)
σ	peak width parameter of the Gaussian peak
σ_1	peak width parameter of the narrowest peak present in the chromatogram
σ_2	peak width parameter of the widest peak present in the chromatogram
σ_a	standard deviation of single-component peak areas
σ_{av}	average peak width
σ_b	standard deviation of separate bands
$\theta(\omega)$	characteristic function
ξ	random variable
ω	frequency
$w(\mathbf{k})$	weight function

LITERATURE CITED

(1) Felinger, A.; Pasti, L.; Dondi, F. *Anal. Chem.* **1990**, *62*, 1846.
(2) Felinger, A.; Pasti, L.; Reschiglian, P.; Dondi, F. *Anal. Chem.* **1990**, *62*, 1854.
(3) Davis, J. M.; Giddings, J. C. *Anal. Chem.* **1983**, *55*, 418.
(4) Martin, M.; Guiochon, G. *Anal. Chem.* **1985**, *57*, 289.
(5) Davis, J. M.; Giddings, J. C. *J. Chromatogr.* **1984**, *289*, 277.
(6) Davis, J. M.; Giddings, J. C. *Anal. Chem.* **1985**, *57*, 2168.
(7) Davis, J. M.; Giddings, J. C. *Anal. Chem.* **1985**, *57*, 2178.
(8) Herman, D. P.; Gonnord, M. F.; Guiochon, G. *Anal. Chem.* **1984**, *56*, 995.
(9) Martin, M.; Herman, D. P.; Guiochon, G. *Anal. Chem.* **1986**, *58*, 2200.
(10) El Fallah, M. Z.; Martin, M. *Chromatographia* **1987**, *24*, 115.
(11) F. Dondi, unpublished results.
(12) Blanc-Lapierre, A.; Foret, R. *Theory of Random Functions*; Gordon and Breach, Science Publishers: New York 1965; Vol. 1, p 150.
(13) Bracewell, R. N. *The Fourier Transform and Its Applications*; McGraw-Hill: New York, 1986.
(14) Feller, W. *An Introduction to Probability Theory and Its Applications*, 2nd ed.; John Wiley & Sons: New York, 1971; Vol. II.
(15) Jenkins, G. M.; Watts, D. G. *Spectral Analysis and Its Applications*; Holden-Day: San Francisco, 1968.
(16) Abramovitz, M.; Segun, I. A. *Handbook of Mathematical Functions*; Dover Publications: New York, 1965.

RECEIVED for review May 15, 1991. Accepted August 19, 1991. This work was made possible by the financial support of the Italian Ministry of the University and the Scientific Research (MURST), the Italian Research Council (CNR), and the Hungarian Academy of Science.

Hydrolytically Stable Bonded Chromatographic Phases Prepared through Hydrosilation of Olefins on a Hydride-Modified Silica Intermediate

Junior E. Sandoval* and Joseph J. Pesek

Department of Chemistry, San Jose State University, San Jose, California 95192

A novel method for the preparation of bonded stationary phases is described in which a hydrocarbonaceous moiety is bound to silica surfaces through a direct silicon–carbon linkage. An established method involving the chlorination and reduction of silica was used to prepare an intermediate material containing fairly stable silicon hydride species. In the present report, such an intermediate was reacted with terminal vinyl organic functionalities in the presence of a platinum catalyst. IR and NMR spectroscopic evidence confirmed the attachment of hydrocarbonaceous ligands onto the silica surface. Typical alkyl surface densities were 4.4 and 2.5 μmol/m² for octyl and octadecyl groups, respectively. The extent of coverage was found to be strongly dependent on olefin concentration and reaction temperature. When compared to the corresponding organosilanization product, the bonded silica was shown to have improved hydrolytic stability toward aqueous solutions containing trifluoroacetic acid.

INTRODUCTION

Organosilanization, a surface-modification procedure derived from "silane-coupling" methodology (*1*), may now be considered a well-established synthetic technique for the preparation of high-performance liquid chromatography (HPLC) column packings. Typically, porous, particulate silicas are reacted with organosilanes to yield an Si–R functionality attached to the support through an Si–O–Si (siloxane) linkage:

$$|\text{Si–OH} + \text{R}_{4-n}\text{SiX}_n \rightarrow |\text{Si–OSiX}_{n-1}\text{R}_{4-n} + \text{HX} \quad (1)$$

Where n = 1–3, R is an alkyl or substituted alkyl group, X is an easily hydrolyzable group such as halide, amine, alkoxy, or acyloxy, and the vertical line represents the support's surface. When di- or trifunctional silanes (n = 2, 3) are reacted with silica in the presence of a known amount of water, an organic layer is formed, the thickness of which may vary according to the reaction conditions. Traditionally, these so-called "polymeric" bonded phases have been considered disadvantageous with respect to their monomeric (n = 1) counterparts, presumably because of difficulties associated with control of the polymerization process which frequently results in irreproducible phase thickness and limited column efficiency (*2, 3*). Additionally, they show a tendency to contribute additional silanols to the bonded phase because, due to steric constrains, only a fraction of the silanol groups formed upon hydrolysis is eliminated via condensation. More recently, however, improved polymeric bonded phases have been prepared and shown to provide not only synthesis reproducibility comparable to that of monomeric bonded phases but also a better separation toward certain polyaromatic hydrocarbon mixtures (*4*).

When a monofunctional silane is used, only a single surface–silane linkage is possible and, consequently, an intrinsically reproducible monolayer is formed. A vast majority of commercially available reversed phases are prepared using chlorodimethylalkylsilane reagents, according to the reaction

$$|\text{Si–OH} + \text{Cl–Si(CH}_3)_2\text{–R} \xrightarrow[\text{solvent}]{\text{base}} |\text{Si–O–Si(CH}_3)_2\text{–R} + \text{HCl} \quad (2)$$

Monomeric bonded phases can also be prepared by reaction of silica under rigorously anhydrous conditions with polyfunctional silanes. They have the shortcoming, though, that residual X groups can be readily hydrolyzed when exposed to aqueous mobile phases, and therefore also contribute additional silanols to the phase.

Bonded silicas produced from monofunctional silanes have been the most thoroughly studied and have found wide use in a variety of analytical as well as preparative applications. The extensive usage of these bonded materials does not necessarily imply that they meet all requirements with respect to column stability and performance. On the contrary, monomeric bonded phases are subject to serious effects arising primarily from an unsatisfactory hydrolytic stability of the Si–O–Si–C linkage, particularly under moderately acidic or slightly alkaline elution conditions, and to a lesser extent from a relatively limited organic coverage. Poor hydrolytic stability and incomplete surface coverage both result in the exposure of a substantial number of surface silanols, groups which are thought to be primarily responsible for the residual adsorption phenomena that plague silica-based separation materials (*5*). One of the most striking cases of these "silanophilic" interactions occurs perhaps in the separation of certain compounds containing amino or other similar groups, particularly biomolecules. For instance, many proteins may interact very strongly with unreacted silanols leading to excessive band tailing or incomplete recovery of one or more solutes.

The problem of limited stability of the Si–O–Si–C linkage in current bonded phases has received a lot of attention in recent years (*6–10*). For instance, to achieve satisfactory reversed-phase separations of certain proteins, it is often desirable to incorporate in the mobile phase dilute aqueous solutions such as phosphate, at pH 2–3, or trifluoroacetic acid (*6, 7*). These mobile phases have been shown to be particularly aggressive toward the bonded ligand and, with virtually no exception, lead to the gradual loss of a significant fraction of the bonded material and a concomitant increase of silanol exposure. Poor long-term precision and potential fraction contamination are the two most evident deleterious effects arising from phase deterioration. Fraction contamination can be particularly disadvantageous in the case of preparative separations.

In an effort to overcome such problems, other organosilane reagents have been developed. Two related approaches have been proposed in which either the methyl groups of the organosilane reagent (eq 2) were replaced by bulkier groups or a "bidentate" silanizing reagent was used (*11–13*). In both cases the new groups serve to shield the unreacted silanols as well as the hydrolytically labile linkage that bonds the silane to the support. Although this steric protection has resulted in significantly improved bonded phases, the synthetic pro-

0003-2700/91/0363-2634$02.50/0

cedures still involve the formation of hydrolytically unstable Si–O–Si–C linkages.

In a different approach, bonded silicas bearing direct Si–C linkages have been developed (*14–16*). They involve the sequential reaction of the silica substrate with a chlorinating reagent (e.g., thionyl chloride) and a proper alkylating reagent (e.g., a Grignard or organolithium compound):

$$|\text{Si–OH} \xrightarrow{\text{SOCl}_2} |\text{Si–Cl} \xrightarrow{\text{R–M}} |\text{Si–R} \qquad (3)$$

where –M = –Li or –MgBr. In principle, this method should provide not only a closer attachment and a denser coverage of organic functionalities but also a more hydrolytically stable bonded phase than that obtained by the corresponding Si–O–Si–C linkage. However, the wide usage of a chlorination/Grignard or chlorination/organolithium reaction scheme as a routine method to modify silica substrates has been hindered by several factors. One factor is that the two-step halogenation/alkylation sequence is significantly more difficult to carry out than the one-step organosilanization procedure. Difficulties associated with the removal of residual salts which may be occluded in the porous silica matrix during the alkylation process is also an important factor which has contributed to the limited usage of this synthetic approach. Finally, but no less important, the preparation of the alkylation reagent exhibits strong interferences with many reactive functionalities. As clearly pointed out by Morisson and Boyd (*17*), "the great reactivity which makes a Grignard reagent so useful in many synthetic approaches seriously limits its applicability". The organic group, R, in the Grignard reagent reacts with acidic groups to form the corresponding hydrocarbon species R–H. Additionally, it readily adds to carbon–oxygen or carbon–nitrogen multiple bonds. It seems clear therefore that only a very limited number of organic functionalities may be present in the halide compound from which a Grignard reagent can be prepared. Being even more reactive than the corresponding Grignard reagent, an organolithium reagent should exhibit the same limitations described above to a similar or greater extent. Such limitations, of course, greatly hinder the versatility of this approach. It is therefore desirable to address the shortcomings of existing bonded packings by applying an alternate silane chemistry which should combine the superior coverage and hydrolytic stability of direct Si–C linkages with the preparation simplicity of organosilanization.

Because of its minimal interferences with many reactive organic functionalities and the relative ease with which it is carried out, the catalytic hydrosilation (addition of silicon hydride, SiH) of terminal olefins represents a promising alternative to produce bonded chromatographic phases, provided that a suitable support containing surface silane species is available. In a previous work we prepared such an intermediate support by sequentially chlorinating and reducing silica with $SOCl_2$/toluene and $LiAlH_4$/ether, respectively. Treatment of the "reduced" silica with dilute HCl then follows to remove chemisorbed aluminum byproducts (*18, 19*).

Hydrosilation is normally carried out in the presence of a metal catalyst. A variety of inorganic and organic complexes of transition metals such as platinum, rhodium, palladium, ruthenium, iridium, and nickel (group VIII) appear to be very effective catalysts for the reaction. The catalyst often consists of a solution of a halide, olefin, carbonyl, or phosphine complex of the transition metal. A 2-propanol solution of hexachloroplatinic acid ("Speier's catalyst") is one of the most commonly used forms. Normally 10^{-7} to 10^{-4} mol of platinum/mol of silicon hydride is sufficient for an effective hydrosilation. An "induction period" is often required before the addition becomes manifest. Then, a highly exothermic reaction occurs, which, when relatively large amounts are involved, may lead to hazardous situations if heat is not efficient and rapidly dissipated. For simple liquid olefins no additional solvent is normally required. For highly reactive olefins (particularly those with a strong tendency to polymerize, e.g., methacrylates, epoxides, etc.) a solvent such as toluene, benzene, saturated hydrocarbons, chloroform, etc. is normally used. In general, the reaction is conveniently carried out under dry conditions, at temperatures ranging from ambient to a full reflux. Typically, an excess of the olefin with respect to the available silicon hydride groups is used. The magnitude of such an excess depends on the nature of the substituents in the olefin. Highly reactive reagents (epoxy-containing olefins, for instance) require a 10–50% molar excess while simple (unsubstituted) olefins usually permit a 10-fold molar excess or more.

The most important goal of this work is to explore the feasibility of preparing bonded phases via hydrosilation of olefins on a hydrosilane-containing silica support:

$$|\text{Si–H} + \text{CH}_2{=}\text{CH–R} \xrightarrow{\text{Pt cat.}} |\text{Si–CH}_2\text{CH}_2\text{–R} \qquad (4)$$

The heterogeneous reaction should result in the formation of an anti-Markovnikov adduct at the silica surface.

EXPERIMENTAL SECTION

Materials. 1-Octene (Aldrich Chemical Co.) and 1-octadecene (Sigma Chemical Co.) were used as received. When required, toluene and other solvents (EM Industries Inc.) were dried with calcium hydride and distilled before use. Trifluoroacetic acid (TFA) was also used as received. A 100 mM hexachloroplatinic acid (37.5% as Pt, Aldrich Chemical Co.) solution in 2-propanol and a 50 mM dicyclopentadienylplatinum(II) chloride solution in chloroform were used as catalysts for hydrosilation. The diolefin–Pt(II) complex was prepared according to Apfel et al. (*20*). The method, based on procedures developed by Drew and Doyle (*21*), involved the reaction of hexachloroplatinic acid and dicyclopentadiene in aqueus acetic acid solution. Bonded phases were prepared from single batches of 40 μm particle diameter Partisil-40 (Whatman Inc., Clifton, NJ) and 5.6 μm Vydac 101TPB (Separations Group, Hesperia, CA). The specific surface area and mean pore diameter (Brunauer–Emmett–Teller (BET) nitrogen adsorption) were determined as 315.3 m^2/g and 90.3 Å, respectively, for Partisil-40 and 88.8 m^2/g and 334 Å for Vydac 101TPB.

Instrumentation. The spectrometric methods used have been previously described (*18*). The BET isotherms were obtained with a Micromeritics Model ASAP 2400 at Chevron Research and Technology (Richmond, CA). Carbon determinations were made at the Department of Chemistry, University of California (Berkeley, CA) by a conventional combustion method. Precision of the carbon determination was evaluated by repeated submission of the same sample over a period of about 6 months. A relative standard deviation of ±1.2% resulted for a total of 10 independent measurements.

Silica Derivatization. Hydride silica intermediates were prepared by a chlorination/reduction sequence on the native silica according to a procedure previously described (*18, 19*). Prior to hydrosilation, the hydride silica was dried at 110 °C for 6 h or more. In a typical preparation of an octyl-bonded silica, 75 mL of 1-octene (density 0.715 g/cm^3, 97% purity) containing 255 μL of freshly prepared 100 mM hexachloroplatinic acid solution in 2-propanol was heated to about 60–70 °C while being agitated magnetically for about 1 h (a clear solution was obtained after about 15–20 min of mixing). A 5-g sample of hydride intermediate substrate was then slowly added to the olefin/catalyst solution, and the reaction was allowed to proceed for at least 24 h at 100 ± 2 °C. The mixture was then centrifuged and the solid washed with three 40-mL portions of toluene followed by similar washings with dichloromethane and diethyl ether. After the solvent was removed, the solid was dried under vacuum at 110 °C overnight. A similar procedure, this time with 1-octadecene (density 0.79 g/cm^3, 99% purity) instead of 1-octene, was followed to prepare an octadecyl-bonded silica. Alternatively, an equivalent molar amount of 50 mM dicyclopentadienylplatinum(II) chloride in chloroform was used as catalyst. When required, conventional octyl- and octadecyl–dimethylsilyl silicas were prepared from

Partisil-40 according to the procedures described by Berendsen et al. (*22*, *23*).

Long-Term Hydrolytic Stability Test. A 0.75-g amount of bonded phase material was suspended in 1 mL of dioxane by magnetically stirring for 5 min. Then, 40 mL of an aqueous 0.1% v/v TFA solution containing 20% v/v dioxane was carefully added. The mixture was magnetically agitated at room temperature for 12 h. After this period, a 2-mL aliquot of the well-agitated suspension was taken and the liquid of the remaining mother suspension was removed by centrifugation. A fresh treating solution was added and the hydrolysis continued for a new 12-h period. After each sampling, the volume of the treating solution was decreased so as to maintain a constant liquid-to-solid ratio during the entire process. The procedure was repeated over a total time of about 100 h. The silica from each 2-mL aliquot sample was washed consecutively with 3-mL portions of 1:1 v/v THF/water, THF, and finally diethyl ether. The solid was dried at 110 °C under vacuum for several hours and its remaining carbon content determined. The decrease in carbon content (percent by weight), or its corresponding molar surface coverage (μmol/m^2), is a direct measure of the loss of bonded material from the support. The test was performed on an octyl-bonded silica prepared using (hydrided) Vydac 101TPB as the support. For comparison purposes, a parallel test was also performed on a commercially prepared (via a conventional silanization procedure) non-end-capped octyldimethylsilyl–silica. The starting silica support was the same for both the commercial batch and the hydrosilation product.

Surface Coverage. The concentration, α_R, of surface-bonded groups was obtained from the carbon content of the bonded material along with the BET specific surface area of the substrate before bonding (i.e., the hydride intermediate). Since the hydride–silica intermediate is a surface-modified substrate, a *monolayer* of organic groups should result from surface hydrosilation and, therefore, the equation proposed by Berendsen and de Galan (*22*) can be used:

$$\alpha_R\ (\mu\text{mol/m}^2) = 10^6 p_c/(10^2 M_c n_c - p_c M_R) S_{BET} \qquad (5)$$

where p_c is the carbon percentage by weight of the bonded material (after correction from any carbon present before bonding), n_c is the number of carbon atoms in the bonded organic group (in this case, the olefin), S_{BET} is the specific surface area (m^2/g) of the hydride substrate, M_R is the molecular weight of the olefin, and M_c is the atomic weight of carbon. Notice that since the bonding reaction is an *addition*, the atomic weight of hydrogen (M_H) does not need to be subtracted from the molecular weight of the bonded molecule as in the case of conventional organosilanization in which one hydrogen atom is lost during the surface (substitution) reaction (*22*). Additionally, the S_{BET} value does not refer to the original (native) silica but rather to the hydride intermediate.

RESULTS AND DISCUSSION

Spectroscopy. The substantial structural changes taking place on the silica surface (namely, formation of Si–C linkages at the expense of Si–H species) permit unequivocal characterization of the addition product by spectroscopic as well as chemical methods. Figure 1 shows the DRIFT spectral changes that take place upon silica derivatization, from a native substrate (curve A), through the hydride intermediate (curve B), to an octyl (curve C) or octadecyl (curve D) bonded phase. The appearance of strong stretching bands in the 3000–2800-cm^{-1} region concomitant with a substantial decline of the Si–H stretching band at 2260 cm^{-1} clearly indicates chemical bonding to the silica surface.

Another way of proving that the olefins indeed undergo Si–H addition at the silica surface is by means of solid-state NMR spectroscopy. Figures 2 and 3 show the ^{13}C cross polarization-magnetic angle spinning (CP-MAS) NMR spectra of the octyl- and octadecyl-bonded phases. On the basis of previous reports of studies involving conventional bonded silicas (*24*, *25*), resonance positions can be readily assigned. The peak positions are virtually the same for both bonded silicas, as expected, with only changes in intensity due to the difference in chain length. The peak near 12 ppm can be

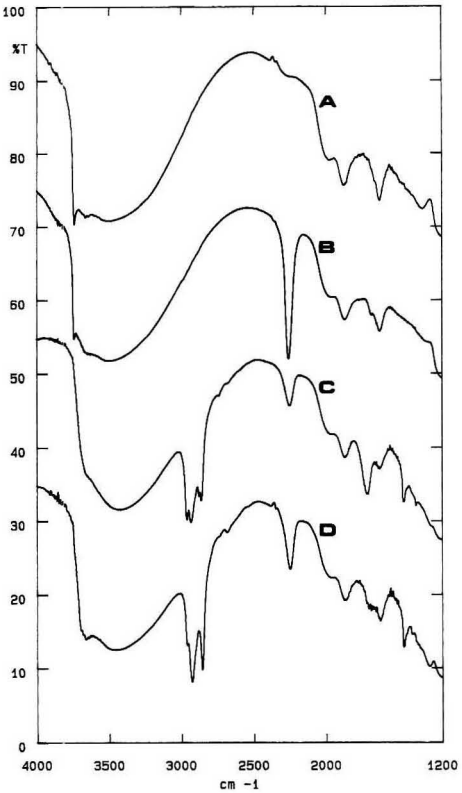

Figure 1. Partial DRIFT spectra of a silica (Partisil-40) after derivatization: (A) native silica; (B) hydride intermediate prepared via a chlorination/reduction sequence; (C) octyl-bonded phase; (D) octadecyl-bonded phase. For better illustration, the ordinates were contracted by a common factor and the curves were moved downward. Ordinate units are therefore arbitrary.

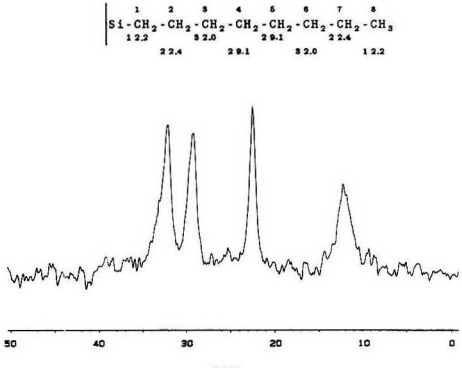

Figure 2. ^{13}C CP-MAS NMR spectrum of an octyl-bonded phase.

assigned to the combined contributions from the terminal methyl group of the alkyl chain (C_8 and C_{18} for octyl- and octadecyl–silica, respectively) and the methylene group which

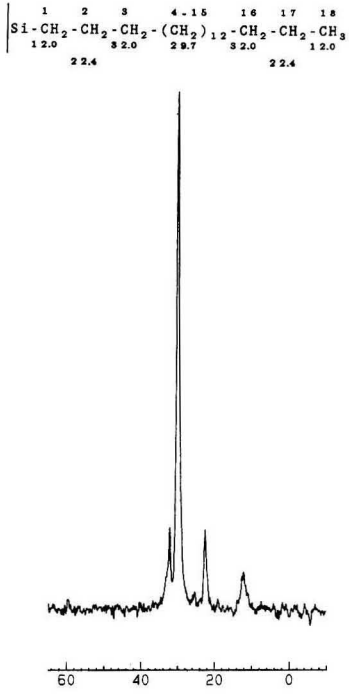

Figure 3. ^{13}C CP-MAS NMR spectrum of an octadecyl-bonded phase.

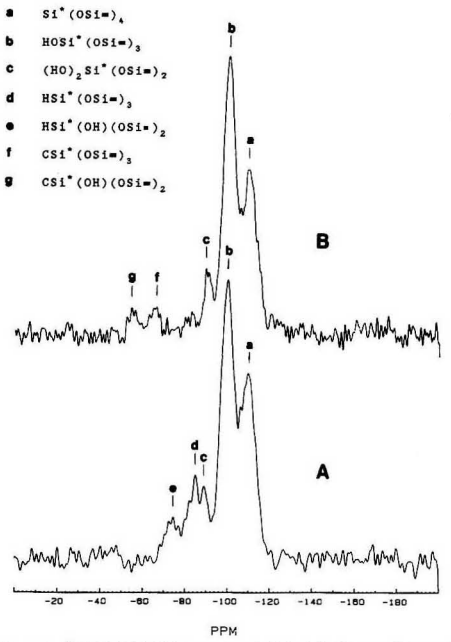

Figure 4. ^{29}Si CP-MAS NMR spectra of (A) hydride intermediate and (B) octyl-bonded silica.

is directly attached to the surface silicon atom (C_1 for both silicas), i.e. the carbon involved in the direct bonding of the terminal olefin to the hydride in the hydrosilation reaction. The peak at 22.4 ppm can be assigned to $C_2 + C_7$ (octyl–silica), and $C_2 + C_{17}$ (octadecyl–silica) composites, while the resonance at 32.0 ppm can be assigned to $C_3 + C_6$ (octyl) and $C_3 + C_{16}$ (octadecyl) composites. The peak near 29 ppm is a composite which represents the remainder of the alkyl chain, i.e., carbon atoms $C_4 + C_5$ (octyl), and C_4 through C_{15} (octadecyl). The last peak, of course, is the dominant absorption in the octadecyl–silica spectrum. It is not surprising that the ^{13}C CP-MAS NMR spectra of our bonded materials closely resemble those of the corresponding polymeric bonded silicas (*24*), since both contain a single type of alkyl group attached to silicon.

With ^{29}Si CP–MAS NMR spectrometry it is possible to obtain further insight into the structure of the hydride intermediate as well as the C_8 and C_{18} product phases. Curve A of Figure 4 is the spectrum of the hydride intermediate showing five distinct peaks. Three of them have been observed in several previous studies (*26*, *27*). These are the peaks at −110.4 ppm, which represents framework Si*(OSi≡)$_4$ structures, −100.9 ppm, which represents surface single silanols, HOSi*(OSi≡)$_3$, and −89.3 ppm, which represents surface geminal silanols, (HO)$_2$Si*(OSi≡)$_2$. The new peak at −85.3 ppm in the spectrum can be assigned to the hydride H—Si*(OSi≡)$_3$ species, in agreement with the resonance at −85.5 ppm observed by Engelhardt et al. on an oligomeric hydrosiloxane material, $(HSiO_{3/2})_8$ (*28*). The other new resonance at about −74.8 ppm can be tentatively assigned to the H—Si*(OH)(OSi≡)$_2$ group. Curve B of Figure 4 shows the ^{29}Si CP-MAS NMR spectrum for the C_8 product. The three peaks at −110.2, −100.2, −100.8, and −89.9 ppm are as described above. The peaks near −85 and −75 ppm have virtually disappeared due to the bonding reaction. Two new peaks at −66.2 and −54.6 ppm have now appeared in the spectrum. These have been previously assigned to CSi*(OSi≡)$_3$ and C(HO)-Si*(OSi≡)$_2$, respectively (*27*). The spectrum of the C_{18} phase (not shown) exhibits the same characteristics as the spectrum of the C_8 product described above. In all cases for ^{29}Si CP-MAS NMR spectra, the relative intensities of the peaks vary considerably depending on the contact time used (*26*).

Surface Coverage. A typical plot of alkyl surface coverage as a function of reaction time at 100 ± 2 °C is shown in Figure 5. Similarly with other surface modification processes, a major fraction of the total surface coverage occurs during the early stages of the reaction, while at longer times, increases in surface coverage are progressively less pronounced. Figure 5 also suggests a decrease in alkyl coverage with increasing carbon chain length (curve A vs B). This observation should, however, be interpreted with caution. Both olefins, 1-octene and 1-octadecene, were used as neat liquids. Their molar concentrations are about 6.18 and 3.10 M, respectively, being in a ratio of 1.99 at room temperature (assuming a similar thermal expansion coefficient for both olefins, this ratio should not be significantly different at the reaction temperature). The corresponding ratio of surface coverages, $\alpha_{octyl}/\alpha_{octadecyl}$, is approximately constant (as suggested by the close parallelism of the two curves) averaging 1.89 ± 0.14 (nine data points), a value which approaches that of the molarity ratio. This finding suggests independence of hydrosilation yield from carbon chain length, a behavior which appears to oppose that of conventional silanization (*29*, *30*). Additional experimental evidence should be obtained to further substantiate this point. Equality of coverage and concentration ratios also suggests first-order kinetics with respect to the olefin. Indeed, a roughly linear relationship was found between surface coverage and

Table I. Surface Coverages of Bonded Silica Phases[a]

silica support	S_{BET}, m^2/g	anchored group	n	M_R	% C	α_R, $\mu mol/m^2$
Partisil-40	296.7	$-C_8H_{17}$	8	112.22	11.00	4.43
Partisil-40	315.3	$-OSi(CH_3)_2C_8H_{17}$	10	170.37	12.85	4.15
Partisil-40	296.7	$-C_{18}H_{37}$	18	252.49	13.40	2.48
Partisil-40	315.3	$-OSi(CH_3)_2C_{18}H_{37}$	20	310.64	20.45	3.67
Vydac 101TPB	89.1	$-C_8H_{17}$	8	112.22	2.10	2.51
Vydac 101TPB	88.8	$-OSi(CH_3)_2C_8H_{17}$	10	170.37	1.78	1.71

[a] As defined for eq 5.

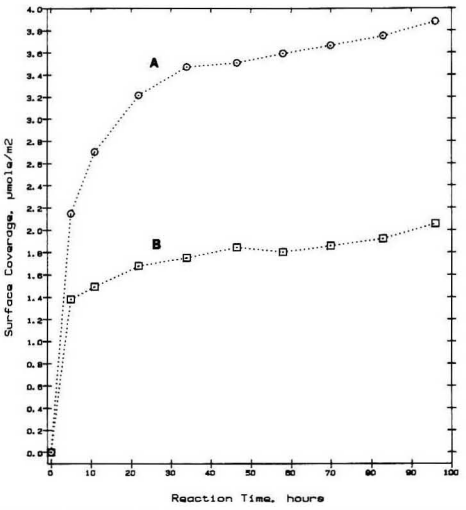

Figure 5. Effect of reaction time on alkyl surface coverage for the hydrosilation of (A) 1-octene and (B) 1-octadecene on a hydride-modified silica (Partisil-40).

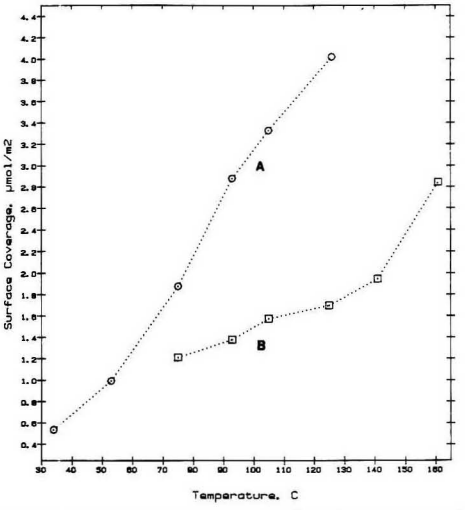

Figure 6. Surface coverage as a function of reaction temperature of the hydrosilation of (A) 1-octene and (B) 1-octadecene on a hydride-modified silica (Partisil-40) with a 20-h reaction time.

olefin concentration (linear fitting results for 1-octadecene were intercept = 0.04 ± 0.08, slope = 0.45 ± 0.04, R^2 = 0.9791).

Surface coverage is also strongly dependent on the temperature of reaction, as illustrated by Figure 6. The data advocate the use of high reaction temperatures to obtain maximum surface coverage. The highest allowed temperature is, however, limited by the boiling point of the liquid olefin and the thermal stabilities of the olefin, the product, and particularly, the catalyst. It was observed that for a 24-h hydrosilation darkening of the product was appreciable at about 110 °C, being more pronounced on the C_{18} phase at higher temperatures and with longer reaction times. It has been known that hydrosilation may be accompanied by some darkening of the reaction mixture, concomitant with a decline of catalyst activity (*31–33*). The observation has been attributed to irreversible reduction of the metal catalyst by the hydrosilane. The extent of catalyst reduction depends on the reaction temperature and the nature of the transition metal and complexing ligands, as well as the structure of the hydrosilane and the olefin. Presumably, the metal precipitates in the form of extremely fine particles which, in the case of the hydride-modified silica, may remain trapped inside the porous support. Although extensive darkening of the bonded silica product was observed, Figure 6 also suggests that, even at the higher temperatures used, the catalyst was still active. When electron spectrometry for chemical analysis (ESCA) was used to examine the bonded products, only one of the octadecyl–silicas (datum for 140 °C) exhibited traces of platinum (the detection limit of the instrument used was about 0.2 atom %). Whether the presence of minute amounts of platinum adversely affects the chromatographic performance of the bonded silicas has not been yet determined. The eventual lack of such a deletereous effect would not be without precedent: when investigating the in situ bonding of alkyldimethylchlorosilanes (prepared via olefin hydrosilation with dimethylchlorosilane) on silica, Shih-Hsien et al. (*34*) found that the presence of adsorbed platinum did not have any observable effect on the bonded phase's performance.

A reaction temperature of about 100 °C along with 60 h of reaction time were routinely used during this preliminary work. Table I shows typical alkyl surface coverages obtained from hydrosilation on two different silicas. For comparison purposes, coverages obtained from conventional silanization on the same batches of silica are also shown. It can be seen that, for a given silica substrate, somewhat improved surface group density was obtained from hydrosilation in the case of C_8 bonded materials. On the other hand, conventional organosilanization appears to perform better in the case of C_{18} phases. Note, however, that the coverage values obtained through conventional organosilanization appear to be near the upper end of the range normally found in the literature (roughly, 3.0–4.0 and 2.5–3.5 $\mu mol/m^2$ for C_8 and C_{18} packings, respectively) (*23, 30*). Additionally, it should be recalled that uncertainties for calculated α_{alkyl} values are normally around 5% and in some cases as high as 10%.

Surprisingly enough, Table I also suggests that, for hydrosilation as well as organosilanization, a narrower pore silica resulted in greater octyl coverages. In the case of hydrosilation,

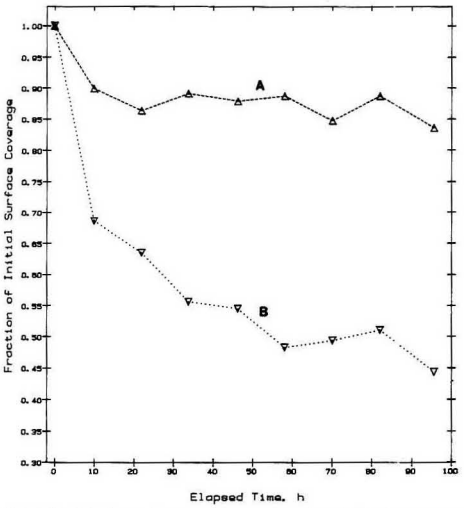

Figure 7. Relative surface coverage of octyl-bonded Vydac 101TPB silicas as a function of hydrolysis time. Prolonged treatment was at room temperature in 0.1% v/v TFA aqueous solution containing 20% v/v dioxane: (A) octyl–silica prepared by hydrosilation; (B) octyl–dimethylsilyl silica by silanization from a commercial procedure.

a cursory examination of the DRIFT spectrum of the C_8-bonded wide-pore support (not shown) reveals that no remaining Si–H stretching band was present; i.e., virtually all the silicon hydride groups were consumed by the reaction with the olefin. A C_{18} product from the same substrate showed the same spectral characteristic. Therefore, the low availability of hydride sites rather than a lack of efficiency in hydrosilation appears to be the factor limiting alkyl coverage on wide-pore Vydac TPB silicas. If one assumes that, compared to their isolated counterparts, associated silanols exhibit a lower reactivity toward chlorination *and* organosilanization, then the unusually low yields on wide-pore Vydacs can be readily rationalized in terms of the predominantly associated silanol population on these silicas (*35*, *36*).

The use of equivalent amounts of dicyclopentadienylplatinum(II) chloride instead of Speier's catalyst resulted essentially in the same level of surface coverage, provided that other reaction conditions remained the same.

Hydrolytic Stability. Assuming that good column-handling practices are observed by the chromatographer, hydrolytic stability of a reversed-phase packing is perhaps the most important factor determining the frequency with which columns are discharged after use. Due to the superior hydrolytic stability of the Si–C bond as compared to that of Si–O–Si–C linkages, we anticipated improved stability for the hydrosilation product over that of the organosilanization analogue. In order to estimate the extent of bonded-phase deterioration, selected bonded materials were subjected to prolonged exposure to a water/dioxane solution containing 0.1% v/v TFA. The amount of remaining bonded ligand was obtained from elemental carbon determinations on sample aliquots periodically taken from the reaction vessel. The plot in Figure 7 clearly shows that the rate of degradation of the silica modified via hydrosilation (present work) is significantly lower than that of the same substrate modified via organosilanization. At the end of the test, the commercial product had lost about 50% of its initial coverage while, under identical conditions, the hydrosilation product lost only about 15% of its starting alkyl load. It should also be noticed in Figure 7

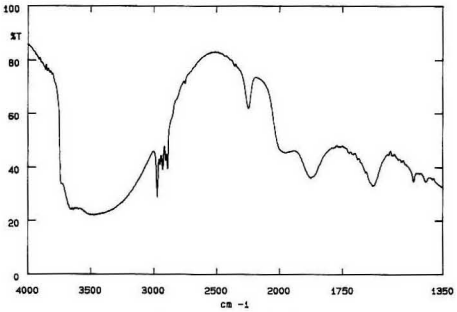

Figure 8. Partial DRIFT spectrum of a hydride-modified silica (Partisil-40) reacted with ethylene gas. C–H stretching bands are at 2971 cm^{-1} (CH_3, antisymmetric), 2950 cm^{-1} (CH_2, antisymmetric), 2929 and 2904 cm^{-1} (CH_3, symmetric), and 2890 cm^{-1} (CH_2 symmetric). C–H bending bands are at 1467 and 1418 cm^{-1}.

that a major fraction of the total losses occurs during the early stages of the long-term hydrolysis. This is in good agreement with the observations of Kirkland and co-workers (*7*, *13*) when monitoring the loss of chromatographic retention for a number of bonded silicas.

Hydrosilane "End-Capping". Similarly with any surface modification procedure, the sites of the bonding reaction will eventually become sterically hindered at some point and, consequently, not all of the Si–H sites will be converted to Si–C. In some instances, it may be desirable to remove as many of the remaining hydrides as possible by means of a "hydride end-capping" procedure which follows the primary bonding reaction. Ethylene gas can be conveniently used for this purpose since it offers the smallest possible steric hindrance in olefin addition. Once the main bonding reaction is considered complete, the ethylene gas can be introduced into the reactor and maintained at high pressure. The reaction can then be continued for an additional period of time. The need for hydride end-capping might be particularly critical when aqueous alkaline solutions are used. Under these conditions and the assumption that efficient shielding is not provided by the bonded alkyl groups, hydride groups can be rapidly hydrolyzed, generating hydrogen gas, with deleterious effects occurring during the course of a separation. Under acidic conditions, on the other hand, silicon hydride groups are virtually indefinitely stable and, therefore, hydride end-capping may not be necessary.

In order to explore the feasibility of hydrosilane end-capping with ethylene, a C_2-bonded silica was prepared by merely bubbling the gas through a hydrided silica/toluene suspension containing dicyclopentadienylplatinum(II) chloride catalyst, at 60 °C for 18 h. Addition of the hydride silica was preceded by an induction period of about 1 h at the same temperature. The resultant product had an ethyl coverage of about 2.3 $\mu mol/m^2$, an acceptable value, given the mild reaction conditions (pressure and temperature) used. Its DRIFT spectrum (see Figure 8) depicts a number of C–H stretching and bending bands in good agreement with previously reported data for silicon–ethyl linkages (*37*).

Versatility of Hydrosilation. In general, the hydrosilation reaction has a great deal of versatility. This is due to the fact that relatively few reactive functionalities interfere with the olefinic addition. Thus, catalytic hydrosilation can be used to attach to silicon organic moieties containing a wide variety of functional groups such as alkyl, nitrile, amine, epoxy, etc. (*38*, *39*). Although the ester group does not seem to interfere with the hydrosilation reaction, addition to the carbonyl group of aldehydes and ketones frequently takes

place. This seems to be particularly true for α,β-unsaturated carbonyls. A similar behavior is exhibited by unsaturated nitriles as well as epoxides of 1,3-dienes. By using olefins whose C=C bond is separated from the heteroatom unsaturation by at least a methylene ($-CH_2-$) group, normal 1,2-addition can be readily achieved. It should be pointed out that, in fact, the great versatility of the existing organosilanization methodology (eq 1) is largely due to the freedom from interference of the hydrosilation reaction. Such a reaction is the most commonly used method to prepare a great variety of organosilanization reagents:

$$X-\underset{R'}{\overset{R'}{Si}}-H + CH_2=CH-R \xrightarrow{\text{Pt cat.}} X-\underset{R'}{\overset{R'}{Si}}-CH_2CH_2-R \quad (6)$$

where R′ = CH_3- or X and R and X are as defined for eq 1. In some cases, olefin hydrosilation provides the only pathway on which an organosilanization reagent can be made. A coupling reagent such as [(methacryloxy)propyl]trimethoxysilane (useful in gel capillary electrophoresis) or a surface modifier such as (glycidoxypropyl)trimethoxysilane (useful, among other things, in the preparation of affinity chromatography supports) cannot be prepared by means of a Grignard reagent, due to the reasons discussed above.

Mechanism of Hydrosilation. The mechanistic aspects of hydrosilation in the homogeneous phase have been described elsewhere (*31–33*, *38*). If one assumes that the same mechanism scheme is applicable to the reaction in the heterogeneous phase, the surface hydrosilation of olefins catalyzed by platinum(II) complexes should proceed as shown in Figure 9. During the induction period a catalytically active (olefin)·Pt^{II} complex (i) is formed. Oxidative addition of the silicon hydride to the metal generates an (olefin)·$Pt^{IV}H(-Si\equiv)$ intermediate (ii). Hydride addition to the olefin then gives an (alkyl)·$Pt^{IV}(-Si\equiv)$ complex (iii), presumably stabilized by coordination of more olefin. Finally, reductive elimination of alkylsilane occurs, regenerating the starting (olefin)·Pt^{II} complex. It should be noted that the whole process takes place around the coordination sphere of the transition-metal catalyst. When Pt(0) complexes are used, the oxidation state of the metal in species i–iii should be lowered by 2 units (*32*, *33*).

Most experimental facts related to olefin hydrosilation (predominance of the terminal adduct, olefin isomerization, stereochemistry at the silicon atom, reductive catalyst deactivation, etc.) have been explained in terms of the proposed mechanism. The well-known effect of oxygen as a cocatalyst has, however, yet to be elucidated. It appears that areation of the reaction mixture is often required for the reaction to start and/or to be sustained. It has been suggested that an oxygen-containing ligand constitutes the active catalytic species (*40*).

The similar coverages obtained with the Speier's catalyst (hexachloroplatinic acid in 2-propanol) and cyclopentadienylplatinum(II) chloride can be easily interpreted if one considers that the active species in the Speier's catalyst corresponds to a (propene)·Pt^{II} complex, as demonstrated by Benkeser and Kang (*41*). Like (cyclopentadienyl)·Pt^{II}, the propene complex readily exchanges ligands with the bonding olefin (eq 4) and produces the starting species (i) of Figure 9.

When olefin hydrosilation occurs on a hydrided silica surface, other factors in addition to those found in the homogeneous counterpart, play a fundamental role in determining the reaction's yield. The maximum surface density of alkyl groups is ultimately limited by the mean pore size of the silica substrate, the cross-sectional area of the anchored groups, and perhaps more importantly, the additional size exclusion requirement imposed by the reaction's intermediates. In other words, the accessibility of the surface active sites (SiH) is largely governed by the physical size of the "olefin carrier" (i) and subsequent species (ii and iii) derived from it. The subject of size exlusion has been discussed by Cheng and McCown (*30*) with regard to conventional organosilanization, while mechanistic aspects have been discussed by Kinkel and Unger (*42*). The size-exclusion requirement of organosilanization can thus be considered in the light of the pentacoordinated intermediate typical of bimolecular nucleophilic substitution reactions (S_N2):

Presumably, the base used (see eq 2) is likely to assist in removal of hydronium and/or weakening of the Si–Cl bond (*42*) and, therefore, increases somewhat the size-exclusion value. Without going over molecular size calculations, it is apparent that the steric requirement for surface organosilanization is less stringent than that for surface hydrosilation. The lower-than-expected coverages obtained from hydrosilation in comparison to those for organosilanization can now be explained, at least partially, from the larger size-exclusion value associated with olefin hydrosilation. Interestingly enough, formation of Si–C linkages by alkylation of a chlorinated surface (eq 3) involves the formation of another S_N2 intermediate. Here, the alkylating group is the nucleophile while the pentacoordinate species occurs around the surface's silicon atom:

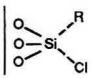

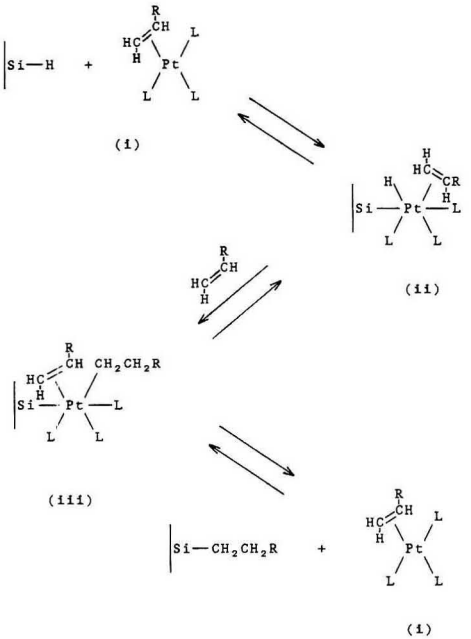

Figure 9. Reaction mechanism scheme for surface olefin hydrosilation catalyzed by platinum(II) complexes. L = halide, olefin, carbonyl, phosphine, etc.

Given the immobility of the surface silicon, the pentacoordinate intermediate is likely to be formed through a flank-side attack of the nucleophile (*43*). In contrast, in organosilanization the surface silanol is the nucleophile and the pentacoordinate intermediate occurs around the reagent's silicon atom which is slightly removed from the surface. Again, the relatively high coverages obtained from alkylation of chlorinated silicas (*14*, *15*) can be rationalized in the light of the less stringent size exclusion requirement associated with Grignard and organolithium reagents. These observations, however, have to be substantiated by appropriate experiments.

The chemical nature of the catalyst is, obviously, another important factor which requires further examination, as it relates to olefin hydrosilation on hydrided silica supports. Fortunately, there seems to be a plethora of group VIII transition-metal complexes from which to choose.

CONCLUSIONS

Olefin hydrosilation provides a suitable method for the preparation of silica-based bonded stationary phases for chromatography. The method allows good alkyl coverages as well as improved hydrolytic stability toward aggressive mobile phases such as those containing aqueous TFA. The hydrolytic advantage of direct Si–C linkages can be achieved without the difficulties that occur when such a linkage is obtained by the known sequential reaction with a chlorinating reagent and an alkylating reagent such as Grignard or organolithium. Additionally, the intrinsic freedom from interference makes hydrosilation a particularly convenient approach to attach virtually any organic functionality to a hydride-modified support, resulting in a remarkably versatile separation material. In principle, virtually all currently available silica-based bonded phases are amenable to being prepared by olefin hydrosilation on the hydrided substrate. This might result in a new generation of bonded silicas with improved hydrolytic stability. Thus, surface hydrosilation of olefins not only combines the superior hydrolytic stability of direct Si–C linkages with a simplicity approaching that of currently available silanization procedures but also provides a versatile separation support suitable for virtually any application. For instance, these features may prove valuable for the chemical modification of the inner wall of fused-silica capillaries used in high-performance capillary electrophoresis.

Future developments are expected to improve the whole synthetic process by applying a simpler and more efficient method to prepare the hydride intermediate, thus avoiding the drudgeries associated with the chlorination/reduction sequence. In addition, for optimal bonding, evaluation of a number of group VIII transition-metal catalysts is required. Work is currently underway in our laboratory along these lines.

ACKNOWLEDGMENT

John Fetzer and Wilt Biggs of Chevron Research and Technology are gratefully acknowledged for the BET analysis. The authors acknowledge the skillful synthetic work of Susan Ferline during the early stages of this research.

LITERATURE CITED

(1) Plueddemann, E. P. *Silane Coupling Reagents*; Plenum Press: New York, 1982.
(2) Unger, K. K. *Porous Silica*. Its Properties and Use as Support in Column Liquid Chromatography; *Journal of Chromatography Library*; Elsevier Scientific Publishing Co.: New York, 1979; Vol. 16.
(3) Majors, R. E. *J. Chromatogr. Sci.* **1974**, *12*, 767–778.
(4) Sander, L. C.; Wise, S. A. *Anal. Chem.* **1984**, *56*, 504–510.
(5) Nawrocki, J. *Chromatographia* **1991**, *31*, 177–192 and 193–205.
(6) Glajch, J. L.; Gluckman, J. C.; Charikofsky, J. G.; Minor, J. M.; Kirkland, J. J. *J. Chromatogr.* **1985**, *318*, 23–39.
(7) Glajch, J. L.; Kirkland, J. J.; Köhler, J. *J. Chromatogr.* **1987**, *384*, 81–90.
(8) Sagliano, N.; Floyd, T. R.; Hartwick, R. A.; Dibussolo, J. M.; Miller, N. T. *J. Chromatogr.* **1988**, *443*, 155–172.
(9) Hetem, M. J. J.; de Haan, J. W.; Claessens, H. A.; van de Ven, L. J. M.; Cramers, C. A.; Kinkel, J. N. *Anal. Chem.* **1990**, *62*, 2288–2296.
(10) Hetem, M. J. J.; de Haan, J. W.; Claessens, H. A.; van de Ven, L. J. M.; Cramers, C. A.; Wijnem, P. W. J. G.; Kinkel, J. N. *Anal. Chem.* **1990**, *62*, 2296–2300.
(11) Glajch, J. L.; Kirkland, J. J. U.S. Patent 4 705 725, 1987.
(12) Glajch, J. L.; Kirkland, J. J.; U.S. Patent 4 746 572, 1988.
(13) Kirkland, J. J.; Glajch, J. L.; Farlee, R. D. *Anal. Chem.* **1989**, *61*, 2–11.
(14) Locke, D. C.; Schmermund, J. T.; Banner, B. *Anal. Chem.* **1972**, *44*, 90–92.
(15) Unger, K.; Thomas, W.; Adrian, P. *Kolloid Z. Z. Polym.* **1973**, *251*, 45–52.
(16) Pesek, J. J.; Swedberg, S. A. *J. Chromatogr.* **1986**, *361*, 83–92.
(17) Morrison, R. T.; Boyd, R. N. *Organic Chemistry*; 3rd ed.; Allyn and Bacon, Inc.: Boston, 1974; pp 512–513.
(18) Sandoval, J. E.; Pesek, J. J. *Anal. Chem.* **1989**, *61*, 2067–2075.
(19) Sandoval, J. E.; Pesek, J. J. U.S. Patent 5 017 540, 1991.
(20) Apfel, M. A.; Finkelmann, H.; Janini, G. M.; Laub, R. J.; Luehrmann, B. H.; Price, A.; Roberts, W. L.; Shaw, T. J.; Smith, C. A. *Anal. Chem.* **1985**, *57*, 651–658.
(21) Drew, D.; Doyle, J. R. In *Inorganic Synthesis*; Vol. XIII, Cotton, F. A., Ed., McGraw-Hill Book Co., Inc.: New York, 1972; Vol. XIII, pp 47–52.
(22) Berendsen, G. E.; De Galan, L. *J. Liq. Chromatogr.* **1978**, *1*, 561–586.
(23) Berendsen, G. E.; Pikaart, K. A.; De Galan, L. *J. Liq. Chromatogr.* **1980**, *3*, 1437–1464.
(24) Bayer, E.; Albert, K.; Reiners, J.; Nieder, M.; Müller, D. *J. Chromatogr.* **1983**, *264*, 197–213.
(25) Bayer, E.; Paulus, A.; Peters, B.; Laupp, G.; Reiners, J.; Albert, K. *J. Chromatogr.* **1986**, *364*, 25–37.
(26) Marciel, G. E.; Sindorf, D. W. *J. Am. Chem. Soc.* **1980**, *102*, 7606–7607.
(27) Sindorf, D. W.; Marciel, G. E. *J. Am. Chem. Soc.* **1983**, *105*, 3767–3776.
(28) Engelhardt, G.; Jancke, H.; Lippmaa, E.; Samoson, A. *J. Organomet. Chem.* **1981**, *210*, 295–301.
(29) Roumeliotis, P.; Unger, K. K. *J. Chromatogr.* **1978**, *149*, 211–224.
(30) Cheng, W.; McCown, M. *J. Chromatogr.* **1985**, *318*, 173–185.
(31) Chalk, A. J.; Harrod, J. F. *J. Am. Chem. Soc.* **1965**, *87*, 16–21.
(32) Harrod, J. F.; Chalk, A. J. In *Organic Synthesis via Metal Carbonyls*; Wender, I., Pino, P., Eds.; John Wiley & Sons: New York, 1977; Vol. 2, pp 673–704.
(33) Speier, J. L. *Adv. Organomet. Chem.* **1979**, *17*, 407–447.
(34) Shih-Hsien, H.; Fazio, S. D.; Tomellini, S. A.; Crowther, J. B.; Hartwick, R. A. *Chromatographia* **1985**, *20*, 161–163.
(35) Köhler, J.; Chase, D. B.; Farlee, R. D.; Vega, A. J.; Kirkland, J. J. *J. Chromatogr.* **1986**, *352*, 275–305.
(36) Köhler, J.; Kirkland, J. J. *J. Chromatogr.* **1987**, *385*, 125–150.
(37) Smith, A. L. *Spectrochim. Acta* **1960**, *16*, 87–105.
(38) Eaborn, C.; Bott, R. W. In *Organometallic Compounds of the Group IV Elements*. *The Bond to Carbon*; MacDiarmid, A. G., Ed.; Marcel Dekker: New York, 1968; Chapter 2, Vol. I, Part I.
(39) Lukevics, E.; Belyakova, Z. V.; Pomerantseva, M. G.; Voronkov, M. G. *J. Organomet. Chem. Libr.* **1977**, *5*, 1–179.
(40) Zhang, X.; Lu, X.; Zhang, R.; Duan, H. *Cuihua Xuebao* **1986**, *7*, 378–382.
(41) Benkeser, R. A.; Kang, J. *J. Organomet. Chem.* **1980**, *185*, C9–C12.
(42) Kinkel, J. N.; Unger, K. K. *J. Chromatogr.* **1984**, *316*, 193–200.
(43) Corriu, R. J. P.; Guerin, C. *J. Organomet. Chem.* **1980**, *198*, 231–320.

RECEIVED for review June 17, 1991. Accepted August 23, 1991. This work was supported in part by the National Science Foundation through Grant No. CHE-8814849 and by The Separations Group.

Centrifugal Partition Chromatography of Palladium(II) and the Influence of Chemical Kinetic Factors on Separation Efficiency

Y. Surakitbanharn, S. Muralidharan,* and H. Freiser

Strategic Metals Recovery Research Facility, Department of Chemistry, University of Arizona, Tucson, Arizona 85721

Separation efficiencies in the centrifugal partition chromatographic (CPC) method for the distributing species, a palladium ion complex and an organic solute (3-picoline) for the heptane:water phase pair have been compared. The column efficiency for the Pd(II)–TOPO (trioctylphosphine oxide) system ($N = 500 \pm 40$) has been found to be significantly less than for the 3-picoline system ($N = 1280 \pm 80$) at a flow rate of 0.50 ± 0.05 mL/min and is dependent on its distribution ratio. The behavior of the Pd(II)–TOPO system in CPC can be attributed to the slow kinetics of back-extraction of the $PdCl_2(TOPO)_2$ complex. The dissociation rate constant for this complex in aqueous solution has been determined to be $168 \pm 8\ M^{-1}\ s^{-1}$ by the stopped-flow kinetics procedure. This kinetic study revealed that the parameter channel equivalent of a theoretical plate (CETP), which is analogous to the reduced plate height, can be correlated to the half-life for the back-extraction and the distribution ratio of Pd(II). These findings have general application to all chromatographic separations involving metal complex formation and dissociation because reaction kinetics too fast to be observed by ordinary means will have a significant effect on chromatographic efficiency.

INTRODUCTION

Centrifugal partition chromatography (CPC), a countercurrent liquid–liquid distribution technique, has been widely used for the separation of organic compounds, biological materials, and natural products (*1*, *2*). It has been only recently that this technique has been applied for the separations of metal ions (*3*, *4*). We were the first to demonstrate the efficient separation by CPC of adjacent lanthanides including the separation of both light and heavy lanthanides in a single run using gradient pH elution (*5*). We were also the first to achieve the separation by CPC of palladium(II) from platinum(II), rhodium(III), and iridium(III) (*6*). These studies revealed that, under comparable conditions, CPC efficiencies for metal ion separations were significantly lower, by a factor of 4–5, than those regularly seen for organic compounds (*7*). Separations of metal ions by CPC involves formation and dissociation of extractable complexes using suitable ligands, most usually dissolved in the stationary organic phase. Further, the column efficiency is also a function of the distribution ratio of a given metal species, unlike the case of the organic compounds. Similar low efficiencies and the dependence of these efficiencies on the distribution ratios of the extracted metal species are also observed in the separation of metals by derivatized solid supports (*8*). Generally, in chromatography the column efficiency is constant for a given set of operating conditions, exhibiting no dependence on the distribution ratios of the species being separated. This puzzling observation in metal separations, which is yet to be addressed, prompted us to undertake a systematic investigation of the influence of chemical kinetic factors on the efficiencies of metal separations by liquid chromatography. CPC, being a liquid–liquid separation technique, has the advantage over HPLC for elucidating the influence of chemical kinetic factors on chemical separations without the interference from the adsorption–desorption processes of the analyte encountered in HPLC.

This study describes our efforts to determine whether, and in what manner, chemical factors, in contrast to simple solvation and desolvation as well as mass-transfer factors, were responsible for the differences in CPC efficiencies for metals and organic separations. CPC studies coupled with solution kinetic studies using stopped flow has allowed us to clearly establish the influence of chemical kinetics on CPC column efficiencies and correlate them to the half-lives of the chemical reaction responsible for the lowered chromatographic efficiencies. These are discussed in this paper.

EXPERIMENTAL SECTION

Apparatus. A Sanki, Co., Japan, assembly consisting of a Model SPL centrifuge containing six analytical/semipreparative cartridges each having 400 channels (2400 total channels), a Model CPC FCU-V loop injector, and a Model LBP-V pump were used for CPC experiments. The current setup has been modified to obtain an internal volume of 120 mL compared to our original work on the separation of lanthanides where the internal volume was 130 mL (*5*).

A UV–vis spectrophotometric detector (Model 770, Schoeffel Instrument Co.) with a 0.1-mL cell volume and 8-mm path length was used. It was set at 238 nm and 255 nm for Pd(II) and 3-picoline experiments, respectively. Data were acquired every 10 s using an IBM/PC interfaced to the detector and a DASH-8 program (Metrabyte Co.).

A Hi-Tech Scientific stopped flow SHU spectrophotometer was used for the kinetic study of the formation and dissociation of the Pd(II) and TOPO complex. Data acquisition and treatment were accomplished with the associated Hi-Tech software. Pd(II) and TOPO as well as chloride (NaCl) were dissolved in aqueous solutions of various concentrations of surfactant (0.7–4% Triton X-100). The kinetics was monitored at 420 nm.

The viscosities of heptane solutions of TOPO were measured using an Ostwald viscometer.

Reagents. Trioctylphosphine oxide, TOPO (kindly supplied by Dr. Richard Boyle of American Cyanamid Co.), was recrystallized from acetone (mp = 53–54 °C). All other reagents were of analytical grade. Metal-free heptane and water solutions were equilibrated overnight before use. Palladium stock solutions (10^{-2} M) were prepared by dissolving a weighed quantity of palladium(II) chloride (59.9% Pd, Alfa Products) in 0.10 M HCl solution. 3-Picoline (Eastman Kodak Co.) was purified by distillation before use. The stock solution of 10^{-2} M 3-picoline was prepared in water. Succinic acid buffer of pH = 6.10 (3.88×10^{-3} M succinic acid and 6.94×10^{-3} M NaOH) was prepared using Perrin's method (*9*). Deionized–distilled water was used throughout this study.

Procedure. All CPC, kinetic, and viscosity measurements were performed at 25 °C. CPC experiments were conducted with 0.1–0.5 M TOPO in heptane as the stationary phase and an aqueous phase at pH 3 and appropriate chloride concentration (using NaCl) as the mobile phase, pumped in the descending mode. Equilibration of the two phases at 800 rpm resulted in 20 mL of heptane and 100 mL of water. A 1-mL aliquot of palladium stock solution (10^{-3} M) was injected into the CPC system for each run. Flow rates between 0.5 and 4.0 mL/min were used in these experiments.

The experimental configuration for the 3-picoline experiment was identical to that for palladium except that the detection

0003-2700/91/0363-2642$02.50/0

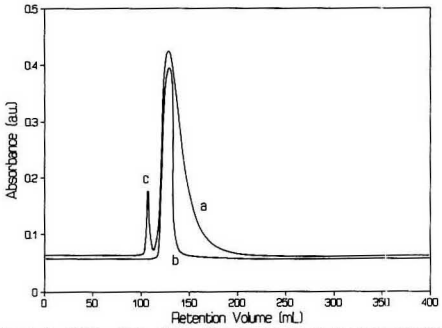

Figure 1. Comparison of the chromatograms at identical retention volumes (132 mL) of (a) Pd(II) ([TOPO] = 0.3 M, [Cl⁻] = 0.1 M.) and (b) 3-picoline (pH = 6.10). The origin of the dead volume peak (c) is uncertain.

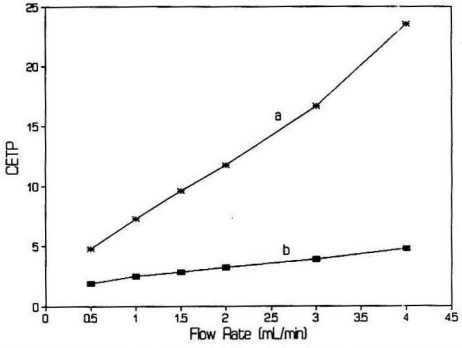

Figure 2. Van Deemter type plot for (a) the Pd(II)–TOPO system at 0.1 M [TOPO], 10^{-2} M [Cl⁻] and pH = 3 and (b) 10^{-3} M 3-picoline in succinic acid buffer of pH = 6.10.

wavelength was set at 255 nm. The mobile phase was adjusted to pH 6.10 using succinic acid buffer before injecting 1 mL of 10^{-3} M 3-picoline.

RESULTS AND DISCUSSION

Comparison of CPC Efficiencies of Pd(II) and 3-Picoline. We have completely characterized the extraction of Pd(II) by TOPO by batch solvent extraction and CPC, in terms of the nature of the Pd(II) species extracted and the dependence of the distribution ratio of this species on the concentrations of TOPO and Cl⁻ (*6*). It was shown that Pd(II) was extracted as the $PdCl_2(TOPO)_2$ complex and that the distribution ratio increased with [TOPO] and decreased with [Cl⁻].

We define the term CETP, channel equivalent of a theoretical plate ($2400/N$), which is the equivalent of reduced plate height, to characterize the separation efficiency of CPC. The dependence of CETP on flow rates of Pd(II) and 3-picoline were compared in the heptane:water system. The peak widths for palladium and 3-picoline at the same retention volume and flow rate of 2.0 mL/min are compared in Figure 1, which shows a significantly lower efficiency for Pd(II) compared to 3-picoline. It is evident from Figure 2 that the CETP for Pd is higher than that for 3-picoline and that it exhibited a greater sensitivity to flow rate. The Pd(II) and 3-picoline separations became less efficient (higher CETP) with increasing flow rate, analogous to conventional liquid chromatography.

Chromatographic efficiency is typically limited by various types of diffusion processes which are operating for both

Table I. CETP and *D* Values for 3-Picoline and Pd(II) at Different TOPO and Chloride Concentrations at a Flow Rate of 2.00 mL/min

[TOPO], M	η, cp	3-picoline CETP[a]	3-picoline *D*	[Cl⁻], M	Pd(II) CETP	Pd(II) $t_{1/2}$, s[b]	Pd(II) *D*
0.0	0.386	3.2	0.9				
0.2	0.485	3.6		0.1	10	2.2	0.4
0.3	0.556	3.9		0.1	17	3.3	0.9
0.4	0.643	4.2		0.1	25	4.4	1.4
0.5	0.738	4.4		0.1	33	5.5	2.8
0.5	0.738	4.4		0.05	68	11.0	8.3
0.5	0.738	4.4		0.20	13	2.7	0.6
0.5	0.738	4.4		0.30	11	1.1	0.4

[a] Calculated values except in pure heptane. [b] Calculated from eq 6.

3-picoline and Pd(II). Simple diffusion alone cannot account for the significantly lower efficiency for Pd(II), however, even when the effect of TOPO on increasing the viscosity, η, of heptane solution is taken into account. The CETP values of 3-picoline at the viscosities of TOPO solutions in heptane were calculated from the CETP value in pure heptane by assuming a linear relationship between CETP and $\eta^{0.5}$, given the narrow range of viscosities, as indicated by the Knox equation (*10*). As seen from Table I, the viscosity of TOPO solution in heptane and the CETP values for 3-picoline and Pd(II) increase with the concentration of TOPO. The CETP values for Pd remain distinctly higher, indicating that viscosity alone does not account for the increase in CETP for Pd with increasing TOPO concentration. It is also evident from this table that the CETP values for Pd(II) are dependent on its distribution ratio. The CETP values are larger at higher distribution ratios, indicating poorer column efficiencies at higher *D* values. The additional peak broadening in the case of Pd(II) compared to 3-picoline under identical conditions and at the higher distribution ratios of Pd(II) must arise from chemical kinetic factors. Approximately 50% of the 3-picoline molecules are protonated at pH = 6.1 (pK_a = 6), at which its CPC chromatograms were obtained. The deprotonation reaction will not cause CPC band broadening in the case of 3-picoline, as it is very rapid and indeed is termed diffusion controlled. In the manner of the Van Deemter and Knox equations in which the reduced plate height is seen as a sum of contributions from various factors, we can express the observed CETP for Pd ($CETP_{obs}$) as a sum of contributions from diffusion ($CETP_{dif}$) and chemical kinetics ($CETP_{CK}$) (eq 1).

$$CETP_{obs} = CETP_{dif} + CETP_{CK} \quad (1)$$

We can isolate the contribution due to the chemical kinetics to the observed CETP for Pd(II) by subtracting the CETP values for 3-picoline at the appropriate TOPO concentrations. We shall show that $CETP_{CK}$ is related to the half-life for the kinetics of back-extraction of the $PdCl_2(TOPO)_2$ complex and the *D* value of Pd(II).

A further examination of the involvement of chemical kinetic factors in the CPC efficiency for Pd(II) was obtained by studying the dependence of CETP on the concentration of chloride in the aqueous phase and the concentration of TOPO in the heptane stationary phase. It is evident from eq 2 that the distribution ratio of Pd(II) should depend on

$$PdCl_2(TOPO)_2 + 2Cl^- \rightleftharpoons PdCl_4^{2-} + 2TOPO \quad (2)$$

the chloride and TOPO concentrations, with *D* being directly proportional to $[TOPO]^2$ and inversely proportional to $[Cl^-]^2$. It is not obvious, however, that CETP should depend on these concentrations as well. It was found that increasing [Cl⁻] and decreasing [TOPO] provided better CPC efficiencies for Pd(II)

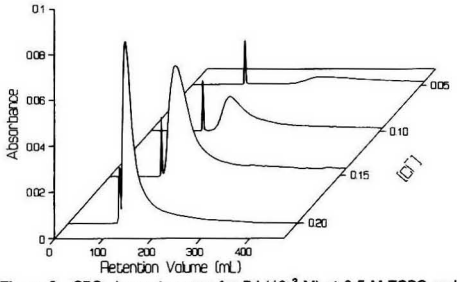

Figure 3. CPC chromatograms for Pd (10^{-3} M) at 0.5 M TOPO and [Cl^-] = 0.05–0.2 M.

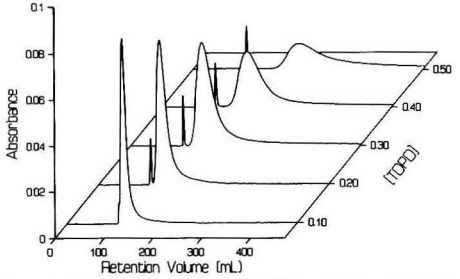

Figure 4. CPC chromatograms for Pd (10^{-3} M) at 0.05 M chloride and [TOPO] = 0.1–0.5 M.

(Figures 3 and 4). As may be seen, CETP is directly proportional to [TOPO] and inversely proportional to [Cl^-] (Table I). These observations are consistent with the hypothesis that the kinetics of the back-extraction reaction, eq 2, is the major factor in affecting the CPC efficiency for Pd(II).

Study of the Back-Extraction of the $PdCl_2(TOPO)_2$ Complex Using Stopped Flow. Since the CPC results indicated the involvement of slow chemical kinetics, a systematic study of the kinetics of the process of extraction and back-extraction of Pd(II) seemed in order. We learned from preliminary experiments of extraction and back-extraction of Pd(II) by TOPO in the heptane:water system using the microporous Teflon phase separator (MTPS) (*11*), that these kinetics were too fast to be measured by this system which can measure half-lives 5 s and longer.

In order to understand the influence of the kinetics of formation and dissociation of $PdCl_2(TOPO)_2$ on CETP, we resorted to stopped-flow analysis and examined the kinetics in the presence of micelles, which as we have demonstrated earlier, provide excellent models for extraction systems (*12*). The micellar system containing up to 4% Triton X-100, a neutral surfactant, to solubilize TOPO was chosen to compare the formation and dissociation rates of $PdCl_2(TOPO)_2$. The formation of $PdCl_2(TOPO)_2$ under a variety of conditions was too fast even for the stopped-flow apparatus (limit of $t_{1/2}$ = 0.4 ms). The dissociation kinetics of $PdCl_2(TOPO)_2$ could be followed by the stopped-flow method.

The $PdCl_2(TOPO)_2$ complex was formed in the Triton X-100 system using 10^{-3} M Pd(II). The dissociation of this complex under pseudo-first-order conditions in [Cl^-] was monitored as a function of [Triton X-100], [Cl^-], and [TOPO]. The observed pseudo-first-order rate constant was independent of the Triton X-100 concentration (Table II), indicating that the dissociation of $PdCl_2(TOPO)_2$ occurred essentially in the bulk aqueous phase. This also indicated that no appreciable dissociation occurred in the micellar phase and that mass transfer of $PdCl_2(TOPO)_2$ between the bulk aqueous and the bulk micellar phases was rapid.

Table II. Variation of k_{obs} with Triton X-100, Chloride, and TOPO Concentrations

[Triton X-100], M	[Cl^-], M	10^4[TOPO], M	k_{obs}, s^{-1}
0.011	0.1	1	15.99
0.016	0.1	1	17.05
0.032	0.1	1	17.97
0.064	0.1	1	16.49
0.016	0.05	1	7.90
0.016	0.2	1	32.18
0.016	0.3	1	46.59
0.016	0.4	1	61.36
0.016	0.5	1	80.64
0.016	0.6	1	96.54
0.016	0.5	5	75.00
0.016	0.5	10	66.72
0.016	0.5	20	56.50
0.016	0.5	30	47.52

The value of k_{obs} increased with increasing [Cl^-] at constant [TOPO] and decreased with increasing [TOPO] at constant [Cl^-]. These observations can be rationalized on the basis of the mechanism in eqs 3–5 for the decomposition of $PdCl_2(TOPO)_2$. The rapid preequilibrium step, eq 3, and the

$$PdCl_2(TOPO)_2 \underset{\text{fast}}{\overset{K}{\rightleftharpoons}} PdCl_2(TOPO) + TOPO \quad (3)$$

$$PdCl_2(TOPO) + Cl^- \xrightarrow[\text{slow}]{k_2} PdCl_3^- + TOPO \quad (4)$$

$$PdCl_3^- + Cl^- \xrightarrow[\text{fast}]{} PdCl_4^{2-} \quad (5)$$

rate-limiting step, eq 4, yield the following expression for k_{obs} under pseudo-first-order conditions in [Cl^-]:

$$k_{obs} = \frac{k_2 K}{K + [TOPO]}[Cl^-] \quad (6)$$

Equation 6 can be rewritten as

$$\frac{[Cl^-]}{k_{obs}} = \frac{1}{k_2} + \frac{1}{Kk_2}[TOPO] \quad (7)$$

The plot of [Cl^-]/k_{obs} as a function of [TOPO] yielded a straight line. The k_2 and K values derived from the intercept and slope of this plot are 168 ± 8 M^{-1} s^{-1} and 0.004 ± 0.0002 M, respectively. Equation 6 indicates two limiting cases, $K \gg$ [TOPO] and $K \ll$ [TOPO] (eqs 8 and 9). Equation 8 is encountered in stopped-flow experiments at 10^{-4} M TOPO where k_{obs} is linear in [Cl^-] (Table II). These observed rate

$$k_{obs} = k_2[Cl^-] \quad (8)$$

$$k_{obs} = \frac{k_2 K}{[TOPO]}[Cl^-] \quad (9)$$

constants yield a k_2 value of 158 ± 4 M^{-1} s^{-1} which is in excellent agreement with the value from eq 7. Equation 9 indicates that $t_{1/2} \propto$ [TOPO]/[Cl^-] ($t_{1/2} = \ln 2/k_{obs}$). It is evident from Table I and Figures 3 and 4 that CETP has a similar relationship to [TOPO] and [Cl^-].

Plotting the difference in the CETP for Pd and 3-picoline to eliminate the contribution from viscosity changes (eq 1) at constant [Cl^-] as a function of $t_{1/2}$ yielded a straight line with slope 6.4 ± 0.2. A similar plot at constant [TOPO] yielded a straight line with slope 5.9 ± 0.3. The CETP determined chromatographically is thus a measure of the half-life for the kinetics of back-extraction of $PdCl_2(TOPO)_2$. It is also evident that the dependence of CETP on [TOPO] and [Cl^-] is different from the dependence of the D value of Pd(II) on these concentratins (eq 2). Interestingly, we find that CETP is directly proportional to $D^{0.5}$ (Table I). Such a relation is

not obvious from the basic chromatographic equations used to calculate the D value from retention volume and the efficiency from the retention volume and the peak width. The relationship between CETP and $t_{1/2}$ and CETP and D have become evident through the independent elucidation of the mechanism of the kinetics of back-extraction of $PdCl_2(TOPO)_2$ using the stopped-flow technique.

This analysis of chromatographic efficiency in separations involving the distribution of metal complexes clearly reveals the influence of the kinetics of complex formation and dissociation on the chromatographic efficiencies and affords a semiquantitative description of the relevant kinetic parameters.

CONCLUSIONS

The differences in the CETP values for the Pd(II) and 3-picoline systems at a given flow rate are attributed to the slow kinetics of back-extraction of the $PdCl_2(TOPO)_2$ complex. The CETP for the Pd(II) system is directly proportional to the $t_{1/2}$ for the kinetics of back-extraction of the $PdCl_2(TOPO)_2$ complex. This strong correlation between CETP and stopped-flow solution kinetics has allowed us to attribute unequivocally that the band broadening in the Pd(II) system is due to the slow kinetics of dissociation of the extracted Pd complex. Thus CPC not only provides useful clues as to the chemical kinetics of extraction and back-extraction but also enables the correlation of column efficiencies with independently measured chemical kinetic parameters. CPC offers an advantage over HPLC in this regard. Such correlations are difficult in HPLC due to interference from the adsorption and the desorption of the analyte on the solid support. Further, the kinetic information obtained from the correlation of column efficiencies with distribution ratios, as demonstrated here, can be used to improve the CPC efficiency.

The customary screening of extraction reactions involving single-stage equilibrations serve not only to determine D values but also to enable one to discard reactions which are too slow to be chromatographically useful. Even when these experiments indicate that extraction reactions are too fast to be measured by ordinary means, the sensitivity of CPC and related chromatographic techniques to reaction rates are dramatically greater. Slow reactions that have half-lives of even ca. 1 s will begin to adversely affect the observed column efficiency. Conversely, observation of efficiencies lower than otherwise expected, provides a qualitative index of slow reaction kinetics. Although our study is focused on extraction reactions involving metal complexation, these will apply to any process in which the transferring species is formed (and dissociated) by slow kinetics.

LITERATURE CITED

(1) Marston, A.; Borel, C.; Hostettmann, K. *J. Chromatogr.* **1988**, *450*, 91–99.
(2) Bruening, R. C.; Oltz, E. M.; Furukawa, J.; Nakanishi, K. *J. Am. Chem. Soc.* **1985**, *107*, 5298–5300.
(3) Araki, T.; Okazawa, Y.; Asai, H.; Ando, J. *J. Liq. Chromatogr.* **1988**, *11*, 2487–2506.
(4) Akiba, K.; Swai, S.; Nakamura, S.; Murayama, W. *J. Liq. Chromatogr.* **1988**, *11*, 2517–2536.
(5) Muralidharan, S.; Cai, R.; Freiser, H. *J. Liq. Chromatogr.* **1990**, *13*, 3651–3672.
(6) Surakitbanharn, Y.; Muralidharan, S.; Freiser, H. *Solv. Extr. Ion Exch.* **1991**, *9*, 45–49.
(7) Berthod, A.; Armstrong, D. W. *J. Liq. Chromatogr.* **1988**, *11*, 567–583.
(8) Braun, T.; Ghersini, G. *Extraction Chromatography*; Elsevier: New York, 1975.
(9) Perrin, D. D. *Aust. J. Chem.* **1963**, *16*, 572–578.
(10) Knox, J. H. *J. Chromatogr. Sci.* **1980**, *18*, 453.
(11) Watarai, H.; Cunningham, L.; Freiser, H. *Anal. Chem.* **1982**, *54*, 2390–2392.
(12) Muralidharan, S.; Yu, W.; Tagashira, S.; Freiser, H. *Langmuir* **1990**, *6*, 1190–1196.

RECEIVED for review May 29, 1991. Accepted August 19, 1991. This research was supported by a grant from NASA.

Multivariate Statistics for Large Data Sets: Applications to Individual Aerosol Particles

Thomas W. Shattuck,*[1] Mark S. Germani,[2] and Peter R. Buseck

Chemistry and Geology Departments, Arizona State University, Tempe, Arizona 85287

Cluster, discriminant, correlation, and principal component analysis were used for data reduction of the elemental compositions of atmospheric aerosol particles. To verify the methods used, cluster analysis was performed on (1) four clay minerals, (2) U.S.G.S. standard basalt particles, and (3) a complex Phoenix aerosol sample. A generalized scheme was developed for seed-point selection, the determination of the number of clusters, and cluster evaluation. Analysis of variance and testing of cluster significance were used as objective criteria for the evaluation of each step in the scheme. Cluster analysis was effective for determining the types of particles that occurred in the Phoenix aerosol. Discriminant analysis, based on the Phoenix clusters, and analysis of the variance of a multisample data set of aerosol particles from Chandler, a neighboring community to Phoenix, were used to test seed-point selection methods and centroid sets. Correlation and principal component analysis of the Chandler set were used to assess cluster significance and temporal emission patterns. The temporal patterns in Chandler correlated well with upper level wind directions.

1. INTRODUCTION

1.1. Motivation. Cluster, discriminant, correlation, and principal component analysis are well-developed multivariate statistical techniques that have recently been used for data reduction of data sets containing individual atmospheric aerosol particle compositions (*1–3*). The determination of the composition, size, and morphology of aerosol particles has played an important role in the study of air quality (*4–7*). Aerosol particles in the respirable size range affect human health and may be important vectors for the introduction into the body of heavy metals, asbestiform minerals, and other deleterious substances. The need for multivariate analysis arose as an outgrowth of an ongoing study into the composition and character of particles in the Phoenix aerosol (*8–13*). However, the methods developed in this study are useful for any large data sets.

The greater Phoenix area, with a population of 1.5 million, is surrounded by large areas having low population densities. Its arid climate and the possibilities for long-range particle transport make Phoenix an ideal area for studying inorganic particulate aerosols.

Automated techniques using a scanning electron microscope (SEM) and energy-dispersive, X-ray emission spectroscopy (EDS) have been developed that are capable of rapidly measuring the elemental compositions and sizes of aerosol particles (*3, 14*). A typical study includes results on many hundreds of particles in each of a large number of samples. The analysis of this wealth of information is made more tractable by data reduction techniques that reveal underlying trends. The methods discussed in this study are cluster, discriminant, correlation, and principal component analysis. Bernard, Van Grieken, and Eisma (*15*) have applied cluster and discriminant analysis to single-particle elemental compositions obtained by EDS of estuarine particles.

The objectives of this study were (1) to develop cluster analysis techniques for the rapid identification of aerosol particle types, (2) to assess methods for the evaluation of cluster analyses, and (3) to apply the methods in a long-term sampling program. These objectives were achieved through the study of four distinct sets of samples, selected and designed to test each of the methods.

1.2. Cluster Analysis. There are three goals for cluster analysis of atmospheric aerosols. (a) The first is to identify the types of particles that occur in the aerosol. Ideally, every particle type in the aerosol is represented by a cluster. Difficulties arise because in Phoenix about 75% of the particles are crustal in origin (*4, 5*). To distinguish the mineral types of these crustal particles, it is necessary to identify clusters that exhibit a wide composition range and/or extensive overlap. It is also important not to miss the less abundant anthropogenic particle types, many of which have compositions different from the crustal particles. Examples of the latter include ammonium and sodium sulfates, lead chlorides and bromides, and more exotic particles associated with specific industries.

(b) The second goal of cluster analysis is to reduce the mass of data to a tractable size, but in a way that emission patterns can be easily discerned. Instead of 1000 or more individual observations, cluster analysis groups the data so that the particles in each cluster have similar compositions. Each cluster is represented by a centroid, which is the average composition of the members of the cluster. The results of the cluster analysis are the centroid compositions and the number of particles assigned to each cluster (particle type). These cluster occupations represent a tremendous reduction in the volume of data without significant loss of information.

(c) The third goal of cluster analysis is to discern particles with unusual compositions; particles greater than a chosen maximum distance distance from all centroids are left unassigned. These unassigned particles generally account for less than 10% of a data set.

The success of a cluster analysis in meeting these goals is assessed by analysis of variance (ANOVA), which measures the ability of a centroid set to model the data. Tests of cluster significance measure how well clusters are separated from each other. These tests are carried out by ANOVA of the members of pairs of clusters.

Three studies of increasing complexity are discussed, culminating in a complex aerosol sample. The single-particle sample in the clay study is a mixture of clay-type minerals; ripidolite, montmorillonite, nontronite, and muscovite mica. The basalt study contains particles from a basalt standard, obtained from the United States Geological Survey (USGS). The Phoenix study is a representative sample from the Phoenix aerosol.

1.3. Discriminant Analysis. In a sampling program, samples are taken over a series of sampling periods at different

[1] On sabbitical leave from Colby College, Waterville, ME 04901.
[2] Current address: McCrone Associates, 850 Pasquinelli Dr., Westmont, IL 60559.

0003-2700/91/0363-2646$02.50/0

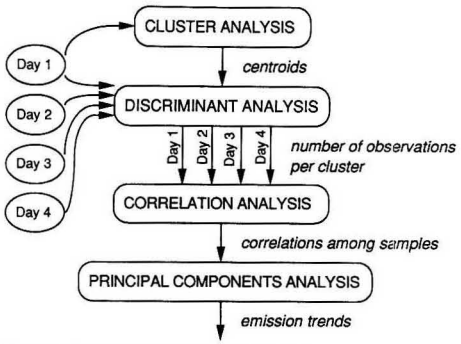

Figure 1. Procedure for multisample analysis.

sites. Discriminant analysis is used for particle classification of these samples. Discriminant analysis classifies the particles in a sample into particle types. The chemical compositions for the types are determined by the centroid set from the cluster analysis of a representative sample. Since a centroid set from a single sample is used to classify particles in samples from a group that may represent widely differing conditions, it is important to assess the ability of the cluster set to model the variability among the samples of the group. Multisample ANOVA is used for this purpose.

ANOVA of the multisample data set can also be used to guide several steps in the cluster analysis of the representative sample. Multisample ANOVA provides objective criteria for choosing the best seed-point method, the number of seed points to use, and the best cluster analysis algorithm. In this way, a centroid set is tailored for use in classification.

1.4. Correlation and Principal Component Analysis. The results from discriminant analysis are used to study temporal and spatial emission patterns. This work has resulted in the general multisample procedure outlined below and diagrammed in Figure 1. This procedure is useful whenever the same set of particle types are expected throughout the sampling study.

(*a*) *Cluster Analysis.* A representative sample is studied by cluster analysis to identify the particle types in the aerosol.

(*b*) *Discriminant Analysis.* The clusters determined in step a are used as a training set for discriminant analysis of the remaining samples. Discriminant analysis yields the particle occupation for each cluster for every sample, based on a consistent set of particle types.

(*c*) *Correlation Analysis.* This particle occupation versus particle occupation correlation matrix is formed to determine the correlations among the occupations of the different particle types.

(*d*) *Principal Component Analysis.* If significant structure appears in the correlation matrix, it is used as a basis for principal component analysis to try to identify particle sources or to find underlying trends that correlate with meterological conditions.

This procedure was used for the Chandler study as an example of a long-term sampling program. This study consists of a nine-sample data set taken in Chandler, 27 km southeast of Phoenix, over a 2-week period. The Phoenix study clusters were used in the discriminant analysis.

Principal component analysis is commonly used in aerosol particle chemistry (e.g. refs 16 and 17), but is has been restricted to analysis of bulk particulate samples. Individual particle data show the distribution of elements among particles and therefore provide clearer patterns for determining sources and trends.

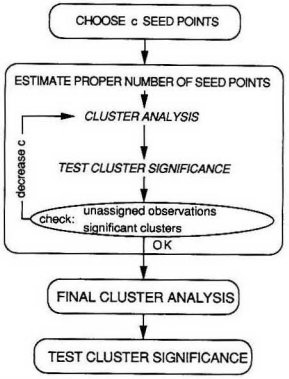

Figure 2. General scheme for cluster analysis.

Correlation analysis can also be used to judge cluster significance (separation). Assignments to a pair of clusters that overlap will show positive correlations because particles from one cluster will be misclassified to the other cluster in the overlap region. Correlation analysis is, therefore, a useful adjunct to tests of cluster significance.

2. THEORY

2.1. Cluster Analysis. The four steps in nonhierarchical cluster analysis are diagrammed in Figure 2. The first step is to choose seed points, which are approximate points from which to begin cluster analysis. The second is to approximate the number of clusters necessary to describe the data set. The third is to apply an algorithm to classify the observations into clusters and to calculate the centroids for each cluster. Lastly, statistical significance tests are applied to determine if the clusters are well-separated. Details of the procedures discussed below are given by refs 1 and 18–23.

2.1.1. Data Preparation. In the spectrum of X-rays produced by a sample in the scanning electron microscope, a range of X-ray energies called a region of interest, or ROI, is chosen as representative of each element in the sample. The raw ROI data, obtained as discussed in Anderson et al. (*5*) and Germani and Buseck (*14*), are converted to relative intensities. If p elements have been determined, and the ROI integral for particle i and element j is denoted ROI_{ij}, then the relative intensity, x_{ij}, is calculated as

$$x_{ij} = \mathrm{ROI}_{ij} / \sum_{m=1}^{p} \mathrm{ROI}_{im} \qquad (1)$$

Since light elements ($Z < \mathrm{Na}$) are not determined and the EDS sensitivity varies greatly from element to element, these relative intensities deviate from the true concentrations. However, it is only necessary to establish a unique pattern for each particle type for cluster analysis; the true concentration is not needed. If necessary, concentrations can be obtained subsequently for particles having compositions coinciding with the centroid.

The Euclidean distance measure is used in these studies. The squared Euclidean distance between an observation i and centroid k taken over p variables is

$$d_{ik}^2 = \sum_{j=1}^{p} (x_{ij} - \bar{x}_j^k)^2 \qquad (2)$$

where x_{ij} and $\bar{x}_j^k$ are the jth relative intensities for the observation and centroid, respectively. Saucy et al. (*7*) have also applied cluster analysis to Arctic aerosol particulates. They used a χ square and an angle-based distance measure in ad-

dition to Euclidean distances.

Data normalization is not used in this study for cluster analysis since it is desired to concentrate on the major elements, which have large standard deviations. Many values for the relative intensities of minor elements are zero, because of the minimum ROI cutoffs discussed in ref 14. This data treatment gives artifically low values for the standard deviations of such variables and correspondingly too great a weight after normalization. Data normalization also increases the noise in the data set caused by analytical uncertainty in the data.

2.1.2. Seed-Point Determination. Seed points are observations or averages of observations from the data set, and they serve as rough approximations for cluster centroids in the first iteration of cluster analysis. Seven methods were tested (Table II), which are discussed in detail in ref 1. The "refine" procedure is the first refinement method from the FASTCLUS procedure in the SAS statistics package (*22*). In the "merge" procedure (*1*), the data set is scanned to find the closest pair of observations. The second of this pair is rejected as a possible seed point. Merging is repeated until a few observations remain, and these remaining observations are then used as the seed-point set. Nearest centrotype sorting is discussed in ref 19. The last four seed-point methods are standard hierarchical techniques (*18*). For use in seed-point determination, the cluster merge list is traced backwards to the stage giving the same number of clusters as the desired number of seed points. The observations in each cluster are then averaged to yield the seed points.

The effectiveness of seed-point selection is determined less by the algorithm than by the way the seed-point algorithm is applied. To be effective, seed-point selection must be fast, and all the important clusters must be identified. With some of the seven methods listed above, it is impractically slow to scan a large data set (e.g., 1000 observations) for seed points. Instead, a subset is chosen as trial seed points, and then one of the seven methods is applied to reduce the number further. This initial subset is chosen in two ways: (1) a consecutive group of observations is chosen from the full data set, or (2) the minimum seed-point separation method of Tou and Gonzalez (*23*) is used. For construction of the trial subset, the choice of the minimum seed-point separation distance in the Tou and Gonzalez method is not critical and is chosen to be small compared to the expected between-cluster separations.

For simple data sets, seed-points are obtained in one step by constructing the trial subset and then applying one of the seed-point methods. However, for more complex data sets, a two-round procedure is necessary to ensure that all prominent clusters have been found:

Round 1:

(a) Seed points are chosen.
(b) Cluster analysis is performed on the full data set.
(c) Unassigned observations are collected.

Round 2:

(a) Additional seed points are chosen from the unassigned observations.
(b) Cluster analysis is performed on the unassigned observations.
(c) The centroids from clusters containing a large number of particles in step 2b are combined with the centroids from step 1b.

The combined set of centroids is then used as seed points for cluster analysis on the full data set.

As additional assurance that all the important clusters have been located, the two-round procedure is performed using several different seed-point selection algorithms and the results are compared. The ANOVA and tests of cluster significance discussed in sections 2.1.5 and 2.3 are helpful when comparing different seed-point selection algorithms.

2.1.3. Cluster Algorithm. The Forgy variety of K-means cluster analysis (*18, 20*) is used because of its speed for large data sets. The centroid for cluster k is given by the components $\bar{x}_j^k$ for all variables j. The average is

$$\bar{x}_j^k = \frac{1}{n^k} \sum_{i=1}^{n^k} x_{ij}^k \tag{3}$$

for the n^k observations, x_{ij}^k, in the cluster. Cluster centroids are updated at the end of each assignment cycle. Outliers are excluded by choosing a maximum distance for cluster assignment.

2.1.4. Analysis of Variance. For each sample, several sets of clusters are generated using different seed-point selection methods. It is necessary to compare each alternative cluster set to determine which best models the data. ANOVA is used for this purpose (cf. ref 24). The sample, modeled by c clusters on p variables, has

$$n = \sum_{k=1}^{c} n^k \tag{4}$$

assigned observations. The grand mean for variable j over the assigned observations is

$$\bar{\bar{x}}_j = \frac{1}{n} \sum_{k=1}^{c} n^k \bar{x}_j^k \tag{5}$$

(Note that a single bar over an x indicates a centroid, while two bars indicate grand means over the data set.) The total sum of squared deviations over the assigned observations, t, with

$$t = \sum_{j=1}^{p} \sum_{k=1}^{c} \sum_{i=1}^{n^k} (x_{ij}^k - \bar{\bar{x}}_j)^2 \tag{6}$$

decomposes as

$$t = b + w \tag{7}$$

where the between-clusters sum of squared deviations, b, is

$$b = \sum_{j=1}^{p} \sum_{k=1}^{c} n^k (\bar{x}_j^k - \bar{\bar{x}}_j)^2 \tag{8}$$

and w is the within-clusters sum of squared deviations

$$w = \sum_{j=1}^{p} \sum_{k=1}^{c} \sum_{i=1}^{n^k} (x_{ij}^k - \bar{x}_j^k)^2 \tag{9}$$

The variance ratio, hereafter denoted the f ratio, is

$$f = \frac{b/p(c-1)}{w/p(n-c)} \tag{10}$$

The cluster set giving the largest f ratio best models the data. That is, a large f ratio shows that the variability within clusters is smaller than the distance between clusters. However, only assigned observations are included, so comparisons of the f ratio can only be made among cluster sets with comparable numbers of assigned observations.

The ability of a cluster set to model all the observations in a sample, and not just the assigned observations, is measured by the ratio of the total sum of squared deviations of all the observations to the total sum of squared deviations of the assigned observations. This ratio, R, is given by

$$R = \frac{T/p(N-1)}{t'/p(n-1)} \tag{11}$$

where T is the total sum of squared deviations from the grand sample mean over all observations. Note that lower case letters are reserved for sums over just the assigned observations, and upper case, for sums over all the observations. T is

$$T = \sum_{j=1}^{p} \sum_{i=1}^{N} (x_{ij} - \bar{\bar{X}}_j)^2 \tag{12}$$

with N the total number of observations in the data set. The grand mean over all the observations for variable j is

$$\bar{\bar{X}}_j = \frac{1}{N} \sum_{i=1}^{N} x_{ij} \tag{13}$$

For consistency, the sum of squared deviations of the assigned observations must be calculated from the same mean, so that

$$t' = \sum_{j=1}^{p} \sum_{k=1}^{c} \sum_{i=1}^{n^k} (x_{ij}{}^k - \bar{\bar{X}}_j)^2 \tag{14}$$

An R ratio close to one indicates that the total sum of squares is well-represented by the cluster model.

2.1.5. Cluster Significance. The goals for significance testing using ANOVA are (1) to estimate the number of clusters that are needed to adequately represent the data set, and (2) to identify the amount of overlap between the various clusters. Although qualitative and semiquantitative tests exist, none is completely satisfactory. We chose the simplest ANOVA method, the sum-of-squares ratio test, based on eqs 3–9.

The sum-of-squares ratio test compares two clusters, r and q, by finding the ratio of the between-clusters sum of squares, $b^{r,q}$, to the within-clusters sum of squares, $w^{r,q}$. These sums are calculated using eqs 8 and 9; however, the sums extend over just clusters r and q, rather than all c clusters. The test statistic is then

$$c^{r,q} = b^{r,q}/w^{r,q} \tag{15}$$

The c statistic is used to test the significance of pairs of clusters under the null hypothesis that the observations are a sample from a single normal population. Hartigan (*20*) and Engelman and Hartigan (*25*) compiled a set of percentage points (critical values) for c. The suitability of these percentage points for this study is discussed in ref 1. A low confidence level (50%) is normally chosen when the percentage points are applied to overcome a tendency of the test to be too stringent.

The sum-of-squares ratio test with the Engelman and Hartigan percentage points is a rough but useful measure of cluster separation. A test failure indicates a significant overlap between a pair of clusters. The ability to detect overlapping clusters is also useful for estimating the number of clusters in the data set. The process is diagrammed in the second box in Figure 2. The initial cluster analysis is intentionally performed with too many seed points. The seed point that gives the largest number of test failures is rejected, and cluster analysis is repeated with the smaller seed-point set. After each subsequent cycle, the seed point with the largest number of test failures is rejected and cluster analysis is repeated. This process continues until the number of unassigned particles begins to increase rapidly and the number of significant clusters decreases.

2.1.6. General Clustering Scheme. A general strategy for cluster analysis of complex samples is shown in Figure 2. The steps, using the above techniques, are

Step i. Seed points are chosen with the two-round procedure, using the seed-point method judged best by ANOVA tests.

Step ii. The proper number of clusters is estimated by successive application of tests of cluster significance and seed-point deletion.

Step iii. The final cluster analysis is performed.

Step iv. The final cluster set is evaluated using ANOVA and tests of cluster significance.

The completion of each of these steps is necessary but not sufficient for a successful analysis. Chemical insight must also be used to guide each step.

2.2. Discriminant Analysis. Nearest centroid discriminant analysis is useful for large multisample data sets. A centroid set is chosen that represents the particle types found in the group of samples. The Euclidean distance from an observation to each centroid is calculated. The observation is assigned to the particle type whose centroid is nearest. To avoid the classification of outliers, a maximum distance for assignment is used. This maximum distance must be carefully chosen: too small a value classifies too few observations. Too large a maximum distance classifies too many unusual particles that are better left in the unassigned group.

2.3. Multisample Analysis of Variance. ANOVA is also used to test the validity of centroid sets for use in discriminant analysis for a multisample study. A centroid set will not adequately model the variability in the multisample study if many of the particles that appear are not represented or if the resulting clusters do not include the range of compositions found for each type. Since the ANOVA is now taken over all clusters and several samples, the single-sample ANOVA presented in eqs 4–14 must be modified by the addition of the sum over all samples. The total sum-of-squares decomposition holds over all samples if the daily cluster centroids are used to calculate b and w, rather than the centroid set used for the discriminant analysis. The R ratio is diagnostic in a multisample study. If new types of particles appear that are not represented by the centroid set, the number of unassigned particles will increase or the compositional range within the existing clusters will increase. These factors increase R. An R ratio close to one shows that the multisample data set is well-represented by the cluster model.

3. EXPERIMENTAL SECTION

3.1. Sample Preparation. For the clay study, Ca–montmorillonte (Texas), ripidolite (chlorite, California), and nontronite samples, all from the University of Missouri clay minerals repository, were ground in an agate mortar and pestle. A sheet of muscovite was washed in ethanol and ground in a ceramic mortar and pestle. The ground samples were separately suspended in distilled water. The distilled water was filtered through 0.4-μm membrane filters before use. The suspensions were filtered onto 0.4-μm polycarbonate Nucleopore filters. A 1-cm^2 portion of each filter was mounted on a carbon stub using carbon cement and coated with 20 nm of carbon in a Denton vacuum evaporator.

The sample preparation for the basalt study is discussed in ref 14. For the Phoenix study, the Phoenix, AZ, aerosol sample was taken on 34th St in downtown Phoenix on Feb 22, 1982. For the Chandler study, a series of nine aerosol samples was collected over a 2-week period in 1982 at a site in Chandler, AZ. The Phoenix and Chandler samples were collected on 8-μm Nucleopore filters, and therefore represented the "coarse fraction" of the aerosol. The ground-level wind direction and speed were monitored continuously during sample collection. Two 8-h samples were collected each day, a.m. and p.m. Details are given by Anderson et al. (*5*) and by Germani and Buseck (*14*). Morning samples from 8-μm filters were used for the present study, except for Feb 22, when unavailability dictated the use of the p.m. sample. No samples were collected on rainy days, which occurred several times during the sampling period.

The imaging conditions and data collection techniques are discussed in refs 5 and 14. A beam current of 300 pA was used to avoid excessive sample heating. A 60-s X-ray acquisition time was necessary to obtain adequate signal-to-noise ratios for the

Table I. Region of Interest (ROI) Energy Ranges

element	energy range, keV	element	energy range, keV
Na	0.88–1.12	Zn	8.40–8.84
Mg	1.12–1.36	Ge	9.60–10.12
Al	1.32–1.60	As	10.28–10.84
Si	1.56–1.92	Se	10.96–11.52
P	1.84–2.16	Br	11.60–12.20
S	2.12–2.52	Zr	15.44–16.08
Cl	2.48–2.80	Pd	2.80–2.92
K	3.12–3.52	Ag	2.88–3.12
Ca	3.48–3.88	Cd	3.92–4.08
Ti	4.32–4.68	Sn	4.12–4.28
V	4.76–5.16	Ba	5.60–6.80
Cr	5.20–5.68	W	8.20–8.56
Mn	5.68–6.12	Au	11.28–11.80
Fe	6.12–6.64	Hg	9.84–10.16
Ni	7.12–7.76	Pb	12.24–13.00
Cu	7.78–8.40		

Table II. Seed-Point Determination for the Clay Study

	clay type[a]			
method	mont-morillonite	non-tronite	ripido-lite	musco-vite
refine	+	+	–[b]	+
merge	+	+	–[b]	+
nearest centrotype	+	+	+	+
single linkage	–	+	+	–
complete linkage	+	+	+	+
av linkage	+	+	+	+
Ward's method	+	+	+	+

[a] + indicates a seed point was found in this cluster. [b] Particle 1 in Figure 3 was chosen as a seed point representing this cluster.

heavier elements (e.g., Sn, Br, Hg, and Pb). The ROI energy ranges are given in Table I. ROI integrals with values less than 3 times the standard deviation of the background were set to zero (*14*).

3.2. Statistical Analysis. All the statistical methods were implemented in an interactive, menu-driven Fortran Program, EXPLOR. Other reports using this program are refs 5 and 7. The program includes extensive capabilities for data manipulation and graphics. The interactive nature of the program was important for the development of the schemes used in this study. The program is highly modular, so that new methods are easily added. The modules may also be quickly assembled into stand-alone applications for repetitive analyses. Versions are availble for VAX series computers under UNIX and VMS operating systems.

4. RESULTS AND DISCUSSION

4.1. Clay Study. The clay minerals study was designed to test the seven seed-point methods and the ability of K-means analysis to cluster and distinguish among chemically similar phases. The data set consisted of 19 Ca–montmorillonite, 10 nontronite, 49 ripidolite, and 54 muscovite particles, with relative intensities for Mg, Al, Si, Fe, K, Ca, and Ti (Figure 3). Table II shows the results from seed-point searches with each of the seven seed-point methods. Nearest centrotype sorting, complete linkage, average linkage, and Ward's method found a seed point for each of the four types of clays. The refine and merge methods chose particle 1, which is a nontronite particle, instead of a ripidolite particle. Single linkage found seed points in the nontronite and ripidolite groups, particle 1, and at a composition intermediate between the Ca–montmorillonite and muscovite clusters. Therefore, single linkage did not find a suitable set of seed points for this data set.

Forgy K-means analysis using the nearest centrotype, complete linkage, average linkage, and Ward's seed points converged to the clusters shown in Figure 3. The refine and merge methods also converged to the same clusters, as long

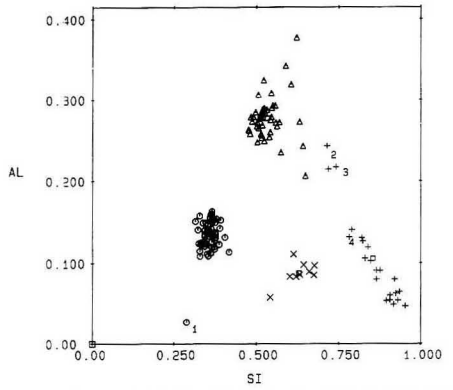

Figure 3. Scatter plot of Si and Al for the clay study clusters. The centroids are shown as squares. Particles 1–4 are misclassified by K-means cluster analysis. (Triangles) muscovite; (circles) ripidolite; (X) nontronite; (+) Ca–montmorillonite.

Table III. Clay Study Centroids, Given as Relative Intensities

cluster	Mg	Al	Si	Fe	K	Ca
nontronite		0.088	0.630	0.233		0.039
Ca–montmorillonite		0.105	0.854	0.011	0.008	0.015
ripidolite	0.095	0.132	0.355	0.410		
muscovite		0.277	0.533	0.022	0.156	

as the maximum distance for cluster assignment was greater than or equal to 0.2. The cluster centroids are given in Table III. The closest centroids were for nontronite and Ca–montmorillonite. The distance between the nontronite and Ca–montmorillonite centroids was 0.317, as compared to the standard deviation of the within-cluster distances of 0.075 and 0.096, respectively. Convergence of the single-linkage seed points to the same four clusters was dependent on the order of the observations in the data matrix. For some sequences, single linkage classified nontronite and Ca–montmorillonite particles into the same cluster, leaving particle 1 in its own single-member cluster.

Particles 1–4 are misclassified; however, Figure 3 and similar scatter plots for the other elemental intensities visually showed these misclassifications to be reasonable. The misclassifications of the particles arose because of natural variability and analytical uncertainty.

In summary, the refine, merge, and single-linkage methods were more likely to find clusters of atypical composition, but they were, therefore, more susceptible to outliers than the four other methods. Single linkage was the only method that failed, under a wide range of circumstances, to delineate the four clay-particle types. The other seed-point methods, on the application of K-means cluster analysis, produced four well-defined clusters.

The clay minerals cluster analysis showed the ability of K-means to easily discriminate among similar mineral types. The maximum distance for cluster assignment was important for defining the clusters. A large maximum distance was able to compensate for less than optimal seed points. In the following studies, however, care was taken to keep the maximum distance small enough so that the cluster analysis did not counteract the ability of a seed-point method to find clusters of atypical composition and/or small occupation.

4.2. Basalt Study. Data on 942 particles from USGS standard basalt BHVO-1 were analyzed. Only elements Na,

Table IV. Basalt Cluster Centroids, Given as Relative Intensities

cluster	Mg	Al	Si	Fe	K	Ca	Ti	identity
1	0.03	0.01	0.53	0.14		0.26	0.01	pyroxene
2		0.17	0.60	0.01		0.22		plagioclase
3			0.12	0.65		0.01	0.19	ilmenite
4		0.01	0.94	0.01	0.02			quartz
5		0.02	0.34	0.50	0.05	0.06	0.15	mixed ilmenite
6		0.07	0.74	0.06	0.05	0.07	0.01	glass
7	0.04	0.01	0.51	0.23		0.19	0.01	pyroxene
8			0.04	0.83		0.01	0.10	iron oxide
9	0.14		0.48	0.35		0.01		olivine
10		0.12	0.62	0.05	0.21			feldspar
11		0.99						alumina

Mg, Al, Si, Fe, K, Ca, and Ti had sufficient concentrations in most of the particles to be useful. The deletion from the data set of all other elements produced a data set of 933 particles. Two of those deleted were apatite particles.

Using the method of Tou and Gonzales (*23*), 70 trial seed points were chosen using a seed-point separation distance of 0.05. These 70 seed points were reduced to 15 using the merge method. The Forgy variety of K-means cluster analysis was used to generate cluster assignments and centroids. A small maximum disance for cluster assignment of 0.15 was used to yield the best possible discrimination among closely spaced clusters. This round gave the first seven clusters listed in Table IV, leaving 100 particles unassigned. Cluster 6 was designated as a glass (a common constituent of basalt) because of the variable amounts of K and Si and the wide variability of the other elements from particle to particle.

Tests of significance were applied using the Engelman and Hartigan percentage points at 50% confidence. The only completely significant cluster (i.e., no test failures) was number 3, ilmenite. Clusters 1, 2, 4, and 5 exhibited one cluster significance test failure each, while clusters 6 and 7 exhibited two test failures each. However, neither cluster 6 or 7 could be deleted without markedly increasing the number of unassigned particles. Clusters 1 and 2 were the closest clusters in the data set, but they did not show a mutual test failure. The clear separation of these clusters underscored the importance of considering the dispersion within clusters, as well as the distance between clusters, in tests of significance.

Since the number of unassigned particles was so large, a second round of cluster analysis was performed (section 2.1.2), yielding four additional clusters (Table IV). However, the addition of these centroids to the original set of seven only decreased the number of unassigned particles to 71. The average number of significance test failures for the original seven centroid set was 1.1 per cluster. The inclusion of the four second-round clusters increased the average number of test failures to 2.2 for the full 11-centroid set. The olivine cluster strongly overlapped with the pyroxene and plagioclase clusters. The general feldspar cluster (no. 10) strongly overlapped with the pyroxene (no. 7), plagioclase, and glass cluster. Unlike other data sets, the iron oxide cluster was not totally significant because of the overlap with the ilmenite cluster. The ilmenite and iron oxide clusters appeared to be part of a single elongated cluster that was arbitrarily divided, when the composition of the particles was plotted versus Fe and Ti. These clusters may represent a Fe–Ti solid solution series of magnetite–ilmenite intergrowths (*26*).

A sample of USGS standard granite G-2 particles was also analyzed in the same fashion (*2*, *14*); however, only the first round of clustering was necessary. The difficulty in adequately characterizing the basalt data set, as compared to the granite set, seems to lie in an increased variability in the composition of the particles in many of the mineral clusters. Basalt is extremely fine grained; moreover it commonly contains long thin crystals that are intimately intergrown with one another. Thus, a granite will be likely to break into discrete mineral grains when crushed whereas a basalt will not. Basalt cluster 5 is a likely candidate for such aggregate particles, and is therefore listed as "mixed ilmenite".

Table V. Seed-Point Trials for the Phoenix Sample and Final Results Using the 20-Centroid Set

method	unassigned particles	av no. of test failures	*f* ratio	*R* ratio
refine	67	8.2	1047	1.0922
merge	76	7.8	1125	1.0864
nearest centrotype	77	6.0	1184	1.0882
single linkage	67	7.9	1052	1.0922
complete linkage	76	5.9	1184	1.0875
av linkage	78	7.5	1143	1.0874
Ward's	76	6.0	1185	1.0875
20-centroid set	42	2.5	1178	1.0110

The number of unassigned particles for the basalt sample could have been decreased by using a larger maximum distance for cluster assignment, but this distance was purposely held small to yield optimal discrimination among closely spaced clusters. The number of clusters to use was somewhat ambiguous. The end use of this centroid set was for mass balance calculations (*2*, *14*), where there was no penalty for a large number of clusters. Since better results were obtained with a larger number of clusters, the full 11-cluster set plus apatite was used in the mass balance calculations.

4.3. Phoenix Study. 4.3.1. Seed-Point Methods. A sample from downtown Phoenix was chosen as representative and used to obtain clusters for the Phoenix aerosol study. This sample was selected because it had high relative intensities of many elements and, because of the central location of the sampling site, it was expected to have most of the types of particles found throughout the Phoenix basin. The 1000-particle data set consisted of relative intensities for 19 elements: Na, Mg, Al, Si, P, S, Cl, K, Ca, Ti, Cr, Mn, Fe, Ni, Cu, Zn, As, Br, and Pb. To test the seven seed-point methods, each method was applied, in turn, to the first 70 observations in the data set in order to produce 20 seed points. These seed points were used in K-means cluster analysis, with a maximum distance for cluster assignment of 0.3. The 20-trial centroids for each seed-point method, so obtained, were used in tests of cluster significance and ANOVA (Table V). There was no unequivocal choice of the best seed-point method to use. The refine and single linkage algorithms were best, considering the number of unassigned particles. Complete linkage gave the best test failure results, with the Engelman and Hartigan percentage points at 50% confidence. Ward's method yielded the best model, based on the *f* ratio criterion. The *R* ratio showed that the merge method best modeled the total variance of the sample, even though the number of unassigned particles was not the smallest. Therefore, the merge method was chosen for further work. The use of the Chandler study and multisample ANOVA to assess seed-point mehods is discussed below.

4.3.2. Clustering. Following the general scheme of section 2.1.6 with the merge method, 35 seed points were chosen from the Phoenix sample. On the basis of the sum-of-squares ratio, seed points were eliminated, yielding a 20-centroid set. The centroids are listed for relative intensities greater than 0.01 (Table VI). The last centroid, which is not listed, has a 0.65 relative intensity for Cr and resulted from residues in the etching solution used to manufacture the polycarbonate filters. This cluster is called the Cr-artifact cluster. The relative intensities are highly distorted from the true compositions of

Table VI. Centroids from the Phoenix Study, Given as Relative Intensities

	Na	Mg	Al	Si	Fe	K	Ca	S	P	Cl	Ti	Mn	Zn	As	Br	Pb
1				0.05	0.92						0.01					
2		0.01	0.08	0.54	0.09	0.04	0.21	0.02								
3		0.02	0.02	0.18	0.05	0.01	0.68	0.01	0.01	0.01						
4			0.11	0.61	0.03	0.23	0.02									
5			0.01	0.13			0.45	0.37		0.02				0.01		
6		0.04	0.06	0.51	0.26	0.06	0.04	0.01			0.02					
7			0.06	0.09	0.03	0.01	0.03	0.43	0.01	0.04			0.01	0.16	0.04	0.09
8				0.06	0.02		0.91	0.01								
9		0.01	0.12	0.61	0.10	0.09	0.05	0.01								
10				0.99												
11	0.01		0.09	0.75	0.05	0.04	0.05									
12		0.01	0.03	0.35	0.08	0.03	0.45	0.01		0.03	0.01					
13	0.06			0.13	0.01	0.03		0.78								
14			0.01	0.08	0.01			0.61						0.18	0.01	0.10
15		0.04	0.05	0.37	0.45	0.02	0.03	0.01			0.01					
16	0.04			0.13	0.51	0.01	0.03	0.05	0.01	0.01	0.01	0.03	0.14	0.01		
17			0.09						0.01	0.88						
18	0.01			0.13	0.01	0.40	0.16			0.28			0.01			
19			0.02	0.08	0.23		0.01				0.66					

Table VII. Cluster Compositions for Phoenix Sample

cluster	elemental compn[a]	similar mineral	% occupation	significance test failures
1	Fe	magnetite	7	
2	Si Ca Fe Al	epidote	6	6
3	Ca Si Fe	pyroxene	4	3
4	Si K Al Fe	orthoclase	7	4
5	Ca S *Si*	gypsum	1	3
6	Si Fe Al K	biotite	4	4
7	Pb Cl Br		3	4
8	Ca	calcite	3	1
9	Si Al K Fe	muscovite	15	5
10	Si	quartz	19	
11	Si Al Fe Ca	albite/montmorillonite	14	3
12	Ca Si Fe	tremolite/actinolite	2	4
13	S *Si* Na		1	2
14	Pb *Si*		3	2
15	Fe Si Al Mg	chlorite	2	2
16	Ti Fe *Si*		0.5	1
17	Fe Zn *Si* S		1	1
18	Ti *Si*	rutile	2	1
19	K Cl Ca *Si*		0.5	4
	unassigned		4	

[a] *Si* indicates that Si may be present in the particles or may result from a spectral artifact (carbon absorption edge).

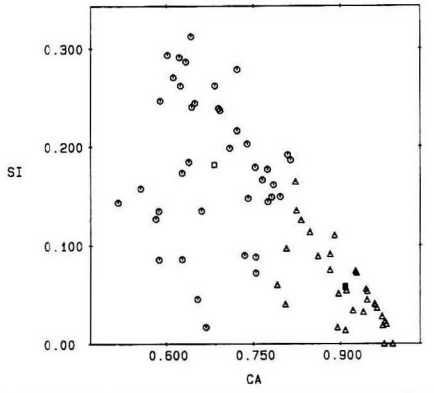

Figure 4. Scatter plot of Ca and Al for Phoenix study clusters 3 and 8: (circles) cluster 3, pyroxene; (triangles) cluster 8, calcite.

the particles because no corrections are made for spectral artifacts, line overlap, atomic number (Z), absorption (A), or fluorescence (F) (*1*). Relative intensities for Si less than 15% are suspect because the carbon absorption edge can give a small integral when no Si is present. The most important elements, in order of decreasing relative intensity, and the relative percentages of particles in each cluster are listed in Table VII. Only 4% of the particles remained unassigned, most of which are rich in heavy metals.

There was considerable ambiguity in the composition of the particles in each cluster, since light elemens (Z < Na) were not determined by EDS. For example, the Fe cluster could have contained iron metal, iron–carbon alloys, or iron oxide particles. The particles in a cluster could have been produced by a variety of sources. The particles in the Ca cluster could have been calcite entrained in the aerosol by automobiles, particles from cement manufacture, or CaO from combustion sources (*4*).

Assuming the particles were of crustal origin, suggestions for mineral types in each cluster were made by comparison with the relative intensities measured for authentic mineral samples (Table VII). The possible minerals were chosen from those previously identified in the Phoenix aerosol by Post and Buseck (*4*), and Pewe et al. (*27*). The structures of albite and montmorillonite are very different. However, they are not distinguishable on the basis of relative intensities, given the large compositional variability of these minerals and the low sensitivity of EDS for Na.

The number of significance test failures for each cluster is also listed in Table VII. Clusters 1, 10, and the Cr-artifact cluster gave no significance test failures. Removing any of these centroids decreased the number of clusters with no test failures and produced a large increase in the number of unassigned particles. Scatter plots of the cluster pairs that gave significance test failures showed that clusters 3 and 8 (Figure 4) and clusters 7 and 14 appeared to be single elongated clusters that had been arbitrarily divided.

The f ratios and R ratios for the Phoenix sample are included in Table V. Compared to the centroid sets formed to test the seed-point selection methods, the 20-centroid set yielded a considerable improvement in the R ratio, indicating an improved ability to model the data set. This result came from a large decrease in the number of unassigned particles. However, the moderate f ratio showed that there was some sacrifice for the improved R ratio, which resulted from an increased variability of the composition of the larger clusters.

Table VIII. Seed-Point Trials Applied to the Nine Chandler Samples and Final Results Using the 20-Centroid Set

method	unassigned	*f* ratio	*R* ratio
refine	973	276.5	1.4937
merge	996	288.3	1.4820
nearest centrotype	1004	300.0	1.4946
single linkage	973	277.0	1.4935
complete linkage	995	297.4	1.4909
av linkage	999	293.3	1.4841
Ward's	1001	301.4	1.4920
20-centroid set	638	382.8	1.1780

The composite discriminatory power (*28*) was used to determine the effect each variable had on the formation of each cluster. In order of decreasing discriminatory power, Si, Fe, Ca, S, K, and Al were the most important elements for separating the clusters. The high discriminatory power of S resulted from several factors. (1) Clusters 5 and 13 contained large amounts of S. (2) Many clusters had small amounts of S. Clusters 2, 3, 6, 9, 12, 15, and 18 had relative intensities for S between 1% and 5%. (3) The overlap of the Pb–M and S–K X-ray lines in the EDS spectra produced large counts for the sulfur ROI in clusters that contained significant amounts of Pb. In particular, clusters 7 and 14 had large relative intensites for S in addition to Pb, even though no S may have been present. Sulfur, therefore, played an important role in determining the structure of the data set. The large apparent abundance for As in centroids 7 and 14 was caused by overlap of Pb–L and As–K X-ray lines. For these reasons, S and As were not listed as major elements for clusters 7 and 14 in Table VII. The ratio of S and As relative intensities to Pb was consistent with only Pb being present in the particles. However, the characteristic pattern of As and S was an important distinguishing characteristic for clusters 7 and 14. Attempts to strip the relative intensities of S and As from these particles would have made the identification of Pb-containing particles more difficult. The problem caused by the overlap of the Pb, S, and As X-ray lines was that a particle with large amounts of As and S might have been misclassified.

In summary, the maximum distance for cluster assignment was chosen to yield a few unassigned particles. The large maximum distance gave a coarser structure than the basalt study, that is, more large occupation clusters and fewer small occupation clusters. However, the large maximum distance did not result in an overly coarse structure, since 13 clusters with occupations less than 5% of the total were found. The lack of sensitivity to the seed-point method used showed that the data set was well-structured for this degree of coarseness. Larger differences between the seed-point methods would have resulted from a smaller maximum distance for cluster assignment.

4.4. Chandler Study. 4.4.1. Phoenix Seed Points. The multisample Chandler data set was used to help assess the best seed-point method to use for cluster analysis in the Phoenix study. Each of the seven seed-point sets was used in a trial K-means cluster analysis, with a maximum distance for cluster assignment of 0.3, to produce 20 trial centroids. The trial-centroid sets were used, in turn, in discriminant analysis to classify the particles from the nine-sample Chandler set. ANOVA results are listed in Table VIII. There was no clearly superior seed-point method, but the variation among seed-point methods was larger than that obtained for the Phoenix sample alone. The merge method gave the best *R* ratio, in agreement with the single-sample ANOVA results. Therefore, the merge method, as reported above, was chosen for further work because it best modeled the variability in the nine-sample data set.

4.4.2. Discriminant Analysis. The 20-centroid set determined in the Phoenix study (Table VI) was used in nearest centroid discriminant analysis to classify the particles in the nine samples collected in Chandler (Table IX). A maximum distance for cluster assignment was chosen that was 3 times the standard deviation of the within-cluster distances of the largest cluster in the Phoenix study. The ANOVA results for the final 20-centroid set are listed in Table VIII. The number of assigned particles, the *f* ratio, and the *R* ratio show considerable improvement over the trial centroid sets discussed in section 4.4.1.

In the Phoenix study, quartz was the most common particle type. In Chandler, muscovite and albite/montmorillonite were more abundant, in agreement with Post and Buseck (*4*). Chandler is dominated by large housing developments and therefore is much less industrial than central Phoenix. The residential environment was reflected in the smaller number of particles in the Fe-rich (no. 1), Ti-rich (nos. 16 and 18), and Pb-rich (nos. 7 and 14) clusters in Chandler.

4.4.3. Correlation Analysis. The relative number of particles in each cluster was used to calculate the covariance and correlation matrices (*29*, *30*) of the cluster assignments (Table IX) over the nine-sample study. The resulting assignment correlation matrix is given in Table X. The small number of particles in some clusters created a large uncertainty for many correlations; therefore, only correlations with absolute values greater than 0.50 are listed. Many of the clusters dominated by crustal material do not correlate well with each other from day to day. For example, the correlation coefficients between orthoclase (no. 4) and, in turn, muscovite (no. 9), albite/montmorillonite (no. 11), epidote (no. 2), biotite (no. 6), and quartz (no. 10) were all less than 0.50.

The assignment correlation matrix was used to explore the significance (separation) of the various clusters, as an adjunct to the sum-of-squares ratio test used in section 4.3.2. A large positive correlation between two clusters could have arisen in two ways: the clusters overlapped, or the particles came from the same source or sources having the same temporal pattern of emissions. The lack of correlation between two

Table IX. Classification of Chandler Samples Using the 20-Centroid Set[a]

	cluster																	
date	1	2	3	4	5	6	7	8	9	10	11	12	13	14	15	16	17	18	19
Feb 22	18	34	18	37	6	22	2	6	95	39	91	16	15	3	6	1	3	1	0
Feb 23	11	62	43	55	9	21	9	32	162	74	171	30	9	9	24	0	13	1	0
Feb 24	7	13	15	31	2	13	0	8	114	29	101	8	6	1	6	0	1	0	0
Feb 26	14	23	8	30	1	23	1	9	114	55	105	11	5	4	6	0	3	1	8
Feb 27	17	23	8	36	10	18	4	5	85	74	94	15	22	7	11	0	4	1	4
Feb 28	22	24	10	47	4	20	3	7	108	53	108	8	13	5	11	1	1	0	0
March 3	10	36	28	30	6	20	2	43	104	57	119	21	7	2	6	0	2	0	1
March 4	6	49	8	29	4	17	5	16	102	48	104	17	2	4	7	1	2	0	3
March 5	3	19	18	24	3	11	2	15	33	29	67	17	5	5	5	3	0	6	3

[a] Entries are the number of particles in each cluster.

Table X. Chandler Study Assignment Correlation Matrix

	C1	C2	C3	C4	C5	C6	C7	C8	C9	C10	C11	C12	C13	C14	C15	C16	C17	C18	C19
C1	1.00		−0.52	0.61		0.69		−0.65				−0.65	0.72						
C2		1.00					0.70					0.52							
C3	−0.52		1.00			−0.54		0.62		−0.60		0.57							−0.51
C4	0.61			1.00				−0.72				−0.63	0.52						
C5					1.00					0.54		0.74							
C6	0.69		−0.54			1.00													
C7		0.70					1.00							0.63	0.64		0.57		
C8	−0.65		0.62	−0.72				1.00				0.56	−0.56						
C9									1.00		0.90	−0.65		−0.65		−0.73		−0.77	
C10			−0.60		0.54					1.00			0.51						
C11									0.90		1.00			−0.66		−0.58		−0.58	
C12	−0.65	0.52	0.57	−0.63				0.56	−0.65			1.00						0.54	
C13	0.72			0.52	0.74			−0.56		0.51			1.00						
C14							0.63		−0.65		−0.66			1.00	0.51				
C15							0.64							0.51	1.00		0.74		
C16								−0.73		−0.58						1.00	−0.51	0.89	
C17							0.57								0.74	−0.51	1.00		
C18								−0.77		−0.58	0.54					0.89		1.00	
C19			−0.51																1.00

Table XI. Principal Component Analysis for the Chandler Study

cluster	P1	P2	P3	P4	similar mineral
1	0.04	−0.30	−0.05	−0.12	magnetite
2	−0.05	0.27	0.70	−0.58	epidote
3	−0.05	0.36	−0.26	0.09	pyroxene
4	0.08	−0.17	−0.26	−0.24	orthoclase
6	0.03	−0.11	0.03	−0.09	biotite
8	−0.09	0.50	0.18	0.49	calcite
9	0.91	0.01	0.12	−0.03	muscovite
10	−0.03	−0.48	0.55	0.53	quartz
11	0.38	0.24	−0.08	0.23	albite/montmorillonite
12	−0.10	0.16	0.09	−0.03	tremolite/actinolite
13	−0.03	−0.31	−0.09	0.01	$(NH_4)_2SO_4$, Na_2SO_4
15	0.01	−0.03	0.03	0.00	ripidolite/chlorite
eigenvalues	4.42×10^{-3}		1.19×10^{-3}	5.68×10^{-4}	3.77×10^{-4}

clusters showed that significant overlap was unlikely.

The only pairs of clusters that exhibited a mutual significance test failure and a correlation coefficient greater than 0.6 were pairs 9–11, 16–18, 15–17, 7–14, and 3–8. There was a surprising lack of correlation between the clusters in the data set as compared to the number of significance test failures using the sum-of-squares ratio test (section 4.3.2). This showed that the sum-of-squares ratio test, while useful, may have been too stringent.

The high correlation between these five pairs was reasonable from the point of view of compositional similarity and the possibility of common sources. For example, the particles in clusters 3 and 8 could have been derived from the wear of traffic on concrete roads (*4*), the Pb-rich clusters (nos. 7 and 14) were almost certainly from vehicle emissions, and the particles in cluster 17 (Fe, Zn, *Si*, S) and the chlorite cluster (no. 15) might have been agglomerates of small iron oxide and dust particles produced by foundry activity.

4.4.4. Principal Component Analysis. Principal component analysis was useful for clarifying the structure in the assignment covariance or correlation matrix (*29, 30*). Clusters with an average number of particles, over the 9 days, less than or equal to nine particles were deleted to avoid the statistical noise inherent in such small numbers. The first four principal components of the nine-sample covariance matrix are listed in Table XI. The first two components accounted for 80.6% of the variation in the data set.

The first principal component (P1) showed a large contribution from clusters 9 (muscovite) and 11 (albite/montmorillonite). This association resulted from the large overlap between the two clusters, as discussed in section 4.4.3. The

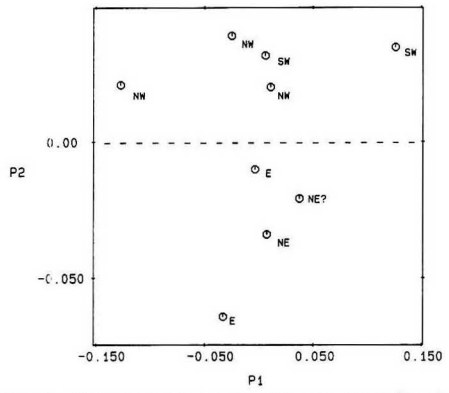

Figure 5. Principal component scores for the nine-sample Chandler study, based on the principal components listed in Table XI. Upper level wind directions for each sample are shown.

second principal component (P2) was more complex but was dominated by cluster 8 (calcite). The relative ordering of the principal component scores of the nine samples on P2, almost exactly, paralleled the assignments for the calcite cluster (Table IX).

The principal component scores for each Chandler sample are plotted in Figure 5. The axes are the vectors corresponding to the first two principal components. To verify that the pattern observed in Figure 5 truly represented the data, the principal component analysis was repeated in several different ways.

The principal components listed in Table XI were calculated using the relative number of particles in covariance about the mean (*29*). Principal component analysis was repeated using the relative and absolute number of particles in covariance about the origin, covariance about the mean, correlation about the origin, and correlation about the mean (the traditional correlation matrix). Only for absolute numbers and covariance about the origin and mean did no single principal component show the ordering of the samples on P2 in Figure 5. However, scatter plots of P3 versus P2 showed the expected ordering diagonally between P3 and P2, which showed that P2 and P3 in linear combination were equivalent to the desired principal component in Table XI. In addition, target testing and short circuit data reproduction (*29*) with

the principal components in Table XI showed that the set of principal components calculated from absolute numbers and covariance about the mean were equivalent. Therefore, the structure shown in Figure 5 is inherent in the data set no matter the scaling or transformation used to preprocess the data.

The pattern of samples in Figure 5 did not correlate well with ground-level wind direction, speed, or occurrence of rain. However, the pattern of scores on the second principal component did correlate well with U.S. Weather Service data for upper level winds at 850 mbar recorded at Winslow, AZ (Figure 5). Wind data were missing for Feb 26; however, the position of a low-pressure area in southern Arizona at that time was consistent with a northeasterly wind during the sample period, and so is shown with a question mark in Figure 5. The wind direction for the sampling period immediately following was from the east.

All the samples taken during westerly prevailing winds had positive scores on P2, and those with easterly winds (including the Feb 26 sample) had negative scores on P2. Positive scores corresponded to high assignments for the calcite and pyroxene clusters and low assignments for the $Na_2SO_4/(NH_4)_2SO_4$ cluster. Samples with positive scores also tended to have fewer quartz and magnetite particles. The sources responsible for this east–west variation are not clear.

5. CONCLUSIONS

5.1. Methods. Relative intensities rather than concentrations are adequate for representing the compositions of aerosol particles for cluster analysis. K-means cluster analysis is a simple, fast, and sufficient tool for the analysis of data sets of complex aerosol particles. The maximum distance for cluster assignment tailors these methods for different goals. For particle recognition, a small maximum distance for cluster assignment allows the best discrimination among particle types. For data reduction and recognition of unusual particles, a large maximum distance for cluster assignment is useful. A large maximum distance assures that most of the particles in the data set are represented in the cluster assignments and, conversely, that only unusual particles are left unassigned. No one set of centroids is optimal for each goal.

Testing of cluster significance is critical for determining the number of clusters to use for a given data set, as well as for assessing the amount of overlap between clusters when the analysis is complete. Classical ANOVA, which measures the ability of a centroid set to model the data, is a useful adjunct to tests of cluster significance for comparing seed-point methods, for determining the number of clusters, and for final assessments. A necessary analysis of variance when some observations remain unassigned is the R ratio, which in some cases may be the most diagnostic of ANOVA techniques. While the f and R ratios are useful for comparing methods, they are limited in an absolute sense for evaluating the quality of results.

If a multisample data set is available, multisample ANOVA aids in the determination of the best seed-point methods and the ability of a centroid set to model data under a wide range of circumstances. Rather than pooling the observations over a sampling study (7), keeping samples separate allows the determination of possible variations from day-to-day and the ability of a centroid set to model that variability. After a centroid set is accepted, the process may be reversed so that the homogeneity of the particle types from sample to sample may be assessed. The number of assigned observations and the single-sample and multisample R ratios are useful measures of the ability of a centroid set to model sample-to-sample variability.

Following discriminant analysis, the calculation of the assignment covariance matrix plays the dual role of (1) providing an additional test for judging the significance of clusters and (2) uncovering underlying trends in the temporal (or spatial) emission patterns.

The results of the procedures in this study are a comprehensive set of tools for solving a wide variety of problems in aerosol environmental chemistry, and for large data sets in general.

5.2. Applications. The clay study shows the suitability of K-means cluster analysis for chemically similar phases. Both the seed-point method and the maximum distance for cluster assignment play a role in the sensitivity to outliers and the coarseness of the clustering. The refine, merge, and single-linkage seed-point methods, coupled with a small maximum distance for cluster assignment, provide a finer structure by optimizing the search for clusters of small occupation or atypical composition. But these conditions also increase the tendency to choose outliers as seed points. On the other hand, nearest centrotype, average linkage, and Ward's method, coupled with a larger maximum distance, emphasize the major clusters, thereby leading to a coarser structure to the clustering.

The importance of tests of cluster significance as a guide to the selection of the proper number of clusters is evident in the basalt study. It is important in this testing to consider the dispersion within clusters as well as the distances between clusters. Even then, the best choice for the number of clusters for the analysis is, in part, determined by the prospective use of the centroids.

For the Phoenix study, no clear choice of seed-point method is evident. Any one of the methods would probably suffice. However, the scheme in which the seed-point method is applied has a large effect on the outcome. The scheme suggested in this study uses the two-round procedure for seed-point selection and the repeated application of tests of significance and cluster analysis to determine the proper number of centroids. The final 20-centroid set provides a good balance between clusters with large and small occupations. The natural variability of the aerosol particles produces overlap between many of the clusters in the final set, as detected by tests of significance. In the basalt and Phoenix studies two or more spherical clusters are used to model a single nonspherical cluster. This usage overcomes the inherent spherical nature of K-means clustering but is responsible for some of the significance test failures.

The Chandler multiday sampling study is used to aid the evaluation of seed-point selection methods for the Phoenix sample. Again, no clear best choice of seed-point method is evident, but the variation in the test results is larger from method to method than the results using only a single sample. The small number of large positive day-to-day correlations in cluster assignments shows that most of the clusters are well-resolved, which suggests that the sum-of-squares test may be too stringent. The temporal emission patterns, displayed using principal components scores, show a marked correlation with upper level wind directions.

Cluster analysis is a necessary tool for data reduction of complex aerosol data sets. The particle types determined help to uncover underlying sources and trends in particle emission through the use of discriminant, correlation, and principle component analysis. Tests of significance and ANOVA are needed to judge seed-point methods, to determine the number of clusters for analysis, and to assess the ability of a centroid set to model the data. The Phoenix and Chandler studies show that single-particle EDS analysis provides a wealth of information not available from other techniques.

Registry No. Na, 7440-23-5; Mg, 7439-95-4; Al, 7429-90-5; Si, 7440-21-3; P, 7723-14-0; S, 7704-34-9; Cl, 7782-50-5; K, 7440-09-7; Ca, 7440-70-2; Ti, 7440-32-6; V, 7440-62-2; Cr, 7440-47-3; Mn, 7439-96-5; Fe, 7439-89-6; Ni, 7440-02-0; Cu, 7440-50-8; Zn,

7440-66-6; Ge, 7440-56-4; As, 7440-38-2; Se, 7782-49-2; Br, 7726-95-6; Zr, 7440-67-7; Pd, 7440-05-3; Ag, 7440-22-4; Cd, 7440-43-9; Sn, 7440-31-5; Ba, 7440-39-3; W, 7440-33-7; Au, 7440-57-5; Hg, 7439-97-6; Pb, 7439-92-1; montronite, 12174-06-0; montmorillonite, 1318-93-0; ripidolite, 12414-36-7; muscovite, 1318-94-1.

LITERATURE CITED

(1) Shattuck, T. W.; Germani, M. S.; Buseck, P. R. In *Environmental Applications of Chemometrics*; Breen, J. J., Robinson, P. E., Eds.; ACS Symposium Series No. 292; American Chemical Society: Washington, DC, 1985; Chapter 9.
(2) Shattuck, T. W.; Germani, M. S.; Buseck, P. R. In *Proceedings: Fifth Annual Symposium on Recent Advances in Pollutant Monitoring of Ambient Air and Stationary Sources*, Environmental Protection Agency, Raleigh, NC, May 1985; EPA/600/9-85/029; Environmental Protection Agency: Research Triangle Park, NC, 1986; pp 130–133.
(3) Kim, D.; Hopke, P. K. *Aerosol Sci. Technol.* **1988**, *9*, 133–151.
(4) Post, J. T.; Buseck, P. R. *Environ. Sci. Technol.* **1984**, *18*, 35–42.
(5) Anderson, J. R.; Aggett, F. J.; Buseck, P. R.; Germani, M. S.; Shattuck, T. W. *Environ. Sci. Technol.* **1988**, *22*, 811–818.
(6) Kim, D. S.; Hopke, P. K.; Casuccio, G. S.; Lee, R. J.; Miller, S. E.; Sverdrup, G. M.; Garber, R. W. *Atmos. Environ.* **1989**, *23*, 81–84.
(7) Saucy, D. A.; Anderson, J. R.; Buseck, P. R. *Atmos. Environ.* **1987**, *21*, 1649–1657.
(8) Buseck, P. R.; Anderson, J. R.; Dea, J. Y.; Aggett, F. J.; Germani, M. S.; Shattuck, T. W. In *Proc.—APCA Annu. Meet.* 1986, 79th (Vol. 2), 86/26.1.
(9) Armstrong, J. T.; Buseck, P. R. *Electron Microsc. X-Ray Appl. Environ. Occup. Health Anal.* **1978**, *2*, 211–228.
(10) Bradley, J. P.; Goodman, P.; Chan, I. Y. T.; Buseck, P. R. *Environ. Sci. Technol.* **1981**, *15*, 1208–1212.
(11) Bradley, J. P.; Buseck, P. R. *Nature* **1983**, *306*, 770–772.
(12) Buseck, P. R.; Bradley, J. P. In *Heterogeneous Atmospheric Chemistry*; Schryer, D. R., Ed.; Geophysical Monograph No. 26; American Geophysical Union: Washington, DC, 1982; pp 57–76.
(13) Thomas, E.; Buseck, P. R. *Atmos. Environ.* **1983**, *17*, 2299–2301.
(14) Germani, M. S.; Buseck, P. R. *Anal. Chem.* **1991**, *63*, 2232–2237.
(15) Bernard, P. C.; Van Grieken, R. E.; Eisma, D. *Environ. Sci. Technol.* **1986**, *20*, 467–73.
(16) Gaarenstrom, P. D.; Preone, S. P.; Moyers, J. L. *Environ. Sci. Technol.* **1977**, *11*, 795.
(17) Hopke, P. K.; Alpert, D. J.; Roscoe, B. A. *Comput. Chem.* **1983**, 7 (3), 149.
(18) Anderberg, M. R. *Cluster Analysis for Application*; Academic Press: New York, 1973.
(19) Massart, D. L.; Kaufman, L. *The Interpretation of Analytical Chemical Data by the Use of Cluster Analysis*; Wiley: New York, 1983; p 107.
(20) Hartigan, J. A. *Clustering Algorithms*; Wiley: New York, 1975; p 97.
(21) Johnson, R. A.; Wichern, D. W. *Applied Multivariate Statistical Analysis*; Printice-Hall: Englewood Cliffs, NJ, 1982.
(22) SAS Institute Inc. *SAS User's Guide: Statistics*; SAS Institute Inc.: Cary, NC, 1982; pp 417–434.
(23) Tou, J. T.; Gonzalez, R. C. *Pattern Recognition Principles*; Addison-Wesley: Reading, MA, 1974; pp 90–92.
(24) Dixon, W. J. *BMDP Statistical Software, 1983 Printing with Additions*; University of California Press: Berkeley, 1983; pp 466–467.
(25) Engelman, L.; Hartigan, J. A. *J. Am. Stat. Assoc.* **1969**, *64*, 1647–1648.
(26) Deer, W. A.; Howie, R. A.; Zussman, J. *An Introduction to the Rock Forming Minerals*; Wiley: London, 1966; pp 412–413.
(27) Pewe, T. L.; Pewe, E. A.; Pewe, R. H.; Journaux, A.; Slatt, R. M. *Spec. Pap.—Geol. Soc. Am.* 1981, No. 186.
(28) Wold, S.; Sjostrom, M. In *Chemometrics, Theory and Application*; Kowalski, B. R., Ed.; ACS Symposium Series No. 52; American Chemical Society: Washington, DC, 1977; pp 243–281.
(29) Malinowski, E. R.; Howery, D. G. *Factor Analysis in Chemistry*; Wiley: New York, 1980.
(30) Johnson, R. A.; Wichern, D. W. *Applied Multivariate Statistical Analysis*; Prentice-Hall: Englewood Cliffs, NJ, 1982; pp 243–281.

RECEIVED for review January 17, 1991. Revised manuscript received August 12, 1991. Accepted August 22, 1991. Financial support for this work was provided by grants from the Atmospheric Chemistry Division of the National Science Foundation. Preliminary results were presented at the 188th National Meeting of the American Chemical Society, Philadelphia, PA, Aug 1984, at the Fifth Annual Symposium on Recent Advances in Pollutant Monitoring of Ambient Air and Stationary Sources, Environmental Protection Agency, Raleigh, NC, May 1985, and the 17th Northeast Regional Meeting of the American Chemical Society, Rochester, NY, Nov 1987.

TECHNICAL NOTES

Two-Dimensional Ion-Pairing Reversed-Phase Chromatography of Nucleosides and Nucleotides on Polymeric and Silica Stationary-Phase Supports

Robert L. St. Claire, III

Department of Drug Metabolism, Glaxo Research Institute, Research Triangle Park, North Carolina 27709

INTRODUCTION

Improved techniques for the analysis of mixtures of nucleosides and nucleotides are in demand as a result of the use of these classes of compounds in studies directed at suppressing the human immunodeficiency virus (HIV) (*1*). A desired technique would be one that could measure multiple, nonradiolabeled therapeutic nucleoside analogues and their respective phosphates simultaneously from a single biological sample containing an excess of endogenous nucleosides and nucleotides. Such a technique has not as yet been reported.

The most popular chromatographic technique applied to the separation of nucleotides is reversed-phase ion-pairing HPLC using the tetrabutylammonium ion as an agent to impart added hydrophobicity to the nucleotides (*2–7*). Some applications of ion-pairing HPLC (*3–6*) have included separations of relatively simple mixtures of endogenous nucleosides and nucleotides. However, as such mixtures become more complex and include therapeutic nucleoside analogues and their respective phosphates, the probability increases that nucleoside and nucleotides will coelute.

For the chromatographic analysis of a complex biological matrix, some form of sample clean-up, such as solid-phase extraction (SPE), often precedes the HPLC separation method. There are few reports on the application of SPE, in an ion-pairing mode. The ion-pairing SPE of both anionic (*8*) and cationic compounds (*9*) was reported.

This report describes a two-dimensional separation system in which ion-pairing solid-phase extraction and ion-pairing HPLC are combined for the analysis of 13 nucleosides and mono-, di-, and triphosphate nucleotides. Central to this approach is a novel ion-pairing solid-phase extraction procedure that relies on the use of a polymeric stationary-phase support as opposed to the widely used silica-based solid supports.

EXPERIMENTAL SECTION

Reagents. 2′,3′-Dideoxyguanosine (ddG), 2′,3′-dideoxyadenosine (ddA), and 2′,3′-dideoxyguanosine 5′-triphosphate (ddGTP) were obtained from ICN Biochemicals Inc. (Costa Mesa, CA). 2′-Deoxyguanosine 5′-monophosphate (dGMP), 2′-deoxyadenosine 5′-monophosphate (dAMP), 2′-deoxyguanosine 5′-diphosphate (dGDP), adenosine 5′-diphosphate (ADP), N^6-methy-2′-deoxyadenosine (mdA), N^6-methyladenosine 5′-monophosphate (mAMP), 3′-azido-3′-deoxythymidine (AZT), 2′-deoxyadenosine 5′-triphosphate (dATP), and 2′,3′-dideoxyadenosine 5′-triphosphate (ddATP) were obtained from Sigma Chemical Co. (St. Louis, MO). 2′-Deoxyadenosine (dA) was obtained from Aldrich Chemical Co. (Milwaukee, WI). Because these nucleosides and nucleotides have the potential to interact with processes involved in the replication of human genetic material, they should be handled in a safe and appropriate manner. HPLC grade tetrabutylammonium hydroxide (TBAH) (1 M solution) was received from Fisher (Fair Lawn, NJ).

Apparatus. The 1.0-mL capacity Polysorb MP-1 solid-phase extraction columns with 100 mg of packing were obtained from Interaction Chemicals Inc. (Mountain View, CA). The 1.0-mL capacity Bond Elute C_{18} solid-phase extraction column with 100 mg of packing was obtained from Analytichem International (Harbor City, CA). The HPLC column, a 150 × 4.6 mm Adsorbosphere HS C_{18} with 3 μm diameter packing, was purchased from Alltech Associates Inc. (Deerfield, IL). A 10 × 4.6 mm matching guard column from the same source was also included. Vacuum aspiration for solid-phase extraction was provided with a Vac Elute SPS 24 manifold (Analytichem International). The HPLC system consisted of a Model 400 solvent delivery system and Model 783A programmable absorbance detector (Applied Biosystems Inc., Ramsey, NJ). Data acquisition employed the PE Nelson Turbochrom II with a Series 900 interface (Perkin Elmer Nelson Systems, Inc., Cupertino, CA).

Procedures. *HPLC Conditions.* The mobile-phase buffer for this study contained 0.05 M ammonium phosphate monobasic with 2.0 mM TBAH. The pH of this solution was adjusted to 6.5 with ammonium hydroxide. The final mobile phase was prepared by adding acetonitrile to this buffer to a concentration of 7.0% (v/v). A mobile-phase flow rate of 1.0 mL/min and a column temperature of 35 °C were utilized. Typically, the column was allowed to equilibrate under these conditions for 1–2 h prior to the start of analysis. The injection volume for all studies was 50 μL. UV detection at 252 nm with a rise time of 1.0 s was employed. Data acquisition was conducted with a sampling rate of 2.0 points/s.

Sample Preparation. A 1.0-mL aqueous solution of all nucleosides and nucleotides was prepared that contained 37.5%, by volume, of the HPLC mobile-phase buffer. The concentrations (μM) of the nucleosides were AZT (1.1), dA (0.53), ddA (0.70), ddG (0.38), and mdA (0.60). The concentrations (μM) of the nucleotides were ADP (0.45), dAMP (0.70), dATP (0.34), ddATP (0.72), ddGTP (0.43), dGDP (0.26), dGMP (0.41), and mAMP (0.65). This sample was analyzed directly by HPLC, as well as used in its entirety for the solid-phase extraction studies described below.

Solid-Phase Extraction with MP-1 C_{18} Columns. The following scheme outlines the SPE procedure used. (1) Wash the column with 2.0 mL of methanol. (2) Wash the column with HPLC mobile-phase buffer (500 μL × 2). (3) Slowly (0.5–1.0 mL/min) load 1.0 mL of the sample onto the column. (4) Wash the column with water (500 μL × 2). (5) Elute fraction 1 (nucleosides) with 1.0 mL of 50% methanol in water (v/v). (6) Wash the column with 1.0 mL of 50% methanol in water (v/v). (7) Elute fraction 2 (nucleotides) with 1.0 mL of 0.26 M ammonium phosphate buffer, pH 6.5, containing 50% methanol (v/v). (8) Dry down fractions 1 and 2 at 40 °C under N_2 for 1.5 h. (9) Reconstitute each fraction in 375 μL of HPLC mobile-phase buffer plus 625 μL of water. This sample was analyzed by using the HPLC conditions described earlier.

Solid-Phase Extraction with Bond Elute C_{18} Columns. The extraction scheme follows the same steps as described for the MP-1 columns above with the following exceptions. In addition to processing an identical sample in a manner identical with that described for the MP-1 column above, two additional samples were examined in a modified manner. In place of the HPLC mobile-phase buffer (with 2.0 mM TBAH) used in the sample preparation and in extraction step 2 described above, phosphate buffers with 4.0 and 8.0 mM TBAH were substituted.

Modified Method for Solid-Phase Extraction on MP-1 Columns. (1) Wash the column with 2.0 mL of methanol. (2) Wash the column with HPLC mobile-phase buffer (500 μL × 2). (3) Load a 1.0-mL solution containing 250 μL of water and 750 μL

0003-2700/91/0363-2657$02.50/0

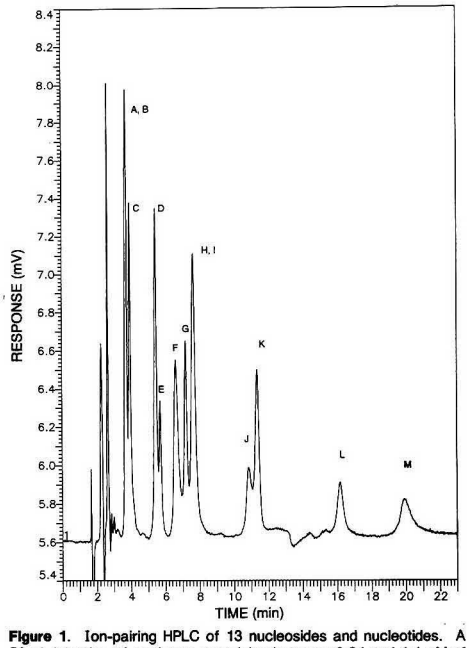

Figure 1. Ion-pairing HPLC of 13 nucleosides and nucleotides. A 50-μL injection of a mixture containing between 0.34 and 1.1 μM of each of the following compounds was employed: (A) and (B) (ddG,-dGMP); (C) dA; (D) dAMP; (E) dGDP; (F) ddA; (G) ADP; (H) and (I) (mAMP,mdA); (J) ddGTP; (K) AZT; (L) dATP; (M) ddATP.

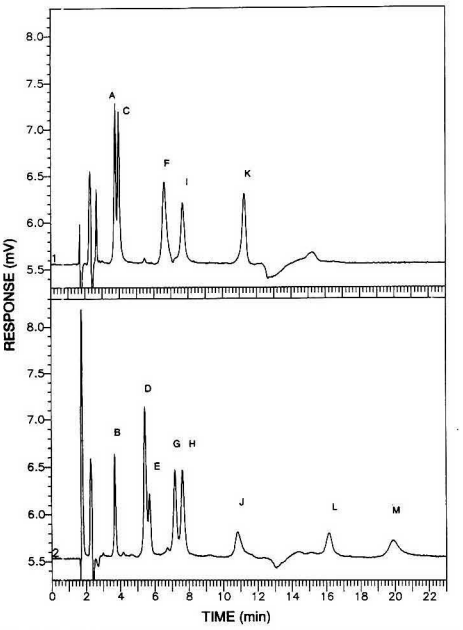

Figure 2. Ion-pairing HPLC of fractions recovered from the MP-1 solid-phase extraction column. Figure 2(upper) represents the following nucleosides extracted: (A) ddG; (C) dA; (F) ddA; (I) mdA; (K) AZT. Figure 2(lower) represents the following nucleotides extracted: (B) dGMP; (D) dAMP; (E) dGDP; (G) ADP; (H) mAMP; (J) ddGTP; (L) dATP; (M) ddATP.

of HPLC mobile-phase buffer. (4) Wash the column with water (500 μL × 2). (5) Wash the column with 2.0 mL of 50% methanol in water. (6) Wash the column with 1.0 mL of 0.26 M ammonium phosphate buffer, pH 6.5, containing 50% methanol (v/v). (7) Wash the column with 1.0 mL of 0.05 M ammonium phosphate buffer, pH 6.5 (no TBAH). (8) Load a 1.0-mL aqueous sample with 75% v/v of 0.05 M ammonium phosphate buffer, pH 6.5 (no TBAH), that contains dAMP, ddGTP, ddGDP, dGMP, and mdA at the same concentrations as for the original sample described earlier. The remaining steps follow steps 4–9 of the original method for the MP-1 C_{18} columns.

RESULTS AND DISCUSSION

Ion-Pairing HPLC of Nucleosides and Nucleotides. The separation of 13 nucleosides and nucleotides using ion-pairing liquid chromatography is shown in Figure 1. Compounds ddG, dGMP (peaks A, B) and mAMP, mdA (peaks H, I) are not resolved. A less than desirable resolution occurs between ddGTP and AZT (peaks J, K). The TBAH concentration in the mobile phase represents what was experimentally determined to be optimum and is consistent with what is recommended in the literature (*4*). For optimum nucleotide peak shape, TBAH also needs to be present in the sample prior to injection onto the HPLC system. All attempts at developing a gradient elution method in this ion-pairing mode proved unsuccessful. Under a variety of gradient elution profiles (increasing acetonitrile concentration at a fixed mobile-phase concentration of TBAH) a large positive base-line shift consistently compromised the detection of the later eluting nucleotide triphosphates. It is suspected that this effect results in part from the effect the increasing acetonitrile concentration is having on the distribution of the ion-pairing agent between the mobile phase and the stationary phase.

Solid-Phase Extraction with MP-1 C_{18} Columns. Figure 2(upper) is a chromatogram of the reconstituted neutral nucleosides, while Figure 2(lower) is a chromatogram of the reconstituted anionic nucleotides. The extraction efficiencies of dA, ddA, dAMP, dGDP, dATP, and ddATP were all determined to be 90% or greater. The combination of ion-pairing SPE with ion-pairing HPLC yielded a separation of nucleosides and nucleotides (ddG, dGMP, mAMP, mdA, ddGTP, and AZT) not possible with ion-pairing HPLC alone.

The TBAH concentration used in sample preparation and in step 2 of this SPE procedure was examined briefly. There was no advantage in increasing the TBAH concentration in the buffer above 2.0 mM. However when a TBAH concentration of 1.0 mM was used, nucleotide triphosphates began to elute prior to fraction 2.

The effect of the wash solvent composition utilized in step 4 was examined. When the water was replaced with 10% methanol in water (v/v), the extraction efficiencies of ddG and dA were reduced to 10%.

The effect of the ammonium phosphate concentration in the buffer used to elute the nucleotides in step 7 was also examined. In addition to 0.26 M ammonium phosphate utilized for this SPE procedure, other concentrations examined included 0.13, 0.052, and 0.026 M. The nucleotide triphosphates did not elute off the column (using the same elution volume) when the buffer concentration was reduced below 0.26 M. This effect of ionic strength on the capacity factor is consistent with the role that the overall ionic equilibrium has on ion-pairing liquid chromatography (2). Although the results were not presented in this report, this two-dimensional ion-pairing separation scheme was successfully applied to the analysis of nucleoside analogues and their phosphate metabolites in tissue culture.

Solid-Phase Extraction with Bond Elute C_{18} Columns. When the same SPE procedure utilized for the MP-1 columns was applied to the Bond Elute columns, all nucleosides and nucleotides eluted together in fraction 1 (step 5) with nearly 100% extraction efficiency. The only exception was dATP, which had a 60% extraction efficiency due the fact that it had already begun to be eluted from the column with the proceeding wash procedure, step 4. Increasing the TBAH concentration (2 mM) used in sample preparation and step 2 to 4.0 and 8.0 mM failed to effect the adsorption of the nucleotides. Clearly, the adsorption characteristics of the Bond Elute SPE columns (C_{18} stationary phase bonded to silica) differ under these ion-pairing conditions from the MP-1 C_{18} columns.

Retention Mechanism Studies on MP-1 C_{18} Columns. The MP-1 SPE column contains a C_{18} stationary phase bonded to a polystyrene–divinylbenzene support. According to the manufacturer, this material behaves more like C_{18} silica-based columns than conventional polymeric reversed-phase ("PRP") materials. In order to gain some understanding of the ion-pairing phenomena occurring on the MP-1 phase, the original extraction method was modified. First, an analyte-free sample containing TBAH was processed on an MP-1 column in the original manner (steps 1–7). Following this procedure, the SPE column was reused for the extraction of a TBAH-free sample containing analyte. This sample was processed as described for the original method except that the phosphate buffer used in step 2 was also TBAH-free. A chromatogram of the original mixture prior to SPE is shown in Figure 3(upper). Chromatograms of nucleosides and nucleotides eluted with this modified SPE procedure are shown in Figures 3(middle),(lower), respectively. The extraction efficiencies for mdA, dGMP, ddAMP, and dGDP were 90% or greater. The extraction efficiency for dGMP was 60%. Between the step when the TBAH-containing aqueous solution was loaded onto the column and the step when the TBAH-free analyte solution was loaded onto the column, approximately 20 column volumes of TBAH-free aqueous solution and 30 column volumes of TBAH-free aqueous solution with 50% methanol passed through the column. Despite this column conditioning, the selective extraction of the nucleotides in the absence of any aqueous TBAH was still demonstrated (Figure 3(lower)). This data would imply that sufficient TBAH had adsorbed onto the stationary phase and remained there, despite extensive column washing, to yield an ion-exchange/reversed-phase surface with enough capacity to retain the molar quantity of nucleotides examined in this study.

Reports on the HPLC and SPE applications of the MP-1 stationary phase have not detailed retention mechanisms that might be unique to this phase when utilized in an ion-pairing mode. Abidi (*10*) did a comparison study in which the retentive characteristics of five different HPLC stationary phases, including MP-1, were examined under various ion-pairing conditions. However, no direct comparison between MP-1 and ODS was done in an anionic ion-pairing mode with the tetrabutylammonium ion. In a recent report (*9*) the manufacturer of the MP-1 stationary phase described a SPE scheme using the MP-1 packing and hexanesulfonic acid to extract amphetamine and methamphetamine. This report attributes the retention of these drugs to the hydrophobic interaction between the ion pair (drug–hexanesulfonic acid) and the stationary phase. Similar explanations have been given to the retention of analytes under ion-pairing conditions on conventional silica-based ODS phases as well (*7*).

Krstulovic and Brown (*11*) have published a review that examines the various equilibria models that have been proposed to explain the ion-pairing phenomena. In one model

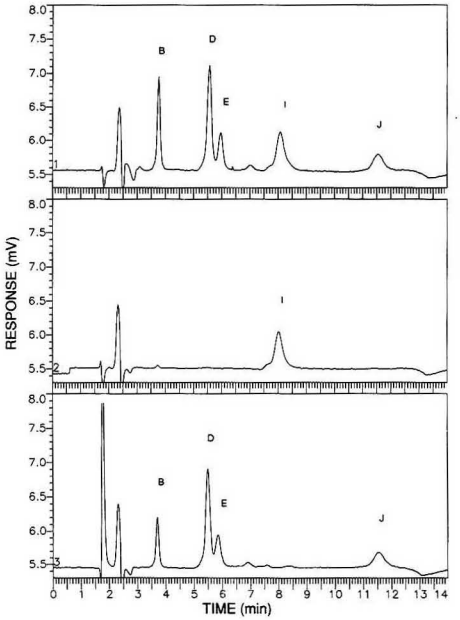

Figure 3. Ion-pairing HPLC of one nucleoside and four nucleotides utilized in the modified SPE procedure on an MP-1 column. Figure 3(upper) represents a 50-μL injection of a nonextracted mixture containing between 0.26 and 0.72 μM of the following compounds: (B) dGMP; (D) dAMP; (E) dGDP; (I) mdA; (J) ddGTP. Figure 3(middle) represents the HPLC of extracted nucleosides. Peak identity is listed in Figure 3(upper). Figure 3(lower) represents the HPLC of extracted nucleotides. Peak identities are listed in Figure 3(upper).

it is postulated that the hydrophobic ion-pairing reagent adsorbs to the nonpolar stationary phase, forming a modified stationary phase with an ion-exchange character. Retention of the ionic solute then occurs through coulombic interaction with the charged surface of the modified stationary phase. The results of this present study with MP-1 and TBAH would indicate that this form of equilibria is playing a major role in the retention of the nucleotides examined here. One possible explanation for the apparently lower capacity of the ODS packing verses the MP-1 column in this study may originate from the fact that the ODS packing has a negative charge associated with it (ionized residual silanols at pH 6.5). The MP-1 phase has no charge. Depending on steric issues, some of the tetrabutylammonium ions associated with the ODS surface might have the opportunity to be in a coulombic association with the silanolates and not the analyte.

CONCLUSIONS

This two-dimensional approach should afford a versatile system for the simultaneous analysis of both charged and neutral compounds in a complex mixture in a manner never before possible with the sole use of silica-based stationary-phase support materials. Specifically, this technique should be useful in the simultaneous measurement of therapeutic nucleoside analogues and their phosphate metabolites in biological samples containing excess endogenous nucleosides and nucleotides. More detailed studies on the capacity differences between the MP-1 and silica-based ODS phases are recommended to better understand the relationship between the stationary-phase support material and the equilibria re-

sponsible for the ion-pairing phenomena demonstrated here.

LITERATURE CITED

(1) Hao, Zhang; Cooney, David A.; Hartman, Neil R.; Perno, Carlo F.; Fridland, Arnold; DeVico, Anthony L.; Samgadharan, M. G.; Broder, Samuel; Johns, David G. *Mol. Pharmacol.* **1988**, *34*, 431–435.
(2) Mack, D. O.; Reed, V. L.; Smith, L. D. *J. Liq. Chromatogr.* **1985**, *8* (4), 591–602.
(3) Webster, D. R.; Boston, G. D.; Paton, D. M. *J. Liq. Chromatogr.* **1985**, *8* (4), 603–618.
(4) Pimenov, A. M.; Tikhonov, Yu. V.; Meisner, I. S.; Toguzov, R. T. *J. Chromatogr.* **1986**, *395*, 221–227.
(5) Werner, Andreas; Siems, Werner; Schmidt, Heike; Rapoport, Iris; Gerber, Gerhard, *J. Chromatogr.* **1987**, *421*, 257–265.
(6) Hammer, Donald F.; Unverferth, Donald V.; Kelly, Robert E.; Harvan, Paula A.; Altschuld, Ruth A. *Anal. Biochem.* **1988**, *169*, 300–305.
(7) Tekkanat, Kim K.; Fox, Irving H. *Clin. Chem.* **1988**, *34* (5), 925–932.
(8) Jones, Clifton W.; Chmel, Herman. *Clin. Chem.* **1988**, *34* (10), 2155–2156.
(9) Patel, Ragina M.; Benson, James R.; Hometchko, David. *LC—GC* **1990**, *8* (2), 152–158.
(10) Abidi, S. L. *J. Liq. Chromatogr.* **1989**, *12* (4), 595–611.
(11) Krstulovic, A. M.; Brown, P. R. *Reversed-Phase High-Performance Liquid Chromatography, Theory, Practice and Biomedical Applications*; John Wiley and Sons: New York, 1982; Chapter 6.

RECEIVED for review December 10, 1990. Revised manuscript received July 1, 1991. Accepted July 10, 1991.

Argon Inductively Coupled Plasma Mass Spectrometry with Thermospray, Ultrasonic, and Pneumatic Nebulization

Akbar Montaser,* Hsiaoming Tan, Izumi Ishii,[1] Sang-Ho Nam, and Mingxiang Cai

Department of Chemistry, The George Washington University, Washington, D.C. 20052

INTRODUCTION

Pneumatic (PN) and ultrasonic nebulizers (USN) have been the most common sample introduction systems (*1–3*) for argon inductively coupled plasma mass spectrometry (Ar ICPMS). Electrothermal vaporization interfaces (*4*), direct injection nebulizers (*5*), and a PN coupled to a membrane separator (*6*) also have been evaluated for introduction of aqueous solutions into the Ar ICPMS system. With thermospray nebulization, detection limits were improved in ICP atomic emission spectrometry by up to a factor of 50 compared to pneumatic nebulization (*7–8*). In a preliminary study, Meyer et al. (*9*) reported the use of a thermospray nebulizer for Ar ICPMS and noted 1.5 times more count rate for Ce^+ and Tb^+ compared to that with pneumatic nebulization. Thus far, no extensive studies have been conducted on the analytical potential of the thermospray nebulizer for Ar ICPMS, particularly when the combination thermospray nebulizer–membrane separator (TNMS) is used for removing solvents from aerosol (*10–12*). Relatedly, the utility of cryogenic desolvation used in tandem with the USN has not been reported for Ar ICPMS in terms of ion kinetic energy and interferences arising from oxide and doubly charged species. For pneumatic nebulization, such studies have been documented for Ar ICPMS (*13–16*).

In this study, we present results on the utility of the TNMS for Ar ICPMS in comparison to the USN and the PN used with and without desolvation. These studies were conducted with a new instrumental arrangement that included a Delsi-Nermag quadrupole mass spectrometer (Delsi-Nermag, Argenteuil, France) coupled in this work to a solid-state, crystal-controlled 40.68-MHz ICP system. Analytical and fundamental characteristics were compared for three nebulization systems in terms of detection limits, ratios of doubly charged to singly charged ions, oxide ion to analyte ion ratios, precision, and ion kinetic energies. These properties also were measured when cryogenic cooling was used to achieve maximum desolvation for the USN. Thus, this report not only provides information on the comparative performance of three nebulization systems, but it describes for the first time aspects and features of a new instrumental arrangement for Ar ICPMS.

* To whom correspondence should be addressed.
[1] Present address: Patent Division, Chemical Abstract Services, 2540 Olentangy River Rd., Columbus, OH 43210.

EXPERIMENTAL SECTION

1. Instrumentation and Operating Conditions. Details of the experimental system are summarized in Table I and are shown in Figure 1. The previous report (*19*) on the Delsi-Nermag ICPMS system was concerned with the use of a free-running 56-MHz generator. In our study, a crystal-controlled, 40.68-MHz ICP system (Table I) is coupled to the mass spectrometer.

Aside from the ICP system, three major differences exist between this and the commonly used ICPMS instruments (*20*). First, two quadrupoles are used for ion transmission and mass separation. Second, no photon stops or obstacles are present in the ion trajectory for the mass spectrometer. Third, an off-axis, *analogue* mass detector known as "Coniphot" is used to detect positive ions. In this detector (Figure 1) ions are directed to a dynode where electrons are generated. These electrons then are amplified via a micro channel plate and are transferred to a scintillator where electromagnetic radiation is produced. The resulting photons pass through a light guide to impinge on the cathode of a standard photomultiplier tube (PMT) held at atmospheric pressure. The signal is amplified at the detector by a current-to-voltage converter (Gain = 10^7 V/A) and is transferred to a 12-bit analog-to-digital converter. For maximum sensitivity and signal-to-noise ratio, the PMT normally is operated at −680 V.

2. Thermospray Nebulizer and Membrane Separator. This system (Figure 2 and Tables I and II) consists of a thermospray nebulizer, a spray chamber made from stainless steel, and a membrane separator which possesses a Teflon membrane mounted on an aluminum holder. The system is typically used for interfacing a liquid chromatograph to a mass spectrometer (*21*, *22*).

The aqueous solution is delivered to the thermospray nebulizer by a high-pressure pump (Table I). Test solution is introduced into an electrothermally heated capillary, converted into a fine spray (*9*, *23–25*), and transported by carrier argon gas through a heated spray chamber. Large droplets condensed on the chamber are removed by a peristaltic pump attached to the drain tube. The membrane separator, connected to the outlet of spray chamber, isolates water vapor from the desolvated aerosol prior to injection into the ICP. Even though Teflon membrane is hydrophobic (*26*, *27*), water vapor selectively diffuses through the membrane. Therefore, a sufficient sweep gas flow must be used to remove solvent vapor. A disposable gas purifier (Model DGP-125, Labclear, Oakland, CA) is installed on the argon gas line to remove the water moisture. Methanol should be introduced into the TNMS at the end of each experiment to prevent rusting.

3. Optimization Procedure and Test Solutions. The mass spectrometer was set to provide 0.5–1 mass resolution over the entire mass range. The operating conditions for the ICPMS system were optimized by maximizing the ion intensity for ^{208}Pb.

0003-2700/91/0363-2660$02.50/0

Table I. Experimental Facilities

I. Mass Spectrometer

PLASMASS (Delsi-Nermag, Argenteuil, France) ICPMS system shown in Figure 1 (mass range = 0–300 amu; microprocessor assisted, adjustable resolution between 0.5 and 4 amu; scan speed = 2000 amu/s) consists of the following:

(1) a nickel sampler (0.9-mm orifice, inside and outside cone angles of 90 and 120°, respectively) and a stainless steel skimmer (0.6-mm orifice, inside and outside cone angles of 100 and 120°, respectively) with its tip located 8 mm behind the sampler (the sample is water cooled, and both cones are grounded; the interface contains an optical port for viewing possible auxiliary discharges between the cones)

(2) an analyzer quadrupole (35 cm long) and a prefilter quadrupole (12 cm long) with a rod diameter of 15.6 mm

(3) an input lens system made of a cylindrical lens to focus the ion beam from the plasma, a quadrupole used as a transmission lens, and an exit plate

(4) a Coniphot detector (see Figure 1 and text)

(5) a three-stage, differentially pumped vacuum system with

(1) a 33 m^3/h mechanical pump on the interface stage

(2) a 33 m^3/h mechanical pump and a 700 L/s water-cooled diffusion pump on intermediate stage

(3) a 20 m^3/h mechanical pump and a 135 L/s water-cooled diffusion pump on analyzer stage (diffusion pumps were water cooled)

(6) a PC-AT type-80286 based computer (WYSEpc 286, WYSE Technology, San Jose, CA) with a typical VGA color display and a laser jet printer; menu-driven software (Version 2.30)

II. ICP and Sample Introduction Systems

(1) a solid-state, 1.6-kW, 40.68-MHz crystal-controlled generator (Model ICP 16, RF Plasma Products, Inc., Voorhees, NJ) with an automatic phase and magnitude matching network (*17*)

(2) a 3.5-turn load coil (top turn grounded) used with a Fassel-type torch (a copper strap was soldered near the edge of the coil and was bolted to the torch housing assembly; a silver braid was attached circumferentially on the sampler interface; the end of the silver braid was connected to the copper strap attached to the coil)

(3) the torch housing assembly and the impedance matching network (*17*) mounted on grounded X-Y-Z translation stages

(4) a mass flow controller (Model 8240, Matheson Gas Co., East Rutherford, NJ) used for the nebulizer injector gas line (other components for the gas lines were similar to those used on a typical ICP system; boil-off from liquid argon (MG Industries, Valley Forge, PA) was used)

(5) sample delivery units: a peristaltic pump (Minipuls 2, Rainin Instrument Co., Woburn, MA) for the ultrasonic and pneumatic nebulizers; a high-pressure pump (Model SP 8700, Spectra Physics, San Jose, CA) for the thermospray nebulizer

(6) an ultrasonic nebulizer and the associated desolvation unit (Model U-5000, CETAC Technologies, Inc., Omaha, NE) (the fluid level in the drain lines of the spray chamber and condenser were regulated separately by peristaltic pumps; see ref 18 for a description of the cryogenic desolvation unit)

(7) a pneumatic nebulizer (Model 5601, RF Plasma Products, Inc.) with a Scott-type spray chamber, with/without a desolvation unit (the desolvation system for the ultrasonic nebulizer (see item 6) was used)

(8) a thermospray nebulizer (Universal Interface, VESTEC Corp., Houston, TX)

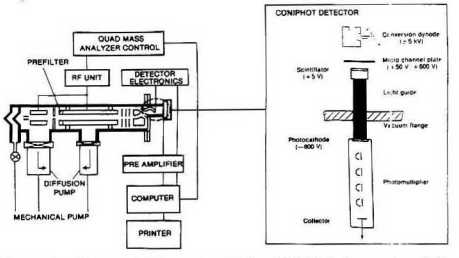

Figure 1. Schematic diagrams of the ICPMS instrument and the Coniphot detector (Delsi-Nermag Instruments, with permission).

The resulting conditions (Table II) were used for all measurements.

Except for measurement of ion kinetic energies (see next section) and oxide ratios for which a 100 ng/mL multielement solution was used, all measurements were conducted with a 10 ng/mL solution. Solutions were prepared in 2–5% ultrapure nitric acid (National Institute of Standards and Technologies, Gaithersburg, MD) from reagent grade chemicals or ICPAES standards (SPEX Industries, Edison, NJ). For the studies with the TNMS, no nitric acid was added to the solution because the spray chamber was made from stainless steel. Test solutions for the TNMS were degassed with helium to ensure stable operation for the high-pressure pump.

4. Measurement of Ion Kinetic Energy Distribution. For accurate measurement of ion energies (*28*), the entire input lens system (the cylindrical lens, the prefilter quadrupole, and the exit plate) was grounded. Typically, sensitivity was reduced approximately 10-fold in this mode of operation. Distributions of ion kinetic energy were measured by applying a retarding potential to the prefilter element (Figure 1) located just before the analyzer quadrupole and recording net ion intensities of Li, Mn, Ni, Cu, Zn, Cd, and Pb. The resulting curves of the ion signals vs the retarding potential were differentiated. The width of the energy distribution at half-height and the most probable energy are approximate measures of ion energies (*28*). In this work, the width of distribution at half-height was measured. The retarding potential was varied in steps of 1 V.

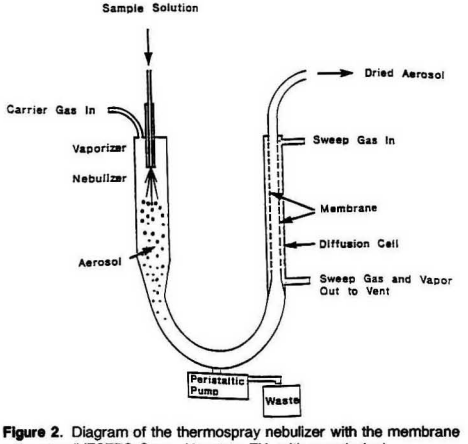

Figure 2. Diagram of the thermospray nebulizer with the membrane separator (VESTEC Corp., Houston, TX, with permission).

RESULTS AND DISCUSSION

1. Short- and Long-Term Precisions. The percent relative standard deviation (% RSD) was calculated for 60 successive scans recorded in 10 min for ultrasonic and pneumatic nebulization of a 10 ng/mL multielement solution containing Mn, Ni, Cu, Zn, Cd, Ce, and Mn. The integration time for each mass (one point per peak) was 0.6 s. Short-term precision in the range 2.6–5.2% RSD was calculated when the

Table II. Operating Conditions for the Ar ICPMS System

ICP System	
forward rf power, kW	1
reflected power, W	0
frequency, MHz	40.68
sampling position (above load coil), mm	15, on-center
outer gas flow rate, L/min	20
intermediate gas flow rate, L/min	1.5
injector gas flow rate, L/min	
(a) ultrasonic and pneumatic nebulizer	0.85; 0.5–1.1, see text
(b) thermospray nebulizer	1
Sample Introduction Systems	
solution uptake rate, mL/min	
(a) thermospray nebulizer	1
(b) ultrasonic and pneumatic nebulizer	2
desolvation unit, heating chamber temp, °C	+150
desolvation unit, condenser temp, °C	+5, 0, –5, see text
cryogenic desolvation unit, temp, °C	–78, see ref 18
parameters for thermospray nebulizer	
(a) nebulizer tip, μm	37.5, 75, see text
(b) sweep gas flow rate, L/min	4.4
(c) carrier gas flow rate, L/min	1.8
(d) vaporizer probe, °C	120
(e) tip temp, °C	200–220
(f) desolvation chamber temp, °C	90–95
(g) membrane separator temp, °C	62
Mass Spectrometer and Detector	
interface region, Torr	1
first quadrupole region, Torr	5.4×10^{-5}
second quadrupole region, Torr	1.8×10^{-6}
voltage on PMT for the Coniphot detector, V	–400 to –680, see text
ion-optics settings, V	
Q1 offset (input lens system)	–132
prefilter	–87
post analyzer deviator 1	–33
post analyzer deviator 2	–53
post analyzer deviator 3	–174

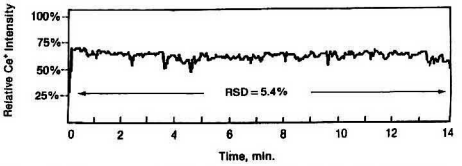

Figure 3. Short-term stability of the Ce^+ signal using the TNMS (3-s integration time).

Table III. Detection Limits (pg/mL) for Aqueous Samples Injected in the Ar ICPMS[a-c]

element	isotope	USN	TNMS	PN with desolvation	PN without desolvation
Mn	55	0.5	2	2	5
Ni	58	2	1	9	30
Co	59	1	3	8	10
Cu	64	2	3	10	20
Zn	65	7	3	60	180
Cd	114	5	8	40	170
In	115	1.5		5	10
Cs	133	0.4	1	2	4
Ba	137	0.5	1	2	4
Ce	140	0.2	1	1	10
Nd	144	2	5	7	20
Pb	208	0.4	0.5	3	35
Bi	209	0.6		3	20
Th	232	1		4	17
U	238	1	2	3	10

[a] The detection limit is defined as the concentration giving a signal equivalent to 3 times the noise, calculated from the standard deviation of 11 repetitive measurement with 3-s integration of the background intensity. Background intensity was measured at either mass 242 or 260. [b] The analyte concentration was 10 ng/mL. [c] The pneumatic nebulizer was used with a desolvation system which consisted of a heating chamber (150 °C) and a condenser (–5 °C).

USN was used. These values were consistently larger than the RSDs (2.1–3.5%) obtained with the PN. No significant improvements in % RSDs were noted for an integration time of 10 s when an USN was used. For comparison, Vickers et al. (*29*) reported short-term precision of 1.25% RSD for their 40.68-MHz ICPMS system when 30 consecutive 10-s integrations were averaged for pneumatic nebulization of a 1 μg/mL solution of barium.

Long-term precision was measured every 10 min over 4 h with a 0.6-s integration time at each mass for a 10 ng/mL multielement solution. The % RSDs measured ranged between 4.3 and 5.8% and 2.5 and 4.2%, respectively, when the USN and PN were used. Again, for a 10-s integration time, little improvement in % RSDs were noted for ultrasonic nebulization. Similar long-term precisions have been reported for other ICPMS systems (*20*, *30*, *31*).

Figure 3 shows the typical signal stability achieved with the TNMS after it was operated for 40 min to reach stable operating temperatures. A 10 ng/mL solution of Ce was nebulized for approximately 14 min. The % RSDs measured were 3.7 and 5.4% for 8 and 14 min, respectively, roughly twice the values measured with a PN. For the membrane separator coupled to a PN used in Ar ICPAES, Gustavsson and Hietala (*10*) reported % RSDs of 3.6, 2.2, and 0.5% after 1, 2, and 3 h of operation, respectively. On the basis of these studies, higher % RSDs should be expected when a membrane separator is coupled to other nebulization systems such as a USN. Relatedly, a longer wash-out time must be allowed when a membrane separator is used. For example, the length of wash-out times, for the signal to decrease to less than 1% of the original level, was generally 1.5–2.5 min for the elements tested compared to the period measured for USN (80 s).

2. Detection Limits. A thermospray nebulizer produces aerosol with smaller droplet diameter as compared to the PN (*23*, *32*). As a result, more particles are transported to the ICP by the injector gas to produce larger signals (*8*, *23*, *32*). In general, analyte transport efficiency is enhanced as the orifice size for the nebulizer tip is reduced (*8*, *32*). Two replaceable nebulizer tips, with i.d.'s of 37.5 and 75 μm, were tested in our studies. The net ion intensities for ^{63}Cu, ^{64}Zn, ^{114}Cd, ^{140}Ce, and ^{208}Pb with a 37.5-μm orifice were greater by a factor of 1.2–2.5 compared to results obtained with the 75-μm tip. However, tip clogging occurred more frequently with the 37.5-μm orifice, especially when the nebulizer was operated at elevated temperature (*32*, *33*).

Detection limits are shown in Table III for Ar ICPMS for nebulization with the USN, TNMS, and PN used with and without desolvation. A 75-μm tip was used for the TNMS, and the integration time was 3 s/mass (one point per peak) for all measurements. Compared to those obtained with the PN used with or without a desolvation system, respectively, detection limits were improved by a factor of up to 20 and 60 for Mn, Ni, Co, Cu, Zn, Cd, Cs, Ba, Ce, Nd, Pb, and U. For the same set of elements, a USN provided detection limits which were generally lower than those of TNMS by a factor of 2–5.

Compared to a PN used with no desolvation, detection limits were improved by a factor of 6–87 with ultrasonic nebulization. When aerosol desolvation was used for the PN,

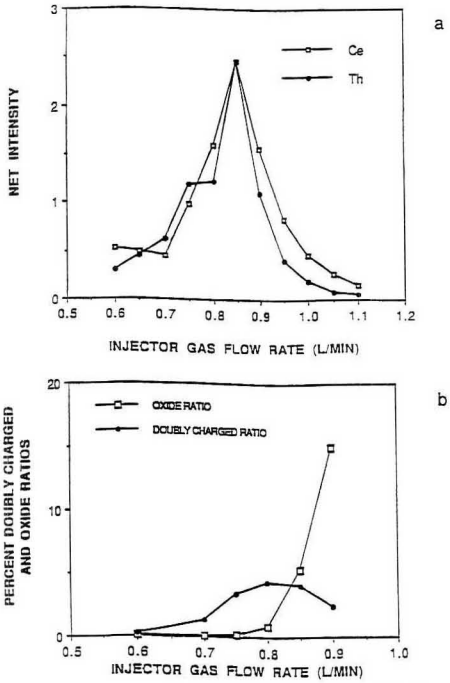

Figure 4. Effect of injector gas flow on ion signals (V) for $^{140}Ce^+$ and $^{232}Th^+$ (a), and oxides and doubly charged ions for Ce (b). The ultrasonic nebulizer was used. The condenser temperature for the USN was held at −5 °C.

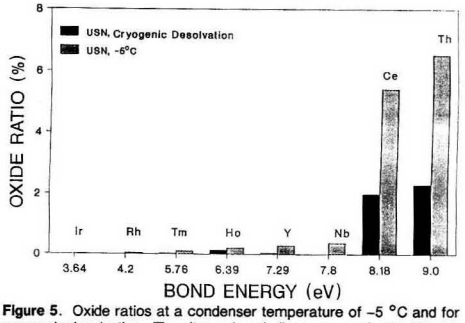

Figure 5. Oxide ratios at a condenser temperature of −5 °C and for cryogenic desolvation. The ultrasonic nebulizer was used. The injector gas flow and the forward power were 0.85 L/min and 1 kW, respectively. Bond energies were taken from ref 37. Ideally, the dissociation energy of the molecular ion (MO^+), not that of the neutral molecule (MO), must be used in the comparison of the oxide levels, but such data are not readily available.

results for the USN were still superior by a factor of 3–8. Improvements in detection limits also have been reported (*34*) for other ICPMS instruments when aerosol desolvation has been used for the PN. For this ICPMS system, aerosol desolvation significantly improved detection limits.

Detection limits were also measured for Mn, Ni, Cu, Zn, Cd, Ce, and Pb when cryogenic cooling was applied to the desolvated aerosol from the USN. Except for Ce for which the detection limit was improved only by a factor of 2, results for the other elements were degraded by a factor of 2–3. This degradation may lead to desolvation-type interferences (*35*), especially for complex matrices. No such behavior was reported by Houk and co-workers (*18*) for elements present in organic solvents.

In general, the detection limits measured in this work for a PN used with desolvation are comparable, for most elements tested, to those reported for other systems (*20*, *30*, *31*), despite differences in ion optics, analyzers, detection systems, and the integration periods used. Thus, all quadrupole-based ICPMS systems are capable of providing detection limits in the parts-per-trillion range. These detection limits can be improved by approximately a factor of 10 when double-focusing instruments are used (*36*).

3. Oxides and Doubly Charged Species. The effect of injector gas flow on ion signal and the ratios of the oxides and doubly charged to singly charged ion (MO^+/M^+, and M^{+2}/M^+) have been explored for the PN extensively (*14–16*, *20*, *30*, *31*). However, no detailed data have been published for thermospray nebulizer or a USN. Figure 4 shows these effects for Ce and Th for the USN. These ions are selected for this study because of the large bond energies (*37*) of the cerium oxide (8.18 eV for MO) and thorium oxide (9.00 eV for MO) and the relatively low first ionization energies of Ce (5.57 eV) and Th (6.2 eV). Ionic and neutral molecular bonds may exhibit substantially different bond strengths (*37*, *38*). Ideally, the dissociation energy of the molecular ion (MO^+), not that of the neutral molecule (MO), must be used in the comparison of the oxide levels, but such data are not readily available. Maximum ion intensities for Ce and Th occur at an injector gas flow of 0.85 L/min. Under such conditions, oxide ratios of 5.4 and 6.5% and doubly charged ion ratios of 4.1 and 2.9% are measured for Ce and Th, respectively. These ratios are reduced at lower injector gas flow rates, but with reduced sensitivities for the metal ions. Other investigators (*29*) have reported oxide and doubly charged ratios of 7.9 and 17.1% for 40.68-MHz Ar ICPMS when a PN was used to nebulize Ce solution into the plasma. The lower oxide and doubly charged ratios shown in Figure 4 for Ce may be attributed to the efficiency of the desolvation system in reducing the solvent load of the plasma. Lam and McLaren (*39*) noted a similar reduction for uranium oxide when partial desolvation was used for their PN.

Two sets of data for eight ions are presented in Figure 5 to illustrate the effect of cryogenic desolvation on the reduction of oxide levels as a function of bond energy of the neutral oxides (*37*, *38*, *40*). In both cases, the injector gas flow and the condenser temperature were 0.85 L/min and −5 °C, respectively, except that cryogenic cooling was applied to the desolvated aerosol in one case. As expected, a direct relationship was generally observed between the oxide levels and the bond energies of the neutral oxides. At higher condenser temperatures and higher injector gas flow rates, larger levels of oxides were observed. The lowest oxide levels were measured when cryogenic cooling was applied to the desolvated aerosol from the USN.

Typical oxide ratios are presented for nine elements in Table IV for the USN at a condenser temperature of −5 °C as the injector gas flow rate is changed. In general, higher oxide levels were observed as the injector gas flow was increased. For the sampling position of 15 mm and at injector gas flow rates higher than 0.95 L/min, the sampler was well inside the initial radiation zone (IRZ), and therefore, high oxide levels were measured.

A comparison of MO^+/M^+ ratios of various elements for nebulization with the TNMS and USN is now relevant. The percent MO^+/M^+ values for Yb, Tm, Ho, Y, and Ce were 0.001 (0.00), 0.00 (0.10), 0.002 (0.21), 0.1 (0.29), and 1.3 (5.4) for TNMS as compared to the results shown in parentheses for

Table IV. Oxide Ratios for Ultrasonic Nebulization Measured for a 1-kW Ar ICPMS

element	isotope	bond energy,[a] eV		Mo^+/M^+ (%) injector flow rate, L/min						
		MO	MO^+	0.80	0.85	0.90	0.95	1.0	1.05	1.1
Ir	193	3.64		0.01	0.01	0.07	0.13	0.39	0.36	0.72
Yb	171	3.97		0.05		0.12	0.16	1.22	1.09	1.78
Rh	103	4.20		0.03	0.04	0.01	0.03	0.10	0.14	0.11
Tm	169	5.76	4.92	0.08	0.10	0.22	0.80	2.75	2.58	5.0
Ho	165	6.39	6.24	0.08	0.21	0.87	1.98	6.00	8.01	12.6
Y	89	7.29	7.89	0.06	0.29	2.57	11.3	19.1	29.1	36.9
Tb	159	7.30	7.33	1.60	2.38	6.73	16.0	23.9	35.8	41.9
Nb	93	7.80		0.11	0.38	1.40	4.65	8.36	12.3	15.9
Ce	140	8.18	8.80	0.84	5.40	15.6	46.0	50.4	65.8	117
Th	232	9.00		2.03	6.53	19.6	30.9	42.0	64.6	66.6

[a] Bond energies for MO and MO^+ (Tm, Ho, Tb, Ce) were taken from refs 37 and 38, respectively. Bond energy for YO^+ was calculated by us on the basis of data in refs 37, 38, and 40. Ideally, the dissociation energy of the molecular ion (MO^+), not that of the neutral molecule (MO), must be used in the comparison of the oxide levels, but such data are not readily available.

USN. Thus, MO^+/M^+ ratios measured for the TNMS were less than those obtained for USN, by a factor of 3 and 4 in the case of Y and Ce, which form strong oxides. Again, note that these ratios were measured when maximum metal ion intensities were recorded at injector gas flows of 0.85 and 1 L/min for the USN and TNMS, respectively. At lower injector gas flow rates, oxide ratios (and also ion signals) were reduced. These data also revealed that the TNMS approach was as effective as the USN–cryogenic desolvation in reducing oxide levels.

For the TNMS, the Ce^{2+}/Ce measured was 6.0% as compared to 4.1% for the USN. As stated earlier, the level of doubly charged ion for the 40.68-MHz ICP is higher than that for the 27.1-MHz plasma (*29*).

4. Ion Kinetic Energies. The magnitude of ion kinetic energy is indicative of the strength of secondary discharges at the sampling interface of ICPMS instruments. Several investigators (*16, 28, 41–45*) have reduced secondary discharges at the ICPMS interface by minimizing the plasma potential. These efforts are significant in minimizing the formation of doubly charged ions and in extending the lifetime of the sampler and skimmer. Although secondary discharges may not be visually observed, they may still persist in the ICPMS interface (*46, 47*). In general, more intense interface-related discharges have been noted for the 40.68- vs 27.1-MHz ICP (*29*), particularly when no center-tapped load coil is used or an electrostatic shield is not interposed between the induction coil and the plasma torch (*42–45*).

Figure 6 shows ion kinetic energies measured for Li, Mn, Ni, Cu, Cd, and Pb for three neublization systems: (1) the USN operated at three condenser temperatures, (2) the USN coupled to the cryogenic desolvation unit, and (3) the TNMS. As the condenser temperature for the USN was raised from −5 to +5 °C, with the cryogenic cooling system disconnected, ion kinetic energies usually increased, except for the ^7Li ion. The increase in ion kinetic energy is attributed to enhanced solvent loading as the temperature is increased. For the mass range 7–208, ion kinetic energies measured ranged between 5 and 12 eV. In general, the magnitudes of these ion kinetic energies are similar to or lower than the results reported for other ICPMS systems (*16, 20, 28, 30, 31, 41, 48*) used with the PN. However, no clear trend, as described in ref 28, of ion kinetic energy with ion mass is noted. The lowest ion kinetic energies (5.0–7.7 eV) were obtained when cryogenic cooling was applied to the desolvated aerosol from the USN or when the TNMS was used.

The low values measured for ion kinetic energies indicate that the sampling interface used in this work is not subject to strong secondary discharges. No $^{58}Ni^+$ signal from the sampler was observed. Because ion kinetic energy usually

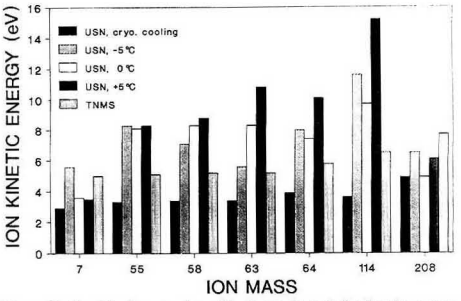

Figure 6. Ion kinetic energies with ultrasonic nebulization (at a condenser temperature of −5 °C), ultrasonic nebulization coupled with cryogenic desolvation, and thermospray nebulization coupled to the membrane separator. The injector gas flows were 0.85 and 1 L/min for ultrasonic and thermospray nebulization, respectively.

increased with condenser temperature and the ratio of doubly charged to singly charged metal ion increased initially with the injector gas flow rate (Figure 4), we can only conclude that a week secondary discharge should persist at the sampling interface.

In view of the recent publication on direct injection nebulizer (*5*), two points should be emphasized here for this TNMS. First, compared to a direct injection nebulizer (*5*), the TNMS introduces desolvated aerosol into the plasma, therefore reducing MO^+/M^+ ratios. Further reduction in oxide levels is feasible by using mixed-gas plasmas (*13, 39, 49–53*). Second, for the current TNMS, most components are made from stainless steel and the system is principally designed for use with organic solution in LC/MS. To fully utilize the potentials of TNMS for analysis of inorganic samples in acid medium, a nonmetallic system should be devised. In addition, test solutions should be introduced in the flow injection mode to reduce the wash-out time with the TNMS.

CONCLUSIONS

The utility of the thermospray nebulizer with a membrane separator (TNMS) was demonstrated in comparison to the ultrasonic nebulizer (USN) and pneumatic nebulizer (PN) for argon inductively coupled plasma mass spectrometry (Ar ICPMS). Parts-per-trillion detection limits were obtained with the TNMS by using a new instrumental arrangement for ICPMS that incorporated an analogue detector. Compared to the PN used with or without a desolvation system, respectively, detection limits were improved for the TNMS by a factor of up to 20 and 60, but the USN provided detection

limits which were lower than those obtained with the TNMS by a factor of 2-5. When cryogenic desolvation was used in tandem with the USN, detection limits were degraded by a factor of 2-3, except for Ce for which the detection limit was improved only by a factor of 2. The lowest ion kinetic energies (5.0-7.7 eV) and oxide levels were obtained when USN-cryogenic desolvation or the TNMS was used.

ACKNOWLEDGMENT

Special thanks to L. West, J. Ott, and R. Spangler of RF Plasma Products, Inc., M. L. Vestal, J. Dixon, C. R. Blakley, and J. Wilkies of VESTEC Corp., and W. B. Sisson, J. A. Easterling, and W.F. Syner of the Food and Drug Administration for significant contributions during the course of this work. We thank R. H. Clifford, S. P. Dolan of our group, R. S. Houk of Iowa State University, and S. Chan of CETAC Technologies, Inc. for their helpful suggestions during the course of this research and D. W. Golightly of Ross Laboratory for his constructive comments in the preparation of this manuscript.

LITERATURE CITED

(1) Gustavsson, A. In *Inductively Coupled Plasmas in Analytical Atomic Spectrometry*; Montaser, A., Golightly, D. W., Eds.; VCH: New York, 1987, Chapter 11 (see also references cited therein).
(2) Broekaert, J. A. C.; Boumans, P. W. J. M. In *Inductively Coupled Plasma Emission Spectroscopy*; Boumans, P. W. J. M., Ed.; John Wiley & Sons: New York, 1987; Vol. I, Chapter 6 (see also references cited therein).
(3) *Application of Inductively Coupled Plasma Mass Spectrometry*; Date, A. R., Gray, A. L., Eds.; Blackie and Son Ltd.: London, 1989; 254 pp.
(4) Shen, W. L.; Caruso, J. A.; Fricke, F. L.; Satzger, R. D. *J. Anal. At. Spectrom.* **1990**, *5*, 451-455 (see also references cited therein).
(5) Wiederin, D. R.; Smith, F. G.; Houk, R. S. *Anal. Chem.* **1991**, *63*, 219-225 (see also references cited therein).
(6) McLaren, J. W.; Lam, J. W.; Gustavsson, A. *Spectrochim. Acta* **1990**, *45B*, 1091-1094 (see also references cited therein).
(7) Roychowdhury, S. B.; Koropchak, J. A. *Anal. Chem.* **1990**, *62*, 484-489.
(8) Koropchak, J. A.; Aryamanya-Mugisha, H.; Winn, D. H. *J. Anal. At. Spectrom.* **1988**, *3*, 799-802.
(9) Meyer, G. A.; Roeck, J. S.; Vestal, M. L. *ICP Inf. Newsl.* **1985**, *10*, 955-963.
(10) Gustavsson, A.; Hietala, P. *Spectrochim. Acta* **1990**, *45B*, 1103-1108.
(11) Backstrom, K.; Gustavsson, A.; Hietala, P. *Spectrochim. Acta* **1989**, *44B*, 1041-1048.
(12) Gustavsson, A. *Spectrochim. Acta* **1988**, *43B*, 917-922.
(13) McLaren, J. W.; Lam, J. W.; Gustavsson, A. *Spectrochim. Acta* **1990**, *45B*, 1091-1094.
(14) Zhu, G.; Browner, R. F. *J. Anal. At. Spectrom.* **1988**, *3*, 781-789.
(15) Hutton, R. C.; Eaton, A. N. *J. Anal. At. Spectrom.* **1987**, *2*, 595-598.
(16) Tsukahara, R.; Kubota, M. *Spectrochim. Acta* **1990**, *45B*, 581-589.
(17) Montaser, A.; Ishii, I.; Clifford, R. H.; Sinex, S. A.; Capar, S. G. *Anal. Chem.* **1989**, *61*, 2589-2592.
(18) Wiederin, D. R.; Houk, R. S.; Winge, R. K.; D'Silva, A. P. *Anal. Chem.* **1990**, *62*, 1155-1160.
(19) Allain, P.; Mauras, Y.; Douge, C.; Jaunault, L.; Delaporte, T.; Beaugrand, C. *Analyst* **1990**, *115*, 813-815.
(20) Horlick, G.; Tan, S. H.; Vaughan, M. A.; Shao, Y. In *Inductively Coupled Plasmas in Analytical Atomic Spectrometry*; Montaser, A., Golightly, D. W., Eds., VCH: New York, 1987; Chapter 10 (see also references cited therein).
(21) Blakley, C. R.; Vestal, M. L. *Anal. Chem.* **1983**, *55*, 750-754.
(22) Vestal, M. L. *Science* **1984**, *226*, 275-281.
(23) Schwartz, S. A.; Meyer, G. A. *Spectrochim. Acta* **1986**, *41B*, 1287-1298.
(24) Peng, R.; Tiggelman, J. J.; de Loos-Vollebregt, M. T. C. *Spectrochim. Acta* **1990**, *45B*, 189-199.
(25) Margaretha, T. C. D.; Johan, J. T.; Pim, C. B.; Christian, D. *J. Anal. At. Spectrom.* **1989**, *4*, 213-217.
(26) Barnes, R. M.; Wang, X. *J. Anal. At. Spectrom.* **1988**, *3*, 1083-1089.
(27) Wang, X.; Barnes, R. M. *J. Anal. At. Spectrom.* **1988**, *3*, 1091-1095.
(28) Fulford, J. E.; Douglas, D. J. *Appl. Spectrosc.* **1986**, *40*, 971-974.
(29) Vickers, G. H.; Wilson, D. A.; Hieftje, G. M. *J. Anal. At. Spectrom.* **1989**, *4*, 749-754.
(30) Date, A. R., Gray, A. L., Eds. *The Application of Inductively Coupled Plasma Mass Spectrometry*; Chapman & Hall: London, 1988; 224 pp.
(31) Takahashi, J.; Hara, R. *Anal. Sci.* **1988**, *4*, 331-333.
(32) Koropchak, A.; Winn, D. H. *Appl. Spectrosc.* **1987**, *41*, 1311-1318.
(33) Elgersma, J. W.; Maessen, F. J. M. J.; Niessen, W. M. A. *Spectrochim. Acta* **1986**, *41B*, 1217-1220.
(34) Browner, R. F.; Tarr, M. A.; Nwogu, V.; Ruiz, A.; Zhu, G. Sample Introduction Systems in Plasma Spectrometry: The Current Status and the Future Directions. Presented at the 1990 FACSS Meeting, Cleveland, OH.
(35) Boumans, P. W. J. M.; De Boer, F. J. *Spectrochim. Acta* **1976**, *31B*, 355-375.
(36) Bradshaw, N.; Hall, E. F. H.; Sanderson, N. E. *J. Anal. At. Spectrom.* **1989**, *4*, 801-803.
(37) Huber, K. P.; Hertzberg, G. *Constants of Diatomic Molecules*; Van Nostand Reinhold Co.: New York, 1979.
(38) Ackermann, R. J.; Raut, E. G.; Thorn, R. J. *J. Chem. Phys.* **1988**, *65*, 1027-1031.
(39) Lam, J. W.; McLaren, J. W. *J. Anal. At. Spectrom.* **1990**, *5*, 419-424.
(40) Rauh, E. G.; Ackermann, R. J. *J. Chem. Phys.* **1974**, *60*, 1396-1400.
(41) Tsukahara, R.; Kubota, M. *Spectrochim. Acta* **1990**, *45B*, 779-787.
(42) Douglas, D. J.; French, J. B. *Spectrochim. Acta* **1986**, *41B*, 197-204.
(43) Gray, A. L.; Houk, R. S.; Williams, J. G. *J. Anal. At. Spectrom.* **1987**, *2*, 13-20.
(44) Jakubowski, N.; Raeymaekers, B. J.; Broekaert, J. A. C; Stuewer, D. *Spectrochim. Acta* **1989**, *44B*, 219-228.
(45) Miseki, K. U.S. Pat. No. 4 804 838, Feb 14, 1989.
(46) Lim, H. B.; Houk, R. S. *Spectrochim. Acta* **1990**, *45B*, 453-461.
(47) Grain, J. S.; Smith, F. G.; Houk, R. S. *Spectrochim. Acta* **1990**, *45B*, 249-259.
(48) Kim, Y.; Kawaguchi, H.; Tanaka, T.; Mizuike, A. *Spectrochim. Acta* **1990**, *45B*, 333-339.
(49) Lam, J. W. H.; Horlick, G. *Spectrochim. Acta* **1990**, *45B*, 1313-1325.
(50) Evans, E. H.; Ebdon, L. *J. Anal. At. Spectrom.* **1989**, *4*, 299-300.
(51) Evans, E. H.; Ebdon, L. *J. Anal. At. Spectrom.* **1990**, *5*, 425-430.
(52) Beauchemin, D.; Craig, J. M. *Proceedings of the 3rd Surry Conference on Plasma Source Mass Spectrometry*; Royal Society of Chemistry: London, 1990; No. 85, pp 25-42.
(53) Beauchemin, D.; Craig, J. M. *Spectrochim. Acta* **1991**, *46B*, 603-614.

RECEIVED for review June 7, 1991. Accepted August 16, 1991. This work was sponsored by the U.S. Department of Energy under Grant No. DEFG05-87-13659 and by the U.S. Geological Survey (through D.C. Water Resources Research Center) under Project No. 14-08-0001-G1554-03. The ultrasonic nebulizer and the ICP system used in this work were gifts from CETAC Technologies, Inc. and RF Plasma Products, Inc., respectively. The thermospray nebulizer was loaned by VESTEC Corp.

Fabrication and Evaluation of a Shielded Ultramicroelectrode for Submicrosecond Electroanalytical Chemistry

Satoshi Nomura, Koichi Nozaki,[1] and Satoshi Okazaki*

Department of Chemistry, Faculty of Science, Kyoto University, Kyoto 606-01, Japan

INTRODUCTION

The development of electrochemical measurements with micro or submicrosecond time resolution is one of the most interesting topics in recent electroanalytical chemistry. These novel measurements, including fast scan cyclic voltammetry (FSCV) (*1-4*) and chronoamperometry (*1-3*) have been made possible by the special characteristics of ultramicroelectrodes (UME) (*5*). However, in transient techniques, observed current signals are more sensitive to poor UME construction than in steady-state measurements (*3, 6*). In addition,

* To whom correspondence should be sent.
[1] Present address: Department of Chemistry, College of General Education, Osaka University, Osaka 560, Japan.

0003-2700/91/0363-2665$02.50/0

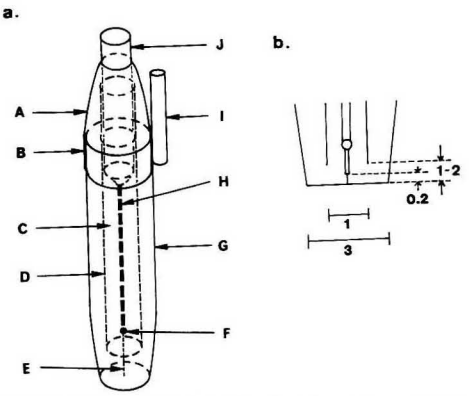

Figure 1. Diagram of a shielded microelectrode (SME) assembly (a) and the dimensions (in mm) (b): (A) epoxy resin; (B) copper foil; (C) capillary tube (i.d. 0.85 mm, o.d. 1.65 mm); (D) aluminum foil; (E) microwire; (F) weld point; (G) soft-glass tube (i.d. 2 mm, o.d. 4 mm); (H) Au lead wire; (I) terminal for shielding; (J) terminal for working.

Wightman et al. recently pointed out that the stray capacitance formed between the electrode material and the solution increases the background current in FSCV (*7*). Although various methods for fabricating UMEs have been reported (*8–10*), little attention has been paid to the fabrication of UMEs which meet the special requirements of these transient techniques. Difficulties in UME fabrication are among the most serious obstacles facing chemists seeking to make these transient techniques practical. Therefore, in a previous study, we developed a fabrication method for a UME which can be used for FSCV or chronoamperometry over a microsecond time scale (*1*).

We now report further improvement of this UME. The fabrication procedure was improved to increase the reliability and durability of the UME. To remove the stray capacitance, the internal conductor was completely shielded and a shielded ultramicroelectrode (SME) was fabricated. With this SME stray capacitance was found to be less than 0.1 pF and significant practical advantages were obtained in FSCV and chronoamperometry.

EXPERIMENTAL SECTION

System Configuration of FSCV. The details of the construction of the fast response potentiostat and the current transducer have been previously described (*1*).

Electrode Materials and Chemicals. Platinum microwire (10 μm in diameter) and Wollaston wire (5 and 2 μm in diameter) (99.99%, purchased from Japan Lamp Industry Co., Ltd.) were used as electrode materials.

The chemicals were prepared in the same way as previously described (*1*).

Electrochemical Cell. A conventional 5-μm-diameter UME was fabricated by sealing the microwire using the electric furnace described below. Electrical contact between the microwire and lead wire was made by a mercury drop.

The surface of the electrode was polished using 0.3- and then 0.05-μm alumina on suede before each measurement. A double-junctioned assembly of a Pt/(I_3^-, I^-) reference electrode was employed (*11*). Platinum wire, 0.5 mm in diameter, was used as an auxiliary electrode. The temperature of the electrochemical cell was kept at 25 ± 0.1 °C.

Design and Fabrication of the SME. Figure 1 shows the configuration of the SME. Platinum microwire or Wollaston wire 2 mm in length was directly connected to an Au lead wire (50 μm in diameter, 6 cm in length) by spot welding using a spark from a pair of graphite rods (8 mm in diameter) and a 2–5-V ac. A

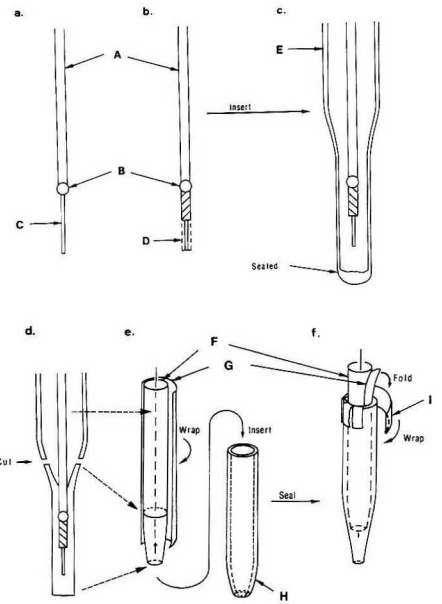

Figure 2. Fabrication procedure for the SME: (A) Au lead wire; (B) weld point; (C) Pt microwire; (D) Wollaston wire (silver coating was removed later; see text); (E) soft-glass tube; (F) capillary tube (i.d. 0.85 mm, o.d. 1.65 mm); (G) aluminum foil; (H) soft-glass tube; (I) copper foil.

soft-glass tube (i.d. 2 mm., o.d. 4 mm) was drawn to give a fine pipet, as illustrated in Figure 2c. The Pt microwire connected to the Au lead wire was inserted into the pipet so that the microwire was positioned at the capillary part (i.d. 0.3–0.4 mm) and was then rinsed with 2 mL of acetone. The Wollaston wire was inserted into the pipet with its tip 2 mm outside of the capillary. The silver coating on the tip (0.5–1 mm) was removed by dipping the tip into 50% nitric acid solution for 15 min. After etching the coated silver, the lead wire was pulled up so that the microwire was positioned at the capillary part. The microwire was rinsed with 2 mL of distilled water, dilute ammonia, distilled water, and acetone, in that order. After the tip of the capillary part was sealed using a methane flame, the capillary part was inserted into an electric furnace, which was fabricated by winding a Nichrome coil around a ceramic tube (i.d. 8 mm). The microwire was sealed into the capillary by gradually increasing the temperature of the furnace (20 °C/min) while the inside of the pipet remained under vacuum. The temperature was kept at optimum (670 ± 10 °C) for 20 min and then lowered to 450 ± 10 °C for annealing. After 10 min of annealing, the capillary was cooled down to room temperature. The sealed capillary was cut 5 mm above the sealed part (Figure 2d). The Au lead wire was inserted into another capillary tube (i.d. 0.85 mm, o.d. 1.65 mm) so that the exposed Au lead wire was covered by a new capillary (Figure 2e). Then, the two capillaries were tightly wrapped with aluminum foil, keeping the tip of the microwire exposed. The whole assembly was inserted into another pipet of the same size (Figure 2e), and then, the unwrapped part of the inner capillary was again sealed using the electric furnace. Finally, the Au lead wire was soldered to a gold-plated terminal. The exposed aluminum foil was folded out and wrapped with copper foil (Figure 2f). The terminal and the copper foil were fixed using epoxy resin. Another gold-plated terminal was soldered to the copper foil. The microwire was exposed from the electrode surface using rough polishing paper.

Scanning electron microscopy (SEM) was used to confirm that the microwire was completely sealed into the glass capillary. The electrode radius (r, μm) was obtained from SEM.

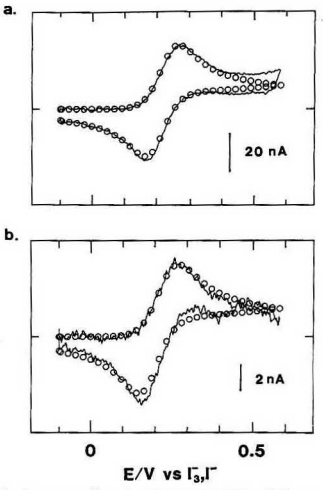

Figure 3. Fast scan cyclic voltammograms of 1 mM ferrocene in AN with 0.6 M $TEAPF_6$ at 10 kV/s after background subtraction (solid line) and calculated voltammograms after the ohmic drop compensation (O): (a) SME 5 μm and (b) 2 μm in diameter.

RESULTS AND DISCUSSION

Parts a and b of Figure 3 show voltammograms of 1 mM ferrocene in acetonitrile (AN) containing 0.6 M tetraethylammonium hexafluorophosphate ($TEAPF_6$) obtained at a scan rate of 10 kV/s with a 5- and 2-μm-diameter SME, respectively. Simulated voltammograms based on reversible electron transfer are also shown. In the case of the simulated voltammograms, ohmic potential drop was compensated by iterative calculations as described previously (*1*). There was excellent agreement between the observed and simulated voltammograms, which indicates that the SME were well constructed. This also confirms that there was no overcompensation of the ohmic potential drop, which indicates that there was no large stray capacitance (*7*).

The apparent double-layer capacitance ($C_{dl,app}$, μF) and the calculated double-layer capacitance ($C_{dl,cal}$, μF) of the conventional UME and the SME were compared to confirm that shielding reduced the stray capacitance. $C_{dl,app}$ values were obtained from the residual current (i_c, A) observed at a scan rate of 10 kV/s in AN containing 0.1 M $TEAPF_6$ according to eq 1 where v is the scan rate (V/s). $C_{dl,cal}$ values were

$$i_c = vC_{dl,app} \quad (1)$$

obtained from r and the double-layer capacitance per unit area in this media (9.9 μF/cm^2). This value was calculated from the $C_{dl,app}$ of a 0.5-mm-diameter Pt electrode and was in good agreement with the typical value in AN containing 0.1 M electrolyte (10 μF/cm^2) (*7*, *12*). The results are listed in Table I.

Positive deviations of $C_{dl,app}$ from $C_{dl,cal}$ and differences in $C_{dl,app}$ depending on the portion of the electrode immersed into the solution observed with the conventional UME were greatly decreased with the SME. Furthermore with the SME, there was excellent agreement between $C_{dl,app}$ and $C_{dl,cal}$, regardless of the depth to which the electrode was immersed when the internal shielding was used, i.e., keeping the internal aluminum foil on the SME at the ground potential. This shows that the internal shielding removed the stray capacitance of the UME.

In FSCV, background current is significantly larger than in conventional CV. In such a condition, the reduction in background current due to a smaller $C_{dl,app}$ is very useful, because otherwise a large fraction of the dynamic range available for amplification is lost (*7*). A constant $C_{dl,app}$ regardless of the portion of the electrode immersed can give a reproducible background current value and is also useful in subtracting the background current.

Figure 4 shows transient current responses in chronoamperometry measured with 5- and 10-μm-diameter SMEs (the internal shield was used) and with the coventional UME in which the electrode potential was stepped from −500 to −200 mV. In order to observe detailed profiles of the charging current, measurements were carried out in a high-resistance AN solution containing 0.01 M $TEAPF_6$. As shown in Figure 4, the current response in chronoamperometry consisted of two components with different time constants (currents A and

Table I. Comparison between Apparent Double-Layer Capacitances ($C_{dl,app}$) and Calculated Double-Layer Capacitances ($C_{dl,cal}$) of the Conventional UME and Various Sizes of SMEs

electrode type	r, μm[a]	$C_{dl,app}$, pF[b]	$C_{dl,cal}$, pF
conventional UME	2.90	6.15 ± 0.12[c] 11.8 ± 0.2[d]	2.6
SME			
unshielded[e]	5.25 ± 0.1	10.0 ± 0.2[c]	8.6
shielded[f]		8.35 ± 0.2[c]	
SME			
unshielded	2.90 ± 0.1	4.75 ± 0.1[c]	2.6
unshielded		5.25 ± 0.1[d]	
shielded		3.05 ± 0.15[c]	
shielded		2.95 ± 0.15[d]	
SME			
unshielded	1.23 ± 0.1	2.54 ± 0.05[c]	0.47
shielded		0.42 ± 0.03[c]	

[a] The radius as measured by SEM. [b] Values obtained from three independent measurements. [c] The tip of the electrode was shallowly (ca. 1 mm) immersed into the solution. [d] The tip of the electrode was deeply (ca. 10 mm) immersed into the solution. [e] Without keeping the internal aluminum foil of the SME at the ground potential. [f] With the internal aluminum foil of the SME kept at the ground potential.

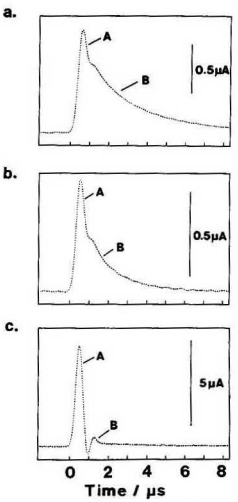

Figure 4. Fast response chronoamperograms recorded from experiments in a high-resistance AN solution containing 0.01 M $TEAPF_6$ with various electrodes: (a) SME, 10 μm in diameter; (b) SME, 5 μm in diameter; (c) conventional UME, 5 μm in diameter.

B). Current A is the charging current for the stray capacitance of the UME. The apparent response of this current was delayed due to the band-pass limitation of the current transducer (0.2 μs) regardless of electrode size and design. However, the peak intensity of current A increases with the amount of stray capacitance of the electrode in such condition that the current response is delayed due to band-pass limitation. Therefore, the higher current A observed with the conventional UME can be explained by the presence of more stray capacitance. On the other hand, current B decayed exponentially with various time constants corresponding to the various electrode sizes, i.e., 2.8 and 1.5 μs at 10 and 5 μm in diameter, respectively. This can be attributed to the charging current for double-layer capacitance. Indeed, these time constants were in good agreements with the cell-time constants (τ, s) predicted from eq 2, where ρ is the uncompensated specific resistance of the medium (650 Ω cm), and R_{us} (Ω) is the solution resistance.

$$\tau = R_{us}C_{dl,cal} = C_{dl,cal}\rho/4r \qquad (2)$$

The presence of current A did not cause any delay in current B. However, as shown in Figure 4c, it is difficult to distinguish these components when the former is much larger than the latter, that is, when the stray capacitance of the UME is significantly larger than the double-layer capacitance. In such a case, current responses originating from stray capacitance can be mistakenly interpreted as electrochemical responses. Therefore, internal shielding of the UME is necessary for precise measurement of electrochemical responses including faradaic responses in chronoamperometry.

Another important property of the SME is its permanent, low-resistance junction between the microwire and the Au lead wire, which is obtained by arc welding. This junction helps a great deal in increasing the reliability and durability of the SME and also in reducing the consumption of the expensive microwire to only a few millimeters. These additional features of the SME can give practical benefits to many chemists who are interested in transient electrochemical techniques.

LITERATURE CITED

(1) Nozaki, K.; Oyama, M.; Hatano, H.; Okazaki, S. *J. Electroanal. Chem. Interfacial Electrochem.* **1989**, *270*, 191–204.
(2) Wipf, D. O.; Wightman, R. M. *Acc. Chem. Res.* **1990**, *23*, 64–70.
(3) Andrieux, C. P.; Hapiot, P.; Saveant, J. M. *Chem. Rev.* **1990**, *90*, 723–738.
(4) Andrieux, C. P.; Hapiot, P.; Saveant, J. M. *Electroanalysis* **1990**, *2*, 183–193.
(5) Robinson, R. S.; McCreery, R. L. *Anal. Chem.* **1981**, *52*, 997–1001.
(6) Wightman, R. M.; Wipf, D. O. In *Electroanalytical Chemistry*; Bard, A. J., Ed.; Marcel Dekker Inc.: New York, 1989; Vol. 15, pp 268–353.
(7) Wipf, D. O.; Michael, A. C.; Wightman, R. M. *J. Electroanal. Chem. Interfacial Electrochem.* **1989**, *269*, 15–25.
(8) Bond, A. M.; Fleishmann, M.; Robinson, J. *J. Electroanal. Chem. Interfacial Electrochem.* **1984**, *168*, 299–312.
(9) Fleishmann, M.; Pons, S.; Rolinson, D.; Schmidt, P. *Ultramicroelectrodes*; Detatech Systems: Morganton, NC, 1987.
(10) Bear, C. D.; Stone, N. J.; Sweigart, D. A. *Anal. Chem.* **1988**, *60*, 188–191.
(11) Coetzee, J. F.; Gardner, C. W., Jr. *Anal. Chem.* **1982**, *54*, 2530–2532.
(12) Howell, J. O.; Wightman, R. M. *Anal. Chem.* **1984**, *56*, 524–529.

RECEIVED for review June 3, 1991. Accepted August 23, 1991.

Long Optical Path Thin-Layer Spectroelectrochemistry in a Liquid Chromatographic Ultraviolet–Visible Absorbance Detector Cell

Thomas R. Nagy and James L. Anderson*

Department of Chemistry, School of Chemical Sciences, University of Georgia, Athens, Georgia 30602

Spectroelectrochemical flow cell (SEFC) detectors of small volume offer novel possibilities for enhanced analytical selectivity as well as characterization of reaction pathways in applications such as high-performance liquid chromatography (HPLC) or flow injection analysis (FIA). Although numerous stationary spectroelectrochemical cells have been reported (*1–33*), with both short (*1–12*) and long (*13–33*) optical paths, only several applications to flowing solutions have been reported, with short (*3*) or long (*13, 14, 21, 25, 30–32*) optical path lengths. Occasional reports have also appeared in which separate electrochemical and spectroscopic detectors have been used in series in a single flow stream (*34*). Electrochemical flow detector design and applications have been reviewed (*35, 36*).

Two general classes of spectroelectrochemical cells have the small volume which is needed for use in a flow stream. One class is based on optically transparent thin-layer electrode (OTTLE) cells, in which light passes along a short path perpendicular to an optically transparent electrode (OTE) consisting of a transparent conductor (*1, 4*) or a meshed or porous conductor (*7–9*). Cells based on specular reflection with a short optical path would also fall in this category. The short optical path length of OTTLE cell limits optical sensitivity and detection limits.

A second class of spectroelectrochemical cells is based on a long optical path thin-layer electrode (LOPTLE) with the optical beam parallel (or nearly so) to the surface of the electrode. Both planar (*20–23, 25, 27–33*) and tubular (*24*) geometries have been successfully applied, as has a multiple specular reflectance cell geometry (*18*). The LOPTLE design can have significantly higher optical sensitivity due to a much longer optical path than feasible in the OTTLE design.

The OTTLE and LOPTLE cells reported to date have exhibited various problems of material compatibility, optical alignment, and optical signal/noise ratio. We report here a tubular flow-through spectroelectrochemical LOPTLE cell which overcomes many of these limitations by incorporation of a tubular working electrode into a conventional HPLC UV–visible absorbance detector cell. This approach exploits the optimized optical alignment and signal/noise ratio of modern HPLC detectors. We demonstrate simultaneous electrochemical and optical absorption detection of analytes by FIA and discuss factors governing signal/noise ratio and interferences due to interaction between detectors in a flow stream. We also describe application of the LOPTLE cell for stopped-flow spectropotentiostatic titrations.

EXPERIMENTAL SECTION

The spectroelectrochemical cells were fabricated for these experiments by modifying a UV–visible HPLC detector cell of standard z-type configuration. The modified cell is shown in Figure 1. A tubular platinum working electrode (WE) (AESAR, Seabrook, NH, inner diameter 1.32 ± 0.03 mm, outer diameter 1.57 ± 0.03 mm, length 10.0 ± 0.1 mm) was press-fit into the optical path of a Kel-F flow cell (Schoeffel, Westwood, NJ), which had been drilled out to a diameter ca. 0.03 mm undersize to ensure a tight leak-free fitting. Electrical contact to the WE was made

0003-2700/91/0363-2668$02.50/0

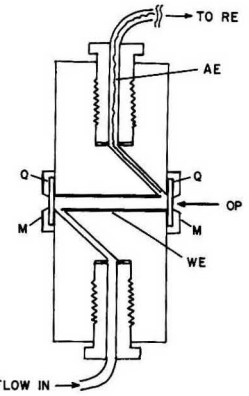

Figure 1. Schematic of spectroelectrochemical cell: (OP) optical path; (Q) quartz window; (M) mask aperture and window retainer.

through a small hole in the cell body drilled perpendicular to the optical path. A platinum wire was inserted into the hole and brought in contact with the WE. The contact wire was sealed into place using Epo-Tek H2OE electrically conductive silver epoxy (Epoxy Technology, Billerica, MA). A gold WE cell was also constructed in much the same way as the platinum cell. A gold wire (Aldrich, Milwaukee, WI) of 2.00 mm diameter was press-fitted into a different Kel-F cuvette. A 0.40 ± 0.03 mm diameter hole was drilled through the center of the wire to create a tubular electrode. The tube length was measured to be 9.00 ± 0.03 mm after fabrication was completed.

Solution entered through the bottom of the cell and exited out the top. Inlet and outlet ports used $^1/_{16}$-in. Teflon tubing and Fingertight fittings. UV quartz windows were placed at the ends of the optical path. The windows were kept in place by two opposing axially centered window flanges with nominally 1 mm diameter apertures, held together by three screws which passed through holes already present in the Kel-F cell.

Electrochemical measurements were made with a Model CV-1B potentiostat (Bioanalytical Systems, West Lafayette, IN) and recorded with a dual-pen strip chart recorder (Linear) and an IBM-PC equipped with a LabMaster digital interface (Scientific Solutions, Solon, OH). The electrochemical cell was composed of a platinum or gold WE, a platinum wire as the auxiliary electrode (AE), and a Ag/AgCl (4.0 M KCl) reference electrode (RE). All potentials are reported relative to this reference electrode. The platinum AE was brought as close to the WE as possible in an effort to decrease iR drop. The RE was located ca. 10 cm further downstream in a small reservior, as close to the other electrodes as size constraints permitted.

The spectrophotometer employed was a Model SF769Z Spectroflow monitor UV–visible LC detector (Kratos, Westwood, NJ). This optical unit had no scanning capabilities, and hence, a single wavelength was monitored. The absorption maximum for ferricyanide at 418 nm (*21*, *24*) was observed at a setting of 421 nm due to a 3-nm wavelength offset on the spectrophotometer.

A flow injection system was used to introduce the sample to the spectroelectrochemical cell in both the flowing stream and stationary solution experiments. The system included a Varian Model 8500 LC pump and pneumatically controlled injector (Valco) or a manually controlled injector (Rheodyne). A sample loop of 3.69 mL made of Teflon tubing was used in the flow injection experiments to ensure attainment of a steady-state response to facilitate comparison of experiment and theory. A 100-μL stainless steel sample loop was used for the stopped-flow analyses. Flow rates were varied in the FIA experiments. For stopped-flow analyses, a flow rate of ca. 80 μL/min was used to introduce the sample into the cell.

Reagent grade $K_3Fe(CN)_6$, $K_4Fe(CN)_6$, and KNO_3 were from J. T. Baker. All solutions were prepared daily in distilled–deionized water and filtered through a Nylon-66 filter with a 0.2 μm pore size (Rainin, Woburn, MA). All solutions were degassed with helium.

RESULTS AND DISCUSSION

FIA Experiments. Meschi and Johnson (*37*) examined the amperometric response of tubular electrodes applied to flow injection determinations. They showed that peak current, i_p, and steady-state current, i_{ss}, were related by the equation

$$i_p = i_{ss}\{\mathrm{erf}[V_S U^{1/2}/(4\pi a_T^2 K^{1/2}(0.5V_S + V_R)^{1/2})]\} = i_{ss}\{\mathrm{erf}(X)\}$$

where V_S equals the sample volume (cm^3), V_R equals the dead volume (cm^3), U equals volume flow rate (cm^3/s), a_T equals radius of the connecting tubing (cm), and K equals the dispersion coefficient (cm^2/s) expressible as

$$K = U^2/(48\pi^2 a_T^2 D)$$

where D is the diffusion coefficient of the analyte (cm^2/s) and X represents the composite argument of the error function. The dispersion coefficient varies with flow rate but is otherwise fixed for a given tube geometry and analyte diffusion coefficient. The steady-state current i_{ss} is predicted by Levich's equation (*38*, *39*):

$$i_{ss} = 5.24 \times 10^5 nCD^{2/3}L^{2/3}U^{1/3}$$

where C is the bulk concentration of the substance diffusing (mol/cm^3) and L is the tube's length (cm). The expression is valid under laminar flow conditions and only when the diffusion layer thickness is small compared to the tube radius.

Remarkably, when the above constraints are valid, the current at a tubular flow-through electrode is independent of the tube radius when expressed in terms of volume flow rate. The ratio of the diffusion layer thickness δ_x to the tubular electrode radius a_e is dependent only on the distance from the tube entrance (*37*), the volume flow rate, and analyte diffusion coefficient: $\delta_x/a_e = [\pi^2 Dx/(2U)]^{1/3}$. The latter equation is strictly valid only for $\delta_x/a_e \ll 1$, such that flow velocity varies approximately linearly with distance from the channel wall. At sufficiently slow flow rates, the equation will underestimate δ_x due to neglect of the parabolic dependence of flow rate with distance from the channel wall. At constant volume flow rate and distance, the ratio of diffusion layer thickness to tube radius is constant and independent of tube radius. This result has important consequences for selection of tube radius of an optical detector in the flow mode, as seen below.

Experiments under traditional FIA conditions (injection and dead volumes of 20 μL; data not shown) gave typical FIA response. Much larger injection volumes (3.69 mL) were used for the FIA experiments presented here solely to ensure that $V_S \gg V_R$ so that erf(X) approached 1.0 and hence, i_p equaled i_{ss}. A log–log plot of amperometric response vs volume flow rate for FIA of ca. 0.10 mM ferricyanide yielded a slope of 0.325 with a correlation coefficient of 0.996, in good agreement with the expected value of $^1/_3$, for V_S = 3.69 cm^3, V_R = 0.185 cm^3, and connecting tubing radius a_T = 0.040 cm, with a tubular platinum WE of radius a_e = 0.061 cm and length L = 1.00 cm, at an applied potential of 0 V vs Ag/AgCl. Figure 2 illustrates both amperometric and absorptometric response for a sequence of flow injection experiments at flow rates ranging from 0.33 to 1.33 mL/min under the above conditions.

Calculation of the absorbance of a tubular flow-through spectroelectrochemical detector requires integration across a spatially inhomogeneous zone in which local concentration varies both axially and radially. An approximate treatment was achieved by dividing the cell into two radial zones, corresponding to the diffusion layer zone and the undisturbed bulk solution zone. The absorbance of the diffusion layer zone was approximated by assuming a linear variation of concen-

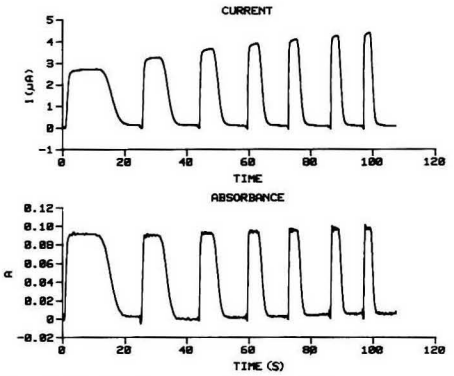

Figure 2. Flow injection amperometric and spectrophotometric responses at a 1.32 mm diameter, 1.00 cm long platinum tubular electrode. Flow rates are 0.33–1.33 mL/min (left to right) in 0.17 mL/min increments. Digitally acquired absorbance data have been Fourier-smoothed using a boxcar apodization function to reject high-frequency noise.

tration across the diffusion layer (*30*) and integrating the absorbance of reactant plus product both axially and radially. The effect on the absorbance of this zone was explicitly treated for a peripheral optical mask occluding the region closest to the tube wall. The absorbance of the undisturbed bulk zone was set equal to the reactant absorbance.

Because it is more accurate to integrate transmittance than absorbance (*40*), the relative contributions of the absorbances of the two zones were treated by averaging the transmittances weighted by the relative cross section of the two zones. For the absorbances encountered here ($A \leq 0.1$), the error of this approximation is small (less than 3%). The resulting expression for absorbance is

$$A = -\log\left(\Phi_\delta 10^{-A_\delta} + \Phi_b 10^{-A_R^*}\right)$$

where Φ_δ is the fraction of beam intensity and A_δ is the absorbance (reactant and product) in the diffusion layer zone; Φ_b is the fraction of beam intensity and A_R^* is the reactant absorbance in the undisturbed bulk zone. If intensity may be assumed to be uniform, $\Phi_b = (a - m\delta_L)^2/(a_m)^2$ and $\Phi_\delta = 1 - \Phi_b$, where m is a small multiplier (here assumed equal to 1) correcting for extent of depletion beyond the linear diffusion layer limit, δ_L is the diffusion layer thickness at the trailing edge of the tube, and a_m is the inner radius of the mask occluding part of the beam.

The absorbance in the diffusion layer, A_δ, is given by the expression (*41*)

$$A_\delta = C_R^* L\{(\epsilon_R - \epsilon_P)[\tfrac{2}{3} - 3f^2/4 + f^4/8 - (m\delta_L/2a) \times (\tfrac{8}{15} - f^3 + f^5/5)] + \epsilon_P[1 - f - (m\delta_L/2a)(1 - f^2)]\}/\{[1 - (m\delta_L/2a)(1 + f)](1 - f)\}$$

where C_R^* is the bulk reactant concentration, ϵ_R and ϵ_P are reactant and product molar absorptivities, and f is the ratio of the occluded portion of the tube radius to the augmented diffusion layer thickness $m\delta_L$. Evaluation of the above expressions reveals that for the cell described here, with mask/tube ratio $a_m/a = 0.8$ (mask occluding only the outer 20% of the tube radius), the absorbance of a reactant chromophore will deviate from the undisturbed value for a diffusion-controlled electrode reaction by less than 5% for flow rates greater than 0.1 mL/min and by less than 1% for flow rates greater than 0.25 mL/min, for a species with diffusion coefficient 7×10^{-6} cm^2/s, such as ferricyanide in aqueous solution. The near constancy of absorbance response of an absorbing reactant in Figure 2 for a wide range of flow rates illustrates the effectiveness of masking to block the optical beam in the diffusion layer and to decouple the absorbance response from the current response. The nearly constant absorbance response contrasts markedly with the conventional flow rate dependence of current response. In the absence of a mask, the absorbance response would be measurably smaller at the slowest flow rates than at the highest flow rates, in a trend opposing the trend for current. For a much higher diffusion coefficient of 3×10^{-5} cm^2/s, found in less viscous media such as acetonitrile, deviation from the undisturbed absorbance will be less than 5% at flow rates greater than 0.5 mL/min and less than 1% at flow rates greater than 1 mL/min. Thus, a masked cell offers the significant advantage of minimal interaction between the electrochemical and optical detector signals when independent response in the same cell is desired.

Optical detection limits for the platinum and gold electrode cells were estimated on the basis of the S/N ratio obtained at a flow rate of 0.50 mL/min. Using ferricyanide (molar absorptivity 1023 at 418 nm) as the chromophoric sample, detection limits of 1.4 and 2.9 μM were obtained for the platinum and gold electrode cells, respectively. Both these detection limits are ca. 10 times better than those attained using thin-layer cells in optical systems not optimized for small-aperture cells (*31*). The higher detection limit for the gold cell resulted from increased noise due to the loss of light throughput with the small-radius cell, particularly due to deviation of the drilled hole from the optical axis by ca. 0.02 cm from entrance to exit. Detection limits based on electrochemical response were not determined, as electrochemical detection limits are significantly lower than optical detection limits.

Current response were also used to calculate concentration of the analyte in the sample. These concentration calculations were compared to concentration values based on absorbance response with no potential applied to the cell at a series of flow rates. For the first data set, the mean concentration based on absorbance was 9.37×10^{-6} M (relative standard deviation (RSD) = 0.2%), compared to a mean of 8.97×10^{-6} M (RSD = 1.1%) based on current response, a relative deviation of +4.3%. The second data set yielded mean concentrations of 8.99×10^{-5} M (RSD = 1.2%) and 9.32×10^{-5} M (RSD = 1.4%) for absorbance and current calculations respectively, a relative deviation of −3.7%. Thus the between-run variability is significantly greater than within-run variability. Between-run variability within one detection method is comparable to the within-run variability between detection methods, and either absorbance or current measurements may indicate higher concentration for any run.

Multipotential Step Chronoabsorptometry. The cell described here is also suitable for experiments with stationary solutions. In a double potential step spectropotentiostatic experiment for a $Fe(CN)_6^{3-}$ solution, the potential was stepped from 0.5 V vs AgCl, where the oxidized species $Fe(CN)_6^{3-}$ is stable, to 0 V, where the reduced product $Fe(CN)_6^{4-}$ is stable, and back, first removing and then restoring the chromophore. The time needed to achieve 95% electrolysis, based on a 95% change in absorbance, was approximately 330 s for the tubular electrode with a 1.32 mm diameter. This value compared well with a predicted electrolysis time (*24*) of 334 s.

Figure 3 shows the results from a complete spectropotentiostatic experiment. Current was monitored to determine complete electrolysis for each applied potential. A 100-μL sample loop was used to introduce a 0.20 mM ferricyanide solution into the flow system. Flow was stopped near the absorbance maximum. Since calculations in this method were based on relative absorbance values, it was not necessary to

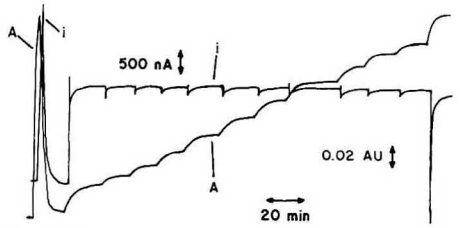

Figure 3. Spectropotentiostatic absorbance–time data for reduction followed by oxidative titration (raw data, no smoothing) of 0.20 mM ferricyanide, 0.20 M KNO_3. Applied potentials (from left to right) were initially 0.000 V and then stepped to 0.500, 0.000, 0.200, 0.210, 0.230, 0.240, 0.250, 0.260, 0.270, 0.280, 0.290, 0.300, and 0.500 V. Conditions: Pt tubular electrode; path length = 1.00 cm; radius = 0.066 cm; cell volume = 0.0137 mL.

know the exact concentration in the cell.

The sample was injected at an applied potential of 0.500 V, and flow was stopped. After reduction at 0 V, the potential was stepped to 0.200 V and then increased stepwise after attainment of equilibrium in 0.010 V increments to 0.300 V and finally to 0.500 V. A Nernst plot of applied potential vs log ($[Fe(CN)_6^{3-}]/[Fe(CN)_6^{4-}]$) derived from absorbance measurements at 418 nm gave $E^{\circ\prime}$ = 0.253 vs Ag/AgCl/4 M KCl and n = 0.94, respectively, for 0.20 mM initial ferricyanide concentration, using a platinum tubular electrode with L = 1.00 cm, a_e = 0.066 cm, and total cell volume of 13.7 μL. Both $E^{\circ\prime}$ and n values are in good agreement with published values (*20*, *24*, *42*).

The tubular spectroelectrochemical cell described here is a thin-layer cell with a long optical path parallel to the electrode. When the electrochemical cell is coupled with the spectrophotometer, great care must be used to ensure that proper optical alignment is achieved. By incorporation of the electrochemical cell into a standard UV–visible absorbance detector cell, optical alignment has already been constructed into the system. Thin-layer cells are usually epoxied together such that they cannot be dismantled. The cell construction presented here allows for the cell to be taken apart and inspected. Cell windows can be cleaned or replaced. The choice of epoxy used in thin-layer cells also limits the use of solvents. Most epoxies are slowly dissolved by organic solvents. This newly designed spectroelectrochemical cell using the tubular electrode exposes no epoxy to the solvent, making it amenable to all types of solvents. This characteristic makes the cell practical for LC detection since most LC eluents contain a significant amount of organic solvents.

Detection limits were calculated on the basis of the experimental absorbance data for the case of a chromophoric sample. Detection limits were improved by a factor of 10 in comparison with comparable thin-layer cells, due to the improved noise characteristics of the HPLC detector. Still lower detection limits and higher sensitivity would be expected for samples with high molar absorptivities (as much as 10–100-fold for molar absorptivity of 10^4–10^5 M^{-1} cm^{-1}).

Absorbance response due to the electrochemical generation or consumption of a chromophore in a flow experiment increases with the ratio of the diffusion layer thickness to the tubular electrode radius. As shown earlier, this fraction is predicted to be independent of the electrode radius at a constant volume flow rate, because the opposing effects of cross section and linear velocity cancel. The optimization of radius involves a tradeoff of the signal/noise ratio (S/N), which will suffer when the radius is too small due to a loss of throughput, vs dead volume, which grows with the square of the radius and adversely affects resolution and sensitivity in HPLC and FIA when the radius is too large. A larger cell diameter would paradoxically be an advantage for spatially resolved absorbance measurements such as diffusion layer imaging (*19*, *23*, *27*, *33*), by increasing the effective aperture and hence the S/N ratio for observation of a particular fraction of the concentration profile vs distance.

The stopped-flow spectropotentiostatic experiment took approximately 2.5 h to complete 13 potential steps and subsequent equilibration, because of the large diameter (1.32 mm) of the platinum electrode, averaging just under 12 min to complete all operations of each step. This time, which is an important consideration for efficient experimentation or for samples of limited stability, can be dramatically reduced by decreasing the electrode radius, since electrolysis time is proportional to the square of the radius. If shot noise is dominant, the optical S/N ratio should vary linearly with the radius. For example, the gold electrode (0.4 mm diameter) showed only a 2-fold degradation in S/N ratio for a ca. 3-fold reduction in diameter, despite serious misalignment of the tube with respect to the optical axis, while affording a nearly 10-fold decrease in electrolysis time.

Optimization of cell dimensions can be achieved once minimum acceptable levels of charge and absorbance uncertainty are set, in conjunction with a maximum allowable electrolysis time to determine the minimum and maximum feasible cell volumes. Complete electrolysis can be expected to require less than 1 min per optical step for electrode diameters less than 0.56 mm, a size intermediate between the two electrode assemblies discussed here.

Tubular electrodes have advantages (*24*) and disadvantages (*35*) relative to other electrode geometries. Tubular electrodes are not easily polished because they are enclosed surfaces with small diameters. Some popular electrode materials cannot be used, such as carbon paste, or liquid mercury, although an amalgam of mercury on gold can be used. Extreme iR drop situations can develop with tubular electrode use due to difficulties placing the auxiliary and reference electrodes close to the working electrode. Despite the disadvantages, tubular electrodes do offer long optical path lengths. The electrode material need not be optically transparent. The electrolysis time experienced with tubular electrodes is short due to cylindrical diffusion and a small electrolysis volume. A cylindrical cell will exhibit faster electrolysis times and significantly lower dead volume than a planar thin-layer cell whose thickness is equal to the tubular electrode diameter (*24*). In contrast, a planar thin-layer cell is expected to exhibit a faster electrolysis time than a tubular cell of equal cross-sectional area and dead volume, because the planar cell can be made thinner on the axis of diffusion and wider in the plane of the electrode to admit the same light flux (and hence comparable S/N ratio) as transmitted by the tubular electrode cell. Perhaps most importantly, tubular electrodes are easily fabricated in a geometry compatible with commercially available HPLC detector optics. A small hole can be drilled through an electrode material such as gold or graphite (*24*), or conductive tubing can be readily obtained. The advantage of having a long optical path length coupled with flow in a tubular geometric shape makes tubular electrodes a practical choice for spectroelectrochemical detection.

The spectroelectrochemical cell described herein is the first such detector to employ a tubular electrode as part of a standard HPLC flow-through UV–visible detector cell. This combination allows for detection of electroactive and/or UV–visible absorbing species. Hence, this type of cell can accommodate a wide range of species without the need for changing detectors. In addition to the steady-state flow-through and stopped-flow spectroelectrochemical titration applications described here, the applicability of this cell for HPLC or FIA detection has also been demonstrated (data not

shown), using the much smaller injection volumes (20 μL) required for optimum resolution in these experiments.

LITERATURE CITED

(1) Heineman, W. R. *Anal. Chem.* **1978**, *40*, 390A–402A.
(2) Anderson, C. W.; Halsall, H. B.; Heineman, W. R. *Anal. Biochem.* **1979**, *93*, 366–372.
(3) Pinkerton, T. J.; Hajidazeh, K.; Deutsch, E.; Heineman, W. R. *Anal. Chem.* **1980**, *52*, 1542–1544.
(4) Heineman, W. R.; Hawkridge, F. M.; Blount, H. N. In *Electroanalytical Chemistry: A Series of Advances*; Bard, A. J., Ed.; Marcel Dekker: New York, 1984; Vol. 13, pp 1–16.
(5) Condit, D. A.; Herrera, M. E.; Stankovich, M. T.; Curran, D. J. *Anal. Chem.* **1984**, *56*, 2909–2914.
(6) Lin, X. Q.; Kadish, K. M. *Anal. Chem.* **1986**, *58*, 1493–1497.
(7) Norvell, V. E.; Mamantov, G. *Anal. Chem.* **1977**, *49*, 1470–1472.
(8) DeWald, H. D.; Watkins, J. W., II; Elder, R. C.; Heineman, W. R. *Anal. Chem.* **1986**, *58*, 2968–2975.
(9) Ward, E. H.; Hussey, C. L. *Anal. Chem.* **1987**, *59*, 213–217.
(10) Nevin, W. A.; Lever, A. B. P. *Anal. Chem.* **1988**, *60*, 727–730.
(11) Zhang, C.; Park, S. M. *Anal. Chem.* **1988**, *60*, 1639–1642.
(12) Flowers, P. A.; Mamantov, G. *Anal. Chem.* **1989**, *61*, 190–192.
(13) Anderson, J. L.; Kincaid, J. R. *Appl. Spectrosc.* **1978**, *32*, 356–362.
(14) Anderson, J. L. *Anal. Chem.* **1979**, *51*, 2312–2315.
(15) Tyson, J. F.; West, T. S. *Talanta* **1979**, *26*, 117–125.
(16) Prulksma, R.; McCreery, R. L. *Anal. Chem.* **1979**, *51*, 2253–2257.
(17) Skully, J. P.; McCreery, R. L. *Anal. Chem.* **1980**, *52*, 1885–1889.
(18) Baumgartner, C. E.; Marks, G. T.; Aikens, D. A.; Richtol, H. H. *Anal. Chem.* **1980**, *52*, 267–270.
(19) Prulksma, R.; McCreery, R. L. *Anal. Chem.* **1981**, *53*, 202–206.
(20) Simone, M. J.; Heineman, W. R.; Kreishman, G. P. *Anal. Chem.* **1982**, *54*, 2382–2384.
(21) Brewster, J. D.; Anderson, J. L. *Anal. Chem.* **1982**, *54*, 2560–2566.
(22) Zak, J.; Porter, M. D.; Kuwana, T. *Anal. Chem.* **1983**, *55*, 2219–2222.
(23) Fukunaka, Y.; Denpo, K.; Iwata, M.; Marukoka, K.; Kondo, Y. *J. Electrochem. Soc.* **1983**, *130*, 2492–2500.
(24) Porter, M. D.; Kuwana, T. *Anal. Chem.* **1984**, *56*, 529–534.
(25) Anderson, J. L.; Brewster, J. D. Fiber Optic Thin-Layer Cell. U.S. Patent 4,540,280, 1985.
(26) Tyson, J. F. *Talanta* **1986**, *33*, 51–54.
(27) Jan, C. C.; McCreery, R. L. *Anal. Chem.* **1986**, *58*, 2771–2777.
(28) Pawliszyn, J.; Weber, M. F.; Dignam, M. J.; Mandelis, A.; Venter, R. D.; Park, S. M. *Anal. Chem.* **1986**, *58*, 236–239.
(29) Pawliszyn, J.; Weber, M. F.; Dignam, M. J.; Mandelis, A.; Venter, R. D.; Park, S. M. *Anal. Chem.* **1986**, *58*, 239–242.
(30) Fosdick, L. E.; Anderson, J. L. *Anal. Chem.* **1988**, *60*, 156–162.
(31) Fosdick, L. E.; Anderson, J. L. *Anal. Chem.* **1988**, *60*, 163–168.
(32) Gui, Y.; Soper, S. A.; Kuwana, T. *Anal. Chem.* **1988**, *60*, 1645–1648.
(33) Wu, H. P.; McCreery, R. L. *J. Electrochem. Soc.* **1989**, *136*, 1375–1379.
(34) Clark, G. J.; Goodin, R. R.; Smiley, J. W. *Anal. Chem.* **1985**, *57*, 2223–2228.
(35) Kissinger, P. In *Liquid Chromatography Detectors*; Vickrey, T. M., Ed.; Marcel Dekker: New York, 1983; pp 151–154.
(36) Stulik, K.; Pacakova, V. *CRC Crit. Rev. Anal. Chem.* **1984**, *14*, 297–351.
(37) Meschi, P. L.; Johnson, D. C. *Anal. Chim. Acta* **1981**, *124*, 303–314.
(38) Levich, V. G. *Physicochemical Hydrodynamics*; Prentice-Hall: Englewood Cliffs, NJ, 1962; pp 112–116.
(39) Blaedel, W. J.; Olson, C. L.; Sharma, L. R. *Anal. Chem.* **1963**, *35*, 2100–2103.
(40) Brewster, J. D.; Anderson, J. L. *Appl. Spectrosc.* **1989**, *43*, 710–714.
(41) Anderson, J. L. Unpublished results, University of Georgia, 1991.
(42) DeAngelis, T. P.; Heineman, W. R. *J. Chem. Educ.* **1976**, *53*, 594–597.

RECEIVED for review June 10, 1991. Accepted September 3, 1991.

CORRECTION

Preparation and Study of Two Benzo-Crown Ether Polysiloxane Stationary Phases for Capillary Gas Chromatography

Cai-ying Wu, Xi-chun Zhou, Zhao-rui Zeng, Xue-ran Lu, and Li-fong Zhang (*Anal. Chem.* **1991**, *63*, 1874–1879).

The locants in the compound names given in Figure 2 and elsewhere (lines 2–4 in the abstract, lines 2 and 3 of the last paragraph in the Introduction, lines 2–4 of the first paragraph in the Experimental Section, lines 2 and 3 of the second paragraph in the Experimental Section, and line 4 of the third paragraph in the Experimental Section) are incorrect. The correct names are as follows:

2,3-benzo-8-[(propenyloxy)methyl]-15-crown-5
2,3-benzo-8-[(propenyloxy)methyl]-18-crown-6

NEW! Combined IR/MS

New research grade GC/LC/MS/DS gives you more than you'd expect...

1. MS Engine: *the* high performance, mid-priced quadrupole mass spectrometer. Its open structure keeps all your application options open.

2. Low picogram to low femtogram sensitivity, full-scan and SIM.

3. Research versatility with GC/MS, thermospray and particle beam LC/MS, EI, CI, NCI, DCI, DIP.

4. Autoswitching, programmable EI/CI source for ease of use.

5. Differential pumping for flexibility and optimum CI.

6. Optional 2000 amu mass range for high molecular weight analysis.

7. New thermospray source for higher sensitivity and increased fragmentation.

8. New higher sensitivity particle beam LC/MS for EI, CI and NCI spectra.

9. Multitasking MS ChemStation (HP-UX series) with X-Window System based software for efficient operation and easy networking.

10. GC/IR/MS system classifies and confirms unknowns in a single injection.

...for less than you'd expect.

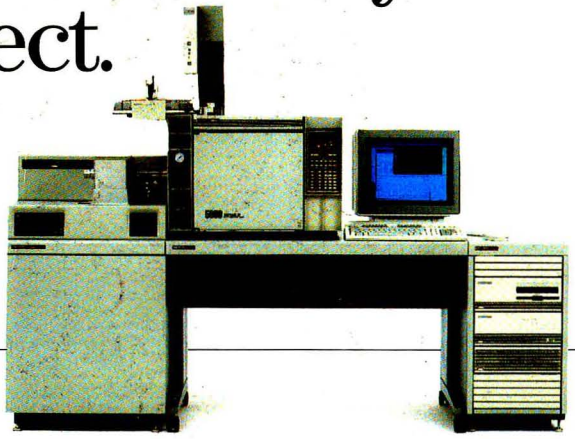

Our new MS Engine system brings you the highest performance in its class. At the lowest price in its class.* Along with the sensitivity, reproducibility, versatility and reliability you need for demanding research, methods development and service laboratory applications. Add to this HP's acclaimed quality, reliability and support, and the deal gets even better.

The MS platform for the 1990s, this flexible system combines HP's advanced GC, LC and FTIR technologies plus our multitasking MS ChemStation with X-Windows. For information, call **1 800 334-3110, Ext. 10246.**

HEWLETT PACKARD

* Under $130,000 (U.S. list price) for a complete standard GC/MS/DS system, including EI/CI source.

CIRCLE 62 ON READER SERVICE CARD